CURRENT ADVANCES IN GENETIC DEMENTIA AND AGING

EDITED BY: Jun Xu, Ulises Gomez-Pinedo, Daojun Hong, Jun Liu and Yuzhen Xu

PUBLISHED IN: Frontiers in Aging Neuroscience and Frontiers in Cellular Neuroscience

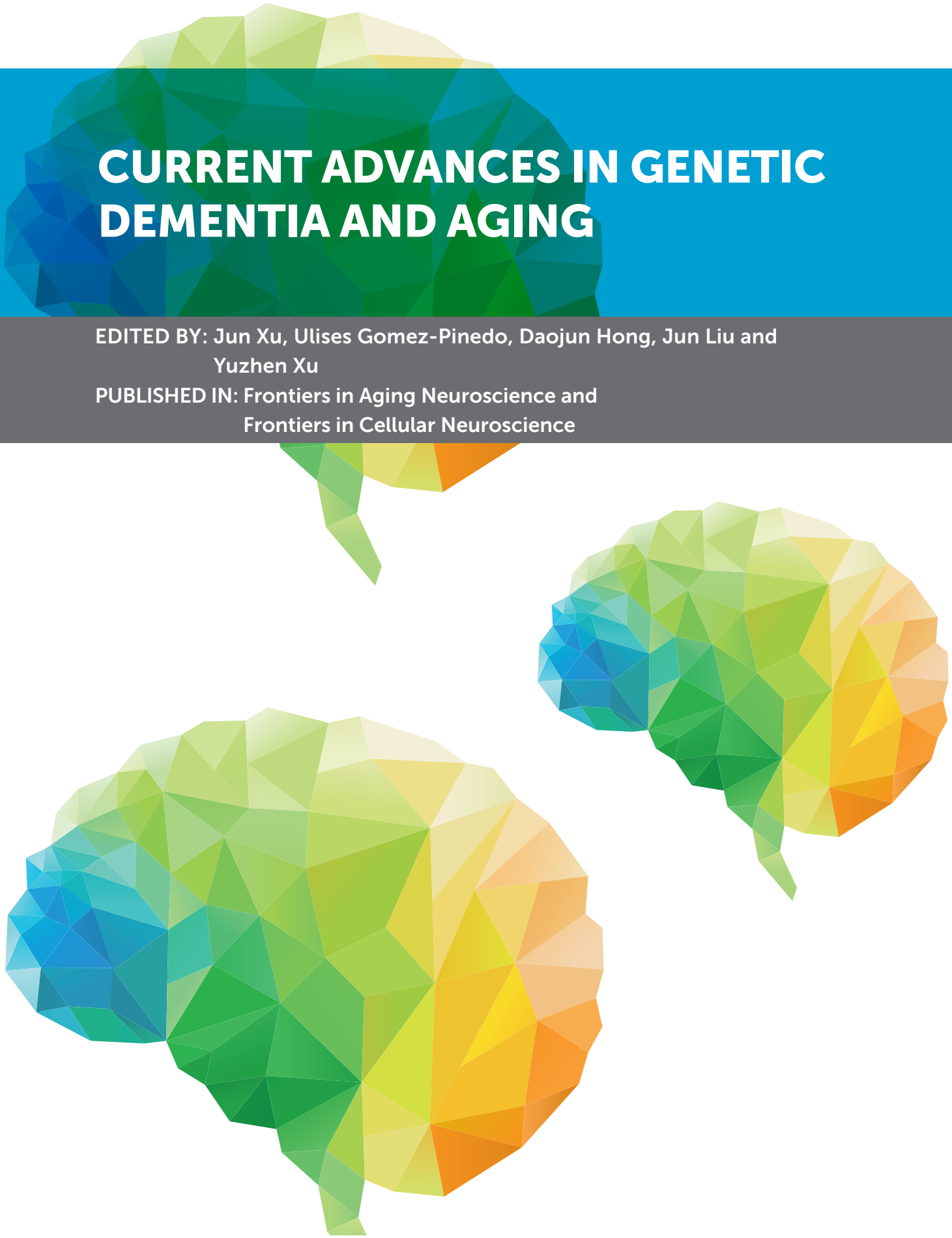

frontiers Research Topics

ISSN 1664-8714
ISBN 978-2-83250-155-9
DOI 10.3389/978-2-83250-155-9

About Frontiers

Frontiers is more than just an open-access publisher of scholarly articles: it is a pioneering approach to the world of academia, radically improving the way scholarly research is managed. The grand vision of Frontiers is a world where all people have an equal opportunity to seek, share and generate knowledge. Frontiers provides immediate and permanent online open access to all its publications, but this alone is not enough to realize our grand goals.

Frontiers Journal Series

The Frontiers Journal Series is a multi-tier and interdisciplinary set of open-access, online journals, promising a paradigm shift from the current review, selection and dissemination processes in academic publishing. All Frontiers journals are driven by researchers for researchers; therefore, they constitute a service to the scholarly community. At the same time, the Frontiers Journal Series operates on a revolutionary invention, the tiered publishing system, initially addressing specific communities of scholars, and gradually climbing up to broader public understanding, thus serving the interests of the lay society, too.

Dedication to Quality

Each Frontiers article is a landmark of the highest quality, thanks to genuinely collaborative interactions between authors and review editors, who include some of the world's best academicians. Research must be certified by peers before entering a stream of knowledge that may eventually reach the public - and shape society; therefore, Frontiers only applies the most rigorous and unbiased reviews.
Frontiers revolutionizes research publishing by freely delivering the most outstanding research, evaluated with no bias from both the academic and social point of view. By applying the most advanced information technologies, Frontiers is catapulting scholarly publishing into a new generation.

What are Frontiers Research Topics?

Frontiers Research Topics are very popular trademarks of the Frontiers Journals Series: they are collections of at least ten articles, all centered on a particular subject. With their unique mix of varied contributions from Original Research to Review Articles, Frontiers Research Topics unify the most influential researchers, the latest key findings and historical advances in a hot research area! Find out more on how to host your own Frontiers Research Topic or contribute to one as an author by contacting the Frontiers Editorial Office: frontiersin.org/about/contact

CURRENT ADVANCES IN GENETIC DEMENTIA AND AGING

Topic Editors:
Jun Xu, Capital Medical University, China
Ulises Gomez-Pinedo, Institute of Neurosciences, Health Research Institute of Hospital Clínico San Carlos, Spain
Daojun Hong, The First Affiliated Hospital of Nanchang University, China
Jun Liu, The Second Affiliated Hospital of Guangzhou Medical University, China
Yuzhen Xu, Tongji University, China

Citation: Xu, J., Gomez-Pinedo, U., Hong, D., Liu, J., Xu, Y., eds. (2022). Current Advances in Genetic Dementia and Aging. Lausanne: Frontiers Media SA.
doi: 10.3389/978-2-83250-155-9

Table of Contents

frontiers | Frontiers in Aging Neuroscience

TYPE Editorial
PUBLISHED 14 September 2022
DOI 10.3389/fnagi.2022.1020547

OPEN ACCESS

EDITED AND REVIEWED BY
Jorge Busciglio,
University of California, Irvine,
United States

*CORRESPONDENCE
Jun Xu
neurojun@126.com

SPECIALTY SECTION
This article was submitted to Cellular and Molecular Mechanisms of Brain-aging, a section of the journal Frontiers in Aging Neuroscience

RECEIVED 16 August 2022
ACCEPTED 31 August 2022
PUBLISHED 14 September 2022

CITATION
Xu Y, Hong D, Gomez-Pinedo U, Liu J and Xu J (2022) Editorial: Current advances in genetic dementia and aging.
Front. Aging Neurosci. 14:1020547.
doi: 10.3389/fnagi.2022.1020547

Editorial: Current advances in genetic dementia and aging

Yuzhen Xu[1], Daojun Hong[2], Ulises Gomez-Pinedo[3], Jun Liu[4] and Jun Xu[5,6]*

[1]School of Medicine, Tongji University, Shanghai, China, [2]Department of Neurology, The First Affiliated Hospital of Nanchang University, Nanchang, China, [3]Laboratory of Neurobiology, Department of Neurology, Institute of Neurosciences, IdISSC, Hospital Clínico San Carlos, Universidad Complutense de Madrid, Madrid, Spain, [4]Department of Neurology, The Second Affiliated Hospital, Guangzhou Medical University, Guangzhou, China, [5]Department of Neurology, Beijing Tiantan Hospital, Capital Medical University, Beijing, China, [6]China National Clinical Research Center for Neurological Diseases, Beijing Tiantan Hospital, Capital Medical University, Beijing, China

KEYWORDS

dementia, Alzheimer's disease (AD), polygenic, neuroimaging, Aβ/tau

Editorial on the Research Topic
Current advances in genetic dementia and aging

Cognitive impairment and dementia have become a serious global public-health issue associated with severe disability. Alzheimer's disease (AD) is a multifarious polygenic disease that is the most common cause of dementia in the elderly. Early-onset AD (EOAD) accounts for approximately 5–10% of all cases of AD and can be caused by mutations in amyloid precursor protein (APP), presenilin 1 (PSEN1), and presenilin 2 (PSEN2). According to Orozco-Barajas et al. PSEN1 A431E is the most reported variants related to EOAD. Besides, more than 40 other genetic variants combine to cause late-onset AD (LOAD) with a lifetime prevalence of 22–95%; when demographic factors are included in the risk score along with APOE ε4 and other risk genes, AD prediction accuracy will exceed 66% (Koriath et al., 2021). And other APOE ε4-independent LOAD, with the lowest risk of development, is significantly more likely to be caused by random conditions than by genetic factors. Previous studies have shown that patients with cerebrovascular illness are more likely to develop dementia. The role of modifiable vascular risk factors can play a role, such as hypertension, diabetes, hyperlipidemia and so on (Appleton et al., 2017; Yen et al., 2022). Strategies to prevent cerebrovascular illness hold great potential to delay the incidence of cognitive impairment or dementia.

Neuroimaging advancements could help in better understanding of AD neuropathologic changes *in vivo*. Zeng et al. have found that vascular hyperintensity on FLAIR images has important implications for cerebrovascular disease, for instance, large-vessel stenosis/occlusion, Moyamoya disease and transient ischemic attack, but it cannot be used as a neuroimaging marker of impaired cerebral hemodynamics or good collateral circulation. Resting-state functional magnetic resonance imaging (rs-fMRI) researches have found that individuals with age-related macular degeneration exhibit abnormal functional connection and regional homogeneity

in Liu et al. and Xiao et al. In addition, patients with mild cognitive impairment have regional homogeneity dysfunction, but their signal intensity in several brain regions is higher than in normal controls. These results may be related to the neural network excitation and inhibition of different regions (Wu et al.). Mai et al. have found that an AD-resemblance atrophy index, based on structural magnetic resonance imaging, can be used to predict the risk of progression from MCI to AD dementia. It is also beneficial to construct a more accurate risk prediction model for AD.

Polygenic risk score combined small effect SNPs is a useful approach to identify individuals at higher risk of LOAD. Mendelian randomization studies have found that AD genetic susceptibility is negatively associated with gout, but not be causally, and genetic associations between LOAD and other cardiometabolic risk factors have been reported (Fu et al.; Li et al.). Increasing attention is now being directed to intestinal flora, Zhang et al. have found that significantly greater numbers of genus Helicobacter is observed in diabetic mice than in wild mice and diabetes may be intricately linked to increased risk for developing neuro-inflammation, which potentially induce age-related cognitive impairment.

The amyloid hypothesis is widely accepted as the core pathology of AD, and amyloid-beta deposition is posited to be the initiating factor in AD. Amyloid-beta may suppress the expression of SIRT1, an essential aging regulator, and promote aging-associated DNA damage. Interestingly, Aspirin could upregulate SIRT1 expression and rescue cells from senescence (Li et al.). Moreover, the accumulation of tau neurofibrillary tangles is a major pathological hallmark of AD. Qian et al. have proved that KRAS and PIK3R1 gene, as core genes associated with abnormal infiltration of peripheral immune cells, are strongly associated with the severity of tau pathology.

Many attempts have been made to prevent or postpone dementia progression, such as exercise, nutritional supplementation and medications. Chen et al. indicate that exercise may be significant to prevent AD through upregulating the expression profile of miR-215-5p to prevent neuronal cell necrosis. Based on molecular dynamical simulations and kinetic studies, Kang et al. confirm that Baicalein can contribute to protect patients with atrophic rhinitis against the development and progression of MCI by targeting the cytochrome C protein.

Author contributions

JX composed the main outline of the editorial. YX drafted the manuscript. All authors contributed to the article and approved the submitted version.

Funding

This study was supported by the National Key Research and Development Program of China (2021YFC2500103), the National Natural Science Foundation (Grant Nos. 82071187, 81870821, and 81471215), and Beijing Youth Talent Team Support Program (2018000021223TD08).

Acknowledgments

We would like to thank all the authors who participated in the subject collection and all the reviewers who were involved in the review process, and we are very grateful to all the editors who assisted us in processing the manuscripts.

Conflict of interest

The authors declare that the research was conducted in the absence of any commercial or financial relationships that could be construed as a potential conflict of interest.

Publisher's note

References

Appleton, J. P., Scutt, P., Sprigg, N., and Bath, P. M. (2017). Hypercholesterolaemia and vascular dementia. *Clin. Sci.* 131, 1561–1578. doi: 10.1042/CS20160382

Koriath, C. A. M., Kenny, J., Ryan, N. S., Rohrer, J. D., Schott, J. M., Houlden, H., et al. (2021). Genetic testing in dementia - utility and clinical strategies. *Neurology* 17, 23–36. doi: 10.1038/s41582-020-00416-1

Yen, F. S., Wei, J. C., Yip, H. T., Hwu, C. M., and Hsu, C. C. (2022). Diabetes, Hypertension, and the Risk of Dementia. *J Alzheimer's disease: JAD.* (preprint). doi: 10.3233/JAD-220207

frontiers in Aging Neuroscience

REVIEW
published: 09 December 2021
doi: 10.3389/fnagi.2021.792840

Recent Advances in Basic Research for CSF1R-Microglial Encephalopathy

Yan-Li Wang[1†], Fang-Ze Wang[2†], Runzhi Li[1], Jiwei Jiang[1], Xiangrong Liu[3] and Jun Xu[1]*

[1] Department of Neurology, Beijing Tiantan Hospital, Capital Medical University, Beijing, China, [2] Department of Cardiology, Weifang People's Hospital, Weifang, China, [3] China National Clinical Research Center for Neurological Diseases, Beijing Tiantan Hospital, Capital Medical University, Beijing, China

Colony-stimulating factor-1 receptor-microglial encephalopathy is a rare rapidly progressive dementia resulting from colony-stimulating factor-1 receptor (CSF1R) mutations, also named pigmentary orthochromatic leukodystrophy (POLD), hereditary diffuse leukoencephalopathy with spheroids (HDLS), adult-onset leukoencephalopathy with axonal spheroids, and pigmented glia (ALSP) and CSF1R-related leukoencephalopathy. *CSF1R* is primarily expressed in microglia and mutations normally directly lead to changes in microglial number and function. Many animal models have been constructed to explore pathogenic mechanisms and potential therapeutic strategies, including zebrafish, mice, and rat models which are with *CSF1R* monogenic mutation, biallelic or tri-allelic deletion, or *CSF1R*-null. Although there is no cure for patients with CSF1R-microglial encephalopathy, microglial replacement therapy has become a topical research area. This review summarizes *CSF1R*-related pathogenetic mutation sites and mechanisms, especially the feasibility of the microglia-original immunotherapy.

Keywords: CSF1R-microglial encephalopathy, microglia, dementia, mutation, pathophysiological mechanism, microglial replacement

OPEN ACCESS

Edited by:
Robert Adam Harris, Karolinska Institutet (KI), Sweden

Reviewed by:
Dejan Baskic, University of Kragujevac, Serbia
Huidong Tang, Shanghai Jiao Tong University, China

***Correspondence:**
Jun Xu
xujun@ccmu.edu.cn

† These authors have contributed equally to this work

Received: *11 October 2021*
Accepted: *16 November 2021*
Published: *09 December 2021*

Citation:
Wang Y-L, Wang F-Z, Li R, Jiang J, Liu X and Xu J (2021) Recent Advances in Basic Research for CSF1R-Microglial Encephalopathy. Front. Aging Neurosci. 13:792840. doi: 10.3389/fnagi.2021.792840

INTRODUCTION

Colony-stimulating factor-1 receptor -microglial encephalopathy, microglia-original dementia, is a rare autosomal dominant disease caused by mutations in the colony-stimulating factor-1 receptor (CSF1R) gene resulting in microglial dysfunction. Clinically, it is manifested by progressive cognitive decline, motor impairment accompanied by mental behavioral abnormalities. CSF1R-microglial encephalopathy typically presents as rapidly progressive dementia. The peak age of onset is 8–72 years (mean 42 years) and the prognosis is poor with a median survival of 2–30 years (mean 6 years) (Lynch et al., 2019). This review discusses the pathophysiology, corresponding animal models, and management options of CSF1R-microglial encephalopathy to promote clinical awareness.

HISTORICAL BACKGROUND AND NOMENCLATURE

Colony-stimulating factor-1 receptor (CSF1R)-microglial encephalopathy was also known as pigmentary orthochromatic leukodystrophy (POLD), hereditary diffuse leukoencephalopathy with

spheroids (HDLS), adult-onset leukoencephalopathy with axonal spheroids, and pigmented glia (ALSP), and CSF1R-related leukoencephalopathy. The naming process was shown in **Figure 1**.

The study Marotti et al. (2004) found that there are many similarities between the original brain sections of the first POLD diagnosed in 1936 and the brain autopsy sections of HDLS families confirmed in 1984, including white matter degeneration, corpus callosum atrophy, pigmented glia, neuroaxonal spheroids and demyelination, and so forth. Besides, the clinical manifestations of POLD are quite similar to HDLS. Thus, it is inferred that POLD and HDLS to be the same disease (i.e., ALSP). The diagnostic criteria for these rare diseases are mostly based on sporadic cases and small case series. Therefore, rare diseases are easily classified as the same disease, when with similar clinical and pathological features. And known nomenclature might simply be an expression of pathological changes, ignoring microglia-original abnormalities.

In recent years, genome-wide association (GWAS) and whole exome/genome sequencing (WES/WGS), have been widely used for mutational analysis in rare diseases. With a common causal gene CSF1R being identified, HDLS and POLD were reconfirmed to be the same disease. And this evidence provides genetic evidence for ALSP diagnostics (Rademakers et al., 2011; Nicholson et al., 2013). But no mutations in the CSF1R gene were found in the first confirmed family of HDLS in 1984 (Sundal et al., 2013). Besides, many patients have typical ALSP clinical manifestations, including progressive cognitive decline, motor impairment, and mental behavioral abnormalities, but no CSF1R mutation (Lynch et al., 2016). Therefore, ALSP is further divided into CSF1R- related leukoencephalopathy, AARS2- related leukoencephalopathy, and CSF1R/AARS2-negative ALSP (Konno et al., 2018). Currently, whether leukodystrophy is the same concept as leukoencephalopathy remains controversial. Microglial dysfunction caused by mutations in the CSF1R gene has been put forward as the fundamental pathogenetic mechanism of this rare disease (Prinz and Priller, 2014). Hence, this review summarized the current basic research with the term "CSF1R-microglial encephalopathy."

CSF1R MUTATION SITES

The colony-stimulating factor-1 receptor (*CSF1R*) gene is located on chromosome 5q32 and includes 22 exons that encode cellular membrane proteins. CSF1R is a receptor tyrosine kinase made up of 5 functional domains: 5 immunoglobulin-like motifs in the extracellular domain, a transmembrane domain (TM), a juxtamembrane domain (JMD), a kinase insertion domain (KID), and dichotomous tyrosine kinase domains (TKDs). Most gene mutations are located at the tyrosine kinase domain of CSF1R encoded by exons 12–21, and no disease-associated mutations located in exon 16 have been discovered yet. As of October 2021, a total of 114 mutation sites has been reported globally, including 93 missense mutations, 4 nonsense mutations (red), 4 insertions or deletions (blue), 7 frameshift mutations (green), and 13 splice-site mutations (**Figure 2**; Konno et al., 2018; Lai et al., 2020; Zhuang et al., 2020; Ayrignac et al., 2021; Chu et al., 2021; Du et al., 2021; Kındış et al., 2021; Sohn et al., 2021; Tipton et al., 2021; Tsai et al., 2021).

PATHOPHYSIOLOGICAL MECHANISMS

In the central nervous system, CSF1R is predominantly expressed on microglia. *CSF1R* knockout leads to a decrease in the number of microglia and exists a high spatial heterogeneity (Prinz and Priller, 2014). Cerebellar CSF1R expression seems to be low when compared with cortex, hippocampus, and striatum in Csf1r-EGFP transgenic mice (Hawley et al., 2018). *In vitro* studies have found that *CSF1R* mutations would lead to autophosphorylation of tyrosine residues lost through two mechanisms, specifically one possibility is a dominant-negative mechanism and the other with loss of function. Mutations located in the juxtamembrane domain and the kinase insert region, which assembles into homodimers and heterodimers, resulting in the inhibition of kinase activity, thereby suppressing phosphorylation of its downstream targets (Rademakers et al., 2011; Leng et al., 2019). Mutations located in the tyrosine kinase domain, which result in the inactivation of a tyrosine kinase, fail to continue signal transduction (Pridans et al., 2013).

The haploinsufficiency of the *CSF1R* gene could result in the lack of microglia in the *CSF1R*-null zebrafish model, including an overall decrease of microglia and a region-specific reduction (Oosterhof et al., 2019). Based on RNA sequencing results for zebrafish of wide-type, biallelic deletion and tri-allelic deletion of *CSF1R*, lack of CSF1R might also up-regulate genes related to immune response processes, including chemokine genes and chemokine receptor genes and down-regulated genes related to nervous system development and neuronal differentiation (Oosterhof et al., 2018). Besides, changes in CSF1R could affect microglial distribution, so the abnormal distribution of microglia is clearly seen in the *CSF1R* tri-allelic deletion of the zebrafish model (Oosterhof et al., 2018). The results of necropsy indicated that residual microglia had a strong proliferative ability though the numbers of microglia in specific brain regions were significantly reduced (Tada et al., 2016).

The *CSF1R* gene expression is increased in response to brain injury marginally expressed in the hippocampus, neurons and neural stem cells, this suggests a neuroprotective role for CSF1R (Luo et al., 2013). Systemic Csf1r-knockout mice can exhibit osteopetrosis, reduction in marrow hematopoiesis, and defection in reproductive function, impairment in olfactory capacity, and reduction in mononuclear phagocyte, including microglia (Dai et al., 2002; Li et al., 2006; Chitu et al., 2016). And the most prominent difference was the length of survival time. *CSF1R*-null mice only had a median survival of 6 weeks, and a significant reduction of microglia is the most obvious feature additionally with enlarged ventricle and skeletal dysplasia (Guo et al., 2019). Because the early lethality

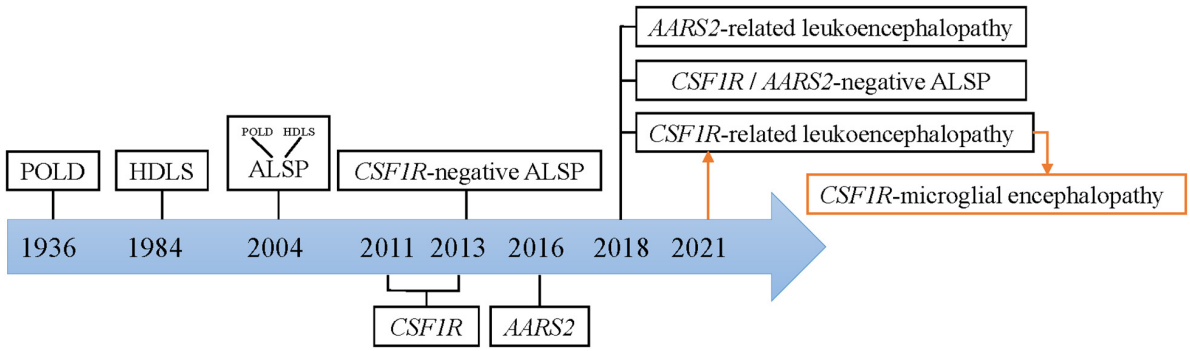

FIGURE 1 | Nomenclature of CSF1R-microglial encephalopathy.

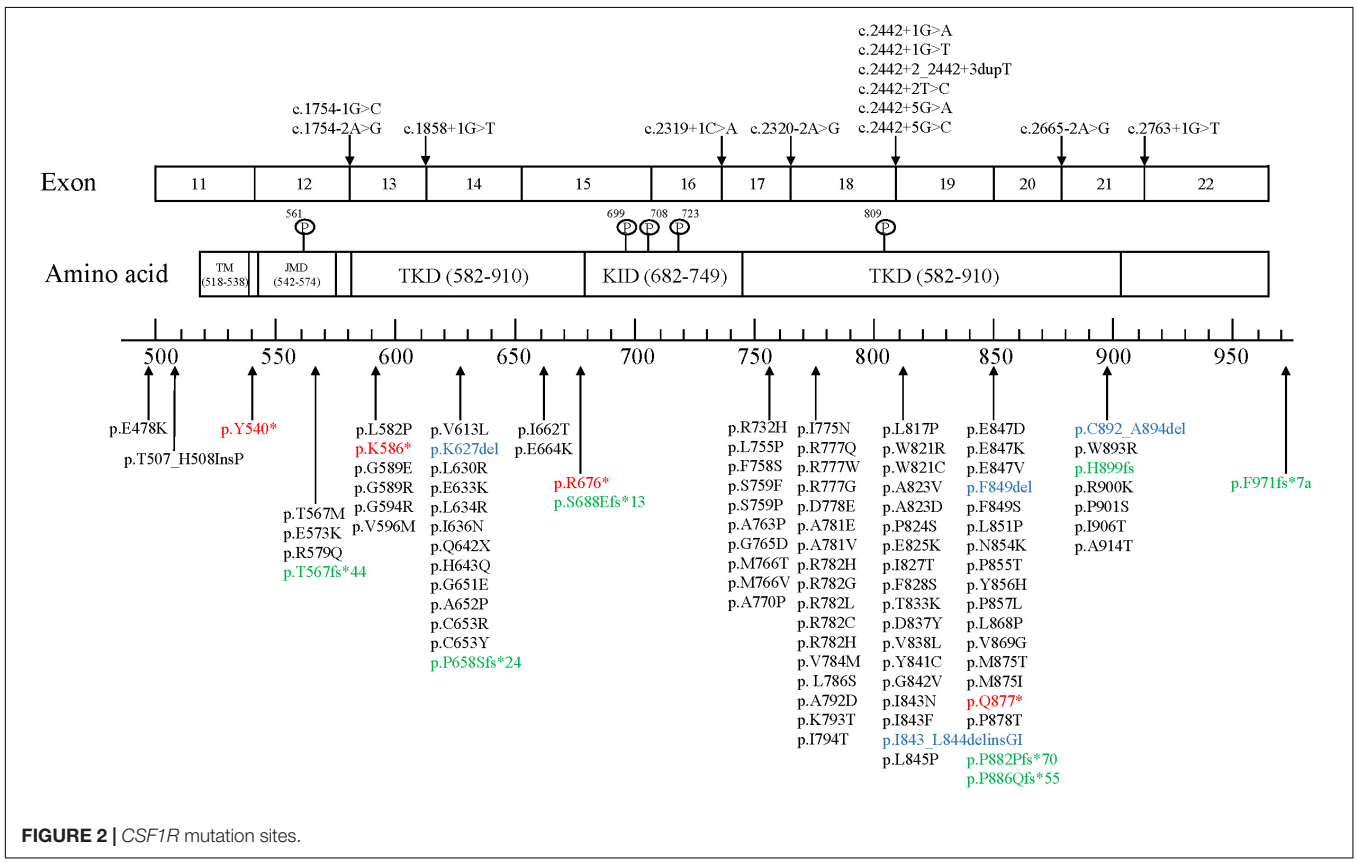

FIGURE 2 | *CSF1R* mutation sites.

of this model is high, the *CSF1R*-null mice model is not suitable to investigate neurodegenerative disease. Although the conditional Csf1r-knockout mice can selectively suppress CSF1R expression and make microglia absent, the mouse phenotype is not clinically consistent with CSF1R-microglial encephalopathy (Rojo et al., 2019). Homozygous infants with *CSF1R* deletion suffer death within 1 year of birth, accompanied by microglial deficiency, macrocephaly, and osteopetrosis (Oosterhof et al., 2019). Microglia are fully absent in the *CSF1R*-null rat model showed growth retardation, skeletal abnormality, and infertility, but most brain structural without abnormality and the rat can survive to adulthood (Guo et al., 2019). Therefore, the *CSF1R*-null rat model poses a possibility for long-term follow-up effects of different interventions.

It is also found in the *CSF1R*-null zebrafish model that the expression of neuronal transcription factor CUX1 is significantly decreased (Oosterhof et al., 2019). Additionally, CUX1 is a transcription factor associated with axonal projections indicating that reducing the number of CUX1+ neurons may lead to the hypoplastic corpus callosum (Oosterhof et al., 2019). Mice with *CSF1R* ± monogenic mutation are viable, fertile, and without skeletal abnormalities, but then may present cognitive decline, depression, and anxiety (Guo et al., 2019). It is found that *CSF1R*

interacts with *TRME2* through the transmembrane region and thereby regulates each other by Cheng et al. (2021). *CSF1R* knockdown markedly increases the *TREM2* mRNA levels and *TRME2* suppression results in elevated mRNA and protein levels of CSF1R. Thus, the phenotype of Trem2-deficient microglia can be rescued by activating CSF1R signaling (Cheng et al., 2021). It has been reported, CSF2 expression is increased in both the Csf1r± mice model and patients with *CSF1R*-microglial encephalopathy (Chitu et al., 2020). Targeted disruption of the murine Csf2 allele could suppress microgliosis, inhibit oxidative stress and improve microglial dysfunction, and ameliorate spatial memory, depression-like behavior, olfactory dysfunction, and motor coordination (Chitu et al., 2020).

MICROGLIAL REPLACEMENT THERAPY

Experimental mouse models of reduced *CSF1R* expression levels indicate that the absence of microglia could contribute to repopulated niche by the newly microglia. However, the source of the repopulated microglia is yet to be fully confirmed. Using different modified mouse lines, Huang et al. (2018) demonstrate that the repopulated microglia is from the proliferation of surviving microglia (<1%). Furthermore, based on findings of $Cx3cr1^{CreER/+}R26^{DTA/+}$ mice, microglia-like cells could be produced by infiltration of peripheral monocytes into the brain (Lund et al., 2018). Both types are not mutually exclusive and can happen at the same time.

BASED ON THE PROLIFERATION OF RESIDENT MICROGLIA

Specific inhibitors of CSF1R target and purge 99% microglia in the CNS and cross the blood-brain barrier, but neither mouse abnormal behavior nor cognitive decline was observed. Microglial numbers return to normal levels 1 week after inhibitor withdrawal (Elmore et al., 2014). After a 28-day repopulation, microglial morphology has been reproduced rejuvenation. And dendrite complexity has been recovered in hippocampal neurons of 24-month mice (Elmore et al., 2018). Microglial repopulation contributes to reversing the expression of all these genes related to actin cytoskeleton remodeling and synaptogenesis, inducing neurogenesis and ameliorating age-related memory impairment (Elmore et al., 2018; Willis et al., 2020). Furthermore, some trials of PLX5622 have found that small molecule inhibitors can affect not only brain microglia, but also bone marrow-derived macrophages, tissue macrophages, and circulating monocytes (Lei et al., 2020). Therefore, the application of CSF1R inhibitor to patients with CSF1R-microglial encephalopathy should be cautiously considered. A study, in which adult CSF1R± mice were treated with persistent low-grade PLX5622 at different stages of the disease, has found that modulating microglial phenotypes could reverse presynaptic and ECM alterations induced by *CSF1R* haploinsufficiency and improved cognition without altering neuronal populations. This finding suggests that microglia are viable targets for therapeutic intervention early in the disease (Arreola et al., 2021).

BASED ON TRANSPLANTATION OF MICROGLIA-LIKE CELLS

Microglia-like cells differentiated by allogeneic bone marrow transplantation (BMT) have the option to replace 92.66% of resident microglia in the brain. Normally, microglia replacement by BMT (mrBMT) remains at resting-state. While in response to inflammatory stimuli, microglia-like cells are activated performing the immune function (Xu et al., 2020). Peripheral blood-derived microglia-like cells (mrPB) can replace 80.74% of resident microglia, and acquire mature phenotype to monitor intracellular environmental stabilization after 30 days (Xu et al., 2020). Single-cell RNA sequencing reveals that microglia-like cells have macrophage-like properties, which is different from the yolk sac-derived CNS resident microglia epigenetically (Lund et al., 2018; Xu et al., 2020). The novel replacement therapies are suitable for neonatal and adult mice. Clinically, bone marrow transplantation and peripheral blood graft hold promise for the treatment of CSF1R-microglial encephalopathy.

BASED ON HEMATOPOIETIC STEM CELL TRANSPLANTATION

Microglia replacement by exogenous microglia transplantation (mrMT) shares very similar morphology and RNA expression profiling of resident microglial (Xu et al., 2020). It is difficult to acquire sufficient endogenous microglia for therapeutic transplantation, so with the help of hematopoietic stem cell transplantation (HSCT), protein expression is normalized for CSF1R in replacement wide-type microglia and the inhibited CSF1R pathways are activated. Patients achieve stable disease with relatively stable expanded disability status score and decreased volume of white matter hyperintensities 6–30 months after undergoing transplantation (Mochel et al., 2019). If HSCT could be performed early in the disease, survival could extend beyond 15 years and patients may have normal communication abilities (Eichler et al., 2016). Donor chimerism reaches 100%, 9 months after transplantation, besides, cognitive and motor impairment are markedly improved and hyperintensities of the foci completely regress after 28 months (Gelfand et al., 2020). And stabilizing effects of HSCT have been found in the largest longitudinal study of 7 patients with CSF1R-microglial encephalopathy receiving HSCT, containing motor capacity, cognition, radiographic severity, and white matter lesion burden (Tipton et al., 2021).

CONCLUSION AND OUTLOOK

At present, works of research on the mechanism of CSF1R-microglial encephalopathy are still few and lack animal models with missense mutations. The emerging microglial replacement therapy is a reliable modality to relieve clinical symptoms

and extend survival. But further experimental studies and clinical trials with long-term follow-up are still needed to assess potential risks.

AUTHOR CONTRIBUTIONS

JX and XL conceived and designed the study. Y-LW and F-ZW contributed to the generation of the manuscript. RL and JJ helped revise the manuscript. All authors contributed to the editing of the manuscript.

FUNDING

This study was supported by the National Natural Science Foundation (Grant Numbers 82071187, 81870821, and 81471215) and the Beijing Youth Talent Team Support Program (2018000021223TD08).

ACKNOWLEDGMENTS

We would like to thank Jin-ming Han who inspired our research.

REFERENCES

Arreola, M. A., Soni, N., Crapser, J. D., Hohsfield, L. A., Elmore, M. R. P., Matheos, D. P., et al. (2021). icroglial dyshomeostasis drives perineuronal net and synaptic loss in a Csf1R(+/-) mouse model of Alsp, which can be rescued via Csf1R inhibitors. *Sci. Adv.* 7:eabg1601. doi: 10.1126/sciadv.abg1601

Ayrignac, X., Carra-Dalliere, C., Codjia, P., Mouzat, K., Castelnovo, G., Ellie, E., et al. (2021). Evaluation of CSF1R-related adult onset leukoencephalopathy with axonal spheroids and pigmented glia diagnostic criteria. *Eur. J. Neurol.* doi: 10.1111/ene.15115

Cheng, B., Li, X., Dai, K., Duan, S., Rong, Z., Chen, Y., et al. (2021). Triggering receptor expressed on myeloid cells-2 (TREM2) interacts with colony-stimulating factor 1 receptor (CSF1R) but is not necessary for CSF1/CSF1R-mediated microglial survival. *Front. Immunol.* 12:633796. doi: 10.3389/fimmu.2021.633796

Chitu, V., Biundo, F., Shlager, G. G. L., Park, E. S., Wang, P., Gulinello, M. E., et al. (2020). Microglial homeostasis requires balanced CSF-1/CSF-2 receptor signaling. *Cell Rep.* 30, 3004–3019.e3005. doi: 10.1016/j.celrep.2020.02.028

Chitu, V., Gokhan, Ş, Nandi, S., Mehler, M. F., and Stanley, E. R. (2016). Emerging roles for CSF-1 receptor and its ligands in the nervous system. *Trends Neurosci.* 39, 378–393. doi: 10.1016/j.tins.2016.03.005

Chu, M., Wang, D. X., Cui, Y., Kong, Y., Liu, L., Xie, K. X., et al. (2021). Three novel mutations in Chinese patients with CSF1R-related leukoencephalopathy. *Ann. Transl. Med.* 9:1072. doi: 10.21037/atm-21-217

Dai, X. M., Ryan, G. R., Hapel, A. J., Dominguez, M. G., Russell, R. G., Kapp, S., et al. (2002). Targeted disruption of the mouse colony-stimulating factor 1 receptor gene results in osteopetrosis, mononuclear phagocyte deficiency, increased primitive progenitor cell frequencies, and reproductive defects. *Blood* 99, 111–120. doi: 10.1182/blood.v99.1.111

Du, Q., Wang, M., and Zhou, H. (2021). A novel mutation in CSF1R associated with hereditary diffuse leukoencephalopathy with spheroids. *Neurol. Sci.* doi: 10.1007/s10072-021-05296-x

Eichler, F. S., Li, J., Guo, Y., Caruso, P. A., Bjonnes, A. C., Pan, J., et al. (2016). CSF1R mosaicism in a family with hereditary diffuse leukoencephalopathy with spheroids. *Brain* 139(Pt 6), 1666–1672. doi: 10.1093/brain/aww066

Elmore, M. R., Najafi, A. R., Koike, M. A., Dagher, N. N., Spangenberg, E. E., Rice, R. A., et al. (2014). Colony-stimulating factor 1 receptor signaling is necessary for microglia viability, unmasking a microglia progenitor cell in the adult brain. *Neuron* 82, 380–397. doi: 10.1016/j.neuron.2014.02.040

Elmore, M. R. P., Hohsfield, L. A., Kramar, E. A., Soreq, L., Lee, R. J., Pham, S. T., et al. (2018). Replacement of microglia in the aged brain reverses cognitive, synaptic, and neuronal deficits in mice. *Aging Cell* 17:e12832. doi: 10.1111/acel.12832

Gelfand, J. M., Greenfield, A. L., Barkovich, M., Mendelsohn, B. A., Van Haren, K., Hess, C. P., et al. (2020). Allogeneic HSCT for adult-onset leukoencephalopathy with spheroids and pigmented glia. *Brain* 143, 503–511. doi: 10.1093/brain/awz390

Guo, L., Bertola, D. R., Takanohashi, A., Saito, A., Segawa, Y., Yokota, T., et al. (2019). Bi-allelic CSF1R mutations cause skeletal dysplasia of dysosteosclerosis-pyle disease spectrum and degenerative encephalopathy with brain malformation. *Am. J. Hum. Genet.* 104, 925–935. doi: 10.1016/j.ajhg.2019.03.004

Hawley, C. A., Rojo, R., Raper, A., Sauter, K. A., Lisowski, Z. M., Grabert, K., et al. (2018). Csf1r-mApple transgene expression and ligand binding in vivo reveal dynamics of CSF1R expression within the mononuclear phagocyte system. *J. Immunol.* 200, 2209–2223. doi: 10.4049/jimmunol.1701488

Huang, Y., Xu, Z., Xiong, S., Sun, F., Qin, G., Hu, G., et al. (2018). Repopulated microglia are solely derived from the proliferation of residual microglia after acute depletion. *Nat. Neurosci.* 21, 530–540. doi: 10.1038/s41593-018-0090-8

Kındış, E., Simsek-Kiper, P., Koşukcu, C., Taşkıran, E. Z., Göçmen, R., Utine, E., et al. (2021). Further expanding the mutational spectrum of brain abnormalities, neurodegeneration, and dysosteosclerosis: a rare disorder with neurologic regression and skeletal features. *Am. J. Med. Genet. A* 185, 1888–1896. doi: 10.1002/ajmg.a.62179

Konno, T., Kasanuki, K., Ikeuchi, T., Dickson, D. W., and Wszolek, Z. K. (2018). CSF1R-related leukoencephalopathy: a major player in primary microgliopathies. *Neurology* 91, 1092–1104. doi: 10.1212/wnl.0000000000006642

Lai, J., Tu, H., Tan, J. Y., Lim, W. K., Zeng, L., and Ng, A. (2020). A novel T567M mutation outside the tyrosine kinase domain of CSF1R with clinical and radiological features of HDLS. *Neurology* 94:15.

Lei, F., Cui, N., Zhou, C., Chodosh, J., Vavvas, D. G., and Paschalis, E. I. (2020). CSF1R inhibition by a small-molecule inhibitor is not microglia specific; affecting hematopoiesis and the function of macrophages. *Proc. Natl. Acad. Sci. U.S.A.* 117, 23336–23338. doi: 10.1073/pnas.1922788117

Leng, C., Lu, L., Wang, G., Zhang, Y., Xu, Y., Lin, X., et al. (2019). A novel dominant-negative mutation of the CSF1R gene causes adult-onset leukoencephalopathy with axonal spheroids and pigmented glia. *Am. J. Transl. Res.* 11, 6093–6101.

Li, J., Chen, K., Zhu, L., and Pollard, J. W. (2006). Conditional deletion of the colony stimulating factor-1 receptor (c-fms proto-oncogene) in mice. *Genesis* 44, 328–335. doi: 10.1002/dvg.20219

Lund, H., Pieber, M., Parsa, R., Han, J., Grommisch, D., Ewing, E., et al. (2018). Competitive repopulation of an empty microglial niche yields functionally distinct subsets of microglia-like cells. *Nat. Commun.* 9:4845. doi: 10.1038/s41467-018-07295-7

Luo, J., Elwood, F., Britschgi, M., Villeda, S., Zhang, H., Ding, Z., et al. (2013). Colony-stimulating factor 1 receptor (CSF1R) signaling in injured neurons facilitates protection and survival. *J. Exp. Med.* 210, 157–172. doi: 10.1084/jem.20120412

Lynch, D. S., Wade, C., Paiva, A. R. B., John, N., Kinsella, J. A., Merwick, Á, et al. (2019). Practical approach to the diagnosis of adult-onset leukodystrophies: an updated guide in the genomic era. *J. Neurol. Neurosurg. Psychiatry* 90, 543–554. doi: 10.1136/jnnp-2018-319481

Lynch, D. S., Zhang, W. J., Lakshmanan, R., Kinsella, J. A., Uzun, G. A., Karbay, M., et al. (2016). Analysis of mutations in AARS2 in a series of CSF1R-negative patients with adult-onset leukoencephalopathy with axonal spheroids and pigmented glia. *JAMA Neurol.* 73, 1433–1439. doi: 10.1001/jamaneurol.2016.2229

Marotti, J. D., Tobias, S., Fratkin, J. D., Powers, J. M., and Rhodes, C. H. (2004). Adult onset leukodystrophy with neuroaxonal spheroids and pigmented glia: report of a family, historical perspective, and review of the literature. *Acta Neuropathol.* 107, 481–488. doi: 10.1007/s00401-004-0847-x

Mochel, F., Delorme, C., Czernecki, V., Froger, J., Cormier, F., Ellie, E., et al. (2019). Haematopoietic stem cell transplantation in CSF1R-related adult-onset

leukoencephalopathy with axonal spheroids and pigmented glia. *J. Neurol. Neurosurg. Psychiatry* 90, 1375–1376. doi: 10.1136/jnnp-2019-320701

Nicholson, A. M., Baker, M. C., Finch, N. A., Rutherford, N. J., Wider, C., Graff-Radford, N. R., et al. (2013). CSF1R mutations link POLD and HDLS as a single disease entity. *Neurology* 80, 1033–1040. doi: 10.1212/WNL.0b013e31828726a7

Oosterhof, N., Chang, I. J., Karimiani, E. G., Kuil, L. E., Jensen, D. M., Daza, R., et al. (2019). Homozygous mutations in CSF1R cause a pediatric-onset leukoencephalopathy and can result in congenital absence of microglia. *Am. J. Hum. Genet.* 104, 936–947. doi: 10.1016/j.ajhg.2019.03.010

Oosterhof, N., Kuil, L. E., van der Linde, H. C., Burm, S. M., Berdowski, W., van Ijcken, W. F. J., et al. (2018). Colony-Stimulating Factor 1 Receptor (CSF1R) regulates microglia density and distribution, but not microglia differentiation in vivo. *Cell Rep.* 24, 1203–1217.e1206. doi: 10.1016/j.celrep.2018.06.113

Pridans, C., Sauter, K. A., Baer, K., Kissel, H., and Hume, D. A. (2013). CSF1R mutations in hereditary diffuse leukoencephalopathy with spheroids are loss of function. *Sci. Rep.* 3:3013. doi: 10.1038/srep03013

Prinz, M., and Priller, J. (2014). Microglia and brain macrophages in the molecular age: from origin to neuropsychiatric disease. *Nat. Rev. Neurosci.* 15, 300–312. doi: 10.1038/nrn3722

Rademakers, R., Baker, M., Nicholson, A. M., Rutherford, N. J., Finch, N., Soto-Ortolaza, A., et al. (2011). Mutations in the colony stimulating factor 1 receptor (CSF1R) gene cause hereditary diffuse leukoencephalopathy with spheroids. *Nat. Genet.* 44, 200–205. doi: 10.1038/ng.1027

Rojo, R., Raper, A., Ozdemir, D. D., Lefevre, L., Grabert, K., Wollscheid-Lengeling, E., et al. (2019). Deletion of a Csf1r enhancer selectively impacts CSF1R expression and development of tissue macrophage populations. *Nat. Commun.* 10:3215. doi: 10.1038/s41467-019-11053-8

Sohn, E. H., Lee, J., Lee, A. Y., and Shin, J. H. (2021). A case of *CSF1R*-related leukoencephalopathy: serial neuroimaging and neuropsychological tests. *Neurocase* doi: 10.1080/13554794.2021.1981947

Sundal, C., Fujioka, S., Van Gerpen, J. A., Wider, C., Nicholson, A. M., Baker, M., et al. (2013). Parkinsonian features in hereditary diffuse leukoencephalopathy with spheroids (HDLS) and CSF1R mutations. *Parkinsonism Relat. Disord.* 19, 869–877. doi: 10.1016/j.parkreldis.2013.05.013

Tada, M., Konno, T., Tada, M., Tezuka, T., Miura, T., Mezaki, N., et al. (2016). Characteristic microglial features in patients with hereditary diffuse leukoencephalopathy with spheroids. *Ann. Neurol.* 80, 554–565. doi: 10.1002/ana.24754

Tipton, P. W., Kenney-Jung, D., Rush, B. K., Middlebrooks, E. H., Nascene, D., Singh, B., et al. (2021). Treatment of CSF1R-Related leukoencephalopathy: breaking new ground. *Mov. Disord.* doi: 10.1002/mds.28734

Tsai, P. C., Fuh, J. L., Yang, C. C., Chang, A., Lien, L. M., Wang, P. N., et al. (2021). Clinical and genetic characterization of adult-onset leukoencephalopathy caused by CSF1R mutations. *Ann. Clin. Transl. Neurol.* 8, 2121–2131. doi: 10.1002/acn3.51467

Willis, E. F., MacDonald, K. P. A., Nguyen, Q. H., Garrido, A. L., Gillespie, E. R., Harley, S. B. R., et al. (2020). Repopulating microglia promote brain repair in an IL-6-dependent manner. *Cell* 180, 833–846.e816. doi: 10.1016/j.cell.2020.02.013

Xu, Z., Rao, Y., Huang, Y., Zhou, T., Feng, R., Xiong, S., et al. (2020). Efficient strategies for microglia replacement in the central nervous system. *Cell Rep.* 32:108041. doi: 10.1016/j.celrep.2020.108041

Zhuang, L. P., Liu, C. Y., Li, Y. X., Huang, H. P., and Zou, Z. Y. (2020). Clinical features and genetic characteristics of hereditary diffuse leukoencephalopathy with spheroids due to CSF1R mutation: a case report and literature review. *Ann. Transl. Med.* 8:11. doi: 10.21037/atm.2019.12.17

Conflict of Interest: The authors declare that the research was conducted in the absence of any commercial or financial relationships that could be construed as a potential conflict of interest.

Publisher's Note: All claims expressed in this article are solely those of the authors and do not necessarily represent those of their affiliated organizations, or those of the publisher, the editors and the reviewers. Any product that may be evaluated in this article, or claim that may be made by its manufacturer, is not guaranteed or endorsed by the publisher.

frontiers in Aging Neuroscience

REVIEW
published: 16 December 2021
doi: 10.3389/fnagi.2021.790626

Fluid-Attenuated Inversion Recovery Vascular Hyperintensity in Cerebrovascular Disease: A Review for Radiologists and Clinicians

Lichuan Zeng[1], Jinxin Chen[2], Huaqiang Liao[1], Qu Wang[3], Mingguo Xie[1] and Wenbin Wu[2]**

[1] Department of Radiology, Hospital of Chengdu University of Traditional Chinese Medicine, Chengdu, China, [2] Department of Geriatrics, Hospital of Chengdu University of Traditional Chinese Medicine, Chengdu, China, [3] Department of Ultrasound, Hospital of Chengdu University of Traditional Chinese Medicine, Chengdu, China

Neuroradiological methods play important roles in neurology, especially in cerebrovascular diseases. Fluid-attenuated inversion recovery (FLAIR) vascular hyperintensity (FVH) is frequently encountered in patients with acute ischemic stroke and significant intracranial arterial stenosis or occlusion. The mechanisms underlying this phenomenon and the clinical implications of FVH have been a matter of debate. FVH is associated with large-vessel occlusion or severe stenosis, as well as impaired hemodynamics. Possible explanations suggested for its appearance include stationary blood and slow antegrade or retrograde filling of the leptomeningeal collateral circulation. However, the prognostic value of the presence of FVH has been controversial. FVH can also be observed in patients with transient ischemic attack (TIA), which may have different pathomechanisms. Its presence can help clinicians to identify patients who have a higher risk of stroke after TIA. In this review article, we aim to describe the mechanism and influencing factors of FVH, as well as its clinical significance in patients with cerebrovascular disease.

Keywords: fluid-attenuated inversion recovery, FLAIR vascular hyperintensity, collateral circulation, transient ischemic attack, stroke

OPEN ACCESS

Edited by:
Yuzhen Xu,
Tongji University, China

Reviewed by:
Peng Lu,
Beijing Normal University, China
S. P. Li,
University of Macau, Macao SAR, China

****Correspondence:***
Mingguo Xie
767030837@qq.com
Wenbin Wu
wwb1201@vip.sina.com

Specialty section:
This article was submitted to Neuroinflammation and Neuropathy, a section of the journal Frontiers in Aging Neuroscience

Received: *07 October 2021*
Accepted: *26 November 2021*
Published: *16 December 2021*

Citation:
Zeng L, Chen J, Liao H, Wang Q, Xie M and Wu W (2021) Fluid-Attenuated Inversion Recovery Vascular Hyperintensity in Cerebrovascular Disease: A Review for Radiologists and Clinicians. Front. Aging Neurosci. 13:790626. doi: 10.3389/fnagi.2021.790626

INTRODUCTION

Cerebrovascular diseases are harmful to human life because they have high mortality and disability rates. Fluid-attenuated inversion recovery (FLAIR) is widely used for the diagnosis of various intracranial diseases and is now recommended as a part of the routine protocol for magnetic resonance imaging (MRI) of stroke. FLAIR vascular hyperintensity (FVH) was first described in 1999 in a series of patients with acute stroke and subacute stroke (Cosnard et al., 1999). This finding has also been termed "hyperintense vessels on FLAIR," the "hyperintense vessel sign," and the "ivy sign" in the literature (Girot et al., 2007; Hacein-Bey et al., 2014; Lee et al., 2016; Nam et al., 2017; Grosch et al., 2020). FVHs are defined as focal, serpentine, or linear hyperintensities that are best visualized within the Sylvian fissure and are associated with large-vessel occlusion or stenosis (Lee et al., 2021). This neuroimaging sign has been observed not only in large-vessel stenoocclusive disease due to atherosclerosis but also in other diseases, such as Moyamoya disease and transient ischemic attack (TIA). FVH may be an important neuroimaging marker, and clinicians and radiologists should be trained to look for its presence.

FLAIR vascular hyperintensity is most likely to represent slow arterial blood flow, which is frequently encountered in patients with acute ischemic stroke. Slow blood flow is interpreted as slow retrograde flow in leptomeningeal collaterals or antegrade flow that corresponds to impaired hemodynamics (Nam et al., 2018). FVH may thus be of clinical significance in predicting cerebrovascular disease, especially when magnetic resonance angiography (MRA) is unavailable. However, the associations of FVH with clinical outcomes remain controversial. FVH may represent slow collateral flow that is effective in maintaining perfusion to penumbral regions, restricting the progression of ischemic lesions, and improving outcomes (Dong and Nao, 2019; Yuan et al., 2019; Derraz et al., 2021). On the other hand, FVH has been observed to correspond to perfusion deficits, larger lesions, and poor outcomes (Nam et al., 2017; Kim et al., 2019; Zhu et al., 2020; Wang et al., 2021). In this review article, we aim to review the current understanding of the physiology and clinical significance of FVH. This underappreciated neuroimaging sign may have important clinical implications.

MECHANISM AND INCIDENCE OF FLAIR VASCULAR HYPERINTENSITY

The exact pathophysiology of FVH has not yet been clearly defined, but its associations with acute large-artery occlusion and chronic arterial stenosis have been widely accepted. FVHs are classified into distal and proximal FVHs according to their extent and location (**Figure 1**), which have different clinical implications (Azizyan et al., 2011). Distal FVH is defined as FVH that is present in the M3 and/or distal segments of the MCA (Yoshioka et al., 2013; Nam et al., 2017). Proximal FVH is defined as FVH that extends only within the territories of the M1 and/or M2 segments of the MCA (Shin et al., 2020; Li et al., 2021). Initially, some authors linked FVH to intraluminal thrombus, whereas other studies suggested that FVH might reflect slow arterial blood flow rather than intraluminal thrombus (Sanossian et al., 2009). FVH is associated with the leptomeningeal collateral circulation in arterial occlusive lesions. Stationary blood and slow antegrade flow have been suggested as possible explanations for proximal FVH. Slow retrograde collateral circulation has been regarded as the mechanism of distal FVH (**Figure 2**). FVHs are frequently detected in patients with acute cerebral infarction accompanied by significant stenosis or arterial occlusion of the middle cerebral artery (MCA) and internal carotid artery (ICA). FVHs can also be observed in posterior cerebral artery territory, but it is much less reported than in MCA and ICA, for the anatomical characteristics of the PCA including a short and tortuous pathway compared with that of the MCA.

Previous studies have attributed the presence of FVH to large-artery disease, leptomeningeal collateral flow, and local alterations in hemodynamics (Jiang et al., 2019; Bourcier et al., 2020; Derraz et al., 2021; Lee et al., 2021; Maruyama et al., 2021). This hypothesis has been corroborated by several observations that reported the presence of FVH together with large-vessel stenosis or occlusion. Alterations in hemodynamics, such as stationary blood and slow blood flow, often from the collateral circulation through leptomeningeal anastomoses, have been suggested to be the leading cause of FVH (Lee et al., 2021). Ahn et al. (2016) investigated the influence of differences in blood flow velocity on the presentation of FVHs. As the flow velocity increased, the signal intensity of FVHs decreased. This finding is consistent with the theory based on slow blood flow. Patients with cerebral infarction exhibited a higher frequency of FVH than patients with TIA, which suggests that the frequency of FVH might be correlated with the severity of ischemia.

FLAIR vascular hyperintensity has frequently been encountered in patients with acute ischemic stroke and significant intracranial arterial stenosis or occlusion, and it has also been observed in patients with chronic intracerebral arterial stenoocclusive disease. The frequency of FVHs has varied immensely between different studies. FVH signs on FLAIR have been reported to be observed in 45–100% of patients with acute ischemic stroke, primarily in strokes involving the MCA territory. Shin et al. (2020) showed that proximal FVH was observed in 71/105 (67.6%) patients who presented with hyperacute infarction of the MCA. A lower prevalence of FVH has been reported in distal occlusions and posterior strokes or when the onset-to-imaging time increased. One possible explanation for these results is the heterogeneity of the patients in the studies. A great many variables might affect the presentation of FVHs.

FACTORS INFLUENCING FLAIR VASCULAR HYPERINTENSITIES

Many factors may influence the presence and extent of FVHs, of which the blood flow velocity is regarded as the most important. A quantitative MRI study (Ahn et al., 2016) of a phantom using different flow velocities would help to define the exact range of flow velocities that cause FVH. The signal intensities of FVHs on conventional FLAIR were minimal at a flow velocity of 11.3 cm/s, but as flow velocities decreased the signal intensities increased. Hence, a decrease in blood flow velocity will result in an increase in signal intensity in the respective vessel on FLAIR imaging. On the other hand, Ahn et al. (2016) reported that MRI parameters, such as the echo time (TE) and flip angle (FA), and the periodically rotated overlapping parallel lines with enhanced reconstruction (PROPELLER) technique were independent factors that influenced the intensity of FVHs. As the TE increased, the signal intensity of FVHs decreased. In contrast, as the FA of the refocusing pulse increased, the intensity of FVHs increased, and the PROPELLER technique significantly increased the intensity of FVHs (Ahn et al., 2015).

The average time interval between symptom onset and imaging might be another important factor that influences the presence of FVH. Many studies have examined the time course of FVH in acute and subacute cerebral infarctions of the MCA territory, and the results showed that the frequency of FVH declined over time (Aoki et al., 2020). Maeda et al. (2001) reported that FVH was seen in 100% of examinations carried out less than 24 h after symptom onset but only 50% of examinations performed 10–13 days after symptom onset. The presence of

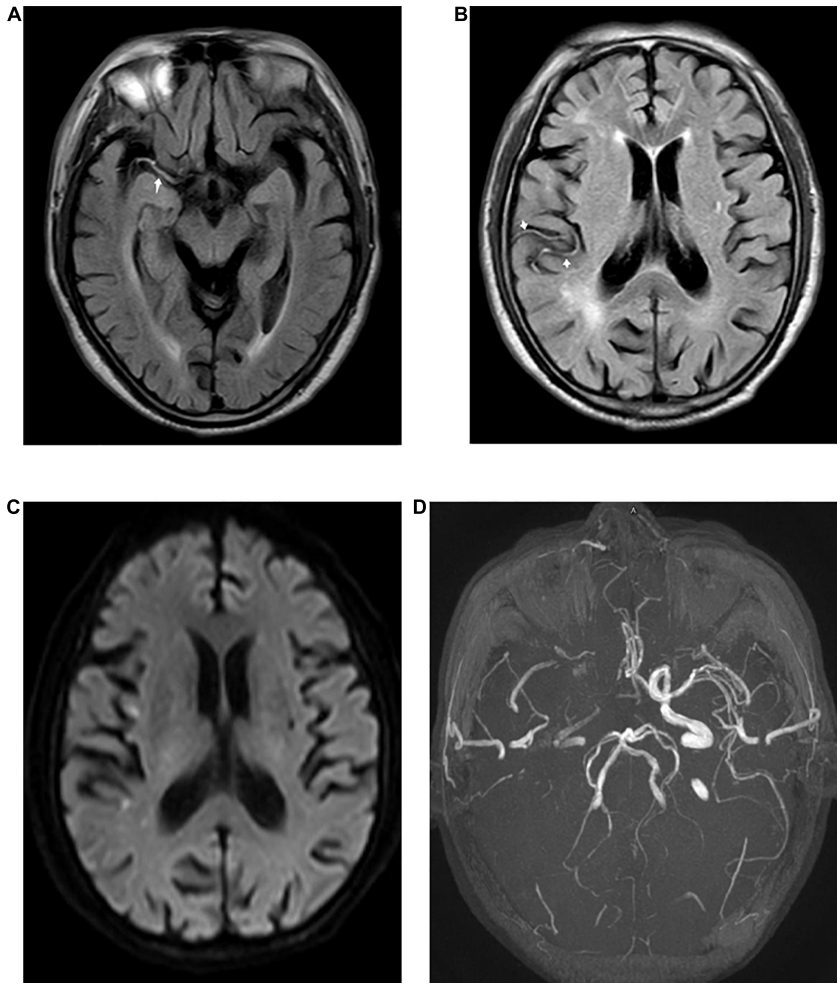

FIGURE 1 | Fluid-attenuated inversion recovery (FLAIR) vascular hyperintensity (FVH) detected in a 73-year-old male patient with acute stroke. Proximal FVH in the Sylvian fissure [**(A)**, arrow] and distal FVH [**(B)**, arrow] in the right temporal lobe were detected in FLAIR images. Diffusion-weighted imaging (DWI) **(C)** shows acute ischemic infarction in the territory of the right middle cerebral artery (MCA). A time-of-flight magnetic resonance imaging (MRI) sequence **(D)** shows the right MCA and an occlusion of the internal carotid artery (ICA).

FVH is associated with the time interval between stroke onset and MRI scanning. FVH can be a temporary phenomenon that commonly disappears within the first 24–36 h after stroke onset. FVH is recognized as a marker of slow blood flow induced by severe stenosis or occlusion of vessels. A previous study (Liu et al., 2011) suggested that there was a significant positive correlation between the intensity of FVH and the degree of stenosis of the M1 segment.

EVALUATION METHODS

Several approaches have been proposed for investigating the extent of FVHs. Lee et al. (2009) graded distal FVHs as absent, subtle, and prominent. Subtle FVH was defined as FVH present over less than one third of the perfusion lesion, whereas prominent FVH was defined as FVH present over more than one third of the perfusion lesion. Olindo et al. (2012) reported a scoring system based on a rostrocaudal extension of FVH. They analyzed horizontal FLAIR images from the first appearance of the M1 segment of the MCA to the 10th image. On each slice, absence of FVH scored 0 points, whereas if one or more FVHs were recognized this scored 1 point. The resulting FVH scores thus ranged from 0 to 10 after 10 images were analyzed.

The Alberta stroke program early computerized tomography score (ASPECTS) was a widely used method for assessing computerized tomography scans in patients with acute ischemic stroke (Barber et al., 2000). The scores on ASPECTS for seven cortical areas (insula and M1–M6) were used to assign FVH scores according to the spatial distribution of MCA. The insula and M1–M3 were defined as corresponding to the level of the basal ganglia, and M4–M6 were defined as corresponding to the level of the ventricles immediately above the basal ganglia, as follows: M1, anterior cortex of MCA; M2, lateral cortex of MCA; M3, posterior cerebral cortex of MCA; and M4, M5, and M6, the anterior, lateral, and posterior MCA territories immediately

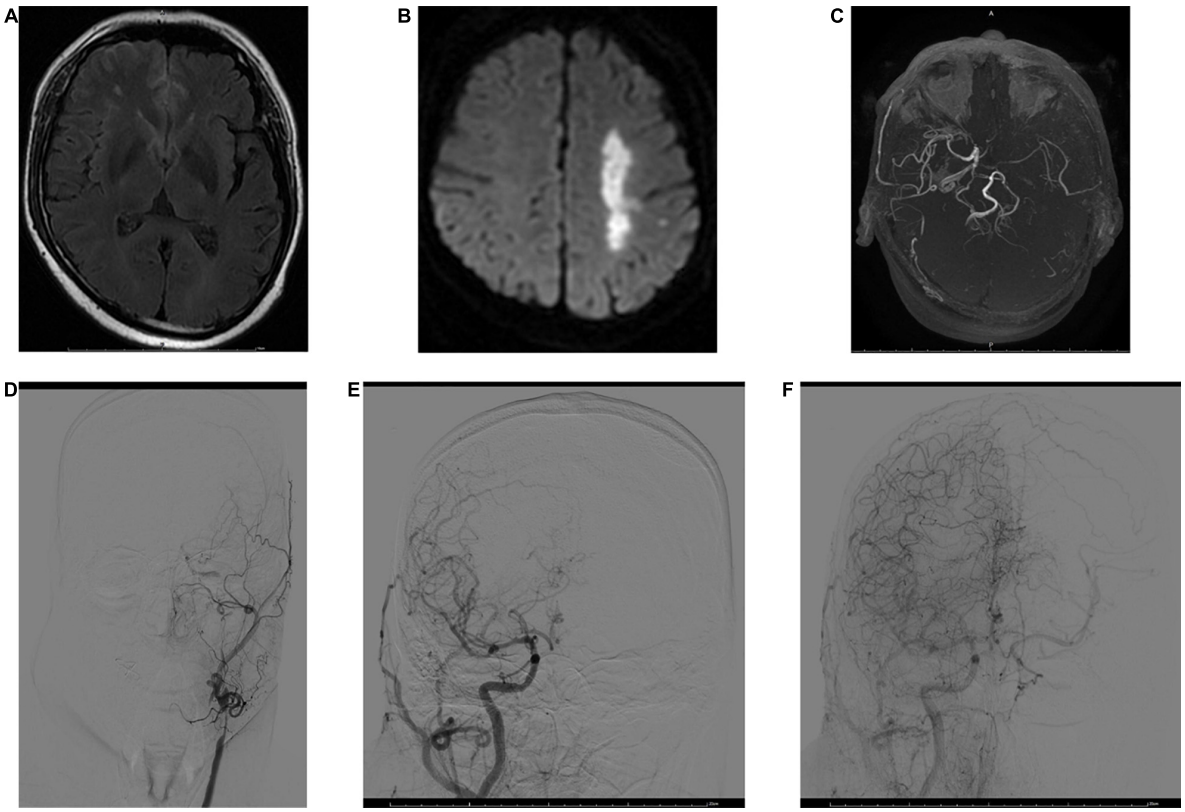

FIGURE 2 | MRI and digital subtraction angiography (DSA) images obtained 3 h after stroke onset in a 53-year-old male. FVHs were observed at the left temporooccipital junction **(A)**. DWI shows acute infarction in the territory of the left MCA **(B)**. FVHs located beyond the DWI lesions, indicating an FVH–DWI mismatch. Magnetic resonance angiography (MRA) **(C)** shows near-occlusion of the left MCA and ICA. A DSA image obtained soon afterward demonstrates stenosis of the left common carotid artery and occlusion of the ICA **(D)**. Angiograms of the right common carotid artery in anteroposterior view in the early arterial phase **(E)** and late arterial phase **(F)** show good retrograde filling of the leptomeningeal collateral circulation in the left hemisphere.

superior to M1, M2, and M3, respectively. The FVH score on ASPECTS, which is based on the number of territories that are positive for FVH, is more widely accepted and applied in clinical practice.

CLINICAL APPLICATIONS

Prediction of Arterial Stenosis or Occlusion

FLAIR vascular hyperintensities are most frequently identified in patients with persistent large-vessel stenosis or occlusion and acute ischemic stroke. FVH has demonstrated excellent diagnostic performance for the identification of large-vessel occlusion, especially in MCA and ICA. Many studies have assessed the accuracy of FVH for the confirmation and location of a large-vessel occlusion. They reported that FVH had excellent sensitivity (76–98%) and specificity (69.8–86%) for the identification of a large-vessel occlusion (Shin et al., 2020). In some FVH positive patients without large-vessel occlusion, atrial fibrillation was thought be an important factor. As for some FVH false negative patients, it is believed that these patients often have good collateral circulation and do not have slow blood flow conditions to form FVH signs.

FLAIR vascular hyperintensities frequently appear in patients with acute ischemic stroke and can, in fact, also be seen in TIA patients. Yoshioka et al. (2013) performed a retrospective analysis of TIA patients and analyzed the relationship between distal hyperintense vessels, severe large-artery stenosis or occlusion, and clinical presentation. They found that FVH was independently associated with severe large-artery stenosis or occlusion in TIA patients. FVH can be regarded as a marker of large-vessel occlusion, which is known to increase the short-term risk of stroke. The presence of FVH on initial FLAIR MRI may be a clue to the presence of persistent large-vessel stenosis or occlusion and the possibility of subsequent stroke. This sign is important, especially when MRA is unavailable to document the presence or absence of large-vessel stenosis or occlusion.

Collaterals

The collateral vessels can maximize the odds of survival of a high volume of brain tissue by sustaining the ischemic penumbra. Most patients with acute stroke who have robust collaterals usually have better clinical outcomes. FVH in collaterals could

serve as good evidence of hemodynamic impairment in patients with cerebral infarction and TIA. Liu et al. (2011) investigated the relationship between the location of FVH and the pattern of collateral flow by comparing findings on FLAIR images with those obtained by digital subtraction angiography. The results demonstrated that the location of FVH is an indicator of the pattern of collateral flow: FVH located within the Sylvian fissure mainly indicates antegrade collateral flow across the residual M1 segment; FVH present in the cerebral sulci at the temporooccipital junction usually represents retrograde leptomeningeal collateral flow from the anterior cerebral artery to the MCA; and FVH expanding to the cerebral sulci of the frontal and parietal lobes represents retrograde leptomeningeal collateral flow via the posterior cerebral artery to the MCA. FVH is a non-invasive indicator of both perfusion defects and collateral flow and has been evaluated in many studies of ischemic stroke. Some studies found that FVH represents insufficient collateralization and is associated with poor functional outcomes. However, other studies have reported that FVH is indicative of sufficient collateralization and has good prognostic value.

Perfusion Abnormalities and FLAIR Vascular Hyperintensity–Diffusion-Weighted Imaging Mismatch

FLAIR vascular hyperintensities are common in patients with acute ischemic stroke and represent marked hemodynamic impairment and slow retrograde flow in the ischemic territory due to intracranial stenoocclusive disease. The presence of FVH in acute ischemic stroke may indicate cerebral hypoperfusion. The FVH sign is associated with larger lesion volumes on perfusion-weighted imaging (PWI) and mismatches between PWI and DWI volumes in acute stroke. Prominent or extended FVHs indicate large areas of salvageable tissue and greater potential benefits from recanalization. Patients in an FVH-positive group exhibited more severe hemodynamic impairment than those in an FVH-negative group (Gawlitza et al., 2014). A quantitative analysis of the perfusion parameters also revealed that perfusion was more severely compromised and widely disturbed in an FVH-positive group (Nomura et al., 2020).

The FVH score has been strongly associated with the area of hypoperfusion and the extent of prolongation of mean transit time, which suggests that the presence of FVH is representative of impaired cerebrovascular autoregulation. FVH can even sometimes be observed during the hyperacute phase of ischemic stroke. A previous study showed that patients with lower FVH scores were more likely to have smaller penumbras on computed tomography perfusion imaging and larger infarct volumes. The presence of FVH may be especially important in instances where MRA or perfusion imaging is not available or images are degraded by artifacts.

An FVH–DWI mismatch is considered to be present when FVH extends beyond the boundaries of the DWI cortical lesion (**Figure 2**). Legrand et al. (2015) reported that an FVH–DWI mismatch predicted the presence of a PWI–DWI mismatch with a sensitivity of 92% and a specificity of 64%. A PWI–DWI mismatch is thought to represent the ischemic penumbra or ischemia without permanent cellular damage. An FVH–DWI mismatch was associated with a smaller initial infarct and greater infarct growth after thrombolysis, even though the final infarcts remained smaller. Jiang et al. (2020a) also reported that an FVH–DWI mismatch group had smaller DWI volumes on admission and on follow-up but lower DWI volume growth than a group with no FVH–DWI mismatch.

Whether an FVH–DWI mismatch is a primary indicator of clinical outcomes in acute ischemic stroke is controversial. Jiang et al. (2020b) assessed the association between FVH–DWI mismatch and functional outcomes in patients with acute stroke receiving endovascular therapy. Patients with an FVH–DWI mismatch had higher FVH scores, smaller DWI volumes, and better functional outcomes than patients without an FVH–DWI mismatch. Wang et al. (2020) found that FVH–DWI mismatch was positively correlated with and independently associated with complete revascularization. They found that a group with good functional outcomes had higher FVH scores, higher FVH–DWI mismatch ratios, and higher complete revascularization ratios than a group with poor functional outcomes.

FLAIR vascular hyperintensity located beyond the boundaries of the DWI lesion reflects impaired yet viable tissue. This tissue recovers its function when recanalization is achieved, which explains why patients with an FVH–DWI mismatch are more likely to have favorable outcomes. PWI–DWI mismatch has been proposed for use in selecting patients with acute stroke for recanalization therapy. FVH–DWI mismatch provides an alternative to PWI–DWI mismatch for selecting patients as candidates for thrombectomy. FVH–DWI mismatch may rapidly identify patients with proximal occlusion who are most likely to benefit from recanalization (Legrand et al., 2016). It may also provide an alternative to PWI–DWI mismatch for identifying candidates for endovascular therapy (Legrand et al., 2019). FVH appearing in the early phase is associated with large-vessel occlusion, a higher National Institutes of Health Stroke Scale (NIHSS) score at admission, and a larger infarct core volume. Over time, FVH represents collateral blood supply to the arterial occlusion, saving more tissue in the ischemic penumbra, and improving the clinical prognosis.

FLAIR Vascular Hyperintensity in Transient Ischemic Attack Patients

Transient ischemic attack is characterized by sudden focal brain dysfunction lasting less than 24 h, which is linked to cerebral or optic ischemia. Patients presenting with transient neurological symptoms have an increased risk of a subsequent stroke. Therefore, the clinical importance of early diagnosis and treatment of TIA should be emphasized to prevent the development of stroke. According to previous studies, the incidence of FVHs in TIA patients was markedly lower than in acute ischemic stroke and varied remarkably from 16 to 39.6% (Dong et al., 2017; Nam et al., 2018). Because some FVHs in TIA patients were proved to be transient and were correlated with symptom resolution, the prior reports may have underestimated the frequency of FVHs. Ding et al. (2020) reported that FVH was

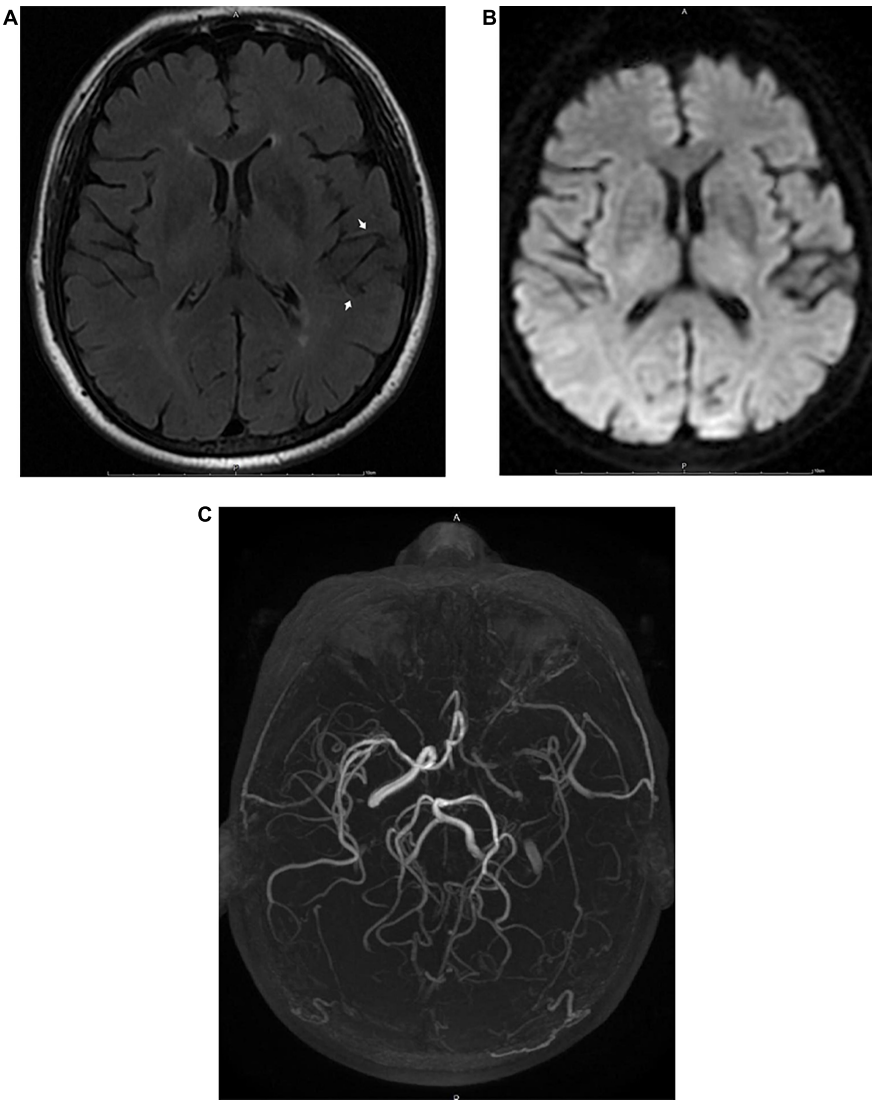

FIGURE 3 | MRI images obtained 6 h after the appearance of the initial symptoms in a 68-year-old male patient with transient ischemic attack. A FLAIR image **(A)** shows FVH in the territory of the left MCA (arrow). There were no abnormalities on DWI **(B)**. Three-dimensional time-of-flight MRA **(C)** shows occlusion of the ipsilateral MCA and ICA.

observed in up to 81.6% (31/38) of hospitalized TIA patients, who had severe stenosis or occlusions. On the another hand, they found that there was no significant difference in the degree of stenosis between FVH-negative and FVH-positive groups, which means that the severity of arterial stenosis did not predict the presence and extent of FVH.

FLAIR vascular hyperintensity has not been fully evaluated in patients with TIA in contrast to ischemic stroke. Two factors – arterial occlusion or stenosis and atrial fibrillation – have been reported to have significant and independent associations with FVH (de Figueiredo et al., 2017). It has been widely accepted that FVH is associated with the presence of significant large-artery stenosis or occlusion, which is an independent risk factor and has a high predictive value for stroke after TIA. FVH is associated with recurrent ischemic stroke events in patients with lesion-negative TIA (Nam et al., 2018). Atrial fibrillation has been specifically associated with transient FVH, and arterial occlusion or stenosis has been associated with persistent FVH. Kobayashi et al. (2013) reported that atrial fibrillation was more common than arterial occlusive lesions in FVH-positive patients. Transient FVH could be caused by early recanalization of emboli in patients with TIA.

FLAIR vascular hyperintensity can predict an oncoming acute ischemic stroke in the 30 days following a TIA (Dong et al., 2017). The occurrence of FVH in patients with TIA may be associated with subsequent ischemic stroke in the corresponding vascular territory. Predicting recurrent ischemic stroke after TIA is important in order to consider adequate strategies for managing patients with TIA. Persistent FVH has been associated with a mechanism of arterial occlusion and an increased risk

of recurrent TIA and ischemic stroke (**Figure 3**). In contrast, transient FVH together with normal MRA findings has been linked to a mechanism of paroxysmal atrial fibrillation but not associated with an increased risk of stroke (Kobayashi et al., 2013). FVH may be of clinical significance in predicting ischemic stroke in a TIA setting, especially when MRA is unavailable.

Association With Functional Outcomes

Many studies have focused on the association between FVHs and clinical outcomes in patients with ischemic stroke. However, the prognostic value of FVH findings is unclear. Some studies demonstrated that the presence of FVHs was associated with severe clinical impairments and poor functional outcomes, (Girot et al., 2007; Kufner et al., 2015; Dong et al., 2017; Nam et al., 2017; Zhu et al., 2020; Wang et al., 2021) whereas other studies indicated that FVHs were correlated with good collateral flow and favorable outcomes (Pérez et al., 2012; Dong and Nao, 2019; Yuan et al., 2019; Aoki et al., 2020; Jiang et al., 2020b; Wang et al., 2020; Zhou et al., 2020b; Derraz et al., 2021). In addition, some other studies proposed that FVH has different clinical significance under different conditions regarding prognostic meaning other than information regarding arterial occlusion (Kim et al., 2016, 2019; Liu et al., 2016; Sakuta et al., 2016; Li et al., 2018, 2021; Jiang et al., 2019; Shang et al., 2019; Zhou et al., 2020a). Studies with prediction of FVH for functional outcomes are summarized in **Tables 1**–**3**. Li et al. (2021) reported that high FVH scores in patients with acute stroke and occlusion or severe stenosis of the MCA tended to indicate severe clinical impairments and poor clinical outcomes, but subgroup analysis showed that high FVH scores represented favorable clinical outcomes in patients with occlusion of the MCA. The results indicated that the clinical significance of FVH differed between patients with severe stenosis of the MCA and patients with occlusion of the MCA.

FLAIR vascular hyperintensity has been recognized as a marker of collateral flow in ischemic stroke, but its relationship with outcomes is still controversial. There is little consensus on the interpretation of prognostic information from FVH studies, which should adopt an accepted standard as a prognostic assessment tool. In previous studies, the populations with stroke that were included were heterogeneous, especially in terms of the time to the initial MRI scan from symptom onset, and patients with proximal and distal FVHs were considered

TABLE 1 | Studies with prediction of FVH for favorable functional outcome.

Author/Year	No. of patients	Mean Age (year) (range)	Standard for favorable functional outcome	Onset to imaging
Derraz et al. (2021)	85	92.4	90-day mRS ≤3	90-day mRS 0–3 group: 180 min 90-day mRS 4–6 group: 219 min
Wang et al. (2020)	72	69.69 (40–82)	3 months mRS score ≤2	Within 6 h
Jiang et al. (2020b)	59	FVH/DWI mismatch: 64.20 ± 14.97 No FVH/DWI mismatch: 71.28 ± 11.10	3 months mRS score ≤2	Within 6 h
Aoki et al. (2020)	72	76 (66–83)	Presence or absence of recanalization assessed by MRA or DSA	FVH(−) group: 9.0 h FVH(+) group: 2.6 h
Zhou et al. (2020b)	293	NA	90-day mRS ≤1	<4.5 h
Yuan et al. (2019)	68	Favorable: 61 (57.5–70.25) Unfavorable: 60 (50.25–64.25)	3 months mRS ≤2	Favorable group: 66 h Unfavorable group: 53.8 h
Dong and Nao (2019)	160	64.01 ± 11.81	90-day mRS ≤2	24.72 ± 16.24 h
Pérez et al. (2012)	70	66	Ischemia progression	Absent/Subtle/Prominent of FVH: 300/280/290 min

FVH, FLAIR vascular hyperintensity; mRS, modified Rankin Scoring; NA, not available.

TABLE 2 | Studies with prediction of FVH for unfavorable functional outcome.

Author/Year	No. of patients	Mean Age (year) (range)	Standard for favorable functional outcome	Onset to imaging	Notes
Nam et al. (2017), Wang et al. (2021)	203	63.3 ± 10.2	mRS at discharge <2	NA	FVH after therapy
Girot et al. (2007), Zhu et al. (2020)	267	66.06 ± 11.76	90-day mRS ≤2	44.44 ± 16.48 h	
Dong et al. (2017), Wang et al. (2021)	154	63.0 ± 11.9	30-day follow-up acute ischemic stroke	Within 72 h	
Nam et al. (2017), Zhu et al. (2020)	325	69	Early neurological deterioration	Within 24 h	Distal FVH
Kufner et al. (2015), Dong et al. (2017)	62	71.4 ± 13.9	3 months mRS ≤2	Visible FHV on ≤4 Sections: 88.5 min Visible FHV on >4 Sections: 93.5 min	
Girot et al. (2007); Kufner et al. (2015)	30	64 (35–92)	1 month mRS ≤2	Within 12 h	Distal FVH

FVH, FLAIR vascular hyperintensity; mRS, modified Rankin Scoring; NA, not available.

TABLE 3 | Studies with prediction of FVH for uncertain functional outcome.

Author/Year	No. of patients	Mean Age (year) (range)	Conclusion
Li et al. (2021)	282	66.66 ± 11.29	In patients with proximal MCA occlusion or stenosis ≥70%, a high FVH score represented severe clinical impairment and poor clinical outcomes In acute ischemic stroke patients with proximal MCA occlusion, a high FVH score represented favorable clinical outcomes
Zhou et al. (2020a)	3,577	NA	FVHs were not associated with functional outcome overall, but were significantly associated with better outcome in those receiving endovascular therapy
Jiang et al. (2019)	37	69.41 ± 12.51	The good functional outcome group had a higher FVH1 (before therapy) score and a lower FVH2 (after therapy) score than the poor functional outcome group
Shang et al. (2019)	459	NA	FVH is associated with unfavorable outcome within 6 h to 14 days of onset, while the wider distribution of distal FLAIR vascular hyperintensity may be favorable beyond 14 days of onset in MCA infarction
Kim et al. (2019)	112	67 (54–79)	For acute stroke patients who do not receive reperfusion therapy, prominent FVH may be independent predictors of an unfavorable outcome In the reperfusion therapy group, there was no association between prominent FVH and the clinical outcome
Li et al. (2018)	38	62.52 ± 13.61	FVH score showed no correlation with 90-day functional clinical outcome and was not sufficient as an independent predictor of short-term clinical outcome
Kim et al. (2016)	87	FVH(−): 70 (61.7–77.0) FVH(+): 71.5 (58.0–76.0)	FVH are associated with relatively severe clinical presentation and non-favorable prognosis in patients with cortical borderzone infarcts, but not in patients with internal borderzone infarcts
Liu et al. (2016)	101	66.2 ± 17.8	Higher FVH-ASPECTS measured outside the DWI lesion is associated with good clinical outcomes FVH-ASPECTS measured inside the DWI lesion was predictive of hemorrhagic transformation
Sakuta et al. (2016)	118	76 ± 9.7	Decrease of FVH after t-PA therapy predicts good outcome in patients receiving

FVH, FLAIR vascular hyperintensity; MCA, middle cerebral artery; ASPECTS, alberta stroke program early computerized tomography score; NA, not available.

together, which potentially confounded tests for significance. Furthermore, studies used different prognostic assessment criteria, including the NIHSS score, Modified Rankin Scale score, and infarct volume on DWI.

The association between FVH and functional outcomes varies with time. Shang et al. (2019) reported that the symptom-to-imaging time might be an important factor when assessing the prognostic value of FVH. FVH is associated with unfavorable outcomes within 6 h to 14 days after onset, whereas a wider distribution of distal FVH may be favorable beyond 14 days after onset in infarction of the MCA. In the majority of studies that showed an association between FVH and good outcomes (Aoki et al., 2020; Jiang et al., 2020b; Wang et al., 2020; Zhou et al., 2020b; Derraz et al., 2021) the symptom-to-imaging time was less than 6 h. In contrast, in most of the studies that demonstrated an association between FVH and poor outcomes (Kim et al., 2016; Dong et al., 2017; Zhu et al., 2020) the symptom-to-imaging time was 12–24 h or longer. FVH might be an imaging marker of leptomeningeal collateral flow within 6 h of symptom onset or within the time window for reperfusion therapy. The extent of FVH may represent the volume of brain parenchyma at risk of ischemia, which could be saved by reperfusion therapy to reduce the final lesion size and improve functional outcomes. This may be the explanation why within this time interval patients with FVH may have better clinical outcomes than patients without FVH. On the other hand, when FVH occurs beyond the time window for reperfusion therapy, the presence of FVH may represent persistent occlusion of a vessel and impaired hemodynamics. Consequently, patients with FVH could be affected more by hemodynamic instability than patients without FVH. This difference might be associated with severe clinical impairments and unfavorable outcomes in patients with FVH during this time interval.

Liu et al. (2016) reported that the pattern of FVHs can serve as an imaging marker for the selection of endovascular therapy in acute occlusion of the MCA. A higher FVH-ASPECTS measured outside the DWI lesion is associated with good clinical outcomes in patients undergoing endovascular therapy, whereas the FVH-ASPECTS measured inside the DWI lesion is predictive of hemorrhagic transformation. It is noteworthy that the prognostic meanings of FVH before and after therapy are different. Jiang et al. (2019) assessed the relationship between functional outcomes and FVH before and after therapy and found that a group with good functional outcomes had higher FVH scores before therapy and lower FVH scores after therapy than a group with poor functional outcomes. FVHs before and after therapy were independently associated with functional outcomes. A high FVH score before therapy is regarded as a marker of good collateral status (Mahdjoub et al., 2018). However, the persistence of FVH after therapy is associated with persistent occlusion of a vessel and a poor functional outcome.

SUMMARY

Although the mechanism underlying FVH remains to be established, this phenomenon is associated with retrograde

collateral blood flow and impaired hemodynamics in the ischemic territory due to intracranial stenoocclusive disease. FVH can be detected in acute infarction and chronic large-vessel occlusion. It is worth noting that FVH occurs in patients with TIA and might be correlated with clinical conditions such as atrial fibrillation and not only with large-vessel occlusion. However, it is still controversial whether FVH may serve as an imaging marker of hemodynamic impairment or good collateral status and may predict patients' prognosis. Many factors should be considered when assessing the prognostic value of FVH, especially for symptom-to-imaging time and differences between before and after treatment. FVH may be an important neuroimaging marker, and radiologists and clinicians should be trained to look for its presence.

AUTHOR CONTRIBUTIONS

LZ and JC: conceptualization. LZ and HL: methodology and writing – original draft preparation. QW and MX: formal analysis and investigation. LZ and WW: writing – reviewing and editing. All authors contributed to the article and approved the submitted version.

FUNDING

This research was funded by the National Key R&D Program of China (2020YFC2003100 and 2020YFC2003104) and "Xing-lin Scholars" Project of Chengdu University of Traditional Chinese Medicine (Grant No. QNXZ2018004).

REFERENCES

Ahn, S. J., Lee, K. Y., Ahn, S. S., Suh, H., Kim, B. S., and Lee, S. K. (2016). Can FLAIR hyperintense vessel (FHV) signs be influenced by varying MR parameters and flow velocities? A flow phantom analysis. *Acta Radiol.* 57, 580–586. doi: 10.1177/0284185115592060

Ahn, S. J., Suh, S. H., Lee, K. Y., Kim, J. H., Seo, K. D., and Lee, S. (2015). Hyperintense Vessels on T2-PROPELLER-FLAIR in Patients with Acute MCA Stroke: prediction of Arterial Stenosis and Perfusion Abnormality. *AJNR Am. J. Neuroradiol.* 36, 2042–2047. doi: 10.3174/ajnr.A4423

Aoki, J., Suzuki, K., Suda, S., Okubo, S., Mishina, M., and Kimura, K. (2020). Negative-FLAIR vascular hyperintensities serve as a marker of no recanalization during hospitalization in acute stroke. *J. Clin. Neurosci.* 72, 233–237. doi: 10.1016/j.jocn.2019.11.032

Azizyan, A., Sanossian, N., Mogensen, M. A., and Liebeskind, D. S. (2011). Fluid-attenuated inversion recovery vascular hyperintensities: an important imaging marker for cerebrovascular disease. *AJNR Am. J. Neuroradiol.* 32, 1771–1775. doi: 10.3174/ajnr.A2265

Barber, P. A., Demchuk, A. M., Zhang, J., and Buchan, A. M. (2000). Validity and reliability of a quantitative computed tomography score in predicting outcome of hyperacute stroke before thrombolytic therapy. ASPECTS Study Group. Alberta Stroke Programme Early CT Score. *Lancet* 355, 1670–1674. doi: 10.1016/s0140-6736(00)02237-6

Bourcier, R., Thiaudière, R., Legrand, L., Daumas-Duport, B., Desal, H., and Boulouis, G. (2020). Accelerated MR Evaluation of Patients with Suspected Large Arterial Vessel Occlusion: diagnostic Performances of the FLAIR Vessel Hyperintensities. *Eur. Neurol.* 83, 389–394. doi: 10.1159/000509077

Cosnard, G., Duprez, T., Grandin, C., Smith, A. M., Munier, T., and Peeters, A. (1999). Fast FLAIR sequence for detecting major vascular abnormalities during the hyperacute phase of stroke: a comparison with MR angiography. *Neuroradiology* 41, 342–346. doi: 10.1007/s002340050761

de Figueiredo, M. M., Júnior, E. A., Alves, M., Vazzoler, M., Miranda, R., and Silva, G. S. (2017). Fluid-Attenuated Inversion Recovery Vascular Hyperintensities in Patients with Transient Ischemic Attack. *J. Stroke Cerebrovasc. Dis.* 26, 2412–2415. doi: 10.1016/j.jstrokecerebrovasdis.2017.05.034

Derraz, I., Ahmed, R., Benali, A., Corti, L., Cagnazzo, F., Dargazanli, C., et al. (2021). FLAIR vascular hyperintensities and functional outcome in nonagenarians with anterior circulation large-vessel ischemic stroke treated with endovascular thrombectomy. *Eur. Radiol.* 31, 7406–7416. doi: 10.1007/s00330-021-07866-1

Ding, B., Chen, Y., Jiang, H., Zhang, H., Huang, J., and Ling, H. W. (2020). Fluid-Attenuated Inversion Recovery Vascular Hyperintensities in Transient Ischemic Attack within the Anterior Circulation. *Biomed. Res. Int.* 2020:7056056. doi: 10.1155/2020/7056056

Dong, X., and Nao, J. (2019). Fluid-attenuated inversion recovery vascular hyperintensities in anterior circulation acute ischemic stroke: associations with cortical brain infarct volume and 90-day prognosis. *Neurol. Sci.* 40, 1675–1682. doi: 10.1007/s10072-019-03909-0

Dong, X., Bai, C., and Nao, J. (2017). Influential factors and clinical significance of fluid-attenuated inversion recovery vascular hyperintensities in transient ischemic attacks of carotid arterial system. *Neuroradiology* 59, 1093–1099. doi: 10.1007/s00234-017-1906-z

Gawlitza, M., Gragert, J., Quäschling, U., and Hoffmann, K. T. (2014). FLAIR-hyperintense vessel sign, diffusion-perfusion mismatch and infarct growth in acute ischemic stroke without vascular recanalisation therapy. *J. Neuroradiol.* 41, 227–233. doi: 10.1016/j.neurad.2013.10.004

Girot, M., Gauvrit, J. Y., Cordonnier, C., Pruvo, J. P., Verdelho, A., Leys, D., et al. (2007). Prognostic value of hyperintense vessel signals on fluid-attenuated inversion recovery sequences in acute cerebral ischemia. *Eur. Neurol.* 57, 75–79. doi: 10.1159/000098055

Grosch, A. S., Kufner, A., Boutitie, F., Cheng, B., Ebinger, M., Endres, M., et al. (2020). Extent of FLAIR Hyperintense Vessels May Modify Treatment Effect of Thrombolysis: a Post hoc Analysis of the WAKE-UP Trial. *Front. Neurol.* 11:623881. doi: 10.3389/fneur.2020.623881

Hacein-Bey, L., Mukundan, G., Shahi, K., Chan, H., and Tajlil, A. T. (2014). Hyperintense ipsilateral cortical sulci on FLAIR imaging in carotid stenosis: ivy sign equivalent from enlarged leptomeningeal collaterals. *Clin. Imaging* 38, 314–317. doi: 10.1016/j.clinimag.2013.12.013

Jiang, L., Chen, Y. C., Zhang, H., Peng, M., Chen, H., Geng, W., et al. (2019). FLAIR vascular hyperintensity in acute stroke is associated with collateralization and functional outcome. *Eur. Radiol.* 29, 4879–4888. doi: 10.1007/s00330-019-06022-0

Jiang, L., Peng, M., Chen, H., Geng, W., Zhao, B., Yin, X., et al. (2020a). Diffusion-weighted imaging (DWI) ischemic volume is related to FLAIR hyperintensity-DWI mismatch and functional outcome after endovascular therapy. *Quant. Imaging Med. Surg.* 10, 356–367. doi: 10.21037/qims.2019.12.05

Jiang, L., Peng, M., Geng, W., Chen, H., Su, H., Zhao, B., et al. (2020b). FLAIR hyperintensities-DWI mismatch in acute stroke: associations with DWI volume and functional outcome. *Brain Imaging Behav.* 14, 1230–1237. doi: 10.1007/s11682-019-00156-x

Kim, D. H., Lee, Y. K., and Cha, J. K. (2019). Prominent FLAIR Vascular Hyperintensity Is a Predictor of Unfavorable Outcomes in Non-thrombolysed Ischemic Stroke Patients With Mild Symptoms and Large Artery Occlusion. *Front. Neurol.* 10:722. doi: 10.3389/fneur.2019.00722

Kim, S. E., Lee, B. I., Kim, S. E., Shin, K. J., Park, J., Park, K. M., et al. (2016). Clinical Significance of Fluid-Attenuated Inversion Recovery Vascular Hyperintensities in Borderzone Infarcts. *Stroke* 47, 1548–1554. doi: 10.1161/STROKEAHA.115.012285

Kobayashi, J., Uehara, T., Toyoda, K., Endo, K., Ohara, T., Fujinami, J., et al. (2013). Clinical significance of fluid-attenuated inversion recovery vascular hyperintensities in transient ischemic attack. *Stroke* 44, 1635–1640. doi: 10.1161/STROKEAHA.111.000787

Kufner, A., Galinovic, I., Ambrosi, V., Nolte, C. H., Endres, M., Fiebach, J. B., et al. (2015). Hyperintense Vessels on FLAIR: hemodynamic Correlates and Response to Thrombolysis. *AJNR Am. J. Neuroradiol.* 36, 1426–1430. doi: 10.3174/ajnr.A4320

Lee, K. Y., Kim, J. W., Park, M., Suh, S. H., and Ahn, S. J. (2021). Interpretation of fluid-attenuated inversion recovery vascular hyperintensity in stroke. *J. Neuroradiol.* S0150-9861, 00034–1. doi: 10.1016/j.neurad.2021.01.009

Lee, K. Y., Latour, L. L., Luby, M., Hsia, A. W., Merino, J. G., and Warach, S. (2009). Distal hyperintense vessels on FLAIR: an MRI marker for collateral circulation in acute stroke? *Neurology* 72, 1134–1139. doi: 10.1212/01.wnl.0000345360.80382.69

Lee, S. H., Seo, K. D., Kim, J. H., Suh, S. H., Ahn, S. J., and Lee, K. Y. (2016). Correlation between Hyperintense Vessels on FLAIR Imaging and Arterial Circulation Time on Cerebral Angiography. *Magn. Reson. Med. Sci.* 15, 105–110. doi: 10.2463/mrms.2015-0006

Legrand, L., Tisserand, M., Turc, G., Edjlali, M., Calvet, D., Trystram, D., et al. (2016). Fluid-Attenuated Inversion Recovery Vascular Hyperintensities-Diffusion-Weighted Imaging Mismatch Identifies Acute Stroke Patients Most Likely to Benefit From Recanalization. *Stroke* 47, 424–427. doi: 10.1161/STROKEAHA.115.010999

Legrand, L., Tisserand, M., Turc, G., Naggara, O., Edjlali, M., Mellerio, C., et al. (2015). Do FLAIR vascular hyperintensities beyond the DWI lesion represent the ischemic penumbra? *AJNR Am. J. Neuroradiol.* 36, 269–274. doi: 10.3174/ajnr.A4088

Legrand, L., Turc, G., Edjlali, M., Beaumont, M., Gautheron, V., Ben, H. W., et al. (2019). Benefit from revascularization after thrombectomy according to FLAIR vascular hyperintensities-DWI mismatch. *Eur. Radiol.* 29, 5567–5576. doi: 10.1007/s00330-019-06094-y

Li, C. C., Hao, X. Z., Tian, J. Q., Yao, Z. W., Feng, X. Y., and Yang, Y. M. (2018). Predictors of short-term outcome in patients with acute middle cerebral artery occlusion: unsuitability of fluid-attenuated inversion recovery vascular hyperintensity scores. *Neural. Regen. Res.* 13, 69–76. doi: 10.4103/1673-5374.224375

Li, G., Huang, R., and Bi, G. (2021). The impact of FLAIR vascular hyperintensity on clinical severity and outcome : a retrospective study in stroke patients with proximal middle cerebral artery stenosis or occlusion. *Neurol. Sci.* 42, 589–598. doi: 10.1007/s10072-020-04513-3

Liu, D., Scalzo, F., Rao, N. M., Hinman, J. D., Kim, D., Ali, L. K., et al. (2016). Fluid-Attenuated Inversion Recovery Vascular Hyperintensity Topography, Novel Imaging Marker for Revascularization in Middle Cerebral Artery Occlusion. *Stroke* 47, 2763–2769. doi: 10.1161/STROKEAHA.116.013953

Liu, W., Xu, G., Yue, X., Wang, X., Ma, M., Zhang, R., et al. (2011). Hyperintense vessels on FLAIR: a useful non-invasive method for assessing intracerebral collaterals. *Eur. J. Radiol.* 80, 786–791. doi: 10.1016/j.ejrad.2010.09.043

Maeda, M., Koshimoto, Y., Uematsu, H., Yamada, H., Kimura, H., Kawamura, Y., et al. (2001). Time course of arterial hyperintensity with fast fluid-attenuated inversion-recovery imaging in acute and subacute middle cerebral arterial infarction. *J. Magn. Reson. Imaging* 13, 987–990. doi: 10.1002/jmri.1142

Mahdjoub, E., Turc, G., Legrand, L., Benzakoun, J., Edjlali, M., Seners, P., et al. (2018). Do Fluid-Attenuated Inversion Recovery Vascular Hyperintensities Represent Good Collaterals before Reperfusion Therapy? *AJNR Am. J. Neuroradiol.* 39, 77–83. doi: 10.3174/ajnr.A5431

Maruyama, D., Yamada, T., Murakami, M., Fujiwara, G., Komaru, Y., Nagakane, Y., et al. (2021). FLAIR vascular hyperintensity with DWI for regional collateral flow and tissue fate in recanalized acute middle cerebral artery occlusion. *Eur. J. Radiol.* 135:109490. doi: 10.1016/j.ejrad.2020.109490

Nam, K. W., Kim, C. K., Kim, T. J., Oh, K., Han, M. K., Ko, S. B., et al. (2018). FLAIR vascular hyperintensities predict early ischemic recurrence in TIA. *Neurology* 90, e738–e744. doi: 10.1212/WNL.0000000000005034

Nam, K. W., Kwon, H. M., Park, S. W., Lim, J. S., Han, M. K., and Lee, Y. S. (2017). Distal hyperintense vessel sign is associated with neurological deterioration in acute ischaemic stroke. *Eur. J. Neurol.* 24, 617–623. doi: 10.1111/ene.13259

Nomura, T., Okamoto, K., Igarashi, H., Watanabe, M., Hasegawa, H., Oishi, M., et al. (2020). Vascular Hyperintensity on Fluid-Attenuated Inversion Recovery Indicates the Severity of Hypoperfusion in Acute Stroke. *J. Stroke Cerebrovasc. Dis.* 29:104467. doi: 10.1016/j.jstrokecerebrovasdis.2019.104467

Olindo, S., Chausson, N., Joux, J., Saint, V. M., Signate, A., Edimonana-Kapute, M., et al. (2012). Fluid-attenuated inversion recovery vascular hyperintensity: an early predictor of clinical outcome in proximal middle cerebral artery occlusion. *Arch. Neurol.* 69, 1462–1468. doi: 10.1001/archneurol.2012.1310

Pérez, D. L. O. N., Hernández-Pérez, M., Domènech, S., Cuadras, P., Massuet, A., Millán, M., et al. (2012). Hyperintensity of distal vessels on FLAIR is associated with slow progression of the infarction in acute ischemic stroke. *Cerebrovasc. Dis.* 34, 376–384. doi: 10.1159/000343658

Sakuta, K., Saji, N., Aoki, J., Sakamoto, Y., Shibazaki, K., Iguchi, Y., et al. (2016). Decrease of Hyperintense Vessels on Fluid-Attenuated Inversion Recovery Predicts Good Outcome in t-PA Patients. *Cerebrovasc. Dis.* 41, 211–218. doi: 10.1159/000443533

Sanossian, N., Saver, J. L., Alger, J. R., Kim, D., Duckwiler, G. R., Jahan, R., et al. (2009). Angiography reveals that fluid-attenuated inversion recovery vascular hyperintensities are due to slow flow, not thrombus. *AJNR Am. J. Neuroradiol.* 30, 564–568. doi: 10.3174/ajnr.A1388

Shang, W. J., Chen, H. B., Shu, L. M., Liao, H. Q., Huang, X. Y., Xiao, S., et al. (2019). The Association between FLAIR Vascular Hyperintensity and Stroke Outcome Varies with Time from Onset. *AJNR Am. J. Neuroradiol.* 40, 1317–1322. doi: 10.3174/ajnr.A6142

Shin, D. H., Han, S. K., Lee, J. H., Choi, P. C., Park, S. O., Lee, Y. H., et al. (2020). Proximal hyper-intense vessel sign on initial FLAIR MRI in hyper-acute middle cerebral artery ischemic stroke: a retrospective observational study. *Acta Radiol.* 62, 922–931. doi: 10.1177/0284185120946718

Wang, E., Wu, C., Yang, D., Zhao, X., Zhao, J., Chang, H., et al. (2021). Association between fluid-attenuated inversion recovery vascular hyperintensity and outcome varies with different lesion patterns in patients with intravenous thrombolysis. *Stroke Vasc. Neurol.* 6, 449–457. doi: 10.1136/svn-2020-000641

Wang, Y., Zhou, Z., and Ding, S. (2020). FLAIR vascular hyperintensity-DWI mismatch most likely to benefit from recanalization and good outcome after stroke. *Medicine* 99:e18665. doi: 10.1097/MD.0000000000018665

Yoshioka, K., Ishibashi, S., Shiraishi, A., Yokota, T., and Mizusawa, H. (2013). Distal hyperintense vessels on FLAIR images predict large-artery stenosis in patients with transient ischemic attack. *Neuroradiology* 55, 165–169. doi: 10.1007/s00234-012-1092-y

Yuan, T., Ren, G., Hu, X., Geng, L., Li, X., Xia, S., et al. (2019). Added assessment of middle cerebral artery and atrial fibrillation to FLAIR vascular hyperintensity-DWI mismatch would improve the outcome prediction of acute infarction in patients with acute internal carotid artery occlusion. *Neurol. Sci.* 40, 2617–2624. doi: 10.1007/s10072-019-04029-5

Zhou, Z., Malavera, A., Yoshimura, S., Delcourt, C., Mair, G., Al-Shahi, S. R., et al. (2020a). Clinical prognosis of FLAIR hyperintense arteries in ischaemic stroke patients: a systematic review and meta-analysis. *J. Neurol. Neurosurg. Psychiatry* 91, 475–482. doi: 10.1136/jnnp-2019-322625

Zhou, Z., Yoshimura, S., Delcourt, C., Lindley, R. I., You, S., Malavera, A., et al. (2020b). Thrombolysis Outcomes in Acute Ischemic Stroke by Fluid-Attenuated Inversion Recovery Hyperintense Arteries. *Stroke* 51, 2240–2243. doi: 10.1161/STROKEAHA.119.028550

Zhu, L., Gong, S., Zhu, X., Zhang, R., Ren, K., Zhu, Z., et al. (2020). FLAIR vascular hyperintensity: an unfavorable marker of early neurological deterioration and short-term prognosis in acute ischemic stroke patients. *Ann. Palliat. Med.* 9, 3144–3151. doi: 10.21037/apm-20-1175

Conflict of Interest: The authors declare that the research was conducted in the absence of any commercial or financial relationships that could be construed as a potential conflict of interest.

Publisher's Note: All claims expressed in this article are solely those of the authors and do not necessarily represent those of their affiliated organizations, or those of the publisher, the editors and the reviewers. Any product that may be evaluated in this article, or claim that may be made by its manufacturer, is not guaranteed or endorsed by the publisher.

frontiers in Aging Neuroscience

ORIGINAL RESEARCH
published: 26 January 2022
doi: 10.3389/fnagi.2021.815562

Gut Microbiota Alteration Is Associated With Cognitive Deficits in Genetically Diabetic (Db/db) Mice During Aging

Jiawei Zhang†, Yaxuan Zhang†, Yuan Yuan, Lan Liu, Yuwu Zhao and Xiuzhe Wang**

Department of Neurology, Shanghai Jiao Tong University Affiliated Sixth People's Hospital, Shanghai, China

Recent studies have revealed that the microbiota may be implicated in diabetes-related cognitive dysfunction. However, the relationship between gut microbiota and cognitive dysfunction during the progression of type 2 diabetes remains elusive. We used 16S rRNA sequencing combined with conventional behavioral tests to explore the longitudinal changes of gut microbiota and cognition in diabetic db/db mice (leptin receptor knockout mice) and their wild-type littermates at different ages. Prussian blue staining was performed to detect the microhemorrhage in the brain, and immunofluorescent study was applied to analyze microglia activation. Moreover, a Meso Scale Discovery kit was used to determine the cytokine levels in the brain. Db/db mice exhibited age dependent pathological characteristics, including cognitive deficits, neuron damage, spontaneous hemorrhages and neuroinflammation. Furthermore, we observed that the diversity and composition of gut microbiota significantly differed between the wild-type and db/db mice during aging. We found that compared to age-matched wild-type mice, genus Helicobacter was significant higher in db/db mice at 18 and 26 weeks. Correlation analysis revealed that Helicobacter is positively associated with Iba-1 positive cells and TNF-α expression. Collectively, our longitudinal study suggests that diabetic cognitive impairment during aging is associated with abnormal gut microbiota composition, which may play a role in the regulation of neuroinflammation.

Keywords: type 2 diabetes, cognitive dysfunction, gut microbiota, neuroinflammation, aging

OPEN ACCESS

Edited by:
Ulises Gomez-Pinedo, Instituto de Investigación Sanitaria del Hospital Clínico San Carlos, Spain

Reviewed by:
Gerard M. Moloney, University College Cork, Ireland
Weidong Le, Dalian Medical University, China

****Correspondence:***
Yuwu Zhao
zhaoyuwu2005@126.com
Xiuzhe Wang
xiuzhewang@hotmail.com

† These authors have contributed equally to this work

Specialty section:
This article was submitted to Neurocognitive Aging and Behavior, a section of the journal Frontiers in Aging Neuroscience

Received: *15 November 2021*
Accepted: *15 December 2021*
Published: *26 January 2022*

Citation:
Zhang J, Zhang Y, Yuan Y, Liu L, Zhao Y and Wang X (2022) Gut Microbiota Alteration Is Associated With Cognitive Deficits in Genetically Diabetic (Db/db) Mice During Aging. Front. Aging Neurosci. 13:815562. doi: 10.3389/fnagi.2021.815562

INTRODUCTION

Type 2 diabetes (T2DM) is a chronic metabolic disorder and its prevalence is on the rise throughout the world. It causes serious complications in various organs, including the central nervous system (Zhao et al., 2019). Numerous studies have reported that diabetic patients have a high risk of developing cognitive impairment which is also termed as "diabetes-related cognitive dysfunction" (Umegaki, 2018; Liu et al., 2020; van Sloten et al., 2020). Diabetes-related cognitive dysfunction is manifested as decreased learning and memory, weakened executive ability, and emotional disturbance. Considering the prevalence of T2DM, diabetes-related cognitive dysfunction will inevitably bring arduous challenges and an immeasurable economic burden to social public health. Nevertheless, the knowledge on diabetes-related cognitive dysfunction is still insufficient, and

available treatments for this complication are currently not effective enough. Therefore, it is imperative to explore the underlying pathogenesis of cognitive dysfunction caused by diabetes, and new strategies to delay or reduce the occurrence of the disease are needed.

As a metabolic disease, T2DM coexists with chronic inflammation, which has been considered as a key factor that contributed to the development of neurodegenerative diseases (Sankar et al., 2020). Studies have shown that neuroinflammation caused by persistent over-activation of microglia is implicated in the pathophysiology of cognitive impairment (Jackson et al., 2020). Activated microglia can release a variety of neurotoxic pro-inflammatory factors including Interleukin 6 (IL-6) and tumor necrosis factor α (TNF-α), which further activates microglia to aggravate neuroinflammation. The etiology of diabetes-related cognitive dysfunction may be multi-factorial. Recent studies have revealed that patients with T2DM and control subjects differed in gut microbiota composition (Karlsson et al., 2013; Bakir-Gungor et al., 2021). Microbiota homeostasis is not only essential for the maintenance of gut health, but also affects central nervous system by regulating the release of neurotransmitters and inflammatory factors (Collins et al., 2012). A number of studies have shown that gut microbiota composition and diversity of Alzheimer's disease patients were different from those of healthy controls (Cattaneo et al., 2017; Sun et al., 2020). However, there are no relevant reports on how the gut microbiota changes with the progression of T2DM and whether it is related to diabetic cognitive dysfunction.

Given the potential role of gut microbiota in diabetes-related cognitive dysfunction, we undertook a comprehensive study to investigate the longitudinal changes of gut microbiota in db/db mice, a typical T2DM rodent model, using 16S ribosomal RNA sequencing combined with conventional behavioral tests and pathological analysis.

MATERIALS AND METHODS

Animals

Male db/db (BKS-Lepr^{em2Cd479}/Gpt) and age-matched WT (wild-type) (C57BLKS/JGpt) mice were purchased from Jiangsu GemPharmatech Biotechnology Co., Ltd. (Jiangsu, China) and housed in a specific pathogen-free animal center under controlled temperature (20–25°C) and light (12 h light/12 h dark) conditions, with water and food available *ad libitum* until 6, 18, and 26 weeks of age. Body weight and fasting blood glucose level was measured at the end of the experiment. All procedures were performed in accordance with the principles outlined in the National Institutes of Health (NIH) Guide for the Care and Use of Laboratory Animals. The study was approved by the ethical committee on animal welfare of Shanghai Jiao Tong University Affiliated Sixth People's Hospital.

Morris Water Maze Test

The Morris Water Maze (MWM) test was performed to measure the spatial learning and memory as we described previously (Zhang J. et al., 2021). The utilized maze consisted of a circular pool (height 50 cm, diameter 120 cm), divided into four quadrants, filled up to a depth of 30 cm with tepid water (25 ± 1°C). A submerged escape platform (10 cm in diameter) 1 cm below the water surface was used for training. The maze was surrounded by curtains with visual cues of four different shapes and sizes placed in the four quadrants. Hidden platform task consisted of four trials per day on 5 consecutive days. Mice were allowed to swim for a maximum trial duration of 60 s and with 10 s on the platform at the end of the trials. During each trial, the latency required to reach the platform was measured as the escape latency. The platform was withdrawn at the sixth day of training for probe trial. The mice were released from the 4th quadrant which is opposite to the target quadrant and allowed to navigate freely for 60 s. During the probe trial, the number of times across the retracted platform, the percentage of time spent in the target quadrant and the average swimming speed were recorded.

Novel Object Recognition Test

The NOR test was performed as described previously with slight modifications (Wang et al., 2020). In brief, on the first day, mice were habituated to experimental apparatus (40 cm × 40 cm × 50 cm) in the absence of objects for 5 min. On the second day, in the training phase, mice were exposed to two identical cubes which were fixed 9 cm from the wall for 5 min. A short-term memory test was performed 1 h later, mice were allowed to explore the apparatus for 5 min in the presence of the familiar cube and the novel triangular object. On the third day, to examine long-term memory, mice were allowed to explore the apparatus for 5 min in the presence of the familiar cube and the novel cylinder. In each phase, the amount of time mice spent exploring each object was recorded and the discrimination index was calculated as [(time with novel object − time with familiar object)/(time with novel object + time with familiar object)].

Nissl Staining

After behavioral experiments, mice were transcardially perfused with 0.9% saline followed by 4% paraformaldehyde. And then the brains were embedding in paraffin and sectioned into 8-μm thick slices by a microtome for further staining. Briefly, the brain sections were deparaffinized, gradually rehydrated in graded concentrations of ethanol, and treated with conventional Nissl staining solution and the images were obtained using an optical microscope (× 100 and × 400).

Prussian Blue Staining

The Prussian blue staining followed the procedures described previously (Villarreal et al., 2017). In short, slides were washed in distilled water and then immersed in a working solution of Prussian blue (5% hydrochloric acid and 5% potassium ferrocyanide). Slides were rinsed with distilled water and then counterstained for 5 min using Nuclear Fast Red. A final series of distilled water washes were performed before dehydration and being coverslipped. Then, the Prussian blue staining images were obtained using an optical microscope (× 40 and × 400).

Immunofluorescence Staining

Paraffin sections were deparaffinized, rehydrated, and subjected to heat-induced antigen retrieval using a microwave, then rinsed in distilled water. The sections were blocked in 3% bovine serum albumin (BSA, Servicebio) for 30 min, and then incubated in anti-Iba-1 primary antibody (1:500, mouse, servicebio) at 4°C overnight. On the second day, the sections were then rinsed in 0.01-M PBS (pH 7.4) and incubated with an anti-mouse HRP-conjugated secondary antibody for 1 h at room temperature. Finally, Immunoreactivity was visualized using diaminobenzidine tetrahydrochloride (DAB), and the sections were stained with hematoxylin and mounted. The localization and distribution of immunoreactive positive cells in the brain were observed using a microscope (× 40 and × 400, IX53, Olympus, Tokyo, Japan).

Meso Scale Discovery for Inflammatory Cytokines

The Meso Scale Discovery kit (MSD, Meso Scale Diagnostics, Rockville, MD, United States) was used for cytokine detection following the manufacturer's instructions. Briefly, the whole brain was lysed and protein supernatants were quantified using a BCA kit. Fifty microliter of sample and standard were added in antibody-coated 96-well plates for incubation followed by washing three times with PBST. And then 25 μl of the prepared detection antibody was added to each well and the plates were sealed with parafilm and shaked at room temperature for 2 h. After washing three times with PBST, 150 μl of reading buffer was added in the plates. Cytokine levels were determined using a MESOTM QuickPlex SQ 120 (Meso Scale Diagnostics, Rockville, MD, United States).

16S rRNA Gene Sequencing of Fecal Samples

DNA from fecal samples was extracted using the E.Z.N.A.® Stool DNA Kit (D4015, Omega, Inc., United States) according to manufacturer's instructions. The V3-V4 region of the prokaryotic (bacterial and archaeal) small-subunit (16S) rRNA gene was amplified with universal primers 341F and 805R. The 5′ ends of the primers were tagged with specific barcodes per sample and sequencing universal primers. The PCR products were purified by AMPure XT beads (Beckman Coulter Genomics, Danvers, MA, United States) and quantified by Qubit (Invitrogen, United States). The amplicon pools were prepared for sequencing and the size and quantity of the amplicon library were assessed on Agilent 2100 Bioanalyzer (Agilent, United States) and with the Library Quantification Kit for Illumina (Kapa Biosciences, Woburn, MA, United States), respectively. The libraries were sequenced on NovaSeq PE250 platform.

Statistical Analysis

Statistical analysis was performed using GraphPad Prism 7 (GraphPad Software Inc., La Jolla, CA). The data were presented as mean ± standard error of the mean (SEM). Differences between groups were performed using one-way analysis of variance (ANOVA) followed by a false discovery rate (FDR) correction for multiple comparisons. Correlation analysis was conducted using Spearman rank correlation analysis. For the hidden-platform training of the Morris water maze test, the escape latency was analyzed by two-way repeated-measures ANOVA followed by Tukey's *post hoc* test. Statistical significance was set at $p < 0.05$.

RESULTS

Learning and Memory Performance Was Impaired in Db/db Mice

Consistent with previous studies, the db/db mice in our study developed T2DM with age. Compared with age-matched WT mice, db/db mice had a phenotype of increased blood glucose and weight gain at 6 weeks, but the phenotype became more obvious as time reached 18 weeks or even 26 weeks (**Figures 1A–C**). To determine the effect of T2DM and age on cognitive function, spatial learning and memory performance was assessed via Morris water maze in 6, 18, and 26 weeks db/db and WT mice. The results revealed that the latency to reach the platform of WT mice was not statistically different acrossing the age, as indicated by a non-significant difference in the latency from 1st to 5th days at the age of 6, 18, and 26 weeks (**Figure 1D**). Db/db mice showed an age-dependent decline in the learning capacity indicated by a significant increase in the escape latency on the 4th and 5th days at the age of 18 and 26 weeks in comparison to 6 weeks (**Figure 1D**). For the factor T2DM, no significant difference was observed in 6-week-old WT and db/db mice. However, a significant effect of T2DM was observed at the age of 18 weeks, with db/db mice consistently taking longer time to reach the platform than WT mice, especially on the 4th and 5th days. A similar performance was observed in 26-week-old db/db mice as compared to age-matched WT mice (**Figure 1D**). To evaluate memory preservation, mice were subjected to a probe trial 24 h after the last training session. The number of times across the retracted platform and the percentage of time spent in the target quadrant were taken as an index of mice's memory capacity. The analysis revealed that 18- and 26-week-old db/db mice showed difficulties remembering where the platform was originally placed and spent significantly shorter time in the target quadrant when compared to the rest of the groups (**Figures 1E,F**), supporting the cognitive impairment observed during the training phase.

We also routinely assessed the motor function of the mice and found that the swimming speed of the db/db mice at 18 and 26 weeks was significantly slower than that of the other groups (**Figure 1G**). To ensure that the cognitive dysfunction observed in the MWM were not attributed to the limitation in locomotor activity, NOR, a test less affected by motor ability, was used to further evaluate the cognitive impairment in mice. The analysis revealed that the discrimination index of WT and db/db mice at the age of 6 weeks was no statistically significant difference. At the age of 18 and 26 weeks, WT mice performed normally as shown by a significantly higher discrimination index for the novel object compared to the familiar object, while no significant difference discrimination index was found for the age-matched

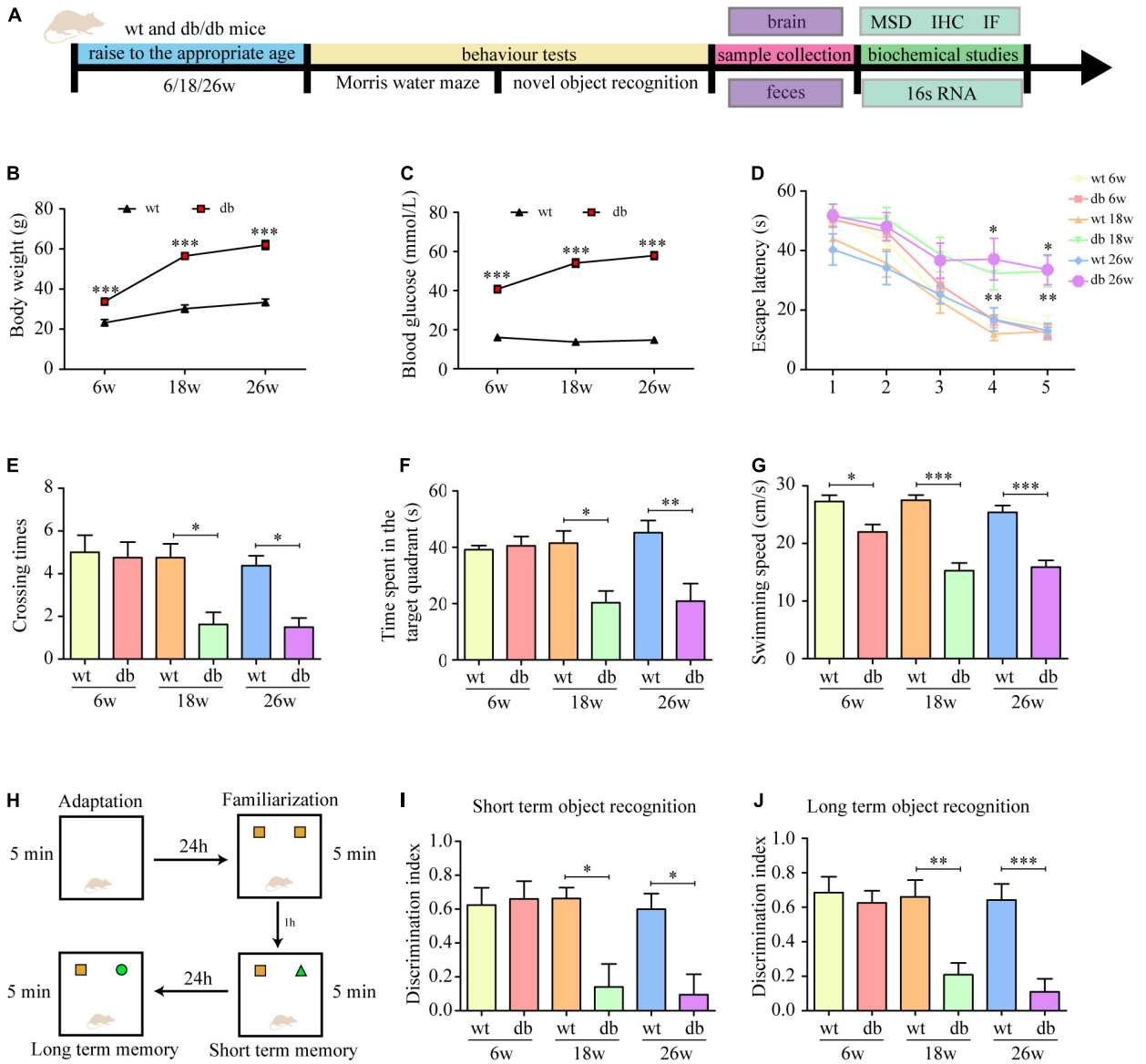

FIGURE 1 | Learning and memory performance was impaired in db/db mice. **(A)** Schematic diagram of the experimental procedure. **(B)** Body weight at different ages. **(C)** Blood glucose at different ages. **(D)** The escape latency of mice in the training trials of the hidden platform task. **(E)** Frequency of platform crossing in the probe trial. **(F)** Percentage of time spent in the target quadrant in the probe trial. **(G)** Swimming speed in the probe trial. **(H)** The experimental design of novel object recognition test. **(I)** The discrimination index of 1 h test trials. **(J)** The discrimination index of 24 h test trials. (n = 8 per group); $^{*}P < 0.05$; $^{**}P < 0.01$; $^{***}P < 0.001$.

db/db mice (**Figures 1H–J**), indicating memory impairment of these mice. Collectively, the results in the behavioral tests indicate that learning and memory performance is impaired during the progression of T2DM in db/db mice.

Brain Pathology Was Severe in Db/db Mice

Subsequently, Nissl staining was performed to assess the pathological morphology of neuronal cells in mouse brain. Nissl body is an indicator that reflects the functional state of neurons. When neurons are damaged, the Nissl bodies would decrease or even disappear. We found that the neurons exhibited a normal morphology with distinct nuclei and abundant Nissl bodies in the cytoplasm in the WT mice of all ages (**Figures 2A–C**). On the other hand, the neurons randomly showed nuclear condensation, sparse Nissl bodies and abnormal staining at 18 and 26 weeks of age in db/db mice (**Figures 2A–C**).

It is reported that microhemorrhage is a common pathological feature of db/db mice. Therefore, Prussian blue staining was used to further detect the microhemorrhage in the brain tissue of each group of mice. The results revealed that only negligible microhemorrhages could be detected in 6-week-old db/db and WT mice. However, significant increase number

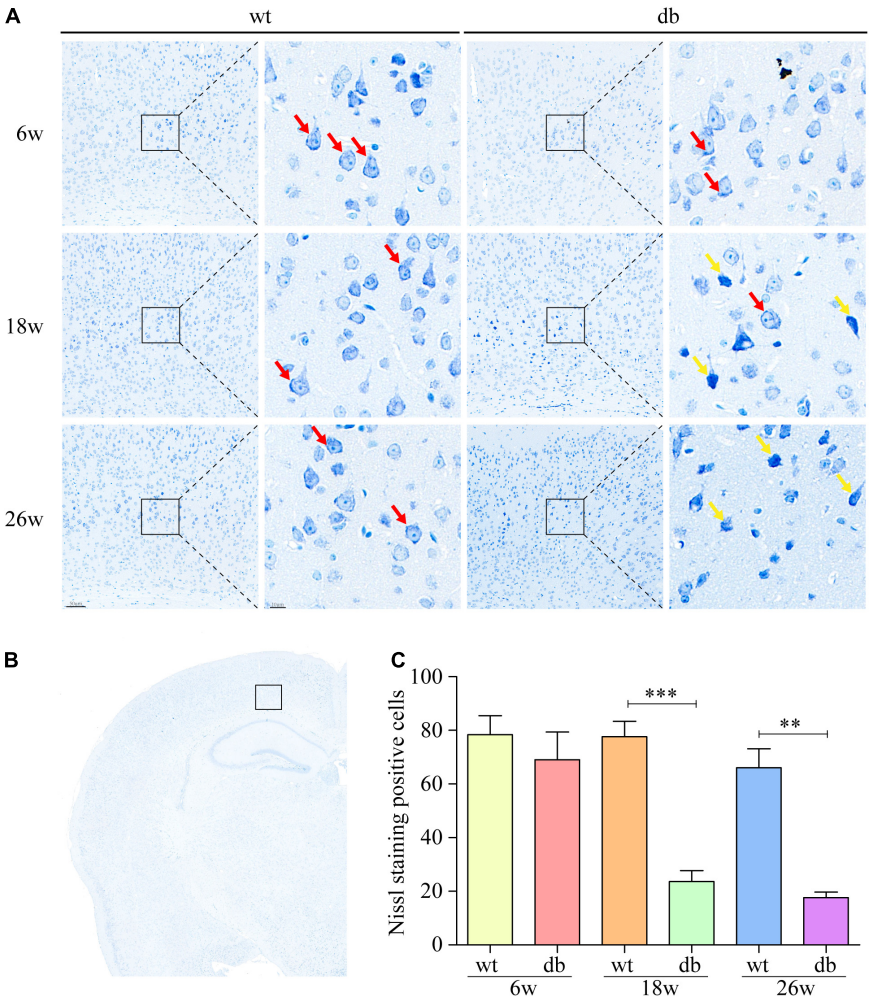

FIGURE 2 | Nissl staining was used to analyze the pathological changes of neuronal cells in mice. **(A,B)** Representative Nissl staining of neurons in the cortex at different ages. Scale bar = 50 or 10 μm. The red arrow points to the Nissl body. The yellow arrow points to damaged neurons. **(C)** Quantitative analysis of Nissl body positive cells. (n = 3 per group); $^{**}P < 0.01$; $^{***}P < 0.001$.

of microhemorrhages were observed in db/db mice at the age of 18 and 26 weeks when compared to age-matched WT mice (**Figures 3A,B**). Taken together, these results indicate that the pathological changes of brain tissues aggravate during the progression of T2DM in db/db mice.

Neuroinflammation Was Prominent in Db/db Mice

To evaluate the role of neuroinflammation on T2DM-mediated cognitive dysfunction and neuron injury, microglial activation was assessed by quantifying Iba-1 immunoreactivity and the production of pro-inflammatory cytokines, including IL-6 and TNF-α. Analysis showed that Iba-1 positive cells in the hippocampus and cortex were not significantly different between db/db and WT mice at 6 weeks of age. At 18 and 26 weeks of age, db/db mice displayed a significant increase of activated microglia in both the hippocampus and cortex compared to the age-matched WT mice (**Figures 4A–C**). We further evaluated the expression of pro-inflammatory cytokines including IL-6 and TNF-α in the whole brain. Analysis by MSD revealed that IL-6 and TNF-α expressions remained unaffected in both WT and db/db mice at 6 weeks of age, whereas a dramatically increase of IL-6 and TNF-α expressions were observed in 18-week-old db/db mice compared with WT mice. At 26 weeks of age, when compared with WT mice, the expression of TNF-α in db/db mice was significantly increased, and the trend of IL-6 expression was consistent with TNF-α but without significant statistical difference (**Figures 4D,E**). The results demonstrate that T2DM could promote microglia activation and subsequent production of pro-inflammatory cytokines in db/db mice with age.

Alterations in Gut Microbiome Composition in Db/db Mice

To delineate the influence of T2DM and age on the diversity of gut microbiota, we use the UpSet plot, an advanced

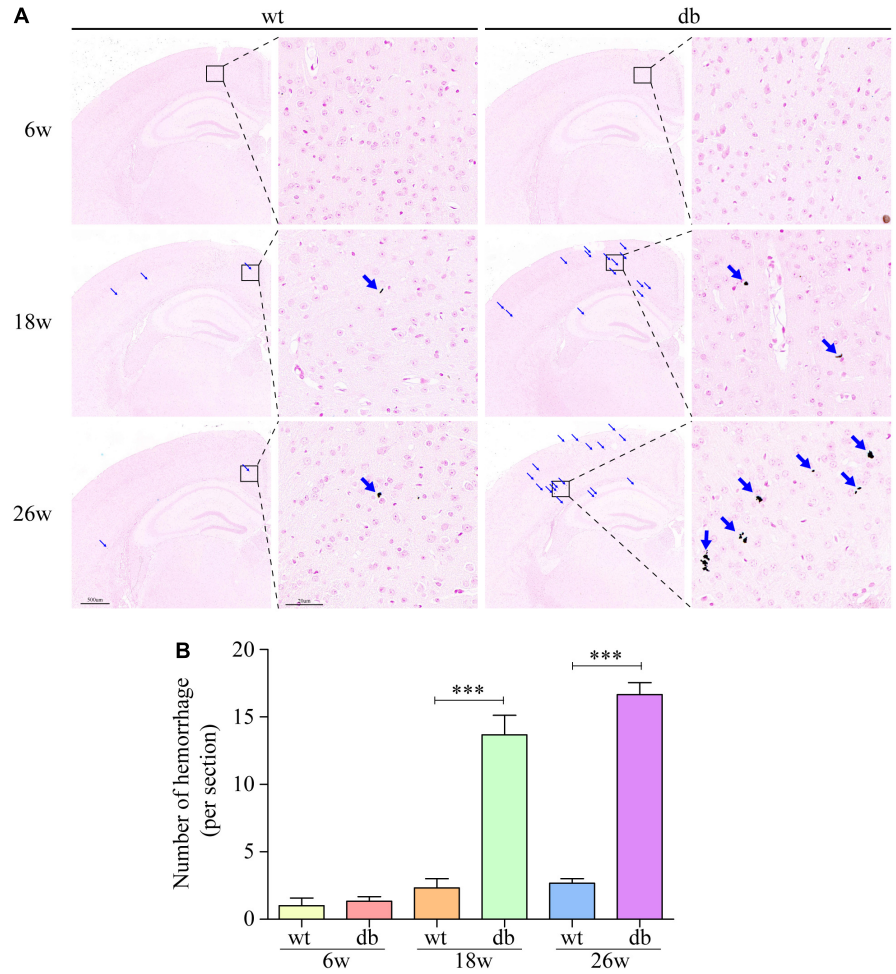

FIGURE 3 | Prussian blue staining was used to detect the microhemorrhage in mice. **(A)** Representative images of hemorrhages in the cortex. Scale bar = 500 or 20 μm. The red arrow points to the hemorrhages. **(B)** Quantitative analysis of hemorrhages. (n = 3 per group); $^{***}P < 0.001$.

Venn diagram, for the quantitative analysis of sets and their intersections (Ballarini et al., 2020). The analysis showed that the number of gut microbiota increased with age in both WT and db/db mice, whereas WT mice increased significantly compared with age-matched db/db mice. Intriguingly, the intersection of db/db mice and age-matched WT mice decreased with age (**Figure 5A**). To further determine the differences of gut microbiota diversity, the alpha and beta diversities were evaluated. The within-sample alpha diversity analysis showed a significant decrease in gut microbial community evenness and richness of 18- and 26-week-old db/db mice compared with age-matched WT mice based on Chao 1, Observed-otus, and Shannon indices. The alpha diversity showed a slight decrease in db/db mice than in WT mice at 6 weeks of age, but the result was not significant difference (**Figures 5B–D**). Principal coordinate analysis (PCoA) based on unweighted Unifrac was used to measure beta diversity and visualize the bacterial composition dissimilarity among each group. The analysis showed that the cluster for db/db mice was similar to WT mice at the age of 6 weeks. Nevertheless, the clusters for db/db mice were clear separated from WT mice at 18 and 26 weeks of age (**Figure 5E**). Overall, these results suggest that both T2DM and age have an effect on the gut microbiota composition of db/db mice.

Differentially Represented Bacterial Taxa in Db/db Mice

The analysis of the gut microbiota composition at the phylum and genus levels showed specific differences between the WT and db/db mice at different ages. Among the common bacterial communities, Bacteroidetes, Firmicutes, Proteobacteria, Actinobacteria, and Verrucomicrobia were the main five phyla present in the gut microbiota of all groups (**Figures 6A,B**). Many studies have shown that obesity and diabetes mellitus are closely related to the ratio of Firmicutes to Bacteroidetes (Ley et al., 2005; Grigor'eva, 2020; Hung et al., 2021). However, the results revealed a slight increase of the Firmicutes/Bacteroidetes ratio in db/db mice than in WT mice at each age, but without significant difference (**Figure 6C**). In addition, no significant differences were observed in microbiota composition between

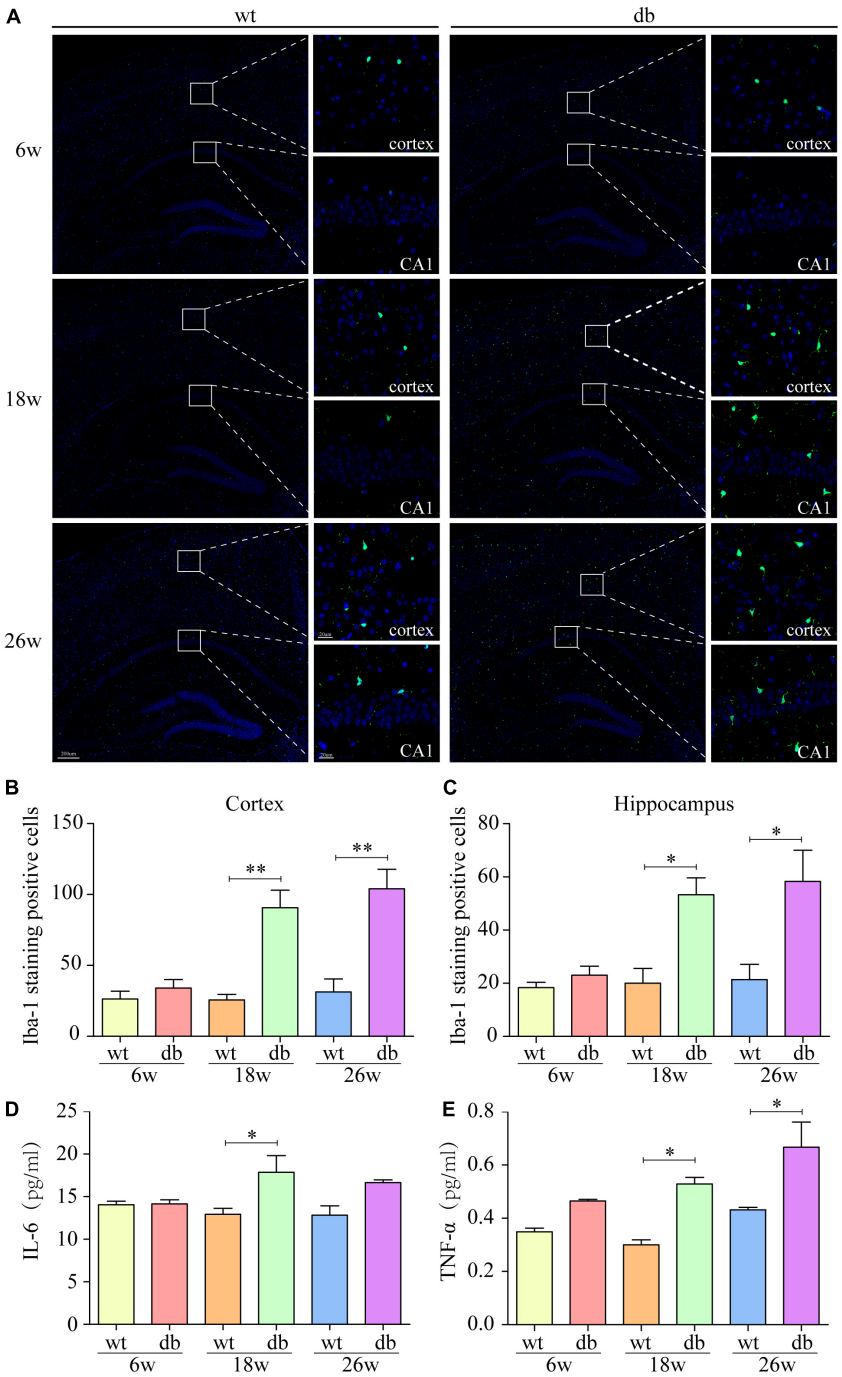

FIGURE 4 | Increased microgliosis and pro-inflammatory cytokines in db/db mice with age. **(A)** Representative immunofluorescent staining of Iba-1-positive microglia in the cortex and hippocampus of mice. Scale bar = 200 or 20 μm. **(B,C)** Quantification of Iba-1-staining positive cells within the cortex or the hippocampus. **(D,E)** MSD was performed to detect the protein levels of IL-6 and TNF-α. (n = 3 per group); $^{*}P < 0.05$; $^{**}P < 0.01$.

the 6-week-old db/db and WT mice at the phylum or genus level (**Figures 6**, **7**). Compared to age-matched WT mice, the relative abundance of phylum Proteobacteria, phylum Deferribacteres, and genus Helicobacter were significant higher in db/db mice at 18 weeks, whereas the relative abundance of genus Akkermansia and genus Barnesiella were significant lower in db/db mice at 18 weeks (**Figures 6D,F**, **7B,E**). Moreover, compared to age-matched WT mice, the relative abundance of phylum Epsilonbacteraeota, genus Helicobacter, and genus Parabacteroides increased significantly in db/db mice at 26 weeks, whereas the relative abundance of genus Akkermansia, genus Barnesiella, genus Bacteroidales-unclassified, and

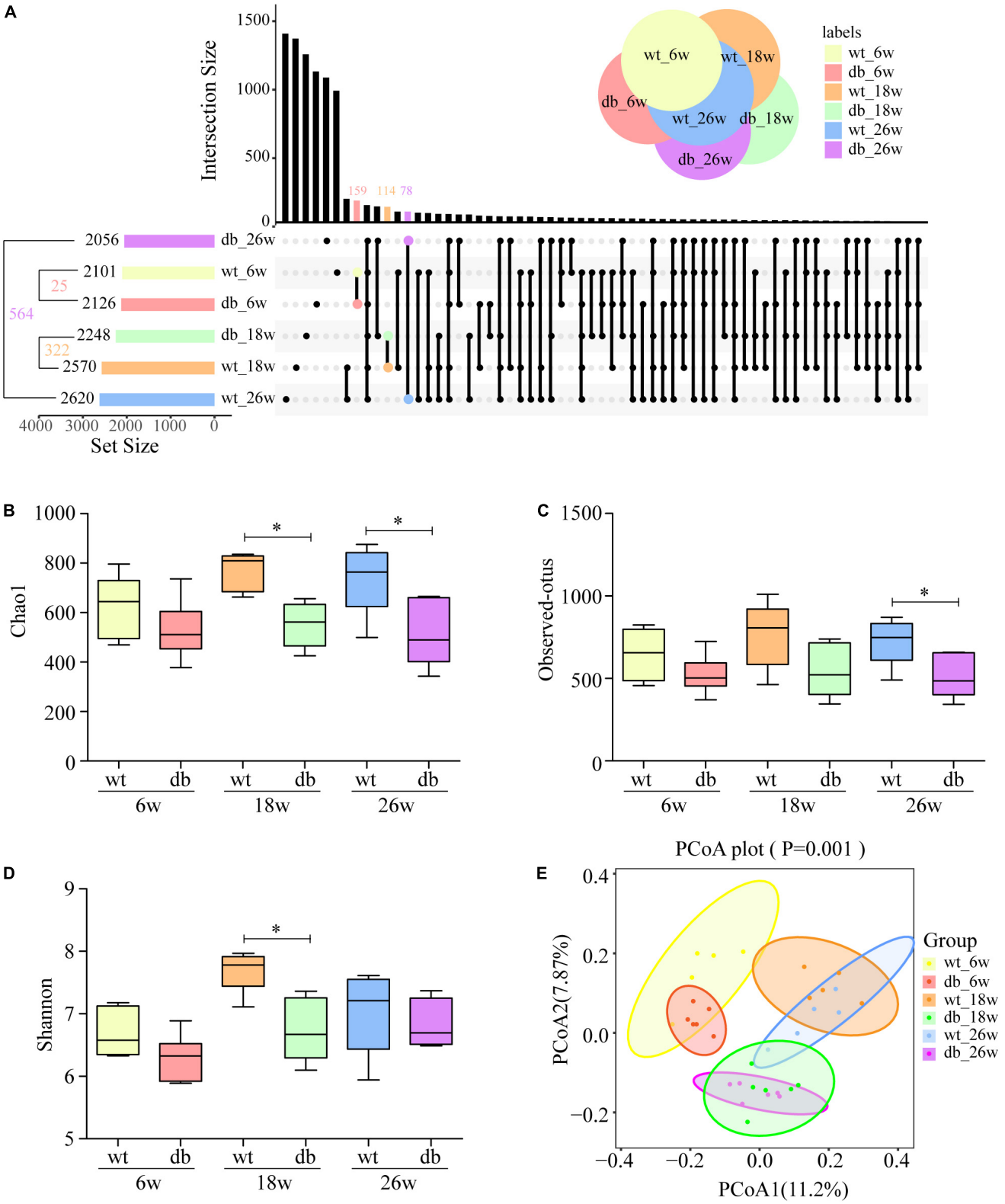

FIGURE 5 | Alpha and beta diversities of the gut microbiota in db/db mice with age. **(A)** UpSet plot for the quantitative analysis of sets and intersections in each group. **(B–D)** Variation in alpha diversity (Chao1, Observed-otus, and Shannon) in mice at different ages. **(E)** PCoA analysis of gut microbiota. (n = 6 per group); $^*P < 0.05$.

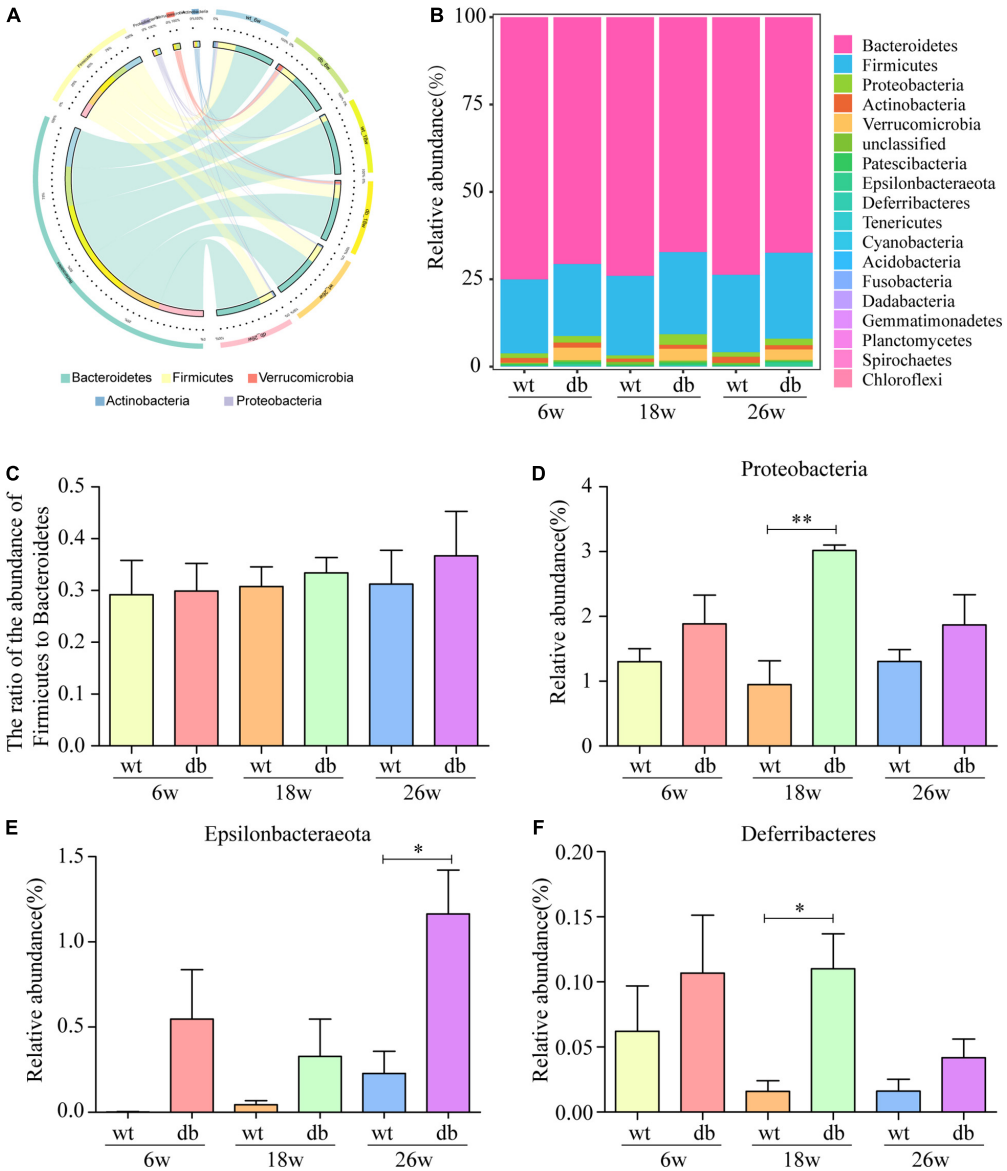

FIGURE 6 | Alteration of gut microbiota composition in db/db mice at the phylum level. **(A,B)** The Circos and bar chart of common bacterial communities in each group. **(C)** The ratio of the abundance of Firmicutes to Bacteroidetes in each group. **(D–F)** The relative abundance of three bacterial communities in each group. (n = 6 per group); *P < 0.05; **P < 0.01.

genus Prevotellaceae-UCG-001 decreased significantly in db/db mice at 26 weeks (**Figures 6E**, **7B–G**). The results above collectively indicate that the abundance of several gut bacteria differ significantly between the WT and db/db mice as T2DM progresses.

Correlation Analysis of Mouse Phenotypes and Gut Bacteria

Spearman correlation analysis was used to evaluate the significant difference between mouse phenotypes and phylum/genus-level gut bacteria. At the phylum level, the relative abundance of Bacteroidetes was positively associated with crossing times and Nissl staining positive cells while negatively correlated with body weight, Iba-1 positive cells, and the expression of TNF-α (**Figure 8A**). Firmicutes was positively correlated with the number of hemorrhage while negatively correlated with crossing times (**Figure 8A**). The change in Epsilonbacteraeota levels was positively associated with body weight, Iba-1 positive cells, and the expression of TNF-α (**Figure 8A**). At the genus level, correlation analysis revealed a positive association between the relative abundance of Helicobacter and body weight, Iba-1 positive cells, and the expression of TNF-α (**Figure 8B**). Muribaculaceae-unclassified was negatively correlated with body weight, blood glucose, Iba-1 positive cells, and the expression of TNF-α (**Figure 8B**).

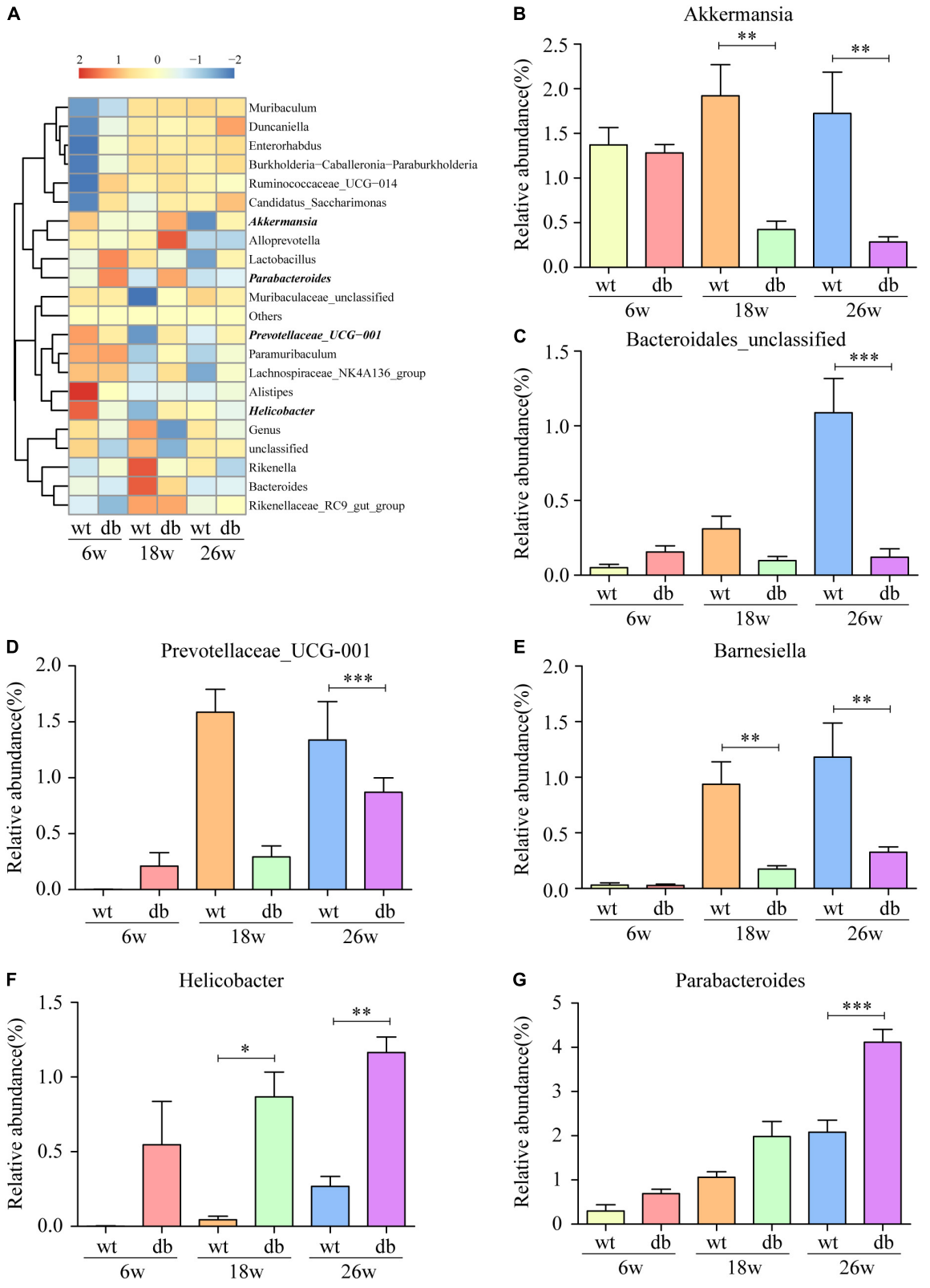

FIGURE 7 | Alteration of gut microbiota composition in db/db mice at the genus level. **(A)** Community heatmap at the genus level. **(B–G)** The relative abundance of six bacterial communities in each group. (n = 6 per group); *P < 0.05; **P < 0.01; ***P < 0.001.

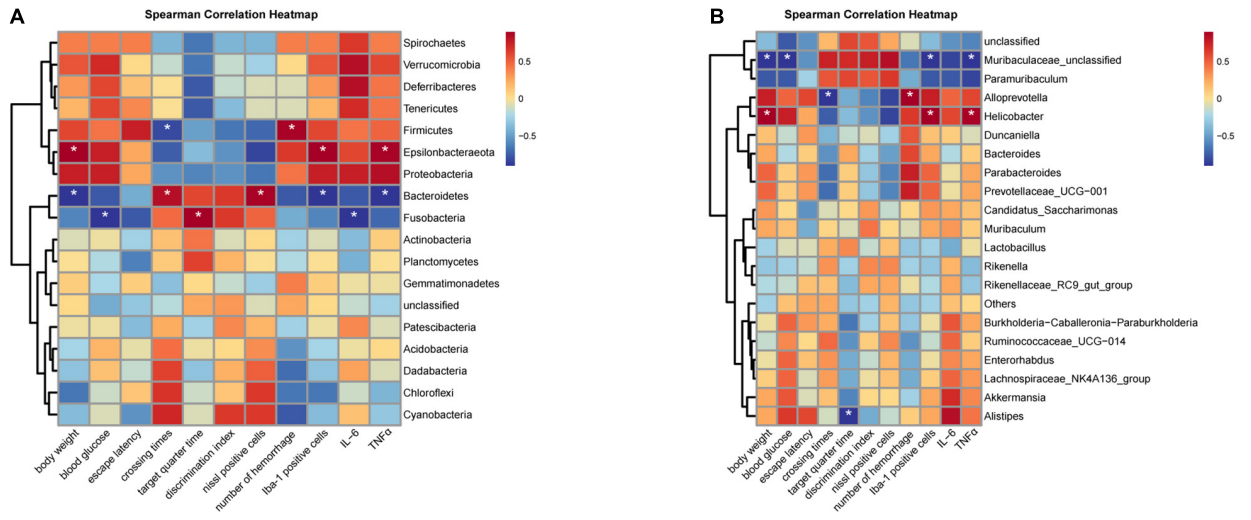

FIGURE 8 | Heatmaps showing correlations between phenotypes and gut microbiota. **(A)** Correlation analysis at the phylum level. **(B)** Correlation analysis at the genus level. (n = 6 per group); *P < 0.05.

DISCUSSION

Recent studies have shown possible links between gut microbiota and T2DM-related cognitive dysfunction (Yu et al., 2019; Zhang Y. et al., 2021). However, there is no report on the relationship between gut microbiota and cognitive dysfunction during the progression of T2DM. Therefore, we investigated the longitudinal changes of gut microbiota and cognition in db/db mice from an early age, using 16S ribosomal RNA sequencing combined with conventional behavioral tests.

In the present study, we used db/db mice, a typical T2DM mouse model, to characterize the natural progression of the metabolic disorder and its effect on pathological changes of the central nervous system, especially cognitive function. Similar to previous reports, we observed that db/db mice exhibited obesity and hyperglycemia phenotypes with age, indicating that a stable T2DM phenotype was formed. It has been reported that aged db/db mice have an increased risk of spontaneous hemorrhage compared with mice without diabetes and are closely related to cognitive deficits (Ramos-Rodriguez et al., 2013). Consistently, our study also found that spontaneous hemorrhage became more pronounced as diabetes progressed in db/db mice. The above data are in accordance with clinical studies that prolonged hyperglycemia is associated with microvascular complications (Kruyt et al., 2010; Luitse et al., 2012). Evidence shows that diabetes is closely related to cognitive dysfunction, and both the level of hyperglycemia and the duration of diabetes are associated with cognitive dysfunction (Rawlings et al., 2019). Recent epidemiological studies have found that compared with non-diabetic individuals, diabetic patients have an increased risk of cognitive dysfunction and even dementia (Huang et al., 2014). The MWM is widely used to assess spatial learning and memory. Previous studies have reported that the cognitive function of diabetic mice is impaired, and it worsens with the prolongation of diabetes (Ramos-Rodriguez et al., 2013). Similar to the previous study, our study found that the pre-diabetic mice (6 weeks of age) performed well at the MWM, but when the db/db mice reached 18 weeks of age, obvious cognitive dysfunction appeared, showing inferior learning and memory performance. Since the swimming speed of db/db mice at 18 and 26 weeks was significantly slower than that of the WT group, it may be considered that the behavioral results were biased due to the high body weight of these mice. However, the swimming speed of obese db/db mice at 6 weeks has already decreased, while spatial learning and memory are almost unaffected, indicating the synergistic effect of diabetes and age. NOR is a test less affected by motor ability (Ennaceur and Delacour, 1988). We further applied NOR analysis and confirmed the reliability of MWM, indicating that learning and memory capacities decrease with the progression of T2DM.

Neuroinflammation, including activation of glial cells and secretion of inflammatory cytokines, is increasingly recognized as the underlying pathogenesis of diabetes-associated cognitive dysfunction (Marioni et al., 2010; Dinel et al., 2011). Iba-1 is widely used as a specific marker of microglia. In the present study, we found that compared with WT mice, the number of Iba-1-positive cells in db/db mice showed a significant increase in the cortex and hippocampus as diabetes progressed, which is in consistent with the previous work where they showed that diabetes-induced cognitive dysfunction was accompanied by microgliosis (Infante-Garcia et al., 2017). It has also been reported that the levels of pro-inflammatory factors IL-6 and TNF-α are significantly increased in both STZ-induced diabetic rats and db/db mice (Miao et al., 2015; Lee and Yang, 2019). Consistently, our study found that the levels of IL-6 and TNF-α in db/db mice at 18 and 26 weeks were significantly higher than those in age-matched WT mice.

The gut microbiota, composed of trillions of symbiotic microorganisms, is essential for host's health and survival (Fung et al., 2017). In addition, microbial diversity usually increases after birth, and microbial composition changes gradually during

late childhood, adolescence, and adulthood (Odamaki et al., 2016; Kundu et al., 2017; Chen et al., 2020). We observed a trend toward increased diversity and richness from 6 to 26 weeks in both WT and db/db mice as indicated by the UpSet plot, Chao 1, Observed-otus, and Shannon indices, suggesting aging is an important factor affecting microbial composition. Moreover, the gut microbiota has been implicated to play an important role in regulating immunity and metabolism (Petra et al., 2015; Ochoa-Reparaz and Kasper, 2016) and in the development of obesity and T2DM (Ten Kulve et al., 2015, 2016; Wijdeveld and Nieuwdorp, 2020). It has been reported that short-chain fatty acids derived from the metabolites of Akkermansia muciniphila can bind to a few G protein-coupled receptors to activate signaling pathways and participate in the regulation of blood glucose levels (Zhai et al., 2019). Previous studies have also shown that abnormal blood glucose levels were related to changes in gut microbiota (Tilg and Moschen, 2014; Wen and Duffy, 2017). The increase in blood glucose has been reported to be accompanied with an decrease in the relative abundance of Bacteroides acidifaciens, Butyricimonas virosa, Bacteroides eggerthii, and Desulfovibrio oxamicus in the gut (Zheng et al., 2021). From PCoA results, we found that the clusters of db/db mice at 18 and 26 weeks were significantly separated from the clusters of age-matched WT mice, indicating that the gut composition changes as T2DM progresses. Furthermore, we observed that the differences in bacterial taxa between the WT and db/db mice increased with age, which coincides with the progression of cognitive dysfunction and microglial activation in db/db mice. Growing evidence reports that the gut microbiota plays a preeminent role in the pathogenesis of central nervous system diseases via the gut–brain axis (Mayer, 2011). Previous study has demonstrated that the gut microbiota composition and relative abundance were strongly associated with cognitive dysfunction in STZ-induced diabetic mice (Yu et al., 2019). We found that compared to age-matched WT mice, the relative abundance of phylum Proteobacteria, phylum Deferribacteres, and genus Helicobacter were significant higher in db/db mice at 18 weeks, whereas the relative abundance of genus Akkermansia and genus Barnesiella were significant lower in db/db mice at 18 weeks. Akkermansia muciniphila, a mucin-degrading bacteria that resides in the mucus layer, is considered as a promising probiotic candidate (Collado et al., 2007). It is reported that the abundance of Akkermansia inversely correlates with obesity and T2DM in mice and humans (Derrien et al., 2004; Belzer and de Vos, 2012; Everard et al., 2013). Recent studies have also shown that Akkermansia treatment reduces hippocampal microgliosis and proinflammatory cytokines by improving gut permeability, ultimately alleviating cognitive dysfunction of high-fat diet-fed mice (Yang et al., 2019). Altered Proteobacteria and Helicobacter composition has been reported to be implicated in inflammatory reactions and cognitive function (Kountouras et al., 2009; Shin et al., 2015; Berrett et al., 2016; Vogt et al., 2017). Similarly, we found that the increase in the relative abundance of Helicobacter is positively associated with body weight, Iba-1 positive cells, and the expression of TNF-α, suggesting that Helicobacter may be a sensitive indicator of neuroinflammation in db/db mice. We also observed that the number of crossing platforms is positively correlated with Bacteroidetes and negatively correlated with Firmicutes. These data provide potential non-invasive biomarkers for the diagnosis of diabetic cognitive dysfunction.

Overall, the current longitudinal research suggests that abnormal gut microbiota composition may contribute to diabetic cognitive impairment by regulating neuroinflammation. Nevertheless, future work is warranted to determine the underlying molecular mechanism of the gut microbiota on the diabetes-related cognitive dysfunction.

DATA AVAILABILITY STATEMENT

The datasets presented in this study can be found in online repositories. The name of the repository and accession number can be found below: National Center for Biotechnology (NCBI) BioProject (https://www.ncbi.nlm.nih.gov/bioproject/, PRJNA784719).

ETHICS STATEMENT

The animal study was reviewed and approved by the Ethical Committee on Animal Welfare of Shanghai Jiao Tong University Affiliated Sixth People's Hospital.

AUTHOR CONTRIBUTIONS

JZ and XW designed the study and contributed to the production of the manuscript. XW and YuZ supervised the research. JZ, YaZ, and YY performed the experiments. JZ and LL analyzed the data. All authors read and approved the final manuscript.

FUNDING

This study was supported by the research grants from National Natural Science Foundation of China (Grant No. 81974158) and National Facility for Translational Medicine (Shanghai) (Grant No. TMSK-2020-122).

REFERENCES

Bakir-Gungor, B., Bulut, O., Jabeer, A., Nalbantoglu, O. U., and Yousef, M. (2021). Discovering Potential Taxonomic Biomarkers of Type 2 Diabetes From Human Gut Microbiota via Different Feature Selection Methods. *Front. Microbiol.* 12:628426. doi: 10.3389/fmicb.2021.628426

Ballarini, N. M., Chiu, Y. D., Konig, F., Posch, M., and Jaki, T. (2020). A critical review of graphics for subgroup analyses in clinical trials. *Pharm. Stat.* 19, 541–560. doi: 10.1002/pst.2012

Belzer, C., and de Vos, W. M. (2012). Microbes inside–from diversity to function: the case of Akkermansia. *ISME J.* 6, 1449–1458. doi: 10.1038/ismej.2012.6

Berrett, A. N., Gale, S. D., Erickson, L. D., Brown, B. L., and Hedges, D. W. (2016). Folate and Inflammatory Markers Moderate the Association

Between *Helicobacter* pylori Exposure and Cognitive Function in US Adults. *Helicobacter* 21, 471–480. doi: 10.1111/hel.12303

Cattaneo, A., Cattane, N., Galluzzi, S., Provasi, S., Lopizzo, N., Festari, C., et al. (2017). Association of brain amyloidosis with pro-inflammatory gut bacterial taxa and peripheral inflammation markers in cognitively impaired elderly. *Neurobiol. Aging* 49, 60–68. doi: 10.1016/j.neurobiolaging.2016.08.019

Chen, Y., Fang, L., Chen, S., Zhou, H., Fan, Y., Lin, L., et al. (2020). Gut Microbiome Alterations Precede Cerebral Amyloidosis and Microglial Pathology in a Mouse Model of Alzheimer's Disease. *Biomed. Res. Int.* 2020:8456596. doi: 10.1155/2020/8456596

Collado, M. C., Derrien, M., Isolauri, E., de Vos, W. M., and Salminen, S. (2007). Intestinal integrity and Akkermansia muciniphila, a mucin-degrading member of the intestinal microbiota present in infants, adults, and the elderly. *Appl. Environ. Microbiol.* 73, 7767–7770. doi: 10.1128/AEM.01477-07

Collins, S. M., Surette, M., and Bercik, P. (2012). The interplay between the intestinal microbiota and the brain. *Nat. Rev. Microbiol.* 10, 735–742.

Derrien, M., Vaughan, E. E., Plugge, C. M., and de Vos, W. M. (2004). Akkermansia muciniphila gen. nov., sp. nov., a human intestinal mucin-degrading bacterium. *Int. J. Syst. Evol. Microbiol.* 54, 1469–1476. doi: 10.1099/ijs.0.02873-0

Dinel, A. L., Andre, C., Aubert, A., Ferreira, G., Laye, S., and Castanon, N. (2011). Cognitive and emotional alterations are related to hippocampal inflammation in a mouse model of metabolic syndrome. *PLoS One* 6:e24325. doi: 10.1371/journal.pone.0024325

Ennaceur, A., and Delacour, J. (1988). A new one-trial test for neurobiological studies of memory in rats. 1: Behavioral data. *Behav. Brain Res.* 31, 47–59. doi: 10.1016/0166-4328(88)90157-x

Everard, A., Belzer, C., Geurts, L., Ouwerkerk, J. P., Druart, C., Bindels, L. B., et al. (2013). Cross-talk between Akkermansia muciniphila and intestinal epithelium controls diet-induced obesity. *Proc. Natl. Acad. Sci. U S A.* 110, 9066–9071. doi: 10.1073/pnas.1219451110

Fung, T. C., Olson, C. A., and Hsiao, E. Y. (2017). Interactions between the microbiota, immune and nervous systems in health and disease. *Nat. Neurosci.* 20, 145–155. doi: 10.1038/nn.4476

Grigor'eva, I. N. (2020). Gallstone Disease, Obesity and the Firmicutes/Bacteroidetes Ratio as a Possible Biomarker of Gut Dysbiosis. *J. Pers. Med.* 11:13. doi: 10.3390/jpm11010013

Huang, C. C., Chung, C. M., Leu, H. B., Lin, L. Y., Chiu, C. C., Hsu, C. Y., et al. (2014). Diabetes mellitus and the risk of Alzheimer's disease: a nationwide population-based study. *PLoS One* 9:e87095. doi: 10.1371/journal.pone.0087095

Hung, W. C., Hung, W. W., Tsai, H. J., Chang, C. C., Chiu, Y. W., Hwang, S. J., et al. (2021). The Association of Targeted Gut Microbiota with Body Composition in Type 2 Diabetes Mellitus. *Int. J. Med. Sci.* 18, 511–519. doi: 10.7150/ijms.51164

Infante-Garcia, C., Jose Ramos-Rodriguez, J., Marin-Zambrana, Y., Teresa Fernandez-Ponce, M., Casas, L., Mantell, C., et al. (2017). Mango leaf extract improves central pathology and cognitive impairment in a type 2 diabetes mouse model. *Brain Pathol.* 27, 499–507. doi: 10.1111/bpa.12433

Jackson, L., Dumanli, S., Johnson, M. H., Fagan, S. C., and Ergul, A. (2020). Microglia knockdown reduces inflammation and preserves cognition in diabetic animals after experimental stroke. *J. Neuroinflamm.* 17:137. doi: 10.1186/s12974-020-01815-3

Karlsson, F. H., Tremaroli, V., Nookaew, I., Bergstrom, G., Behre, C. J., Fagerberg, B., et al. (2013). Gut metagenome in European women with normal, impaired and diabetic glucose control. *Nature* 498, 99–103. doi: 10.1038/nature12198

Kountouras, J., Boziki, M., Gavalas, E., Zavos, C., Grigoriadis, N., Deretzi, G., et al. (2009). Eradication of *Helicobacter* pylori may be beneficial in the management of Alzheimer's disease. *J. Neurol.* 256, 758–767.

Kruyt, N. D., Biessels, G. J., DeVries, J. H., Luitse, M. J., Vermeulen, M., Rinkel, G. J., et al. (2010). Hyperglycemia in aneurysmal subarachnoid hemorrhage: a potentially modifiable risk factor for poor outcome. *J. Cereb. Blood Flow Metab.* 30, 1577–1587. doi: 10.1038/jcbfm.2010.102

Kundu, P., Blacher, E., Elinav, E., and Pettersson, S. (2017). Our Gut Microbiome: The Evolving Inner Self. *Cell* 171, 1481–1493. doi: 10.1016/j.cell.2017.11.024

Lee, H. J., and Yang, S. J. (2019). Supplementation with Nicotinamide Riboside Reduces Brain Inflammation and Improves Cognitive Function in Diabetic Mice. *Int. J. Mol. Sci.* 20:4196. doi: 10.3390/ijms20174196

Ley, R. E., Backhed, F., Turnbaugh, P., Lozupone, C. A., Knight, R. D., and Gordon, J. I. (2005). Obesity alters gut microbial ecology. *Proc. Natl. Acad. Sci. U S A.* 102, 11070–11075. doi: 10.1073/pnas.0504978102

Liu, T., Lee, J. E., Wang, J., Ge, S., and Li, C. (2020). Cognitive Dysfunction in Persons with Type 2 Diabetes Mellitus: A Concept Analysis. *Clin. Nurs. Res.* 29, 339–351. doi: 10.1177/1054773819862973

Luitse, M. J., Biessels, G. J., Rutten, G. E., and Kappelle, L. J. (2012). Diabetes, hyperglycaemia, and acute ischaemic stroke. *Lancet Neurol.* 11, 261–271. doi: 10.1016/s1474-4422(12)70005-4

Marioni, R. E., Strachan, M. W., Reynolds, R. M., Lowe, G. D., Mitchell, R. J., Fowkes, F. G., et al. (2010). Association between raised inflammatory markers and cognitive decline in elderly people with type 2 diabetes: the Edinburgh Type 2 Diabetes Study. *Diabetes* 59, 710–713. doi: 10.2337/db09-1163

Mayer, E. A. (2011). Gut feelings: the emerging biology of gut-brain communication. *Nat. Rev. Neurosci.* 12, 453–466. doi: 10.1038/nrn3071

Miao, Y., He, T., Zhu, Y., Li, W., Wang, B., and Zhong, Y. (2015). Activation of Hippocampal CREB by Rolipram Partially Recovers Balance Between TNF-alpha and IL-10 Levels and Improves Cognitive Deficits in Diabetic Rats. *Cell Mol. Neurobiol.* 35, 1157–1164. doi: 10.1007/s10571-015-0209-3

Ochoa-Reparaz, J., and Kasper, L. H. (2016). The Second Brain: Is the Gut Microbiota a Link Between Obesity and Central Nervous System Disorders? *Curr. Obes. Rep.* 5, 51–64. doi: 10.1007/s13679-016-0191-1

Odamaki, T., Kato, K., Sugahara, H., Hashikura, N., Takahashi, S., Xiao, J. Z., et al. (2016). Age-related changes in gut microbiota composition from newborn to centenarian: a cross-sectional study. *BMC Microbiol.* 16:90. doi: 10.1186/s12866-016-0708-5

Petra, A. I., Panagiotidou, S., Hatziagelaki, E., Stewart, J. M., Conti, P., and Theoharides, T. C. (2015). Gut-Microbiota-Brain Axis and Its Effect on Neuropsychiatric Disorders With Suspected Immune Dysregulation. *Clin. Ther.* 37, 984–995. doi: 10.1016/j.clinthera.2015.04.002

Ramos-Rodriguez, J. J., Ortiz, O., Jimenez-Palomares, M., Kay, K. R., Berrocoso, E., Murillo-Carretero, M. I., et al. (2013). Differential central pathology and cognitive impairment in pre-diabetic and diabetic mice. *Psychoneuroendocrinology* 38, 2462–2475. doi: 10.1016/j.psyneuen.2013.05.010

Rawlings, A. M., Sharrett, A. R., Albert, M. S., Coresh, J., Windham, B. G., Power, M. C., et al. (2019). The Association of Late-Life Diabetes Status and Hyperglycemia With Incident Mild Cognitive Impairment and Dementia: The ARIC Study. *Diab. Care* 42, 1248–1254. doi: 10.2337/dc19-0120

Sankar, S. B., Infante-Garcia, C., Weinstock, L. D., Ramos-Rodriguez, J. J., Hierro-Bujalance, C., Fernandez-Ponce, C., et al. (2020). Amyloid beta and diabetic pathology cooperatively stimulate cytokine expression in an Alzheimer's mouse model. *J. Neuroinflamm.* 17:38. doi: 10.1186/s12974-020-1707-x

Shin, N. R., Whon, T. W., and Bae, J. W. (2015). *Proteobacteria*: microbial signature of dysbiosis in gut microbiota. *Trends Biotechnol.* 33, 496–503. doi: 10.1016/j.tibtech.2015.06.011

Sun, M., Ma, K., Wen, J., Wang, G., Zhang, C., Li, Q., et al. (2020). A Review of the Brain-Gut-Microbiome Axis and the Potential Role of Microbiota in Alzheimer's Disease. *J. Alzheimers Dis.* 73, 849–865. doi: 10.3233/JAD-190872

Ten Kulve, J. S., Veltman, D. J., van Bloemendaal, L., Barkhof, F., Deacon, C. F., Holst, J. J., et al. (2015). Endogenous GLP-1 mediates postprandial reductions in activation in central reward and satiety areas in patients with type 2 diabetes. *Diabetologia* 58, 2688–2698. doi: 10.1007/s00125-015-3754-x

Ten Kulve, J. S., Veltman, D. J., van Bloemendaal, L., Barkhof, F., Drent, M. L., Diamant, M., et al. (2016). Liraglutide Reduces CNS Activation in Response to Visual Food Cues Only After Short-term Treatment in Patients With Type 2 Diabetes. *Diab. Care* 39, 214–221. doi: 10.2337/dc15-0772

Tilg, H., and Moschen, A. R. (2014). Microbiota and diabetes: an evolving relationship. *Gut* 63, 1513–1521. doi: 10.1136/gutjnl-2014-306928

Umegaki, H. (2018). Diabetes-related cognitive dysfunction: Hyperglycemia in the early stage might be a key? *J. Diab. Investig.* 9, 1019–1021. doi: 10.1111/jdi.12808

van Sloten, T. T., Sedaghat, S., Carnethon, M. R., Launer, L. J., and Stehouwer, C. D. A. (2020). Cerebral microvascular complications of type 2 diabetes: stroke, cognitive dysfunction, and depression. *Lancet Diabetes Endocrinol.* 8, 325–336. doi: 10.1016/S2213-8587(19)30405-X

Villarreal, S., Zhao, F., Hyde, L. A., Holder, D., Forest, T., Sondey, M., et al. (2017). Chronic Verubecestat Treatment Suppresses Amyloid

Accumulation in Advanced Aged Tg2576-AbetaPPswe Mice Without Inducing Microhemorrhage. *J. Alzheimers Dis.* 59, 1393–1413. doi: 10.3233/JAD-170056

Vogt, N. M., Kerby, R. L., Dill-McFarland, K. A., Harding, S. J., Merluzzi, A. P., Johnson, S. C., et al. (2017). Gut microbiome alterations in Alzheimer's disease. *Sci. Rep.* 7:13537.

Wang, H. Y., Wu, M., Diao, J. L., Li, J. B., Sun, Y. X., and Xiao, X. Q. (2020). Huperzine A ameliorates obesity-related cognitive performance impairments involving neuronal insulin signaling pathway in mice. *Acta Pharmacol. Sin.* 41, 145–153. doi: 10.1038/s41401-019-0257-1

Wen, L., and Duffy, A. (2017). Factors Influencing the Gut Microbiota, Inflammation, and Type 2 Diabetes. *J. Nutr.* 147, 1468S–1475S. doi: 10.3945/jn.116.240754

Wijdeveld, M., and Nieuwdorp, M. (2020). R IJ: The interaction between microbiome and host central nervous system: the gut-brain axis as a potential new therapeutic target in the treatment of obesity and cardiometabolic disease. *Expert Opin. Ther. Targets* 24, 639–653. doi: 10.1080/14728222.2020.1761958

Yang, Y., Zhong, Z., Wang, B., Xia, X., Yao, W., Huang, L., et al. (2019). Early-life high-fat diet-induced obesity programs hippocampal development and cognitive functions via regulation of gut commensal Akkermansia muciniphila. *Neuropsychopharmacology* 44, 2054–2064. doi: 10.1038/s41386-019-0437-1

Yu, F., Han, W., Zhan, G., Li, S., Xiang, S., Zhu, B., et al. (2019). Abnormal gut microbiota composition contributes to cognitive dysfunction in streptozotocin-induced diabetic mice. *Aging* 11, 3262–3279. doi: 10.18632/aging.101978

Zhai, Q., Feng, S., Arjan, N., and Chen, W. (2019). A next generation probiotic, Akkermansia muciniphila. *Crit. Rev. Food Sci. Nutr.* 59, 3227–3236.

Zhang, J., Zheng, Y., Zhao, Y., Zhang, Y., Liu, Y., Ma, F., et al. (2021). Andrographolide ameliorates neuroinflammation in APP/PS1 transgenic mice. *Int. Immunopharmacol.* 96:107808. doi: 10.1016/j.intimp.2021.107808

Zhang, Y., Lu, S., Yang, Y., Wang, Z., Wang, B., Zhang, B., et al. (2021). The diversity of gut microbiota in type 2 diabetes with or without cognitive impairment. *Aging Clin. Exp. Res.* 33, 589–601. doi: 10.1007/s40520-020-01553-9

Zhao, Q., Zhang, F., Yu, Z., Guo, S., Liu, N., Jiang, Y., et al. (2019). HDAC3 inhibition prevents blood-brain barrier permeability through Nrf2 activation in type 2 diabetes male mice. *J. Neuroinflamm.* 16:103. doi: 10.1186/s12974-019-1495-3

Zheng, S., Wang, Y., Fang, J., Geng, R., Li, M., Zhao, Y., et al. (2021). Oleuropein Ameliorates Advanced Stage of Type 2 Diabetes in db/db Mice by Regulating Gut Microbiota. *Nutrients* 13:2131. doi: 10.3390/nu13072131

Conflict of Interest: The authors declare that the research was conducted in the absence of any commercial or financial relationships that could be construed as a potential conflict of interest.

Publisher's Note: All claims expressed in this article are solely those of the authors and do not necessarily represent those of their affiliated organizations, or those of the publisher, the editors and the reviewers. Any product that may be evaluated in this article, or claim that may be made by its manufacturer, is not guaranteed or endorsed by the publisher.

frontiers in Cellular Neuroscience

CASE REPORT
published: 01 February 2022
doi: 10.3389/fncel.2022.811596

Spinal Muscular Atrophy Type IIIb Complicated by Moyamoya Syndrome: A Case Report and Literature Review

*Jing Li, Xin Li, Liqun Wang and Guode Wu**

Department of Neurology, Lanzhou University Second Hospital, Lanzhou, China

Spinal muscular atrophy (SMA) is an inherited disorder characterized by degeneration of motor neurons and symmetrical muscle weakness and atrophy. Moyamoya syndrome (MMS) or moyamoya disease (MMD) is radiologically defined by chronic cerebrovascular occlusion with abnormal vascular network formation in the skull base. We report herein a 21-year-old female patient with limb weakness and muscular atrophy for 17 years. Electromyography revealed extensive motor neuron damage. Cranial MRA showed occlusion of bilateral anterior and middle cerebral arteries, with increased peripheral blood vessels and collateral circulation. She was diagnosed as SMA type IIIb combined with MMS following genetic testing, in which homozygous deletion of exons 7 and 8 of survival motor neuron (SMN)1 gene and 3 copies of exons 7 and 8 of *SMN2* gene were detected. After treatment, the patient's symptoms improved. Our study found that the rare SMA and MMS co-exist. We speculated that the moyamoya phenomenon may be related to the abnormal regulation of intracranial vascular endothelial cells and smooth muscle cells in proliferation and differentiation caused by functional defects of SMN protein. The relationship between the two diseases needs to be further elucidated in future clinical work.

Keywords: spinal muscular atrophy, *SMN* gene, SMN protein, moyamoya syndrome, moyamoya disease

OPEN ACCESS

Edited by:
Yuzhen Xu,
Tongji University, China

Reviewed by:
Wanjin Chen,
First Affiliated Hospital of Fujian Medical University, China
Tadanori Hamano,
University of Fukui, Japan

****Correspondence:***
Guode Wu
wgdlzh@163.com

Specialty section:
This article was submitted to Cellular Neuropathology, a section of the journal Frontiers in Cellular Neuroscience

Received: *09 November 2021*
Accepted: *11 January 2022*
Published: *01 February 2022*

Citation:
Li J, Li X, Wang L and Wu G (2022) Spinal Muscular Atrophy Type IIIb Complicated by Moyamoya Syndrome: A Case Report and Literature Review. Front. Cell. Neurosci. 16:811596. doi: 10.3389/fncel.2022.811596

INTRODUCTION

Spinal muscular atrophy (SMA) is a rare neuromuscular disease resulting from the deletion or mutation of the survival motor neuron (SMN) 1 gene (Ross and Kwon, 2019). It has a prevalence of about 1/6,000–1/11,000, carrying rate ∼1/35–1/50 (Alías et al., 2014; Gidaro and Servais, 2019). Moyamoya disease (MMD) is an unexplained disease characterized by progressive stenosis and occlusion of the terminal internal carotid arteries (ICAs) and the beginning of its proximal branches, leading to the formation of an abnormal vascular network at the base of the brain (Oshima and Katayama, 2012). Secondary moyamoya disease is named moyamoya syndrome (MMS) if the moyamoya vasculopathy is associated with other diseases (Scott and Smith, 2009; Li et al., 2019). It is commonly seen in sickle cell anemia, neurofibromatosis type I, Down syndrome, and diffuse toxic goiter etc. (Scott and Smith, 2009; Vargiami et al., 2014; Li et al., 2019; Yamani et al., 2020; Nakamura et al., 2021). However, MMS associated with SMA has not been reported. To improve the understanding of the relationship between SMA and moyamoya vasculopathy, the clinical and electrophysiological

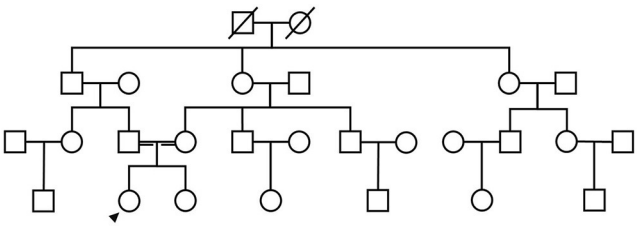

FIGURE 1 | The patient's family diagram shows that the patient's parents were cousins, and the patient (black arrow) was the only SMA patient in the family.

findings, gene detection, and imaging features of a patient with both SMA and MMS were analyzed, the report is as follows.

CASE PRESENTATION

A 21-year-old female undergraduate patient was referred to the Lanzhou University Second Hospital on March 10, 2021, due to limb weakness with muscle atrophy for 17 years. Seventeen years before admission, the patient had limb weakness without obvious inducement, especially in the lower limbs. She could lift the upper limbs and clench the fist but could not hold heavy objects with hands intermittent trembling. The weakness of the lower limbs was mainly manifested as difficulty in squatting and standing up, needing the help of foreign objects to get up, being unable to climb mountains and stairs, sometimes falling. She gradually developed muscle atrophy and thinning of limbs, especially atrophy of upper arms and thighs without limb numbness, coldness, pain, or other paresthesia. She had no abnormal beating sensation of skin and muscles, no fluctuating of symptoms as mild in the morning and severe in the evening, no blepharoptosis or restricted eye movement, no dysphagia or choking cough when drinking water or slurred speech, no weakness of head lifting or neck turning or shoulder shrugging, no dyspnea or cough weakness and so on. Seventeen years ago, her family brought the patient to Tianshui People's Hospital, where X-ray examinations of limbs, shoulder joints, and pelvis were completed. No obvious abnormalities were found in all of them, and no special treatment was given. Three years ago, she was admitted to The Second Xiangya Hospital of Central South University, and her electromyography (EMG) examination showed abnormalities (no report form was found, and neither the patient nor her family members could describe the specific results in detail), which failed to further clarify the diagnosis. Since then, the patient has been treated intermittently with Ginkgo biloba leaf (40 mg/time, three times a day) without significant improvement. During the disease, the above symptoms were not relieved or progressively aggravated. Then the patient was admitted to the inpatient department of neurology in our hospital with "hereditary peripheral neuropathy." The patient's birth history and growth history were unremarkable. The parents were healthy, consanguineous (cousins; **Figure 1**), and none of the other family members exhibited any similar clinical anomalies.

FIGURE 2 | Muscle atrophy in the limbs of the patient, especially the proximal lower limbs. **(A)** Front view and **(B)** Side view.

We first performed neurological and physical examinations of the patient. The patient showed stable vital signs, no obvious abnormalities in cardiopulmonary and abdominal examination, and clear consciousness, fluent speech, good cooperation, appropriate answer to question. A test of higher cortical function was normal. The 12 pairs of cranial nerve examinations were negative. The muscle volume of the proximal limbs decreased (**Figure 2**). The muscle strength of the proximal upper limbs was grade 4, the distal upper limbs grade 4 +, the proximal lower limbs grade 3 +, the distal lower limbs grade 4. The muscle tension of the extremities was normal, the tendon reflex was weakened, the deep and superficial sensation was symmetrical, and the bilateral pathological signs were negative. The bilateral rotation test, finger-nose test, heel-knee-shin test were all stable. The neck was flaccid with no resistance and the meningeal irritation sign was negative. She had arched foot and duck-like gait.

Next, a series of laboratory examinations such as blood, urine and stool routine, liver and kidney functions, electrolytes, coagulation profile, thyroid function test, anemia test, tumor markers detection, myocardial enzyme, plasma ammonia, cortisol rhythm, adrenocorticotropic hormone, and arterial blood gas analysis showed no significant abnormalities. Lumbar puncture pressure was in the normal range. The cerebrospinal fluid routine, biochemical and bacteriological tests were normal. Electrocardiogram (ECG), chest radiography and cardiac color ultrasound showed no significant abnormalities. Furthermore, the patient's EMG showed normal conduction velocity and distal latency of the right ulnar nerve motor nerve while low evoked potential amplitude. Neurogenic lesions were also found in right abductor pollicis brevis, right biceps brachii, left deltoid, left abductor digiti minimi, medial head of right quadriceps femoris, bilateral tibialis anterior muscle, right gastrocnemius, and right rectus abdominis, which indicated extensive neurogenic damage with chronic changes involving the cervical, thoracic, and lumbosacral innervated muscles (**Figure 3**). Abdominal color

		slationary phase				light contraction	motor unit	potential	heavy contraction	potential
	insertional potential	fibrillation potential	positive potential	fasciculation potential	special potential	duration MS	amplitude UV	multiphase %	wave type	amplitude MV
deltoid (L)	——	——	——	——	——	18.7↑	1749↑	50.0	single miscible	5.0
abductor digiti minimi (L)	——	——	——	——	——	15.3↑	1534↑	50.0	pure phase	4.6
abductor pollicis brevis (R)	——	——	——	——	——	16.3↑	1371↑	0	pure phase	5.2
quadriceps femoris (R)	——	——	——	——	——	16.6↑	2525↑	14.3	pure phase	5.8
biceps brachii (R)	——	——	——	——	——	16.3↑	1294↑	33.3	pure phase	5.3
tibialis anterior (L)	——	——	——	——	——	19.4↑	1736↑	83.3	pure phase	6.2
tibialis anterior (R)	——	——	——	——	——	16.7↑	1880↑	60.0	pure phase	5.0
sternocleidomastoid (R)	——	——	——	——	——	10.9	431	0	interference phase	2.3
gastrocnemius (R)	——	2+	2+	——	——	15.1↑	1824↑	0	pure phase	5.4
rectus abdominis (R)	——	——	——	——	——	16.2↑	1047↑	7.7	single miscible	5.4

FIGURE 3 | EMG of the patient shows extensive neurogenic damage with chronic changes involving the cervical, thoracic and lumbosacral innervated muscles. EMG, electromyography.

ultrasound revealed thickened and rough gallbladder wall and multiple high echoes in the inner wall of the gallbladder, thus polyps and inflammatory changes were mostly considered. Cranial magnetic resonance imaging (MRI) scans showed no significant abnormality in the brain parenchymal. Brain magnetic resonance angiography (MRA) scans revealed occlusion of bilateral anterior and middle cerebral arteries, a significant increase in peripheral vessels, and formation of collateral circulation, which suggests moyamoya disease (**Figure 4**).

To confirm the diagnosis, gene detection was performed. Multiplex ligation-dependent probe amplification (MLPA) is considered the gold standard for diagnosing SMA and the next generation sequencing results confirmed that the patient had a homozygous deletion of *SMN1* exons 7 and 8 with zero-copy and 3 copies of *SMN2* exons 7 and 8 (**Figure 5**). Finally, the above series of tests led us to the diagnosis of SMA type IIIb with MMS, and gallbladder polyps with cholecystitis.

In the end, we gave the patient the following treatment plan, low-dose methylprednisolone (20 mg/time, once a day) and idebenone (30 mg/time, three times a day), coenzyme Q10 (10 mg/time, three times a day) were prescribed orally. The patient was discharged on March 19, 2021 and continued oral treatment with the above drugs. During a telephone follow-up on June 20, 2021, the patient reported that the strength of her limbs did not seem to have changed much, but that her hand tremors were relieved when she occasionally lifted heavy objects, and there was no immediate improvement in other aspects. On September 27, 2021, the patient went to the outpatient department of our hospital for follow-up, indicating that the activities of lower limbs were gradually improved, mainly in the form of stronger squatting and standing up, and no falls for the time being. We performed a neurological physical examination of the patient and found that her proximal muscle strength of lower limbs was close to grade 4, that is, between grade 3 + and grade 4, and other physical signs were basically the same as 6 months ago. On December 27, 2021, the patient was followed up again by telephone, and reported that all aspects of performance and activity were similar to those of 3 months earlier. We told the patient to continue taking the medication, and admitted her to the hospital 3 months later for re-examination. The EMG needs to be reviewed again to assess the change of disease compared with the results of the previous year.

The course of the patient's onset and hospital visit, as well as the post-treatment response after the diagnosis was confirmed, are shown in the timeline (**Figure 6**).

DISCUSSION AND CONCLUSION

SMA is an autosomal recessive peripheral neuromuscular disease or lower motor neuron spectrum disease due to progressive degeneration and irreversible loss of anterior horn cells in the spinal cord and brainstem nuclei, leading to progressive muscle weakness and atrophy (Ross and Kwon, 2019), and no effective treatment is available. SMA is one of the main hereditary causes

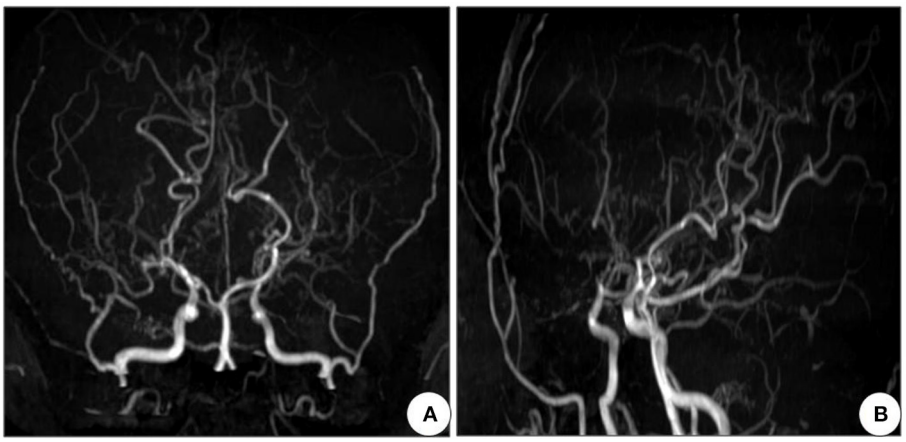

FIGURE 4 | Cranial MRA of the patient shows occlusion of bilateral anterior and middle cerebral arteries, with development of neoformation vessels, suggestive for moyamoya disease. **(A)** Front view and **(B)** Side view. MRA, Magnetic resonance angiography.

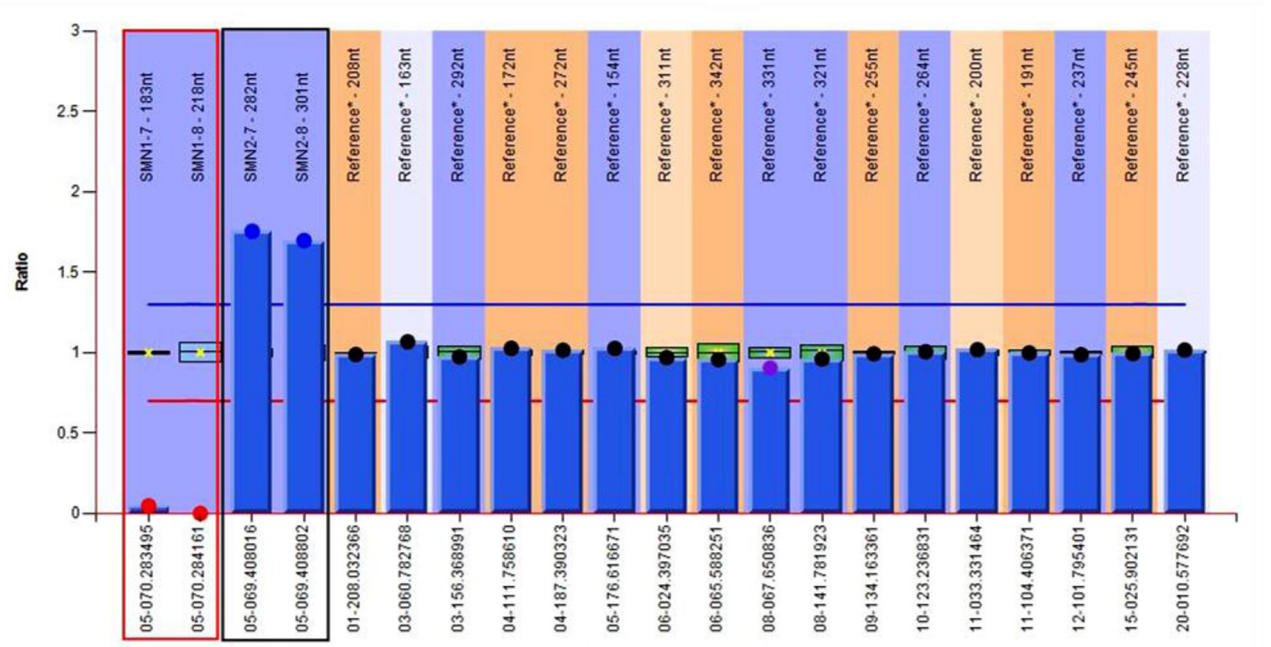

FIGURE 5 | Genetic test results of the patient show 0 copy of exons 7 and 8 of *SMN1*, 3 copies of exons 7 and 8 of *SMN2*. The red region refers to exons 7 and 8 of *SMN1*, and the black one refers to exons 7 and 8 of *SMN2*.

of infant death. SMA was first reported by Guido Werdnig in 1891. Until 1995, when the Lefebvre team identified its causative gene as *SMN1* located in the 5q11.2–13.3 region (Lefebvre et al., 1995). In China, approximately 95% of SMA patients have a homozygous deletion in exon 7 or exons 7 and 8 of *SMN1*, which leads to loss of SMN protein function and thus causes disease (He et al., 2013).

The clinical manifestations of SMA are quite heterogeneous. SMA was classified into four types according to the onset time and the highest attainment of motor function of the patients (Munsat and Davies, 1992). SMA type I is the severe form, also known as Werdnig-Hoffman disease, accounting for about 45% of all forms of SMA, often presenting within 6 months of age with rapidly progressive and symmetrical limb weakness, inability to sit. Most of these children die of respiratory failure before the age of 2 years. SMA type II is the intermediate form, also known as Dubowitz disease, accounting for about 30–40%, with affected infants often presenting in 6–18 months of age. Children with type II usually achieve the ability to sit independently, but cannot stand and walk, and survive over 2 years depending largely on

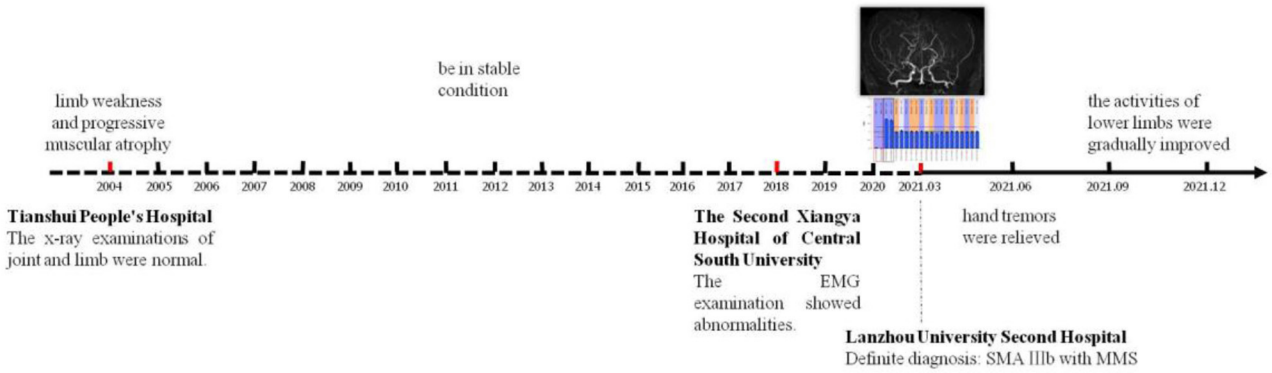

FIGURE 6 | The timeline reflects the whole process from the onset of the disease to the definite diagnosis in our hospital and regular follow-up after treatment.

the occurrence of respiratory complications. SMA type III is the mild or juvenile form, also known as Kugelberg-Welander disease, accounting for about 20%, typically presenting after 18 months. Affected children can walk independently as the disease progresses slowly, and life expectancy is not affected or slightly shortened. This type can be further divided into (1) SMA type IIIa: the onset age is <3 years, and the probability of walking 10 years after onset is 73%; (2) SMA type IIIb: the onset age is more than 3 years, and the probability of waking 10 years after onset is 97%. SMA type IV is the late-onset or adult form, with the onset age 15–60 years, about 35 years for the high incidence age. The onset and progression are more insidious than other types. Individuals with SMA type IV may experience walking difficulties, and their survival time is not different from that of normal subjects.

In this case, the onset of SMA was at 4 years old. The patient presented slow progressive limb weakness and atrophy, with lower limbs heavier than upper limbs, proximal heavier than distal. Physical examination revealed positive signs such as decreased muscle volume of the proximal limbs, poor muscle strength, weakened tendon reflexes, arched foot, and duck-like gait. Chronic motor neuron involvement changes at multiple sites were seen on EMG. These clinical features are highly consistent with SMA, but need to be differentiated from other hereditary motor neuron diseases such as Kennedy's disease and distal hereditary motor neuropathy. Kennedy's disease, also known as spinal bulbar muscular atrophy, can cause muscle weakness and atrophy of limbs and even the whole body. Different from the SMA, Kennedy's disease is an X-linked recessive genetic disorder, usually occurs in middle-aged and elderly men, the main clinical features are male breast development, bulbar muscle involvement and jaw tremor (Breza and Koutsis, 2019). And the distal hereditary motor neuropathy is a length dependent motor nerve damage, mainly involving the distal muscles of the limbs leading to weakness and atrophy, can be presented as "crane leg sign," "hammer finger" (Frasquet et al., 2021), this is highly inconsistent with the patient's proximal muscle involvement. Therefore, Kennedy's disease and distal hereditary motor neuropathy can be ruled out. Genetic testing revealed homozygous deletion of exons 7 and 8 of *SMN1* and 3 copies of exons 7 and 8 of *SMN2*. Due to economic constraints, the patient's parents were unable to undergo genetic testing. But the patient's parents are cousins, so it is possible that the pathogenic gene came from both parents. The diagnosis was confirmed by combining the genetic results. According to the age of onset and motor ability of the patient, the clinical classification was defined as SMA type IIIb. In addition, the cranial MRA showed occlusion of bilateral anterior and middle cerebral arteries, significantly increased peripheral tiny vascular, and collateral circulation formation, which was in accordance with the imaging characteristics of MMD. We searched for relevant literature, but there have been no reports about SMA and moyamoya phenomenon so far. The co-occurrence of rare diseases in a patient may hint more toward a correlation than a co-incidence (Puri et al., 2016). Therefore, we speculated that moyamoya disease is more likely to be a secondary vascular lesion of SMA, so the patient was finally diagnosed with SMA type IIIb with MMS.

MMD was first described by Japanese scholars Takeuchi and Shimizu in 1957 (Oshima and Katayama, 2012). It is a chronic cerebrovascular occlusive disease characterized by severe stenosis or occlusion of the siphon segments of bilateral internal carotid arteries and the beginning of the anterior and middle cerebral arteries found by cerebral angiography, the formation of an abnormal vascular network at the skull base caused by a compensatory proliferation of small vessels such as the leptomeninges and perforating arteries. MMS, also known as Quasi-moyamoya disease, refers to moyamoya disease associated with more than one underlying disease. In a nutshell, MMS is a secondary lesion due to other systemic diseases (Scott and Smith, 2009; Li et al., 2019). The underlying diseases are extensive that covers various aspects and multiple systems, such as hereditary diseases (neurofibromatosis type I and Down syndrome), infectious diseases (tuberculous vasculitis and Epstein-Barr virus infection), inflammatory diseases (systemic lupus erythematosus and Sjogren's syndrome), hematological diseases (sickle cell anemia and spherocytosis), metabolic diseases (abnormal thyroid function or pituitary hormone levels and

pyruvate kinase deficiency), exogenous injuries (head trauma and radiation injury) as well as oral contraceptives or drug taking (Scott and Smith, 2009; Vargiami et al., 2014; Li et al., 2019; Yamani et al., 2020; Nakamura et al., 2021).

At present, no relevant reports on SMA with MMS have been found in literature, so what are the possible mechanisms by which SMA causes moyamoya phenomenon? An in-depth study of *SMN1* shows that abnormal expression of *SMN1* not only affects the function of anterior horn cells of the spinal cord but also leads to the involvement of multiple sites and multiple organs (Gombash et al., 2015; Qian et al., 2019; Besse et al., 2020). The expression of SMN protein is very wide, and Nash et al. (2016) systematically summarized the expression of SMN protein in the digestive system (the gastrointestinal tract such as liver and gallbladder), autonomic nervous system, endocrine system, reproductive system, skeletal system, central nervous system, and vascular system. Therefore, the gallbladder lesions in this patient may be related to the deletion of *SMN1* which affects the expression of SMN protein and in turn involves its digestive system such as liver and gallbladder. In recent years, some studies have found a significant decrease in vascular bed density in skeletal muscle and spinal cord of SMA transgenic mice (Somers et al., 2012, 2016). Thus, the deletion or mutation of *SMN1* may cause developmental defects in peripheral and spinal cord vessels, but the effect on the intracranial vessels is unknown. Ito et al. (2004) reported that a SMA type I child with an abnormally high signal change in the bilateral anterolateral part of the thalamus on cranial MRI, and Shishikura et al. (1983) studied the brains of five children with SMA type I and founded that sensory neuron and thalamic degeneration in addition to severe cell loss in the anterior horn of the spinal cord and cranial nerve motor neurons (V, VII, X, and XII), which indicated that *SMN1* gene defects can lead to intracranial lesions. Animal studies have confirmed that reduced SMN protein levels in SMA mouse models resulted in brain development damage of perinatal mice. Comparative proteomic analysis of the hippocampus in SMA and wild-type mice showed that when SMN protein levels were reduced, the expression levels of proteins that regulate cell proliferation, migration, and development were significantly altered, confirming that SMN protein played a crucial role in brain development (Wishart et al., 2010). Based on this, we speculated that the low expression of SMN protein level in SMA patients may cause developmental disorders by affecting the growth, division, and migration of vascular endothelial cells and smooth muscle cells in the brain, and finally, MMD-like abnormal changes such as progressive vascular stenosis and even occlusion occurred.

In summary, the clinical diagnosis of SMA is mainly based on the clinical features of progressive muscle weakness and atrophy and the electrophysiological changes of typical motor neuron involvement. The final diagnosis depends on the results of *SMN1* gene detection. The coexistence of SMA with moyamoya phenomenon is rare, and the relationship between the two is still unclear, so it deserves to be reported. We consider that it may be related to the dysfunction of SMN protein, which results in the abnormal regulation of proliferation and differentiation of intracranial vascular endothelial cells and smooth muscle cells. However, this view is based on clinical speculation, and the possibility of pure coincidence cannot be ruled out. Perhaps further basic studies or long-term follow-up will tell us the answer.

DATA AVAILABILITY STATEMENT

The original contributions presented in the study are included in the article/supplementary materials, further inquiries can be directed to the corresponding author/s.

ETHICS STATEMENT

The studies involving human participants were reviewed and approved by the Medical Ethics Committee of the Second Hospital of Lanzhou University, which is affiliated to Lanzhou University. The patients/participants provided their written informed consent to participate in this study. Written informed consent was obtained from the individuals for the publication of this case report, including any potentially identifiable images or data contained in this article.

AUTHOR CONTRIBUTIONS

JL and XL collected medical records. JL, XL, LW, and GW all participated in analyzing the condition, confirming the diagnosis, and formulating the treatment plan. JL was responsible for writing the manuscript. All authors have reviewed the manuscript.

FUNDING

This study was supported by the Natural Science Research Fund of Gansu Province (21JR1RA136).

REFERENCES

Alías, L., Barceló, M. J., Bernal, S., Martínez-Hernández, R., Also-Rallo, E., and Vázquez, C. (2014). Improving detection and genetic counseling in carriers of spinal muscular atrophy with two copies of the SMN1 gene. *Clin. Genet.* 85, 470–475. doi: 10.1111/cge.12222

Besse, A., Astord, S., Marais, T., Roda, M., Giroux, B., and Lejeune, F. X. (2020). AAV9-mediated expression of SMN restricted to neurons does not rescue the spinal muscular atrophy phenotype in mice. *Mol. Ther.* 28, 1887–1901. doi: 10.1016/j.ymthe.05, 011

Breza, M., and Koutsis, G. (2019). Kennedy's disease (spinal and bulbar muscular atrophy): a clinically oriented review of a rare disease. *J. Neurol.* 266, 565–573. doi: 10.1007/s00415-018-8968-7

Frasquet, M., Rojas-García, R., Argente-Escrig, H., Vázquez-Costa, J. F., Muelas, N., and Vílchez, J. J. (2021). Distal hereditary motor neuropathies: mutation spectrum and genotype-phenotype

correlation. *Eur. J. Neurol.* 28, 1334–1343. doi: 10.1111/ene.14700

Gidaro, T., and Servais, L. (2019). Nusinersen treatment of spinal muscular atrophy: current knowledge and existing gaps. *Dev. Med. Child Neurol.* 61, 19–24. doi: 10.1111/dmcn.14027

Gombash, S. E., Cowley, C. J., Fitzgerald, J. A., Iyer, C. C., Fried, D., McGovern, V. L., et al. (2015). SMN deficiency disrupts gastrointestinal and enteric nervous system function in mice. *Hum. Mol. Genet.* 24, 3847–3860. doi: 10.1093/hmg/ddv127

He, J., Zhang, Q. J., Lin, Q. F., Chen, Y. F., Lin, X. Z., and Lin, M. T. (2013). Molecular analysis of SMN1, SMN2, NAIP, GTF2H2, and H4F5 genes in 157 Chinese patients with spinal muscular atrophy. *Gene* 518, 325–329. doi: 10.1016/j.gene.12109

Ito, Y., Kumada, S., Uchiyama, A., Saito, K., Osawa, M., and Yagishita, A. (2004). Thalamic lesions in a long-surviving child with spinal muscular atrophy type I: MRI and EEG findings. *Brain Dev.* 26, 53–56. doi: 10.1016/s0387-7604(03)00075-5

Lefebvre, S., Bürglen, L., Reboullet, S., Clermont, O., Burlet, P., Viollet, L., et al. (1995). Identification and characterization of a spinal muscular atrophy-determining gene. *Cell* 80, 155–165. doi: 10.1016/0092-8674(95)90460-3

Li, J., Jin, M., Sun, X., Liu, Y., and Xi, Y. (2019). Imaging of moyamoya disease and moyamoya syndrome: current status. *J. Comput. Assist. Tomogr.* 43, 257–263. doi: 10.1097/RCT.0000000000000834

Munsat, T. L., and Davies, K. E. (1992). International SMA consortium meeting. (26–28 June 1992, Bonn, Germany). *Neuromuscul. Disord.* 2, 423–428. doi: 10.1016/s0960-8966(06)80015-5

Nakamura, H., Sato, K., Yoshimura, S., Hayashi, Y., Izumo, T., and Tokunaga, Y. (2021). Moyamoya disease associated with Graves' disease and Down syndrome: a case report and literature review. *J. Stroke Cerebrovasc. Dis.* 30, 105414. doi: 10.1016/j.jstrokecerebrovasdis.2020.105414

Nash, L. A., Burns, J. K., Chardon, J. W., Kothary, R., and Parks, R. J. (2016). Spinal muscular atrophy: more than a disease of motor neurons?. *Curr. Mol. Med.* 16, 779–792. doi: 10.2174/1566524016666161128113338

Oshima, H., and Katayama, Y. (2012). Discovery of cerebrovascular moyamoya disease: research during the late 1950s and early 1960s. *Childs Nerv. Syst.* 28, 497–500. doi: 10.1007/s00381-012-1708-x

Puri, I., Vibha, D., Prasad, K., and Bhatia, R. (2016). Is congenital melanocytic naevus a link between Hirayama disease and moyamoya pattern: a new syndrome or a co-incidence?. *BMJ Case Rep*. 2016, bcr2015212894. doi: 10.1136./bcr-2015-212894

Qian, X., Du, Y., Jiang, G., Lin, F., and Yao, L. (2019). Survival motor neuron (SMN) protein insufficiency exacerbates renal ischemia/reperfusion injury. *Front. Physiol.* 10, 559. doi: 10.3389/fphys.2019.00559

Ross, L. F., and Kwon, J. M. (2019). Spinal muscular atrophy: past, present, and future. *NeoReviews* 20, e437–e451. doi: 10.1542/neo.20-8-e437

Scott, R. M., and Smith, E. R. (2009). Moyamoya disease and moyamoya syndrome. *N. Engl. J. Med.* 360, 1226–1237. doi: 10.1056/NEJMra0804622

Shishikura, K., Hara, M., Sasaki, Y., and Misugi, K. (1983). A neuropathologic study of Werdnig-Hoffmann disease with special reference to the thalamus and posterior roots. *Acta Neuropathol.* 60, 99–106. doi: 10.1007/BF00685353

Somers, E., Lees, R. D., Hoban, K., Sleigh, J. N., Zhou, H., and Muntoni, F. (2016). Vascular defects and spinal cord hypoxia in spinal muscular atrophy. *Ann. Neurol.* 79, 217–230. doi: 10.1002/ana.24549

Somers, E., Stencel, Z., Wishart, T. M., Gillingwater, T. H., and Parson, S. H. (2012). Density, calibre and ramification of muscle capillaries are altered in a mouse model of severe spinal muscular atrophy. *Neuromuscul. Disord.* 22, 435–442. doi: 10.1016/j.nmd.10021

Vargiami, E., Sapountzi, E., Samakovitis, D., Batzios, S., Kyriazi, M., and Anastasiou, A. (2014). Moyamoya syndrome and neurofibromatosis type 1. *Ital. J. Pediatr.* 40, 59. doi: 10.1186/1824-7288-40-59

Wishart, T. M., Huang, J. P., Murray, L. M., Lamont, D. J., Mutsaers, C. A., and Ross, J. (2010). SMN deficiency disrupts brain development in a mouse model of severe spinal muscular atrophy. *Hum. Mol. Genet.* 19, 4216–4228. doi: 10.1093/hmg/ddq340

Yamani, M., Obaid, E. F., and Hemida, A. H. (2020). Moyamoya syndrome in a 32-year-old male with sickle cell anemia. *Cureus*. 12:e10001. doi: 10.7759/cureus.10001

Conflict of Interest: The authors declare that the research was conducted in the absence of any commercial or financial relationships that could be construed as a potential conflict of interest.

Publisher's Note: All claims expressed in this article are solely those of the authors and do not necessarily represent those of their affiliated organizations, or those of the publisher, the editors and the reviewers. Any product that may be evaluated in this article, or claim that may be made by its manufacturer, is not guaranteed or endorsed by the publisher.

frontiers in Cellular Neuroscience

CASE REPORT
published: 17 February 2022
doi: 10.3389/fncel.2022.856512

Detection of Japanese Encephalitis by Metagenomic Next-Generation Sequencing of Cerebrospinal Fluid: A Case Report and Literature Review

Xin Li[1], *Jing Li*[1], *Guode Wu*[1], *Manxia Wang*[1]* *and Zhang Jing*[2]

[1] Department of Neurology, Lanzhou University Second Hospital, Lanzhou, China, [2] Department of Magnetic Resonance, Lanzhou University Second Hospital, Lanzhou, China

Japanese encephalitis (JE) is an acute viral central nervous system disease, although less than 1% of patients infected with Japanese encephalitis virus (JEV) result in JE, which has an extremely poor prognosis. The Routine detection methods for JEV are time-consuming or limited by hospital conditions, therefore, need the quicker and sensitive techniques to detect JEV. Here, we reported a 14-year-old female who was admitted to our hospital with a severe fever, progressively headache and unconsciousness. Based on the clinical presentation, Preliminary diagnosis on admission indicated central nervous system infection of suspected viral meningoencephalitis or autoimmune encephalitis. The patient's symptoms were unrelieved after being treated with empiric antiviral therapy. Magnetic resonance imaging (MRI) showed that the lesions were located in the bilateral thalamus, head of caudate nucleus, and right lenticular nucleus, so we had to consider the possibility of Flaviviruses infection. We sent the cerebrospinal fluid (CSF) for metagenomic next-generation sequencing (mNGS) immediately, subsequent result suggested the infection caused by JEV. Two days later the results of the serum agglutination test confirmed that virus immunoglobulin M antibody positive. After a week treatment with intravenous immunoglobulin (IVIG), meanwhile, the lumbar puncture was used to check the pressure and various indicators of the CSF again to evaluate the treatment effect, An decrease in the number of WBC indicates, protein and unique RNA reads that the previous experimental treatment was effective, accompany by temperature and consciousness of the patient was normalized. Two weeks after admission, the patient was transferred to the rehabilitation hospital, MR showed the lesions had disappeared completely after 2 months of follow-up. We believed that mNGS may be an effective method for rapid identification of JE.

Keywords: Japanese encephalitis, central nervous system infection, metagenomic next-generation sequencing, Japanese encephalitis virus, epidemic encephalitis B

OPEN ACCESS

Edited by:
Yuzhen Xu,
Tongji University, China

Reviewed by:
Zhiqin Liu,
Xi'an Jiaotong University School of Medicine, China
Lei Liu,
Capital Medical University, China

***Correspondence:**
Manxia Wang
wmx322@aliyun.com

Specialty section:
This article was submitted to Cellular Neuropathology, a section of the journal Frontiers in Cellular Neuroscience

Received: *17 January 2022*
Accepted: *25 January 2022*
Published: *17 February 2022*

Citation:
Li X, Li J, Wu G, Wang M and Jing Z (2022) Detection of Japanese Encephalitis by Metagenomic Next-Generation Sequencing of Cerebrospinal Fluid: A Case Report and Literature Review. Front. Cell. Neurosci. 16:856512. doi: 10.3389/fncel.2022.856512

INTRODUCTION

Japanese encephalitis (JE) is the mosquito-borne, an acute viral central nervous system disease in most temperate areas of Asia and Western Pacific, especially in rural or mountain areas where forest and pig farming (Quan et al., 2020). The mortality rate of JE is 20–30% approximately, and 30–50% of survivors have varying degrees of neurological sequelae (Campbell et al., 2011). The prognosis

of patients depends on identification early and treatment timely, but the conventional methods such as Enzyme-Linked Immunosorbent Assays (ELISA), Reverse Transcriptase Polymerase Chain Reaction (RT-PCR) were time-consuming or limited by hospital conditions. There is an urgent clinical need for a technology that can quickly and accurately identify pathogens, reduce the risk of death due to delayed treatment. Metagenomics next-generation sequencing (mNGS) is a new detection technology, which has the advantages of fast and precise (Wilson et al., 2019). We report the first case of JE diagnosed by using mNGS of cerebrospinal fluid (CSF).

CASE REPORT-1

A 14-year-old female patient was admitted to the Second Hospital of Lanzhou University on July 23rd, 2019 due to fever accompanied by progressively deteriorated headache for 3 days, and progressive unconsciousness for 1 day. She developed fever (her body temperature over 40°C) without obvious predisposing factors on July 20th, 2019, accompanied by headache, mainly mild intermittent throbbing pain in the temporal. The symptoms worsened on the next day, and the headache spread to the occipital and back of the neck and lasted longer. Meanwhile, she developed mild fatigue and sore muscles, which were unresponsive to Paracetamol. On the morning of July 22nd, the headache was significantly aggravated obvious, and the duration was prolonged, accompanied by nausea and vomiting. Her sleep increased and she was not easy to wake up that afternoon. When she was taken to our hospital on July 23rd 2019, she was in mild coma. Routine physical examination on admission showed the body temperature of 39.2°C, pulse of 93 beats/min, respiratory rate of 23 times/min, and blood pressure of 124/82 mmHg. Nervous system examination showed consciousness and poor mental state without obvious abnormalities involving high-level cortical functions or cranial nerves. The muscle strength of the limbs was grade 4+. The muscle tension was normal, and tendon reflexes were present without any pathological signs. The neck was rigid, and the mentosternal distance was 4 fingers. Positive Kernig sign and positive Brudzirnki sign were observed. Blood routine on admission plus CRP showed WBC counts at 9.5×10^9/L, neutrophil ratio NE% of 0.43, lymphocyte ratio LY% of 0.57, and CRP of 29 mg/L. The rest laboratory tests showed no abnormalities. Preliminary diagnosis on admission indicated central nervous system infection of suspected viral meningoencephalitis. Acyclovir 0.5 g/8 h, iv, dexamethasone 10 mg, iv. were administered. Brian magnetic resonance imaging (MRI) revealed hyperintensity involving bilateral thalamus, head of caudate nucleus and right lenticular nucleus on July 24th, 2019 (**Figures 1A–E**). Because of symmetrical thalamic lesions, we have to consider that the patient may suffer from Flaviviruses. Lumbar puncture was subsequently performed with the CSF intracranial pressure of 220 mmH_2O, WBC counts was 90×10^6/L, of which mononuclear cell accounted for 86.9%, and proteins was 1.07 g/L. In the meantime, syphilis antibodies, autoimmune encephalitis antibodies, rheumatism antibodies, respiratory disease antibodies, and tuberculosis antibodies were all tested for negative. The rest examinations showed no abnormalities. In addition, 8 ml of CSF was collected for mNGS (Accurate Decoding Medical Laboratory, Gansu, China) to determine the pathogen. On July 26, the results of mNGS showed a total of 26 unique RNA sequences of Japanese encephalitis virus (JEV), with a coverage rate of 23.9348% (**Figure 2**). In order to confirm the JEV infection, the CSF was collected and sent to the Center for Disease Control and Prevention to test the JEV immunoglobulin M antibody. As the patient's condition did not relieve, we used intravenous gamma globulin empirically. On July 28, the patient's JEV immunoglobulin M antibody was positive. Therefore, the diagnosis of JE was finally confirmed. Subsequently, the patient's clinical symptoms improved, her body temperature was basically normal, and her consciousness recovered. A second lumbar puncture was performed to observed cytological and protein changes in CSF and for mNGS detection again on August 1st, 2019. Analysis of CSF showed a decrease in the number of white blood cells and protein levels (WBC count was 42×10^6/L, of which monocyte percentage for 56.9%, and protein was 0.57 g/L). The result of mNGS detected seven the unique RNA reads of JEV and genome coverage 2.0484% on August 3rd, 2019 (**Figure 3**), which was significantly better than the previous results on July 26th, 2019. After pure antiviral treatment for 5 days, the patient was transferred to the rehabilitation hospital on August 5th, 2019. Follow-up MRI showed that the lesions disappeared completely after2 months, on October 2nd, 2019 (**Figure 1F**).

Through timeline of the patient's clinical symptoms, temperature change process, drug use, mNGS and MRI (**Figure 4**), we can see the patient's treatment process in detail.

DISCUSSION

Japanese encephalitis is also known as epidemic encephalitis B, an acute mosquito-borne viral central nervous system infection caused by JEV, which is mainly prevalent in Asia and the Pacific. The WHO estimates that approximately 67,900 cases of JE are distributed in these epidemic areas, and the incidence rate is about 1.8/10,000 (Solomon, 2006; Wang and Liang, 2015). However, there is a trend that epidemic areas expand (Connor and Bunn, 2017). In 2010, the nucleic acid sequence of the JEV-NS5 segment was detected in the specimens of *Culex pipiens* pollens and birds in northeastern Italy (Platonov et al., 2012; Zeller, 2012). In Africa, JEV nucleic acid was detected from Fiebre amarilla patients through deep sequencing (Simon-Loriere et al., 2017).

A variety of animals can be infected with JEV, including pigs, horses, cattle, sheep, and birds. Among them, pigs are very susceptible to JEV (Le Flohic et al., 2013; Mansfield et al., 2017). Pigs can maintain a state of high-level viremia for a long time after infection. They are the main host and important source of infection for JEV (van den Hurk et al., 2009). Mosquito bite is the main mode of transmission of JE. At present, more than 30 species of mosquitoes are known to be vectors of JE, and the type and number of mosquitoes can affect the incidence and prevalence of JE (Le Flohic et al., 2013). *Culex tritaeniorhynchus*

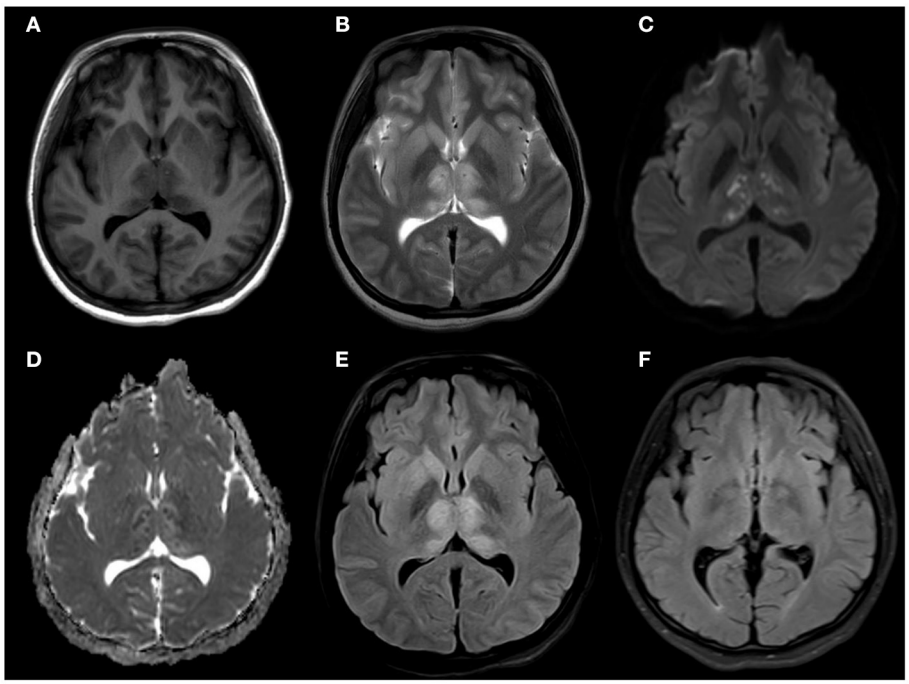

FIGURE 1 | (A) MRI brain axial T1: slightly hypointensity in the symmetric thalamus, head of caudate nucleus, and right lenticular nucleus **(B)** MRI brain axial T2: hyperintensity in the symmetric hippocampus, thalamus, head of caudate nucleus, and right lenticular nucleus. **(C,D)** MRI brain axial diffusion-weighted imaging: isointensity bilateral punctate hyperintensity in the symmetric thalamus, and showed hypointensity in ADC. **(E)** MRI brain axial T2 fluid-attenuated inversion recovery: slightly hyperintensity in the symmetric thalamus, head of caudate nucleus, no mass effect. **(F)** MRI brain axial T2 fluid-attenuated inversion recovery: The lesions had disappeared completely after 2 months.

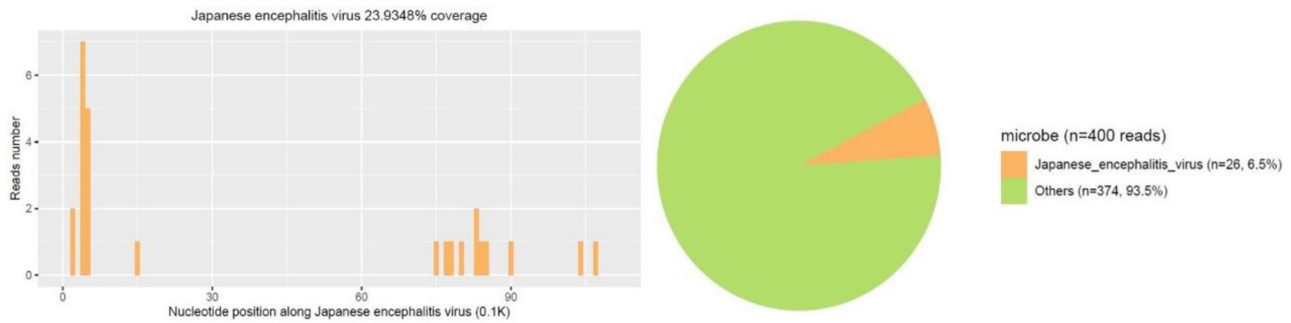

FIGURE 2 | First mNGS result showed a total of 26 unique RNA sequences of Japanese encephalitis virus (JEV), with a coverage of 23.9348% were detected.

is widely distributed among mosquito vectors, and is highly susceptible to JE. It is the most important mosquito species in the transmission of JE (Ghosh and Basu, 2009; Hsieh and St John, 2020). Japanese encephalitis virus (genus Flavivirus; family: Flaviviridae) is a forward single-stranded RNA virus containing an envelope, which is neuroinvasive and neurotoxic in humans (Impoinvil et al., 2011). After humans are bitten by mosquitoes carrying JEV, the virus enters the local skin and lymph nodes through receptor-mediated endocytosis and is replicated in monocyte-macrophages and dendritic cells, causing transient low-level viremia (Banerjee and Tripathi, 2019; Filgueira and Lannes, 2019). Infected cells cross the blood-brain barrier (BBB) through endothelial cell phagocytosis, and induce the production of inflammatory cytokines and chemokines, leading to the destruction of the BBB (Miner and Diamond, 2016; Patabendige et al., 2018; Hsieh and St John, 2020). It is worth noting that the destruction of the BBB is not caused by the virus itself. Inflammatory cytokines or chemokines can reduce the permeability of the BBB by down-regulating tight junction proteins. At the same time, inflammatory cytokines can further impair the BBB by inducing the expression of adhesion molecules on BBB endothelial cells (Chen et al., 2014;

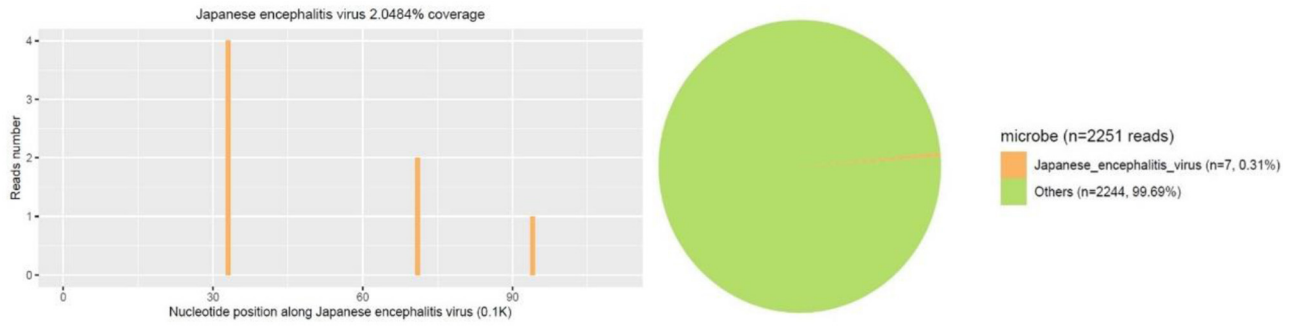

FIGURE 3 | Second mNGS result showed a total of 7 unique RNA sequences of Japanese encephalitis virus (JEV), with a coverage of 2.0484% were detected.

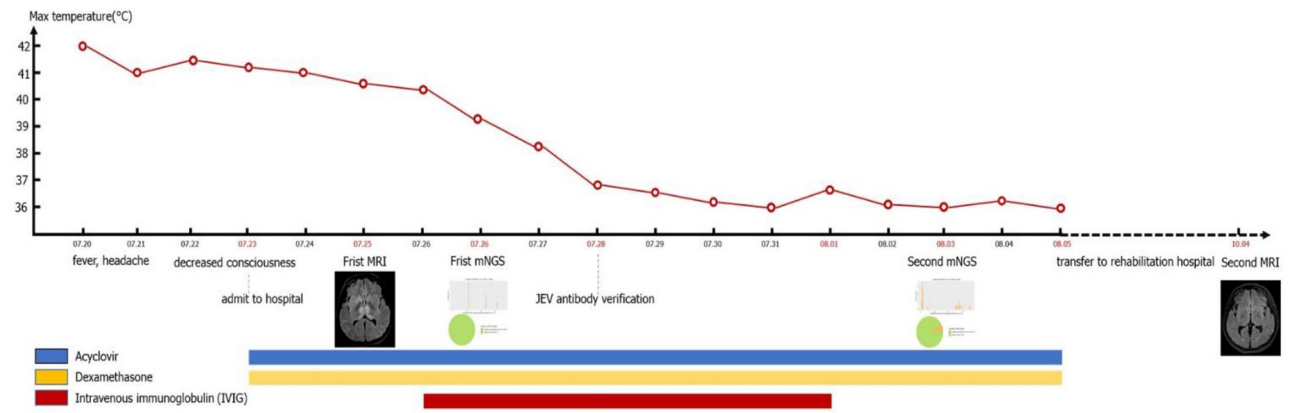

FIGURE 4 | Timeline of the patient's clinical symptoms, temperature change process, drug use, mNGS, and MRI.

Chang et al., 2015). Then the infected cells migrate from the periphery to the central nervous system, trigger humor and cell-mediated immune responses and induce the expression of pro-inflammatory cytokines. The activation of microglia will lead to the overproduction of pro-inflammatory mediators and cause extensive destruction of neurons and symptoms of acute encephalitis (Lannes et al., 2017; Ashraf et al., 2021). The clinical manifestations and prognosis of patients depend on the virulence of the virus and the host immune response. The main clinical manifestations of patients include headache, high fever, disturbance of consciousness, seizures, and even respiratory failure (Basumatary et al., 2013). Rare manifestations include mandibular-facial nerve twisting tremor (Takeuchi et al., 2014), cervical dystonic tremor (Spagnolo et al., 2014), phrenic nerve palsy (Chaudhuri et al., 2021), and upper and mixed upper and lower motor neuron damage (Ghosh et al., 2020). Japanese encephalitis is often secondary to a variety of diseases including Guillain-Barré syndrome (Xiang et al., 2014; Wang et al., 2020), Secondary Parkinson's disease (Tadokoro et al., 2018), anti-N-methyl-D-aspartate receptor encephalitis (Tian et al., 2019; Wang et al., 2020), acute flaccid myelitis (Dev et al., 2020; Shen et al., 2020), cerebral venous sinus thrombosis (Jia et al., 2012) and so on. The patient in this case had typical high fever, headache, and hypoconsciousness, and the clinical symptoms are consistent with the typical clinical manifestations of JE. The imaging manifestations of JE are extensive involvement of the brain and spinal cord. Among which the thalamus and midbrain are the most severely affected, the parietal lobe, frontal lobe, and hippocampus of the brain are significantly affected, and the spinal cord is the least affected. Symmetry of thalamic lesions is the characteristic of JE (Prakash et al., 2004; Handique and Barkataky, 2008; Lai et al., 2008). Magnetic resonance imaging of this case showed lesions in the bilateral thalamus, the head of the caudate nucleus, and the right lenticular nucleus. The lesions showed slightly low signal intensity on T1WI, slightly higher signal intensity on T2WI, and high signal intensity on FLAIR sequence, which is consistent with changes in acute encephalitis. The DWI sequence showed mainly iso-signal intensity mixed with patchy hyperintensity, suggesting that the lesions were mainly vasogenic edema, and a few showed cytotoxic edema. The imaging changes are related to the pathological mechanism of the patient's disease process, and the spot-to-uniform pattern of cytotoxic edema may reflect the pattern of virus replication in the thalamus (Arahata et al., 2019). It was confirmed in animal experiments that the RNA of JEV mainly accumulates in the thalamus and basal ganglia, indicating that

the virus replicates specifically in these areas (Ricklin et al., 2016). Although Neuroimaging features of JE have showed that involvement of temporal lobe and hippocampus is also one of the characteristics in previous study (Handique et al., 2006), the patient in this case did not have hippocampal involvement, and there were no clinically related mental abnormalities and memory impairment, which may be related to her mild condition. Through the characteristics of imaging, we suspected the possibility of flavivirus infection, but due to technical restriction, we can't detect the specific virus type by PCR. After weighing and analyzing the benefits of treatment and the risk of serious consequences of JEV, before completing the confirmatory test of JEV antibodies, we conducted experimental treatment immediately based on the results of mNGS. Although there is no special treatment for JE, early supportive treatment can limit the development of neurological sequelae. Based on previous clinical experience, the patient used antiviral drugs (aciclovir), dexamethasone, and experimentally used intravenous gamma globulin for 5 days. The treatment effect was evaluated based on the unique RNA readings in the CSF samples on July 26, 2019 and August 7, 2019. After 10 days of treatment, the number of JEV readings was reduced from 24 to 7. Fortunately, after 20 days of hospitalization, the patient's condition gradually stabilized and she was transferred to the rehabilitation hospital. A follow-up MRI showed that the lesions disappeared completely after 2 months. As a new detection method, mNGS does not rely on traditional microbial culture and directly performs high-throughput sequencing of nucleic acids in samples. It can quickly and indiscriminately detect pathogenic microorganisms in samples (Salzberg et al., 2016; Gu et al., 2019; Wilson et al., 2019), such as bacteria, viruses, fungi, and parasites, to the difficult infections or rare pathogenic microorganisms especially (Fan et al., 2020; Cao et al., 2021; Liu et al., 2021).

Current next-generation sequencing (NGS) are widely utilized for pathogen identification, but they can only sequence DNA molecules in most cases. While DNA composes the genetic material for pathogenic bacteria and fungi, RNA viruses compose a large fraction of infectious pathogens in central nervous system infectionas well, Flavivirus (including West Nile virus, JE virus and so on), severe fever with thrombocytopenia syndrome virus (SFTSV), for example. It is noteworthy that the severe acute respiratory syndrome coronavirus 2 (SARS-CoV-2) responsible for the coronavirus disease 2019 (COVID-19) which belongs to RNA virus (Manso et al., 2017; Gao, 2018; Wang et al., 2020a,b). Thus, RNA viruses will be neglected from solely DNA-based mNGS, sometimes hindering important diagnoses. Due to the cost of medical economics, mNGS is rarely used for simultaneous detection of RNA and DNA of pathogenic microorganisms in clinical diagnosis, our experience is that when the DNA sequence of pathogenic microorganism is not detected and the treatment effect of the patient is poor, or the patient lives in the epidemic area, or the encephalitis patients with typical symmetrical basal ganglia lesions can directly choose mNGS for RNA detection, or DNA and RNA can be detected together. Although mNGS still has some problems to be solved, such as distinguishing infection from colonization, identifying exogenous nucleic acid pollution, the targeted sequencing are overcoming these defects (Simner et al., 2018).

As far as we know, this is the first clinical case of JE that has been diagnosed using mNGS. We must emphasize the potential value of mNGS in the identification of pathogens of central nervous system infection, because it has the advantages of sensitivity, speediness and accuracy.

DATA AVAILABILITY STATEMENT

The raw data supporting the conclusions of this article will be made available by the authors, without undue reservation.

ETHICS STATEMENT

The studies involving human participants were reviewed and approved by Lanzhou University Second Hospital Ethics Committee. The patients/participants provided their written informed consent to participate in this study. Written informed consent was obtained from the individual(s) for the publication of any potentially identifiable images or data included in this article.

AUTHOR CONTRIBUTIONS

XL and JL contributed to the study design and drafted the manuscript. MW contributed to PCR validation of the data in the literature and edited the manuscript. ZJ contributed to MRI of the data in the literature. GW contributed to supervised writing of the manuscript and critically reviewed the paper. All authors contributed to the article and approved the submitted version.

FUNDING

This work was supported by grants from the Natural Science Foundation of Gansu Province, China (Grant No. 21JR1RA136).

ACKNOWLEDGMENTS

We thank all the subjects who participated in our study.

REFERENCES

Arahata, Y., Fujii, K., Nishimura, T., Uchida, T., Kitazawa, K., and Honda, A. (2019). Longitudinal magnetic resonance imaging changes in Japanese encephalitis. *Brain Dev*. 41, 731–734. doi: 10.1016/j.braindev.2019.04.005

Ashraf, U., Ding, Z., Deng, S., Ye, J., Cao, S., and Chen, Z. (2021). Pathogenicity and virulence of Japanese encephalitis virus: neuroinflammation and neuronal cell damage. *Virulence* 12, 968–980. doi: 10.1080/21505594.2021.1899674

Banerjee, A., and Tripathi, A. (2019). Recent advances in understanding Japanese encephalitis. *F1000Res*. 8, 1915. doi: 10.12688/f1000research.19693.1

Basumatary, L. J., Raja, D., Bhuyan, D., Das, M., Goswami, M., and Kayal, A. K. (2013). Clinical and radiological spectrum of Japanese encephalitis. *J. Neurol. Sci*. 325, 15–21. doi: 10.1016/j.jns.2012.11.007

Campbell, G. L., Hills, S. L., Fischer, M., Jacobson, J. A., Hoke, C. H., Hombach, J. M., et al. (2011). Estimated global incidence of Japanese encephalitis: a systematic review. *Bull.*

World Health Organ. 89, 766–774E. doi: 10.2471/BLT.10.085233

Cao, J., Cai, Q., Su, W., Ge, Z., Zhao, H., Zhou, X., et al. (2021). Case report: metagenomic next-generation sequencing confirmed a case of central nervous system infection with *Brucella melitensis* in non-endemic areas. *Front. Med.* 8, 723197. doi: 10.3389/fmed.2021.723197

Chang, C. Y., Li, J. R., Chen, W. Y., Ou, Y. C., Lai, C. Y., Hu, Y. H., et al. (2015). Disruption of *in vitro* endothelial barrier integrity by Japanese encephalitis virus-Infected astrocytes. *Glia* 63, 1915–1932. doi: 10.1002/glia.22857

Chaudhuri, J., Dubey, S., Ray, B. K., and Biswas, T. (2021). Phrenic nerve palsy in Japanese encephalitis: a rare association. *Acta Neurol. Belg.* 121, 575–576. doi: 10.1007/s13760-020-01433-z

Chen, C. J., Ou, Y. C., Li, J. R., Chang, C. Y., Pan, H. C., Lai, C. Y., et al. (2014). Infection of pericytes *in vitro* by Japanese encephalitis virus disrupts the integrity of the endothelial barrier. *J. Virol.* 88, 1150–1161. doi: 10.1128/JVI.02738-13

Connor, B., and Bunn, W. B. (2017). The changing epidemiology of Japanese encephalitis and new data: the implications for new recommendations for Japanese encephalitis vaccine. *Trop. Dis. Travel Med. Vaccines* 3, 14. doi: 10.1186/s40794-017-0057-x

Dev, N., Kumar, R., Kumawat, A., and Bhowmick, M. (2020). Acute flaccid myelitis caused by japanese encephalitis virus: a rare association. *Ann. Indian Acad. Neurol.* 23, 237–238. doi: 10.4103/aian.AIAN_309_19

Fan, S., Yuan, H., Liu, L., Li, H., Wang, S., Zhao, W., et al. (2020). Pseudorabies virus encephalitis in humans: a case series study. *J. Neurovirol.* 26, 556–564. doi: 10.1007/s13365-020-00855-y

Filgueira, L., and Lannes, N. (2019). Review of emerging japanese encephalitis virus: new aspects and concepts about entry into the brain and inter-cellular spreading. *Pathogens* 8, 111. doi: 10.3390/pathogens8030111

Gao, G. F. (2018). From "A"IV to "Z"IKV: attacks from emerging and re-emerging pathogens. *Cell* 172, 1157–1159. doi: 10.1016/j.cell.2018.02.025

Ghosh, D., and Basu, A. (2009). Japanese encephalitis-a pathological and clinical perspective. *PLoS Negl. Trop. Dis.* 3, e437. doi: 10.1371/journal.pntd.0000437

Ghosh, R., Dubey, S., Chatterjee, S., Kanti Ray, B., and Benito-León, J. (2020). Mixed upper and lower motor neuron damage in Japanese encephalitis virus infection. *Case Rep Neurol.* 12, 482–488. doi: 10.1159/000510711

Gu, W., Miller, S., and Chiu, C. Y. (2019). Clinical metagenomic next-generation sequencing for pathogen detection. *Annu. Rev. Pathol.* 14, 319–338. doi: 10.1146/annurev-pathmechdis-012418-012751

Handique, S. K., and Barkataky, N. (2008). MR imaging in biphasic Japanese encephalitis. *AJNR Am. J. Neuroradiol.* 29, E3. doi: 10.3174/ajnr.A0862

Handique, S. K., Das, R. R., Barman, K., Medhi, N., Saharia, B., Saikia, P., et al. (2006). Temporal lobe involvement in Japanese encephalitis: problems in differential diagnosis. *AJNR Am. J. Neuroradiol.* 27, 1027–1031.

Hsieh, J. T., and St John, A. L. (2020). Japanese encephalitis virus and its mechanisms of neuroinvasion. *PLoS Pathog.* 16, e1008260. doi: 10.1371/journal.ppat.1008260

Impoinvil, D. E., Solomon, T., Schluter, W. W., Rayamajhi, A., Bichha, R. P., Shakya, G., et al. (2011). The spatial heterogeneity between Japanese encephalitis incidence distribution and environmental variables in Nepal. *PLoS ONE* 6, e22192. doi: 10.1371/journal.pone.0022192

Jia, M., Xiong, N., Huang, J., Wang, Y., Zhang, X., Zhang, Z., et al. (2012). Japanese encephalitis accompanied by cerebral venous sinus thrombosis: a case report. *BMC Neurol.* 12, 43. doi: 10.1186/1471-2377-12-43

Lai, C. C., Liu, W. L., Lin, S. C., Hsiao, Y. C., and Ding, L. W. (2008). Diagnostic MR images of Japanese encephalitis. *J. Emerg. Med.* 35, 305–307. doi: 10.1016/j.jemermed.2007.02.042

Lannes, N., Summerfield, A., and Filgueira, L. (2017). Regulation of inflammation in Japanese encephalitis. *J. Neuroinflammation* 14, 158. doi: 10.1186/s12974-017-0931-5

Le Flohic, G., Porphyre, V., Barbazan, P., and Gonzalez, J. P. (2013). Review of climate, landscape, and viral genetics as drivers of the Japanese encephalitis virus ecology. *PLoS Negl. Trop. Dis.* 7, e2208. doi: 10.1371/journal.pntd.0002208

Liu, Y., Zhang, J., Han, B., Du, L., Shi, Z., Wang, C., et al. (2021). Case Report: diagnostic value of metagenomics next generation sequencing in intracranial infection caused by mucor. *Front. Med.* 8, 682758. doi: 10.3389/fmed.2021.682758

Mansfield, K. L., Hernández-Triana, L. M., Banyard, A. C., Fooks, A. R., and Johnson, N. (2017). Japanese encephalitis virus infection, diagnosis and control in domestic animals. *Vet. Microbiol.* 201, 85–92. doi: 10.1016/j.vetmic.2017.01.014

Manso, C. F., Bibby, D. F., and Mbisa, J. L. (2017). Efficient and unbiased metagenomic recovery of RNA virus genomes from human plasma samples. *Sci. Rep.* 7, 4173. doi: 10.1038/s41598-017-02239-5

Miner, J. J., and Diamond, M. S. (2016). Mechanisms of restriction of viral neuroinvasion at the blood-brain barrier. *Curr. Opin. Immunol.* 38, 18–23. doi: 10.1016/j.coi.2015.10.008

Patabendige, A., Michael, B. D., Craig, A. G., and Solomon, T. (2018). Brain microvascular endothelial-astrocyte cell responses following Japanese encephalitis virus infection in an *in vitro* human blood-brain barrier model. *Mol. Cell. Neurosci.* 89, 60–70. doi: 10.1016/j.mcn.2018.04.002

Platonov, A., Rossi, G., Karan, L., Mironov, K., Busani, L., and Rezza, G. (2012). Does the Japanese encephalitis virus (JEV) represent a threat for human health in Europe? Detection of JEV RNA sequences in birds collected in Italy. *Euro Surveill.* 17, 20241. doi: 10.2807/ese.17.32.20241-en

Prakash, M., Kumar, S., and Gupta, R. K. (2004). Diffusion-weighted MR imaging in Japanese encephalitis. *J. Comput. Assist. Tomogr.* 28, 756–761. doi: 10.1097/00004728-200411000-00005

Quan, T. M., Thao, T. T. N., Duy, N. M., Nhat, T. M., and Clapham, H. (2020). Estimates of the global burden of Japanese encephalitis and the impact of vaccination from 2000–2015. *Elife* 9, e51027. doi: 10.7554/eLife.51027

Ricklin, M. E., García-Nicolás, O., Brechbühl, D., Python, S., Zumkehr, B., Nougairede, A., et al. (2016). Vector-free transmission and persistence of Japanese encephalitis virus in pigs. *Nat. Commun.* 7, 10832. doi: 10.1038/ncomms10832

Salzberg, S. L., Breitwieser, F. P., Kumar, A., Hao, H., Burger, P., Rodriguez, F. J., et al. (2016). Next-generation sequencing in neuropathologic diagnosis of infections of the nervous system. *Neurol. Neuroimmunol. Neuroinflamm.* 3, e251. doi: 10.1212/NXI.0000000000000251

Shen, Q., Li, Y., Lu, H., Ning, P., Huang, H., Zhao, Q., et al. (2020). Acute flaccid paralysis as the initial manifestation of Japanese encephalitis: a case report. *Jpn. J. Infect. Dis.* 73, 381–382. doi: 10.7883/yoken.JJID.2019.332

Simner, P. J., Miller, S., and Carroll, K. C. (2018). Understanding the promises and hurdles of metagenomic next-generation sequencing as a diagnostic tool for infectious diseases. *Clin Infect Dis.* 66, 778–788. doi: 10.1093/cid/cix881

Simon-Loriere, E., Faye, O., Prot, M., Casademont, I., Fall, G., Fernandez-Garcia, M. D., et al. (2017). Autochthonous Japanese Encephalitis with yellow fever coinfection in Africa. *N. Engl. J. Med.* 376, 1483–1485. doi: 10.1056/NEJMc1701600

Solomon, T. (2006). Control of Japanese encephalitis–within our grasp?. *N. Engl. J. Med.* 355, 869–871. doi: 10.1056/NEJMp058263

Spagnolo, F., Scomazzoni, F., Fichera, M., Comi, G., and Volontè, M. A. (2014). Secondary cervical dystonic tremor after Japanese encephalitis. *Neurol. Sci.* 35, 491–493. doi: 10.1007/s10072-013-1579-2

Tadokoro, K., Ohta, Y., Sato, K., Maeki, T., Sasaki, R., Takahashi, Y., et al. (2018). A Japanese encephalitis patient presenting with parkinsonism with corresponding laterality of magnetic resonance and dopamine transporter imaging findings. *Intern. Med.* 57, 2243–2246. doi: 10.2169/internalmedicine.0337-17

Takeuchi, T., Miyamoto, R., Osaki, Y., Takasaki, T., Yamamoto, N., Sato, K., et al. (2014). Slow mandibulo-faciolingual wiggling tremor associated with Japanese encephalitis. *Mov. Disord. Clin. Pract.* 1, 368–370. doi: 10.1002/mdc3.12074

Tian, M., Li, J., Lei, W., and Shu, X. (2019). Japanese encephalitis virus-induced anti-N-methyl-D-aspartate receptor encephalitis: a case report and review of literature. *Neuropediatrics* 50, 111–115. doi: 10.1055/s-0038-1675607

van den Hurk, A. F., Ritchie, S. A., and Mackenzie, J. S. (2009). Ecology and geographical expansion of Japanese encephalitis virus. *Annu. Rev. Entomol.* 54, 17–35. doi: 10.1146/annurev.ento.54.110807.090510

Wang, C., Gong, L., Zeng, Z., Zhang, J., Guan, H., Chen, L., et al. (2020a). Genome-based analysis of SFTSV causing severe encephalitis with brain lesions. *J. Neurovirol.* 26, 181–187. doi: 10.1007/s13365-019-00816-0

Wang, C., Horby, P. W., Hayden, F. G., and Gao, G. F. (2020b). A novel coronavirus outbreak of global health concern. *Lancet* 395, 470–473. doi: 10.1016/S0140-6736(20)30185-9

Wang, C. J., Zeng, Z. L., Zhang, F. S., and Guo, S. G. (2020). Clinical features of adult anti-N-methyl-d-aspartate receptor encephalitis after Japanese encephalitis. *J. Neurol. Sci*. 417, 117080. doi: 10.1016/j.jns.2020.117080

Wang, G., Li, H., Yang, X., Guo, T., Wang, L., Zhao, Z., et al. (2020). Guillain-Barré syndrome associated with JEV infection. *N. Engl. J. Med*. 383, 1188–1190. doi: 10.1056/NEJMc1916977

Wang, H., and Liang, G. (2015). Epidemiology of Japanese encephalitis: past, present, and future prospects. *Ther. Clin. Risk Manag*. 11, 435–448. doi: 10.2147/TCRM.S51168

Wilson, M. R., Sample, H. A., Zorn, K. C., Arevalo, S., Yu, G., Neuhaus, J., et al. (2019). Clinical metagenomic sequencing for diagnosis of meningitis and encephalitis. *N. Engl. J. Med*. 380, 2327–2340. doi: 10.1056/NEJMoa1803396

Xiang, J. Y., Zhang, Y. H., Tan, Z. R., Huang, J., and Zhao, Y. W. (2014). Guillain-Barré syndrome associated with Japanese encephalitis virus infection in China. *Viral Immunol*. 27, 418–420. doi: 10.1089/vim.2014.0049

Zeller, H. (2012). Is Japanese encephalitis emerging in Europe? *Euro Surveill*. 17, 20242. doi: 10.2807/ese.17.32.20242-en

Conflict of Interest: The authors declare that the research was conducted in the absence of any commercial or financial relationships that could be construed as a potential conflict of interest.

frontiers in Aging Neuroscience

ORIGINAL RESEARCH
published: 15 March 2022
doi: 10.3389/fnagi.2022.800375

Phenome-Wide Association Study of Polygenic Risk Score for Alzheimer's Disease in Electronic Health Records

*Mingzhou Fu[1,2], UCLA Precision Health Data Discovery Repository Working Group, UCLA Precision Health ATLAS Working Group and Timothy S. Chang[1]**

[1] Movement Disorders Program, Department of Neurology, David Geffen School of Medicine, University of California, Los Angeles, Los Angeles, CA, United States, [2] Medical Informatics Home Area, Department of Bioinformatics, University of California, Los Angeles, Los Angeles, CA, United States

Alzheimer's disease (AD) is the most common form of dementia and a growing public health burden in the United States. Significant progress has been made in identifying genetic risk for AD, but limited studies have investigated how AD genetic risk may be associated with other disease conditions in an unbiased fashion. In this study, we conducted a phenome-wide association study (PheWAS) by genetic ancestry groups within a large academic health system using the polygenic risk score (PRS) for AD. PRS was calculated using LDpred2 with genome-wide association study (GWAS) summary statistics. Phenotypes were extracted from electronic health record (EHR) diagnosis codes and mapped to more clinically meaningful phecodes. Logistic regression with Firth's bias correction was used for PRS phenotype analyses. Mendelian randomization was used to examine causality in significant PheWAS associations. Our results showed a strong association between AD PRS and AD phenotype in European ancestry (OR = 1.26, 95% CI: 1.13, 1.40). Among a total of 1,515 PheWAS tests within the European sample, we observed strong associations of AD PRS with AD and related phenotypes, which include mild cognitive impairment (MCI), memory loss, and dementias. We observed a phenome-wide significant association between AD PRS and gouty arthropathy (OR = 0.90, adjusted p = 0.05). Further causal inference tests with Mendelian randomization showed that gout was not causally associated with AD. We concluded that genetic predisposition of AD was negatively associated with gout, but gout was not a causal risk factor for AD. Our study evaluated AD PRS in a real-world EHR setting and provided evidence that AD PRS may help to identify individuals who are genetically at risk of AD and other related phenotypes. We identified non-neurodegenerative diseases associated with AD PRS, which is essential to understand the genetic architecture of AD and potential side effects of drugs targeting genetic risk factors of AD. Together, these findings expand our understanding of AD genetic and clinical risk factors, which provide a framework for continued research in aging with the growing number of real-world EHR linked with genetic data.

Keywords: Alzheimer's disease, polygenic risk score, phenome-wide association study, electronic health record, Mendelian randomization

OPEN ACCESS

Edited by:
Yuzhen Xu,
Tongji University, China

Reviewed by:
Duncan McLauchlan,
Cardiff University, United Kingdom
Gita A. Pathak,
Yale University, United States

***Correspondence:**
Timothy S. Chang
timothychang@mednet.ucla.edu

Specialty section:
This article was submitted to Alzheimer's Disease and Related Dementias, a section of the journal Frontiers in Aging Neuroscience

Received: *23 October 2021*
Accepted: *04 February 2022*
Published: *15 March 2022*

Citation:
Fu M, UCLA Precision Health Data Discovery Repository Working Group, UCLA Precision Health ATLAS Working Group and Chang TS (2022) Phenome-Wide Association Study of Polygenic Risk Score for Alzheimer's Disease in Electronic Health Records. Front. Aging Neurosci. 14:800375. doi: 10.3389/fnagi.2022.800375

INTRODUCTION

Dementia is one of the largest unmet medical needs worldwide. Alzheimer's disease (AD) is the most prevalent form of dementia, which accounts for 60–70% of the total cases (Alzheimer's Association, 2021). In the United States, an estimated 6.2 million individuals aged 65 and older are living with AD, which results in an economic cost of $355 billion (Alzheimer's Association, 2021). Multiple factors, both genetic and environmental, are associated with AD (Xu et al., 2015). Genome-wide association studies (GWASs) have identified multiple common variants, which together contribute to 7.1% of the risk for AD (Kunkle et al., 2019). Well-established genetic risk factors include the ε4 allele of the apolipoprotein E (*APOE*) gene, the five repeat allele of very low-density lipoprotein receptor (*VLDL-R*) gene, and deletion in exon 18 of the α2 macroglobulin (*A2M*) gene (Tilley et al., 1998). Environmental factors, such as air pollution, dyslipidemia, and type 2 diabetes, are also associated with higher risk of AD (Tsuno and Homma, 2009; Fu et al., 2021; Ware et al., 2021). Given the large public health burden, determining the relationship between AD genetic risk and other disease conditions can improve our understanding of the genetic architecture of AD and disease conditions that may be the risk factors for AD.

A phenome-wide association study (PheWAS) can identify the shared genetic etiology between AD and other diseases. A PheWAS is considered a genotype-to-phenotype approach where multiple phenotypes are tested for association with one genetic loci (Hebbring, 2014). As a way of exploring gene-disease associations, PheWAS has been used by investigators with extensively phenotyped cohorts such as large biobanks (Bycroft et al., 2018) and electronic health record (EHR) systems (Denny et al., 2013).

To define phenotypes, PheWASs use computable phenotypes derived from EHR databases. Standard PheWASs have primarily focused on correlating single-nucleotide polymorphisms (SNPs) to a spectrum of phenotypes, which may result in limited power due to the small effect size of each SNP (Fritsche et al., 2018). A polygenic risk score (PRS) is a summary score calculated by aggregating the risk carried by multiple genetic variants, weighted by their effect sizes from a GWAS (Escott-Price et al., 2015). As a measurement of genetic liability to a trait, the PRS has shown promise in predicting human complex traits and diseases and may facilitate early detection, risk stratification, and prevention of common complex diseases (Chatterjee et al., 2016). For instance, one study reported an area under the curve (AUC) of 0.57 using *APOE* region only to predict AD (Tosto et al., 2017), whereas another study reported an AUC of 0.84 with an AD PRS using more than 2,00,000 variants including *APOE* (Escott-Price et al., 2017).

Because a PheWAS identifies multiple phenotypes associated with AD genetic risk, it is possible that these PheWAS significant phenotypes are the causal risk factors for AD. For example, AD genetic risk may lead to a PheWAS significant phenotype, which may lead to AD. Mendelian randomization (MR) is a method using genetic variants as the instrumental variables to assess causality between two phenotypes known as the exposure and the outcome. It is analogous to a randomized control trial where individuals are randomized to carry genetic variants that may modify the risk of an exposure. Since genetic variants are fixed at conception, preceding the onset of health disorders and environmental exposures, MR can overcome many drawbacks of observational studies, such as confounding and reverse causation (Smith and Ebrahim, 2003).

Our study is the first to perform a comprehensive PheWAS from AD PRS in an academic health center EHR with different ancestry populations. We first constructed AD PRS based on the largest AD GWAS (Kunkle et al., 2019). Then, we linked EHR information with genotypic data to explore phenotype associations of AD genetic risk. When a PRS-based PheWAS led to the association with other phenotypes (e.g., gout), we performed MR to evaluate their causal relationships.

SUBJECTS AND METHODS

University of California, Los Angeles ATLAS Cohort

Participants were recruited through University of California, Los Angeles (UCLA) Health System. Written informed consent was obtained from the participants for the study of remnant biosamples in the UCLA ATLAS Precision Health Biobank (Chang et al., 2021; GenomicsDB, 2021; Johnson et al., 2021). Genetic data obtained from remnant biosamples as described below were linked to the deidentified EHR from the UCLA Health System known as the UCLA Data Discovery Repository (DDR), developed under the auspices of the UCLA Health Office of Health Informatics Analytics and the UCLA Institute of Precision Health. This study was considered human subject research exempt because all genetic and EHRs were deidentified (UCLA IRB# 21-000435).

Data Preprocessing

Genotyping and Sample Quality Control

Genotype collection, quality control, processing, and imputation were performed by the UCLA ATLAS Precision Health Biobank (GenomicsDB, 2021; Johnson et al., 2021). Briefly, DNA was extracted from participant blood samples and genotyped on a custom Illumina Global Screening Array that included a standard GWAS backbone and an additional set of pathogenic variants selected from ClinVar (Landrum et al., 2018). Preprocessing of the genotyped data includes removing contaminated samples, unmapped SNPs, high missing rate samples, high missing rate SNPs, duplicates, and performing strand flip (PLINK v.1.90) (Chang et al., 2015; Johnson et al., 2021). After performing array-level genotype quality control, genotypes were imputed from the Michigan Imputation Server (2021). After filtered by $R^2 > 0.90$ and minor allele frequency (MAF) > 0.01, 8,048,268 polymorphic variants and 30,118 participants remained.

Population stratification, defined as the presence of systematic allele frequency differences between populations, can distort the true effect estimates between genetic variants and disease (Price et al., 2006). To adjust for population stratification, we conducted all analyses within samples of the same genetic ancestry group. We inferred samples' genetic ancestry by projecting all genotyped

samples into the principal components (PCs) space of the 1,000 Genome Project (phase 3) (Internationalgenome1000, 2021) reference panel using the R package "bigsnpr" (Privé et al., 2018). We limited the principal component analysis (PCA) to variants that were shared between the 1,000 Genome reference and the UCLA ATLAS data, had a MAF $>$ 0.01, and remained after linkage disequilibrium (LD) clumping ($R^2 > 0.2$, prioritizing variants by higher minor allele counts). PCs were stored and used for further association tests. Genetic ancestry of each sample was inferred using k-nearest neighbor (k-NN) (Altman, 1992) (multiclass classification) with the first 20 PCs of the genotyped data. Genetic ancestry classes were assigned to European, African, American, East Asian, or South Asian ancestry. We compared patients' inferred genetic ancestry with self-reported race or ethnicity, and results are shown in **Supplementary Table 1**.

Phenotype Generation

International Classification of Disease (ICD) codes are standard diagnosis codes used in the EHR. ICD codes are arranged hierarchically to describe diseases and syndromes. It has fine granularity but are considered too detailed to represent clinically meaningful phenotypes and to replicate known genetic associations (Wei et al., 2017). Instead, we used phecodes in our study to reduce complexity of phenotypes in the EHR. Phecodes are defined as a combination of ICD codes and have been validated by experts to better represent clinical disease phenotypes (Denny et al., 2010). As such, this improves power to detect an association by increasing the number of cases and reducing multiple hypothesis testing. We extracted the diagnosis data (ICD-9/10 codes) from all types of encounters (including appointment, hospital encounter, office visit, history, telephone, patient message, orders, transcribed document, scanned document, billing encounter, refill, letter, laboratory visit, health maintenance letter, procedure pass, ancillary orders, historical scanned document, and ancillary procedure) from the UCLA EHR and mapped the ICD codes to phecodes using the R package "PheWAS" (Carroll et al., 2014). Cases for a given PheWAS code were defined if an individual had at least one assignment of that phecode in their longitudinal records. The remaining individuals that did not have phecodes from exclusion criteria previously defined (Carroll et al., 2014) were considered as control subjects. In each ancestry sample, we only tested phenotypes with $\geq$ 50 cases and $\geq$ 50 controls to increase statistical power in the PheWAS analyses. A total of 1,515 case–control studies were generated for further analyses.

Construction of Alzheimer's Disease Polygenic Risk Score

To construct the AD PRS, we used the summary statistics of a late-onset AD GWAS conducted by Kunkle et al. (2019) in which included 21,982 cases and 41,944 controls (N SNP = 11,480,632). Variant positions were converted to GRCh38 using variant IDs from dbSNP build 151 (UCSC Genome Browsers) (Karolchik et al., 2004). The set of SNPs that overlapped between GWAS summary statistics and ATLAS genotyped data was retained for PRS construction. We also restricted our analyses to only the HapMap3 SNPs and removed outliers (SNPs) from the summary statistics as recommended by Privé et al. (2020). A total of 953,397 SNPs passed the above quality control steps and were used for PRS construction. We then used LDpred2 to build the AD PRS (Privé et al., 2020). For the first step of LDpred2, we used a reference dataset from 1,000 Genome (European samples only, n = 522) to extract overlapping GWAS hits and estimated pairwise LD using the available allele dosages of the corresponding controls. LDpred2 updated weights (β) based on LD information and then the updated weights were applied to all UCLA ATLAS samples accordingly. The PRS was calculated by the sum of an individual's risk allele dosages, weighted by risk allele effect sizes. Namely, for subject j, the PRS was of the form $PRS_j = \sum_i \beta_i G_{ij}$ where β_i was the updated weight for locus i, and G_{ij} was the measured dosage data from the risk allele on locus i in subject j. The same methods were applied to construct AD PRS for each ancestry group. Finally, we normalized all PRSs (mean = 0, standard deviation = 1) to a reference population (the 1,000 Genome, European sample).

Statistical Analysis

To validate the AD PRS, we examined the association between PRS and AD phenotype (phecode = 290.11) using logistic regression. To avoid selection bias introduced by younger, healthier participants, we only selected people aged over 65 without AD as our controls (vs. AD cases). We first determined the PRS quartiles within each ancestry sample, categorized all samples according to these PRS quartiles, and fitted logistic regression adjusting for age, sex, and the first five PCs. We reported area under the receiver operating characteristic (ROC) curve (AUC) (Receiver Operating Characteristic, 2021) and odds ratios (ORs) corresponding to the top vs. the bottom quartile PRS (reference), referred to as PRS OR. We also used continuous PRS as the covariate to increase statistical power.

For our primary PRS PheWAS, we conducted logistic regression for each phenotype, adjusting for age, sex, and the first five PCs. We used Firth's bias reduction method in logistic regression models to avoid the problem of separation, which is introduced by very small observed value of the outcome that leads to large parameter estimates and standard errors in a binary or categorical outcome logistic regression (Wang, 2014). We applied the false discovery rate (FDR) p-value correction to adjust for multiple testing (Korthauer et al., 2019). The results were presented as ORs and raw or adjusted p-values.

For significant PheWAS hits on AD PRS, we first reexamined their associations with AD PRS within non-AD controls only. We also tested their relationship with AD phenotype in our sample using logistic regression and one-sample MR. Confounders used for model adjustments were health conditions that were associated with both phenotypes. The conceptual directed acyclic graph and MR assumptions are shown in **Supplementary Figure 1**. For one-sample MR, sequential probit models were used to calculate the causal effect controlling for confounders at each step (Davies et al., 2018). We also used two-sample MR, which uses large GWAS summary statistics (Hartwig et al., 2016), to test the robustness of our one-sample MR results. In two-sample MR, identified SNPs at significance thresholds (liberal: P < 1E-06; conservative: P < 5E-08) were clumped

for independence using PLINK clumping ($R^2 \leq 0.001$, window size = 10,000 kb) within a European reference panel, where SNPs with the lowest *p*-value were retained. We applied multiple robust methods in our study including inverse variance weighted (IVW, with multiplicative random effects model), MR-Egger, weighted median, and weighted mode. Beta coefficient, standard error, and *p*-value were reported for each method. Finally, we performed multiple sensitivity analyses to test whether those MR assumptions were met. F-statistics was used to check instrumental variable strength, with > 10, which indicates a sufficiently strong instrument (Burgess et al., 2011). Cochran's *Q*-test, MR-Egger intercept, and MR-PRESSO global test were used to examine the existence of horizontal pleiotropy and outliers (Bowden et al., 2018; Verbanck et al., 2018). Additionally, I^2 statistics was calculated as a measure of heterogeneity between causal estimates, with a low I^2 which indicates estimates biased toward the null (Bowden et al., 2016).

All analyses were carried out separately for different genetic ancestries. If not stated otherwise, analyses were performed using R version 4.1.0 (R: The R Project For Statistical Computing, 2019).

RESULTS

The study cohort included 30,118 genotyped samples with EHR data (see summary characteristics of the cohort in **Table 1**). The study cohort contained 54.6% women and the median age was 61 years. Of these samples, 0.92% had a diagnosis of AD. Compared to non-European genetic ancestry samples, the European sample was older and had a lower AD PRS. The African and South Asian samples had a higher proportions of AD cases.

Validation of Alzheimer's Disease Polygenic Risk Score

To validate the construction of AD PRS, we determined the association between AD PRS and AD in our UCLA ATLAS sample by ancestry (**Table 2**). AD PRS was positively associated with AD phenotype in the European and East Asian ancestry sample. After adjusting for age, sex, and first five PCs, European participants falling in the top quartile of AD PRS (>0.954) were associated with 1.81 (95%CI: 1.18, 2.82) times higher odds of AD relative to the bottom quartile (≤ -0.854); the odds were higher in East Asian participants, though with a wider confidence interval (OR = 5.11, 95% CI: 1.09, 37.77). A one standard deviation unit increase in AD PRS was associated with 1.26 (95% CI: 1.13, 1.40) times higher odds of AD in European ancestry and 1.88 (95% CI: 1.22, 2.98) times higher in East Asian ancestry. For European ancestry, the AUC for AD PRS alone to predict AD in the logistic regression model was 0.58 (95% CI: 0.53, 0.63) and increased to 0.79 (95% CI: 0.74, 0.83) with covariates including age, sex, and first five PCs. However, no association was observed between AD PRS and AD in other ancestry groups. Taken results together, the AD PRS built using GWAS summary statistic from European ancestry individuals (Kunkle et al., 2019) was confirmed to be a valid instrument for further analyses in the European and East Asian ancestry but should be used with caution for other ancestry samples.

Alzheimer's Disease Polygenic Risk Score Phenome-Wide Association Study

We evaluated AD PRS across 1515 EHR-derived phenotypes with at least 50 case and control subjects in the European sample as our primary analyses (**Supplementary Table 2A**). Through a PheWAS plot, we present -ln(FDR corrected *p*-values) corresponding to each of the 1,515 association tests for H_0: $\beta_{PRS} = 0$ (**Figure 1**). After FDR *p*-value correction, we found strongest associations of AD PRS with the AD and related phenotypes, which include mild cognitive impairment (MCI) (OR = 1.18, FDR = 0.013), memory loss (OR = 1.10, FDR = 0.004), and dementias (OR = 1.14, FDR = 0.046) (**Table 3**). We observed a borderline association between AD PRS and delirium dementia and amnestic and other cognitive disorders (OR = 1.11, FDR = 0.059). In addition, we identified a PRS association with a secondary trait besides cognitive disorders. We observed an inverse association of AD PRS with gouty arthropathy (OR = 0.90, FDR = 0.05). PRS PheWAS was also conducted in other ancestry samples with phenotypes of at least 50 case and control subjects each (**Supplementary Tables 2B–E**), but no significant associations were found.

Determining Causality Between Alzheimer's Disease and Secondary Phenotypes

To investigate whether the secondary association of gouty arthropathy and AD PRS was due to patients with both AD and gouty arthropathy, we reexamined the AD PRS-gout association after excluding AD cases. After adjusting for the same demographic variables (age, sex, number of follow-up years, and first five genetic PCs), the inverse association between AD PRS and gouty arthropathy was still significant (OR = 0.91, $p = 0.01$). We also evaluated the association between gouty arthropathy and AD phenotype in our European sample. Variables that influence both the exposure (gouty arthropathy) and outcome (AD) can cause a spurious association in observational studies (McNamee, 2005). We performed bivariate analyses to find factors that potentially confound the association between gouty arthropathy and AD (**Supplementary Table 3**). Hypertension, diabetes, stroke, and hyperlipid were significantly associated with both gouty arthropathy and AD. These were adjusted as confounders in subsequent models. Although there was a crude positive association between gouty arthropathy and AD (OR = 2.48, 95% CI: 1.11, 4.79), no significant association was found after adjustments of demographic and comorbidity variables mentioned above (**Table 4**).

Next, we examined whether a lower risk of AD was a consequence of gouty arthropathy with a one-sample MR framework (**Supplementary Figure 1**). A test of inferred causality of gouty arthropathy on AD was conducted using AD PRS as the instrumental variable since its association with gouty arthropathy was statistically significant (**Table 3**), which met the relevance assumption of MR. As shown in **Table 4**, the causality of gouty

TABLE 1 | Demographics and clinical characteristics of UCLA ATLAS sample.[a]

		Genetic ancestry sample					
Characteristic	**All sample** ***n* = 30,118**	**European** ***n* = 19,934**	**African** ***n* = 1,663**	**American** ***n* = 4,991**	**East Asian** ***n* = 2,982**	**South Asian** ***n* = 548**	**Overall *P*-value[b]**
Females, N (%)	16,434 (54.6%)	10,288 (51.6%)	1,027 (61.8%)	3,004 (60.2%)	1,816 (60.9%)	299 (54.6%)	< 0.001*
Age (years), Median [25th;75th]	61.0 [45.0;72.0]	63.0 [48.0;73.0]	60.0 [46.0;71.0]	53.0 [39.0;66.0]	57.0 [42.0;70.0]	49.0 [38.0;66.0]	< 0.001*
Encounters per participant, Median [25th;75th][c]	59.0 [25.0;119]	59.0 [26.0;119]	73.0 [29.0;152]	55.0 [22.0;119]	54.0 [25.0;105]	49.0 [23.0;106]	< 0.001*
Unique diagnosis per participant, Median [25th;75th]	59.0 [32.0;103]	60.0 [33.0;103]	71.0 [38.0;125]	59.0 [29.0;107]	50.0 [28.0;88.0]	51.0 [28.0;83.0]	< 0.001*
Timespan of records (years), Median [25th;75th]	6.00 [3.10;8.10]	6.20 [3.30;8.10]	6.50 [3.30;8.20]	5.20 [2.50;7.90]	5.80 [3.00;8.00]	5.30 [2.90;7.80]	< 0.001*
PRS for Alzheimer's disease, Mean (SD)	0.46 (1.64)	0.16 (1.43)	3.63 (1.58)	0.23 (1.40)	1.07 (1.34)	0.19 (1.39)	< 0.001*
Alzheimer's disease case count, N (%)	241 (0.92%)	168 (0.97%)	15 (1.06%)	34 (0.78%)	17 (0.63%)	7 (1.42%)	0.21

PRS, polygenic risk score; SD, standard deviation.
[a]All the statistics were calculated based on non-missing data for each variable.
[b]Depending whether the row variable is considered as continuous normal distributed (1), continuous non-normal distributed (2) or categorical (3), the following descriptives and tests are performed: 1- mean, sd, and ANOVA; 2- median, 1st and 3rd quartiles, and Kruskal–Wallis test; (3), absolute and relative frequencies and chi-squared or exact Fisher's test when the expected frequency is less than 5 in some cells from chi-square test for categorical variables as appropriate, interpreted as differences between groups.
*[c]All types of encounters extracted from the EHRs were included, see details in section "Subjects and Methods." *significant test statistics ($p < 0.05$).*

TABLE 2 | Associations between AD PRS and AD, UCLA ATLAS sample, by genetic ancestry.[a]

	Categorical (top vs. bottom quartile) PRS			Continuous PRS				
	N[b]	**Odds Ratio (95%CI)**		**N[b]**	**Odds Ratio (95%CI)**		**AUC: PRS alone (95%CI)**	
European	3,829	1.81	(1.18, 2.82)	7,620	1.26	(1.13, 1.40)	0.58	(0.53, 0.63)
African	262	0.91	(0.11, 7.79)	521	0.95	(0.63, 1.41)	0.55	(0.40, 0.70)
American	544	0.62	(0.21, 1.72)	1,084	0.97	(0.74, 1.26)	0.50	(0.40, 0.61)
East Asian	448	5.11	(1.09, 37.77)	905	1.88	(1.22, 2.98)	0.66	(0.53, 0.79)
South Asian	65	0.46	(0.01, 7.46)	123	0.80	(0.40, 1.51)	0.60	(0.31, 0.88)

AD, Alzheimer's Disease; CI, confidence interval; PRS, polygenic risk score.
[a]All the values were based on results from multivariable logistic regression analyses in each sample, in which "no AD" was used as the reference group. ORs were reported from the models which further adjusted for age, sex, and first five PC sets. AUCs were reported from the models with PRS alone.
[b]This number include both AD cases and controls.

arthropathy on AD no longer held after adjusting for the same demographic and comorbidity variables mentioned above (one-sample MR with sequential probit models, $p = 0.06$). The results suggest that gouty arthropathy is not a causal protective factor of AD in our European ancestry sample.

We further tested whether gout is the causal protective risk factors for AD using a two-sample MR approach. This two-sample MR method does not directly test whether AD PRS is the instrumental variable, but rather uses multiple variants below a given *p*-value threshold from GWAS as the instrumental variable. We used the Kunkle et al. (2019) AD GWAS and the gout GWAS conducted by Tin et al. (2019) to perform two-sample MR analyses. Similar to our one-sample MR, no significant causal relationship was consistently found from gout to AD using multiple methods that include IVW, MR-Egger, weighted median, and weighted mode (**Table 5**). The F-statistic indicates adequate instrument strength (liberal: 86.76 > 10; conservative: 123.49 > 10). There was no heterogeneity across different methods or directional pleiotropy found using multiple measures (see "Subjects and Methods"). We also performed a sensitivity analysis to examine the reverse causality of AD on gout. Both one-sample and two-sample MR results showed no causal relationship between AD and gout (**Supplementary Table 4**).

DISCUSSION

Alzheimer's disease is a complex disease determined by interactions between genetic risk factors and environmental modifiers (Baumgart et al., 2015; Xu et al., 2015; Fu et al., 2021; Ware et al., 2021). In our study, we conducted a comprehensive, ancestry specific PheWAS study using cumulative genetic risk of AD in a real-world academic medical center population. We provided evidence for the value of AD PRS to aid in identifying individuals who are genetically at risk of AD, and also other related phenotypes including MCI, memory loss

FIGURE 1 | PheWAS plot for Alzheimer's disease polygenic risk score, European ancestry sample (N = 19,934). 1515 traits (number of cases/controls ≥ 50) are grouped into 17 color-coded categories as shown on the horizontal axis; the p-values for testing the associations of PRS with the traits were adjusted by FDR and transformed to minus natural logarithms, shown on the vertical axis. The size of the dot refers to effect size (OR) of AD PRS on traits. All values were based on results from multivariable logistic regression analyses, in which "no disease/symptom" was used as the reference group, adjusted for age, sex, and first five PCs. The solid horizontal line for adjusted p = 0.05 cutoff.

TABLE 3 | Significant PheWAS results of Alzheimer's disease polygenic risk score in the full European ancestry sample (N = 19,934).[a]

Phecodes	Description	Group	N total	N Cases	N Controls	OR	Raw *P*-value	Adjusted *P*-value[b]
290.11	Alzheimer's disease	Mental disorders	17,290	168	17,122	1.26	3.17E-05	0.015
292.2	Mild cognitive impairment	Mental disorders	17,470	359	17,111	1.18	1.81E-05	0.013
292.3	Memory loss	Mental disorders	18,583	1,470	17,113	1.10	2.88E-06	0.004
290.1	Dementias	Mental disorders	17,585	479	17,106	1.14	1.26E-04	0.046
274.11	Gouty arthropathy	Endocrine/metabolic	19,489	656	18,833	0.90	1.73E-04	0.050

OR, odds ratio.
[a]*All the values were based on results from multivariable logistic regression analyses in each sample, in which "no disease/symptom" was used as the reference group, and adjusted for age, sex, and first five PC sets.*
[b]*The adjusted p-value was calculated by controlling the FDR.*

TABLE 4 | Results of logistic regression and one-sample Mendelian randomization testing associations and causality between gouty arthropathy and Alzheimer's disease, European ancestry (N = 14,511).[a]

	Logistic regression test for association		One-sample MR test for causality	
	Odds ratio (95 CI%)		Beta coefficient[d]	*p*-value
Crude	2.48	(1.11, 4.79)	–29.71	0.04*
Adjusted demographics[b]	1.13	(0.49, 2.28)	–5.71	0.03*
Adjusted health conditions[c]	1.02	(0.44, 2.09)	–3.62	0.06

AD, Alzheimer's disease; CI, Confidence Interval; MR, Mendelian randomization; PRS, polygenic risk score.
[a]*All the values were based on results from multivariable logistic regression analyses in each sample, in which "no Alzheimer's disease" was used as the reference group.*
[b]*Adjusted for age, sex, number of follow-up years, and five ancestry-specific PC sets.*
[c]*Adjusted for history of hypertension, diabetes, stroke, and hyperlipid in addition to variables in b.*
[d]*Beta coefficients for the causal estimates from gouty arthropathy to AD. *significant test statistics ($p < 0.05$).*

and dementias in the European ancestry. We identified non-neurodegenerative diseases, especially gout, associated with AD PRS. Understanding horizontal pleiotropy for AD genetic risk is essential to broaden our understanding for the genetic architecture of AD. These PheWAS results also provide insights on potential side effects of drugs targeting these genetic risk

TABLE 5 | Two-sample Mendelian randomization to test causal relationship between gout status and Alzheimer's disease.[a]

Instrument	Mendelian randomization method	Beta	SE	*P*-value	Sensitivity test	Results
Evaluate gout causal for AD						
Liberal	IVW (fixed effects)	0.022	0.019	0.24	F statistic (combined instrument)	86.76
$p < 1E-06$	IVW (multiplicative random effects)	0.022	0.020	0.25	Cochran's Q (for IVW)	$p = 0.34$
(n_SNP = 48)	MR Egger	0.079	0.032	0.02*	MR-Egger intercept	$p = 0.03$
	Weighted median	0.057	0.029	0.05	MR-PRESSO global test	$p = 0.26$
	Weighted mode	0.054	0.028	0.06	I^2 test	0.99
Conservative	IVW (fixed effects)	0.025	0.021	0.22	F statistic (combined instrument)	123.49
$p < 5E-08$	IVW (multiplicative random effects)	0.025	0.019	0.19	Cochran's Q (for IVW)	$p = 0.67$
(n_SNP = 29)	MR Egger	0.059	0.034	0.10	MR-Egger intercept	$p = 0.22$
	Weighted median	0.054	0.030	0.07	MR-PRESSO global test	$p = 0.20$
	Weighted mode	0.056	0.030	0.08	I^2 test	0.99

IVW, inverse variance weighted; SE, standard error.

[a]*The F-statistics was not able to be calculated because the Kunkle GWAS summary statistics did not report allele frequency. *significant test statistics ($p < 0.05$).*

factors in AD (Nguyen et al., 2019). For example, because AD PRS and gout have a negative association, drugs targeting AD genetic risk factors may increase risk of gout. Finally, we performed thorough analyses evaluating the causality between significant associations, which shows that gout was not a causal risk factor for AD. The evaluation of causality is an important component to infer the temporal order of diseases and better understand protective and risk factors of AD.

We constructed an AD PRS that summarized the aggregated AD genetic risks based on prior GWAS. We found moderate prediction power of the AD PRS in the European and East Asian ancestry sample, but poor predictive power in other non-European ancestry samples. We expected poor performance in non-European ancestry samples as our methods for computing the AD PRS depended on summary statistics from a GWAS including only participants of the European ancestry (Kunkle et al., 2019). Prior studies have found in multiple diseases that PRS constructed from European ancestry GWAS results in poor predictive performance in non-European ancestry populations (Duncan et al., 2019; Martin et al., 2019). Furthermore, we had small sample sizes for PheWAS in non-European ancestry samples (**Table 2**). The significant association of the European GWAS-based AD PRS with East Asian ancestry may be due to some shared genetic architecture for AD genetic risk. Prior studies found associations between a polygenic risk model using significant AD risk loci from European AD GWAS and AD in Chinese cohorts (Xiao et al., 2015; Zhou et al., 2020).

We then performed a primary PheWAS. In the European samples, we observed a significant positive association between AD PRS and AD, along with multiple cognitive phenotypes (MCI, memory loss, and dementias). Prior studies have identified an association of AD PRS with MCI (Logue et al., 2019) and the conversion of MCI to AD (Chaudhury et al., 2019; Logue et al., 2019). Our study further supports that AD PRS is associated with MCI in an EHR cohort. We also observed a borderline association between AD PRS and delirium dementia and amnestic and other cognitive disorders. Whereas it is known Alzheimer's disease and dementias are risk factors for delirium (Fick et al., 2002; Fong et al., 2009), prior work has not evaluated the association of AD PRS and delirium. The association of AD PRS and these cognitive phenotypes including memory loss and dementias may also be due to the fact they are comorbid with or precede a diagnosis of Alzheimer's disease (Varatharajah et al., 2019; Alzheimer's Association, 2021). Our results from an EHR cohort suggest that using AD PRS to predict not only AD but also MCI and delirium should be further explored.

We also found a significant association between gouty arthropathy and AD PRS. We conducted multiple sensitivity analyses to explore whether the associations of AD PRS with gout and AD PRS with AD were driven by horizontal pleiotropy, in which genetic variants convey risk independently to two different phenotypes, or vertical pleiotropy, in which genetic variants convey risk to one phenotype, which in turn raises or lowers risk for the secondary phenotype (Zheutlin et al., 2019). In the European ancestry sample, we observed that gout was not causally related to AD using one-sample and two-sample MR. This result was also consistent with the null association found between gout and AD given by logistic regressions testing gout and AD without considering AD genetic risk and correcting for confounders (**Table 4**). Although gout commonly has an earlier age of onset than AD (Lu et al., 2016), which indicates that there is unlikely to be a causal relationship from AD to gout, we tested for reversal causality from AD to gout in our study as a sensitivity analysis and the null-causal relationship still held. Taken as a whole, gout is a horizontal pleiotropic factor of AD; that is, AD genetic variants have a negative effect on gout, but gout is not a causal risk factor for AD when considering other confounders.

The association of gout with AD has had mixed findings in prior work. Hyperuricemia is the key causal precursor for gout and has been proposed as a mechanistic link to AD (Lu et al., 2016). Uric acid is considered as a major natural antioxidant in plasma that reduces oxidative stress and protects against free radicals, which are elevated in AD (Tuppo and Forman, 2001; Polidori and Mecocci, 2002; Reddy, 2006; Al-Khateeb et al., 2015). Other cross-sectional studies of serum uric acid reported no difference in concentration in AD and MCI patients compared to healthy controls (Polidori and Mecocci, 2002).

There are several distinct aspects to our study. We used LDpred2 method to build our AD PRS. Since association tests in GWASs are typically performed one SNP at a time, the presence of strong correlation structures across the genome, also known as LD, will likely cause bias in the independent effect estimates (Choi et al., 2020). LDpred is a popular method for deriving polygenic scores to account for LD. It implements a Bayesian shrinkage model which uses a prior on effect sizes and LD information from an external reference panel to infer the posterior mean effect size of each SNP (Vilhjálmsson et al., 2015). LDpred2 is an updated version of LDpred that addresses the issues of model misspecification while improving the computational efficiency. Specifically, LDpred2 (auto model) allows the learning of the two LDpred parameters (the proportion of causal variants p and the SNP heritability h^2) from data, which can therefore be applied to data without the need of a validation dataset to choose best-performing hyperparameters (Privé et al., 2020). In addition, we used Firth's corrected logistic regression in our PheWAS analyses. The Firth's bias correction can solve the problem of separation in logistic regression and provide well-controlled type I error rates for unbalanced case–control studies with relatively small sample counts (Wang, 2014). Finally, we used thorough MR analyses to study causal inferences of gout and AD. MR has the advantages of removing unmeasured confounding, and the use of both one-sample and two-sample MR could be complementary to each other. The advantage of one-sample MR is the use of individual participant data rather than summary data, whereas the advantage of two-sample MR is the increased statistical power and thus can provide more robust causal results. However, some assumptions, such as the exclusion restriction assumption, are difficult to completely verify as all true confounders for gout and AD are unknown (Burgess et al., 2015).

There are limitations to this study. Given the non-significant results of AD PRS and AD in non-European ancestry samples, the PheWAS results may not be generalizable to these populations. Although large AD GWAS is not currently available in other ancestry groups, future work should perform PheWAS with AD PRS from ancestry specific GWAS. Because thorough MR analysis did not identify a causal relationship between gout and AD, and MR methods do not consider temporal data, we did not consider the temporal ordering of gout and AD diagnosis.

In summary, this study expands our understanding of AD genetic and clinical risk factors and provides a framework for evaluating horizontal and vertical pleiotropy that can be used in aging research. With the growing number of real-world EHR linked with genetic data, continued research will improve our ability to use genetics, biomarkers, and clinical risk factors, some of which will be causal, for early disease prediction and treatment.

CONSORTIUM/GROUP AND COLLABORATIVE AUTHORS

UCLA Precision Health Data Discovery Repository Working Group: Anna L. Antonio, Maryam Ariannejad, Angela M. Badillo, Brunilda Balliu, Yael Berkovich, Michael Broudy, Tony Dang, Chris Denny, Eleazar Eskin, Eran Halperin, Brian L. Hill, Ankur Jain, Vivek Katakwar, Clara Lajonchere, Clara Magyar, Sheila Minton, Ghouse Mohammed, Ariff Muhamed, Pabba Pavan, Michael A. Pfeffer, Nadav Rakocz, Akos Rudas, Rey Salonga, Timothy J. Sanders, Paul Tung, Vu Vu, and Ailsa Zheng. UCLA Precision Health ATLAS Working Group: Ruth Johnson, Yi Ding, Alec Chiu, Jae-Hoon Sul, Sriram Sankraraman, and Bogdan Pasaniuc.

DATA AVAILABILITY STATEMENT

The data analyzed in this study is subject to the following licenses/restrictions: individual electronic health record data are not publicly available due to patient confidentiality and security concerns. Requests to access these datasets should be directed to corresponding author.

ETHICS STATEMENT

Ethical review and approval was not required for the study on human participants in accordance with the local legislation and institutional requirements. The patients/participants provided their written informed consent to participate in this study.

AUTHOR CONTRIBUTIONS

MF analyzed the data. MF and TC interpreted the data analysis and were major contributors in writing the manuscript. All authors read and approved the final manuscript.

FUNDING

MF was supported by the Summer Mentored Research Fellowship from the Graduate Programs in Bioscience at University of California, Los Angeles. TC was supported by the National Institutes of Health (NIH) National Institute of Aging (NIA) (grant K08AG065519-01A1). The UCLA ATLAS Community Health Initiative in collaboration with UCLA ATLAS Precision Health Biobank is a program of Institute for Precision Health (IPH), which directs and supports the biobanking and genotyping of biospecimen samples from participating UCLA patients in collaboration with the David Geffen School of Medicine, UCLA Clinical and Translational Science Institute and UCLA Health.

ACKNOWLEDGMENTS

We gratefully acknowledge patients who have participated in the UCLA ATLAS Community Health Initiative.

SUPPLEMENTARY MATERIAL

The Supplementary Material for this article can be found online at: https://www.frontiersin.org/articles/10.3389/fnagi.2022.800375/full#supplementary-material

REFERENCES

Al-Khateeb, E., Althaher, A., Al-Khateeb, M., Al-Musawi, H., Azzouqah, O., Al-Shweiki, S., et al. (2015). Relation between uric acid and Alzheimer's disease in elderly jordanians. *J. Alzheimers Dis.* 44, 859–865. doi: 10.3233/Jad-142037

Altman, N. S. (1992). An introduction to kernel and nearest-neighbor nonparametric regression. *Am. Stat.* 46, 175–185. doi: 10.1080/00031305.1992.10475879

Alzheimer's Association (2021). 2021 Alzheimer's disease facts and figures. *Alzheimers Dement.* 17, 327–406. doi: 10.1002/Alz.12328

Baumgart, M., Snyder, H. M., Carrillo, M. C., Fazio, S., Kim, H., and And Johns, H. (2015). Summary of the evidence on modifiable risk factors for cognitive decline and dementia: a population-based perspective. *Alzheimers Dement.* 11, 718–726. doi: 10.1016/J.Jalz.2015.05.016

Bowden, J., Del, Greco M F, Minelli, C., Davey Smith, G., Sheehan, N. A., and Thompson, J. R. (2016). Assessing the suitability of summary data for two-sample mendelian randomization analyses using Mr-Egger regression: the role of the I2 statistic. *Int. J. Epidemiol.* 45, 1961–1974. doi: 10.1093/Ije/Dyw220

Bowden, J., Hemani, G., and Davey Smith, G. (2018). Invited commentary: detecting individual and global horizontal pleiotropy in mendelian randomization-a job for the humble heterogeneity statistic? *Am. J. Epidemiol.* 187, 2681–2685. doi: 10.1093/Aje/Kwy185

Burgess, S., Scott, R. A., Timpson, N. J., Davey Smith, G., Thompson, S. G., and Epic-Interact Consortium (2015). Using published data in mendelian randomization: a blueprint for efficient identification of causal risk factors. *Eur. J. Epidemiol.* 30, 543–552. doi: 10.1007/S10654-015-0011-Z

Burgess, S., Thompson, S. G., and Crp Chd Genetics Collaboration. (2011). Avoiding bias from weak instruments in mendelian randomization studies. *Int. J. Epidemiol.* 40, 755–764. doi: 10.1093/Ije/Dyr036

Bycroft, C., Freeman, C., Petkova, D., Band, G., Elliott, L. T., Sharp, K., et al. (2018). The Uk biobank resource with deep phenotyping and genomic data. *Nature* 562, 203–209. doi: 10.1038/S41586-018-0579-Z

Carroll, R. J., Bastarache, L., and Denny, J. C. (2014). R phewas: data analysis and plotting tools for phenome-wide association studies in the r environment. *Bioinformatics* 30, 2375–2376. doi: 10.1093/Bioinformatics/Btu197

Chang, C. C., Chow, C. C., Tellier, L. C., Vattikuti, S., Purcell, S. M., and Lee, J. J. (2015). Second-generation plink: rising to the challenge of larger and richer datasets. *Gigascience* 4:7. doi: 10.1186/S13742-015-0047-8

Chang, T. S., Ding, Y., Freund, M. K., Johnson, R., Schwarz, T., Yabu, J. M., et al. (2021). Pre-existing conditions in hispanics/latinxs that are covid-19 risk factors. *Iscience* 24:102188. doi: 10.1016/J.Isci.2021.102188

Chatterjee, N., Shi, J., and García-Closas, M. (2016). Developing and evaluating polygenic risk prediction models for stratified disease prevention. *Nat. Rev. Genet.* 17, 392–406. doi: 10.1038/Nrg.2016.27

Chaudhury, S., Brookes, K. J., Patel, T., Fallows, A., Guetta-Baranes, T., Turton, J. C., et al. (2019). Alzheimer's disease polygenic risk score as a predictor of conversion from mild-cognitive impairment. *Transl. Psychiatry* 9:154. doi: 10.1038/S41398-019-0485-7

Choi, S. W., Mak, T. S.-H., and O'reilly, P. F. (2020). Tutorial: a guide to performing polygenic risk score analyses. *Nat. Protoc.* 15, 2759–2772. doi: 10.1038/S41596-020-0353-1

Davies, N. M., Holmes, M. V., and Davey Smith, G. (2018). Reading mendelian randomisation studies: a guide, glossary, and checklist for clinicians. *BMJ* 362:K601. doi: 10.1136/Bmj.K601

Denny, J. C., Bastarache, L., Ritchie, M. D., Carroll, R. J., Zink, R., Mosley, J. D., et al. (2013). Systematic comparison of phenome-wide association study of electronic medical record data and genome-wide association study data. *Nat. Biotechnol.* 31, 1102–1110. doi: 10.1038/Nbt.2749

Denny, J. C., Ritchie, M. D., Basford, M. A., Pulley, J. M., Bastarache, L., Brown-Gentry, K., et al. (2010). Phewas: demonstrating the feasibility of a phenome-wide scan to discover gene-disease associations. *Bioinformatics* 26, 1205–1210. doi: 10.1093/Bioinformatics/Btq126

Duncan, L., Shen, H., Gelaye, B., Meijsen, J., Ressler, K., Feldman, M., et al. (2019). Analysis of polygenic risk score usage and performance in diverse human populations. *Nat. Commun.* 10:3328. doi: 10.1038/S41467-019-11112-0

Escott-Price, V., Myers, A. J., Huentelman, M., and Hardy, J. (2017). Polygenic risk score analysis of pathologically confirmed alzheimer disease. *Ann. Neurol.* 82, 311–314. doi: 10.1002/Ana.24999

Escott-Price, V., Sims, R., Bannister, C., Harold, D., Vronskaya, M., Majounie, E., et al. (2015). Common polygenic variation enhances risk prediction for Alzheimer's disease. *Brain* 138, 3673–3684. doi: 10.1093/Brain/Awv268

Fick, D. M., Agostini, J. V., and Inouye, S. K. (2002). Delirium superimposed on dementia: a systematic review. *J. Am. Geriatr. Soc.* 50, 1723–1732. doi: 10.1046/J.1532-5415.2002.50468.X

Fong, T. G., Jones, R. N., Shi, P., Marcantonio, E. R., Yap, L., Rudolph, J. L., et al. (2009). Delirium accelerates cognitive decline in alzheimer disease. *Neurology* 72, 1570–1575. doi: 10.1212/Wnl.0b013e3181a4129a

Fritsche, L. G., Gruber, S. B., Wu, Z., Schmidt, E. M., Zawistowski, M., Moser, S. E., et al. (2018). Association of polygenic risk scores for multiple cancers in a phenome-wide study: results from the michigan genomics initiative. *Am. J. Hum. Genet.* 102, 1048–1061. doi: 10.1016/J.Ajhg.2018.04.001

Fu, M., Bakulski, K. M., Higgins, C., and Ware, E. B. (2021). Mendelian randomization of dyslipidemia on cognitive impairment among older americans. *Front. Neurol.* 12:660212. doi: 10.3389/Fneur.2021.660212

GenomicsDB (2021). *Ucla Precision Health*. Available online at: https://www.Uclahealth.Org/Precision-Health/Genomicsdb (accessed August 10, 2021).

Hartwig, F. P., Davies, N. M., Hemani, G., and Davey Smith, G. (2016). Two-sample mendelian randomization: avoiding the downsides of a powerful, widely applicable but potentially fallible technique. *Int. J. Epidemiol.* 45, 1717–1726. doi: 10.1093/Ije/Dyx028

Hebbring, S. J. (2014). The challenges, advantages and future of phenome-wide association studies. *Immunology* 141, 157–165. doi: 10.1111/Imm.12195

Internationalgenome1000 (2021). *Genomes | A Deep Catalog Of Human Genetic Variation*. Available online at: https://Www.Internationalgenome.Org/ (accessed August 10, 2021).

Johnson, R., Ding, Y., Venkateswaran, V., Bhattacharya, A., Chiu, A., Schwarz, T., et al. (2021). Leveraging genomic diversity for discovery in an ehr-linked biobank: the ucla atlas community health initiative. *medRxiv* [Preprint] doi: 10.1101/2021.09.22.21263987

Karolchik, D., Hinrichs, A. S., Furey, T. S., Roskin, K. M., Sugnet, C. W., Haussler, D., et al. (2004). The ucsc table browser data retrieval tool. *Nucleic Acids Res.* 32, D493–D496. doi: 10.1093/Nar/Gkh103

Korthauer, K., Kimes, P. K., Duvallet, C., Reyes, A., Subramanian, A., Teng, M., et al. (2019). A practical guide to methods controlling false discoveries in computational biology. *Genome Biol.* 20:118. doi: 10.1186/S13059-019-1716-1

Kunkle, B. W., Grenier-Boley, B., Sims, R., Bis, J. C., Damotte, V., Naj, A. C., et al. (2019). Genetic meta-analysis of diagnosed Alzheimer's disease identifies new risk loci and implicates Aβ, tau, immunity and lipid processing. *Nat. Genet.* 51, 414–430. doi: 10.1038/S41588-019-0358-2

Landrum, M. J., Lee, J. M., Benson, M., Brown, G. R., Chao, C., Chitipiralla, S., et al. (2018). Clinvar: improving access to variant interpretations and supporting evidence. *Nucleic Acids Res.* 46, D1062–D1067. doi: 10.1093/Nar/Gkx1153

Logue, M. W., Panizzon, M. S., Elman, J. A., Gillespie, N. A., Hatton, S. N., Gustavson, D. E., et al. (2019). Use of an Alzheimer's disease polygenic risk score to identify mild cognitive impairment in adults in their 50s. *Mol. Psychiatry* 24, 421–430. doi: 10.1038/S41380-018-0030-8

Lu, N., Dubreuil, M., Zhang, Y., Neogi, T., Rai, S. K., Ascherio, A., et al. (2016). Gout and the risk of Alzheimer's disease: a population-based, bmi-matched cohort study. *Ann. Rheum. Dis.* 75, 547–551. doi: 10.1136/Annrheumdis-2014-206917

Martin, A. R., Kanai, M., Kamatani, Y., Okada, Y., Neale, B. M., and Daly, M. J. (2019). Clinical use of current polygenic risk scores may exacerbate health disparities. *Nat. Genet.* 51, 584–591. doi: 10.1038/S41588-019-0379-X

McNamee, R. (2005). Regression modelling and other methods to control confounding. *Occup. Environ. Med.* 62, 500–506. doi: 10.1136/Oem.2002.001115

Michigan Imputation Server (2021). Available online at: https://imputationserver.sph.umich.edu/index.html#! (accessed August 17, 2021).

Nguyen, P. A., Born, D. A., Deaton, A. M., Nioi, P., and Ward, L. D. (2019). Phenotypes associated with genes encoding drug targets are predictive of clinical trial side effects. *Nat. Commun.* 10:1579. doi: 10.1038/S41467-019-09407-3

Polidori, M. C., and Mecocci, P. (2002). Plasma susceptibility to free radical-induced antioxidant consumption and lipid peroxidation is increased in very old subjects with alzheimer disease. *J. Alzheimers Dis.* 4, 517–522. doi: 10.3233/Jad-2002-4608

Price, A. L., Patterson, N. J., Plenge, R. M., Weinblatt, M. E., Shadick, N. A., and Reich, D. (2006). Principal components analysis corrects for stratification in genome-wide association studies. *Nat. Genet.* 38, 904–909. doi: 10.1038/Ng1847

Privé, F., Arbel, J., and Vilhjálmsson, B. J. (2020). Ldpred2: better, faster, stronger. *Bioinformatics* 36, 5424–5431. doi: 10.1093/Bioinformatics/Btaa1029

Privé, F., Aschard, H., Ziyatdinov, A., and Blum, M. G. B. (2018). Efficient analysis of large-scale genome-wide data with two r packages: bigstatsr and bigsnpr. *Bioinformatics* 34, 2781–2787. doi: 10.1093/Bioinformatics/Bty185

R: The R Project For Statistical Computing (2019). Available online at: https://www.R-Project.Org/ (accessed October 18, 2019).

Receiver Operating Characteristic (2021). *Wikipedia*. Available online at: https://En.Wikipedia.Org/W/Index.Php?Title=Receiver_Operating_Characteristic&Oldid=1035914883 (accessed August 11, 2021).

Reddy, P. H. (2006). Amyloid precursor protein-mediated free radicals and oxidative damage: implications for the development and progression of Alzheimer's disease. *J Neurochem.* 96, 1–13. doi: 10.1111/J.1471-4159.2005.03530.X

Smith, G. D., and Ebrahim, S. (2003). "Mendelian randomization": can genetic epidemiology contribute to understanding environmental determinants of disease? *Int. J. Epidemiol.* 32, 1–22. doi: 10.1093/Ije/Dyg070

Tilley, L., Morgan, K., and Kalsheker, N. (1998). Genetic risk factors in Alzheimer's disease. *Mol. Pathol.* 51, 293–304.

Tin, A., Marten, J., Halperin Kuhns, V. L., Li, Y., Wuttke, M., Kirsten, H., et al. (2019). Target genes, variants, tissues and transcriptional pathways influencing human serum urate levels. *Nat. Genet.* 51, 1459–1474. doi: 10.1038/S41588-019-0504-X

Tosto, G., Bird, T. D., Tsuang, D., Bennett, D. A., Boeve, B. F., Cruchaga, C., et al. (2017). Polygenic risk scores in familial alzheimer disease. *Neurology* 88, 1180–1186. doi: 10.1212/Wnl.0000000000003734

Tsuno, N., and Homma, A. (2009). What is the association between depression and Alzheimer's disease? *Expert Rev. Neurother.* 9, 1667–1676. doi: 10.1586/Ern.09.106

Tuppo, E. E., and Forman, L. J. (2001). Free radical oxidative damage and Alzheimer's disease. *J. Am. Osteopath. Assoc.* 101, S11–S15.

Varatharajah, Y., Ramanan, V. K., Iyer, R., and Vemuri, P. (2019). Predicting short-term mci-to-ad progression using imaging, csf, genetic factors, cognitive resilience, and demographics. *Sci. Rep.* 9:2235. doi: 10.1038/S41598-019-38793-3

Verbanck, M., Chen, C.-Y., Neale, B., and Do, R. (2018). Detection of widespread horizontal pleiotropy in causal relationships inferred from mendelian randomization between complex traits and diseases. *Nat. Genet.* 50, 693–698. doi: 10.1038/S41588-018-0099-7

Vilhjálmsson, B. J., Yang, J., Finucane, H. K., Gusev, A., Lindström, S., Ripke, S., et al. (2015). Modeling linkage disequilibrium increases accuracy of polygenic risk scores. *Am. J. Hum. Genet.* 97, 576–592. doi: 10.1016/J.Ajhg.2015.09.001

Wang, X. (2014). Firth logistic regression for rare variant association tests. *Front. Genet.* 5:187. doi: 10.3389/Fgene.2014.00187

Ware, E. B., Morataya, C., Fu, M., and Bakulski, K. M. (2021). Type 2 diabetes and cognitive status in the health and retirement study: a mendelian randomization approach. *Front. Genet.* 12:634767. doi: 10.3389/Fgene.2021.634767

Wei, W.-Q., Bastarache, L. A., Carroll, R. J., Marlo, J. E., Osterman, T. J., Gamazon, E. R., et al. (2017). Evaluating phecodes, clinical classification software, and Icd-9-cm codes for phenome-wide association studies in the electronic health record. *PLoS One* 12:e0175508. doi: 10.1371/Journal.Pone.0175508

Xiao, Q., Liu, Z.-J., Tao, S., Sun, Y.-M., Jiang, D., Li, H.-L., et al. (2015). Risk prediction for sporadic Alzheimer's disease using genetic risk score in the han chinese population. *Oncotarget* 6, 36955–36964. doi: 10.18632/Oncotarget.6271

Xu, W., Tan, L., Wang, H.-F., Jiang, T., Tan, M.-S., Tan, L., et al. (2015). Meta-analysis of modifiable risk factors for Alzheimer's disease. *J. Neurol. Neurosurg. Psychiatry* 86, 1299–1306. doi: 10.1136/Jnnp-2015-310548

Zheutlin, A. B., Dennis, J., Karlsson Linnér, R., Moscati, A., Restrepo, N., Straub, P., et al. (2019). Penetrance and pleiotropy of polygenic risk scores for schizophrenia in 106,160 patients across four health care systems. *Am. J. Psychiatry* 176, 846–855. doi: 10.1176/Appi.Ajp.2019.18091085

Zhou, X., Chen, Y., Ip, F. C. F., Lai, N. C. H., Li, Y. Y. T., Jiang, Y., et al. (2020). Genetic and polygenic risk score analysis for Alzheimer's disease in the chinese population. *Alzheimers Dement. (Amst)* 12:E12074. doi: 10.1002/Dad2.12074

Conflict of Interest: The authors declare that the research was conducted in the absence of any commercial or financial relationships that could be construed as a potential conflict of interest.

Publisher's Note: All claims expressed in this article are solely those of the authors and do not necessarily represent those of their affiliated organizations, or those of the publisher, the editors and the reviewers. Any product that may be evaluated in this article, or claim that may be made by its manufacturer, is not guaranteed or endorsed by the publisher.

frontiers in Aging Neuroscience

ORIGINAL RESEARCH
published: 21 March 2022
doi: 10.3389/fnagi.2022.854758

Functional Connectivity Hypointensity of Middle Cingulate Gyrus and Thalamus in Age-Related Macular Degeneration Patients: A Resting-State Functional Magnetic Resonance Imaging Study

Ang Xiao[1†], Hai-Jun Li[2†], Qiu-Yu Li[1†], Rong-Bin Liang[1], Hui-Ye Shu[1], Qian-Min Ge[1], Xu-Lin Liao[3], Yi-Cong Pan[1], Jie-Li Wu[4], Ting Su[4,5], Li-Juan Zhang[1], Qiong Zhou[1] and Yi Shao[1]**

[1] Department of Ophthalmology, The First Affiliated Hospital of Nanchang University, Nanchang, China, [2] Department of PET Center and Medical Image Center, The First Affiliated Hospital of Nanchang University, Nanchang, China, [3] Department of Ophthalmology and Visual Sciences, The Chinese University of Hong Kong, Shatin, Hong Kong SAR, China, [4] Department of Ophthalmology, Xiang'an Hospital of Xiamen University, Fujian Provincial Key Laboratory of Ophthalmology and Visual Science, Eye Institute of Xiamen University, Xiamen University School of Medicine, Xiamen, China, [5] Department of Ophthalmology, Massachusetts Eye and Ear, Harvard Medical School, Boston, MA, United States

Objective: Age-related macular degeneration (AMD) causes visual damage and blindness globally. The purpose of this study was to investigate changes in functional connectivity (FC) in AMD patients using resting-state functional magnetic resonance imaging (rs-fMRI).

Subjects and Methods: A total of 23 patients (12 male, 11 female) with AMD were enrolled to the AMD patients group (AMDs), and 17 healthy age-, sex-, and education-matched controls (9 male, 8 female) to the healthy controls group (HCs). All participants underwent rs-fMRI and mean FC values were compared between the two groups.

Results: Significantly higher FC values were found in the inferior frontal gyrus (IFG), superior frontal gyrus (SFG), inferior parietal lobule (IPL), rectal gyrus (RTG), and superior parietal lobule (SPL) in AMDs compared with HCs. Conversely, FC values in the cerebellum posterior lobe (CPL), middle cingulate gyrus (MCG), medulla (MDL), cerebellum anterior lobe (CAL), and thalamus (TLM) were significantly lower in AMDs than in HCs.

Conclusion: This study demonstrated FC abnormalities in many specific cerebral regions in AMD patients, and may provide new insights for exploration of potential pathophysiological mechanism of AMD-induced functional cerebral changes.

Keywords: age-related macular degeneration, rs-fMRI, functional connectivity, middle cingulate gyrus, thalamus

OPEN ACCESS

Edited by:
Yuzhen Xu,
Tongji University, China

Reviewed by:
Yingying Shi,
University of Miami Health System, United States
Wensi Tao,
University of Miami Health System, United States

***Correspondence:**
Qiong Zhou
qiongz-ms@126.com
Yi Shao
freebee99@163.com

† These authors have contributed equally to this work

Specialty section:
This article was submitted to Cellular and Molecular Mechanisms of Brain-aging, a section of the journal Frontiers in Aging Neuroscience

Received: *14 January 2022*
Accepted: *14 February 2022*
Published: *21 March 2022*

Citation:
Xiao A, Li H-J, Li Q-Y, Liang R-B, Shu H-Y, Ge Q-M, Liao X-L, Pan Y-C, Wu J-L, Su T, Zhang L-J, Zhou Q and Shao Y (2022) Functional Connectivity Hypointensity of Middle Cingulate Gyrus and Thalamus in Age-Related Macular Degeneration Patients: A Resting-State Functional Magnetic Resonance Imaging Study. Front. Aging Neurosci. 14:854758. doi: 10.3389/fnagi.2022.854758

INTRODUCTION

As a prevalent, chronic and progressive disease of the macula, age-related macular degeneration (AMD) is the leading cause of central vision impairment worldwide. The prevalence of AMD ranges from 6.8% in Asians to 12.3% in Europeans, is lower in Africans than in Europeans, but similar between Asians and Africans (Kawasaki et al., 2010; Laude et al., 2010; Wong et al., 2014). Major visual impairment occurs mainly in the late stages of AMD in one of two forms: neovascular (wet) AMD and geographic (dry) atrophy. Age is an important risk factor for AMD, other strong and consistent risk factors being darker iris pigmentation (Chakravarthy et al., 2010), previous cataract surgery (Cugati et al., 2006), cigarette smoking (Seddon et al., 1996), and obesity (Seddon et al., 2003). In clinical practice, fundus fluorescein angiography (FFA), optical coherence tomography, and fundus autofluorescence imaging are now extensively applied in diagnosis and to guide management of AMD (Lim et al., 2012). However, these examinations may not be suitable for patients with severe ocular media opacity or significant disease such as heart or renal failure. Advances have been made in disease detection and diagnosis allowing for rapid intervention, monitoring, and amelioration of the disease, improving prognosis, and evaluation.

Resting-state functional magnetic resonance imaging (rs-fMRI) is widely performed to assess cerebrum functional connectivity (FC), which is temporally correlated within resting state functional networks. rs-fMRI is increasingly applied to map the representation of cerebral function in many diseases, such as amyotrophic lateral sclerosis (Douaud et al., 2011), traumatic brain injury (Mayer et al., 2015), stroke (Puig et al., 2018), and Alzheimer's disease (Zhao et al., 2020), and has proven valuable for characterizing and analyzing cerebral activity in the resting state (Damoiseaux et al., 2006; De Luca et al., 2006) and in task performance (Spreng and Grady, 2010). Based on the correlation between the anatomical structure and physiological functions of the retina and cerebrum (Wong et al., 2001b; Patton et al., 2005), the potential of retinopathy to provide indirect indicators of intracerebral lesions has attracted extensive attention (Fuller et al., 2001; Wong et al., 2001a, 2002; Yatsuya et al., 2010). Abnormal spontaneous FC has been observed in ophthalmic diseases such as glaucoma (Li et al., 2017), amblyopia (Ding et al., 2013; Liang et al., 2017), and strabismus (Yan et al., 2019). The frontal, thalamic and temporal cerebral regions comprise the default mode network, which participates in memory, emotional, and cognitive functions (Raichle, 2010; Zhang and Raichle, 2010). Therefore, we hypothesize that FC is abnormal in AMD patients, and that relevant cognition-related or connectivity changes in visual areas may result in anxiety and depression.

To explore this possibility, rs-fMRI was used to measure cerebral FC, promoting an in-depth understanding of the potential neural mechanism of cerebrum visual pathway injury in patients with AMD (**Figure 1**), and allowing better evaluation and improved prognosis for patients.

MATERIALS AND METHODS

Subjects

A total of 23 subjects with AMD (12 males, 11 females) were recruited to the AMD group (AMDs) at the First Affiliated Hospital of Nanchang University (Nanchang, China) according to the inclusion criteria described in previous publications (Seiple et al., 2005; Zuo et al., 2020). Information about the AMD patients is provided in section "Results." Seventeen healthy controls (HCs) (9 male and 8 female subjects) without AMD were recruited to the HCs group. The two groups were matched for age, gender, handedness, educational level, and total intracranial volume. The inclusion criteria for HCs were as follows: (1) no history of AMD or other ocular disease; (2) no MRI contraindications; (3) no history of drug or alcohol abuse; and (4) no neurological or psychiatric diseases.

This study was conducted in accordance with the Declaration of Helsinki, and was approved by the Medical Ethics Committee of the First Affiliated Hospital of Nanchang University. All participants signed declarations of informed consent.

Functional Magnetic Resonance Imaging Parameters

The MRI scans were performed using a 3-T MR scanner (Trio; Siemens, Munich, Germany). T1-weighted (T1W) gradient echo images were acquired using the following parameters: TR/TE 1,900/2.26 ms; gap 0.5 mm; slice thickness 1.0 mm; acquisition matrix 256 × 256; field of view 250 × 250 mm; and flip angle 9°. Functional images were processed using the following parameters: TR/TE 2,000/30 ms; gap 1.2 mm; slice thickness 4.0 mm; acquisition matrix 64 × 64; field of view 220 × 220 mm; flip angle 90°; number of axial slices 29. All participants were awake with eyes closed for the duration of the scan.

Functional Magnetic Resonance Imaging Data Processing

The fMRI data were classified using MRIcro software,[1] and processed using statistical parametric mapping software[2] and the rs-fMRI Data Analysis Toolkit (REST[3]), using the Data Processing Assistant for Resting-State fMRI (DPARSF) software[4] for resting-state fMRI. This methodology has been described previously (Chao-Gan and Yu-Feng, 2010; Huang et al., 2016). The first 10 volumes from each participant were eliminated to ensure the stability of signal values, and images were motion corrected. Data were smoothed using a Gaussian at full width half-maximum of 8 × 8 × 8 mm. Bandpass filtering (0.01–0.08 Hz) and image detrending were applied to reduce the influence of other factors that may lead to errors (Lowe et al., 1998).

[1] www.MRIcro.com
[2] http://www.fil.ion.ucl.ac.uk/spm/
[3] http://www.restfmri.net
[4] http://rfmri.org/DPARSF

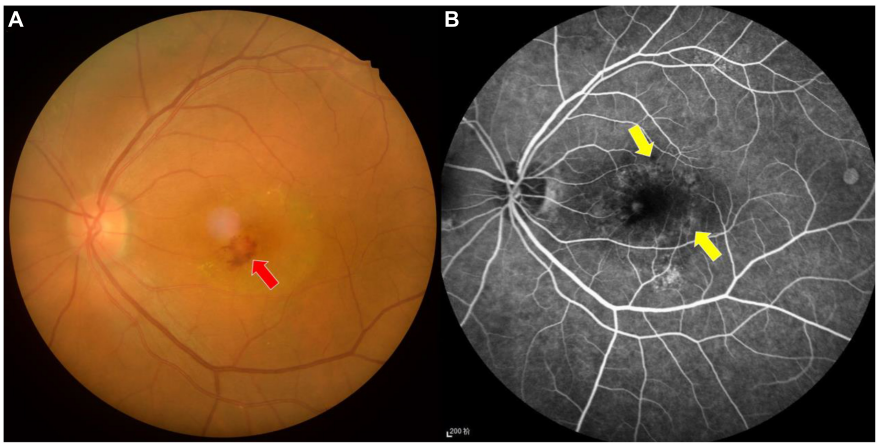

FIGURE 1 | Fundus photograph **(A)** and fluorescence fundus angiography image **(B)** of age-related macular degeneration. The fundus photograph shows bleeding and exudation in the macular area, while the leakage of strong fluorescein spot and shadowing fluorescein at the macular area are shown in the fundus fluorescein angiography image. Red arrow indicates bleeding, and yellow arrows indicate the leakage.

Functional Connectivity Analysis

The GIFT v3.0b toolbox[5] was used for preprocessing analysis (Calhoun et al., 2001), and the rs-fMRI data preprocessing was performed using Data Processing & Analysis for Brain Imaging software (DPABI[6]) (Yan et al., 2016). The generalized linear model and one-way analysis of covariance were used to generate the FC maps. A previously published resting-state network template (Ding et al., 2011) was applied. This approach has been described in detail previously (Li et al., 2019).

Statistical Analyses

SPSS software version 19.0 (IBM Corporation, Armonk, NY, United States) was used to analyze the processed data. Two-sample *t*-tests and Gaussian Random-Field theory were applied to correct for multiple comparisons. The correction parameters were set to voxel-level threshold of 0.005 and cluster-level threshold of 0.05, using a two-sided test. Age, gender, handedness and educational level were regression covariates. *P*-values < 0.05 were considered statistically significant. In addition, receiver operating characteristic (ROC) curves were generated to compare data from specific cerebral regions between the AMDs and HCs.

[5]http://icatb.sourceforge.net/

[6]http://www.rfmri.org/dpabi

TABLE 1 | Clinical characteristics of patients between AMDs and HCs.

Characteristics	AMDs	HCs	*t*-Value	*P*-Values
Male/female	12/11	9/8	0.124	0.972
Age (years)	55.72 ± 5.29	56.33 ± 5.62	−0.361	0.819
Weight (kg)	57.49 ± 7.72	58.41 ± 6.21	−0.484	0.876
Handedness (left/right)	0/23	0/17	NA	NA
Duration (years)	0.83 ± 0.49	NA	NA	NA
Best-corrected VA, left	0.15 ± 0.06*	1.06 ± 0.18	−2.732	0.031
Best-corrected VA, right	0.22 ± 0.09*	1.12 ± 0.34	−3.052	0.028
IOP, left	15.62 ± 3.27*	16.02 ± 4.11	−2.853	0.026
IOP, right	14.63 ± 3.25*	15.64 ± 3.46	−2.792	0.024

*Independent t-tests comparing the two groups (*P < 0.05) represented statistically significant differences.*

AMDs, age-related macular degeneration group; HCs, healthy controls; NA, not applicable; VA, visual acuity; IOP, intraocular pressure.

Correlation Analysis

The Hospital Anxiety and Depression Scale (HADS) was completed by all participants. GraphPad Prism 8 software (GraphPad Inc., San Diego, CA, United States) was used for Pearson's correlation analysis, and to evaluate and plot the linear correlation between HADS scores and mean FC signal values of the middle cingulate gyrus (MCG) and thalamus.

RESULTS

Demographic and Clinical Characteristics

No significant differences in age ($P = 0.819$), weight ($P = 0.876$), or duration ($P > 0.05$) was found between AMDs and HCs. However, intraocular pressure (IOP) and binocular best corrected visual acuity were significantly different ($P < 0.05$) between the two groups. Details are shown in **Table 1**.

Seed Regions of Interest

The different insula subregions for resting-state FC patterns between the AMDs and HCs are shown in **Figure 2**. The ventral anterior insula (vAI) is chiefly connected with the limbic cortices and pregenual anterior cingulate mediating affective processes, while the dorsal anterior insula (dAI) connects with the dorsolateral prefrontal cortex and dorsal anterior cingulate cortex contributing to regulation of cognitive processes. Moreover, the posterior insula (PI) was predominantly connected with sensorimotor cortices. The three insular subregions were considered seed regions of interest to study the variability

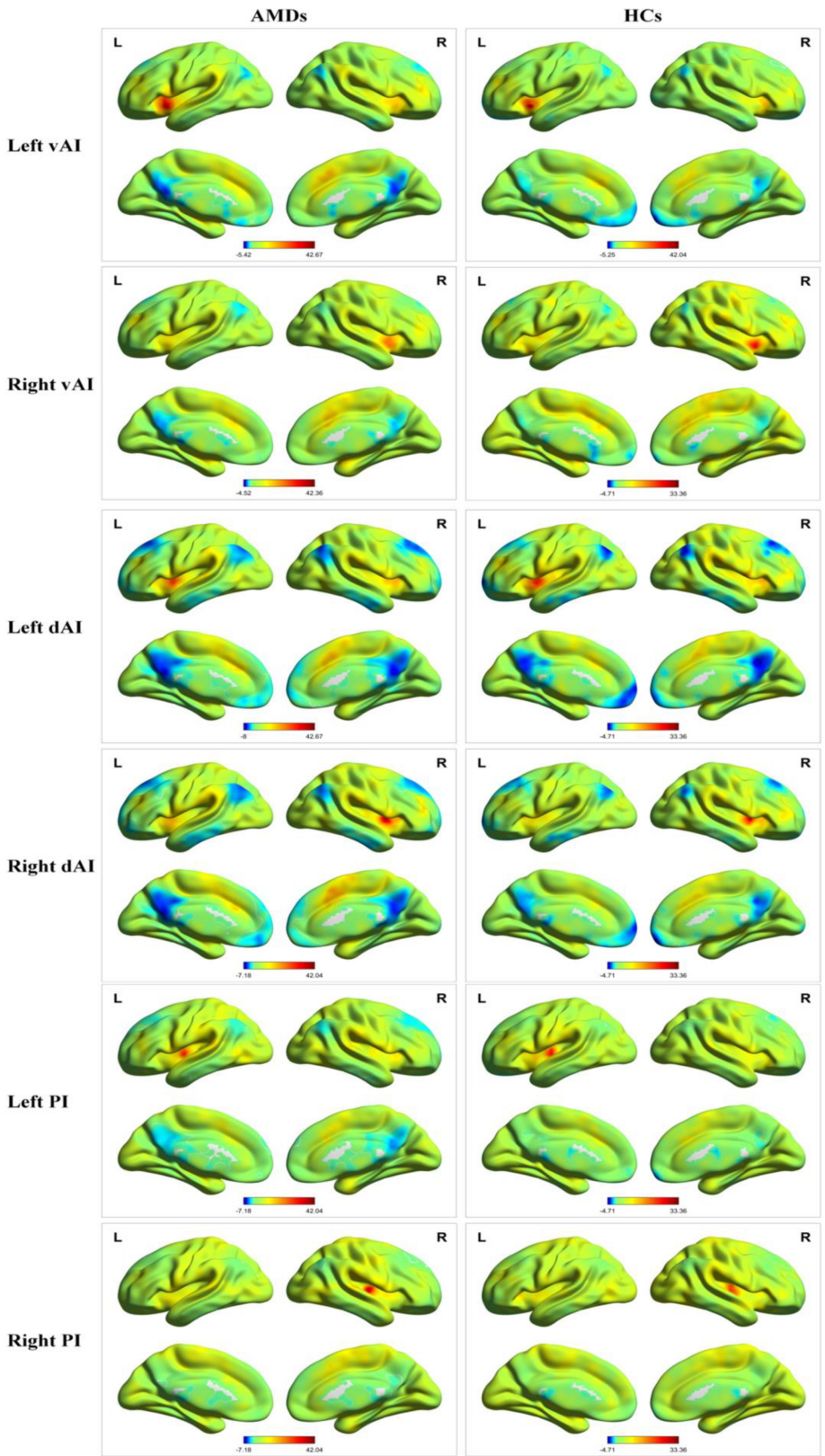

FIGURE 2 | Resting-state functional connectivity patterns of insula subregions in AMDs and HCs. AMDs, age-related macular degeneration group; HCs, healthy controls; vAI, ventral anterior insula; dAI, dorsal anterior insula; PI, posterior insula; L, left; R, right.

TABLE 2 | Cerebral areas showing functional connectivity differences with insular subdivisions between AMDs and HCs.

Seed-ROIs	Cerebral areas	L/R	MNI coordinates			Number of voxels	*t*-Values
			X	*Y*	*Z*		
Left vAI							
	Cerebellum posterior lobe	L	−30	−75	−42	43	−4.547
	Inferior frontal gyrus	L	−12	42	−30	65	4.309
	Superior frontal gyrus	R	12	60	−12	73	4.122
	Inferior parietal lobule	L	−45	−36	42	72	3.945
Right vAI							
	Cerebellum posterior lobe	L/R	6	−75	33	65	−3.478
	Middle cingulate gyrus	L	−9	−12	36	50	−3.609
Left dAI							
	Rectal gyrus	L	−6	36	−27	40	3.986
	Superior parietal lobule	R	33	−63	66	46	5.196
Right dAI							
	Medulla	L	−6	−48	−51	42	−3.478
	Cerebellum posterior lobe	L	−24	−75	−39	68	−4.632
Left PI							
	Cerebellum anterior lobe	R	30	−30	−39	42	−3.908
	Inferior frontal gyrus	L	−12	36	−30	61	4.419
Right PI							
	Thalamus	R	12	−30	0	50	−3.875

Voxel level P < 0.01, AlphaSim corrected.
AMDs, age-related macular degeneration group; HCs, healthy controls; L/R, left/right; vAI, ventral anterior insula; dAI, dorsal anterior insula; PI, posterior insula.

of resting-state FC in specific subregions of the insula for first episode schizophrenia and clinical high risk for psychosis (Li et al., 2019).

Group Differences in Functional Connectivity

The FC in specific cerebral regions are shown in **Table 2** and **Figure 3**. We found that the mean FC values in inferior frontal gyrus (IFG), superior frontal gyrus (SFG), inferior parietal lobule (IPL), rectal gyrus (RTG), and superior parietal lobule (SPL) were statistically significantly higher in AMDs than in HCs, while values in cerebellum posterior lobe (CPL), MCG, medulla (MDL), cerebellum anterior lobe (CAL), and thalamus (TLM) were significantly lower in AMDs.

Receiver Operating Characteristic Curve

Receiver operating characteristic curve analysis was used to verify differences and to explore whether FC values of specific cerebral regions have potential as biomarkers to differentiate patients with and without AMD. The individual areas under the curves (AUCs) of FC values within the range of regions are as follows: left vAI CPL (0.934, $P < 0.001$), IFG (0.854, $P < 0.001$), SFG (0.831, $P < 0.001$), and IPL (0.806, $P = 0.001$); right vAI CPL (0.890, $P < 0.001$) and MCG (0.916, $P < 0.001$) (**Figure 4A**); left dAI RTG (0.821, $P = 0.001$) and SPL (0.841, $P < 0.001$); right dAI MDL (0.951, $P < 0.001$) and CPL (0.957, $P < 0.001$) (**Figure 4B**); left PI CAL (0.980, $P < 0.001$) and IFG (0.834, $P < 0.001$); right PI TLM (0.872, $P < 0.001$) (**Figure 4C**). These findings indicate that the mean FC values of specific cerebral regions can accurately distinguish AMDs from HCs, and may be applied as diagnostic biomarkers.

Correlation Analysis

Statistically significant positive correlations were found between HADS scores and overall FC values in the MCG ($r = 0.8434$, $P < 0.0001$ for anxiety and $r = 0.8116$, $P < 0.0001$ for depression; **Figures 5A,B**), and thalamus ($r = 0.9298$, $P < 0.0001$ for anxiety and $r = 0.8819$, $P < 0.0001$ for depression; **Figures 5C,D**) in AMDs.

DISCUSSION

Foveal scotoma due to macular photoreceptor atrophy in AMD has caused vision loss and blindness for a large number of individuals globally, particularly in developed countries (Rosengarth et al., 2013; Wong et al., 2014). Previous studies in animals (Kaas et al., 1990; Darian-Smith and Gilbert, 1995; Giannikopoulos and Eysel, 2006) and humans (Pascual-Leone et al., 2005; Liu et al., 2007) have demonstrated altered cerebral functions in response to reduced visual input, but the extent of cerebral changes associated with AMD remains unclear and has attracted the attention of many researchers. Our study has indicated that FC values are significantly increased in the IFG, SFG, IPL, RTG, and SPL, and decreased in the CPL, MCG, MDL, CAL, and TLM in AMDs compared with HCs (**Figure 6**). These findings may reflect compensatory changes supporting cerebral performance in AMD patients with vision loss.

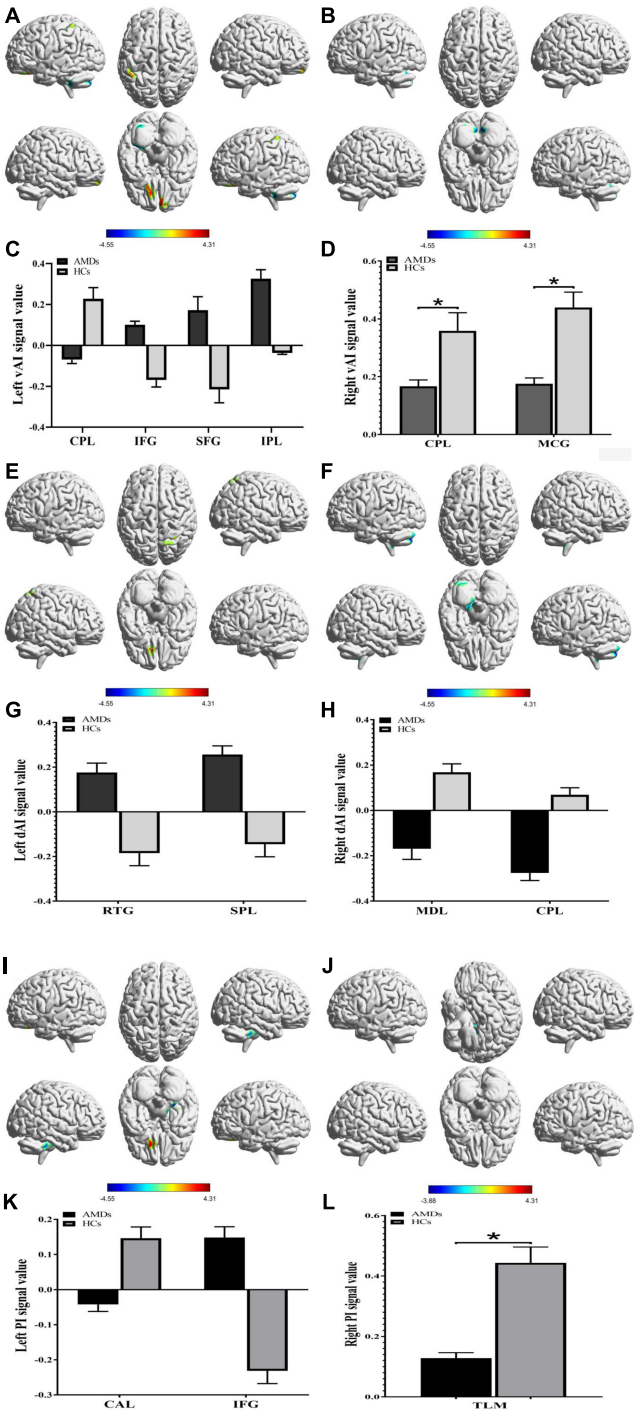

FIGURE 3 | Functional connectivity group differences in insular subregions within different cerebral areas are shown **(A–L)**. **(A,C)**, **(B,D)**, **(E,G)**, **(F,H)**, **(I,K)**, and **(J,L)** show cerebral regions of altered FC in the left vAI, right vAI, left dAI, right dAI, left PI, and right PI, respectively. *$P < 0.01$. AMDs, age-related macular degeneration group; HCs, healthy controls; vAI, ventral anterior insula; dAI, dorsal anterior insula; PI, posterior insula; CPL, cerebellum posterior lobe; IFG, inferior frontal gyrus; SFG, superior frontal gyrus; IPL, inferior parietal lobule; MCG, middle cingulate gyrus; RTG, rectal gyrus; SPL, superior parietal lobule; MDL, medulla; CAL, cerebellum anterior lobe; TLM, thalamus.

Previous MRI research on the impact of AMD on cerebral regions is shown in **Table 3** and the underlying functions of specific areas of the cerebrum are shown in **Table 4**. We could hypothesize that AMD not only causes changes in cerebral FC patterns affecting visual pathways, language, cognitive and memory, but also strengthens internetwork connections *via* a

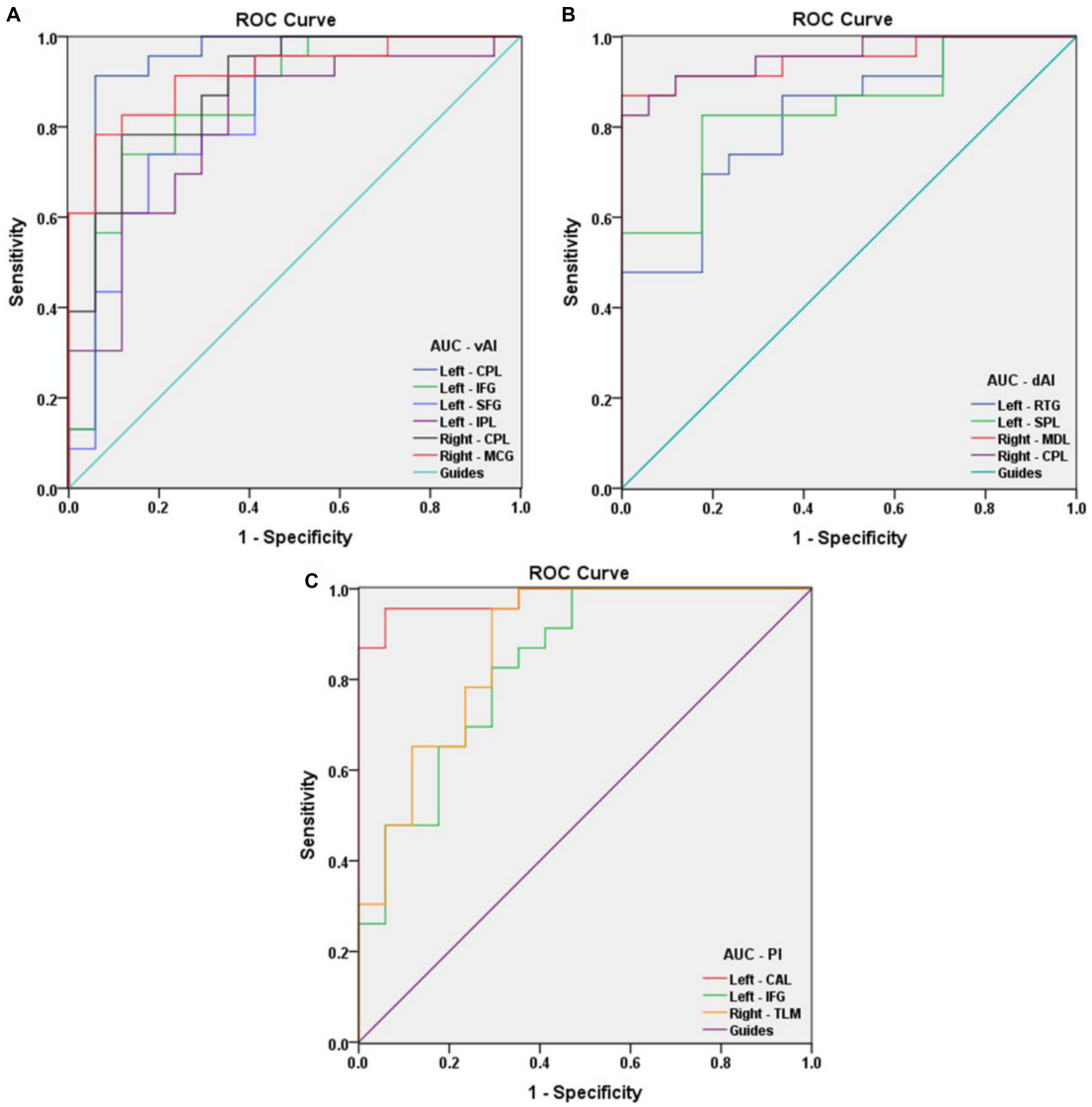

FIGURE 4 | Receiver operating characteristic curve analysis of the mean FC values for the specific cerebral regions. **(A)** The area under the ROC curve of FC values were presented as follows: the CPL (0.934, 95% CI: 0.833–1.000), IFG (0.854, 95% CI: 0.730–0.978), SFG (0.831, 95% CI: 0.696–0.966), and IPL (0.806, 95% CI: 0.666–0.945) in left vAI, CPL (0.890, 95% CI: 0.790–0.990) and MCG (0.916, 95% CI: 0.830–1.000) in right vAI. **(B)** The AUCs of FC values in dAI were as follows: RTG (0.821, 95% CI: 0.693–0.949) and SPL (0.841, 95% CI: 0.719–0.964) in left dAI, MDL (0.951, 95% CI: 0.886–1.000) and CPL (0.957, 95% CI: 0.899–1.000) in right dAI. **(C)** The AUCs of FC values in PI were as follows: CAL (0.980, 95% CI: 0.944–1.000) and IFG (0.834, 95% CI: 0.705–0.962) in left PI, TLM (0.872, 95% CI: 0.758–0.987) in right PI. vAI, ventral anterior insula; dAI, dorsal anterior insula; PI, posterior insula; CPL, cerebellum posterior lobe; IFG, inferior frontal gyrus; SFG, superior frontal gyrus; IPL, inferior parietal lobule; MCG, middle cingulate gyrus; RTG, rectal gyrus; SPL, superior parietal lobule; MDL, medulla; CAL, cerebellum anterior lobe; TLM, thalamus.

loss of inhibitory signals that accompany visual stimulation or contribute to recruitment of new networks to support and complete visually mediated tasks. Whitson et al. (2015) found relatively high resting-state FC values in AMD patients in the IFG, superior temporal gyrus (STG), inferior parietal lobe (IPL), superior parietal lobe (SPL), supramarginal gyrus (SMG), supplementary motor area (SMA), and precentral gyrus (preCG). They also found high connectivity between SMA and SPL as well as SMA, IPL and IFG which are implicated in motor/visuospatial function, with strong connectivity within the reference links and default mode network compared to HCs. Furthermore, the AMDs showed stronger relationships between connectivity and memory performance in the inferior and medial temporal gyri, temporal pole, IFG, SFG, MFG, posterior cingulate cortex, and medial prefrontal cortex compared to control participants, while the resting default mode network in the bilateral posterior cingulate cortex, anterior cingulate cortices, and precuneus were similar in these groups (Zuo et al., 2020). One study indicates that AMDs exhibit increased cerebral activation in a widely distributed cortical network including SPL, IPL, the frontal

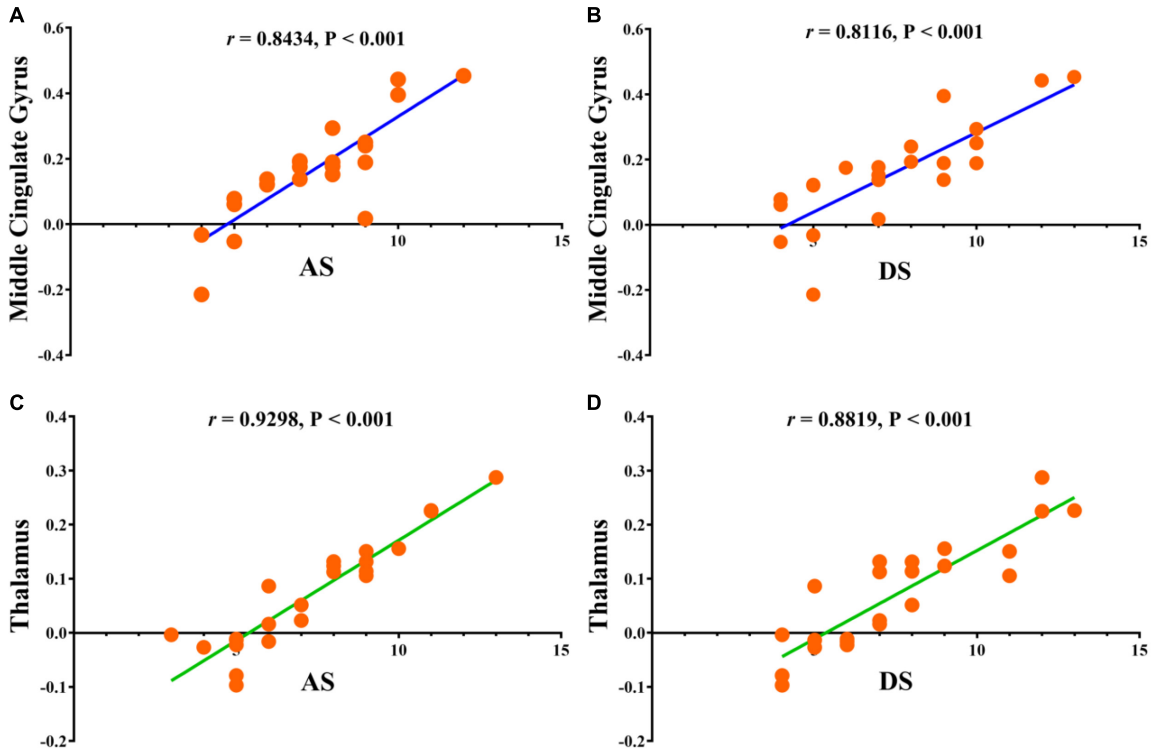

FIGURE 5 | Correlations between the clinical behaviors and FC values in middle cingulate gyrus and thalamus. **(A)** The anxiety scores showed a positive correlation with FC values in middle cingulate gyrus (0.8434, 95% CI: 0.6610–0.9317); **(B)** the depression scores showed a positive correlation with FC values in middle cingulate gyrus (0.8116, 95% CI: 0.6002–0.9170); **(C)** the anxiety scores showed a positive correlation with FC values in thalamus (0.9298, 95% CI: 0.8392–0.9702); **(D)** the depression scores showed a positive correlation with FC values in thalamus (0.8819, 95% CI: 0.7380–0.9491). FC, functional connectivity; AS, anxiety scores; DS, depression scores.

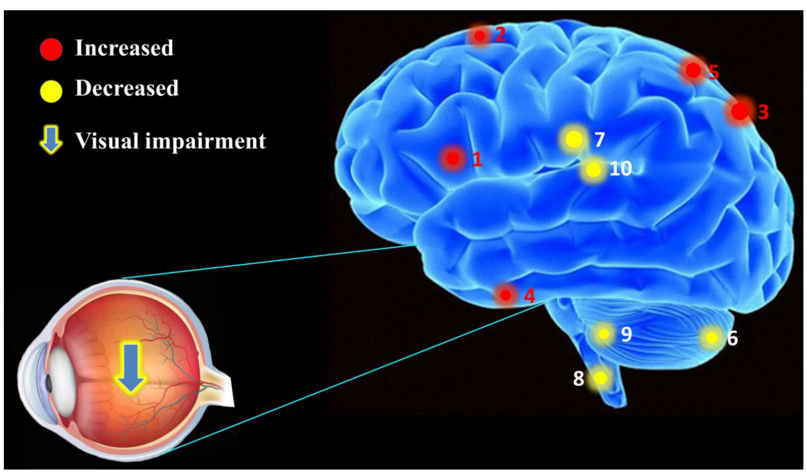

FIGURE 6 | The mean FC values of cerebrum in AMD participants. Compared with HCs, the AMDs showed abnormal signals in specific cerebral regions as followed: 1. inferior frontal gyrus (left vAI, t = 4.309; left PI, t = 4.419), 2. superior frontal gyrus (t = 4.122), 3. inferior parietal lobule (t = 3.945), 4. rectal gyrus (t = 3.986), 5. superior parietal lobule (t = 5.196), 6. cerebellum posterior lobe (left vAI, t = –4.547; right vAI, t = –3.478; right dVI, t = –4.632), 7. middle cingulate gyrus (t = –3.609), 8. medulla (t = –3.478), 9. cerebellum anterior lobe (t = –3.908), and 10. thalamus (t = –3.875).

eye fields, and the prefrontal cortex (Szlyk and Little, 2009). These results directly and indirectly support our findings that the mean FC values in IFG, SFG, IPL, RTG, and SPL are significantly higher in AMDs than in HCs, suggesting that a positively FC was correlated with these specific cerebral regions involved in the regulatory mechanism of AMD to achieve

TABLE 3 | Current research status of fMRI and AMD in specific cerebral regions.

Author (Y)	Average age (Y)	Number (P/HC, M/F)	fMRI	Objective of cerebrum function	Cerebral regions
Little et al., 2008	AMDs, 55–83; Control, 22–78	18 (6/12, 8/10)	Yes	Cortical networks underling oculomotor function	**Increased:** preFC, intraparietal sulci, FEFs, supplementary eye fields; **Decreased:** visual cortex (MT/V5, V2/V3, and V1).
Rosengarth et al., 2013	AMDs, 55–84; Control, 51–83	16 (9/7, 6/10)	Yes	Training-related changes in cerebellum	**Increased:** fusiform gyrus, ITG, and lateral occipital cortex; **No differences:** visual area (V1, V2, and V3).
Zuo et al., 2020	AMDs, 75.3 ± 8.9; Control, 74.5 ± 7.2	83 (42/41, 40/43)	Yes	Quantify the strength of functional connectivity	**Increased:** ITG, MTG, temporal pole, IFG, SFG, MFG, PCC, and medial preFC; **No differences:** bilateral PCC, ACC, and precuneus.
Whitson et al., 2015	AMDs, 79.9 ± 7.5; Control, 68.3 ± 3.4	23 (7/16, 9/14)	Yes	Functional connectivity and phonemic fluency	**Increased:** left IFG, left STG, bilateral IPL, right SPL, right SMG, right SMA, and right precentral gyrus.
Szlyk and Little, 2009	AMDs, 55–83; Control, 54–78	12 (6/6, 5/7)	Yes	Cortical networks underling word recognition and processing	**Increased:** supplementary motor regions, FEFs, IPL and SPL, preFC; **Decreased:** SPL and IPL, primary and secondary visual cortices, FEFs, bilaterally SPL, supplementary motor regions and eye fields, and LFG.

Y, year; P, patient; HC, healthy control; M, male; F, female; AMDs, age-related macular degeneration patients; ITG, inferior temporal gyrus; MTG, medial temporal gyrus; IFG, inferior frontal gyrus; SFG, superior frontal gyrus; MFG, middle frontal gyrus; PCC, posterior cingulate cortex; preFC, prefrontal cortex; ACC, anterior cingulate cortices; STG, superior temporal gyrus; IPL, inferior parietal lobe; SMG, supramarginal gyrus; FEFs, frontal eye fields; SMA, supplementary motor area; SPL, superior parietal lobe; LFG, left fusiform gyrus.

TABLE 4 | Alternation of cerebral regions and its potential effects.

Cerebral regions	Experimental results	Cerebral functions	Anticipate effects
Cerebellum posterior lobe	AMDs < HCs	Coordinate sensory and motor functions, and participate in higher cognitive functions	Dyskinesia and difficulty in fine motion
Inferior frontal gyrus	AMDs > HCs	Involved in language processing and cognitive functions	Bipolar disorder
Superior frontal gyrus	AMDs > HCs	Involved in cognitive and motor control, and the execution of working memory	Parkinson's disease and motor aphasia
Inferior parietal lobule	AMDs > HCs	Involved in the processing of various sensory, perceptual and cognitive functions	Gerstmann's syndrome and Schizophrenia
Middle cingulate gyrus	AMDs < HCs	Manage emotion, cognition, and movement, and integrate visual information	Affective and cognitive dysfunction, visual function abnormals
Rectal gyrus	AMDs > HCs	Decision making, reward processing, planning, and reasoning	Epilepsy
Superior parietal lobule	AMDs > HCs	Participates in somatosensory and working memory, and coordinates visual and motor functions	Cortical sensory disorders, such as loss of position, entity, and recognition
Medulla	AMDs < HCs	Control all non-conscious daily activities	Partial sensory loss, hemiplegia, and hemianopia
Cerebellum anterior lobe	AMDs < HCs	mediating unconscious proprioception, and regulate muscular tension	Cerebellar ataxia
Thalamus	AMDs < HCs	Sensory processing, memory function, emotion, associated with visual function	Emotional problems, endocrine disease, and visual dysfunction

adaptability and plasticity in various functions such as vision, cognition, and memory.

In addition, one study showed significantly increased gray and white matter in the CPL during a period of oculomotor training in AMD compared with controls (Rosengarth et al., 2013), while no difference was found in white matter of the cingulum hippocampus, cingulate, or the thalamus (Yoshimine et al., 2018). In addition, volumetric reductions were found in the optic radiations, lateral geniculate bodies and visual cortex in AMD patients, as the white matter in frontal lobe was decreased in AMD but not in juvenile macular degeneration (Hernowo et al., 2014). The activation with significant clusters showed

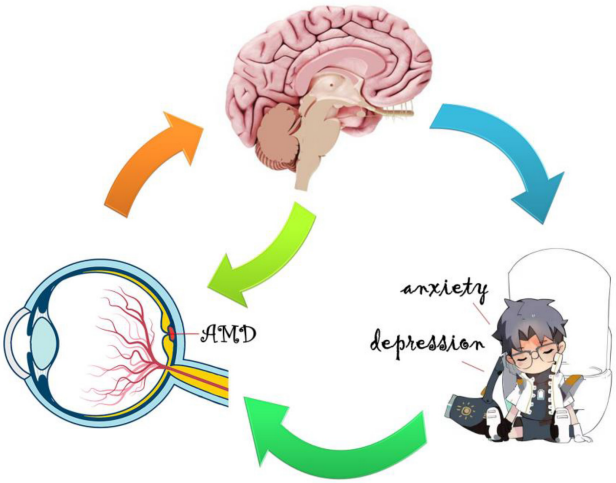

FIGURE 7 | Relationship between FC values and emotional status. The mean FC values presented obvious abnormalities in many specific cerebral regions of AMD patients in contrast to healthy controls, and AMD patients appear to be more prone to anxiety and depression.

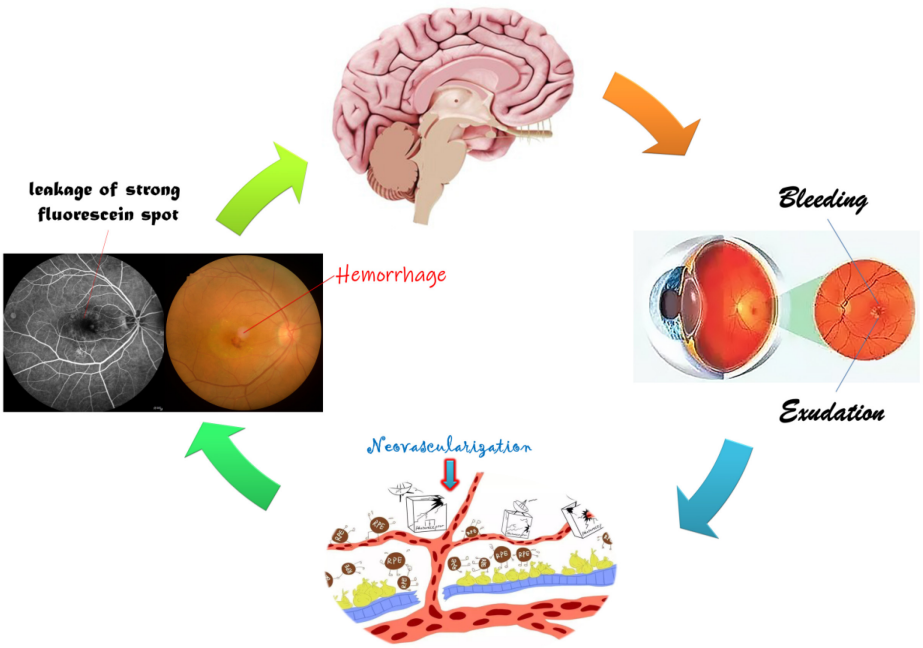

FIGURE 8 | Relationship between FC and clinical manifestation of AMD. The retinal macular is stimulated by a variety of growth factors and inflammatory factors resulting in neovascularization, hemorrhage, and exudation, further leading to visual impairment and changes in specific cerebral regions.

marked reduction in the parietal lobules in AMD patients (Little et al., 2008). Since the lateral geniculate body, optic radiation, and visual cortex are vital parts of the visual pathways, AMD patients may have changes in these specific areas. Szlyk and Little (2009) found decreased activation in the left SPL and IPL, primary and secondary visual cortices, frontal eye fields, bilateral superior parietal regions, supplementary motor regions, eye fields, and left fusiform gyrus in AMD patients relative to controls. However, the results of the present study differ from the above findings due to differences in race, geographical region, inter-individual variations and image data processing, but can fully supplement their research. Previous studies (Hernowo et al., 2014; Prins et al., 2016a,b) reported reduced cortical volume and abnormality of white matter in the visual cortex in AMD. The results of these studies suggest that AMD may cause widespread changes in cerebral regions and suggest a strong association between AMD and changes in specific cerebral regions, and their corresponding major effects, and are further supported by the current work.

Whether changes in cerebral activity are consequential or adaptive in AMD and the exact mechanism underpinning them remains unclear. Apoptosis of retinal nerve cells, especially in the macular area, could affect changes in cerebral tissue properties through transsynaptic degeneration in AMD (Haak et al., 2016; Prins et al., 2016a). This would lead to decreased visual signaling from the defective macula and behavioral factors correlated with loss of visually dependent activities, such as social interaction and reading (Zuo et al., 2020). The frontal lobe, cingulate gyrus, temporal gyrus, and thalamus are involved in cognitive, emotional, and memory functions (Critchley et al., 2004; Seitz et al., 2006; Raichle, 2010; Zhang and Raichle, 2010). Lesions of these cerebral regions are connected with social and emotional behavior, and could lead to anxiety and depression. The AMD group in this study showed significant correlations between connectivity in cerebral regions and HADS scores, indicating that anxiety and depression scores are linked with overall FC values, and that abnormal neural electrical activity may occur in brain regions associated with emotional activity (**Figure 7**). Moreover, AMD may result in specific cerebral regional changes through a variety of mechanisms, including the loss of cognitive stimulation (a consequence of sensory disorder), adaptive restructuring of visual pathways, decreased feedback regulatory signals from visual cortical regions, or by increased metabolic demand in specific cerebral regions, which would present alterations in FC and diminished cognitive ability (Whitson et al., 2015). These changes may promote functional cerebral reorganization in the fronto-parietal control networks (Zhuang et al., 2018) and primary visual cortex (Masuda et al., 2008) in AMD to improve vision and prognosis. The mechanism of cerebral regional changes caused by AMD is a complex process involving many different brain regions and requires more in-depth and comprehensive research.

Based on the above studies (**Table 4** and **Figure 8**), it could be suggested that AMD patients have abnormalities in several cerebral regions. The current study has some limitations. A cross-sectional and observational approach was adopted in this study, and the sample size was small, making it difficult to observe the possible development of cognitive impairment and fMRI changes associated with AMD, so we have not drawn firm conclusions about causality of the described relationships. Therefore, an in-depth, comprehensive and systematic study is needed to elucidate the mechanisms and correlations of AMD-induced changes in brain regions.

CONCLUSION

Our study demonstrated abnormal FC values in specific cerebral regions of AMD patients. These findings can not only supplement the theoretical basis for research on the mechanisms of AMD nerve injury and repair process, but also form a basis for further exploration of the potential pathophysiological mechanisms of AMD-induced functional changes in cerebral regions.

DATA AVAILABILITY STATEMENT

The original contributions presented in the study are included in the article/supplementary material, further inquiries can be directed to the corresponding author/s.

ETHICS STATEMENT

The studies involving human participants were reviewed and all research methods were approved by the Committee of the Medical Ethics of the First Affiliated Hospital of Nanchang University and were in accordance with the 1964 Helsinki declaration and its later amendments or comparable ethical standards. The patients/participants provided their written informed consent to participate in this study.

AUTHOR CONTRIBUTIONS

All authors listed have made a substantial, direct, and intellectual contribution to the work, and approved it for publication.

FUNDING

Jiangxi branch of National Clinical Research Center for ocular disease (No. 20211ZDG02003); Key Research Foundation of Jiangxi Province (Nos. 20181BBG70004 and 20203BBG73059); Excellent Talents Development Project of Jiangxi Province (No. 20192BCBL23020); Natural Science Foundation of Jiangxi Province (No. 20181BAB205034); Grassroots Health Appropriate Technology "Spark Promotion Plan" Project of Jiangxi Province (No. 20188003); Health Development Planning Commission Science Foundation of Jiangxi Province (Nos. 20201032 and 202130210); Health Development Planning Commission Science TCM Foundation of Jiangxi Province (Nos. 2018A060 and 2020A0087); Education Department Foundation of Jiangxi Province (Nos. GJJ200157, GJJ200159, and GJJ200169); and Key Research Foundation of Jiangxi Province (Nos. 20203BBG73058 and 20192BBGL70033).

REFERENCES

Calhoun, V. D., Adali, T., Pearlson, G. D., and Pekar, J. J. (2001). A method for making group inferences from functional MRI data using independent component analysis. *Human Brain Mapp.* 14, 140–151. doi: 10.1002/hbm.1048

Chakravarthy, U., Wong, T. Y., Fletcher, A., Piault, E., Evans, C., Zlateva, G., et al. (2010). Clinical risk factors for age-related macular degeneration: a systematic review and meta-analysis. *BMC Ophthalmol.* 10:31. doi: 10.1186/1471-2415-10-31

Chao-Gan, Y., and Yu-Feng, Z. D. F. (2010). A matlab toolbox for "pipeline" data analysis of resting-state fMRI. *Front. Syst. Neurosci.* 4:13.

Critchley, H. D., Wiens, S., Rotshtein, P., Ohman, A., and Dolan, R. J. (2004). Neural systems supporting interoceptive awareness. *Nat. Neurosci.* 7, 189–195. doi: 10.1038/nn1176

Cugati, S., Mitchell, P., Rochtchina, E., Tan, A. G., Smith, W., and Wang, J. J. (2006). Cataract surgery and the 10-year incidence of age-related maculopathy: the blue mountains eye study. *Ophthalmology* 113, 2020–2025. doi: 10.1016/j.ophtha.2006.05.047

Damoiseaux, J. S., Rombouts, S. A., Barkhof, F., Scheltens, P., Stam, C. J., Smith, S. M., et al. (2006). Consistent resting-state networks across healthy subjects. *Proc. Natl. Acad. Sci. USA* 103, 13848–13853. doi: 10.1073/pnas.0601417103

Darian-Smith, C., and Gilbert, C. D. (1995). Topographic reorganization in the striate cortex of the adult cat and monkey is cortically mediated. *J. Neurosci.* 15, 1631–1647. doi: 10.1523/JNEUROSCI.15-03-01631.1995

De Luca, M., Beckmann, C. F., De Stefano, N., Matthews, P. M., and Smith, S. M. (2006). fMRI resting state networks define distinct modes of long-distance interactions in the human brain. *Neuroimage* 29, 1359–1367. doi: 10.1016/j.neuroimage.2005.08.035

Ding, J. R., Liao, W., Zhang, Z., Mantini, D., Xu, Q., Wu, G. R., et al. (2011). Topological fractionation of resting-state networks. *PLoS One* 6:e26596. doi: 10.1371/journal.pone.0026596

Ding, K., Liu, Y., Yan, X., Lin, X., and Jiang, T. (2013). Altered functional connectivity of the primary visual cortex in subjects with amblyopia. *Neural. Plast.* 2013:612086. doi: 10.1155/2013/612086

Douaud, G., Filippini, N., Knight, S., Talbot, K., and Turner, M. R. (2011). Integration of structural and functional magnetic resonance imaging in amyotrophic lateral sclerosis. *Brain* 134, 3470–3479. doi: 10.1093/brain/awr279

Fuller, J. H., Stevens, L. K., and Wang, S. L. (2001). Risk factors for cardiovascular mortality and morbidity: the WHO mutinational study of vascular disease in diabetes. *Diabetologia* 44:S54. doi: 10.1007/pl00002940

Giannikopoulos, D. V., and Eysel, U. T. (2006). Dynamics and specificity of cortical map reorganization after retinal lesions. *Proc. Natl. Acad. Sci. USA* 103, 10805–10810. doi: 10.1073/pnas.0604539103

Haak, K. V., Morland, A. B., Rubin, G. S., and Cornelissen, F. W. (2016). Preserved retinotopic brain connectivity in macular degeneration. *Ophthal. Physiol. Opt.* 36, 335–343. doi: 10.1111/opo.12279

Hernowo, A. T., Prins, D., Baseler, H. A., Plank, T., Gouws, A. D., Hooymans, J. M., et al. (2014). Morphometric analyses of the visual pathways in macular degeneration. *Cortex* 56, 99–110. doi: 10.1016/j.cortex.2013.01.003

Huang, X., Li, H. J., Ye, L., Zhang, Y., Wei, R., Zhong, Y. L., et al. (2016). Altered regional homogeneity in patients with unilateral acute open-globe injury: a resting-state functional MRI study. *Neuropsychiatr. Dis. Treat.* 12, 1901–1906. doi: 10.2147/NDT.S110541

Kaas, J. H., Krubitzer, L. A., Chino, Y. M., Langston, A. L., Polley, E. H., and Blair, N. (1990). Reorganization of retinotopic cortical maps in adult mammals after lesions of the retina. *Science* 248, 229–231. doi: 10.1126/science.2326637

Kawasaki, R., Yasuda, M., Song, S. J., Chen, S. J., Jonas, J. B., Wang, J. J., et al. (2010). The prevalence of age-related macular degeneration in Asians: a systematic review and meta-analysis. *Ophthalmology* 117, 921–927. doi: 10.1016/j.ophtha.2009.10.007

Laude, A., Cackett, P. D., Vithana, E. N., Yeo, I. Y., Wong, D., Koh, A. H., et al. (2010). Polypoidal choroidal vasculopathy and neovascular age-related macular degeneration: same or different disease? *Prog. Retin. Eye Res.* 29, 19–29. doi: 10.1016/j.preteyeres.2009.10.001

Li, S., Li, P., Gong, H., Jiang, F., Liu, D., Cai, F., et al. (2017). Intrinsic functional connectivity alterations of the primary visual cortex in primary angle-closure glaucoma patients before and after surgery: a resting-state fMRI Study. *Plos One* 12:e0170598. doi: 10.1371/journal.pone.0170598

Li, X. B., Wang, L. B., Xiong, Y. B., Bo, Q. J., He, F., Li, F., et al. (2019). Altered resting-state functional connectivity of the insula in individuals with clinical high-risk and patients with first-episode schizophrenia. *Psychiatry Res.* 282:112608. doi: 10.1016/j.psychres.2019.112608

Liang, M., Xie, B., Yang, H., Yin, X., Wang, H., Yu, L., et al. (2017). Altered interhemispheric functional connectivity in patients with anisometropic and strabismic amblyopia: a resting-state fMRI study. *Neuroradiology* 59, 517–524. doi: 10.1007/s00234-017-1824-0

Lim, L. S., Mitchell, P., Seddon, J. M., Holz, F. G., and Wong, T. Y. (2012). Age-related macular degeneration. *Lancet* 379, 1728–1738.

Little, D. M., Thulborn, K. R., and Szlyk, J. P. (2008). An FMRI study of saccadic and smooth-pursuit eye movement control in patients with age-related macular degeneration. *Invest. Ophthalmol. Vis. Sci.* 49, 1728–1735. doi: 10.1167/iovs.07-0372

Liu, Y., Yu, C., Liang, M., Li, J., Tian, L., Zhou, Y., et al. (2007). Whole brain functional connectivity in the early blind. *Brain* 130, 2085–2096. doi: 10.1093/brain/awm121

Lowe, M. J., Mock, B. J., and Sorenson, J. A. (1998). Functional connectivity in single and multislice echoplanar imaging using resting-state fluctuations. *Neuroimage* 7, 119–132. doi: 10.1006/nimg.1997.0315

Masuda, Y., Dumoulin, S. O., Nakadomari, S., and Wandell, B. A. (2008). V1 projection zone signals in human macular degeneration depend on task, not stimulus. *Cereb. Cortex* 18, 2483–2493. doi: 10.1093/cercor/bhm256

Mayer, A. R., Bellgowan, P. S., and Hanlon, F. M. (2015). Functional magnetic resonance imaging of mild traumatic brain injury. *Neurosci. Biobehav. Rev.* 49, 8–18.

Pascual-Leone, A., Amedi, A., and Fregni, F. (2005). Merabet, LB, The plastic human brain cortex. *Ann. Rev. Neurosci.* 28, 377–401.

Patton, N., Aslam, T., Macgillivray, T., Pattie, A., Deary, I. J., and Dhillon, B. (2005). Retinal vascular image analysis as a potential screening tool for cerebrovascular disease: a rationale based on homology between cerebral and retinal microvasculatures. *J. Anatomy* 206, 319–348. doi: 10.1111/j.1469-7580.2005.00395.x

Prins, D., Hanekamp, S., and Cornelissen, F. W. (2016a). Structural brain MRI studies in eye diseases: are they clinically relevant? A review of current findings. *Acta Ophthalmol.* 94, 113–121. doi: 10.1111/aos.12825

Prins, D., Plank, T., Baseler, H. A., Gouws, A. D., Beer, A., Morland, A. B., et al. (2016b). Surface-based analyses of anatomical properties of the visual cortex in macular degeneration. *PLoS One* 11:e0146684. doi: 10.1371/journal.pone.0146684

Puig, J., Blasco, G., Alberich-Bayarri, A., Schlaug, G., Deco, G., Biarnes, C., et al. (2018). Resting-state functional connectivity magnetic resonance imaging and outcome after acute stroke. *Stroke* 49, 2353–2360. doi: 10.1161/STROKEAHA.118.021319

Raichle, M. (2010). The brain's dark energy. *Sci. Am.* 302, 44–49.

Rosengarth, K., Keck, I., Brandl-Rühle, S., Frolo, J., Hufendiek, K., Greenlee, M. W., et al. (2013). Functional and structural brain modifications induced by oculomotor training in patients with age-related macular degeneration. *Front. Psychol.* 4:428. doi: 10.3389/fpsyg.2013.00428

Seddon, J. M., Cote, J., Davis, N., and Rosner, B. (2003). Progression of age-related macular degeneration: association with body mass index, waist circumference, and waist-hip ratio. *Arch. Ophthalmol.* 121, 785–792. doi: 10.1001/archopht.121.6.785

Seddon, J. M., Willett, W. C., Speizer, F. E., and Hankinson, S. E. (1996). A prospective study of cigarette smoking and age-related macular degeneration in women. *Jama* 276, 1141–1146.

Seiple, W., Szlyk, J. P., McMahon, T., Pulido, J., and Fishman, G. A. (2005). Eye-movement training for reading in patients with age-related macular degeneration. *Invest. Ophthalmol. Visual Sci.* 46, 2886–2896. doi: 10.1167/iovs.04-1296

Seitz, R. J., Nickel, J., and Azari, N. P. (2006). Functional modularity of the medial prefrontal cortex: involvement in human empathy. *Neuropsychology* 20, 743–751. doi: 10.1037/0894-4105.20.6.743

Spreng, R. N., and Grady, C. L. (2010). Patterns of brain activity supporting autobiographical memory, prospection, and theory of mind, and their relationship to the default mode network. *J. Cogn. Neurosci.* 22, 1112–1123. doi: 10.1162/jocn.2009.21282

Szlyk, J. P., and Little, D. M. (2009). An FMRI study of word-level recognition and processing in patients with age-related macular degeneration. *Invest. Ophthalmol. Vis. Sci.* 50, 4487–4495. doi: 10.1167/iovs.08-2258

Whitson, H. E., Chou, Y. H., Potter, G. G., Diaz, M. T., Chen, N. K., Lad, E. M., et al. (2015). Phonemic fluency and brain connectivity in age-related macular degeneration: a pilot study. *Brain Connect.* 5, 126–135. doi: 10.1089/brain.2014.0277

Wong, T. Y., Klein, R., Klein, B. E., Tielsch, J. M., Hubbard, L., and Nieto, F. J. (2001b). Retinal microvascular abnormalities and their relationship with hypertension, cardiovascular disease, and mortality. *Surv. Ophthalmol.* 46, 59–80. doi: 10.1016/s0039-6257(01)00234-x

Wong, T. Y., Klein, R., Couper, D. J., Cooper, L. S., Shahar, E., Hubbard, L. D., et al. (2001a). Retinal microvascular abnormalities and incident stroke: the atherosclerosis risk in communities study. *Lancet* 358, 1134–1140. doi: 10.1016/S0140-6736(01)06253-5

Wong, T. Y., Klein, R., Sharrett, A. R., Couper, D. J., Klein, B. E., Liao, D. P., et al. (2002). Cerebral white matter lesions, retinopathy, and incident clinical stroke. *Jama* 288, 67–74. doi: 10.1001/jama.288.1.67

Wong, W. L., Su, X., Li, X., Cheung, C. M., Klein, R., Cheng, C. Y., et al. (2014). Global prevalence of age-related macular degeneration and disease burden projection for 2020 and 2040: a systematic review and meta-analysis. *Lancet Glob. Health* 2, e106–e116. doi: 10.1016/S2214-109X(13)70145-1

Yan, C. G., Wang, X. D., Zuo, X. N., and Zang, Y. F. D. P. A. B. I. (2016). Data processing & analysis for (resting-state) brain imaging. *Neuroinformatics* 14, 339–351.

Yan, X., Wang, Y., Xu, L., Liu, Y., Song, S., Ding, K., et al. (2019). Altered functional connectivity of the primary visual cortex in adult comitant strabismus: a resting-state functional MRI Study. *Curr. Eye Res.* 44, 316–323. doi: 10.1080/02713683.2018.1540642

Yatsuya, H., Folsom, A. R., Wong, T. Y., Klein, R., Klein, B. E., and Sharrett, A. R. (2010). Retinal microvascular abnormalities and risk of lacunar stroke: atherosclerosis risk in communities study. *Stroke* 41, 1349–1355. doi: 10.1161/STROKEAHA.110.580837

Yoshimine, S., Ogawa, S., Horiguchi, H., Terao, M., Miyazaki, A., Matsumoto, K., et al. (2018). Age-related macular degeneration affects the optic radiation white matter projecting to locations of retinal damage. *Brain Struct. Funct.* 223, 3889–3900. doi: 10.1007/s00429-018-1702-5

Zhang, D., and Raichle, M. E. (2010). Disease and the brain's dark energy. *Nat. Rev. Neurol.* 6, 15–28. doi: 10.1038/nrneurol.2009.198

Zhao, J., Du, Y. H., Ding, X. T., Wang, X. H., and Men, G. Z. (2020). Alteration of functional connectivity in patients with Alzheimer's disease revealed by resting-state functional magnetic resonance imaging. *Neural. Regen. Res.* 15, 285–292. doi: 10.4103/1673-5374.265566

Zhuang, J., Madden, D. J., Duong-Fernandez, X., Chen, N. K., Cousins, S. W., Potter, G. G., et al. (2018). Language processing in age-related macular degeneration associated with unique functional connectivity signatures in the right hemisphere. *Neurobiol. Aging* 63, 65–74. doi: 10.1016/j.neurobiolaging.2017.11.003

Zuo, X., Zhuang, J., Chen, N. K., Cousins, S., Cunha, P., Lad, E. M., et al. (2020). Relationship between neural functional connectivity and memory performance in age-related macular degeneration. *Neurobiol. Aging* 95, 176–185. doi: 10.1016/j.neurobiolaging.2020.07.020

Conflict of Interest: The authors declare that the research was conducted in the absence of any commercial or financial relationships that could be construed as a potential conflict of interest.

Publisher's Note: All claims expressed in this article are solely those of the authors and do not necessarily represent those of their affiliated organizations, or those of the publisher, the editors and the reviewers. Any product that may be evaluated in this article, or claim that may be made by its manufacturer, is not guaranteed or endorsed by the publisher.

frontiers in Aging Neuroscience

ORIGINAL RESEARCH
published: 25 March 2022
doi: 10.3389/fnagi.2022.838141

Body Complexion and Circulating Lipids in the Risk of TDP-43 Related Disorders

Noelia Esteban-García[1†], Luis C. Fernández-Beltrán[1†], Juan Miguel Godoy-Corchuelo[1†], Jose L. Ayala[2], Jordi A. Matias-Guiu[1] and Silvia Corrochano[1]*

[1] Neurological Disorders Group, Hospital Clínico San Carlos, Instituto de Investigación Sanitaria San Carlos (IdISSC), Madrid, Spain, [2] Department of Computer Architecture and Automation, Universidad Complutense de Madrid, Madrid, Spain

OPEN ACCESS

Edited by:
Yuzhen Xu,
Tongji University, China

Reviewed by:
Alejandro A. Canales-Aguirre, CONACYT Centro de Investigación y Asistencia en Tecnología y Diseño del Estado de Jalisco (CIATEJ), Mexico
Ricardo Madrid, Universidad Complutense de Madrid, Spain
Qiying Sun, Central South University, China

***Correspondence:**
Silvia Corrochano
silvia.corrochano@salud.madrid.org

[†] These authors have contributed equally to this work

Specialty section:
This article was submitted to Cellular and Molecular Mechanisms of Brain-aging, a section of the journal Frontiers in Aging Neuroscience

Received: 17 December 2021
Accepted: 04 February 2022
Published: 25 March 2022

Citation:
Esteban-García N, Fernández-Beltrán LC, Godoy-Corchuelo JM, Ayala JL, Matias-Guiu JA and Corrochano S (2022) Body Complexion and Circulating Lipids in the Risk of TDP-43 Related Disorders. Front. Aging Neurosci. 14:838141. doi: 10.3389/fnagi.2022.838141

Objective: Frontotemporal dementia (FTD) and amyotrophic lateral sclerosis (ALS) are two distinct degenerative disorders with overlapping genetics, clinical manifestations, and pathology, including the presence of TDP-43 aggregates in nearly 50% of patients with FTD and 98% of all patients with ALS. Here, we evaluate whether different genetically predicted body lipid metabolic traits are causally associated with the risk of FTD with TDP-43 aggregates, compare it to their causal role in the risk of ALS, and identify genetic variants shared between these two TDP43 related disorders in relation to lipid metabolic traits.

Methods: We conducted two-sample Mendelian randomization analyses (2SMR) to evaluate the causal association of 9 body complexion and 9 circulating lipids traits with the risk of FTD with TDP-43 aggregates and the risk of ALS. The inverse-variance weighted method was the primary analysis, followed by secondary sensitive analyses. We then looked for common genetic variants between FTD and ALS in relation to lipid metabolic traits.

Results: Genetically increased trunk-predicted mass, fat-free mass, and higher circulating triglycerides levels were suggestively associated with a higher risk of FTD with TDP-43 aggregates. Circulating lipids, mainly LDL cholesterol, were causally associated with a higher risk of ALS. We identified two genetic variants, *EIF4ENIF1 and HNRNPK,* in relation to body complexion and circulating lipids shared between FTD with TDP-43 aggregates and ALS.

Conclusion: This work provides evidence that body complexion and circulating lipids traits impact differentially on the risk of FTD and ALS, suggesting new and specific interventional approaches in the control of body lipid metabolism for FTD and ALS, and identified *HNRNPK* as a potential link between circulating lipids levels and these disorders.

Keywords: amyotrophic lateral sclerosis, frontotemporal dementia, lipid metabolism, Mendelian randomization, TDP-43 related disorders

INTRODUCTION

Frontotemporal lobar degeneration (FTLD) encompasses a spectrum of severe neurodegenerative disorders with several degrees of behavioral, language, cognitive, and motor symptoms. Frontotemporal dementia (FTD) is characterized by neuronal degeneration of the frontal and anterior temporal lobes of the brain. It is the second most common cause of early onset dementia (age < 65) and the third in patients > 65 years (Seltman and Matthews, 2012; Coyle-Gilchrist et al., 2016; Manzoni and Ferrari, 2021). Currently, there is no treatment for FTD.

Frontotemporal dementia is mainly sporadic. However, genetics plays a key role in up to 30% of the cases (Manzoni and Ferrari, 2021). So far, more than 20 genes involved in the development of FTLD have been identified. The protein aggregates, being the largest group characterized by positive inclusions of TAR DNA binding protein 43 (TDP-43), e.g., FTLD TDP subtype, are a hallmark of these disorders. Interestingly, in amyotrophic lateral sclerosis (ALS), another degenerative debilitating disorder, TDP-43 aggregates are found in up to 98% of the cases studied (Neumann et al., 2006; Geser et al., 2009). ALS is a neurodegenerative fatal disorder characterized by the loss of upper and lower motor neurons of the brain and spinal cord leading to muscle atrophy and death (Kiernan et al., 2011). ALS and FTD are two ends of a spectrum of disorders with several mixed intermediate forms (Ferrari et al., 2011). There are some genes that can cause both ALS or FTD or mixed forms (DeJesus-Hernandez et al., 2011; Xi et al., 2014; Karch et al., 2018; Raffaele et al., 2019). There might be some missing genetics that could help to shed light not only on these complex disorders, but also on the influence of environmental risk factors. Especially, the weight and circulating lipids are complex traits that have been previously associated with ALS (Dupuis et al., 2008; Paganoni et al., 2011), and to a much lesser extent with FTD. The weight seems to be delineating the clinical form along the spectrum, with the smaller weight at the ALS end and the highest weight in the FTD end of the spectrum (Ahmed et al., 2014). Association studies have revealed that patients with FTD have lipid metabolism alterations (Kim et al., 2018a; Ahmed et al., 2019). This highlights the need to deepen in their association and potential causal relation since adiposity and metabolic traits have become a global health problem. Additionally, the identification of genetic variants that might be influencing the clinical form within the ALS/FTD spectrum of disorders could help predict the impact of these lipid metabolic risk factors and assist with the stratification of patients within the spectrum.

Here, we hypothesized that some of the genetic variants that impact in body lipid metabolic traits could be influencing the development of particular clinical forms of TDP-43 proteionopathies within the spectrum of disorders of FTD and ALS. To assess this hypothesis, we used an analytical tool known as Mendelian randomization analysis (MR) of 2 samples (2SMR) (Hemani et al., 2018), which allows for the identification of overlapping genetic variants between several risk factors and the disease of interest. Thus, we performed a 2SMR study using the most up-to-date GWAS summary data related to lipid metabolism in two main blocks: (i) body complexion; and, (ii) circulating lipids, with an FTLD TDP subtype GWAS summary data, and, in parallel, another study with GWAS of ALS (**Figure 1**). After the comparison of the two studies, we obtained all the significant SNPs in FTLD TDP subtype and in ALS, and we identified two genetic variants in relation to lipid metabolic traits shared between the two diseases of interest.

MATERIALS AND METHODS

Genome-Wide Association Studies Summary Data for Body Complexion and Circulating Lipids (Exposures)

We used summary population-level data to conduct the method of 2SMR to evaluate the possible causal relationship between different variables related to body lipid metabolism and FTLD TDP subtype, and compared it to their role in ALS, a related TDP-43 proteinopathy. We conducted a Pubmed search as well as the MR-base catalog search of the most recent GWAS studies (until December 2020) for lifelong lipid metabolism traits, in particular those related to body composition, body shape and lipid levels in blood. We selected GWAS datasets using the following criteria: (i) GWAS with the most recent publication date; (ii) GWAS that have not been used in this type of analysis before; (iii) those with larger sample sizes; and, (iv) GWAS that have the data curated and were in the MR base catalog.

The exposure traits were separated into two groups: (i) Body complexion and adiposity, and (ii) circulating lipids. In the body complexion and adiposity group we included 9 traits: "Extreme body mass index," "body mass index" (BMI), "waist-to-hip ratio" (WHR), "body fat percentage" (BF%), "trunk predicted mass," "trunk fat-free mass," "appendicular lean mass," "impedance whole body," "whole Body fat mass." In the circulating lipids group, we included 9 traits: "Total triglycerides" (TG), "total cholesterol"(TC), "LDL cholesterol" (LDL), "HDL cholesterol" (HDL), "linoleic acid," "docosahexaenoate" (DHA), "omega 3-fatty acid," "omega 6-fatty acid," "total fatty acids." The characteristics of the selected GWAS are detailed in **Supplementary Table 1**.

Genome-Wide Association Analysis Data for Frontotemporal Dementia and Amyotrophic Lateral Sclerosis (Outcomes)

We used the summary statistics from a GWAS of frontotemporal lobar degeneration with TDP-43 inclusions (FTLD TDP subtype) from 2010, with 3,020 cases in the study (Van Deerlin et al., 2010). We also ran the same study for the outcome ALS, in this case using the GWAS from 2018, gathering an *N* of 80,610 with 20,806 cases and 59,804 controls, and 10,031,630 variants in the analysis (Nicolas et al., 2018). All the populations are of European ancestry (**Supplementary Table 1**).

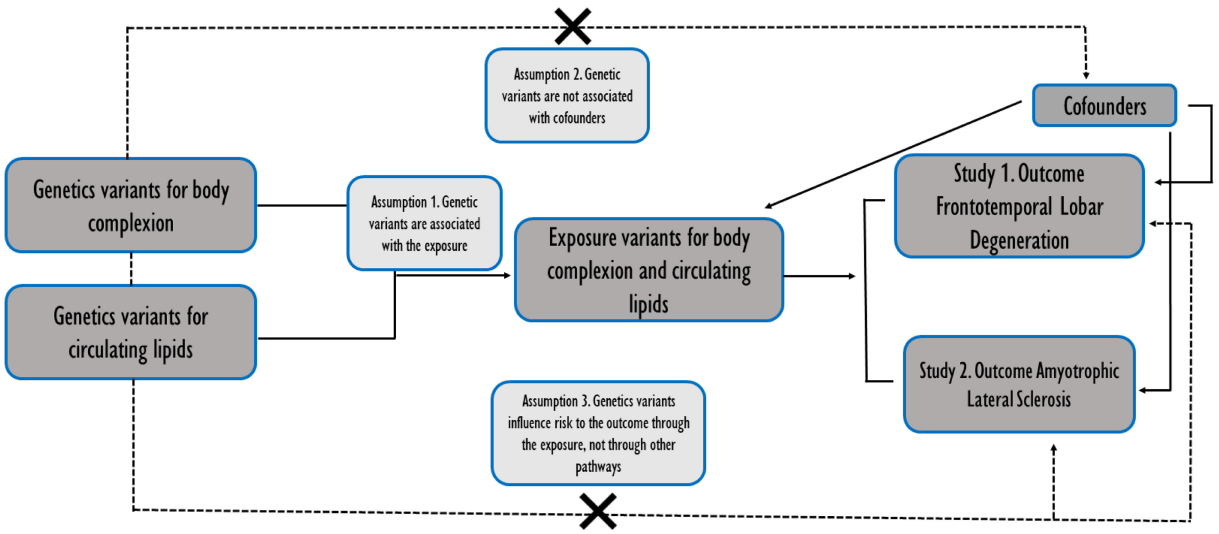

FIGURE 1 | Schematic representation of the two independent studies conducted in parallel. Assumptions of a two-sample Mendelian randomization analyses between the exposures (body complexion and circulating lipids traits) and the outcomes (the risk of frontotemporal dementia TDP43 subtype and amyotrophic lateral sclerosis). Broken lines represent potential pleiotropic or direct causal effects between variables that would violate Mendelian randomization assumptions.

The Two-Sample Mendelian Randomization Analyses

We used an algorithm developed by Hemani et al. (2018) and implemented it into the TwoSampleMR R package (version 4.26). We used RStudio 1.4.1717 (2021) and R 4.1.1 software to perform the MR analyses. This data package offers a curated database containing summarized GWAS. This approach determines whether an exposure is causally associated with an outcome. Along these lines, the MR analysis carried out was supported by three assumptions: (i) That instrumental variables (IVs) are significantly associated with body complexion and adiposity and circulating lipids; (ii) IVs are not associated with confounding factors; (iii) the risk of the two outcomes, ALS or FTD, is only influenced by IVs (**Figure 1**).

For each of the individual 2SMR analyses performed, the IVs used for each trait were identified. This identification is based on the odds ratios per allele (beta) and standard estimates (SE) for all single nucleotide polymorphisms (SNPs), using a statistically driven approach that identifies SNPs that are significantly associated with exposure, setting the threshold p-values of $< 5 \times 10^{-8}$. The applied algorithm then extracts those SNPs from the outcome (from FTLD TDP subtype and ALS GWAS datasets in this case), thereby selecting the SNPs found in both the exposure and outcome datasets. For the SNPs present in the exposure that are not present in the outcome data, it applies a clustering method using proxies ($r_2 > 0.9$). With all these SNPs, a harmonization of the data sets is carried out to ensure that the effect of the size of the SNPs is homogenized. The total number of IVs used on each of the 2SMR analyses conducted for FTD and ALS are shown in **Figures 2A,B**, respectively.

The causal association between the exposures (the lipid metabolism traits) and the outcome (FTD or ALS) was primarily assessed by the inverse variance weighted (IVW) method, and the traits were considered to have an effect when the p-value was < 0.05. Multiple comparisons were corrected using the Bonferroni-corrected method. The IVW method has some assumptions on the independence of the genetic variants, assuming no horizontal pleiotropy that might be influencing the relation by other pathways (Burgess et al., 2013). As such, we used other sensitivity methods that account for pleiotropy to support the findings, including the MR-Egger regression, the Simple median, and the weighted median. To ensure the robustness of the significance of our results, we performed a leave-a-SNP-out analysis to detect the heterogeneity of the analyses.

We used the scatter plot to visualize how each SNP from the exposure used in the analysis was associated with the outcome, with a potential representation of the causal effect estimation of each of the SNPs.

Identification of Shared Body Lipid Metabolisms Genetic Variants in Frontotemporal Dementia and Amyotrophic Lateral Sclerosis

From all of the 2SMR analyses performed, we extracted all the SNPs from body complexion and circulating lipid levels that were significantly associated with FTD TDP subtype, and we did the same for all the SNPs significantly associated with ALS, thus creating two lists of putative genetic variants influencing those two diseases, separating them by the type of trait they belong to (body complexion or circulating lipids). We then evaluated specificities and communalities of the SNPs between the two outcomes (FTD and ALS) using Venn diagrams. We used bioinformatics open resources as tools to examine the biological function of those SNPs, including dsSNP, GnomAD, ClinVar, and functional biological interactions using String.

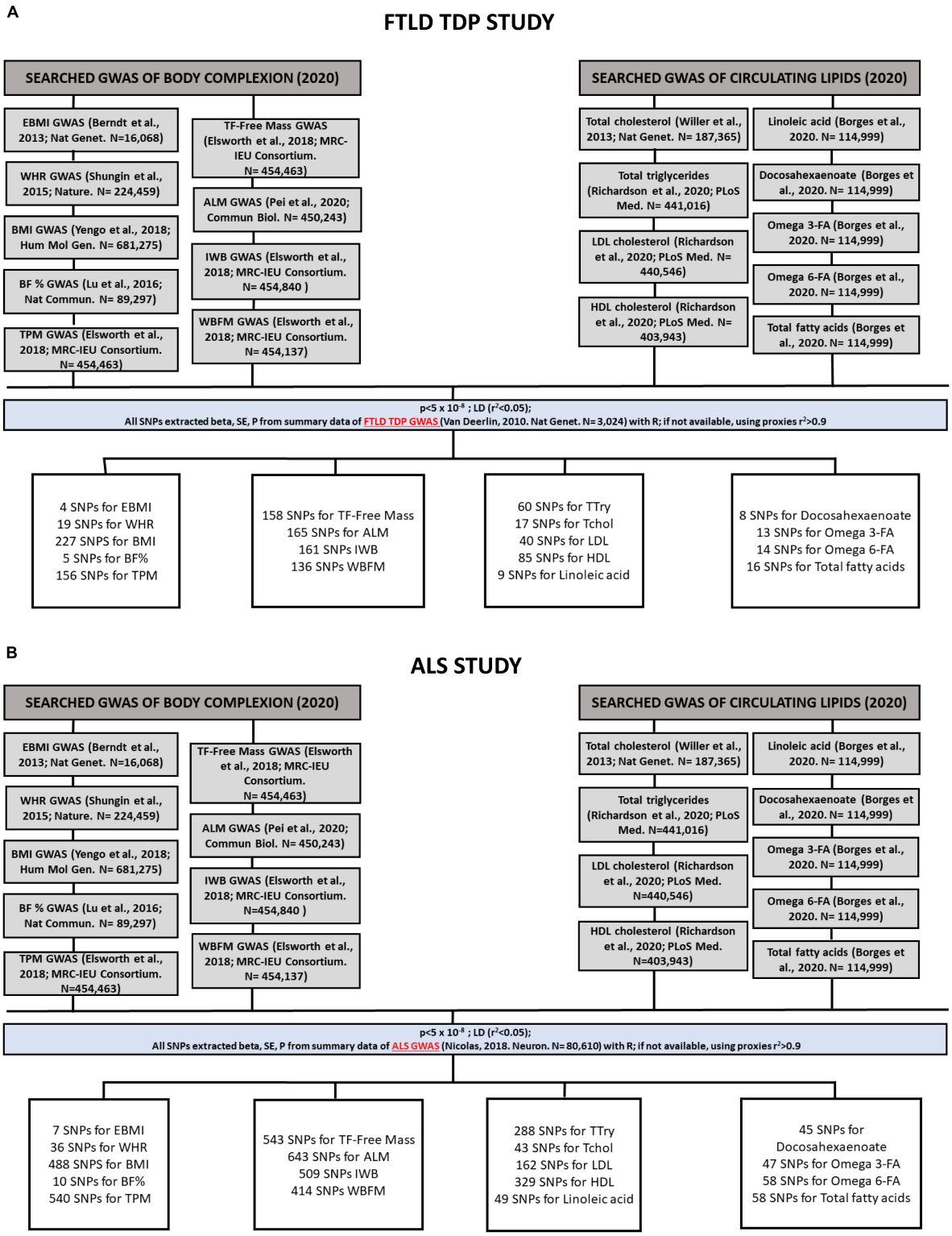

FIGURE 2 | Flowchart followed by the process of identification and selection of genome-wide association studies (GWAS) and the SNPs used as instrumental variables (IVs) that have been included in the Mendelian randomization analyses of FTLD TDP subtype **(A)** and ALS **(B)**. In the body complexion group we included 9 traits: "Extreme body mass index," "body mass index" (BMI), "waist-to-hip ratio" (WHR), "body fat percentage" (BF%), "trunk predicted mass," "trunk fat-free mass," "appendicular lean mass," "impedance whole body," "whole body fat mass." In the circulating lipids group we included 9 traits: "Total triglycerides" (TG), "total cholesterol"(TC), "LDL cholesterol" (LDL), "HDL cholesterol" (HDL), "linoleic acid," "docosahexaenoate" (DHA), "omega 3-fatty acid," "omega 6-fatty acid," and "total fatty acids."

RESULTS

Our main aim was to identify the genetically determined causal role of body lipid metabolism on the risk of FTD. In particular, we used the FTD with TDP-43 inclusion subtype as it is the pathological form that is more associated with ALS in the spectrum of disorders. Thus, we also ran the same study in parallel on ALS so that we could then compare similarities and specificities of the potential genetic influences of body lipid metabolism on the risk of these two disorders (**Figure 1**). For each disease (outcome), FTLD TDP subtype (**Figure 2A**) or ALS (**Figure 2B**), we analyzed the causal effect of a total of 9 traits included in the category of body complexion and another 9 traits that fall in the category of circulating lipids.

Two-Sample Mendelian Randomization Analysis of Body Composition and Circulating Lipids on the Risk of Frontotemporal Dementia TAR DNA Binding Protein 43 Subtype

In relation to FTLD TDP subtype, among the group of 9 traits that fall in the category of the body complexion, the trunk-predicted mass (p = 0.008, OR = 3.27, 95% CI = 1.35–7.95) and the trunk-predicted fat-free mass (p = 0.01, OR = 3.14, 95% CI = 1.30–7.54) are suggested to increase the risk of FTD by the IVW method. The simple median method was able to sustain those results, especially in the case of trunk-predicted mass (p = 0.039), and close but not significant for the trunk-predicted fat-free mass (p = 0.055). Unfortunately, the results were not supported by the MR-Egger method (**Figure 3A**). A list of all the SNPs used in the analysis of the 9 traits on FTD are displayed in **Supplementary Tables 2–10**. Regarding the circulating lipid levels group, none of the 9 traits analyzed were significantly found to be genetically causally associated with FTD by the IVW method (**Figure 3B**). Genetically predicted "total triglycerides" showed a trend to be causally associated with FTD by the IVW method (p = 0.06, OR = 1.9, 95% CI = 0.96–3.7) and it was significantly associated by the weighted median method (p = 0.04, OR = 2.5, 95% CI = 1.02–6.36). A list of all the SNPs (IVs) used in the analysis of the 9 circulating lipid traits on FTD is displayed in the **Supplementary Tables 11–19**.

Two-Sample Mendelian Randomization Analysis of Body Composition and Circulating Lipids on the Risk of Amyotrophic Lateral Sclerosis

The same study was conducted in parallel with ALS as the outcome. The primary analysis of IVW method did not find any significant causal association of the 9 body complexion traits with ALS (**Figure 4A**). The "extreme body mass index" (Extreme BMI) was found to be significant by the weighted median (p = 0.016, OR = 0.92, 95% CI = 0.85–0.98) and by simple median (p = 0.02, OR = 0.91, 95% CI = 0.85–0.99) methods, but the analysis was not rigorously significant by the IVW method (p = 0.08, OR = 0.93, 95% CI = 0.87–1.00). The "body fat percentage" (BF%) trait also presented a trend of potential inverse causal effect on ALS found significant by the MR-Egger method (p = 0.035, OR = 0.15, 95% CI = 0.03–0.65), consistent with a previous analysis by Zhang et al. (2020), although none of the other sensitive analyses supported those findings. The leave-one-out analysis of BF% identified the SNP rs6857 to be driving much of the effect, which is consistent with the previous analysis (Zhang et al., 2020). The leave-one-out analysis of extreme BMI identified the SNP rs11127483 to be driving much of the effect. Thus, the 1-SD increase in extreme BMI and in BF% is not rigorously associated with a lower risk of ALS, but more data and experiments are needed to clarify and support those results. A list of all the SNPs used in these analyses can be found in **Supplementary Tables 2–10**. From the 9 circulating lipids traits, we found that "total cholesterol" (p = 0.011, OR = 1.11, 95% CI = 1.02–1.2), "LDL cholesterol" (p = 0.034, OR = 1.11, 95% CI = 1.01–1.21), "linoleic acid" (p = 0.022, OR = 1.12, 95% CI = 1.016–1.24), and "omega-6 fatty acid" (p = 0.033, OR = 1.12, 95% CI = 1.00–1.25) were causally associated to ALS by the primary method IVW (**Figure 4B**). Out of the four blood lipid traits, only the "LDL cholesterol" was found supported significant by the weight median (p = 0.037, OR = 1.15, 95% CI = 1.00–1.32) and the weight mode (p = 0.015, OR = 1.16, 95% CI = 1.03–1.31) sensitive analysis. The list of IVs used in these analyses can be found in **Supplementary Tables 11–19**. The leave-one-out analysis showed no evidence of outlier SNPs.

The effect of the individual SNPs on the trunk predicted mass and fat-free mass vs. the effect on FTD is shown in **Figure 5**. The effect of the SNPs on the extreme BMI and BF% vs. their effect on ALS is represented in a scatter plot in **Figure 6A**. The effect of circulating lipids (total cholesterol, LDL cholesterol, linoleic acid and omega 6 fatty acid) vs. their effect on ALS is shown in scatter plots in **Figure 6B**.

Identification of Shared and Specific Single Nucleotide Polymorphisms in Frontotemporal Dementia TAR DNA Binding Protein 43 Subtype and Amyotrophic Lateral Sclerosis in Relation to Body Lipid Metabolism

In addition, we decided to look for the SNPs that showed a significant effect on the outcomes of FTLD TDP subtype and ALS and compared them with the idea that there could be some shared genetics regarding body lipid metabolism in these two disorders with pathological TDP43 hallmark overlap. Thus, we used all the results from the two studies and extracted the list of all the SNPs that were individually significantly associated with each of the outcomes, FTD and ALS. From the 9 traits in the group of body complexion (using the list of SNPs extracted from **Supplementary Tables 2–10**), we found a total of 43 SNPs that were significantly associated with FTD and a total of 218 SNPs significantly associated with ALS. We then compared the SNPs that were exclusively or commonly found between FTD and ALS, as shown in the Venn diagrams (**Figure 7A**), and identified only one SNP in common, rs5753630

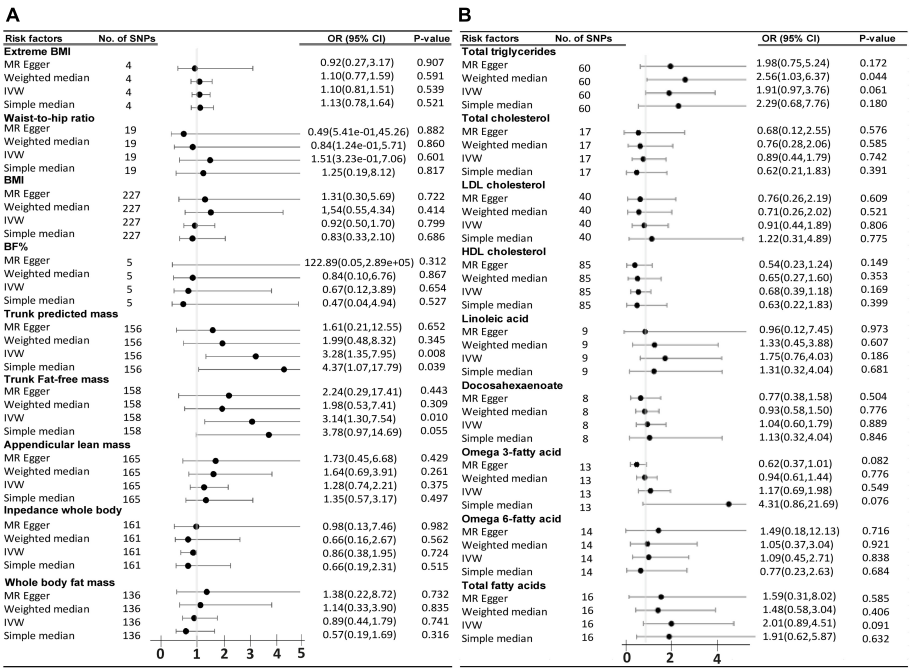

FIGURE 3 | Odds ratio (OR) and forest plot for the causal association with the risk of frontotemporal dementia with TDP43 aggregates by, **(A)** Body complexion traits, and **(B)** Circulating lipids traits. BMI, body mass index; BF%, body fat percentage; CI, confidence interval; IVW, inverse variance weighted; SNPs, single nucleotide polymorphisms.

[chr22:31465964 (GRCh38.p13)]. The rs5753630 variant falls on an intron region of the *EIF4ENIF1* gene (eukaryotic translation initiation factor 4E nuclear import factor 1), which encodes a nucleocytoplasmic shuttle protein involved in the regulation of translation initiation. We conducted further analysis of pathway enrichment to investigate if those 43 and 218 differential SNPs in FTD and ALS, respectively, are related to a biological function or a pathway. From the 43 SNPs specific of the FTLD TDP subtype and body complexion, we found that 32 SNPs have associated genes, and most of them have alternative splicing (data not shown).

Next, we performed the same analysis for the total of SNPs that were significantly associated with FTD and ALS from the study of circulating lipid traits (using the list of SNPs extracted from **Supplementary Tables 11–19**). We found 12 SNPs that were significant from the FTD study and 89 SNPs in the ALS study from all the 9 lipid traits analyzed. We then looked for any common SNPs between the two outcomes in relation to circulating lipids and identified one SNP, rs696825 [chr9:83968161 (GRCh38.p13)] (**Figure 7B**). The rs696825 variant falls on the 3‘ Prime UTR of the gene *HNRNPK* (heterogeneous nuclear ribonucleoprotein K), which encodes an hnRNP RNA binding protein involved in RNA processing. Interestingly, this protein has recently been found mislocalized in the cytoplasm and associated with FTLD pathology (Bampton et al., 2021). Remarkably, this protein seems to control the cytoplasmic aggregation of TDP43 (Moujalled et al., 2015). Finally, we run further enrichment analysis on the significant SNPs related to circulating lipid traits identified in the ALS and FTD studies. From the 89 SNPs of the ALS study, we found functional enrichment in the cholesterol homeostasis pathway (GO:42632). The list with all the SNPs used in this section can be found in **Supplementary Table 20**.

DISCUSSION

We conducted two independent studies in parallel to evaluate the effect of genetically predicted body complexion and circulating lipids on the risk of FTLD TDP subtype and on ALS and compared their effects in these two TDP-43 related diseases (Liscic et al., 2008) that are also part of a spectrum of disorders. We found that body trunk mass and triglycerides levels could be more relevant for the risk of FTLD TDP subtype, and on the contrary, the levels of LDL cholesterol, and possibly linoleic and omega 6 fatty acids, play a more important role in the risk of ALS. Moreover, we identified two genetic variants shared in the two studies conducted on FTD and ALS. These two variants are located in two genes that encode proteins with role in RNA metabolism which is a well-documented pathological mechanism operating in these disorders. Emerging evidence shows that lipid metabolic alterations as another important pathological mechanism contributing to these multifactorial complex disorders etiology (Burg et al., 2021; Fernández-Beltrán et al., 2021; Lee et al., 2021).

This is, to our knowledge, the first time that this type of MR analysis has been done to evaluate the genetically predicted causal association of these particular body complexions and circulating

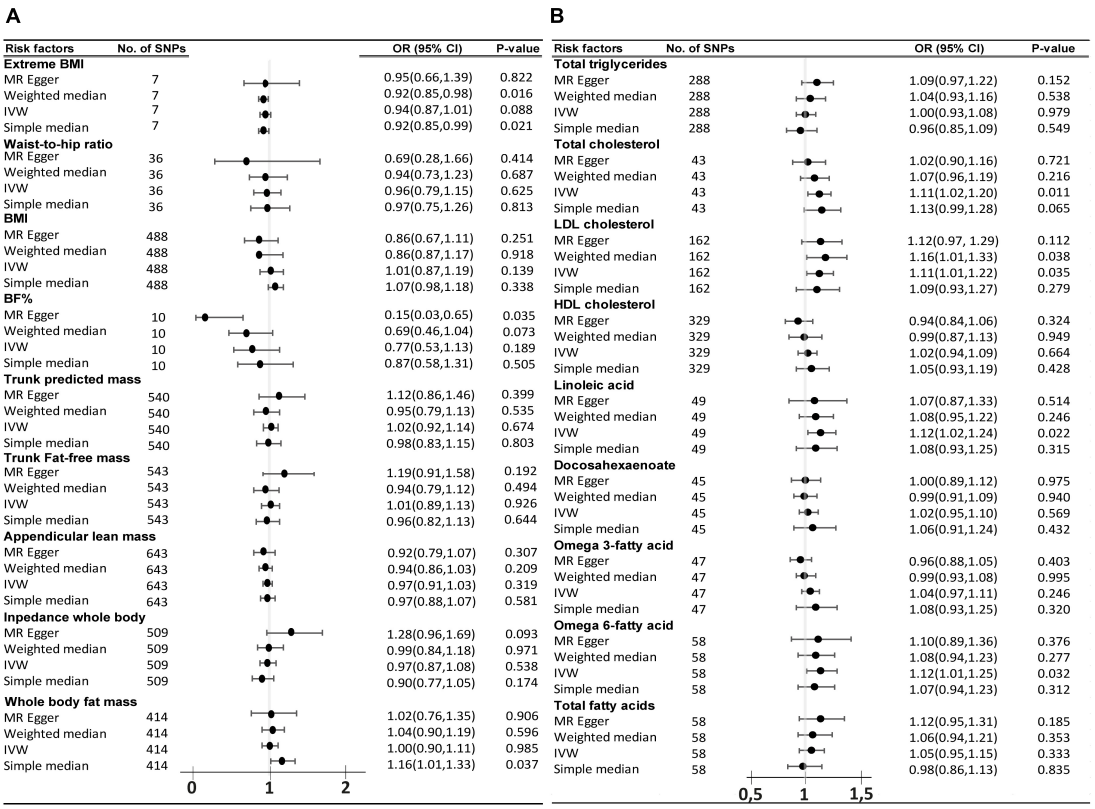

FIGURE 4 | Odds ratio (OR) and forest plot for the causal association with the risk of ALS by, **(A)** body composition and, **(B)** circulating lipids. BMI, body mass index, BF%, body fat percentage, CI, confidence interval, IVW, inverse variance weighted, SNPs, single nucleotide polymorphisms.

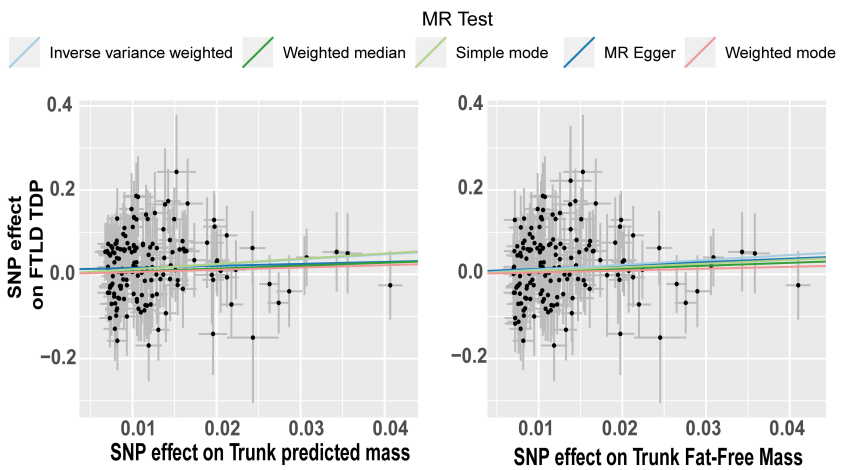

FIGURE 5 | Scatterplot of single nucleotide polymorphism (SNP) potential effects on trunk mass vs. frontotemporal lobar degeneration with TDP43. The slope of each line corresponds to the estimated Mendelian randomization (MR) effect per method. Significant changes in SNPs related to predict trunk mass and trunk fat-free mass are associated as a risk factor in FTLD TDP subtype.

lipids traits on the risk of FTLD TDP subtype. We conducted the same study on ALS in parallel and compared the results of the two studies. There is a previous study using 2SMR with 5 different traits of lifelong adiposity on the risk of ALS, but our study encompasses a more extensive focus with 18 updated GWAS datasets that have not been used for ALS before, except for only two traits (BMI and extreme BMI), which are coincident with a previous study (Zhang et al., 2020). There is another

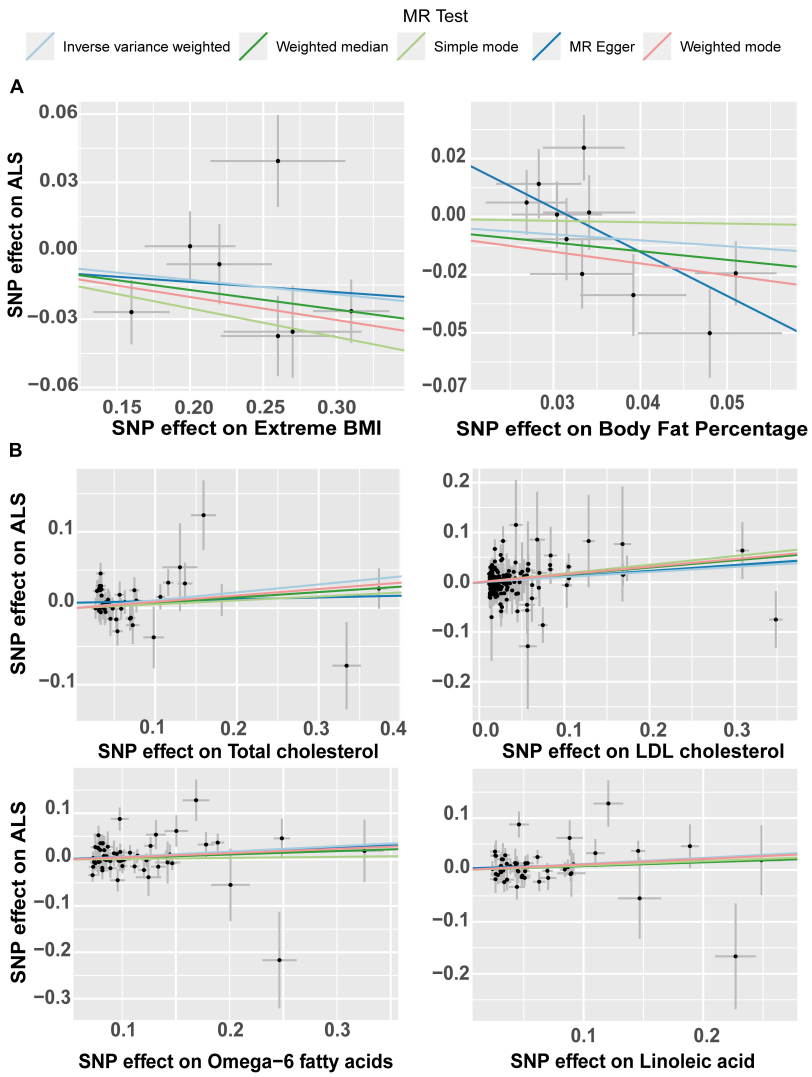

FIGURE 6 | Scatter plot of single nucleotide polymorphism (SNP) potential effects on body lipid metabolic traits vs. amyotrophic lateral sclerosis (ALS). The slope of each line corresponds to the estimated Mendelian randomization (MR) effect per method. **(A)** Scatter plots show the comparison of the SNPs effects on extreme BMI (body mass index) and body fat percentage (BF%) vs. ALS**. (B)** Scatterplots of single nucleotide polymorphism (SNP) potential effects on total cholesterol, LDL cholesterol, Omega-6 fatty acid and linoleic fatty acid, vs. amyotrophic lateral sclerosis (ALS). LDL, low density lipoprotein.

interesting study using this approach for ALS using all the GWAS available at the time. In that study, they found that higher levels of LDL cholesterol in blood increases the risk of ALS (Bandres-Ciga et al., 2019). There is one more study which also identified that LDL cholesterol was causally associated with a higher risk of ALS (Zeng and Zhou, 2019). Here, we have been able to replicate those results even though we have used a different and updated GWAS data set for LDL cholesterol. We also found other suggestive associations that were not evaluated in those two previous studies. Thus, for both diseases, FTD and ALS, this work presents novel and interesting results.

We have shown, for the first time, that genetically predicted 1-SD increase in trunk mass and fat-free mass (lean mass) are suggestively associated with a higher risk of FTD (TDP43 subtype). More anthropometric measures should be conducted routinely in the clinic to verify this association. Body metabolic measurements done in observational association studies on FTLD have previously reported higher BMI and visceral fat mass in FTLD patients in comparison to healthy controls, as well as in patients with Alzheimer disease (Ahmed et al., 2019). Our analysis did not support a genetically causal association of BMI and fat mass with FTLD TDP subtype. Similarly, we could not find a significant causal relation of any of the 9 traits analyzed for body composition and anthropometric measures with the risk of ALS, except for a suggestive association of higher body fat percentage (BF%) and extreme BMI with lower risk of ALS, which would be in line with previous studies (Zhang et al., 2020).

In relation to the study of the causal association of blood circulating lipids on FTD, only the genetically predicted 1-SD increase triglycerides (TG) blood levels were suggestively

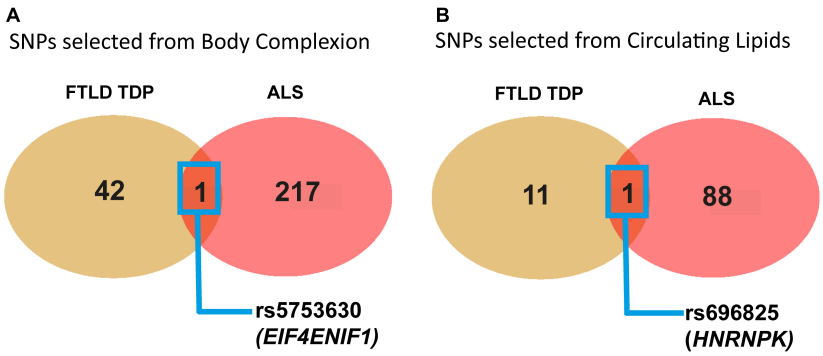

FIGURE 7 | Graphical representation of the identification of common significant SNPs in relation to body complexion and circulating lipids shared between FTD TDP43 subtype and ALS. **(A)** Venn diagram showing the common significant SNPs between FTLD TDP subtype and ALS from the 9 traits in relation to the body complexion group. The only genetic variant found in common is rs5753630, with *EIF4ENIF1* as near gene. **(B)** Venn diagram showing the common significant SNPs between FTD and ALS from the 9 traits in relation to the circulating lipid traits. The only genetic variant found in common is rs696825 that falls in the 3′UTR of the *HNRNPK* gene.

associated with a higher risk of FTLD TDP subtype. Interestingly, previous blood lipid measurements in observational studies found hypertriglyceridemia in patients with behavioral variant FTD (bvFTD) vs. healthy controls and patients with Alzheimer disease (AD) (Kim et al., 2018a,b). Similarly, in another observational study comparing circulating lipid levels in bvFTD, ALS, as well as mixed forms of ALS-FTD, higher TG, and lower HDL cholesterol levels were found in all the groups compared to healthy controls (Ahmed et al., 2017; Kim et al., 2018a). None of the other circulating lipids traits, including HDL cholesterol, was causally associated with FTD in our study. We corroborated the previous causal association of 1-SD genetically predicted higher levels of LDL with the increased risk of ALS (Bandres-Ciga et al., 2019; Zeng and Zhou, 2019), even though we used an updated data source for the LDL trait. We found a novel suggested causal association with ALS in relation to circulating fatty acids, such as linoleic acid and the omega-6 fatty acid levels. It is well known that altered lipidemia is a clinical phenotype in patients with ALS (Dupuis et al., 2008; Paganoni et al., 2011), although this is the first time it is shown that these fatty acids could be also causally associated. Again, it is interesting to observe that not all the circulating lipids influence the risk of FTLD TDP subtype and ALS in the same way. These differences support the idea that different exposures (risk factors) might define the clinical manifestation of diseases with TDP-43 pathology.

The RNA processing disruption is a well-documented pathological mechanism in ALS and FTD. It is very interesting to observe that the two SNPs identified in common between ALS and FTLD TDP subtype, in relation to body complexion and circulating lipid levels, fall under genes related to RNA processing functions. It is very remarkable that even though the significantly associated circulating lipid traits were different between FTD and ALS, we could identify a common significant genetic variant in the *HNRNPK* gene in both the diseases. This gene is widely expressed in neuronal tissue and encodes for the hnRNP K protein. Similar to TDP-43, which is also a family member of hnRNP proteins, this protein binds to RNA and has a role in RNA processing and maturation. This protein is altered in models of ALS with TDP43 mutation (Moujalled et al., 2017), and most recently, it has been found mislocalized in patients with FTLD (Bampton et al., 2021). Curiously, it has been shown that hnRNP K phosphorylation controls the aggregation of TDP-43 in the cytosol (Moujalled et al., 2017). These findings suggest that HNRNPK could be a potential molecular causal link between the lipid metabolic alterations and ALS/FTD spectrum of disorders. Similarly, *HNRNPA1*, another gene that encodes a hnRNP protein that forms a functional complex with hnRNP K, affects the splicing and regulation of *HMGCR* (3-hydroxy-3-methylglutaryl-Coenzyme A reductase), the rate-limiting enzyme in the biosynthesis of cholesterol, impacting the intracellular cholesterol metabolism (Yu et al., 2014). Even more, TDP-43 regulates the splicing of hnRNP A1 (Deshaies et al., 2018). Further clinical and functional studies are needed to corroborate the potential role of HNRNPK in lipid homeostasis and TDP-43 pathology and understand whether there is a causal relation between altered body lipid metabolism and RNA processing in FTD and ALS.

There are some limitations in this study. First, all the MR studies might be subjected to pleiotropy since it is difficult to rule out linear relations between the risk factors and the diseases we studied. Second, we used European ancestry population mainly for the GWAS data we selected to reduce population stratification bias, but this might be difficult with the extension of these results to other genetic background populations. Third, all MR results are dependent on the SNPs used as instrumental variables in the particular trait data. Those could be different or updated with time, and thus it could potentially have a different result when performing the analysis after actualizing the data at a different time. In this particular case, we could identify new association trends between linoleic acid and omega 6 fatty acid levels with the risk of ALS by using updated databases and comparing with previous analysis results (Bandres-Ciga et al., 2019; Zeng and Zhou, 2019) that found no association. In general, the number of IVs used in the analysis with ALS is larger than

those used in the analysis with FTD, partly due to the SNPs panels on each of the GWAS studies, which is more updated and extensive in the ALS GWAS (from 2018) than in the FTD GWAS study (from 2010), and also the sample size is much larger in the ALS GWAS (n = 80,610) compared to the FTD GWAS (n = 3,024). Therefore, all these parameters impact on the total number of SNPs detected that could then be used as IVs for the 2SMR analyses. Finally, here we limited the study to a specific FTLD subtype, and so the findings cannot be generalized to different clinical forms of FTLD. At the same time, this can also be perceived as a strength of the study since by performing the analysis with a particular FTLD type, we might be helping the identification of specific risk factors in the different subtypes, in this case the FTLD TDP subtype, supporting the stratification of patients and understanding in the clinic. Thus, the findings from the FTD with TDP-43 aggregates described in this study are very promising and opens the door for future analysis using new updated FTD GWAS databases, ideally with different FTLD forms GWAS datasets so that we could analyze the effect of all body lipid metabolic traits of interests in the different clinical forms of FTLD.

CONCLUSION

We found that genetic variants associated with circulating lipids and body composition are differentially involved in the risk of FTLD TDP subtype and ALS. In this regard, our study suggests that higher LDL cholesterol and fatty acid levels could potentially have a causal role in the risk of ALS, but further experimental and clinical studies are needed to confirm these findings. Conversely, for FTD, the prevention and intervention strategies could be aimed to lower circulating triglycerides levels. These differences support the idea that different exposures (risk factors) might define clinical manifestation of diseases within the spectrum. These findings emphasize the need to study lipid metabolism in these complex disorders, and for more research on the causal role of circulating lipids the possibility to modify them for prevention or treatment, or even use them in the stratification of patients. We also identified HNRNPK as a potential candidate that could serve as a link between circulating lipids and ALS/FTD with TDP-43 pathology. Extensive experimental research is needed to confirm these findings.

DATA AVAILABILITY STATEMENT

The original contributions presented in the study are included in the article/**Supplementary Material**, further inquiries can be directed to the corresponding author/s.

AUTHOR CONTRIBUTIONS

JM-G and SC: conceptualization and funding acquisition. NE-G, LF-B, JG-C, and JA: methodology. NE-G, LF-B, and JA: software, validation, formal analysis, and data curation. NE-G, LF-B, JM-C, JA, JM-G, and SC: writing—review and editing. JA, JM-G, and SC: supervision. All authors have read and agreed to the published version of the manuscript.

FUNDING

SC was supported by Consejería de Educación de la Comunidad de Madrid, through the Atracción de Talento Program (Grant No. "2018-T1/BMD-10731") and the Spanish Minister of Science, (Grant No. PID2020-1153-70RB-100). JM-G was supported by the Instituto de Salud Carlos III through the project INT20/00079 (co-funded by European Regional Development Fund "A way to make Europe").

ACKNOWLEDGMENTS

We thank all the people who have participated in all the genome association studies and all the studies that have made the data publicly available.

SUPPLEMENTARY MATERIAL

The Supplementary Material for this article can be found online at: https://www.frontiersin.org/articles/10.3389/fnagi.2022.838141/full#supplementary-material

REFERENCES

Ahmed, R. M., Highton-Williamson, E., Caga, J., Thornton, N., Ramsey, E., Zoing, M., et al. (2017). Lipid metabolism and survival across the frontotemporal dementia–amyotrophic lateral sclerosis spectrum: relationships to eating behavior and cognition. *J. Alzheimers Dis.* 61, 773–783. doi: 10.3233/JAD-170660

Ahmed, R. M., Landin-Romero, R., Liang, C. T., Keogh, J. M., Henning, E., Strikwerda-Brown, C., et al. (2019). Neural networks associated with body composition in frontotemporal dementia. *Ann. Clin. Transl. Neurol.* 6, 1707–1717. doi: 10.1002/acn3.50869

Ahmed, R. M., Mioshi, E., Caga, J., Shibata, M., Zoing, M., Bartley, L., et al. (2014). Body mass index delineates ALS from FTD: implications for metabolic health. *J. Neurol.* 261, 1774–1780. doi: 10.1007/s00415-014-7416-6

Bampton, A., Gatt, A., Humphrey, J., Cappelli, S., Bhattacharya, D., Foti, S., et al. (2021). HnRNP K mislocalisation is a novel protein pathology of frontotemporal lobar degeneration and ageing and leads to cryptic splicing. *Acta Neuropathol.* 142, 609–627. doi: 10.1007/s00401-021-02340-0

Bandres-Ciga, S., Noyce, A. J., Hemani, G., Nicolas, A., Calvo, A., Mora, G., et al. (2019). Shared polygenic risk and causal inferences in amyotrophic lateral sclerosis. *Ann. Neurol.* 85, 470–481. doi: 10.1002/ana.25431

Burg, T., Rossaert, E., Moisse, M., Van Damme, P., and Van Den Bosch, L. (2021). Histone deacetylase inhibition regulates lipid homeostasis in a mouse model of amyotrophic lateral sclerosis. *Int. J. Mol. Sci.* 22:11224. doi: 10.3390/ijms222011224

Burgess, S., Butterworth, A., and Thompson, S. G. (2013). Mendelian randomization analysis with multiple genetic variants using summarized data. *Genet. Epidemiol.* 37, 658–665. doi: 10.1002/gepi.21758

Coyle-Gilchrist, I. T. S., Dick, K. M., Patterson, K., Rodríquez, P. V., Wehmann, E., Wilcox, A., et al. (2016). Prevalence, characteristics, and survival of frontotemporal lobar degeneration syndromes. *Neurology* 86, 1736–1743. doi: 10.1212/WNL.0000000000002638

DeJesus-Hernandez, M., Mackenzie, I. R., Boeve, B. F., Boxer, A. L., Baker, M., Rutherford, N. J., et al. (2011). Expanded GGGGCC hexanucleotide repeat in noncoding region of C9ORF72 causes chromosome 9p–linked FTD and ALS. *Neuron* 72, 245–256. doi: 10.1016/j.neuron.2011.09.011

Deshaies, J. E., Shkreta, L., Moszczynski, A. J., Sidibé, H., Semmler, S., Fouillen, A., et al. (2018). TDP-43 regulates the alternative splicing of hnRNP A1 to yield an aggregation–prone variant in amyotrophic lateral sclerosis. *Brain* 141, 1320–1333.

Dupuis, L., Corcia, P., and Fergani, A. (2008). Gonzalez De aguilar JL, Bonnefont–Rousselot D, Bittar R, et al. Dyslipidemia is a protective factor in amyotrophic lateral sclerosis symbol. *Neurology* 70, 1004–1009. doi: 10.1212/01.wnl.0000285080.70324.27

Fernández-Beltrán, L. C., Godoy-Corchuelo, J. M., Losa-Fontangordo, M., Williams, D., Matias-Guiu, J., and Corrochano, S. (2021). A transcriptomic meta–analysis shows lipid metabolism dysregulation as an early pathological mechanism in the spinal cord of sod1 mice. *Int. J. Mol. Sci.* 22:9553. doi: 10.3390/ijms22179553

Ferrari, R., Kapogiannis, D., Huey, E. D., and Momeni, P. (2011). Huey E, Momeni P. FTD and ALS: a tale of two diseases. *Curr. Alzheimer Res.* 8, 273–294. doi: 10.2174/156720511795563700

Geser, F., Martinez-Lage, M., Robinson, J., Uryu, K., Neumann, M., Brandmeir, N. J., et al. (2009). Clinical and pathological continuum of multisystem TDP–43 proteinopathies. *Arch. Neurol.* 66, 180–189. doi: 10.1001/archneurol.2008.558

Hemani, G., Zheng, J., Elsworth, B., Wade, K. H., Haberland, V., Baird, D., et al. (2018). The MR–base platform supports systematic causal inference across the human phenome. *eLife* 7:e34408. doi: 10.7554/eLife.34408

Karch, C. M., Wen, N., Fan, C. C., Yokoyama, J. S., Kouri, N., Ross, O. A., et al. (2018). Selective genetic overlap between amyotrophic lateral sclerosis and diseases of the frontotemporal dementia spectrum. *JAMA Neurol.* 75, 860–875. doi: 10.1001/jamaneurol.2018.0372

Kiernan, M. C., Vucic, S., Cheah, B. C., Turner, M. R., Eisen, A., Hardiman, O., et al. (2011). Amyotrophic lateral sclerosis. *Lancet* 377, 942–955.

Kim, W. S., He, Y., Phan, K., Ahmed, R. M., Rye, K.-A., Piguet, O., et al. (2018a). Altered high density lipoprotein composition in behavioral variant frontotemporal dementia. *Front. Neurosci.* 12:847. doi: 10.3389/fnins.2018.00847

Kim, W. S., Jary, E., Pickford, R., He, Y., Ahmed, R. M., Piguet, O., et al. (2018b). Lipidomics analysis of behavioral variant frontotemporal dementia: a scope for biomarker development. *Front. Neurol.* 9:104. doi: 10.3389/fneur.2018.00104

Lee, H., Lee, J. J., Park, N. Y., Dubey, S. K., Kim, T., Ruan, K., et al. (2021). Multi–omic analysis of selectively vulnerable motor neuron subtypes implicates altered lipid metabolism in ALS. *Nat. Neurosci.* 24, 1673–1685. doi: 10.1038/s41593-021-00944-z

Liscic, R. M., Grinberg, L. T., Zidar, J., Gitcho, M. A., and Cairns, N. J. (2008). ALS and FTLD: two faces of TDP-43 proteinopathy. *Eur. J. Neurol.* 15, 772–780. doi: 10.1111/j.1468-1331.2008.02195.x

Manzoni, C., and Ferrari, R. (2021). Mendelian and sporadic FTD: disease risk and avenues from genetics to disease pathways through in silico modelling. *Adv. Exp. Med. Biol.* 1281, 283–296. doi: 10.1007/978-3-030-51140-1_17

Moujalled, D., Grubman, A., Acevedo, K., Yang, S., Ke, Y. D., Moujalled, D. M., et al. (2017). TDP-43 mutations causing amyotrophic lateral sclerosis are associated with altered expression of RNA–binding protein hnRNP K and affect the Nrf2 antioxidant pathway. *Hum. Mol. Genet.* 26, 1732–1746. doi: 10.1093/hmg/ddx093

Moujalled, D., James, J. L., Yang, S., Zhang, K., Duncan, C., Moujalled, D. M., et al. (2015). Phosphorylation of hnRNP K by cyclin–dependent kinase 2 controls cytosolic accumulation of TDP-43. *Hum. Mol. Genet.* 24, 1655–1669. doi: 10.1093/hmg/ddu578

Neumann, M., Sampathu, D. M., Kwong, L. K., Truax, A. C., Micsenyi, M. C., Chou, T. T., et al. (2006). Ubiquitinated TDP-43 in frontotemporal lobar degeneration and amyotrophic lateral sclerosis. *Science* 314, 130–133.

Nicolas, A., Kenna, K., Renton, A. E., Ticozzi, N., Faghri, F., Chia, R., et al. (2018). Genome–wide analyses identify KIF5A as a novel ALS gene. *Neuron* 97, 1268-1283.e6. doi: 10.1016/j.neuron.2018.02.027

Paganoni, S., Deng, J., Jaffa, M., Cudkowicz, M. E., and Wills, A. M. (2011). Body mass index, not dyslipidemia, is an independent predictor of survival in amyotrophic lateral sclerosis. *Muscle Nerve* 44, 20–24. doi: 10.1002/mus.22114

Raffaele, F., Claudia, M., and John, H. (2019). Genetics and molecular mechanisms of frontotemporal lobar degeneration: an update and future avenues. *Neurobiol. Aging* 78, 98–110. doi: 10.1016/j.neurobiolaging.2019.02.006

Seltman, R. E., and Matthews, B. R. (2012). Frontotemporal lobar degeneration: epidemiology, pathology, diagnosis and management. *CNS Drugs* 26, 841–870. doi: 10.2165/11640070-000000000-00000

Van Deerlin, V. M., Sleiman, P. M. A., Martinez-Lage, M., Chen-Plotkin, A., Wang, L. S., Graff-Radford, N. R., et al. (2010). Common variants at 7p21 are associated with frontotemporal lobar degeneration with TDP-43 inclusions. *Nat. Genet.* 42, 234–239. doi: 10.1038/ng.536

Xi, Z., Yunusova, Y., Van Blitterswijk, M., Dib, S., Ghani, M., Moreno, D., et al. (2014). Identical twins with the C9ORF72 repeat expansion are discordant for ALS. *Neurology* 83, 1476–1478. doi: 10.1212/WNL.0000000000000886

Yu, C. Y., Theusch, E., Lo, K., Mangravite, L. M., Naidoo, D., Kutilova, M., et al. (2014). HNRNPA1 regulates HMGCR alternative splicing and modulates cellular cholesterol metabolism. *Hum. Mol. Genet.* 23, 319–332. doi: 10.1093/hmg/ddt422

Zeng, P., and Zhou, X. (2019). Causal effects of blood lipids on amyotrophic lateral sclerosis: a mendelian randomization study. *Hum. Mol. Genet.* 28, 688–697. doi: 10.1093/hmg/ddy384

Zhang, L., Tang, L., Huang, T., and Fan, D. (2020). Life course adiposity and amyotrophic lateral sclerosis: a mendelian randomization study. *Ann. Neurol.* 87, 434–441.

Conflict of Interest: The authors declare that the research was conducted in the absence of any commercial or financial relationships that could be construed as a potential conflict of interest.

The reviewer RM declared a shared affiliation with one of the authors, JA to the handling editor at time of review.

Publisher's Note: All claims expressed in this article are solely those of the authors and do not necessarily represent those of their affiliated organizations, or those of the publisher, the editors and the reviewers. Any product that may be evaluated in this article, or claim that may be made by its manufacturer, is not guaranteed or endorsed by the publisher.

frontiers | Frontiers in Aging Neuroscience

ORIGINAL RESEARCH
published: 14 April 2022
doi: 10.3389/fnagi.2022.877281

Regional Homogeneity in Patients With Mild Cognitive Impairment: A Resting-State Functional Magnetic Resonance Imaging Study

*Yu-Qian Wu[1†], Yi-Ning Wang[1†], Li-Juan Zhang[1†], Li-Qi Liu[1], Yi-Cong Pan[1], Ting Su[2], Xu-Lin Liao[3], Hui-Ye Shu[1], Min Kang[1], Ping Ying[1], San-Hua Xu[1] and Yi Shao[1]**

[1] Department of Ophthalmology and Neurology, The First Affiliated Hospital of Nanchang University, Nanchang, China,
[2] Department of Ophthalmology, Massachusetts Eye and Ear, Harvard Medical School, Boston, MA, United States,
[3] Department of Ophthalmology and Visual Sciences, The Chinese University of Hong Kong, Sha Tin, Hong Kong SAR, China

OPEN ACCESS

Edited by:
Yuzhen Xu,
Tongji University, China

Reviewed by:
Guanghui Liu,
Fujian Provincial People's Hospital, China
Hua Wang,
Central South University, China

***Correspondence:**
Yi Shao
freebee99@163.com

[†] These authors have contributed equally to this work

Specialty section:
This article was submitted to Cellular and Molecular Mechanisms of Brain-aging, a section of the journal Frontiers in Aging Neuroscience

Received: 16 February 2022
Accepted: 22 March 2022
Published: 14 April 2022

Citation:
Wu Y-Q, Wang Y-N, Zhang L-J, Liu L-Q, Pan Y-C, Su T, Liao X-L, Shu H-Y, Kang M, Ying P, Xu S-H and Shao Y (2022) Regional Homogeneity in Patients With Mild Cognitive Impairment: A Resting-State Functional Magnetic Resonance Imaging Study. Front. Aging Neurosci. 14:877281. doi: 10.3389/fnagi.2022.877281

Objective: To analyze the potential changes in brain neural networks in resting state functional magnetic resonance imaging (rs-fMRI) scans by regional homogeneity (ReHo) in patients with mild cognitive impairment (MCI).

Methods: We recruited and selected 24 volunteers, including 12 patients (6 men and 6 women) with MCI and 12 healthy controls matched by age, sex, and lifestyle. All subjects were examined with rs-fMRI to evaluate changes in neural network connectivity, and the data were analyzed by ReHo method. Correlation analysis was used to investigate the relationship between ReHo values and clinical features in different brain regions of MCI patients. The severity of MCI was determined by the Mini-Mental State Examination (MMSE) scale.

Results: The signals of the right cerebellum areas 4 and 5, left superior temporal, right superior temporal, left fusiform, and left orbital middle frontal gyri in the patient group were significantly higher than those in the normal group ($P < 0.01$ by t-test of paired samples). The signal intensity of the right inferior temporal and left inferior temporal gyri was significantly lower than that of the normal group ($P < 0.01$). The ReHO value for the left inferior temporal gyrus correlated negatively with disease duration, and the value for the right inferior temporal gyrus correlated positively with MMSE scores.

Conclusion: Mild cognitive impairment in patients with pre- Alzheimer's disease may be related to the excitation and inhibition of neural networks in these regions. This may have a certain guiding significance for clinical diagnosis.

Keywords: rs-fMRI, mild cognitive impairment, ReHo, spontaneous brain activity, Alzheimer's disease

INTRODUCTION

Cognitive decline is common in older adults, including dementia, delirium, depression, language problems, inattention, and low literacy levels (D'Atri et al., 2021). Mild cognitive impairment (MCI) is an intermediate stage of cognitive decline between normal aging and dementia in which people have memory problems or other cognitive abnormalities but have not yet

reached the severity of dementia; therefore, the condition has little impact on daily living. MCI is common in the elderly, with a prevalence at age 65 of 6%. Because of the slow progression of the disease, a simple history and neurological examination alone are not enough to confirm the diagnosis. Studies have shown that 37–80% of dementia is not clinically diagnosed, suggesting that cognitive impairment is difficult to detect without screening tools (D'Atri et al., 2021). The most common cause of mild cognitive impairment is Alzheimer's disease (AD) (Yukimasa, 2017).

AD is a series of primary degenerative encephalopathies occurring in middle-aged and older adults (Yukimasa, 2017). The incidence of AD is closely related to several factors such as age, genetics, and environment that produce common pathological changes concerning metabolism, blood vessels, and inflammation (Yukimasa, 2010). In terms of metabolism, previous studies that explored the independent and reciprocal effects of curcumin on the brain and liver have shown that curcumin injection prior to Aβ deposition can prevent AD in APP/PS1 mice, suggesting that curcumin may significantly affect the elimination of Aβ42 in cerebral blood transport and peripheral circulation (Yepes, 2021). Cerebrovascular disease mainly presents symptoms of progressive memory loss, MCI, distraction, affective disorder, personality changes, and other characteristics. Alzheimer's disease often presents as a persistent disorder of high-level neural function (Wu et al., 2021). It has been reported that in APP/PS1 mice, a double transgenic mouse model of AD, female mice developed Aβ plaque load in the dentate gyrus layer at an early stage. There was also a significant neuroinflammatory activation of astrocytes and microglia (Jung et al., 2019). In addition, some studies have shown that magnetic resonance imaging (MRI)-based assessment of brain atrophy can be used to evaluate and stage Alzheimer's disease, which laid a foundation for the specific neuroimaging changes in the brain of our study (Bijttebier et al., 2021). Researchers have indicated that it is now possible to measure tau and amyloid beta (Aβ) protein in the brain. Analyses of the association among neuroimaging findings, clinical phenotype, and age were performed as a way to investigate how different neuroimaging modalities relate to disease mechanisms; hence, it is possible to elaborate on the specific cause of, as well as the course of, Alzheimer's disease (Benitez et al., 2021; Roberts et al., 2021).

Aβ has been shown to accumulate in the retina of patients with MCI, and this phenomenon may appear before accumulation in the brain (Mei et al., 2020). Detecting an accumulation of Aβ in the eye may prove to be a useful clinical method for early diagnosis of AD before the onset of clinical symptoms, but the relevant diagnostic approach needs to be further developed (**Figure 1**).

Despite these advances, there is still a lack of strong evidence that can be used as a basis for the clinical diagnosis of AD. MRI is a non-invasive diagnostic technique used in the medical and biomedical fields to evaluate nervous system structure and neurological function (Zang et al., 2004). Resting-state functional magnetic resonance imaging (rs-fMRI) allows measurements of brain activity at rest, and its use has evolved rapidly in recent years (Jiang et al., 2021). Regional homogeneity (ReHo) is a technique for analyzing rs-fMRI results that has been normally applied in clinical practice. Recent studies on the application of the ReHo method to analyze neuroimaging changes are shown in **Table 1** (Tononi et al., 1998; Xiang et al., 2018; Liao et al., 2019; Shao et al., 2019; Wen et al., 2019; Li et al., 2020; Guo et al., 2021). By calculating the Kendall coefficient consistency of voxel dynamic fluctuation time-series in a specific cluster, the local synchronization of spontaneous rs-fMRI signals is explored, which represents essential data for normal brain activity (Fang et al., 2021; Gaubert et al., 2021). Brain dysfunction in patients may lead to changes in synchronization of neurons in the brain, which adversely affects neural information processing, and thus reflects numerical differences from people with normal brain activity.

The severity of dementia can be determined based on the results of neuropsychological assessments. The commonly used clinical tool is the Mini-Mental State Examination (MMSE)

TABLE 1 | REHO method applied in neurogenic disease and ophthalmologic.

References	Years	Disease
Guo et al. (2021)	2019	Classical trigeminal neuralgia
Xiang et al. (2018)	2019	Retinal vein occlusion
Wen et al. (2019)	2019	Diabetic retinopathy
Li et al. (2020)	2019	Strabismus and amblyopia
Liao et al. (2019)	2021	Diabetic optic neuropathy
Shao et al. (2019)	2021	Thyroid-associated ophthalmopathy
Tononi et al. (1998)	2020	Parkinson

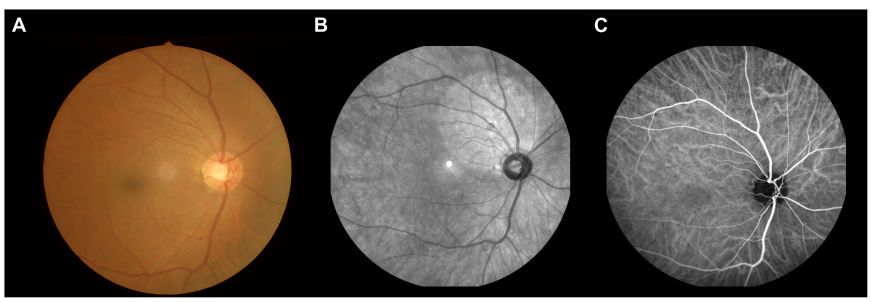

FIGURE 1 | An example of MCI. **(A)** Fundus photography; **(B)** fundus fluorescein angiography; **(C)** indocyanine green angiography. MCI, mild cognitive impairment.

TABLE 2 | Demographic characteristic of the enrolled subjects.

Condition	MCI	HC	*t*	*P*
Subject	12	12	NA	>0.99
Age (y)	64.33 ± 7.01	64.00 ± 6.18	0.124	0.595
Gender (M:F)	6:6	6:6	NA	NA
Duration (month)	12.00 ± 15.42	NA	4.766	<0.001*
SBP	128.92 ± 12.00	130.5 ± 10.83	–0.339	0.593
DBP	76.08 ± 12.15	76.17 ± 10.57	–0.018	0.593
HR	70.01 ± 9.16	70.42 ± 8.36	–0.091	0.922
Barthel index	99.58 ± 1.44	100	/	/
Best-corrected V A-left eye	0.29 ± 0.10	0.23 ± 0.06	1.967	0.164
Best-corrected V A-right eye	0.28 ± 0.12	0.21 ± 0.08	1.591	0.078
S100β	0.18 ± 0.09	2.71 ± 1.05	–8.327	<0.001*
MMSE	21.42 ± 4.56	27.83 ± 2.52	–4.266	0.125

**P < 0.05 Independent t-tests comparing two groups.*
MCI, mild cognitive impairment; HC, Healthy control; NA, not applicable; SBP, systolic blood pressure; DBP, diastolic blood pressure; HR, heart rate.

Scale (0–30 points; lower scores represent more severe cognitive impairment) (Cheng et al., 2019).

Receiver operating characteristics (ROC) curve analysis is a tool that can describe diagnostic accuracy in medical research, and the area under the curve (AUC) often serves as one of the criteria for comparison. A larger AUC implies a higher correlation, which in turn represents a higher diagnostic accuracy (Dong et al., 2021).

MATERIALS AND METHODS

Participants

A total of 24 volunteers were chosen for this study, including 12 patients (6 men and 6 women) with MCI and 12 healthy controls (HC) matched by age, gender, and lifestyle from the Ophthalmology Department of the First Affiliated Hospital of Nanchang University Hospital. The inclusion criteria for participants with MCI were as follows: (1) Age $\geq$ 45 years; (2) chief complaint of memory decline and MMSE $<$ 27 points; (3) Barthel index for ability to perform activities of daily living $\geq$ 90 points; and (4) recent cranial MRI suggesting no parenchymal brain lesions. The exclusion criteria for participants with MCI were the following: (1) vascular dementia, Parkinson dementia, frontotemporal lobar degeneration and other types of dementia, cognitive impairment due to other causes, acute cerebral hemorrhage, cerebral infarction, and intracranial space occupying lesions; (2) other psychiatric disorders, such as severe affective disorder or current evidence of depression; (3) visual and hearing impairment; and (4) severe dementia.

Inclusion criteria for the HC group were as follows: (1) Age $\geq$ 45 years; (2) routine brain MRI without obvious abnormalities; (3) no memory problems and an MMSE score $\geq$ 27 points; (4) no neurological, psychiatric, and cardiovascular diseases; (5) no drug or alcohol addiction; and (6) able to undergo MRI.

The medical ethics committee of the First Affiliated Hospital of Nanchang University approved all research methods which were in accordance with the 1964 Declaration of Helsinki and its later amendments or comparable ethical standards. The purpose, method, and potential risks of participating in the study were explained to all participants, and all participants signed an informed consent form.

Magnetic Resonance Imaging Parameters

All subjects were scanned with a 3-Tesla magnetic resonance scanner (Trio, Siemens, Munich, Germany). They were instructed to keep their eyes closed, but to remain awake and relaxed until the end of the scan. Using a three-dimensional spoiled gradient-recalled echo sequence in the MRI, relevant data was then obtained. Imaging parameters of the T1 and T2 sequences for 176 traverse images were as follows: TR = 1,900 ms, TE = 2.26 ms, thickness = 1.0 mm, gap = 0.5 mm, acquisition matrix = 256 × 56, field of view = 250 × 250 mm, and flip angle = 9°. Imaging parameters for 240 functional images were as follows: TR = 2,000 ms, TE = 30 ms, thickness = 4.0 mm, gap = 1.2 mm, acquisition matrix = 64 × 64, flip angle = 90°, field of view = 220 × 220 mm, and 29 axial. Scanning times were 5 and 10 min, respectively.

Data Analysis for Resting State Functional Magnetic Resonance Imaging

The MRIcro software[1] was used to organize the data, including classifying the data and deleting the incomplete data. Moreover, Statistical Parametric Mapping (SPM; The MathWorks, Inc.)[2] and the Data Processing Assistant for rs-fMRI software (DPARSFA; version 4.0; Institute of Psychology, Chinese Academy of Sciences)[3] were used to analyze the data. The regions of interest (ROI) in patients with MCI and HC were divided with the RESTing-state fMRI data analysis toolkit (REST). The echo planar imaging was used to standardize the rs-fMRI images,

[1]www.MRIcro.com
[2]http://www.fil.ion.ucl.ac.uk/spm
[3]http://rfmri.org/DPARSF

which met the spatial standards of the Montreal Institute of Neurology (MNI).

Participant 3 was excluded because his head movements were > 3 mm and the rest of his head movements were < 3 mm and well matched.

Statistical Analysis

We used SPSS software, version 22.0 (International Business Machines Corporation, Inc. (IBM), Armonk, New York, United States) in this study to analyze changes in brain neural signal fluctuations (i.e., ReHo values). Paired samples *t*-tests were used to test whether the two means were the same overall. In general, the larger the *t*-value, the more likely it is to be statistically relevant. We considered results significant if $P<0.05$. Multiple comparison correction used Gaussian Random Field (GRF) with a voxel level threshold of 0.005 and a cluster level threshold of 0.05 for two-sided tests. ROC curve analysis was used to compare the rs-fMRI values of the two groups. This represents

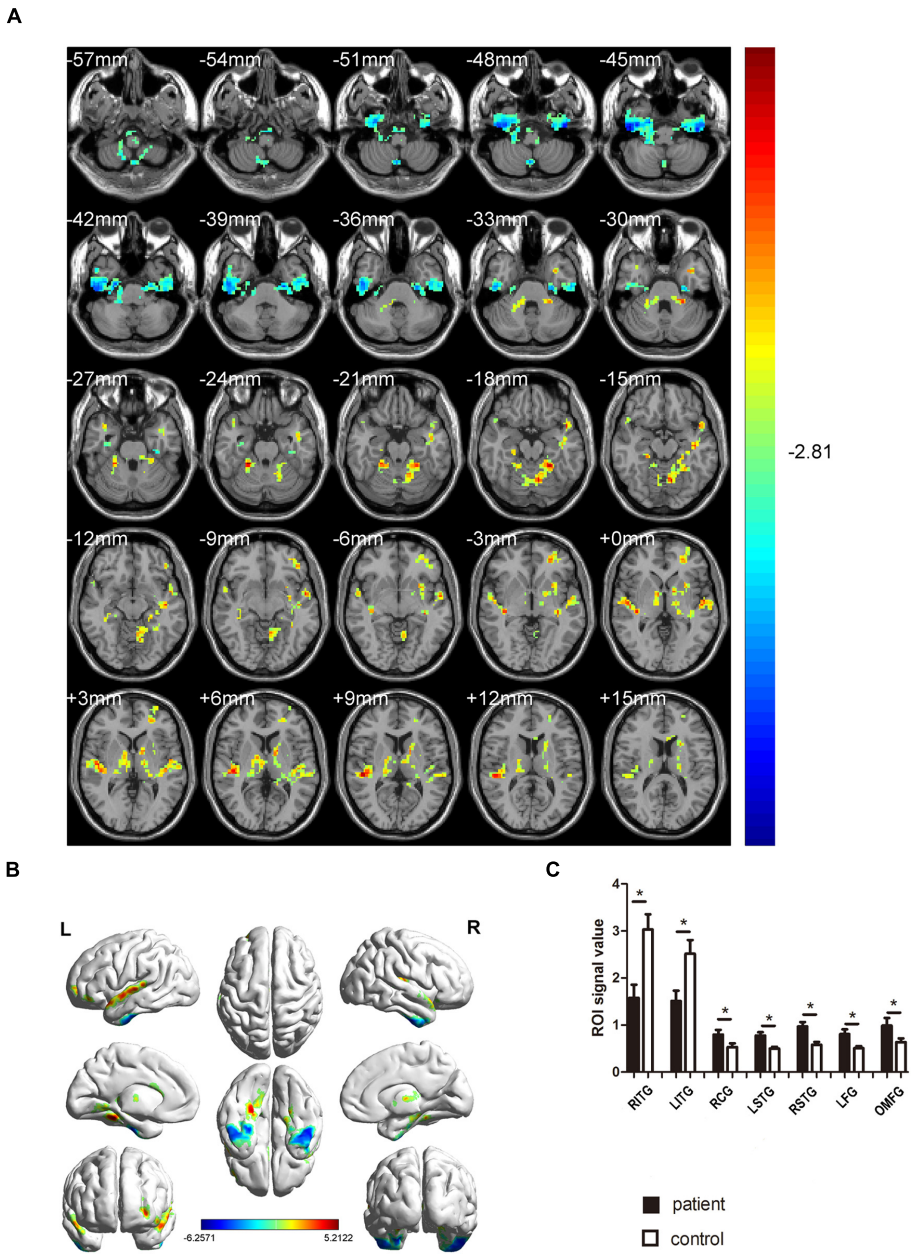

FIGURE 2 | Comparison of ReHo values in MCI and HC groups. **(A)** Differences in ReHo were found in RCG, LSTG, RSTG, LFG, and OMFG, RITG, and LITG. **(B)** The stereoscopic form of the cerebrum. The red area indicates an increase in ReHo value; the blue indicates a decrease in ReHo value. (GRF correction, the cluster-level: $P < 0.05$; two-tailed, with voxel level $P < 0.005$). **(C)** The Mean ReHo value between MCIs and control group. ReHo, regional homogeneity; MCI, mild cognitive impairment; HC, healthy controls. *$P < 0.05$ Independent t-tests comparing two groups.

how accurate rs-fMRI values are in the diagnosis of MCI. The AUC was of primary interest, and represents the diagnostic yield in this analysis. AUC > 0.9 was considered as a numerical value that represents high diagnostic accuracy.

Brain-Behavior Correlation Analysis

We collected clinical data from all study participants, including MMSE scores and disease duration, to find correlations between these data and the mean ReHo values of the different brain regions studied. Pearson correlation was analyzed with GraphPad Prism 8 software (GraphPad Inc., San Diego, CA, United States) to evaluate and graph the linear correlation between MMSE scores, duration of MCI and ReHo values.

RESULTS

Demographics

There was no significant difference in mean age between the MCI and HC groups (64.33 ± 7.01 and 64.00 ± 6.18 year, respectively; $P = 0.595$). There was no significant difference in the male to female ratio between the MCI and HC groups. The average MMSE scores of the MCI group was 21.42 ± 4.56 ($P = 0.125$). The average duration of the MCI was 12.00 ± 15.42 months ($P < 0.001$). A detailed summary of the data is presented in **Table 2**.

Regional Homogeneity Differences

In contrast with the HC group, the ReHo values of MCI patients for the right inferior temporal gyrus (RITG) and the left inferior gyrus (LITG) exhibited significantly lower in **Figures 2A,B** (blue) and **Table 3**. At the same time, the ReHo values of MCI patients were increased in the right cerebellar gyrus areas 4 and 5 (RCG), left superior temporal gyrus (LSTG), right superior temporal gyrus (RSTG), left fusiform gyrus (LFG), and left orbital middle frontal gyrus (OMFG) as shown in **Figures 2A,B** (red) and **Table 3** ($P < 0.01$, using GRF theory for multiple comparisons, $z > 2.3$, $P < 0.01$, cluster > 40 voxels, AlphaSim has been corrected).

Receiver Operating Characteristics Curve

Considering the abnormal activity of certain brain regions in MCI patients, we analyzed the diagnostic value of ReHo for MCI by ROC curve analysis. In this study, the AUC value was 1.000 ($P<0.0001$; 95% CI: 1.000–1.000) for LITG, RITG, LSTG, RSTG, LFG, and OMFG; meanwhile the AUC value was 0.985 ($P < 0.01$; 95% CI: 0.946–1.000) for RCG (**Figure 3**). These results show that ReHo values in these brain regions showed significant differences between patients with MCI and healthy controls.

Correlation Analysis

In patients with MCI, the ReHO value in LITG ($r^2 = 0.852$, $P < 0.001$) correlated negatively with disease duration, and the ReHO value in RITG ($r^2 = 0.879$, $P < 0.001$) correlated positively with the MMSE (**Figure 4**).

TABLE 3 | Brain areas with different ReHo values between MCIs and HCs.

Brain areas(aal)	MNI coordinates			BA	Number of voxels	*T*-value
	X	Y	Z			
HC > MCI						
RITG	48	–15	–45	–	114	–6.2571
LITG	–45	–15	–48	–	65	–5.4858
HC < MCI						
RCG	24	–39	–24	98	117	5.2122
LSTG	–54	–9	0	81	136	4.7359
RSTG	51	–27	9	82	125	4.9241
LFG	–24	–42	–18	55	312	4.8765
OMFG	–27	48	–3	–	121	4.2007

The statistical threshold was set at the voxel level with $P < 0.05$ for multiple comparisons using Gaussian Random Field theory ($z > 2.3$, $P < 0.01$, cluster > 40 voxels, AlphaSim corrected).

ReHo, regional homogeneity; BA, Brodmann area; HCs, healthy controls; MNI, Montreal Neurological Institute. RITG, the right inferior temporal gyrus; LITG, the right inferior temporal gyrus; RCG, the cerebellum superior; LSTG, the left superior temporal gyrus; RSTG, the right superior temporal gyrus; LFG, the left fusiform gyrus; OMFG, the left orbital middle frontal gyrus.

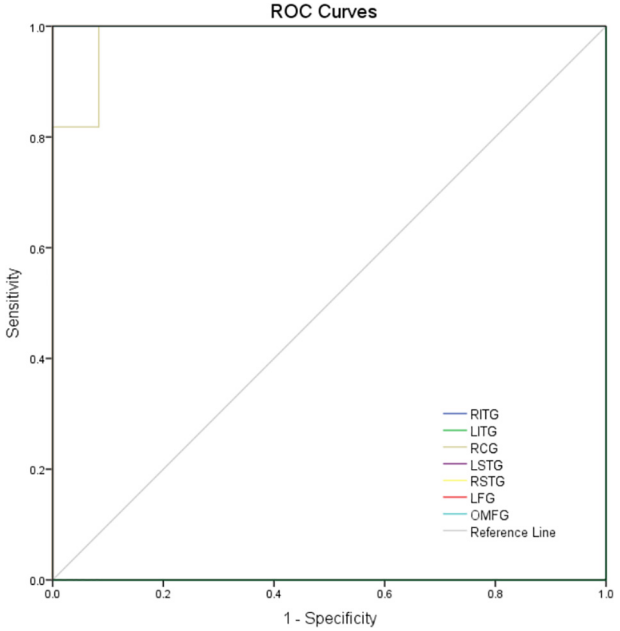

FIGURE 3 | ROC curve analysis of the mean ReHo values for altered brain regions. The area under the ROC curve were 1.000, ($p<0.0001$; 95% CI: 1.000–1.000) for LITG, RITG, LSTG, RSTG, LFG, and OMFG; 0.985 ($p < 0.01$; 95% CI: 0.946–1.000) for RCG. AUC, area under the curve; ROC, receiver operating characteristic.

DISCUSSION

The rs-fMRI provides insight into abnormal electrical activity in patients' brains during a disease state. In this study we use the ReHo method to measure abnormal activity in specific brain regions, and has been widely used in the diagnosis, treatment, and

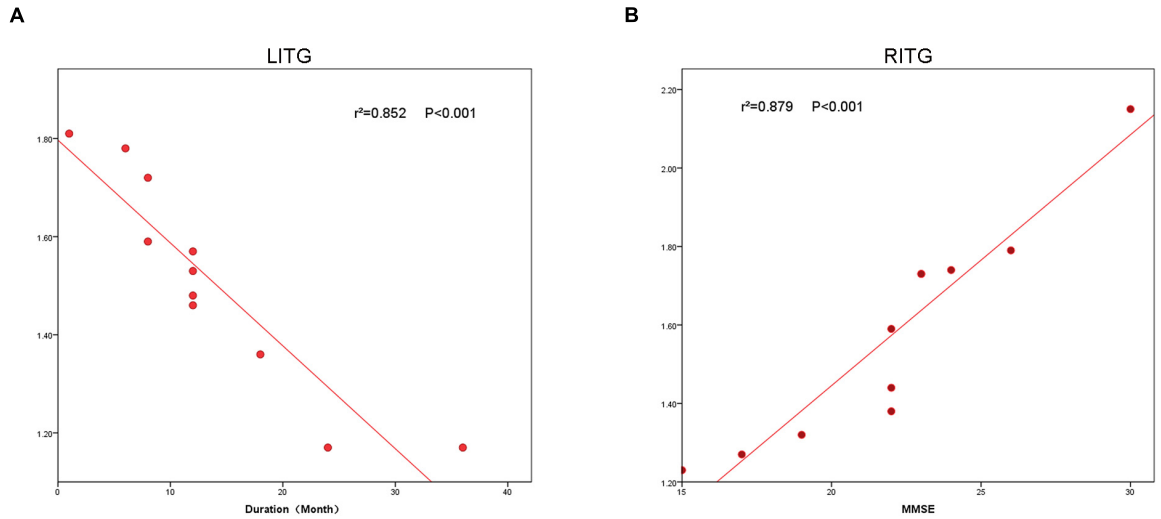

FIGURE 4 | The correlation between the ReHo value of LITG, RITG and the duration **(A),** and MMSE **(B)**. In the Alzheimer's disease group, the ReHo value of LITG showed a negative correlation with duration (r^2 = 0.852, P < 0.0001). The ReHo value of the RITG was positively correlated with MMSE (r^2 = 0.879, P < 0.0001). ReHo, regional homogeneity; MCI, mild cognitive impairment.

prognosis of various craniocerebral injuries, ophthalmic diseases, and related neurological diseases (Gu et al., 2022).

Hypointensity in the LITG area may be associated with auditory naming disorder in mild cognitive impairment; however, there are few specific functional studies on LITG (Takamura et al., 2021). Some studies found that activation of language networks and task-related functional connectivity exist in the left temporal lobe, and there was activation of the LITG area during auditory naming in the clinical naming experiment (Mitchell et al., 2020). In some studies, rs-fMRI values of individuals with cognitive decline due to sleep deprivation are represented in LITG, specifically by attenuated alterations in the effective connectivity of LITG with other brain regions (Lyu et al., 2021). Previous studies have shown that significant genetic overlap exists between hearing loss and AD, and that a polygenic risk score for AD can significantly predict hearing loss in an independent cohort, suggesting that there is a correlation between damage in this brain region and genetic risk, but the specific correlation remains to be further studied (Kang et al., 2021). In our study, we demonstrated that the MCI patients show decreased ReHo values in the LITG, which indicates auditory naming dysfunction. In addition, we found a negative correlation between the ReHo signal value of LITG and the duration of MCI; thus, the longer the duration of the disease, the lower the ReHo signal value of this brain region.

Some studies have shown that the RITG may be related to the consciousness of important emotional significance. Alfredson et al. (2010) studied the changes in temporal lobe blood flow in volunteers who listened to standard music vs. important emotional music. Measurements were made during silence, individually selected emotional music, and standard neutral music. The RITG showed a significant (p < 0.01) increase in regional cerebral blood flow (rCBF) when the emotional music was compared to silence. A temporal lobe asymmetry (right > left) during emotional music was also significant (p < 0.01) (Alfredson et al., 2010). In addition, another study demonstrated increased signal in the RITG and a positive correlation with alertness in patients with right temporal lobe epilepsy. The significant decrease in RITG signal found in this study for the MCI group may be related to the reduced response to important affective meanings seen in patients with MCI (Gellersen et al., 2021). This may be related to the abnormal mental behavior of AD patients; that is, positive mental symptoms such as agitation, anxiety, and mania as well as negative mental symptoms such as depression and indifference caused by cerebral cortex damage (**Figure 5**). Furthermore, the ReHo value of RITG showed a significant positive correlation

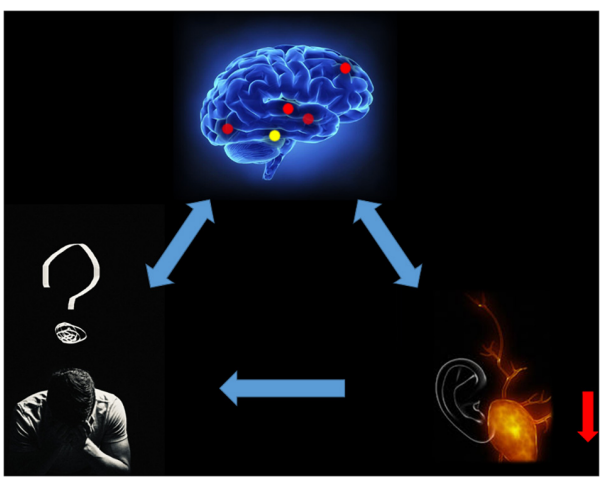

FIGURE 5 | Relationship between MRI images and clinical manifestations in MCI. MCI, mild cognitive impairment.

with the MMSE score of MCI patients, and data processing also showed a significant negative correlation between the signal intensity of this brain region and the length of the disease. This result implies that the ReHo value of RITG can be indirectly correlated with MMSE scores to determine the severity of MCI.

We speculate that ReHo values in patients with MCI decrease in RITG and LITG represented by the auditory naming and hearing loss, and important affective disorders may be associated with abnormal mental activity. Emotions such as agitation, mania or depression, apathy and hearing loss caused by decreased quality of life may also affect the degree of MCI (**Figure 6**).

The cerebellum in general has control over sensorimotor and vestibular components, and additionally influences cognitive, emotional, and autonomic function (Xu et al., 2021). A previous meta-analysis of cerebellar gray matter loss in normal aging and AD by Shah et al. (2013) found that gradient 3 (which captures lateralization differences in cognitive function) was significantly different in normal aging compared with AD, indicating slight functional differences between left and right cerebellar atrophy regions. The exact function of the RCG region is not fully understood; however, compared with the HCs, the ReHo value of this region was significantly increased in this study, which may be related to the changes in autonomic and cognitive function of MCI patients.

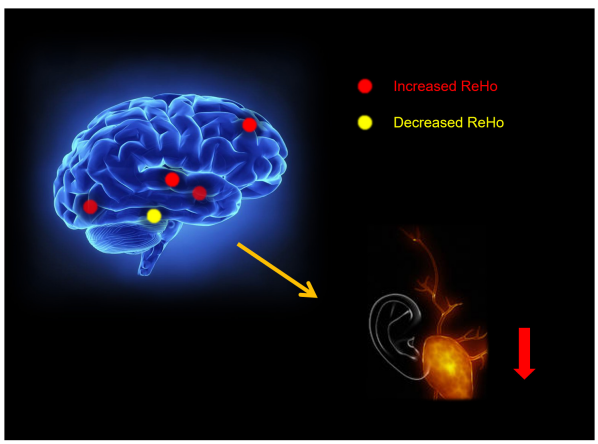

FIGURE 6 | The hearing loss results of brain activity.

A major function of the superior temporal gyrus is extracting meaningful linguistic features from speech inputs, and is strongly modulated by learning knowledge and perceived goals (Zhongwei et al., 2017). There is some evidence that the right STG functions in allocentric neglect deficits (Mao et al., 2021). The significantly lower signal in this region in the MCI group in the present study may be related to the altered perception of language in patients with MCI.

The fusiform gyrus may be associated with face processing, and the high signal expression in LFG found in this study may be associated with altered face processing ability in patients with MCI (Zuo et al., 2013). Gerłowska et al. (2021) stated that further research on facial expression patterns of the older adults can reduce misunderstandings and improve patients' quality of life. Therefore, we can speculate that stimulation targeting of these brain regions can significantly improve the facial expression patterns of AD patients and thus improve their quality of life.

There are few studies on the function of OMFG. Some studies suggest that the signal changes of OMFG are related to the changes in neurological function of patients with anxiety and depression. Previous studies have found that patients with severe anxiety and depression had significantly lower amplitude of low-frequency fluctuation values in the brain regions, means that the brain regions activity obviously changed (Zhao et al., 2019). In our study, the MCI patients ReHo values for the OMFG were significantly higher compared to HCs: thus, we hypothesize that it is possible to identify patients with complications of anxiety and depression by monitoring the changes in signal values in this brain region. However, we did not evaluate anxiety and depression scores for study participants that would allow us to prove a relationship between the degree of signal changes and the degree of anxiety and depression; thus, this association remains to be studied further. Please refer to **Table 4** for the changes of ReHo values in brain regions and their effects on brain function.

This study has some limitations. First of all, the different lengths of scanning time and the occurrence of multiple body movements during the rs-fMRI scanning process will produce different qualities of images in the scanning results; thus, there are avoidable errors in the obtained values. Reducing these individual differences may improve the specificity and accuracy of our analysis. Secondly, the sample size was small, and further and more accurate studies with a larger sample size

TABLE 4 | Brain areas alteration and its potential impact.

Brain areas	Experimental result	Function
Inferior temporal gyrus	HCs > MCIs	Related to cognitive learning and object memory, emotional processing
Fusiform gyri	HCs < MCIs	Face recognition,Secondary classification and recognition of objects
Superior temporal gyri	HCs < MCIs	Responsible for extracting meaningful linguistic features from speech inputs
Right cerebellum areas 4 and 5	HCs < MCIs	control over sensorimotor and vestibular components
Left orbital middle frontal gyri	HCs < MCIs	Related to the changes of neurological function in patients with anxiety and depression

HCs, healthy controls; MCI, mild cognitive impairment.

are needed to validate our findings. This may explain why we failed to find positive results in the process of verifying the correlation between the course of disease and MMSE score and the degree of signal value change for each brain region.

Our results showed that all MCI patients had varying degrees of increased or decreased abnormal electrical signals in rs-fMRI imaging of the brain regions we explored, which may reflect the pathogenesis of AD and identify potential risk factors. These ReHo values can be used to help clinicians diagnose and assess the severity of MCI.

CONCLUSION

This paper analyzed the alterations in ReHo of fMRI signals in a resting state. Alterations in the functional connectivity patterns of regions of interest and whole brain analyses were in turn analyzed to deduce the pathogenesis of MCI as well as disease progression. This may provide some diagnostic basis for clinical practice, as well as some significance for patient prognosis.

DATA AVAILABILITY STATEMENT

The raw data supporting the conclusions of this article will be made available by the authors, without undue reservation.

ETHICS STATEMENT

The studies involving human participants were reviewed and approved by the First Affiliated Hospital of Nanchang University. The patients/participants provided their written informed consent to participate in this study.

AUTHOR CONTRIBUTIONS

Y-QW, Y-NW, and L-JZ analyzed the data and draft the manuscript. L-QL, Y-CP, TS, and X-LL assisted with data interpretation and figure composing. H-YS, MK, PY, and S-HX collected the data. YS conceived, designed and directed the study, and final revised and approved the manuscript. All authors contributed to the article and approved the submitted version.

FUNDING

This work was supported by the National Natural Science Foundation (No. 82160195), the Central Government Guides Local Science and Technology Development Foundation (No. 20211ZDG02003), and the Key Research Foundation of Jiangxi Province (Nos. 20181BBG70004 and 20203BBG73059).

REFERENCES

Alfredson, B. B., Risberg, J., Hagberg, B., and Gustafson, L. (2010). Right temporal lobe activation when listening to emotionally significant music. *Appl. Neuropsychol.* 11, 161–166. doi: 10.1207/s15324826an1103_4

Benitez, D. P., Jiang, S., Wood, J., Wang, R., Hall, C. M., Peerboom, C., et al. (2021). Knock-in models related to Alzheimer's disease: synaptic transmission, plaques and the role of microglia. *Mol. Neurodegener.* 16:47. doi: 10.1186/s13024-021-00457-0

Bijttebier, S., Theunis, C., Jahouh, F., Martins, D. R., Verhemeldonck, M., Grauwen, K., et al. (2021). Development of immunoprecipitation – two-dimensional liquid chromatography – mass spectrometry methodology as biomarker read-out to quantify phosphorylated tau in cerebrospinal fluid from Alzheimer disease patients. *J. Chromatogr.* 1651:462299. doi: 10.1016/j.chroma.2021.462299

Cheng, J., Yang, H., and Zhang, J. (2019). Donepezil's effects on brain functions of patients with Alzheimer disease: a regional homogeneity study based on resting-state functional magnetic resonance imaging. *Clin. Neuropharmacol.* 42, 42–48. doi: 10.1097/WNF.0000000000000324

D'Atri, A., Scarpelli, S., Gorgoni, M., Truglia, I., Lauri, G., Cordone, S., et al. (2021). EEG alterations during wake and sleep in mild cognitive impairment and Alzheimer's disease. *iScience* 24:102386. doi: 10.1016/j.isci.2021.102386

Dong, W. J., Su, T., Li, C. Q., Shu, Y. Q., Shi, W. Q., Min, Y. L., et al. (2021). Altered brain network centrality in patients with retinal vein occlusion: a resting-state fMRI study. *Int. J. Ophthalmol.* 14, 1741–1747. doi: 10.18240/ijo.2021.11.14

Fang, M., Strand, K., Zhang, J., Totillo, M., Signorile, J. F., Galvin, J. E., et al. (2021). Retinal vessel density correlates with cognitive function in older adults. *Exp. Gerontol.* 152:111433. doi: 10.1016/j.exger.2021.111433

Gaubert, S., Houot, M., Raimondo, F., Ansart, M., Corsi, M. C., Naccache, L., et al. (2021). Machine learning approach to screen for preclinical Alzheimer's disease. *Neurobiol. Aging* 105, 205–216. doi: 10.1016/j.neurobiolaging.2021.04.024

Gellersen, H. M., Guell, X., and Sami, S. (2021). Differential vulnerability of the cerebellum in healthy ageing and Alzheimer's disease. *Neuroimage Clin.* 30:102605. doi: 10.1016/j.nicl.2021.102605

Gerłowska, J., Dmitruk, K., and Rejdak, K. (2021). Facial emotion mimicry in older adults with and without cognitive impairments due to Alzheimer's disease. *AIMS Neurosci.* 8, 226–238. doi: 10.3934/Neuroscience.2021012

Gu, X. Q., Liu, Y., Gu, J. B., Li, L. F., Fu, L. L., and Han, X. M. (2022). Correlations between hippocampal functional connectivity, structural changes, and clinical data in patients with relapsing-remitting multiple sclerosis: a case-control study using multimodal magnetic resonance imaging. *Neural Regen. Res.* 17, 1115–1124. doi: 10.4103/1673-5374.324855

Guo, G. Y., Zhang, L. J., Li, B., Liang, R. B., Ge, Q. M., Shu, H. Y., et al. (2021). Altered spontaneous brain activity in patients with diabetic optic neuropathy: a resting-state functional magnetic resonance imaging study using regional homogeneity. *World J. Diabetes* 12, 278–291. doi: 10.4239/wjd.v12.i3.278

Jiang, Y. P., Yang, Y. C., Tang, L. Y., Ge, Q. M., Shi, W. Q., Su, T., et al. (2021). Altered spontaneous brain activity patterns in dysthyroid optic neuropathy: a resting-state fMRI study. *J. Integr. Neurosci.* 20, 375–383. doi: 10.31083/j.jin2002037

Jung, F., Kazemifar, S., Bartha, R., and Rajakumar, N. (2019). Semiautomated assessment of the anterior cingulate cortex in Alzheimer's disease. *J. Neuroimaging* 29, 376–382. doi: 10.1111/jon.12598

Kang, D. W., Wang, S. M., Um, Y. H., Na, H. R., Kim, N. Y., Lee, C. U., et al. (2021). Distinctive association of the functional connectivity of the posterior cingulate cortex on memory performances in early and late amnestic mild cognitive impairment patients. *Front. Aging Neurosci.* 13:696735. doi: 10.3389/fnagi.2021.696735

Li, M. G., Liu, T. F., Zhang, T. H., Chen, Z. Y., Nie, B. B., Lou, X., et al. (2020). Alterations of regional homogeneity in Parkinson's disease with mild cognitive impairment: a prelimin ary resting-state fMRI study. *Neuroradiology* 62, 327–334. doi: 10.1007/s00234-019-02333-7

Liao, X. L., Yuan, Q., Shi, W. Q., Li, B., Su, T., Lin, Q., et al. (2019). Altered brain activity in patients with diabetic retinopathy using regional homogeneity: a resting-state FMRI Study. *Endocr. Pract.* 25, 320–327. doi: 10.4158/EP-2018-0517

Lyu, H., Jiao, J., Feng, G., Wang, X., Sun, B., Zhao, Z., et al. (2021). Abnormal causal connectivity of left superior temporal gyrus in drug-naïve first- episode adolescent-onset schizophrenia: a resting-state fMRI study. *Psychiatry Res. Neuroimaging* 315:111330. doi: 10.1016/j.pscychresns.2021.111330

Mao, Y., Liao, Z., Liu, X., Li, T., Hu, J., Le, D., et al. (2021). Disrupted balance of long and short-range functional connectivity density in Alzheimer's disease (AD) and mild cognitive impairment (MCI) patients: a resting-state fMRI study. *Ann. Transl. Med.* 9:65. doi: 10.21037/atm-20-7019

Mei, X., Yang, M., Zhu, L., Zhou, Q., Li, X., Chen, Z., et al. (2020). Retinal levels of amyloid beta correlate with cerebral levels of amyloid beta in young APPswe/PS1dE9 transgenic mice before onset of Alzheimer's disease. *Behav. Neurol.* 2020:1574816. doi: 10.1155/2020/1574816

Mitchell, B. L., Thorp, J. G., Evans, D. M., Nyholt, D. R., Martin, N. G., and Lupton, M. K. (2020). Exploring the genetic relationship between hearing impairment and Alzheimer's disease. *Alzheimers Dement.* 12:e12108. doi: 10.1002/dad2.12108

Roberts, S., Gardner, C., Jiang, Z., Abedi, A., Buser, Z., and Wang, J. C. (2021). Analysis of trends in lumbar disc degeneration using kinematic MRI. *Clin. Imaging* 79, 136–141. doi: 10.1016/j.clinimag.2021.04.028

Shah, P. P., Spaldo, N., Barrett, A. M., and Chen, P. (2013). Assessment and functional impact of allocentric neglect: a reminder from a case study. *Clin. Neuropsychol.* 27, 840–863. doi: 10.1080/13854046.2013.783120

Shao, Y., Li, Q. H., Li, B., Lin, Q., Su, T., Shi, W. Q., et al. (2019). Altered brain activity in patients with strabismus and amblyopia detected by analysis of regional homogeneity: a resting state functional magnetic resonance imaging study. *Mol. Med. Rep.* 19, 4832–4840. doi: 10.3892/mmr.2019.10147

Takamura, Y., Fujii, S., Ohmatsu, S., Ikuno, K., Tanaka, K., Manji, A., et al. (2021). Interaction between spatial neglect and attention deficit in patients with right hemisphere damage. *Cortex* 141, 331–346. doi: 10.1016/j.cortex.2021.03.036

Tononi, G., McIntosh, A. R., Russell, D. P., and Edelman, G. M. (1998). Functional clustering: identifying strongly interactive brain regions in neuroimaging data. *Neuroimage* 7, 133–149. doi: 10.1006/nimg.1997.0313

Wen, S. M., Min, Y. L., Yuan, Q., Li, B., Lin, Q., Zhu, P. W., et al. (2019). Altered spontaneous brain activity in retinal vein occlusion as determined by regional homogeneity: a resting-state fMRI study. *Acta Radiol.* 60, 1695–1702. doi: 10.1177/0284185119845089

Wu, X., Shen, Q., Zhang, Z., Zhang, D., Gu, Y., and Xing, D. (2021). Photoactivation of TGFβ/SMAD signaling pathway ameliorates adult hippocampal neurogenesis in Alzheimer's disease model. *Stem Cell Res. Ther.* 12:345. doi: 10.1186/s13287-021-02399-2

Xu, J., Dong, H., Li, N., Wang, Z., Guo, F., Wei, J., et al. (2021). Weighted RSA: an improved framework on the perception of audio-visual affective speech in left insula and superior temporal gyrus. *Neuroscience* 469, 46–58. doi: 10.1016/j.neuroscience.2021.06.002

Xiang, C. Q., Liu, W. F., Xu, Q. H., Su, T., Yong-Qiang, S., Min, Y. L., et al. (2018). Altered spontaneous brain activity in patients with classical trigeminal neuralgia using regional homogeneity: a resting-state functional MRI study. *Pain Pract.* 19, 397Ű406. doi: 10.1111/papr.12753

Yepes, M. (2021). The plasminogen activating system in the pathogenesis of Alzheimer's disease. *Neural Regen. Res.* 16, 1973–1977. doi: 10.4103/1673-5374.308076

Yukimasa, T. (2010). "10P-E-6 the relationship between fractal dimension of brain CT images and the scores on the MMSE in senile dementia of Alzheimer type preliminary report(room E international session)," in *Proceedings of the Annual Conference of Biomedical Fuzzy Systems Association*. doi: 10.24466/pacbfsa.23.0_341

Yukimasa, T. (2017). Fractal analysis of brain CT image in Senile dementia of Alzheimer type (new development of SOFT science in BMFSA2009-AMAMI). *Int. J. Biomed. Soft Comput. Hum. Sci.* 16, 81–86.

Zang, Y., Jiang, T., Lu, Y., He, Y., and Tian, L. (2004). Regional homogeneity approach to fMRI data analysis. *Neuroimage* 22, 394–400. doi: 10.1016/j.neuroimage.2003.12.030

Zhao, P., Yan, R., Wang, X., Geng, J., Chattun, M. R., Wang, Q., et al. (2019). Reduced resting state neural activity in the right orbital part of middle frontal gyrus in anxious depression. *Front. Psychiatry* 10:994. doi: 10.3389/fpsyt.2019.00994

Zhongwei, G., Xiaozheng, L., Jiapeng, L., Fuquan, W., Hongtao, H., Xingli, C., et al. (2017). Fractional amplitude of low-frequency fluctuations is disrupted in Alzheimer's disease with depression. *Clin. Neurophysiol.* 128, 1344—-1349. doi: 10.1016/j.clinph.2017.05.003

Zuo, X.-N., Xu, T., Jiang, L., Yang, Z., Cao, X. Y., He, Y., et al. (2013). Toward reliable characterization of functional homogeneity in the human brain: preprocessing, scan duration, imaging resolution and computational space. *Neuroimage* 65, 374–386. doi: 10.1016/j.neuroimage.2012.10.017

Conflict of Interest: The authors declare that the research was conducted in the absence of any commercial or financial relationships that could be construed as a potential conflict of interest.

Publisher's Note: All claims expressed in this article are solely those of the authors and do not necessarily represent those of their affiliated organizations, or those of the publisher, the editors and the reviewers. Any product that may be evaluated in this article, or claim that may be made by its manufacturer, is not guaranteed or endorsed by the publisher.

frontiers | Frontiers in Aging Neuroscience

MINI REVIEW
published: 14 April 2022
doi: 10.3389/fnagi.2022.849443

Associations of Polygenic Risk Score for Late-Onset Alzheimer's Disease With Biomarkers

Qiaojun Li[1], Xingping Lv[2], Fei Jin[3], Kun Liao[2], Liyuan Gao[2] and Jiayuan Xu[4]*

[1] School of Information Engineering, Tianjin University of Commerce, Tianjin, China, [2] School of Sciences, Tianjin University of Commerce, Tianjin, China, [3] Department of Molecular Imaging, Qingdao Central Hospital, Qingdao University, Qingdao, China, [4] Department of Radiology and Tianjin Key Laboratory of Functional Imaging, Tianjin Medical University General Hospital, Tianjin, China

Late-onset Alzheimer's disease (LOAD) is a common irreversible neurodegenerative disease with heterogeneous genetic characteristics. Identifying the biological biomarkers with the potential to predict the conversion from normal controls to LOAD is clinically important for early interventions of LOAD and clinical treatment. The polygenic risk score for LOAD (AD-PRS) has been reported the potential possibility for reliably identifying individuals with risk of developing LOAD recently. To investigate the external phenotype changes resulting from LOAD and the underlying etiology, we summarize the comprehensive associations of AD-PRS with multiple biomarkers, including neuroimaging, cerebrospinal fluid and plasma biomarkers, cardiovascular risk factors, cognitive behavior, and mental health. This systematic review helps improve the understanding of the biomarkers with potential predictive value for LOAD and further optimizing the prediction and accurate treatment of LOAD.

Keywords: late onset Alzheimer's disease, polygenic risk score, biomarker, prediction, brain

OPEN ACCESS

Edited by:
Panteleimon Giannakopoulos, Université de Genève, Switzerland

Reviewed by:
Keeley Brookes, Nottingham Trent University, United Kingdom
Anbupalam Thalamuthu, University of New South Wales, Australia

****Correspondence:***
Qiaojun Li
liqiaojun@tjcu.edu.cn

Specialty section:
This article was submitted to Alzheimer's Disease and Related Dementias, a section of the journal Frontiers in Aging Neuroscience

Received: *06 January 2022*
Accepted: *14 March 2022*
Published: *14 April 2022*

Citation:
Li Q, Lv X, Jin F, Liao K, Gao L and Xu J (2022) Associations of Polygenic Risk Score for Late-Onset Alzheimer's Disease With Biomarkers. Front. Aging Neurosci. 14:849443. doi: 10.3389/fnagi.2022.849443

INTRODUCTION

Alzheimer's disease (AD) which accounts for about 70% of dementia is an irreversible progressive polygenic neurodegenerative disease with insidious onset (Kametani and Hasegawa, 2018; Breijyeh and Karaman, 2020; Tank et al., 2022). By age at onset, AD can be classified into early-onset AD (EOAD) and late-onset AD (LOAD). EOAD is an autosomal dominant disease with heritability of more than 70% (Gatz et al., 2006; Wingo et al., 2012) and three responsible mutated genes, the amyloid protein precursor gene (*APP*), presenilin-1 gene (*PSEN1*), and presenilin-2 gene (*PSEN2*), were found to mainly dominate the production, aggregation, and clearance of amyloid β-protein (Aβ) (Cacace et al., 2016). Unlike the EOAD, LOAD occurs in more than 95% of the AD patients with a relatively complex polygenetic mechanism (Zhu et al., 2015; Xiao et al., 2017), and the related external phenotype changes in the very early stage. Although aducanumab can reduce the amyloid deposition in the brain and has been approved by Food and Drug Administration to treat Alzheimer's disease lately, however, controversy about it still exists (Selkoe, 2021; Servick, 2021). Therefore, identifying the biomarkers with the potential to predict the conversion from normal controls to LOAD and the progression of LOAD is clinically very important for early interventions.

In recent years, genome-wide association studies (GWAS) have been widely applied to study complex neuropsychiatric disorders (Ripke et al., 2014; Lello et al., 2019; van der Merwe et al., 2019; Levey et al., 2021; Peyrot and Price, 2021) and more than 200 susceptibility genetic variants have been identified to characterize the polygenetic architecture of LOAD (Chen et al., 2021). To overcome the small effect size of a single genetic variant, some polygenic methods have been developed to quantify the cumulative effects of multiple genetic variants related to complex diseases (Tan et al., 2018; Altmann et al., 2020; Choi et al., 2020), of which the polygenic risk score (PRS) is the most representative and widely used method (Wray et al., 2021). With the release of large-sample GWAS summary statistics for LOAD (Lambert et al., 2013; Weiner et al., 2015; Kunkle et al., 2019), AD-PRS, which measures the cumulative genome-wide-weighted effects of LOAD-risk genetic variants, is being increasingly used with multiple biomarkers to identify the underlying neurobiological mechanisms of LOAD.

In this review, we summarized the research progress of the associations of AD-PRS with multiple biomarkers, including neuroimaging, cerebrospinal fluid, and plasma, cardiovascular risk factors, cognitive behaviors, and mental health. This review is helpful to identify the biomarkers with the potential to predict the occurrence and development of LOAD, which is clinically important for the early diagnosis and interventions of this complex disease. A schematic summary of the related work in this review is shown in **Figure 1** and **Table 1**.

ASSOCIATIONS OF AD-PRS WITH NEUROIMAGING BIOMARKERS

Exploring the structural and functional changes through medical imaging techniques is crucial for understanding LOAD development. Because of the advantages of safety and information abundance, magnetic resonance imaging (MRI) has become prominent among various medical imaging techniques. Of the various modalities of MRI, structure MRI (sMRI), diffusion tensor MRI (dMRI), and functional MRI (fMRI) have been mostly applied to study the underlying neural mechanism of LOAD and its clinical diagnosis and treatment by exploring the correlation between AD-PRS and brain phenotypes.

sMRI is one of the most important avenues to illustrate the brain morphological measures, for example, gray matter volume, cortical surface area, and cortical thickness. Studies have found that AD-PRS was associated with reduced gray matter volume (GMV) in the hippocampus (Axelrud et al., 2018) and its subregions (Heidi et al., 2021), left precuneus and right cingulate gyrus cortex (Li et al., 2018), whereas with increased GMV in the right superior frontal gyrus and caudate (Li et al., 2018). Meanwhile, AD-PRS was found to be associated with decreased surface area in the frontal pole (Xiao et al., 2017), decreased cortical thickness in the bilateral medial temporal cortices (Lee et al., 2021), posterior cingulate cortices (Sabuncu et al., 2012), and bilateral entorhinal cortices (Harrison et al., 2016). The changes of these brain regions are some of the most prominent

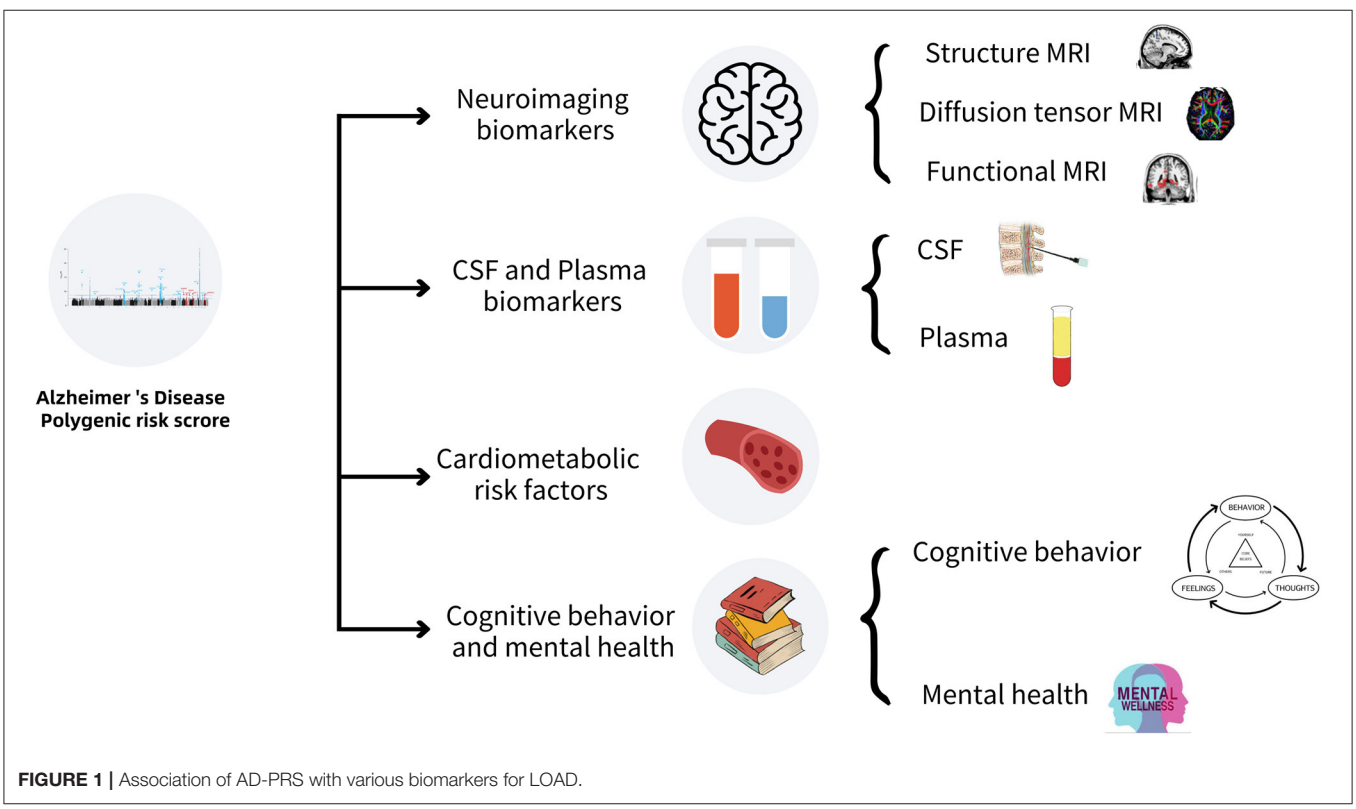

FIGURE 1 | Association of AD-PRS with various biomarkers for LOAD.

TABLE 1 | The work progress in the associations of AD-PRS with multiple biomarkers.

Biomarker	Subfields	Variables	References	Program for PRS	Base sample	Target sample	Correlation		Regression			MRI coordinate	
							r/R2	Sig.	β/OR	Sig.	95%CI	Coordinate [x,y,z]	Sig.
MRI	Structure MRI	GMV in hippocampus	Axelrud et al., 2018	PRSice	IGAP, $n = 74,046$	BHRC, $n = 716$			Left hippocampus: $\beta = -0.301$; right hippocampus: $\beta = -0.319$	-	Left hippocampus: [−0.434,−0.087]; right hippocampus: [−0.468,−0.072]		
		GMV in hippocampal subregions	Heidi et al., 2021	PRSice2	IGAP, $n = 74,046$	UKBB, $n = 17,161$			Left cornu ammonis: $\beta = -0.0209$; Right cornu ammonis: $\beta = -0.0112$	Left cornu ammonis: $p = -0.000629$; Right cornu ammonis: $p = 0.068324$			
		GMV in left precuneus	Li et al., 2018	PLINK	IGAP, $n = 74,046$	Recruited from society, $n = 683$						[−12, −51, 58.5]	$p < 0.05$
		GMV in right cingulate gyrus	Li et al., 2018	PLINK	IGAP, $n = 74,046$	Recruited from society, $n = 683$						[6, 3, 33]	$p < 0.05$
		GMV in right superior frontal gyrus	Li et al., 2018	PLINK	IGAP, $n = 74,046$	Recruited from society, $n = 683$						[6, 66, 1.5]	$p < 0.05$
		GMV in right caudate	Li et al., 2018	PLINK	IGAP, $n = 74,046$	Recruited from society, $n = 683$						[−1.5 ,4.5, 1.5]	$p < 0.05$
		CS in frontal pole	Xiao et al., 2017	PLINK	IGAP, $n = 74,046$	Recruited from society, $n = 231$			-	$p = 0.029$			
		CT in bilateral medial temporal cortex	Lee et al., 2021	PLINK	IGAP, $n = 54,162$	ADNI, $n = 217$	-	-					

(Continued)

TABLE 1 | Continued

Biomarker	Subfields	Variables	References	Program for PRS	Base Sample	Target sample	Correlation		Regression			MRI coordinate	
							r/R2	Sig.	β/OR	Sig.	95%CI	Coordinate [x,y,z]	Sig.
		CT in posterior cingulate cortex	Sabuncu et al., 2012	PLINK	ADNI, $n = 745$	ADNI, $n = 204$	$r = -0.27$	$p < 0.05$					
		CT in entorhinal cortex	Harrison et al., 2016	-	IGAP, $n = 74,046$	UCLA Longevity Center, $n = 45$	unweighted risk score: $r = -0.35$; weighted risk score: $r = -0.35$	unweighted risk score: $p = 0.009$; weighted risk score: $p = 0.009$					
	Diffusion tensor MRI	FA in the right cingulum bundle	Foley et al., 2017	PLINK	IGAP, $n = 54,162$	CUBRIC, $n = 272$	R2 = 0.032	$p = 0.009$					
		FA and MD in inferior occipito-frontal fascicle	Harrison et al., 2020a	-	-	-	-	-					
		FA and MD in superior longitudinal fascicle	Harrison et al., 2020a	-	-	-	-	-					
		FA and MD in cingulum	Harrison et al., 2020a	-	-	-	-	-					
		FA and MD in corpus callosum	Harrison et al., 2020a	-	-	-	-	-					
		MNS of visual subnetwork	Mirza-Davies et al., 2021	PLINK	IGAP, $n = 94,437$	ALSPAC, $n = 562$	$r = -0.19$	$p =$ 1.3E−5					

(Continued)

TABLE 1 | Continued

Biomarker	Subfields	Variables	References	Program for PRS	Base Sample	Target sample	Correlation		Regression			MRI coordinate	
							r/R2	Sig.	β/OR	Sig.	95%CI	Coordinate [x,y,z]	Sig.
	Functional MRI	FC between precuneus and superior temporal gyrus	Axelrud et al., 2019	PRSice	IGAP, $n = 74,046$	BHRC, $n = 636$			discovery sample: β = 0.180; replication sample: β = 0.202	discovery sample: p-adjusted = 0.036; replication sample: $p = 0.031$			
		FC within temporal cortex	Su et al., 2017	gPLINK	-	Recruited from hospital, $n = 218$			left middle temporal gyrus: β = −0.3	left middle temporal gyrus p<0.001			
		Activation in episodic memory processing network	Zhan et al., 2016	-	-	ADNI, $n = 68$						[5, 8, 11]	
		Activation in hippocampus	Chandler et al., 2020	PLINK	CTGLAB, $n =$ 455,258	YA-HCP, $n = 608$			β = 0.102	$p = 0.016$	[0.019, 0.186]		
		Activation in hippocampus ROI	Xiao et al., 2017	PLINK	IGAP, $n = 74,046$	Recruited from society, $n = 231$						Left hippocampal activition: [−39, −24, −15]; right hippocampal activition: [39, −21, 15]	Left hippocampal activition: p < 0.05; right hippocampal activition: p <0.05
		CBF in frontal regions	Chandler et al., 2019	PLINK	IGAP, $n = 74,046$	Recruited from society, $n =75$			β = −0.232	$p = 0.031$			
			Chandler et al., 2021	PRSice	IGAP, $n = 94,437$	ADNI, $n = 90$			β = −0.38	$p = 0.012$	[−0.68, −0.09]		

(Continued)

TABLE 1 | Continued

Biomarker	Subfields	Variables	References	Program for PRS	Base Sample	Target sample	Correlation		Regression			MRI coordinate	
							r/R2	Sig.	β/OR	Sig.	95%CI	Coordinate [x,y,z]	Sig.
CSF and plasma biomarkers	CSF	Aβ42	Skoog et al., 2021	PLINK	IGAP, $n = 94,437$	H70, $n = 303$	include APOE: $r = -0.4092$; exclude APOE:$r = -0.2789$	include APOE: $p = 0.0017$; exclude APOE: $p = 0.1285$					
		T-tau	Porter et al., 2018a	-	IGAP, $n = 74,046$	AIBL, $n = 643$	include APOE: $r = 0.1949$; exclude APOE: $r = 0.1787$	include APOE: $p = 0.1499$; exclude APOE: $p = 0.0348$					
		P-tau	Porter et al., 2018a	-	IGAP, $n = 74,046$	AIBL, $n = 643$	include APOE: $r = 0.1543$; exclude APOE: $r = 0.2044$	include APOE: $p = 0.2563$; exclude APOE: $p = 0.0719$					
		Ration of Aβ42/Aβ40	Li et al., 2020	PLINK	IGAP, $n = 74,046$	Recruited from hospital, $n = 925$	$r = -0.25$	$p < 0.001$					
	Plasma	Clusterin	Morgan et al., 2017	-	IGAP, $n = 74,046$	Recruited from society, $n = 93$	PRS: $r = 0.2$; Immune specific PRS: $r = 0.25$	PRS: $p = 0.05$; Immune specific PRS: $p = 0.02$					
		Complement receptor 1 inhibitor	Morgan et al., 2017	-	IGAP, $n = 74,046$	Recruited from society, $n = 93$	Immune specific PRS: $r = 0.22$	Immune specific PRS: $p = 0.05$					

(Continued)

TABLE 1 | Continued

Biomarker	Subfields	Variables	References	Program for PRS	Base Sample	Target sample	Correlation		Regression			MRI coordinate	
							r/R2	Sig.	β/OR	Sig.	95%CI	Coordinate [x,y,z]	Sig.
		C-reactive protein	Morgan et al., 2017	-	IGAP, $n = 74,046$	Recruited from society, $n = 93$	Immune specific PRS: $r = 0.16$	Immune specific PRS: $p = 0.13$					
		Osteopontin	Zhou et al., 2020	R	-	Recruited from hospital, $n = 829$			$\beta = 0.673$	$p = 5.95E{-}04$			
		Neurocan core protein	Zhou et al., 2020	R	-	Recruited from hospital, $n = 829$			$\beta = 0.411$	$p = 1.94E{-}03$			
		P-tau 181	Zettergren et al., 2021	-	IGAP, $n = 962$	ADNI, $n = 818$			include APOE: $\beta = 0.18 \sim 0.19$ exclude APOE: $\beta = 0.05 \sim 0.11$	include APOE: $p = 3E{-}18 \sim 7E{-}15$ exclude APOE: $p = 3E{-}4 \sim 0.03$			
		Diabetes	Richardson et al., 2019	-	-	UBKK , $n =$ 334,398	-	-					
		Diastolic blood pressure	Richardson et al., 2019	-	-	UBKK , $n =$ 334,398	-	-					
		Mid-life hypertension and obesity	Baumgart et al., 2015	-	-	-	-	-					
		Traumatic brain injury	Baumgart et al., 2015	-	-	-	-	-					
		Coronary heart disease	Elman et al., 2019	PLINK	IGAP, $n = 74,046$	VETSA, $n = 1,329$	-	-					

(Continued)

TABLE 1 | Continued

Biomarker	Subfields	Variables	References	Program for PRS	Base Sample	Target sample	Correlation		Regression			MRI coordinate	
							r/R2	Sig.	β/OR	Sig.	95%CI	Coordinate [x,y,z]	Sig.
		PRS of Coronary artery disease	Elman et al., 2019	PLINK	IGAP, $n = 74,046$	VETSA, $n = 1,329$			$OR = 1.38$	$p = 0.023$	[1.05, 1.83]		
		Height and weight	Korologou-Linden et al., 2019b	PLINK	IGAP, $n = 74,046$	ALSPAC, $n = 7,977$			height-adjusted fat mass: $\beta = 0.59\%$; height-adjusted lean mass: $\beta = 0.04$ kg		height-adjusted fat mass: [−0.92, 2.11]; height-adjusted lean mass: [−0.03, 0.11]		
		Triglyceride	Korologou-Linden et al., 2019b	PLINK	IGAP, $n = 74,046$	ALSPAC, $n = 7,977$	-	-					
		Insulin and C-reactive protein	Korologou-Linden et al., 2019b	PLINK	IGAP, $n = 74,046$	ALSPAC, $n = 7,977$	-	-					
Cognitive behavior and mental health	Cognitive behavior	Immediate memory	Marden et al., 2016	-	IGAP, $n = 74,046$	HRS, $n = 8,253$			non-Hispanic whites: $\beta = -0.058$; non-Hispanic blacks: $\beta = -0.050$		non-Hispanic whites: [−0.074,−0.043]; non-Hispanic blacks: [−0.106,0.006]		
		Verbal episodic memory	Porter et al., 2018b	R	-	AIBL, $n = 226$	include APOE: $r = -0.259$; exclude APOE: $r = -0.208$	include APOE: $p = 0.00003$; exclude APOE: $p = 0.004$					

(Continued)

TABLE 1 | Continued

Biomarker	Subfields	Variables	References	Program for PRS	Base Sample	Target sample	Correlation		Regression			MRI coordinate	
							r/R2	Sig.	β/OR	Sig.	95%CI	Coordinate [x,y,z]	Sig.
		General episodic memory	Li et al., 2018	PLINK	IGAP, $n = 74,046$	Recruited from society, $n = 683$			Working memory 2-back: β = −0.068; Working memory 3-back: β = −0.061	Working memory 2-back: $p = 0.196$; Working memory 3-back: $p = 0.249$			
		Total intelligence quotients	Korologou-Linden et al., 2019a	PLINK	IGAP, $n = 74,046$	ALSPAC, $n = 5,525$			β = −0.04	$p = 0.002$	[−0.07, −0.02]		
		Verbal intelligence quotients	Korologou-Linden et al., 2019a	PLINK	IGAP, $n = 74,046$	ALSPAC, $n = 5,525$			β = −0.04	$p = 0.003$	[−0.07, −0.01]		
		Performance intelligence quotients	Korologou-Linden et al., 2019a	PLINK	IGAP, $n = 74,046$	ALSPAC, $n = 5,525$			β = −0.03	$p = 0.012$	[−0.06, −0.01]		
		Economic behaviors	Shin et al., 2019	-	IGAP, $n = 74,046$	HRS, n =2936			hands-on assets: β = −0.3558; hands-off assets: β = 0.1114	hands-on assets: $p < 0.001$; hands-off assets: $p > 0.05$			
			Ajnakina et al., 2020	PRSice	IGAP, $n = 74,046$	ELSA, n =7039			intermediate wealth: β = −0.13; low wealth: β = −0.21	intermediate wealth: $p = 0.03$; low wealth: $p < 0.001$	intermediate wealth: [−0.24, −0.01]; low wealth: [−0.30, −0.07]		
	Mental health	Delusions	Creese et al., 2019	PRSice	PGC, $n =$ 150,034	ADNI, $n = 3,111$			β = 1.18	$p = 0.001$	[1.06, 1.3]		

(Continued)

TABLE 1 | Continued

Biomarker	Subfields	Variables	References	Program for PRS	Base Sample	Target sample	Correlation		Regression			MRI coordinate	
							r/R2	Sig.	β/OR	Sig.	95%CI	Coordinate [x,y,z]	Sig.
		Schizophrenia	Creese et al., 2019	PRSice	PGC, *n* = 150,034	ADNI, *n* = 3,111			Psychosis wide: *OR* = 1.14; Psychosis narrow: *OR* = 1.16	Psychosis wide: *p* = 0.003; Psychosis narrow: *p* = 0.002	Psychosis wide: [1.05, 1.23]; Psychosis narrow: [1.06, 1.28]		
		Hallucinations	Kusters et al., 2020	PRSice	IGAP, *n* = 74,046	PEG, *n* = 281; PW, *n* = 118			*OR* = 1.37		[1.03, 1.83]		
			Creese et al., 2019	PRSice	PGC, *n* = 150,034	ADNI, *n* = 3,111	-	-					
		Neuroticism	Duberstein et al., 2011	-	-	GEM, *n* = 767			*OR* = 1.36		[1.08, 1.71]		
			Terracciano and Sutin, 2019	-	-	-	-	-					
		Major depression disorder	Xu et al., 2018	PRSice	PGC *n* = 150,034; IGAP *n* = 74,046	ADNI, *n* = 322	-	-					

ADNI, Alzheimer's Disease Neuroimaging Initiative; AIBL, Australian Imaging, Biomarkers and Lifestyle study; ALSPAC, Avon Longitudinal Study of Parents and Children; Aβ, amyloid β-protein; BHRC, Brazilian High Risk Study for Psychiatric Disorders; CBF, cerebral blood flow; CS, cortical surface; CSF, cerebrospinal fluid; CT, cortical thickness; CTGLAB, Complex Ttait Genetics Lab; CUBRIC, Cardiff University; Brain Research Imaging Centre; dMRI, diffusion tensor MRI; ELSA, English Longitudinal Study of Aging; FA, fractional anisotropy; FC, functional connectivity; GEM, Details of the Ginkgo Evaluation of Memory study; GMV, gray matter volume; H70, Gothenburg H70 Birth Cohort Studies; HRS, Health and Retirement Study; IGAP, International Genomics of Alzheimer's Project; MD, mean diffusivity; MNS, mean nodal strength; PEG, The Parkinson's Environment and Gene study; PGC, Psychiatric Genomics Consortium; PRS, polygenic risk score; P-tau, phosphorylated tau; PW, Norwegian ParkWest study; ROI, region of interest; sMRI, structure MRI; T-tau, total tau; UBKK, UK Biobank; UCLA Longevity Center, University of California of Los Angeles Longevity Center; VETSA, Vietnam Era Twin Study of Aging; YA-HCP, Young Human Connectome Project; - , indicates that the information is not mentioned in the original text.

early pathological features of LOAD and can be used as reliable predictive measures for the conversion from normal controls or mild-cognitive impairment to LOAD (Yang et al., 2012).

dMRI is mainly used to measure the microstructural integrity of the white matter through modeling-water diffusivity in the tissue microstructure (Kilimann et al., 2013), with fractional anisotropy (FA) and mean diffusivity as the two most used indices. AD-PRS is associated with decreased FA in the right cingulum bundle in healthy adults (Foley et al., 2017). AD-PRS was also found to be associated with reduced FA and increased mean diffusivity across the whole brain white matter tracts, notably in the inferior occipitofrontal fascicle, superior longitudinal fascicle, cingulum and corpus callosum in the AD patients (Harrison et al., 2020a). Recently, Mirza-Davies et al. (2021) found the visual subnetwork constructed based on dMRI was also correlated with AD-PRS.

fMRI was used to evaluate brain activity by detecting changes associated with blood flow (Smitha et al., 2017), referred to as the blood-oxygen-level-dependent (BOLD) signal in the brain-resting or task-based state. AD-PRS was found to be associated with increased functional connectivity between the right precuneus and the right superior temporal gyrus in the youths, which might impact memory performance and inhibitory control in early life (Axelrud et al., 2019). AD-PRS was also found to be associated with decreased functional connectivity within the temporal cortex in mild-cognitive impairment patients (Su et al., 2017). The hippocampal activation, mostly responsible for episodic memory processing, was severely impaired in the LOAD patients (Zhan et al., 2016; Xiao et al., 2017). However, contrary research findings have been reported between the AD-PRS and hippocampal activation. Chandler et al. (2020) found a significantly positive correlation and Xiao et al. (2017) found a significantly negative correlation during the episodic memory. This divergence may be due to the different task codings and sample size of the studies.

Arterial spin labeling was a functional MRI technology for measuring tissue perfusion to quantify the cerebral blood flow (CBF) in a given period with high time resolution (Rostami et al., 2014). There is a hypothesis proposing that insufficient CBF increases the risk of developing LOAD, leads to the decline of consciousness and dysfunction of LOAD, and even can be treated as an early antecedent of LOAD (Chandler et al., 2021). AD-PRS was found to be negatively correlated with CBF on many brain regions across the younger and older participants, including the frontal pole, middle frontal gyrus, inferior frontal gyrus, insular, frontal medial cortex, and orbitofrontal cortex (Chandler et al., 2019, 2021). These studies may shed light on exploring the key molecular processes that underpin LOAD.

All of the above findings together revealed the close relationship between the cumulative genetic risk of LOAD and the changes in the brain structure and function, providing new perspectives to explain the pathophysiology of LOAD. The combination of the neuroimaging biomarkers with AD-PRS to predict the LOAD development is attracting attention (Harrison et al., 2016, 2020b; Williams et al., 2021) and this is thought to be a promising step toward improving the very early identification of LOAD (Williams et al., 2021).

ASSOCIATIONS OF AD-PRS WITH CEREBROSPINAL FLUID AND PLASMA BIOMARKERS

The concentration determination of Aβ, total tau (T-tau), and phosphorylated tau (P-tau) in the cerebrospinal fluid (CSF) are three classical biomarkers for the clinical diagnosis of LOAD (Lee et al., 2019; Shen et al., 2021). The changes of these measures in the brain occur more than 15 years before the onset of symptoms in LOAD patients (Bateman et al., 2012; Dementia, 2021). More studies devoted to the association analysis of AD-PRS and these biomarkers found that AD-PRS was not only correlated with the CSF levels of Aβ42, Aβ42/Aβ40, T-tau, and P-tau in the older adults (Porter et al., 2018a; Li et al., 2020), but could also predict the incidence rate of LOAD and the age at onset (Li et al., 2020). In addition, there was an interaction between AD-PRS and the Aβ42 pathology status to the neurofilament light (NfL) (Skoog et al., 2021). Moreover, the A/T/N criteria including a combined accumulation of amyloid plaques (A), neurofibrillary tangles composed of tau (T), and neurodegeneration (N) can predict the cognitive decline and clinical progression of LOAD (Soldan et al., 2019; Ebenau et al., 2020) and are recommended to be included in the diagnostic categories of LOAD (Foley et al., 2017). AD-PRS also showed a significant correlation with the A/T/N profiles (Ebenau et al., 2021). A study found that the integration of genetic risk across the AD biomarkers like A/T/N may improve the prediction of the disease progression (Moore et al., 2019).

Various inflammations occur in pathologically vulnerable brain regions in LOAD patients (Akiyama, 2000) and many plasma biomarkers of inflammation are useful for early diagnosis and monitoring the progression of LOAD (Kinney et al., 2018; Naveed et al., 2019). AD-PRS was found to be associated with various increased inflammatory biomarkers in the plasma, such as clusterin, complement receptor 1 inhibitor and C-reactive protein (Morgan et al., 2017), osteopontin and neurocan core protein (Zhou et al., 2020), and P-tau 181 (Zettergren et al., 2021). Similar to other biomarkers, the integration of AD-PRS and inflammatory biomarkers can also greatly improve the sensitivity and specificity of predicting LOAD. These findings not only facilitate the development of genetic tools for assessing the individual risk of LOAD but could also improve our understanding of the underlying mechanisms of this disease.

ASSOCIATIONS OF AD-PRS WITH CARDIOMETABOLIC RISK FACTORS

Many cardiometabolic risk factors are implicated in the etiology of LOAD and are thought to lie on the pathways linking the genetic variants of LOAD (Korologou-Linden et al., 2019b). Of these factors, cardiovascular risk factors are found to increase the incidence of LOAD (Lin et al., 2019), which may be due to the high genetic association between LOAD and many cardiovascular diseases, such as hypertension (Baumgart et al., 2015), coronary heart disease (Elman et al., 2019), diabetes, and diastolic blood pressure (Richardson et al., 2019). AD-PRS was

also found positively associated with other cardiometabolic risk factors such as traumatic brain injury, obesity, and hypertension in adults (Baumgart et al., 2015). However, these associations are not consistent throughout the whole life trajectory. For example, Korologou-linden et al. did not detect evidence to suggest that AD-PRS acts through childhood and adolescent cardiometabolic risk factors (Korologou-Linden et al., 2019b). More studies should be conducted in other large-birth cohorts to examine whether the genetic risk for Alzheimer's disease can be captured in early childhood. If not, further studies should examine whether and why these associations emerge only later, in adulthood, when the variation in the cardiometabolic risk factors is likely to be greater.

The combination of the genetic accumulation risk of LOAD and some vascular risk factors increased the predictive potential of LOAD for the shared genetic heritage (Li et al., 2016). The coronary artery disease (CAD) interacting with the LOAD pathology is highly heritable and CAD-PRS has been widely used to improve cardiovascular risk prediction (Wehby et al., 2018; Elliott et al., 2020; Levin and Rader, 2020). A healthy adult group with higher CAD-PRS and AD-PRS showed a significantly increased risk of developing amnestic mild-cognitive impairment (aMCI) (Elman et al., 2019), which is a state of cognitive deficit that is not severe enough to fulfill the criteria of dementia (Bennett et al., 2002) and showed a much higher probability of developing into LOAD (Chaudhury et al., 2019). In summary, AD-PRS, combined with the PRS of cardiovascular risk factors, has shown a superior predictive value of onset of aMCI and LOAD compared to the independent application of AD-PRS, indicating the importance of infusing multiple PRSs and their interactions.

ASSOCIATION OF AD-PRS WITH COGNITIVE BEHAVIORS AND MENTAL HEALTH

The impairment of episodic memory and decline in advanced cognitive functions are the earliest and most characteristically clinical manifestations of LOAD (Bäckman et al., 2004). In the early stage, cognitive behaviors and mental health of the LOAD patients are partially impaired, which complicate and intertwine with the occurrence and progression of LOAD. Exploring the association between AD-PRS and cognitive functions has aroused many important findings. For example, AD-PRS was reported to be associated with lower total, verbal, and performance intelligence quotients in childhood and adolescence (Korologou-Linden et al., 2019a), whereas no significant associations were identified in the cognitively normal adult individuals (Li et al., 2018). Moreover, increasing studies showed that AD-PRS had a significant negative correlation with immediate memory and verbal episodic memory, which increases the predictive efficiency of conversion from healthy controls to LOAD (Marden et al., 2016; Porter et al., 2018b). It is worth noting that, in a study of Chinese samples, a significant correlation between AD-PRS and episodic memory ability was not found (Li et al., 2018). The inconsistency may be caused by ethnic differences or the evaluation efficiency of different memory scales.

AD-PRS was found to be closely associated with economic behaviors. Individuals with different levels of AD-PRS showed different saving behaviors and wealth composition (Shin et al., 2019), for instance, individuals with higher AD-PRS are more likely to hold less wealth in the Individual Retirement Accounts and to have simpler managed assets, such as fixed deposits, whereas individuals with lower AD-PRS have more complex managed assets, such as stocks (Shin et al., 2019). In addition, it was suggested that the interaction between higher AD-PRS and lower wealth levels would lead to the early-onset age of LOAD and accelerate its development (Ajnakina et al., 2020).

Mental health is also a vital risk factor affecting the onset and progression of LOAD, and up to 50% of LOAD patients have psychosis symptoms, such as hallucinations and delusions (Creese et al., 2019). Studies have shown that AD-PRS is positively correlated with neuroticism (Duberstein et al., 2011; Terracciano and Sutin, 2019) and hallucinations (Kusters et al., 2020). The association between AD-PRS and cognition was also mediated by these two personality traits (Stephan et al., 2018). Further, a combination between AD-PRS and major depression disorder-PRS has been used to study LOAD and their integration would significantly increase the ability to predict conversion from aMCI to LOAD (Xu et al., 2018). The above results indicated that LOAD shared a highly genetic association with mental health disorders.

OPPORTUNITIES AND CHALLENGES FOR AD-PRS APPLICATIONS

AD-PRS has been widely used in many different research fields and has exhibited a huge ability in the prediction of LOAD. However, there was large heterogeneity in AD-PRS considering the huge variations in the calculation pipeline (Choi et al., 2020).

First, the selection of a certain P_T threshold from the GWAS summary statistics of the discovery sample was quite important for building PRS in the target sample, because it determined how many SNPs were included for calculation. In the classic AD-PRS calculation method, only those SNPs less than a predefined P_T threshold were included (Axelrud et al., 2018). Recently, the optimal P_T threshold method was applied widely, in which a series of AD-PRS were typically calculated over a range of thresholds, and the associations between the target trait and each AD-PRS were calculated to find out the best prediction model with the underlying P_T threshold accordingly was set as the optimized P_T threshold in the calculation of PRS (Choi et al., 2020). Second, after identifying the P_T threshold, the calculation strategies of PRS in the target sample also varied. The simple AD-PRS only calculates the number of risk alleles assuming that all SNPs have the same effect on the disease. More commonly, an odds-ratio-weighted PRS was calculated for each individual as the sum of the count of risk alleles multiplied by the corresponding effect sizes across these SNPs. Third, the quality of the base sample and target sample including ethnicity, sample size, and the number of genetic variants used has a great impact on the

AD-PRS and will exert the findings. To date, no consensus has been reached about these points and various strategies have been adopted by researchers, which of course will hamper the utility of the AD-PRS for a clinical diagnosis.

Besides the above points, another important question is whether the APOE-*ε4* should be included for calculating AD-PRS, which is the largest risk factor for LOAD (Kim et al., 2009). At present, the accuracy of predicting the risk of LOAD by using the PRS method is 84% (Escott-Price et al., 2015, 2017). However, by far, the *APOE-ε4* allele (risk) and the *APOE-ε2* allele (protective) contributed the largest to this risk, where the predictive accuracy could reach 0.68 (*APOE-ε4*) and 0.69 (*APOE-ε4*+*APOE-ε2*) in the clinical samples (Escott-Price et al., 2015). An important practical and theoretical consideration is to understand how good AD-PRS is when excluding the *APOE-ε4* gene risk and no consensus has been reached so far. Thus, associations of the AD-PRS with multiple biomarkers adjusting for *APOE* locus or not need to be tested.

It should be noted that, although some limitations about AD-PRS still need to be addressed, the advanced development of large-GWAS studies and data-sharing policies are driving the AD-PRS to be constantly optimized and updated for drawing unambiguous conclusions about LOAD. For example, many researchers have identified that AD-PRS was associated with lower hippocampal volume in different target samples using different $P_T$when using the publicly available International Genomics of Alzheimer's Project (IGAP) as the base sample (Mormino et al., 2016; Axelrud et al., 2018; Heidi et al., 2021; Tank et al., 2022). The underlying reason may be that the base sample from IGAP or UK Biobank is very large which can reduce the deviation caused by a small sample, and also offer the same risk alleles for the AD-PRS calculation which makes the most important risk alleles always included.

In the future, more studies considering the causal inference between AD-PRS, biomarkers, and LOAD occurrence are needed to infer the underlying mechanism of LOAD. Moreover, the application of AD-PRS would also be critical for drug discovery, as drugs targeting proteins encoded in genetic risk loci would be more likely to be successful in phases II and III clinical trials (King et al., 2019). Thus, AD-PRS have a greater utility in biomedical research and personalized precision medicine in the future.

AUTHOR CONTRIBUTIONS

QL, XL, and JX contributed to conception and design of the study. QL and XL wrote the first draft of the manuscript. JX wrote sections of the manuscript. All authors contributed to manuscript revision, read, and approved the submitted version.

FUNDING

This work was supported by the National Natural Science Foundation of China (grant no. 81801687), Science & Technology Development Fund of Tianjin Education Commission for Higher Education (grant no. 2019KJ195), and Open Research Project of The Beijing Key Laboratory of High Dynamic Navigation Technology under grant no. HDN2020102.

REFERENCES

Ajnakina, O., Cadar, D., and Steptoe, A. (2020). Interplay between socioeconomic markers and polygenic predisposition on timing of dementia diagnosis. *J. Am. Geriatr. Soc.* 68, 1529–1536. doi: 10.1111/jgs.16406

Akiyama, H. (2000). Inflammation and Alzheimer's disease. *Neurobiol. Aging* 21, 383–421. doi: 10.1016/S0197-4580(00)00124-X

Altmann, A., Scelsi, M. A., Shoai, M., de Silva, E., Aksman, L. M., Cash, D. M., et al. (2020). A comprehensive analysis of methods for assessing polygenic burden on Alzheimer's disease pathology and risk beyond APOE. *Brain Commun.* 2, fcz047. doi: 10.1093/BRAINCOMMS/FCZ047

Axelrud, L. K., Santoro, M. L., Pine, D. S., Talarico, F., Gadelha, A., Manfro, G. G., et al. (2018). Polygenic risk score for Alzheimer's disease: implications for memory performance and hippocampal volumes in early life. *Am. J. Psychiatry* 175, 555–563. doi: 10.1176/appi.ajp.2017.17050529

Axelrud, L. K., Sato, J. R., Santoro, M. L., Talarico, F., Pine, D. S., Rohde, L. A., et al. (2019). Genetic risk for Alzheimer's disease and functional brain connectivity in children and adolescents. *Neurobiol. Aging* 82, 10–17. doi: 10.1016/j.neurobiolaging.2019.06.011

Bäckman, L., Jones, S., Berger, A. K., Laukka, E. J., and Small, B. J. (2004). Multiple cognitive deficits during the transition to Alzheimer's disease. *J. Intern. Med.* 256, 195–204. doi: 10.1111/j.1365-2796.2004.01386.x

Bateman, R. J., Xiong, C., Benzinger, T. L. S., Fagan, A. M., Goate, A., Fox, N. C., et al. (2012). Clinical and biomarker changes in dominantly inherited Alzheimer's disease. *N. Engl. J. Med.* 367, 795–804. doi: 10.1056/NEJMoa1202753

Baumgart, M., Snyder, H. M., Carrillo, M. C., Fazio, S., Kim, H., and Johns, H. (2015). Summary of the evidence on modifiable risk factors for cognitive decline and dementia: a population-based perspective. *Alzheimers. Dement.* 11, 718–726. doi: 10.1016/j.jalz.2015.05.016

Bennett, D. A., Wilson, R. S., Schneider, J. A., Evans, D. A., Beckett, L. A., Aggarwal, N. T., et al. (2002). Natural history of mild cognitive impairment in older persons. *Neurology* 59, 198–205. doi: 10.1212/WNL.59.2.198

Breijyeh, Z., and Karaman, R. (2020). Comprehensive review on Alzheimer's disease: causes and treatment. *Molecules* 25, 5789. doi: 10.3390/molecules25245789

Cacace, R., Sleegers, K., and Van Broeckhoven, C. (2016). Molecular genetics of early-onset Alzheimer's disease revisited. *Alzheimers Dement.* 12, 733–748. doi: 10.1016/J.JALZ.2016.01.012

Chandler, H. L., Hodgetts, C. J., Caseras, X., Murphy, K., and Lancaster, T. M. (2020). Polygenic risk for Alzheimer's disease shapes hippocampal scene-selectivity. *Neuropsychopharmacology* 45, 1171–1178. doi: 10.1038/s41386-019-0595-1

Chandler, H. L., Wise, R. G., Linden, D. E., Williams, J., Murphy, K., Lancaster, T. M., et al. (2021). Alzheimer's genetic risk effects on cerebral blood flow are spatially consistent and proximal to gene expression across the lifespan. *bioRxiv*. doi: 10.1101/2020.12.31.424949

Chandler, H. L., Wise, R. G., Murphy, K., Tansey, K. E., Linden, D. E. J., and Lancaster, T. M. (2019). Polygenic impact of common genetic risk loci for Alzheimer's disease on cerebral blood flow in young individuals. *Sci. Rep.* 9, 467. doi: 10.1038/s41598-018-36820-3

Chaudhury, S., Brookes, K. J., Patel, T., Fallows, A., Guetta-Baranes, T., Turton, J. C., et al. (2019). Alzheimer's disease polygenic risk score as a predictor of conversion from mild-cognitive impairment. *Transl. Psychiatry* 9, 154. doi: 10.1038/s41398-019-0485-7

Chen, H.-H., Petty, L. E., Sha, J., Zhao, Y., Kuzma, A., Valladares, O., et al. (2021). Genetically regulated expression in late-onset Alzheimer's disease

implicates risk genes within known and novel loci. *Transl. Psychiatry* 11, 618. doi: 10.1038/s41398-021-01677-0

Choi, S. W., Mak, T. S.-H., and O'Reilly, P. F. (2020). Tutorial: a guide to performing polygenic risk score analyses. *Nat. Protoc.* 15, 2759–2772. doi: 10.1038/s41596-020-0353-1

Creese, B., Vassos, E., Bergh, S., Athanasiu, L., Johar, I., Rongve, A., et al. (2019). Examining the association between genetic liability for schizophrenia and psychotic symptoms in Alzheimer's disease. *Transl. Psychiatry* 9, 273. doi: 10.1038/s41398-019-0592-5

Dementia, A., (2021) Alzheimer's disease facts and figures. *Alzheimers Dement.* 17, 327–406. doi: 10.1002/alz.12328

Duberstein, P. R., Chapman, B. P., Tindle, H. A., Sink, K. M., Bamonti, P., Robbins, J., et al. (2011). Personality and risk for Alzheimer's disease in adults 72 years of age and older: a 6-year follow-up. *Psychol. Aging* 26, 351–362. doi: 10.1037/a0021377

Ebenau, J. L., Lee, S. J., Hulsman, M., Tesi, N., Jansen, I. E., Verberk, I. M. W., et al. (2021). Risk of dementia in APOE ε4 carriers is mitigated by a polygenic risk score. *Alzheimers Dement.* 13, 1–9. doi: 10.1002/dad2.12229

Ebenau, J. L., Timmers, T., Wesselman, L. M. P., Verberk, I. M. W., Verfaillie, S. C. J., Slot, R. E. R., et al. (2020). ATN classification and clinical progression in subjective cognitive decline. *Neurology* 95, e46–e58. doi: 10.1212/WNL.0000000000009724

Elliott, J., Bodinier, B., Bond, T. A., Chadeau-Hyam, M., Evangelou, E., Moons, K. G. M., et al. (2020). Predictive accuracy of a polygenic risk score–enhanced prediction model vs a clinical risk score for coronary artery disease. *JAMA* 323, 636. doi: 10.1001/jama.2019.22241

Elman, J. A., Panizzon, M. S., Logue, M. W., Gillespie, N. A., Neale, M. C., Reynolds, C. A., et al. (2019). Genetic risk for coronary heart disease alters the influence of Alzheimer's genetic risk on mild cognitive impairment. *Neurobiol. Aging* 84, 237.e5–237.e12. doi: 10.1016/j.neurobiolaging.2019.06.001

Escott-Price, V., Myers, A. J., Huentelman, M., and Hardy, J. (2017). Polygenic risk score analysis of pathologically confirmed Alzheimer disease. *Ann. Neurol.* 82, 311–314. doi: 10.1002/ana.24999

Escott-Price, V., Sims, R., Bannister, C., Harold, D., Vronskaya, M., Majounie, E., et al. (2015). Common polygenic variation enhances risk prediction for Alzheimer's disease. *Brain* 138, 3673–3684. doi: 10.1093/brain/awv268

Foley, S. F., Tansey, K. E., Caseras, X., Lancaster, T., Bracht, T., Parker, G., et al. (2017). Multimodal brain imaging reveals structural differences in Alzheimer's disease polygenic risk carriers: a study in healthy young adults. *Biol. Psychiatry* 81, 154–161. doi: 10.1016/j.biopsych.2016.02.033

Gatz, M., Reynolds, C. A., Fratiglioni, L., Johansson, B., Mortimer, J. A., Berg, S., et al. (2006). Role of genes and environments for explaining Alzheimer disease. *Arch. Gen. Psychiatry* 63, 168. doi: 10.1001/archpsyc.63.2.168

Harrison, J. R., Bhatia, S., Tan, Z. X., Mirza-Davies, A., Benkert, H., Tax, C. M. W., et al. (2020a). Imaging Alzheimer's genetic risk using diffusion MRI: a systematic review. *Neuroimage Clin.* 27, 102359. doi: 10.1016/j.nicl.2020.102359

Harrison, J. R., Mistry, S., Muskett, N., and Escott-Price, V. (2020b). From polygenic scores to precision medicine in Alzheimer's disease: a systematic review. *J. Alzheimer's Dis.* 74, 1271–1283. doi: 10.3233/JAD-191233

Harrison, T. M., Mahmood, Z., Lau, E. P., Karacozoff, A. M., Burggren, A. C., Small, G. W., et al. (2016). An Alzheimer's disease genetic risk score predicts longitudinal thinning of hippocampal complex subregions in healthy older adults. *eNeuro* 3, ENEURO.0098-16. doi: 10.1523/ENEURO.0098-16.2016

Heidi, T. A., Jiang, J., Koch, F., and Mather, K. A., Wen, W., et al. (2021). Associations between Alzheimer's disease polygenic risk scores and hippocampal subfield volumes in 17,161 UK Biobank participants. *Neurobiol. Aging* 98, 108–115. doi: 10.1016/j.neurobiolaging.2020.11.002

Kametani, F., and Hasegawa, M. (2018). Reconsideration of amyloid hypothesis and tau hypothesis in Alzheimer's disease. *Front. Neurosci.* 12, 25. doi: 10.3389/FNINS.2018.00025

Kilimann, I., Likitjaroen, Y., Hampel, H., and Teipel, S. (2013). Diffusion tensor imaging to determine effects of antidementive treatment on cerebral structural connectivity in Alzheimer's disease. *Curr. Pharm. Des.* 19, 6416–6425. doi: 10.2174/1381612811319360003

Kim, J., Basak, J. M., and Holtzman, D. M. (2009). The role of apolipoprotein E in Alzheimer's disease. *Neuron* 63, 287–303. doi: 10.1016/j.neuron.2009.06.026

King, E. A., Davis, J. W., and Degner, J. F. (2019). Are drug targets with genetic support twice as likely to be approved? Revised estimates of the impact of genetic support for drug mechanisms on the probability of drug approval. *PLoS Genet.* 15, e1008489. doi: 10.1371/journal.pgen.1008489

Kinney, J. W., Bemiller, S. M., Murtishaw, A. S., Leisgang, A. M., Salazar, A. M., and Lamb, B. T. (2018). Inflammation as a central mechanism in Alzheimer's disease. *Alzheimer's Dement. Transl. Res. Clin. Interv.* 4, 575–590. doi: 10.1016/j.trci.2018.06.014

Korologou-Linden, R., Anderson, E. L., Jones, H. J., Davey Smith, G., Howe, L. D., and Stergiakouli, E. (2019a). Polygenic risk scores for Alzheimer's disease, and academic achievement, cognitive and behavioural measures in children from the general population. *Int. J. Epidemiol.* 48, 1972–1980. doi: 10.1093/ije/dyz080

Korologou-Linden, R., O'Keeffe, L., Howe, L. D., Davey-Smith, G., Jones, H. J., Anderson, E. L., et al. (2019b). Polygenic risk score for Alzheimer's disease and trajectories of cardiometabolic risk factors in children. *Wellcome Open Res.* 4, 125. doi: 10.12688/wellcomeopenres.15359.1

Kunkle, B. W., Grenier-Boley, B., Sims, R., Bis, J. C., Damotte, V., Naj, A. C., et al. (2019). Genetic meta-analysis of diagnosed Alzheimer's disease identifies new risk loci and implicates Aβ, tau, immunity and lipid processing. *Nat. Genet.* 51, 414–430. doi: 10.1038/s41588-019-0358-2

Kusters, C. D. J., Paul, K. C., Folle, A. D., Keener, A. M., Bronstein, J. M., Dobricic, V., et al. (2020). Genetic risk scores and hallucinations in patients with Parkinson disease. *Neurol. Genet.* 6, e492. doi: 10.1212/NXG.0000000000000492

Lambert, J.-C., Ibrahim-Verbaas, C. A., Harold, D., Naj, A. C., Sims, R., Bellenguez, C., et al. (2013). Meta-analysis of 74,046 individuals identifies 11 new susceptibility loci for Alzheimer's disease. *Nat. Genet.* 45, 1452–1458. doi: 10.1038/ng.2802

Lee, J. C., Kim, S. J., Hong, S., and Kim, Y. S. (2019). Diagnosis of Alzheimer's disease utilizing amyloid and tau as fluid biomarkers. *Exp. Mol. Med.* 51, 1–10. doi: 10.1038/s12276-019-0250-2

Lee, Y., Jeon, S., Kang, S. W., Park, M., Baik, K., Yoo, H. S., et al. (2021). Interaction of CSF α-synuclein and amyloid beta in cognition and cortical atrophy. *Alzheimer's Dement.* 13, 1–12. doi: 10.1002/dad2.12177

Lello, L., Raben, T. G., Yong, S. Y., Tellier, L. C. A. M., and Hsu, S. D. H. (2019). Genomic prediction of 16 complex disease risks including heart attack, diabetes, breast and prostate cancer. *Sci. Rep.* 9, 15286. doi: 10.1038/s41598-019-51258-x

Levey, D. F., Stein, M. B., Wendt, F. R., Pathak, G. A., Zhou, H., Aslan, M., et al. (2021). Bi-ancestral depression GWAS in the Million Veteran Program and meta-analysis in andgt;1.2 million individuals highlight new therapeutic directions. *Nat. Neurosci.* 24, 954–963. doi: 10.1038/s41593-021-00860-2

Levin, M. G., and Rader, D. J. (2020). Polygenic risk scores and coronary artery disease. *Circulation* 141, 637–640. doi: 10.1161/CIRCULATIONAHA.119.044770

Li, J., Zhang, X., Li, A., Liu, S., Qin, W., Yu, C., et al. (2018). Polygenic risk for Alzheimer's disease influences precuneal volume in two independent general populations. *Neurobiol. Aging* 64, 116–122. doi: 10.1016/j.neurobiolaging.2017.12.022

Li, J.-Q. Q., Tan, L. L., Wang, H.-F. F., Tan, M.-S. S., Tan, L. L., Xu, W., et al. (2016). Risk factors for predicting progression from mild cognitive impairment to Alzheimer's disease: a systematic review and meta-analysis of cohort studies. *J. Neurol. Neurosurg. Psychiatry* 87, 476–484. doi: 10.1136/jnnp-2014-310095

Li, W.-W., Wang, Z., Fan, D.-Y., Shen, Y.-Y., Chen, D.-W., Li, H.-Y., et al. (2020). Association of polygenic risk score with age at onset and cerebrospinal fluid biomarkers of Alzheimer's disease in a Chinese cohort. *Neurosci. Bull.* 36, 696–704. doi: 10.1007/s12264-020-00469-8

Lin, Y., Smith, A. V., Aspelund, T., Betensky, R. A., Smoller, J. W., Gudnason, V., et al. (2019). Genetic overlap between vascular pathologies and Alzheimer's dementia and potential causal mechanisms. *Alzheimers Dement.* 15, 65–75. doi: 10.1016/j.jalz.2018.08.002

Marden, J. R., Mayeda, E. R., Walter, S., Vivot, A., Tchetgen Tchetgen, E. J., Kawachi, I., et al. (2016). Using an Alzheimer disease polygenic risk score to predict memory decline in black and white americans over 14 years of follow-up. *Alzheimer Dis. Assoc. Disord.* 30, 195–202. doi: 10.1097/WAD.0000000000000137

Mirza-Davies, A., Foley, S., Caseras, X., Baker, E., Holmans, P., Escott-Price, V., et al. (2021). The impact of genetic risk for Alzheimer's disease on the structural brain networks of young adults. *bioRxiv*. doi: 10.1101/2021.09.22.461338

Moore, A. M., Filshtein, T. J., Dumitrescu, L., Harrati, A., Elahi, F., Mormino, E. C., et al. (2019). A/T/N polygenic risk score for cognitive decline in old age Annah. *bioRxiv*. doi: 10.1101/838847

Morgan, A. R., Touchard, S., O'Hagan, C., Sims, R., Majounie, E., Escott-Price, V., et al. (2017). The correlation between inflammatory biomarkers and polygenic risk score in Alzheimer's disease. *J. Alzheimers Dis.* 56, 25–36. doi: 10.3233/JAD-160889

Mormino, E. C., Sperling, R. A., Holmes, A. J., Buckner, R. L., De Jager, P. L., Smoller, J. W., et al. (2016). Polygenic risk of Alzheimer disease is associated with early- and late-life processes. *Neurology* 87, 481–488. doi: 10.1212/WNL.0000000000002922

Naveed, M., Mubeen, S., Khan, A., Ibrahim, S., and Meer, B. (2019). Plasma biomarkers: potent screeners of Alzheimer's disease. *Am. J. Alzheimers Dis.* 34, 290–301. doi: 10.1177/1533317519848239

Peyrot, W. J., and Price, A. L. (2021). Identifying loci with different allele frequencies among cases of eight psychiatric disorders using CC-GWAS. *Nat. Genet.* 53, 445–454. doi: 10.1038/s41588-021-00787-1

Porter, T., Burnham, S. C., Milicic, L., Savage, G., Maruff, P., Lim, Y. Y., et al. (2018a). Utility of an Alzheimer's disease risk-weighted polygenic risk score for predicting rates of cognitive decline in preclinical Alzheimer's disease: a prospective longitudinal study. *J. Alzheimer's Dis.* 66, 1193–1211. doi: 10.3233/JAD-180713

Porter, T., Burnham, S. C., Savage, G., Lim, Y. Y., Maruff, P., Milicic, L., et al. (2018b). A polygenic risk score derived from episodic memory weighted genetic variants is associated with cognitive decline in preclinical Alzheimer's disease. *Front. Aging Neurosci.* 10, 423. doi: 10.3389/fnagi.2018.00423

Richardson, T. G., Harrison, S., Hemani, G., and Smith, G. D. (2019). An atlas of polygenic risk score associations to highlight putative causal relationships across the human phenome. *eLife* 8, 1–24. doi: 10.7554/eLife.43657

Ripke, S., Neale, B. M., Corvin, A., Walters, J. T. R., Farh, K. H., Holmans, P. A., et al. (2014). Biological insights from 108 schizophrenia-associated genetic loci. *Nature* 511, 421–427. doi: 10.1038/nature13595

Rostami, E., Engquist, H., and Enblad, P. (2014). Imaging of cerebral blood flow in patients with severe traumatic brain injury in the neurointensive care. *Front. Neurol.* 5, 114. doi: 10.3389/fneur.2014.00114

Sabuncu, M. R., Buckner, R. L., Smoller, J. W., Lee, P. H., Fischl, B., Sperling, R. A., et al. (2012). The association between a polygenic Alzheimer score and cortical thickness in clinically normal subjects. *Cereb. Cortex* 22, 2653–2661. doi: 10.1093/cercor/bhr348

Selkoe, D. J. (2021). Treatments for Alzheimer's disease emerge. *Science* 373, 624–626. doi: 10.1126/science.abi6401

Servick, K. (2021). Alzheimer's drug approval spotlights blood tests. *Science* 373, 373–374. doi: 10.1126/science.373.6553.373

Shen, X. N., Huang, Y. Y., Chen, S. D., Guo, Y., Tan, L., Dong, Q., et al. (2021). Plasma phosphorylated-tau181 as a predictive biomarker for Alzheimer's amyloid, tau and FDG PET status. *Transl. Psychiatry* 11, 1–10. doi: 10.1038/s41398-021-01709-9

Shin, S. H., Lillard, D. R., and Bhattacharya, J. (2019). Understanding the correlation between Alzheimer's disease polygenic risk, wealth, and the composition of wealth holdings. *Biodemography Soc. Biol.* 65, 323–350. doi: 10.1080/19485565.2020.1769466

Skoog, I., Kern, S., Najar, J., Guerreiro, R., Bras, J., Waern, M., et al. (2021). A non-APOEPolygenic risk score foralzheimer's disease is associated with cerebrospinal fluid neurofilament light in a representative sample of cognitively unimpaired 70-year olds. *J. Gerontol. Ser. A Biol. Sci. Med. Sci.* 76, 983–990. doi: 10.1093/gerona/glab030

Smitha, K., Akhil Raja, K., Arun, K., Rajesh, P., Thomas, B., Kapilamoorthy, T., et al. (2017). Resting state fMRI: a review on methods in resting state connectivity analysis and resting state networks. *Neuroradiol. J.* 30, 305–317. doi: 10.1177/1971400917697342

Soldan, A., Pettigrew, C., Fagan, A. M., Schindler, S. E., Moghekar, A., Fowler, C., et al. (2019). ATN profiles among cognitively normal individuals and longitudinal cognitive outcomes. *Neurology* 92, e1567–e1579. doi: 10.1212/WNL.0000000000007248

Stephan, Y., Sutin, A. R., Luchetti, M., Caille, P., and Terracciano, A. (2018). Polygenic score for Alzheimer disease and cognition: the mediating role of personality. *J. Psychiatr. Res.* 107, 110. doi: 10.1016/J.JPSYCHIRES.2018.10.015

Su, F., Shu, H., Ye, Q., Xie, C., Yuan, B., Zhang, Z., et al. (2017). Integration of multilocus genetic risk into the default mode network longitudinal trajectory during the Alzheimer's disease process. *J. Alzheimers. Dis.* 56, 491–507. doi: 10.3233/JAD-160787

Tan, C. H., Fan, C. C., Mormino, E. C., Sugrue, L. P., Broce, I. J., Hess, C. P., et al. (2018). Polygenic hazard score: an enrichment marker for Alzheimer's associated amyloid and tau deposition. *Acta Neuropathol.* 135, 85–93. doi: 10.1007/s00401-017-1789-4

Tank, R., Ward, J., Flegal, K. E., Smith, D. J., Bailey, M. E. S., Cavanagh, J., et al. (2022). Association between polygenic risk for Alzheimer's disease, brain structure and cognitive abilities in UK Biobank. *Neuropsychopharmacology* 47, 564–569. doi: 10.1038/s41386-021-01190-4

Terracciano, A., and Sutin, A. R. (2019). Personality and Alzheimer's disease: an integrative review. *Personal. Disord. Theory, Res. Treat.* 10, 4–12. doi: 10.1037/per0000268

van der Merwe, C., Passchier, R., Mufford, M., Ramesar, R., Dalvie, S., and Stein, D. J. (2019). Polygenic risk for schizophrenia and associated brain structural changes: a systematic review. *Compr. Psychiatry* 88, 77–82. doi: 10.1016/j.comppsych.2018.11.014

Wehby, G. L., Domingue, B. W., and Wolinsky, F. D. (2018). Genetic risks for chronic conditions: implications for long-term wellbeing. *J. Gerontol. Ser. A Biol. Sci. Med. Sci.* 73, 477–483. doi: 10.1093/gerona/glx154

Weiner, M. W., Veitch, D. P., Aisen, P. S., Beckett, L. A., Cairns, N. J., Cedarbaum, J., et al. (2015). 2014 Update of the Alzheimer's Disease Neuroimaging Initiative: a review of papers published since its inception. *Alzheimer's Dement.* 11, e1–e120. doi: 10.1016/j.jalz.2014.11.001

Williams, M. E., Elman, J. A., McEvoy, L. K., Andreassen, O. A., Dale, A. M., Eglit, G. M. L., et al. (2021). 12-year prediction of mild cognitive impairment aided by Alzheimer's brain signatures at mean age 56. *Brain Commun.* 3, fcab167. doi: 10.1093/braincomms/fcab167

Wingo, T. S., Lah, J. J., Levey, A. I., and Cutler, D. J. (2012). Autosomal recessive causes likely in early-onset Alzheimer disease. *Arch. Neurol.* 69, 59–64. doi: 10.1001/archneurol.2011.221

Wray, N. R., Lin, T., Austin, J., McGrath, J. J., Hickie, I. B., Murray, G. K., et al. (2021). From basic science to clinical application of polygenic risk scores: a primer. *JAMA Psychiatry* 78, 101–109. doi: 10.1001/jamapsychiatry.2020.3049

Xiao, E., Chen, Q., Goldman, A. L., Tan, H. Y., Healy, K., Zoltick, B., et al. (2017). Late-Onset Alzheimer's disease polygenic risk profile score predicts hippocampal function. *Biol. Psychiatry Cogn. Neurosci. Neuroimaging* 2, 673–679. doi: 10.1016/j.bpsc.2017.08.004

Xu, J., Li, Q., Qin, W., Li, M. J., Zhuo, C., Liu, H., et al. (2018). Neurobiological substrates underlying the effect of genomic risk for depression on the conversion of amnestic mild cognitive impairment. *Brain* 141, 3457–3471. doi: 10.1093/brain/awy277

Yang, J., Pan, P., Song, W., Huang, R., Li, J., Chen, K., et al. (2012). Voxelwise meta-analysis of gray matter anomalies in Alzheimer's disease and mild cognitive impairment using anatomic likelihood estimation. *J. Neurol. Sci.* 316, 21–29. doi: 10.1016/j.jns.2012.02.010

Zettergren, A., Lord, J., Ashton, N. J., Benedet, A. L., Karikari, T. K., Lantero Rodriguez, J., et al. (2021). Association between polygenic risk score of Alzheimer's disease and plasma phosphorylated tau in individuals from the Alzheimer's Disease Neuroimaging Initiative. *Alzheimers. Res. Ther.* 13, 17. doi: 10.1186/s13195-020-00754-8

Zhan, Y., Ma, J., Xu, K., Ding, Y., Cui, Y., Yang, Z., et al. (2016). "Impaired episodic memory network in subjects at high risk for Alzheimer's disease," in *38th Annual International Conference of the IEEE Engineering in Medicine and Biology Society (EMBC)* (Orlando, FL: IEEE), 4017–4020. doi: 10.1109/EMBC.2016.7591608

Zhou, X., Chen, Y., Ip, F. C. F., Lai, N. C. H., Li, Y. Y. T., Jiang, Y., et al. (2020). Genetic and polygenic risk score analysis for Alzheimer's disease in the Chinese population. *Alzheimers Dement.* 12, 1–15. doi: 10.1002/dad2.12074

Zhu, X. C., Tan, L., Wang, H. F., Jiang, T., Cao, L., Wang, C., et al. (2015). Rate of early onset Alzheimer's disease: a systematic review and meta-analysis. *Ann. Transl. Med.* 3, 38. doi: 10.3978/J.ISSN.2305-5839.2015.01.19

Conflict of Interest: The authors declare that the research was conducted in the absence of any commercial or financial relationships that could be construed as a potential conflict of interest.

Publisher's Note: All claims expressed in this article are solely those of the authors and do not necessarily represent those of their affiliated organizations, or those of the publisher, the editors and the reviewers. Any product that may be evaluated in this article, or claim that may be made by its manufacturer, is not guaranteed or endorsed by the publisher.

frontiers | Frontiers in Aging Neuroscience

ORIGINAL RESEARCH
published: 25 April 2022
doi: 10.3389/fnagi.2022.870957

Integrating Lipidomics and Transcriptomics Reveals the Crosstalk Between Oxidative Stress and Neuroinflammation in Central Nervous System Demyelination

Zhi-jie Zhao[1†], Rui-zhe Zheng[1,2†], Xiao-jing Wang[1,3†], Tong-qi Li[4], Xiao-hua Dong[1,5], Chang-yi Zhao[1] and Xin-yuan Li[1*]*

[1] Department of Neurosurgery, Tongren Hospital, Shanghai Jiao Tong University School of Medicine, Shanghai, China, [2] Department of Neurosurgery, Huashan Hospital, Shanghai Medical College, Fudan University, Shanghai, China, [3] Department of Neurology, The First Affiliated Hospital of Anhui Medical University, Hefei, China, [4] Department of Ophthalmology, Shanghai General Hospital, Shanghai Jiao Tong University School of Medicine, Shanghai, China, [5] Hongqiao International Institute of Medicine, Tongren Hospital, Shanghai Jiao Tong University School of Medicine, Shanghai, China

OPEN ACCESS

Edited by:
Yuzhen Xu,
Tongji University, China

Reviewed by:
Jie Tao,
Shanghai General Hospital, China
Yang Jiang,
Tongji University, China
Weiwei Lin,
Zhejiang University, China

***Correspondence:**
Chang-yi Zhao
zcy3712@shtrhospital.com
Xin-yuan Li
lxy2186@shtrhospital.com

† These authors have contributed equally to this work and share first authorship

Specialty section:
This article was submitted to Neuroinflammation and Neuropathy, a section of the journal Frontiers in Aging Neuroscience

Received: 07 February 2022
Accepted: 01 April 2022
Published: 25 April 2022

Citation:
Zhao Z-j, Zheng R-z, Wang X-j, Li T-q, Dong X-h, Zhao C-y and Li X-y (2022) Integrating Lipidomics and Transcriptomics Reveals the Crosstalk Between Oxidative Stress and Neuroinflammation in Central Nervous System Demyelination. Front. Aging Neurosci. 14:870957. doi: 10.3389/fnagi.2022.870957

Multiple sclerosis (MS) is an incurable and progressive neurodegenerative disease that affects more than 2.5 million people worldwide and brings tremendous economic pressures to society. However, the pathophysiology of MS is still not fully elucidated, and there is no effective treatment. Demyelination is thought to be the primary pathophysiological alteration in MS, and our previous study found abnormal lipid metabolism in the demyelinated corpus callosum. Growing evidence indicates that central nervous system (CNS) demyelinating diseases never result from one independent factor, and the simultaneous participation of abnormal lipid metabolism, oxidative stress, and neuroinflammation could potentiate each other in the pathogenesis of MS. Therefore, a single omics analysis cannot provide a full description of any neurodegenerative disease. It has been demonstrated that oxidative stress and neuroinflammation are two reciprocal causative reasons for the progression of MS disease. However, the potential crosstalk between oxidative stress and neuroinflammation remains elusive so far. With an integrated analysis of targeted lipidomics and transcriptomics, our research presents the potential interaction between abnormalities of lipid metabolism, mitochondrial dysfunction, oxidative stress, and neuroinflammation in CNS demyelinating diseases. The findings of this paper may be used to identify possible targets for the therapy of CNS demyelinating diseases.

Keywords: targeted lipidomics, oxidative stress, mitochondrial dysfunction, neuroinflammation, crosstalk

INTRODUCTION

Central nervous system (CNS) demyelinating diseases are characterized by inflammatory stimulation, vascular compression, immune abnormalities, and massive loss of oligodendrocytes (Sen et al., 2019). The destruction of the myelin sheath will lead to neurological disorders, including multiple sclerosis (MS) and cranial nerve disorders (Kim et al., 2021; Saraswat et al., 2021). MS is a progressive, incurable disease that affects more than 2.5 million individuals globally

(Zhao et al., 2020). Patients with MS have a variety of neurological symptoms such as motor impairment, cognitive impairment, depressive tendencies, visual impairment, sleep disturbances, and anxiety tendencies, all of which negatively affect the quality of life and lead to a significant impact on medical and healthcare systems (Shao et al., 2021; Zhao et al., 2021). However, to date, the comprehensive pathogenesis of MS remains unknown, and there is no effective therapy (Meng-Ru et al., 2021).

The pathogenic processes of MS are astoundingly complicated. Previous research has suggested that mitochondrial dysfunction (Luo et al., 2020), oxidative stress (Shiri et al., 2020; Mihai et al., 2021), and neuroinflammation (Meng-Ru et al., 2021; Shao et al., 2021) may be jointly involved in the onset and progression of MS. Cellular energy crisis and increased oxidative stress are consequences of mitochondrial dysfunction. Defective mitochondrial enzyme activity plays a critical role in the development and progression of MS (Lu et al., 2000). Additionally, mitochondrial malfunction and an increase in the formation of reactive oxygen species (ROS) can cause oligodendrocyte destruction (Yeung et al., 2021). Moreover, ROS can interact with biological substances such as DNA or lipids (Shiri et al., 2020). Thus, excessive ROS production can trigger mitochondrial dysfunction, which manifests itself through aberrant gene expression, enzyme activity, and kinetics in the mitochondria (Mao and Reddy, 2010). In addition, it is thought that pro-inflammatory conditions in the CNS accelerate myelin sheath degradation (Shao et al., 2021).

Metabolomics widens our knowledge of small molecule metabolites, which are often considered as biomarkers, end products of cellular metabolism, while their regulatory roles in the genome, transcriptome, and proteome are often overlooked. Our prior investigation discovered an abnormal lipid metabolism in demyelinated central nerve tissue (Zhao et al., 2021). At present, there is no obvious association between abnormal lipid metabolism and mitochondrial dysfunction, oxidative stress, and neuroinflammation in CNS demyelinated tissues. We employed combined targeted lipid metabolomics and transcriptomics to investigate the potential interaction between them in demyelinating tissue of the central nervous system.

Abbreviations: CNS, Central nervous system; MS, Multiple sclerosis; CPZ, Cuprizone; QC, Quality control; SD, Standard deviation; CV, Coefficient of Variation; ANOVA, One-way analysis of variance; VIP, Variable influence on projection; TIC, Total ion flow chromatogram; PCA, Principal component analysis; OPLS-DA, Orthogonal Partial least squares discriminant analysis; PCC, Pearson correlation coefficients; HCA, Hierarchical cluster analysis; DA Score, differential abundance score; PE, Phosphatidylethanolamine; PC, Phosphatidylcholine; DAG, Diacylglycerol; CE, Cholesteryl ester; ROS, Reactive oxygen species; CD14, Monocyte differentiation antigen; MIP-1β, Ccl4, chemokine (C-C motif) ligand 4; MIP-1α, C-C motif chemokine 3; NOX, NADPH oxidase 2; CYBA, Cytochrome b-245, alpha polypeptide; RANTES, C-C motif chemokine 5; mt-Nd1, Mitochondrially encoded NADH dehydrogenase 1; mt-Nd2, Mitochondrially encoded NADH dehydrogenase 2; mt-Nd4, Mitochondrially encoded NADH dehydrogenase 4; mt-Nd4l, Mitochondrially encoded NADH dehydrogenase 4L; mt-Nd5, Mitochondrially encoded NADH dehydrogenase 5; mt-Nd6, Mitochondrially encoded NADH dehydrogenase 6; Uqcr11, Ubiquinol-cytochrome c reductase%2C complex III subunit XI; mt-Cytb, Mitochondrially encoded cytochrome b; mt-Co3, Mitochondrially encoded cytochrome c oxidase III; mt-Co1, Mitochondrially encoded cytochrome c oxidase I; mt-Co2, Mitochondrially encoded cytochrome c oxidase II; Cox8b, Cytochrome c oxidase subunit 8B; mt-Atp6, Mitochondrially encoded ATP synthase 6; mt-Atp8, Mitochondrially encoded ATP synthase 8.

MATERIALS AND METHODS

Animals and Experimental Design

Male C57BL/6 mice (8 weeks old) were purchased from Spelford (Beijing) Biotechnology Company. Mice were housed in an air-conditioned room at 22 ± 1°C with a 12-h light-dark cycle (lights on from 7:00 a.m. to 7:00 p.m.) (Zhao et al., 2021). Food and tap water were freely available. All procedures for the following experiments were approved by the Animal Care and Use Committee, performed by the NIH Guide for the Care and Use of Laboratory Animals.

Twenty male C57BL/6 mice (8 weeks old) were randomly divided into the control group (n = 10) and the cuprizone (CPZ) group (n = 10), and mice in the CPZ group were fed by a diet containing 0.2% cuprizone (reagent purchased from Sigma, custom-made feed from Jiangsu Hershey Feeds). By referring to the literature (Wellman et al., 2020), C57BL/6 male mice were selected to be fed 0.2% cuprizone chow to construct the demyelination model, and we chose continuous feeding (11 weeks) for the CPZ group (Zhao et al., 2021). Then, mice were executed, and the corpus callosum was immediately stored at −80°C for subsequent detection of the targeted lipidomics and transcriptomics.

Corpus Callosum Lipid Extraction

The Corpus Callosum was thawed on ice. Take 20 mg of sample and homogenize with 1 ml of the mixture (including methanol, MTBE, and internal standard mixture) and a steel ball. Remove the pellet and vortex the mixture for 15 min. Add 200 μL of water, vortex for 1 min, and then centrifuge at 4°C for 10 min at 12,000 rpm. Remove 300 μL of supernatant and concentrate. Dissolve the powder with 200 μL of the reagent solution and store it at −80°C. Place the solution in a sample vial for LC-MS/MS analysis. In addition, to investigate the stability of instruments and the reproducibility of the sample, quality control (QC) samples were also prepared by combining equal volumes of each sample.

Acquisition of Targeted Lipidomics Data

HPLC grades of acetonitrile (ACN), methanol (MeOH), isopropanol (IPA), methylene chloride (CH2Cl2), and tert-butyl methyl ether (MTBE) were purchased from Merck (Darmstadt, Germany). HPLC grade formic acid (FA) and ammonium formate (AmFA) were purchased from Sigma-Aldrich (St. Louis, MO, United States). Ultrapure water was obtained using a Milli-Q system (Millipore, Billerica, MA). Lipid standards were purchased from Sigma-Aldrich or Avanti Polar Lipids (Alabaster, AL).

Sample extracts were analyzed using an LC-ESI-MS/MS system (UPLC, ExionLC AD,[1] MS, QTRAP® 6500+ system[2]).

[1]https://sciex.com.cn/

[2]https://sciex.com

The analytical conditions were as follows, UPLC: column, Thermo Accucore™ C30 (2.6 μm, 2.1 mm × 100 mm i.d.); solvent system, A: acetonitrile/water (60/40, V/V, 0.1% formic acid, 10 mmol/L ammonium formate), B: acetonitrile/isopropanol (10/90 VV/V, 0.1% formic acid, 10 mmol) /L ammonium formate); gradient program, A/B (80:20, V/V) at 0 min, 70:30 V/V, 2.0 min, 40:60 V/V, 4 min, 15:85 V/V, 9 min, 10 :90 V/V at 14 min, 5:95 V/V at 15.5 min, 5:95 V/V at 17.3 min, 80:20 V/V V at 17.3 min, 80:20 V/V at 20 min; flow rate, 0.35 mL/min; temperature, 45°C; injection volume: 2 μL. Alternatively, connect the discharge port to an ESI triple quadrupole linear ion trap (QTRAP)-MS.

LIT and triple quadrupole scanning (QQQ) are performed using a triple quadrupole linear ion trap mass spectrometer (QTRAP). The QTRAP® 6500+ LC-MS/MS system is equipped with an ESI turbo ion spray interface operating in positive ion mode and negative ion mode, controlled by Analyst 1.6.3 (Sciex) software. The operating parameters of the ESI source are as follows: ion source, turbo spray; source temperature 500°C; ion spray voltage (IS) 5,500 V (positive), −4,500 V (negative); ion source gas 1 (GS1), gas 2 (GS2), and gas curtain gas (CUR) set to 45, 55, and 35 psi, respectively. QQQ and LIT modes used 10 and 100 μ mol/L polypropylene glycol solution for device tuning and mass calibration in QQQ and LIT modes. QQQ scans were captured as MRM experiments with the collision gas (nitrogen) set to 5 psi. Individual MRM conversions of DP and CE were done by further DP and CE optimization. A specific set of MRM conversions was monitored for each period based on the metabolites eluted during that period.

RNA Sequencing

The process of RNA sequencing includes RNA extraction, RNA detection, library construction, and up-sequencing. Briefly, RNA degradation and contamination were monitored on 1% agarose gels, followed by RNA purity. RNA purity was checked using the NanoPhotometer® spectrophotometer (IMPLEN, CA, United States). Then, the RNA concentration was measured using Qubit® RNA Assay Kit in Qubit®2.0 Flurometer (Life Technologies, CA, United States). After that, RNA integrity was assessed using the RNA Nano 6000 Assay Kit of the Bioanalyzer 2100 system (Agilent Technologies, CA, United States). A total amount of 1 μg RNA per sample was used as input material for the RNA sample preparations. Following the manufacturer's recommendations, the sequencing libraries were generated using NEBNext® Ultra™ RNA Library Prep Kit for Illumina® (NEB, United States), and index codes were added to attribute sequences to each sample.

Purify mRNA from total RNA using poly-T oligo-binding magnetic beads. High-temperature lysis in NEBNext First Strand Synthesis Reaction Buffer (5X) using divalent cations. The first strand of cDNA was synthesized using random hexamer primers and M-MuLV reverse transcriptase (RNase H-). The second strand of the cDNA is then synthesized using DNA polymerase I and RNase H. The remaining prominent ends are converted to flat ends by exonuclease/polymerase activity. After adenylation of the 3′ end of the DNA fragment, the NEBNext splice is ligated to the hairpin loop structure and prepared for hybridization. To preferably select cDNA fragments of 250–300 bp in length, library fragments were purified using the AMPure XP system (Beckman Coulter, Beverly, United States). Then 3 μl USER enzyme (NEB, United States) was used with the size-selected, aptamer-linked cDNA for 15 min at 37°C followed by 5 min at 95°C before PCR. PCR was then performed using Phusion high-fidelity DNA polymerase, universal PCR primers, and index (X) primers. Finally, the PCR products were purified (AMPure XP system), and the quality of the library was assessed on an Agilent Bioanalyzer 2100 system. According to the manufacturer's instructions, index-coded samples were clustered on the cBot cluster generation system using the TruSeq PE Cluster Kit v3-cBot-HS (Illumia). After cluster generation, library preparations were sequenced on the Illumina Hiseq platform, and 125/150 bp double-end reads were generated.

Statistical Analyses

Data Analysis of Lipidomics

Unsupervised principal component analysis (PCA) was performed by R software.[3] The data were scaled with unit variance prior to unsupervised PCA. The results of HCA (hierarchical cluster analysis) for samples and metabolites are shown as heat maps with tree plots etc., while the Pearson correlation coefficients (PCC) between samples were calculated using the cor function in R software and are shown as heat maps. The normalized signal intensity (scale per unit variance) of metabolites was shown as a chromatogram for HCA. Metabolites that were significantly regulated between groups were identified by VIP $\geq$ 1, fold change $\geq$ 1.5 or fold change $\leq$ 0.66, p-value $<$ 0.05. VIP values were extracted from the OPLS-DA results, containing score and alignment plots, and were created using the R package MetaboAnalystR. Before OPLS-DA, the data were log-transformed ($\log_2$) and centered on the mean. Permutation tests (200 permutations) were performed to avoid over-fitting. The identified metabolites were annotated with the help of the kyoto encyclopedia of genes and genomes (KEGG) Compound Database,[4] and the annotated metabolites were then added to the KEGG Pathway Database.[5] Pathways with significantly regulated metabolites were then fed into Metabolite Set Enrichment Analysis (MSEA); in addition, their significance was determined by the p-value of the hypergeometric test's p-values.

Data Analysis of Transcriptomics

Raw data is filtered with fastp (V 0.19.3), mainly by removing reads with adapter; paired reads are removed when sequencing reads contain more than 10% of the number of bases in the read; if a sequencing read contains more than 50% of the number of bases in a low quality read (Q $\leq$ 20), the paired read is removed. All subsequent analyses are based on clear reads. Download the reference genome and its annotation file from the website, build the index using HISAT (V2.1.0) and compare the clean reads to the reference genome. The StringTie (V1.3.4d) was used to predict new genes. StringTie applies a

[3]www.r-project.org

[4]http://www.kegg.jp/kegg/compound/

[5]http://www.kegg.jp/kegg/pathway.html

network streaming algorithm and optionally splices transcripts from scratch. Compared to the soft of Cufflinks, StringTie can create more complete and accurate transcripts; in addition, it is faster than Cufflinks. The featureCounts (V1.6.2) was used to calculate Gene alignment, and then the FPKM was used to calculate each gene based on gene length. DESeq2 (V1.22.1) was used to analyze the differential expression between the two groups and corrected for *P*-values using Benjamini & Hochberg's method. The corrected *P*-value and | $\log_2$foldchange | were used as thresholds for expressing significant differences. The enrichment analysis is performed based on hypergeometric tests. In KEGG, the hypergeometric distribution test is performed in terms of paths; For GO, it is performed in GO terms. The analysis of protein interactions for the differentially expressed genes is based on the STRING database[6] with known and predicted protein-protein interactions. We constructed the network for species present in the database by extracting a list of target genes from the database. Otherwise, we used Blast (v2.7.1+) to compare the target gene sequences with selected reference protein sequences and then constructed the network based on known interactions for the selected reference species.

Integrated Analysis of Targeted Lipidomics and Transcriptomics

Pearson correlation analysis was used to determine the correlation coefficients between differential metabolites and genes. In addition, we selected the differential metabolites and genes with a correlation coefficient >0.6 to plot the map of the correlation network using the Cytoscape software (v3.8.2).

RESULTS

Data Pre-processing and Quality Control of Lipidomics

The Software Analyst (v1.6.3) was used to process mass spectrometry data. The intensity of all ions in the mass spectra at each time point of the mixed QC sample was summed and scanned continuously to obtain the total ions current (TIC) (**Figure 1A**: Negative mode; **Figure 1B**: Positive mode), the multi-matter extracted ion flow spectroscopy was used to draw multi-peak maps of MRM metabolite detection (**Figure 1C**: Negative mode; **Figure 1D**: Positive mode). The horizontal coordinate is the retention time for metabolite detection, and the vertical coordinate is the ion flow intensity. According to the lipid database, the detected lipid metabolites were characterized by mass spectrometry. The mass spectral peaks detected for each substance in the different samples were corrected to ensure accurate quantification.

The instrument's stability was evaluated by overlapping TIC (**Figure 1E**: Negative mode; **Figure 1F**: Positive mode) of the same QC sample. The results showed a high-level overlap of the TIC curves for metabolite detection, suggesting that the signal stability of the mass spectrometer was relatively stable when the same sample was detected at different times, and the signal was steady throughout the analysis processing. The Pearson correlation analysis was performed on the QC samples; the results showed that the testing process is relatively stable (**Figure 1G**). The coefficient of Variation (CV) can reflect the degree of data dispersion. The results of CV showed that in QC samples, the ratio of substances' CV value less than 0.5 was higher than 85%, and the percentage less than 0.3 was higher than 75%, indicating that the experimental data were very stable (**Figure 1H**).

Overall Samples Principal Component Analysis and Cluster Analysis of Lipidomics

The overall samples (includes QC samples) PCA analysis showed a trend of separation for lipid metabolites between the CPZ and control groups (**Figures 2A–D**). The horizontal coordinates of the PCA analysis plot indicate the first principal component, the vertical coordinates indicate the second principal component, and the percentage indicates the contribution of the principal component to the sample variation. Each point in the plot indicates a sample. The plot of principal component univariate statistical process control showed the PC1 of QC samples within plus or minus 3 standard deviations (SD); it indicated that the condition of the instrument is stable (**Figure 2E**). The content of lipid metabolites was normalized using the polar difference method. After normalization, the Hierarchical Cluster Analysis (HCA) was performed by R software (see text footnote 3) to analyze the accumulation pattern of metabolites among different samples (**Figure 2F**).

Lipid Metabolites Composition and Changes in Subclass Content Between Cuprizone Group and Control Group

The statistics of the detected lipid subclasses, proportions of lipid subclasses, and the number of lipid metabolites contained in each sub-classes were shown in **Figures 3A,B**. The changes in lipid subclass content between the CPZ and the control group was shown in **Figure 3C**. The dynamic distribution of lipid content demonstrated the lowest and highest lipid metabolites in the CPZ and control groups, as well as the variation in lipid content across the range (**Figure 3D**). The radar charts showed the trend changes in the content of the lipid metabolites between the CPZ and control groups (**Figures 3E,F**).

Subgroup Principal Component Analysis and Orthogonal Partial Least Squares Discriminant Analysis of Lipid Metabolites Between Cuprizone and Control Groups

The plots of subgroup PCA analysis were shown in **Figure 4**. The ellipse in **Figure 4A** is the confidence intervals of PCA plots, where the horizontal coordinate is the first principal component (PC1), and the vertical coordinate is the second principal component (PC2). According to the two-dimensional (**Figures 4A,B**) and three-dimensional PCA plots (**Figure 4C**), there was a significant trend of separation between the CPZ

[6]http://string-db.org

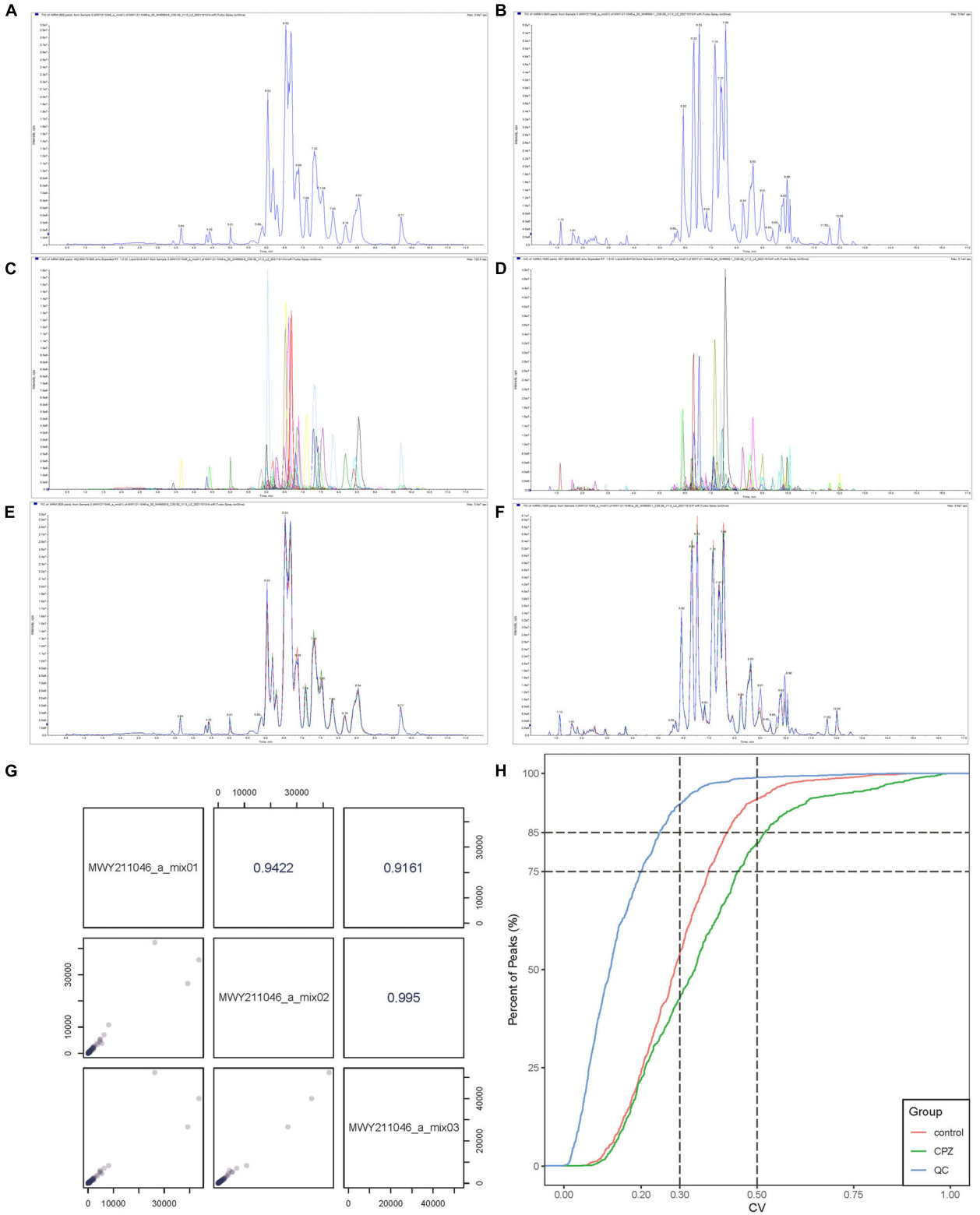

FIGURE 1 | (A) The TIC of mixed QC sample in negative mode. **(B)** The TIC of mixed QC sample in positive mode. **(C)** The MRM of mixed QC sample in negative mode. **(D)** The MRM of mixed QC sample positive mode. **(E)** The overlapping curve of TIC in negative mode. **(F)** The overlapping curve of TIC in positive mode. **(G)** The correlation analysis diagram of QC samples. **(H)** The CV diagram of QC samples.

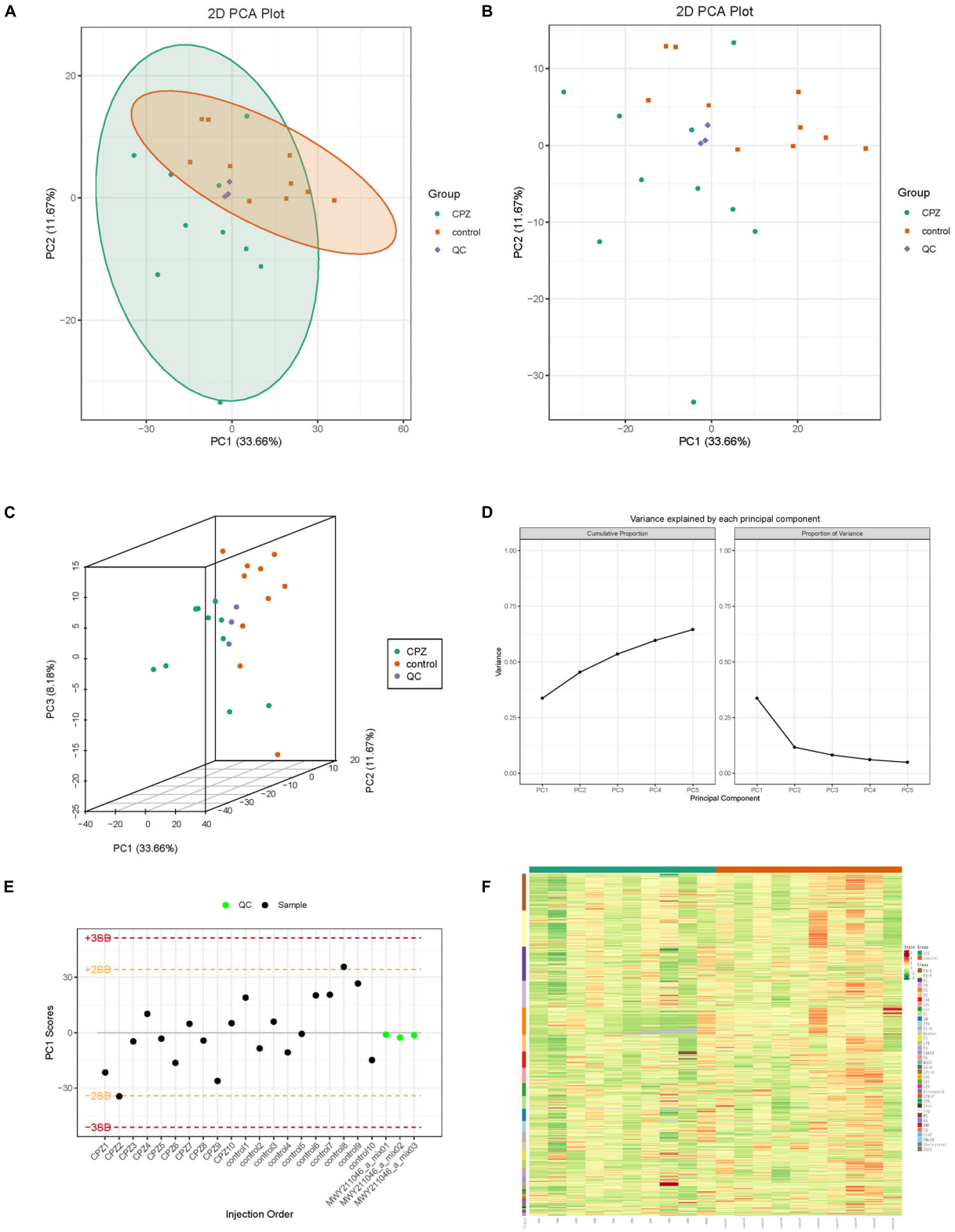

FIGURE 2 | (A,B) The two-dimensional images of the overall samples PCA results. **(C)** The 3D images of the overall samples PCA results. **(D)** The plot of variance explained by each principal component. **(E)** The plot of principal component univariate statistical process control, the horizontal coordinates of the graph are the order of sample testing, the vertical coordinates reflect the values of PC1, and the yellow and red lines define the plus or minus 2 and 3 standard deviation ranges, respectively. The green dots represent QC samples, and the black dots represent test samples. **(F)** Cluster Analysis of Lipidomics.

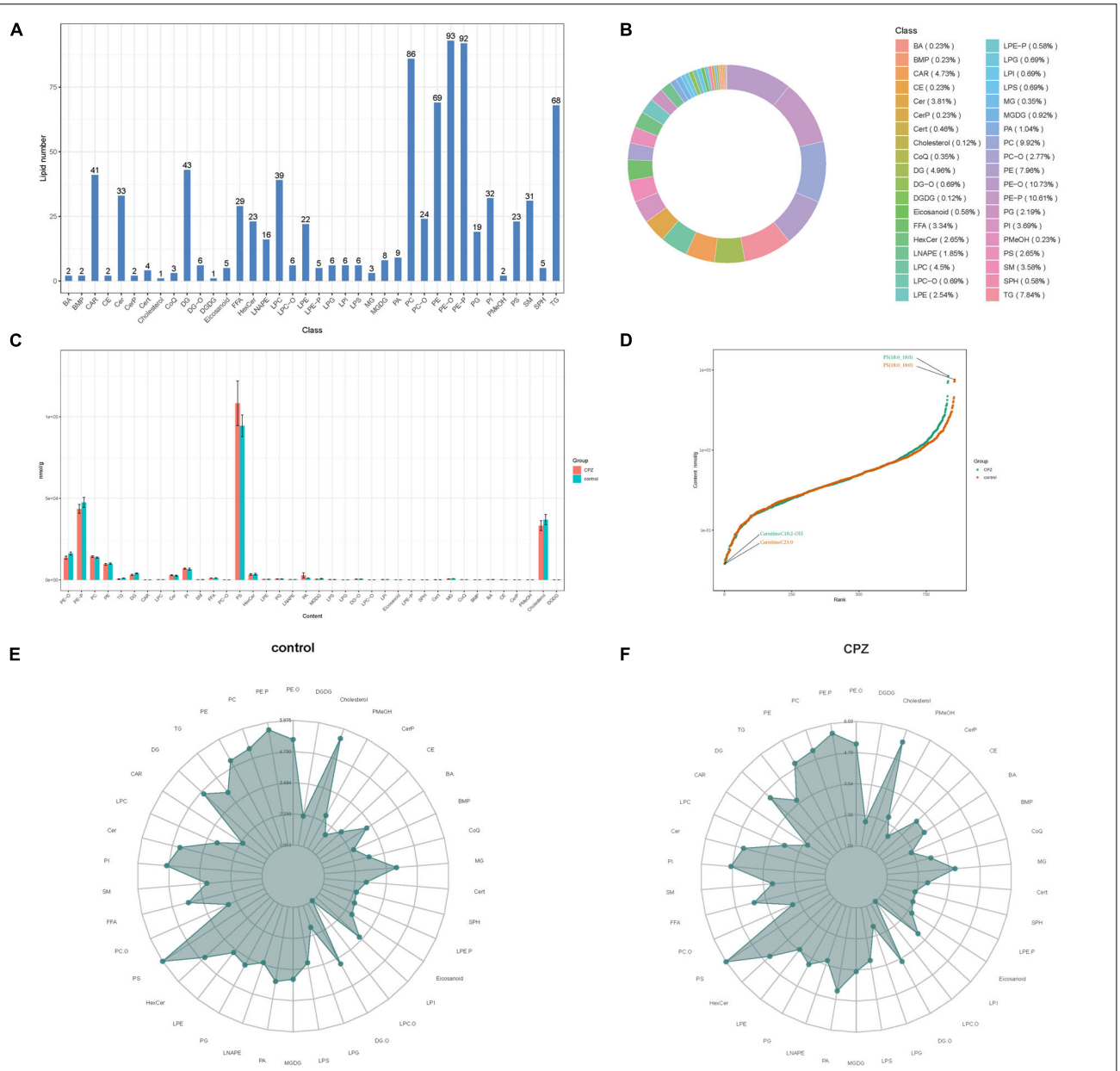

FIGURE 3 | (A) The histogram of lipid subclass. **(B)** The ring diagram of lipid subclass composition (each color represents a lipid subclass, and the area of the color block indicates the proportion of that subclass). **(C)** The histogram of changes in lipid subclass content between CPZ and control groups. **(D)** The plot of dynamic distribution for lipid content (Each point in the graph represents a lipid molecule. The vertical coordinates represent the content corresponding to each lipid molecule, and the lipid molecules with the lowest and highest content are marked. Different color curves represent different groupings). **(E,F)** The radar charts of the content of the lipid metabolites between the CPZ and control groups (The grid lines indicate the LG categorical content, and the green shading consists of the line connecting each categorical content).

and control groups, which indicated a significant difference in lipid metabolites between the CPZ and control groups. The explainable variances of the Top five principal components are shown in **Figure 4D**. The horizontal coordinates indicate the individual principal components, and the vertical coordinates indicate the explainable variances; in addition, the left panel shows the cumulative explainable variances, and the right panel shows the explainable variances of each principal component.

The raw lipidomic data were presented using an OPLS-DA score plot, indicating a clear distinction between CPZ and control groups (**Figure 4E**). The subsequent permutation test of the generated model showed R2X = 0.592, R2Y = 0.995, Q2 = 0.823 (**Figures 4G**), confirming that this model performed reliably in terms of predictive performance. **Figure 4F** shows the S-plot of OPLS-DA in which the metabolites near the upper right and lower left corners indicate differential expression (red dots,

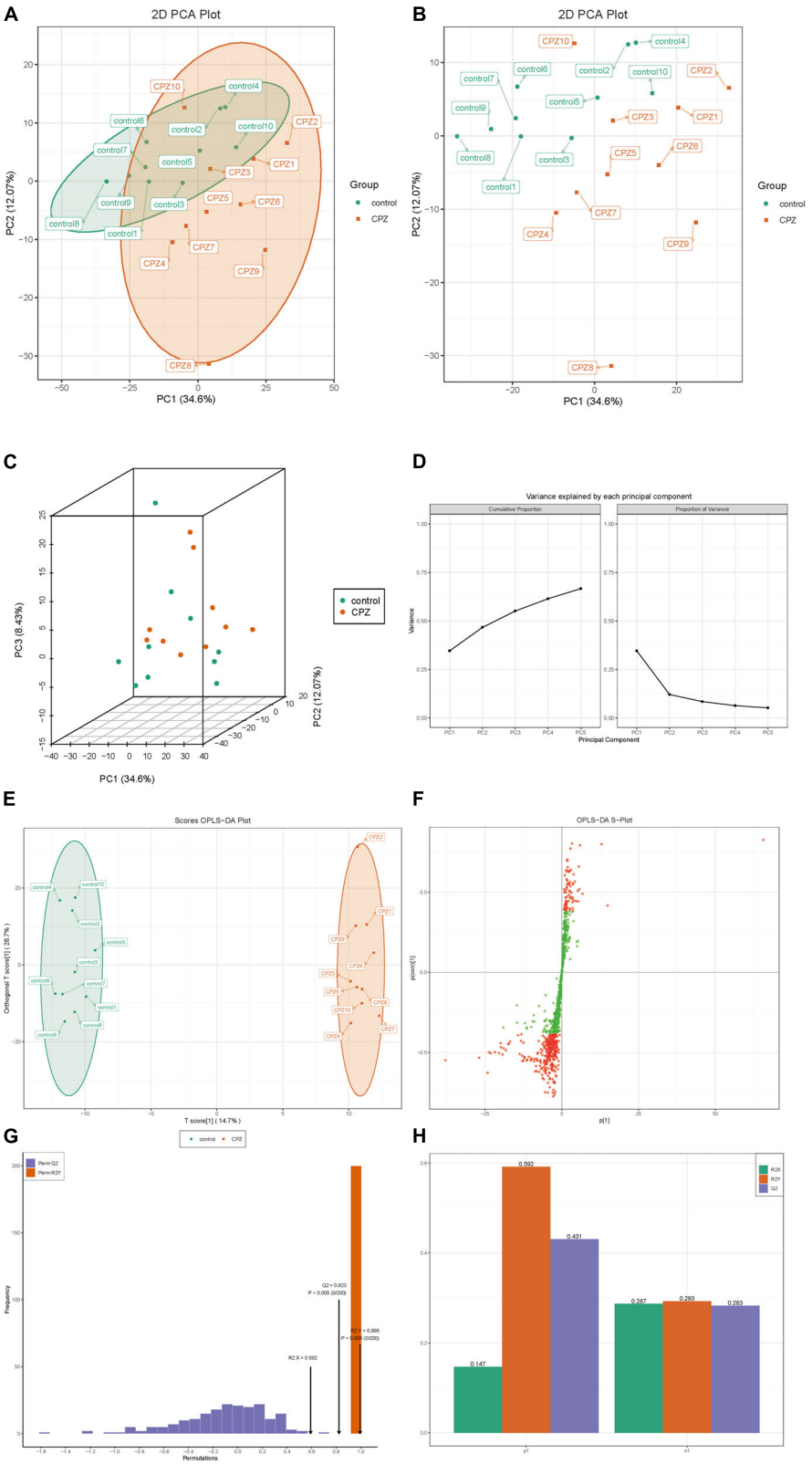

FIGURE 4 | (A,B) The two-dimensional images of the subgroup PCA analysis. **(C)** The 3D images of the subgroup PCA analysis. **(D)** The plot of variance explained by each principal component. **(E)** OPLS-DA score map. **(F)** S-plot of OPLS-DA. **(G)** Permutation test. **(H)** The details of the permutation test.

VIP $\geq$ 1; green dots, VIP $<$ 1). **Figure 4H** shows the details of the permutation test of the OPLS-DA model, including the values of R2X, Q2, and R2Y in orthogonal principal components (o1) and prediction of principal components(p1).

Identification of Lipid Metabolites

A total of 867 lipid metabolites were identified in this study, and 120 significantly different lipid metabolites (fold change $\geq$ 1.5 or fold change $\leq$ 0.66; VIP $\geq$ 1; p-value $<$ 0.05) were screened. Compared to the control group, 8 lipid metabolites were up-regulated, and 112 were down-regulated in the CPZ group. A metabolite bar graph was created based on the magnitude of the Log_2FC values for lipid metabolites (**Figure 5A**). To show the overall differences of metabolite more clearly and visually, the dynamic distribution of metabolite' content difference was plotted based on FC values (**Figure 5B**). Based on the VIP values of the metabolites, a violin plot of the top 50 lipid metabolites was created to show the data distribution and its probability density (**Figure 5C**). The top 20 differential metabolites with the most significant VIP values in the OPLS-DA model were selected to plot the graph of VIP values (**Figure 5D**). Volcano Plot was used to demonstrate the differences in metabolite content between the two groups of samples and the statistical significance of the differences (**Figure 5E**). To facilitate the observation of the variation pattern of metabolite content, we applied normalization (Unit Variance Scaling, UV Scaling) to the raw content of the differential metabolites by row. We plotted the clustering heat map (**Figure 5F**). We used Pearson correlation analysis to determine the correlation of the differential metabolites and created a heat map of the correlation for the differential metabolites (**Figures 5G,H**). The differential metabolite chord diagram is shown in **Figure 5I**, and the plots were made by default for differential metabolites with $|r| > 0.8$ and $P < 0.05$.

Kyoto Encyclopedia of Genes and Genomes Pathway Analysis of Differential Lipid Metabolites

Based on the KEGG annotation information for the differential metabolites, KEGG metabolic pathways containing at least five differential metabolites were selected, and the contents of all differential metabolites in these pathways were clustered and analyzed to investigate better the patterns of changes in the contents of substances in potentially important metabolic pathways in different groupings (**Figure 6A**).

After obtaining the matching information of the differential metabolites, pathway search and regulatory interaction network analysis was performed based on the KEGG database of the corresponding species, and a network plot was presented in **Figure 6B**. In this network plot, the red dot represents a metabolic pathway, the yellow dot represents substance-related regulatory enzyme information, the green dot represents a background substance of a metabolic pathway, the purple dot represents a class of substance molecular module information, the blue dot represents a substance chemical interaction reaction, and the green square represents the difference substance obtained from this comparison.

The differential abundance score (DA Score) (**Figure 6C**) is a pathway-based analysis of metabolic changes, and the score captures the overall changes of all metabolites in a pathway. The DA score reflects the overall change of all metabolites in the metabolic pathway. A score of 1 indicates an up-regulated trend in the expression of all identified metabolites in the pathway and -1 a down-regulated trend in the expression of all identified metabolites in the pathway.

Based on the differential metabolite results, we constructed a KEGG enrichment map (**Figure 6D**) for differential metabolites, the rich factor is the ratio of the number of differentially expressed metabolites in the corresponding pathway to the total number of metabolites annotated by the pathway detection, and a more significant value indicates a greater enrichment. The p-value in the diagram is the hypergeometric test p-value. In the KEGG enrichment map of differential metabolites, the horizontal coordinate indicates the rich factor for each pathway, the vertical coordinate is the name of the pathway, and the color of the dot is the p-value. The size of the dots represents the number of differential metabolites enriched.

The total results of KEGG annotation of differentially significant metabolites were classified according to the type of pathway in KEGG, and the classification diagram is shown in **Figure 6E**.

Transcriptomics Analysis

Quantitative Analysis of Gene Expression

The fragments per kilobase of transcript per million fragments mapped (FPKM) was used to measure the transcript or gene expression level. The box line diagram (**Figure 7A**), violin plot (**Figure 7B**), and density distribution graph (**Figure 7C**) were used to display the dispersion, probability density, and concentrated interval of the gene expression level distribution for each sample, respectively. R (Pearson's correlation coefficient) was used to assess the correlation of biological replicates of samples and the reliability of differentially expressed genes. The closer the R^2 is to 1, the stronger the correlation between the two replicate samples. Our results showed that the R^2 of the samples in this study were all higher than 0.8 (**Figure 7D**). The PCA analysis of the transcriptomics was shown in **Figures 7E,F**. The ellipse is the confidence interval, the horizontal coordinate is the first principal component (PC1), and the vertical coordinate is the second principal component (PC2).

Screen for Differential Genes

In this study, the screening conditions for differential genes were log_2Fold Change $\geq$ 1 and FDR $<$ 0.05. The FPKM of differential genes' centration and normalized expressions was used to map the clustering heat map of hierarchical cluster analysis; the clustering heat map (**Figure 8A**) showed a significant difference for the expression of genes between the control group and CPZ group. The results showed that 206 differential genes were screened, of which 113 were expressed up-regulated and 93 were expressed down-regulated (**Figure 8B**). In addition, the volcano map and M-vs.-A plot of all genes were displaced in **Figures 8C,D**. We used the STRING Protein Interaction Database (see text footnote 6) to map the differential gene protein interaction network (**Figure 8E**).

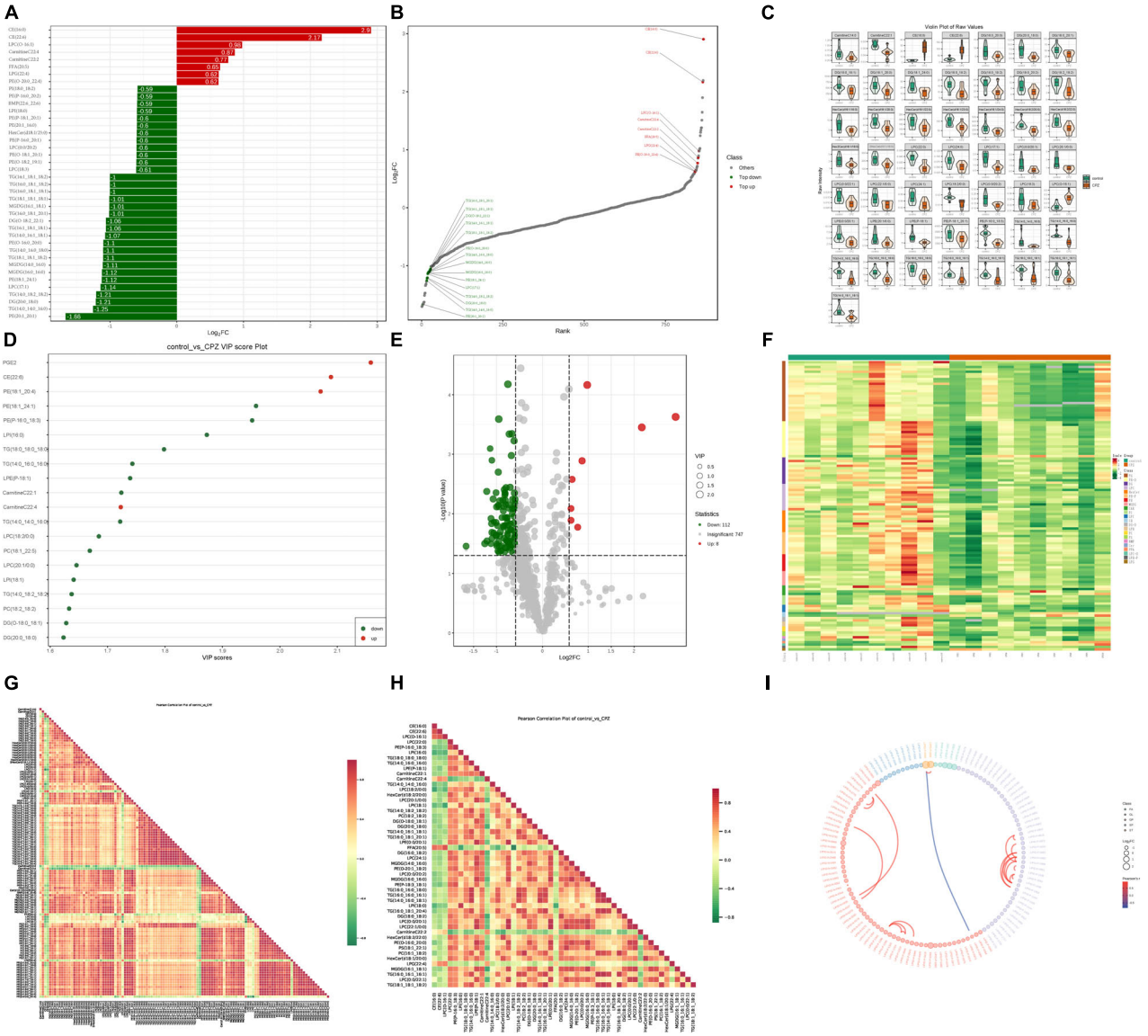

FIGURE 5 | (A) Metabolite bar graph. **(B)** Dynamic distribution of metabolite content differences. **(C)** Metabolite violin diagram. **(D)** Metabolite VIP value chart. **(E)** Volcano Plot of metabolites. **(F)** Metabolite clustering heat map. **(G)** Heat map of the correlation of the all-differential metabolites. **(H)** Heat map of the correlation of the top 50 differential metabolites. **(I)** Differential metabolite chord diagram.

Enrichment Analysis of Difference Genes

Based on the KEGG enrichment analysis results, the top 20 pathways were selected to plot the scatter plot (**Figure 9A**). According to the Reactome enrichment analysis, the top 20 most significant pathways were chosen to draw a scatter plot (**Figure 9B**). In addition, we selected the most significant GO pathways from the GO enrichment results to plot the histogram (**Figure 9C**). Moreover, we make a topGO directed acyclic graph of the GO enriched term, including biological process (**Figure 9D**), cellular component (**Figure 9E**), and molecular function (**Figure 9F**). Explain here that the directed acyclic graph topGO visualizes differentially expressed gene enrichment GO nodes and their hierarchical relationships and is a graphical representation of the results of GO enrichment analysis of differentially expressed genes, with branches defining inclusion relationships and those from top to bottom, representing increasingly specific domains of functional description.

Integrated Analysis of Lipidomics and Transcript Profiles

Correlation analysis was first performed for differential metabolites and genes detected between the control and CPZ groups. The core program of R software was used to calculate the Pearson correlation coefficients for differential metabolites and genes. According to the Pearson's correlation coefficient ($r > 0.6$), the software of Cytoscape was used to plot the map of the total

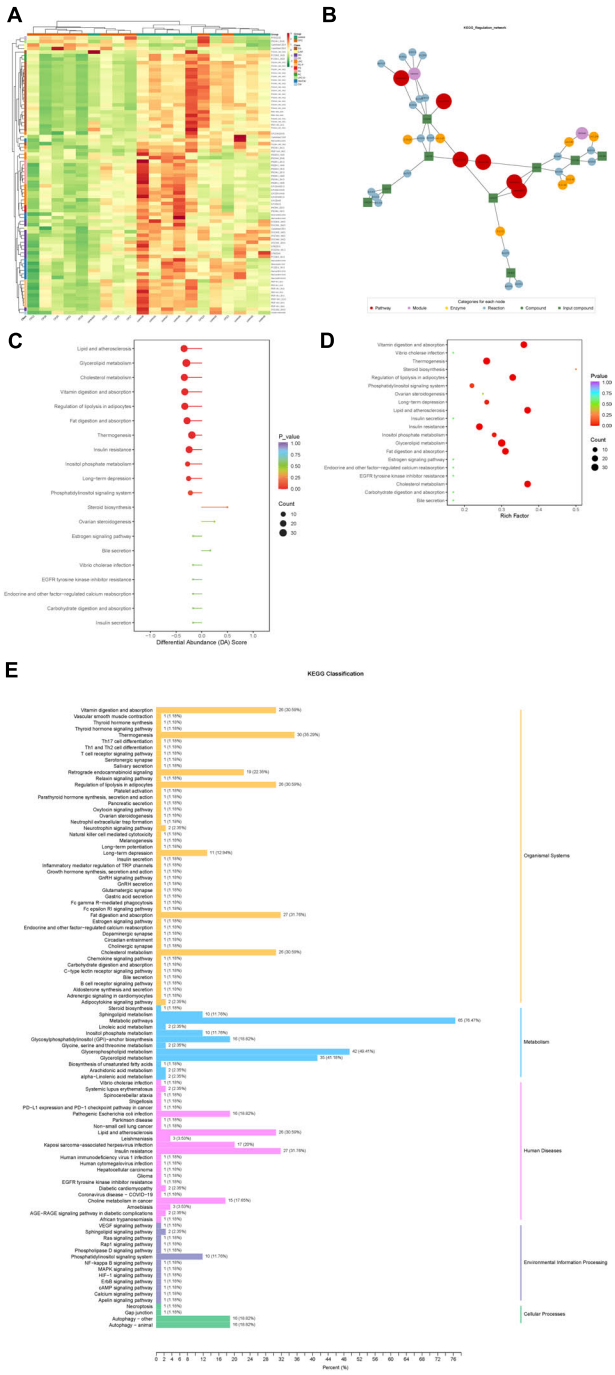

FIGURE 6 | (A) Clustering analysis for different metabolites of KEGG signaling pathway. **(B)** Analysis of the regulatory network for differential metabolites. **(C)** Differential abundance score of differential metabolic pathways. **(D)** KEGG enrichment map of differential metabolites. **(E)** KEGG enrichment analysis of differentially significant lipid metabolites.

correlation network between differential metabolites and genes (**Figure 10A**); in addition, the above result was also displayed as the plot of the heatmap in **Figure 10C**. Based on the results of KEGG enrichment analysis for differential metabolites and genes, we drew a histogram of pathways (**Figure 10B**).

According to the results of KEGG enrichment analysis which was based on the differential metabolites and genes, we choose the MAPK signaling pathway, cAMP signaling pathway, NF-kappa B signaling pathway, HIF-1 signaling pathway, thermogenesis, retrograde endocannabinoid signaling, Parkinson's disease, pathways of neurodegeneration—multiple diseases, lipid, and atherosclerosis which are associated to oxidative stress to plot the **Figure 11A**. In addition, the mitochondrial function-related genes and metabolites were used to draw **Figure 11B**. In summary, we extracted the above results to map **Figure 11C** to show the disorder's biological processes of lipid metabolism and gene expression in CNS demyelinating diseases.

DISCUSSION

Lipid metabolism is a critical component of metabolomics since it is involved in energy transport, intercellular information exchange, and a variety of other biological activities. Targeted lipidomics research has recently emerged as a promising tool for elucidating the probable link between molecular pathways and disease patterns. To present, however, the mechanism through which lipid metabolism, mitochondrial dysfunction, oxidative stress, and neuroinflammation interact to cause the degenerative processes of CNS remyelination remains elusive. Thus, utilizing a self-built database with MRM detection mode, we performed qualitative and quantitative analysis of lipid metabolites in the corpus callosum of mice using the UPLC-MS/MS apparatus, creating detailed lipid profiles for a total of 867 lipids from 38 lipid classes. The KEGG enrichment analysis was performed first in the integrated analysis of lipidomics and transcript profiles. The results showed that the 120 significantly different lipid metabolites and 206 differential genes were mainly enriched in 51 KEGG pathways. By further analysis of the above enrichment pathways revealed that the MAPK signaling pathway, cAMP signaling pathway, NF-kappa B signaling pathway, HIF-1 signaling pathway, thermogenesis, retrograde endocannabinoid signaling, Parkinson's disease, pathways of neurodegeneration—multiple diseases, lipid, and atherosclerosis are associated to oxidative stress. A deeper understanding of the complicated interaction between lipid metabolism, mitochondrial dysfunction, oxidative stress, and neuroinflammation in CNS demyelination may aid in the discovery of novel pharmaceutical targets for neuroprotective therapy. The differentially expressed genes and lipid metabolites from the above pathways related to oxidative stress were utilized to generate a map combining lipid metabolism and gene expression.

Mitochondria play an important role in oxidative phosphorylation, fatty acid oxidation, apoptosis, and calcium homeostasis (Witte et al., 2014). It also constantly generates reactive oxygen species (ROS), which can cause cell damage if the generation of ROS becomes excessive (Lin and Beal, 2006). Due to the brain's high energy requirements, it is particularly susceptible to mitochondrial malfunction, which manifests

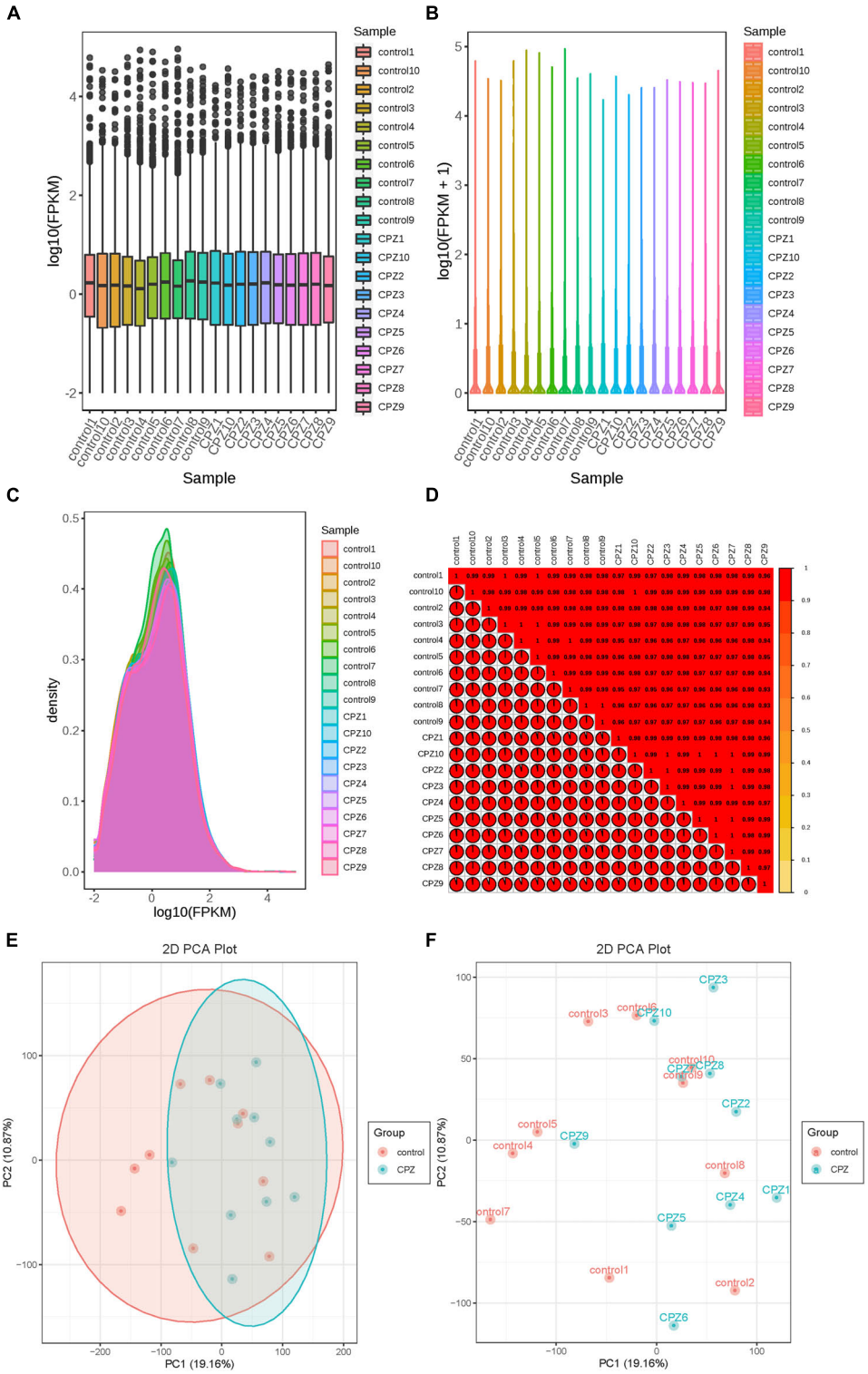

FIGURE 7 | (A) Box line diagram. **(B)** Violin plot. **(C)** Density distribution graph. **(D)** correlation heatmap of R^2. **(E,F)** The plots of PCA.

itself in neurological illnesses (DiMauro et al., 2013). Its malfunction is a significant contributor to reversible neurological impairments in neuroinflammatory illnesses such as multiple sclerosis (Sadeghian et al., 2016). An energy imbalance appears to be a prominent component of the brain and spinal cord in MS (Vidaurre et al., 2014). Up to now, the mechanism of

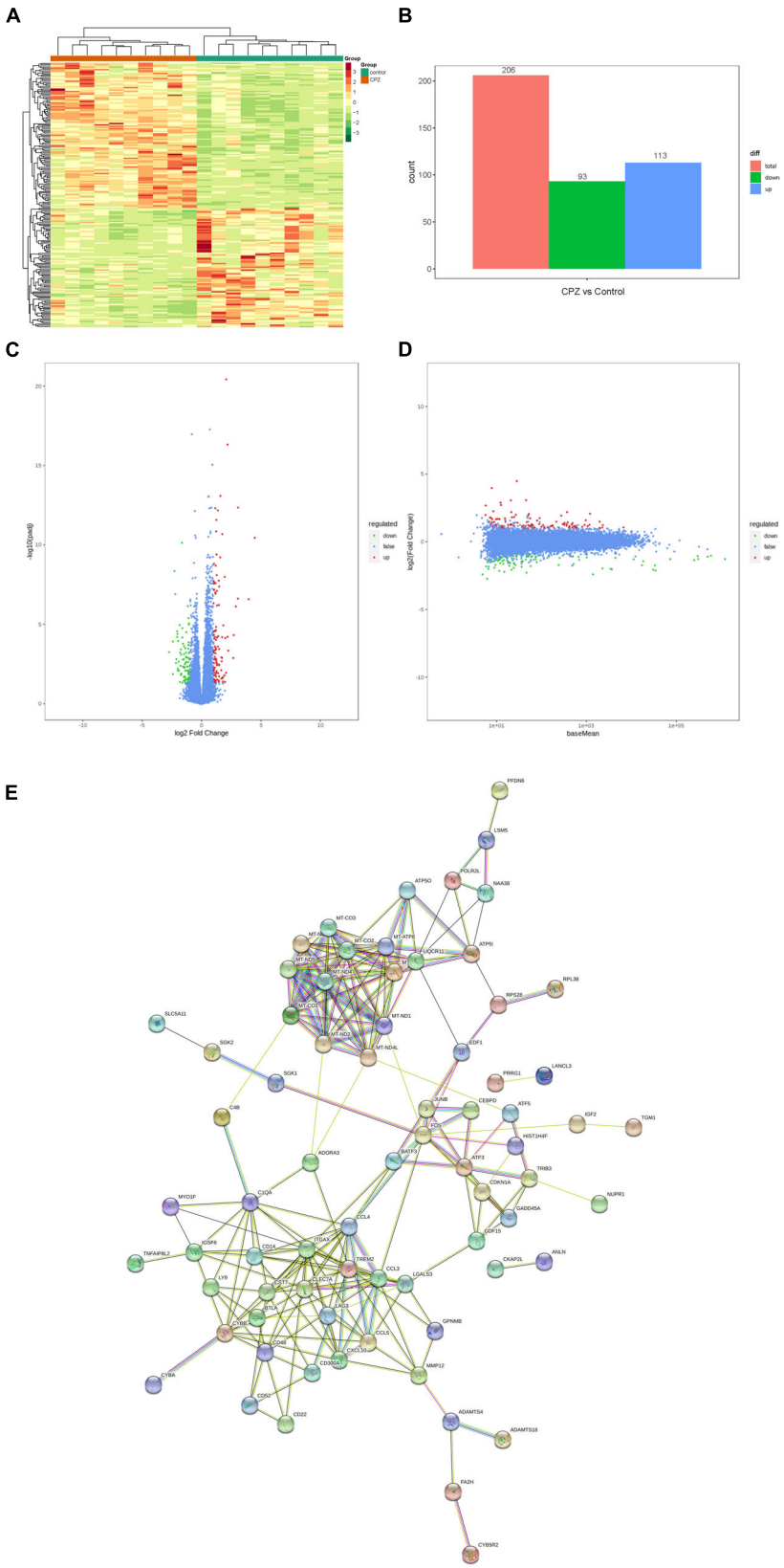

FIGURE 8 | (A) Clustering heat map of FPKM. **(B)** Histogram of differential genes' statistic. **(C,D)** Volcano map and M-vs.-A plot of all genes. **(E)** Differential genes protein interaction network.

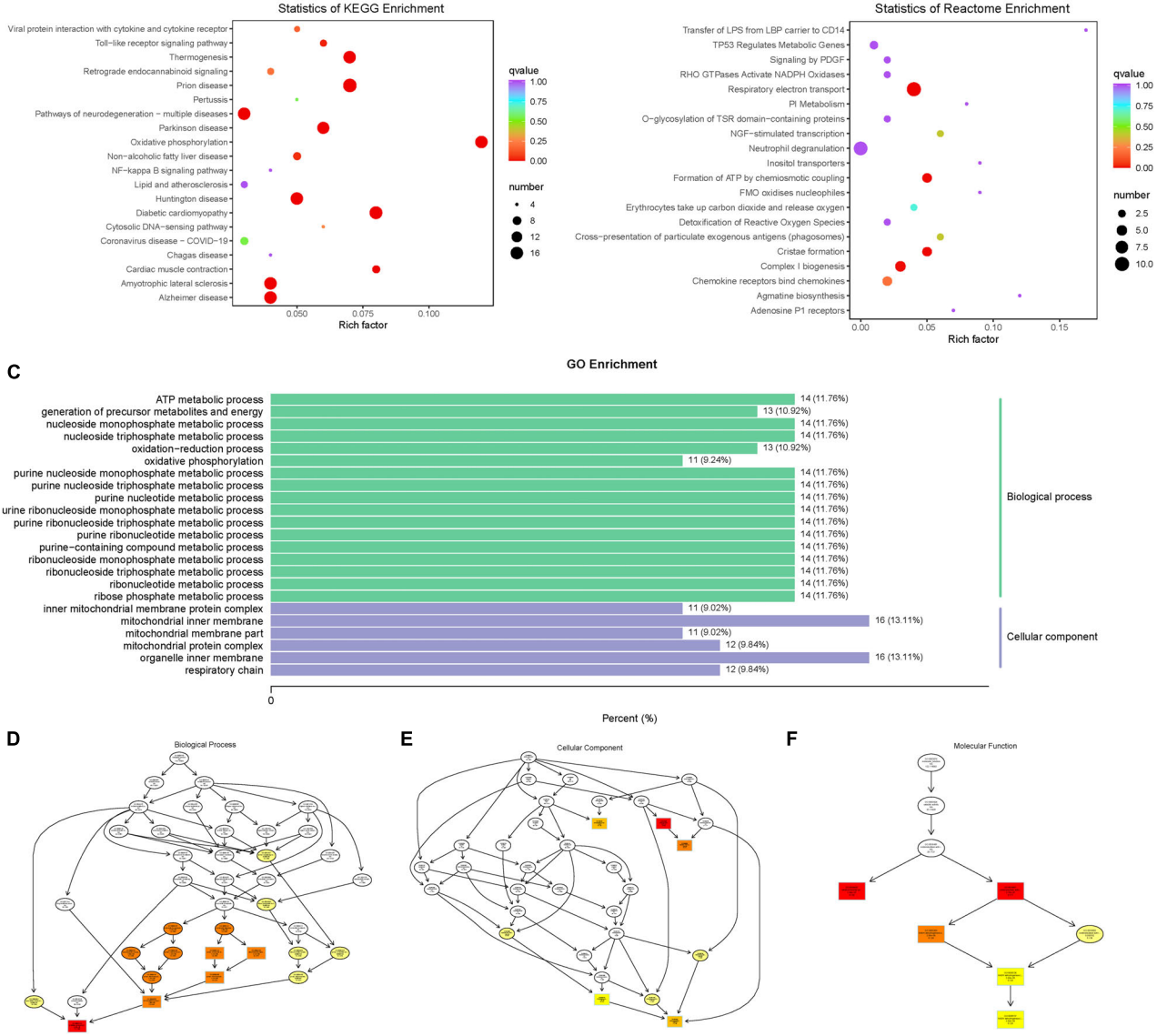

FIGURE 9 | (A) scatter plot of KEGG enrichment analysis. **(B)** scatter plot of Reactome enrichment analysis. **(C)** histogram of GO enrichment analysis. **(D)** topGO directed acyclic graph of a biological process. **(E)** topGO directed acyclic graph of the cellular component. **(F)** topGO directed acyclic graph of molecular function.

mitochondrial dysfunction in CNS demyelinating disorders has not yet been elucidated.

The majority of ATP synthesis is dependent on the system of interconnected ATP synthases (ComplexV) and the mitochondrial electron transport chain, which is composed of four enzymes and is housed within the inner mitochondrial membrane: reduced nicotinamide-de adenine dinucleotide (NADH) dehydrogenase (ComplexI), succinate dehydrogenase (ComplexII), cytochrome c oxidoreductase (ComplexIV) (Mancini et al., 2018). Reduced ComplexI activity, the principal electron entry site into the respiratory chain, is expected to result in a reduction in mitochondrial membrane potential, the rate at which electrons enter and exit the respiratory system (Nicholls, 2002). The results of transcriptomics indicated that the expression of mitochondrially encoded NADH dehydrogenase 1 (mt-Nd1), mitochondrially encoded NADH dehydrogenase 2 (mt-Nd2), mitochondrially encoded NADH dehydrogenase 4 (mt-Nd4), mitochondrially encoded NADH dehydrogenase 4L (mt-Nd4l), mitochondrially encoded NADH dehydrogenase 5 (mt-Nd5) and mitochondrially encoded NADH dehydrogenase 6 (mt-Nd6) were all down-regulated in the CPZ group. The results above demonstrate that ComplexI expression is down-regulated in the demyelinated corpus callosum. Sadeghian et al. (2016) discovered that EAE mice's spinal cords have decreased ComplexI activity, but ComplexII activity remained unaltered. Additionally, our transcriptomics data revealed no significant

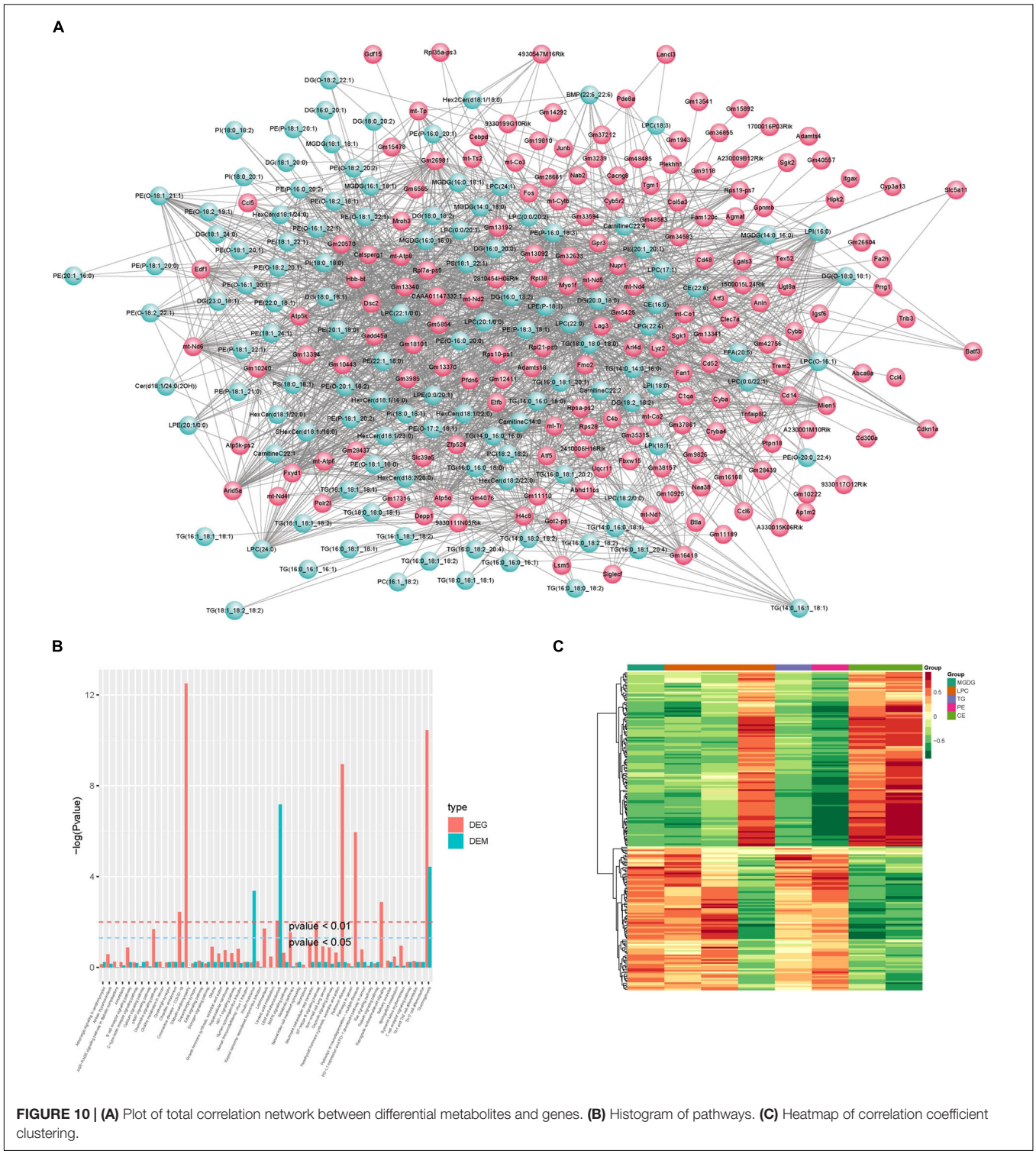

FIGURE 10 | (A) Plot of total correlation network between differential metabolites and genes. **(B)** Histogram of pathways. **(C)** Heatmap of correlation coefficient clustering.

difference in ComplexII levels between the control and CPZ groups. This may imply that ComplexII is relatively stable in the CPZ hypothesis.

In a previous investigation, ComplexIII activity was shown to be considerably increased in the spinal cords of EAE mice (Ng et al., 2019). Our data indicate that the ubiquinol-cytochrome c reductase2C complex III subunit XI (Uqcr11) was up-regulated in ComplexIII (log_2FC: 1.229). On the other hand, cytochrome b (mt-Cytb) expression was decreased (log_2FC: −1.026) in the CPZ group. According to the log_2FC values for Uqcr11 and mt-Cytb, ComplexIII's general trend was up-regulated. This could be to make up for

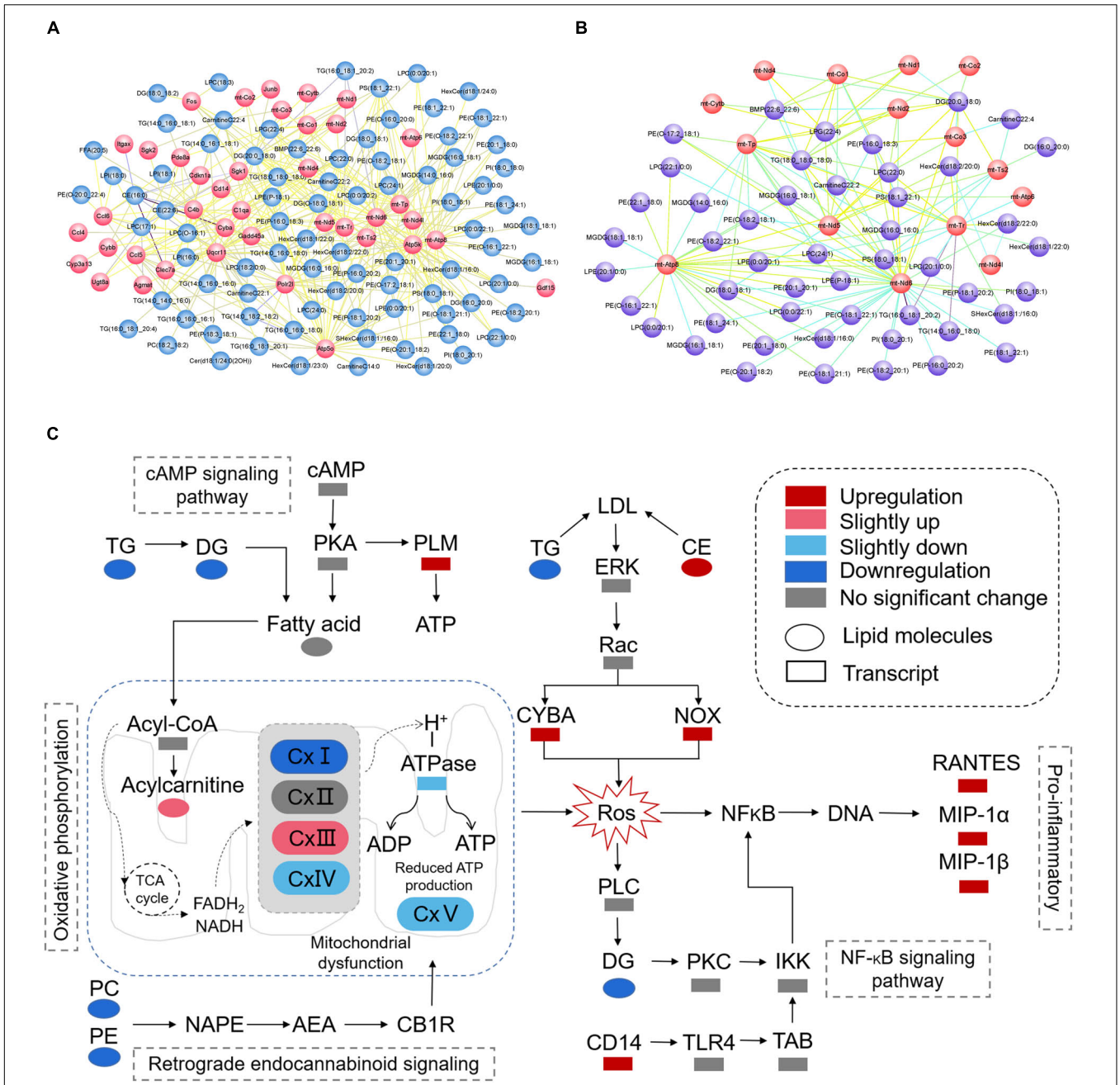

FIGURE 11 | (A) Plot of oxidative stress correlation network. **(B)** Plot of mitochondrial function-related correlation network. **(C)** Pathway representation of mitochondrial dysfunction, oxidative stress, and neuroinflammation-related signaling pathways.

mitochondrial enzymes that have been damaged or to keep the oxidative phosphorylation balance stable during the illness state. Complex IV is critical for mitochondrial function since it is the final component of the electron transport chain and accounts for about 90% of the total oxygen requirement of the cell (DiMauro and Schon, 2003). Additionally, Mahad et al. (2009) discovered that the content of ComplexIV and mitochondria in degenerated axons do not grow in a compensatory manner. Prior research established that exposure to EAE enhanced mitochondrial activity in demyelinated axons, but this increase was not accompanied by an increase in ComplexIV activity in their mitochondria. Additionally, ComplexIV activity was shown to be related to the extent of axonal damage but not to the quantity of mitochondrial material in the demyelinated lesion (Campbell and Mahad, 2018). In the EAE model, the decline in ComplexIV activity may start before there are changes in the structure of axonal mitochondria in the brain (Nikic et al., 2011). Except for cytochrome c oxidase subunit 8B (Cox8b), our results indicated

that the expression of mitochondrially encoded cytochrome c oxidase III (mt-Co3), mitochondrially encoded cytochrome c oxidase I (mt-Co1), and mitochondrially encoded cytochrome c oxidase II (mt-Co2) was all decreased in the CPZ group. Thus, the general trend of ComplexIV expression was decreased in demyelinated corpus callosum tissue. Broadwater et al. (2011) used mass spectrometry to identify proteomic changes associated with mitochondrial respiratory chain complexes in the motor cortex of patients with multiple sclerosis and confirmed a significant decrease in the content of mitochondrial respiratory complexes ComplexIV and ComplexV via western blotting. Both mitochondrial ATP synthase 6 (mt-Atp6) (log_2FC: −1.746) and mitochondrial ATP synthase 8 (mt-Atp8) (log_2FC: −1.711) expression levels were decreased. On the other hand, Atp5o (log_2FC: 1.048) and Atp5k (log_2FC: 1.485) expression levels were increased. Thus, ComplexV's overall tendency was finally down-regulated in the CPZ group.

Overproduction of ROS is intimately linked to caspase activation and cytochrome C release, both of which result in apoptosis (Ott et al., 2007). Oxidative stress caused by ROS can damage mitochondrial membrane lipids, enzyme complexes, and mitochondrial DNA, causing mitochondrial function to be harmed and causing less ATP to be made (Claus et al., 2013). Inflammation of the central nervous system (CNS) is a potent initiator of reactive oxygen species and mitochondrial dysfunction. As a result, limiting inflammation may be a beneficial strategy for avoiding mitochondrial dysfunction and increasing mitochondrial synthesis. Inflammation and neuro-axonal degeneration have been linked to MS, implying that immunological responses may exacerbate neurodegeneration, resulting in irreversible disease progression. This process may be affected by a lack of energy and problems with mitochondria caused by inflammation (Mancini et al., 2018). Furthermore, metabolic alterations may occur prior to demyelination or axonal degeneration (Sadeghian et al., 2016).

Phosphatidylcholine (PC) is the most abundant glycerophospholipid found in cell membranes and accounts for a significant portion of the composition of cell membranes, with phosphatidic acid and choline serving as the primary breakdown products. Phosphatidylethanolamine (PE) is the second most common phospholipid in the body, and it is found in cell and mitochondrial membranes. The results of targeted lipidomics show that both PC and PE concentrations were lowered in the CPZ group, which is consistent with earlier findings. The alteration of PE and PC demonstrated a dysregulation of glycerophospholipid metabolism in the demyelinated corpus callosum. Furthermore, we discovered a triglyceride metabolism abnormality in the demyelinated corpus callosum, with the content of TG and DG both decreasing while the level of cholesteryl ester (CE) was increasing.

Based on the integrated analysis of targeted lipidomics and transcriptomics (**Figures 10**, **11**), the following hypothesis is advanced: by interfering with mitochondrial activity, lower levels of PE and PC, as well as lower levels of TG and DG, in the demyelinated corpus callosum may result in energy depletion and an increase in ROS. In addition, high CE levels and low TG levels may lead to more Cytochrome b-245, alpha polypeptide (CYBA) and NADPH oxidase 2 (NOX) expression in the demyelinated corpus callosum. Interestingly, CYBA and NOX may contribute to an increase in ROS. Finally, higher ROS levels in the body may result in increased expression of pro-inflammatory chemicals such as C-C motif chemokine 5 (RANTES), C-C motif chemokine 3 (MIP-1α), and Ccl4, chemokine (C-C motif) ligand 4 (MIP-1β).

In summary, the beginning and progression of CNS demyelination is a complicated pathological process that may be mediated by a combination of lipidomics and transcriptomics. A single omics analysis may not be able to identify the overall characteristics of demyelination or provide a precise mechanism for how this process takes place completely. By using targeted lipidomics and transcriptomics, we were able to reveal the potential crosstalk between disorders of lipid metabolism, mitochondrial dysfunction, oxidative stress, and neuroinflammation in the corpus callosum of the CPZ model. The results described above may serve as a blueprint for the identification of effective therapeutic targets for the treatment of CNS demyelinating disorders.

DATA AVAILABILITY STATEMENT

The datasets presented in this study can be found in online repositories. The names of the repository/repositories and accession number(s) can be found below: NCBI (accession: PRJNA816699).

ETHICS STATEMENT

The animal study was reviewed and approved by the Laboratory Animal Ethical and Welfare Committee Tong Ren Hospital affiliated to Shanghai Jiao Tong University School of Medicine (AF/SC-11/02.1).

AUTHOR CONTRIBUTIONS

Z-JZ, R-ZZ, X-JW, and X-YL conceived and designed the experiments. Z-JZ, R-ZZ, and C-YZ performed the experiments. C-YZ, X-HD, and T-QL collected the data. X-YL and X-HD contributed the reagents, materials, and analysis tools. Z-JZ and X-JW analyzed the data and wrote the article. X-HD conducted quality control on the articles and guided the submission. All authors read and approved the final manuscript.

FUNDING

This work was supported by the Project of Shanghai Jiao Tong University School of Medicine Hongqiao International Medical Research Institute Open Project Fund (TRYJ2021JC05), the Shanghai Science and Technology Commission (22ZR1457100), and Famous doctor's workshop in Changning District of Shanghai (MYGZS007).

REFERENCES

Broadwater, L., Pandit, A., Clements, R., Azzam, S., Vadnal, J., Sulak, M., et al. (2011). Analysis of the mitochondrial proteome in multiple sclerosis cortex. *Biochim Biophys Acta.* 1812, 630–641. doi: 10.1016/j.bbadis.2011.01.012

Campbell, G., and Mahad, D. J. (2018). Mitochondrial dysfunction and axon degeneration in progressive multiple sclerosis. *FEBS Lett.* 592, 1113–1121. doi: 10.1002/1873-3468.13013

Claus, C., Schonefeld, K., Hubner, D., Chey, S., Reibetanz, U., and Liebert, U. G. (2013). Activity increase in respiratory chain complexes by rubella virus with marginal induction of oxidative stress. *J. Virol.* 87, 8481–8492. doi: 10.1128/JVI.00533-13

DiMauro, S., and Schon, E. A. (2003). Mitochondrial respiratory-chain diseases. *N. Engl. J. Med.* 348, 2656–2668. doi: 10.1056/NEJMra022567

DiMauro, S., Schon, E. A., Carelli, V., and Hirano, M. (2013). The clinical maze of mitochondrial neurology. *Nat. Rev. Neurol.* 9, 429–444. doi: 10.1038/nrneurol.2013.126

Kim, M., Park, S. K., Lee, S., Lee, J. A., and Park, K. (2021). Lateral spread response of different facial muscles during microvascular decompression in hemifacial spasm. *Clin. Neurophysiol.* 132, 2503–2509. doi: 10.1016/j.clinph.2021.07.020

Lin, M. T., and Beal, M. F. (2006). Mitochondrial dysfunction and oxidative stress in neurodegenerative diseases. *Nature* 443, 787–795. doi: 10.1038/nature05292

Lu, F., Selak, M., O'Connor, J., Croul, S., Lorenzana, C., Butunoi, C., et al. (2000). Oxidative damage to mitochondrial dna and activity of mitochondrial enzymes in chronic active lesions of multiple sclerosis. *J. Neurol. Sci.* 177, 95–103. doi: 10.1016/s0022-510x(00)00343-9

Luo, M., Deng, M., Yu, Z., Zhang, Y., Xu, S., Hu, S., et al. (2020). Differential susceptibility and vulnerability of brain cells in c57bl/6 mouse to mitochondrial dysfunction induced by short-term cuprizone exposure. *Front. Neuroanat.* 14:30. doi: 10.3389/fnana.2020.00030

Mahad, D. J., Ziabreva, I., Campbell, G., Lax, N., White, K., Hanson, P. S., et al. (2009). Mitochondrial changes within axons in multiple sclerosis. *Brain* 132, 1161–1174. doi: 10.1093/brain/awp046

Mancini, A., Tantucci, M., Mazzocchetti, P., de Iure, A., Durante, V., Macchioni, L., et al. (2018). Microglial activation and the nitric oxide/cgmp/pkg pathway underlie enhanced neuronal vulnerability to mitochondrial dysfunction in experimental multiple sclerosis. *Neurobiol. Dis.* 113, 97–108. doi: 10.1016/j.nbd.2018.01.002

Mao, P., and Reddy, P. H. (2010). Is multiple sclerosis a mitochondrial disease? *Biochim. Biophys. Acta* 1802, 66–79. doi: 10.1016/j.bbadis.2009.07.002

Meng-Ru, Z., Ruo-Xuan, S., Ming-Yang, Y., Tong, T., Lei, Z., Ying-Bo, Y., et al. (2021). Antagonizing astrocytic platelet activating factor receptor-neuroinflammation for total flavone of epimedium in response to cuprizone demyelination. *Int. Immunopharmacol.* 101:108181. doi: 10.1016/j.intimp.2021.108181

Mihai, D. P., Ungurianu, A., Ciotu, C. I., Fischer, M., Olaru, O. T., Nitulescu, G. M., et al. (2021). Effects of venlafaxine, risperidone and febuxostat on cuprizone-induced demyelination, behavioral deficits and oxidative stress. *Int. J. Mol. Sci.* 22:7183. doi: 10.3390/ijms22137183

Ng, X., Sadeghian, M., Heales, S., and Hargreaves, I. P. (2019). Assessment of mitochondrial dysfunction in experimental autoimmune encephalomyelitis (eae) models of multiple sclerosis. *Int. J. Mol. Sci.* 20:4975. doi: 10.3390/ijms20204975

Nicholls, D. G. (2002). Mitochondrial function and dysfunction in the cell: its relevance to aging and aging-related disease. *Int. J. Biochem. Cell Biol.* 34, 1372–1381. doi: 10.1016/s1357-2725(02)00077-8

Nikic, I., Merkler, D., Sorbara, C., Brinkoetter, M., Kreutzfeldt, M., Bareyre, F. M., et al. (2011). A reversible form of axon damage in experimental autoimmune encephalomyelitis and multiple sclerosis. *Nat. Med.* 17, 495–499. doi: 10.1038/nm.2324

Ott, M., Gogvadze, V., Orrenius, S., and Zhivotovsky, B. (2007). Mitochondria, oxidative stress and cell death. *Apoptosis* 12, 913–922. doi: 10.1007/s10495-007-0756-2

Sadeghian, M., Mastrolia, V., Rezaei, H. A., Mosley, A., Mullali, G., Schiza, D., et al. (2016). Mitochondrial dysfunction is an important cause of neurological deficits in an inflammatory model of multiple sclerosis. *Sci. Rep.* 6:33249. doi: 10.1038/srep33249

Saraswat, D., Shayya, H. J., Polanco, J. J., Tripathi, A., Welliver, R. R., Pol, S. U., et al. (2021). Overcoming the inhibitory microenvironment surrounding oligodendrocyte progenitor cells following experimental demyelination. *Nat. Commun.* 12:1923. doi: 10.1038/s41467-021-22263-4

Sen, M. K., Mahns, D. A., Coorssen, J. R., and Shortland, P. J. (2019). Behavioural phenotypes in the cuprizone model of central nervous system demyelination. *Neurosci. Biobehav. Rev.* 107, 23–46. doi: 10.1016/j.neubiorev.2019.08.008

Shao, Y., Chen, C., Zhu, T., Sun, Z., Li, S., Gong, L., et al. (2021). Trpm2 contributes to neuroinflammation and cognitive deficits in a cuprizone-induced multiple sclerosis model via nlrp3 inflammasome. *Neurobiol. Dis.* 160:105534. doi: 10.1016/j.nbd.2021.105534

Shiri, E., Pasbakhsh, P., Borhani-Haghighi, M., Alizadeh, Z., Nekoonam, S., Mojaverrostami, S., et al. (2020). Mesenchymal stem cells ameliorate cuprizone-induced demyelination by targeting oxidative stress and mitochondrial dysfunction. *Cell. Mol. Neurobiol.* 41, 1467–1481. doi: 10.1007/s10571-020-00910-6

Vidaurre, O. G., Haines, J. D., Katz, S. I., Adula, K. P., Huynh, J. L., McGraw, C. A., et al. (2014). Cerebrospinal fluid ceramides from patients with multiple sclerosis impair neuronal bioenergetics. *Brain* 137, 2271–2286. doi: 10.1093/brain/awu139

Wellman, S. M., Guzman, K., Stieger, K. C., Brink, L. E., Sridhar, S., Dubaniewicz, M. T., et al. (2020). Cuprizone-induced oligodendrocyte loss and demyelination impairs recording performance of chronically implanted neural interfaces. *Biomaterials* 239:119842. doi: 10.1016/j.biomaterials.2020.119842

Witte, M. E., Mahad, D. J., Lassmann, H., and van Horssen, J. (2014). Mitochondrial dysfunction contributes to neurodegeneration in multiple sclerosis. *Trends Mol. Med.* 20, 179–187. doi: 10.1016/j.molmed.2013.11.007

Yeung, A., Tzvetkov, N. T., Georgieva, M. G., Ognyanov, I. V., Kordos, K., Jozwik, A., et al. (2021). Reactive oxygen species and their impact in neurodegenerative diseases: literature landscape analysis. *Antioxid Redox Signal.* 34, 402–420. doi: 10.1089/ars.2019.7952

Zhao, Z., Bao, X. Q., Zhang, Z., Liu, H., and Zhang, D. (2020). Phloroglucinol derivative compound 21 attenuates cuprizone-induced multiple sclerosis mice through promoting remyelination and inhibiting neuroinflammation. *Sci. China Life Sci.* 63, 905–914. doi: 10.1007/s11427-019-9821-2

Zhao, Z., Li, T., Dong, X., Wang, X., Zhang, Z., Zhao, C., et al. (2021). Untargeted metabolomic profiling of cuprizone-induced demyelination in mouse corpus callosum by uplc-orbitrap/ms reveals potential metabolic biomarkers of cns demyelination disorders. *Oxid Med .Cell Longev.* 2021:7093844. doi: 10.1155/2021/7093844

Conflict of Interest: The authors declare that the research was conducted in the absence of any commercial or financial relationships that could be construed as a potential conflict of interest.

The reviewer JT declared a shared affiliation with the author T-QL to the handling editor at the time of review.

frontiers | Frontiers in Aging Neuroscience

ORIGINAL RESEARCH
published: 28 April 2022
doi: 10.3389/fnagi.2022.859492

AD Resemblance Atrophy Index of Brain Magnetic Resonance Imaging in Predicting the Progression of Mild Cognitive Impairment Carrying Apolipoprotein E-ε4 Allele

Yingren Mai[1†], Zhiyu Cao[1†], Jiaxin Xu[1†], Qun Yu[1], Shaoqing Yang[2], Jingyi Tang[1], Lei Zhao[3,4], Wenli Fang[1], Yishan Luo[3,4], Ming Lei[1], Vincent C. T. Mok[3,4,5], Lin Shi[3,4,6], Wang Liao[2], Jun Liu[1,2*] and the Alzheimer's Disease Neuroimaging Initiative[‡]*

[1] Department of Neurology, Sun Yat-sen Memorial Hospital, Sun Yat-sen University, Guangzhou, China, [2] Department of Neurology, The Second Affiliated Hospital of Guangzhou Medical University, Guangzhou, China, [3] BrainNow Research Institute, Shenzhen, China, [4] BrainNow Medical Technology Limited, Shenzhen, China, [5] Division of Neurology, Department of Medicine and Therapeutics, Gerald Choa Neuroscience Centre, Lui Che Woo Institute of Innovative Medicine, The Chinese University of Hong Kong, Shatin, Hong Kong SAR, China, [6] Department of Imaging and Interventional Radiology, The Chinese University of Hong Kong, Shatin, Hong Kong SAR, China

Background and Objective: Early identification is important for timely Alzheimer's disease (AD) treatment. Apolipoprotein E ε4 allele (APOE-ε4) is an important genetic risk factor for sporadic AD. The AD-Resemblance Atrophy Index (RAI)—a structural magnetic resonance imaging-derived composite index—was found to predict the risk of progression from mild cognitive impairment (MCI) to AD. Therefore, we investigated whether the AD-RAI can predict cognitive decline and progression to AD in patients with MCI carrying APOE ε4.

Methods: We included 733 participants with MCI from the Alzheimer's Disease Neuroimaging Initiative Database (ADNI). Their APOE genotypes, cognitive performance, and levels of AD-RAI were assessed at baseline and follow-up. Linear regression models were used to test the correlations between the AD-RAI and baseline cognitive measures, and linear mixed models with random intercepts and slopes were applied to investigate whether AD-RAI and APOE-ε4 can predict the level of cognitive decline. Cox proportional risk regression models were used to test the association of AD-RAI and APOE status with the progression from MCI to AD.

Results: The baseline AD-RAI was higher in the MCI converted to AD group than in the MCI stable group ($P < 0.001$). The AD-RAI was significantly correlated with cognition, and had a synergistic effect with APOE-ε4 to predict the rate of cognitive decline. The AD-RAI predicted the risk and timing of MCI progression to AD. Based on the MCI population carrying APOE-ε4, the median time to progression from MCI to AD was

OPEN ACCESS

Edited by:
Panteleimon Giannakopoulos, Université de Genève, Switzerland

Reviewed by:
Gang Wang, Ruijin Hospital, Shanghai Jiao Tong University School of Medicine, China
Haihong Zhou, Affiliated Hospital of Guangdong Medical University, China

***Correspondence:**
Wang Liao
liaowang@gzhmu.edu.cn
Jun Liu
liujun6@mail.sysu.edu.cn

[†] These authors have contributed equally to this work

[‡] Data used in preparation of this article were in part obtained from the ADNI database (adni.loni.usc.edu). As such, the investigators within the ADNI contributed to the design and implementation of ADNI and/or provided data but did not participate in analysis or writing of this report. A complete listing of ADNI investigators can be found at: http://adni.loni.usc.edu/wp-content/uploads/how_to_apply/ADNI_Acknowledgement_List.pdf

Specialty section:
This article was submitted to Alzheimer's Disease and Related Dementias, a section of the journal Frontiers in Aging Neuroscience

Received: *21 January 2022*
Accepted: *23 March 2022*
Published: *28 April 2022*

24 months if the AD-RAI $>$ 0.5, while the median time to progression from MCI to AD was 96 months for patients with an AD-RAI $\leq$ 0.5.

Conclusion: The AD-RAI can predict the risk of progression to AD in people with MCI carrying APOE ε4, is strongly correlated with cognition, and can predict cognitive decline.

Keywords: Alzheimer's disease, mild cognitive impairment, magnetic resonance imaging, AD resemblance atrophy index, APOE ε4-allele, cognition

INTRODUCTION

With more than 55 million people suffering from dementia worldwide in 2021, the prevalence of dementia has increased dramatically, and is now the most common disease among older people (Scheltens et al., 2021; The Alzheimer's Association, 2021). Alzheimer's disease (AD) is the most common type of dementia, with sporadic AD being the most common. However, the pathogenesis and etiology of AD are not yet fully understood, and treatment options and efficacy are unsatisfactory (Hodson, 2018; Liu et al., 2018; Scheltens et al., 2021). The preclinical stage of AD is mild cognitive impairment (MCI), which mainly manifests as amnesia with the preservation of other cognitive and life skills, but MCI is often considered as a sign of normal aging (Petersen, 2011; Petersen et al., 2014). The early stage of AD is the best time for patients to begin treatment (Sperling et al., 2011), and clinical or community screening to identify MCI is therefore an important tool in AD treatment.

The apolipoprotein E ε4 allele (APOE-ε4) is a key gene associated with sporadic AD, and is one of the major risk factors for AD (Corder et al., 1993; Strittmatter et al., 1993; Genin et al., 2011; Verghese et al., 2011). APOE-ε4 promotes the decrease of β-amyloid (Aβ) degradation and the brain metabolic dysfunction; this exacerbates Aβ plaque formation and tau protein phosphorylation, which in turn accelerates hippocampal atrophy (Jiang et al., 2008; Liu et al., 2015; Zalocusky et al., 2019). The risk of AD is up to 10–60 fold higher in APOE-ε4 homozygous carriers, but the ε4 allele can not identify the onset of AD or predict the rate at which MCI progresses to AD (Farrer et al., 1997). Early identification of people with MCI carrying APOE-ε4 who may progress to AD is important for the aging community and within clinics.

The pathological changes in AD, mainly Aβ deposition, tau protein phosphorylation, and neuronal necrosis, which lead to brain atrophy, can begin decades before the onset of clinical symptoms in patient with MCI (Hardy and Higgins, 1992; Dubois et al., 2021). The diagnostic methods of AD and MCI in terms of pathological examinations include cerebrospinal fluid (CSF) examination and positron emission tomography-computed tomography, but their high cost, invasiveness, and the difficulty in obtaining detection reagents make them unsuitable for routine clinical examination (Molinuevo et al., 2018; Wei et al., 2019). Magnetic resonance imaging (MRI) is a widely used clinical tool to diagnose AD and MCI. MRI is non-invasive, non-radioactive, easy to obtain, inexpensive, and can be used to monitor the progression of AD (Frisoni et al., 2010; Knight et al., 2016). With the development of neuroimaging machine learning, many studies have found that a single MRI metric can predict the risk of MCI progression to AD. For instance, hippocampal atrophy was found to predict the onset of AD in healthy populations decades in advance (Den Heijer et al., 2010). The AD-Resemblance Atrophy Index (AD-RAI) is a whole-brain model-based MRI machine-learning-derived index reflecting the similarity of an individual's atrophy pattern with that of AD patients, and is metric. Our recent study showed that the AD-RAI could accurately distinguish healthy individuals from patients with AD and predict the progression to MCI and AD with a higher accuracy than using a single brain structure (Zhao et al., 2019; Liu et al., 2021; Mai et al., 2021).

In this study, we explored whether the AD-RAI imaging index predicts progression to AD in patients with MCI carrying the APOE ε4 allele. We also analyzed the association between the AD-RAI and cognitive functioning, and whether the AD-RAI predicts cognitive decline.

MATERIALS AND METHODS

Subjects

We used data from study subjects of the multicenter study Alzheimer's Disease Neuroimaging Initiative Database (ADNI), a longitudinal multicenter study established in 2003 with the primary goal of investigating whether MRI, positron emission tomography-computed tomography, other biological markers, and clinical and neuropsychological assessments can be used to measure the progression of MCI and early AD (Mueller et al., 2005). The use of all data was approved by the Institutional Review Board of the ADNI website, and all patients signed an informed consent form. All relevant tests and methods were performed in accordance with relevant guidelines and regulations, and this study was approved by the ADNI Publications Committee.

Data on baseline demographic characteristics, APOE alleles, longitudinal neuropsychological cognitive assessments, and head MRI were collected. Only 733 patients with MCI from the ADNI-1, ADNII-GO/2, and ADNI-3 were included in this study, and detailed inclusion and exclusion criteria can be found on the ADNI website.[1] Briefly, the inclusion criteria in this study were as follows: The diagnosis of MCI was made at first admission (see

[1] http://adni.loni.usc.edu/methods/

diagnostic table for details: DXSUM_PDXCONV_ADNIALL), and patients had a baseline Mini-Mental State Examination (MMSE) scores of 24–30; patients experienced subjective memory decline, as reported by study subjects, informants, and/or clinicians, and objective memory decline was measured by delayed memory scores (scores adjusted by years of education) on the Wechsler Memory Scale; patients had no impairment in other cognitive domains, basic preservation of the ability to perform daily tasks, and the absence of dementia. For the present study, we included patients with MCI who were followed up with diagnostic and neuropsychological assessments for a mean follow-up period of 36 months, with the diagnostic follow-up ranging from 12 to 180 months and the cognitive assessment follow-up ranging from 12 to 192 months. Subjects with MCI were divided into two groups according to their diagnosis during the follow-up period, as follows: subjects with clinical symptoms and cognitive levels that met the diagnostic criteria for likely AD (2011 NIA-AA diagnostic criteria or other AD diagnostic criteria) (Mckhann et al., 2011) during the follow-up period were allocated to the MCI conversion group (MCIc group), while those with MCI who did not convert to normal functioning or to AD at the end of the follow-up period were allocated to the stable MCI group (MCIs group).

Neuropsychological Assessments

The cognitive measures included in our study were the MMSE, Clinical Dementia Rating Scale Sum of Boxes (CDR-SOB), composite scores for memory (ADNI-MEM), and executive functions (ADNI-EF). The ADNI-MEM assessment is a comprehensive tool that integrates all memory items, and its composite z score is based on the three-word recall item from the MMSE, recognition tasks from The Alzheimer's Disease Assessment Scale–Cognitive Subscale (ADAS-Cog), recall from Logical Memory I of the Wechsler Memory Test-Revised, and Rey Auditory Verbal Learning task assessment results (Van Loenhoud et al., 2019). The ADNI-EF reflects the level of executive ability and includes a composite z-score consisting of Category Fluency, the Trail-Making Test, Digit Span Backwards, Wechsler Adult Intelligence Scale–Revised Digit–Symbol Substitution, and 5 Clock Drawing items (Van Loenhoud et al., 2019). The MMSE score indicates the overall cognitive level and the CDR-SOB indicates the level of dementia.

Apolipoprotein E

All study subjects were tested for the APOE genotype. A description of the AOPE sample collection and testing methods can be found.[2] APOE is composed of three types of alleles, ε2/ε2, ε2/ε3, ε3/ε3, ε2/ε4, ε 3/ε4, and ε4/ε4 of different groups of subtype types. Patients were divided into two groups, whereby those with the APOE ε2/ε2, APOE ε2/ε3, and APOE ε3/ε3 were classified as the APOE group that did not carry the ε4 allele (ε4- group), and those with the ε3/ε4 and ε4/ε4 were the APOE group that carried the ε4 allele (ε4 + group). In this study, those carrying the ε2/ε4 phenotype were excluded.

Magnetic Resonance Imaging Acquisition and Processing

The MRI T1-weighted (T1-w) images analyzed in this study were obtained by downloading from the LONI image Data Archive. All images were acquired by Philips, Siemens, and GE scanners at baseline in the study subjects. MRI T1-weighted images in the ADNI database were standardized before uploading, and details of image scanning standards and processing methods can be found in the ADNI-MRI Technical Procedures Manual.[3] All MRI T1-weighted images were analyzed using the AccuBrain® V2.0 Magnetic Resonance Image Analysis System. AccuBrain® is based on a multi-atlas non-rigid registration scheme for brain structure segmentation and quantification, which can automatically quantify 68 brain structure indicators. The accuracy of its hippocampal segmentation and quantification has been verified in multiple datasets (Abrigo et al., 2019). AccuBrain® is a non-open source software and requires an application with BrainNow Medical Technology Limited for the relevant usage rights.

The AD-RAI is a comprehensive index based on the support vector machine model in AccuBrain®, and represents the similarity of an individual's brain atrophy pattern with that in patients with AD. The value range is 0–1, whereby 1 represents a greater similarity. When the AD-RAI $>$ 0.50, an individual is considered to have a brain structure that is more inclined toward AD and is considered more likely to have AD (Zhao et al., 2019; Mai et al., 2021). The AD-RAI status is considered positive when the AD-RAI $>$ 0.5 (AD-RAI+) and negative when the AD-RAI $\leq$ 0.5 (AD-RAI-).

Statistical Analysis

The MCI population at baseline was divided into four categories—the MCIs or MCIc group, and the APOE-ε4 or APOE-ε4+ group. Continuous variables of demographic and clinical characteristics were compared between the two groups using t-tests, and categorical variables were compared using the chi-square test. We also explored the relationships between the AD-RAI, APOE genotypes, and cognitive performance. To do this, we further divided the 733 participants into the four following groups: APOE-ε4+ plus AD-RAI-positive, only APOE-ε4+, only AD-RAI-positive, and both negative. Mann–Whitney U tests were used to compare the baseline cognitive measures among these groups. We further investigated the cross-sectional relationships using linear regression models, in which the interaction between APOE status and the AD-RAI levels was explored. A linear mixed-effects models with random intercept and slopes was used to investigate whether a higher AD-RAI and APOE4 genotype could predict faster cognitive decline of MCI patients. The interactions between AD-RAI, APOE genotype, and time were also tested.

We also investigated whether the AD-RAI and APOE genotypes could predict the rate of conversion from MCI to AD. Kaplan–Meier curves were used to show the survival rate and log-rank tests with Bonferroni correction were used to compare different curves. As we performed six times of comparisons

[2]http://adni.loni.usc.edu/methods/

[3]http://adni.loni.usc.edu/methods/documents/MRIprotocols

(intergroup comparison of the four groups), $P < 0.008(0.05/6)$ were thought to be statistically significant according to the Bonferroni method. Cox-proportional hazard regression models were used to test the association of the AD-RAI and APOE-ε4 on AD conversion. Analyses were performed in APOE-ε4+ and APOE-ε4- groups separately. Age, sex, and years of education were adjusted in these analyses, and hazard ratios (HRs) were reported. Statistical analyses were performed in R software (v. 4.1.0) and IBM SPSS Statistics (v. 25.0.0). Age, sex, and years of education were adjusted in all regression models. Statistical tests were two-tailed and $P < 0.05$ was considered significant. Bonferroni correction was conducted when making out multiple comparisons.

RESULTS

Demographic Characteristics

This study included 426 patients in the MCIs group and 307 in the MCIc group at baseline stage. Demographic information is shown in **Table 1**. The MCIc group was older than the MCIs group ($P = 0.042$) and included a larger proportion of individuals carrying the APOE ε4 allele, but there were no statistical differences in gender or education between the two groups. The MMSE, CDR-SOB, ADNI-MEM, and ADNI-EF scores were statistically different between groups ($P < 0.001$). The AD-RAI was significantly higher in the MCIc group than in the MCIs group ($P < 0.001$).

The 733 patients with MCI included 364 APOE-ε4- and 369 APOE-ε4+ patients. There were no significant differences between the APOE-ε4- and APOE-ε4+ groups in terms of age, sex, or education. In contrast, the APOE-ε4+ group had lower cognitive levels and higher AD-RAI values than the APOE-ε4- group ($P < 0.05$). The results are shown in **Table 1**.

For all 733 patients with MCI, we collected longitudinal cognitive data, and the number of cognitive measure visits was based on participant history taking or diagnostic visits, ranging from 1 to 20 visits per participant, with a median of 5. Details on the number of participants with longitudinal data of cognitive measures and diagnosis are shown in **Table 2**.

The Baseline AD-RAI and APOE-ε4 Status Were Associated Cross-Sectionally With Cognitive Performance

We first compared the cognitive measures (MMSE, CDR-SOB, ADNI-EF, and ADNI-MEM) at baseline between the four groups (APOE-ε4+ plus AD-RAI-positive group, only APOE-ε4+ group, only AD-RAI-positive group, and both negative groups). The two AD-RAI-positive groups both had worse MMSE, ADNI-EF, and ADNI-MEM scores than the other two groups with the same ApoE-ε4 status as them. The APOE-ε4 + plus AD-RAI-positive group performed better in CDR-SOB test than the only APOE-ε4 + group. We also observed better memory performance in the two APOE-ε4- groups than in the other two groups (**Figure 1**).

We further tested the cross-sectional associations of the AD-RAI and APOE-ε4 status with cognitive measures using linear regression models (see **Table 3**). After adjusting for age, sex, and years of education, both the AD-RAI and APOE-ε4 status were associated with a lower MMSE score (APOE-ε4 status: β = -0.37, $P = 0.003$; AD-RAI: β = -0.76, $P < 0.001$), ADNI-EF score (APOE-ε4 status: β = -0.16, $P = 0.008$; AD-RAI: β = -0.39, $P < 0.001$), and ADNI-MEM score (APOE-ε4 status: β = -0.19, $P = 0.023$; AD-RAI: β = -0.42, $P < 0.001$). However, no significant cross-sectional association was found between the APOE-ε4 status and CDR-SOB score (β = 0.10, $P = 0.112$), while AD-RAI status was associated with CDR-SOB scores (β = 0.33, $P < 0.001$).

The Baseline AD-RAI and APOE-ε4 Status Predicted Faster Cognitive Decline

Linear mixed-effects analysis showed that both APOE4 genotype and a baseline AD-RAI > 0.5 could predict faster yearly decline of memory (APOE-ε4 status: $P = 0.005$; AD-RAI: $P < 0.001$) and executive ability (APOE-ε4 status: $P = 0.042$; AD-RAI: $P = 0.007$) and a faster increase of dementia severity (APOE-ε4 status: $P = 0.029$; AD-RAI: $P < 0.001$) over 15 years. We did not observe

TABLE 1 | Demographic and general clinical characteristics by MCI, APOE groups.

	MCIs (n = 426)	MCIc (n = 307)	P_1	APOE-ε4- (n = 364)	APOE-ε4+ (n = 369)	P_2
Age (years), mean ± SD	72.66 ± 7.45	73.77 ± 7.00	0.042	73.59 ± 7.59	72.67 ± 6.94	0.088
Male, n (%)	244 (57.28)	189 (61.56)	0.244	215 (59.07)	218 (59.08)	0.529
Education (years), mean ± SD	15.84 ± 2.92	15.60 ± 2.74	0.760	15.97 ± 2.79	15.77 ± 2.89	0.760
APOE ε4, n (%)	175 (41.07)	113 (63.19)	<0.001	/	/	/
MCIc, n (%)	/	/	/	113 (31.04)	194 (52.57)	<0.001
MMSE, mean ± SD	27.92 ± 1.74	27.12 ± 1.72	<0.001	27.78 ± 1.71	27.39 ± 1.81	0.025
CDR-SOB, mean ± SD	1.31 ± 0.80	1.85 ± 0.93	<0.001	1.47 ± 0.89	1.62 ± 0.90	0.026
AD-MEM, mean ± SD	0.371 ± 0.645	–0.182 ± 0.528	<0.001	0.286 ± 0.677	–0.006 ± 0.605	<0.001
AD-EF, mean ± SD	0.372 ± 0.862	–0.109 ± 0.858	<0.001	0.248 ± 0.927	0.094 ± 0.850	<0.001
AD-RAI, mean ± SD	0.39 ± 0.34	0.64 ± 0.34	<0.001	0.45 ± 0.36	0.53 ± 0.37	0.003

n, number; APOE ε4, apolipoprotein E ε4-allele; MMSE, Mini-mental State Examination; CDR-SOB, Clinical Dementia Rating Scale Sum of Boxes; AD-RAI, AD resemblance atrophy index; P_1, MCIs vs MCIc; P_2, APOE-ε4- vs APOE-ε4+.

any significant association between APOE4 genotype and the yearly rate of decline of MMSE scores among participants with an AD-RAI < 0.5 at baseline ($P = 0.143$). Interestingly, we also found that the APOE4 genotype could further amplify the acceleration of cognitive decline caused by the higher level of AD-RAI. The predictive ability of the AD-RAI and APOE remained significant over 10 years (**Table 4** and **Figure 2**).

The Baseline AD-RAI Predicted the Conversion From MCI to AD in Both APOE ε4+ and APOE ε4- Individuals

This analysis included 733 patients with MCI for whom we had APOE-ε4 test results, the baseline AD-RAI, and longitude diagnosis information for up to 180 months. Kaplan–Meier curves (see **Figure 3**) showed that an AD-RAI > 0.5 (median survival time = 36 months) and an APOE-ε4 + status (median survival time = 48 months) increased the risk of AD conversion. An AD-RAI > 0.5 was associated with an increased risk of AD conversion in both the APOE-ε4 + group (AD-RAI > 0.5, median survival time = 24 months; AD-RAI < 0.5, median survival time = 96 months; $P < 0.001$) and APOE-ε4- group (AD-RAI > 0.5, median survival time = 96 months; AD-RAI < 0.5, median survival time > 180 months; $P < 0.001$). A Cox-proportional hazard regression model showed, after correcting for age, sex, and years of education, that the AD-RAI + ($HR = 2.82$, 95% confidence interval, 2.22–3.58, $P < 0.001$) and APOE-ε4 + ($HR = 2.31$, 95% confidence interval, 1.83–2.92, $P < 0.001$) were still associated with an increased risk of MCI to AD conversion, and there was no interaction between them.

TABLE 2 | Number of participants with longitudinal cognitive measures.

Time-point (month)	Diagnosis	MMSE	CDR-SOB	ADNI-MEM	ADNI-EF
0	733	733	733	733	731
6	53	646	642	646	646
12	116	697	695	699	697
18	44	259	255	259	258
24	127	571	578	575	571
30	3	5	6	5	5
36	121	458	462	469	462
48	0	302	307	322	315
54	3	4	3	6	6
60	39	192	196	212	60
66	3	16	17	24	23
72	23	134	150	165	160
78	4	17	20	30	30
84	19	100	120	135	131
90	3	17	19	33	32
96	27	91	111	102	100
102	0	29	27	26	26
108	0	75	74	57	56
114	8	11	11	9	9
120	15	37	37	28	27
126	3	9	9	7	7
132	6	18	18	12	11
144	2	11	12	11	11
150	3	5	5	5	5
156	1	3	3	2	2
162	0	3	3	0	0
168	0	1	1	1	1
174	2	1	1	2	2
180	1	1	1	0	0
192	0	2	2	0	0

DISCUSSION

This study used data from a multicenter prospective cohort study to examine whether the AD-RAI can predict the risk of progression to AD and the level of cognitive decline in patients with MCI with APOE-ε4. We found that the AD-RAI was higher in the MCI to AD conversion population, that AD-RAI predicted the progression from MCI to AD, and that it was more accurate in predicting progression to AD in patients with MCI carrying APOE-ε4. The AD-RAI predicted cognitive decline and was strongly correlated with cognitive level.

While the effect of APOE-ε4 on cognitive alterations varies according to age, APOE has been reported to significantly affect the rate of memory decline, especially in situational memory, during midlife and early old age (Caselli et al., 2009; Rawle et al., 2018). On analyzing cognitive levels in patients with MCI carrying the ε4 allele and those not carrying the ε4 allele, we found a significant correlation between the AD-RAI and cognitive decline, and a longitudinal study revealed that higher values were associated with faster rates of cognitive decline and a synergistic effect with APOEε4. Cognitive functions such as learning and memory are dependent on hippocampal synaptic plasticity, constant neurogenesis, and communication within the brain's memory network (Anacker and Hen, 2017). APOEε4 has been found to damage cognition-related brain structures and cognition-related pathways, increase tau deposition in medial temporal lobe regions, and accelerate hippocampal atrophy, further leading to cognitive deficits (Cho et al., 2016). Cognition is strongly correlated with atrophy of brain structures, and learning and memory impairments have been associated with atrophy of brain structures such as the hippocampus and amygdala (Yavuz et al., 2007; Sluimer et al., 2008; Guzmán-Vélez et al., 2016). Cognitive decline, such as memory decline, is common in patients with AD, and 90% of amnestic MCI cases progress to AD (Petersen et al., 2005; Hodson, 2018). The AD-RAI is strongly correlated with the composite memory score of the ADNI-MEM (Crane et al., 2012), and the AD-RAI is a composite of characteristic atrophied brain structures associated with AD (Zhao et al., 2019; Mai et al., 2021). Therefore, the AD-RAI can be used as a composite of indexes of cognitive-related brain structures underpinning functions such as memory to predict cognitive decline associated with AD.

Hippocampal atrophy and hippocampal volume are an important markers for diagnosing AD with dementia or as a prognostic biomarker for predicting the transition from MCI to AD, and have been widely used for AD screening

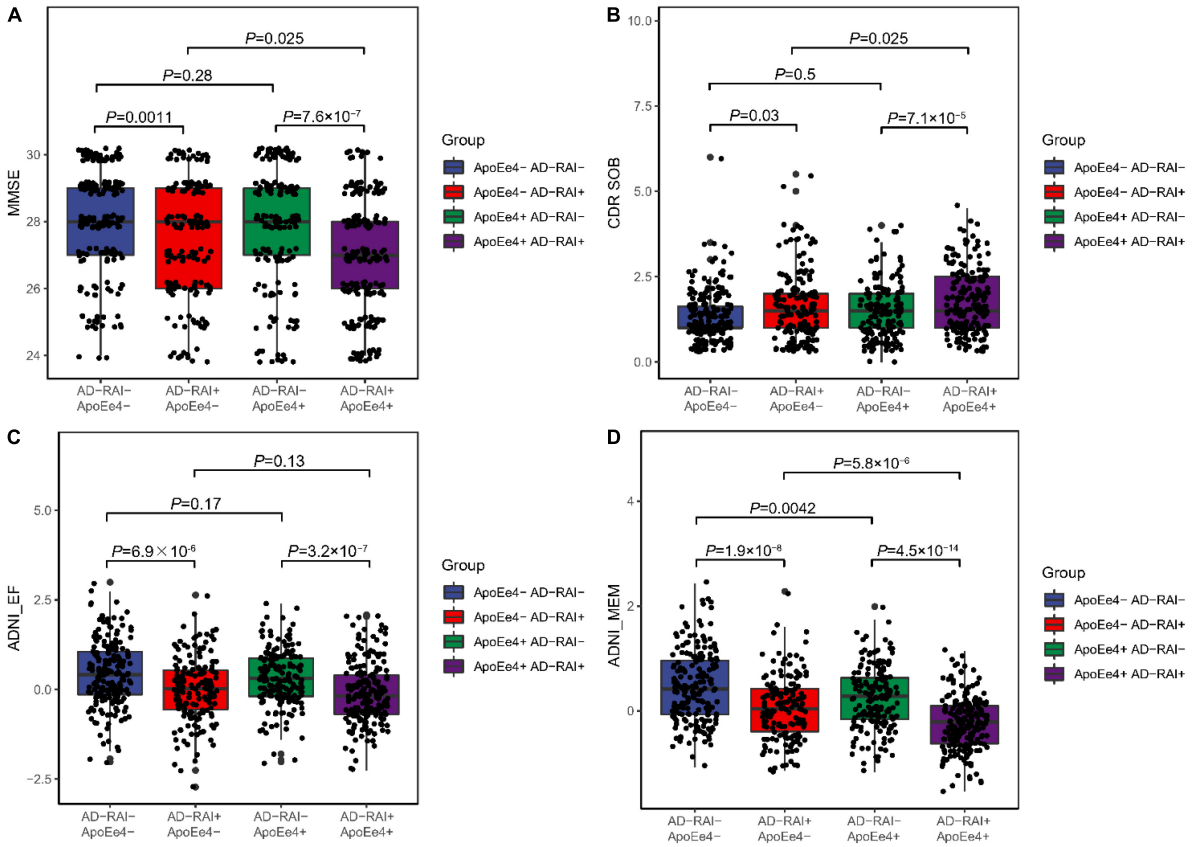

FIGURE 1 | Associations of AD-RAI and APOE ε4 with cognitive measures among MCI patients. We categorized the participants into four groups: APOE-ε4+ plus AD-RAI-positive group (AD-RAI + APOE-ε4+), only APOE-ε4+ group (AD- RAI-, APOE-ε-4+), only AD-RAI-positive group (AD-RAI + APOE-ε4-) and both negative group (AD- RAI-, APOE-ε4-). We found that scores of MMSE **(A)**, ADNI-EF **(C)** and ADNI-MEM **(D)** were significantly higher in the two AD-RAI-positive groups. We also observed better memory performance **(D)** in the two APOE-ε4+ groups. The APOE-ε4+ plus AD-RAI-positive group performed better in CDR-SOB test than the only APOE-ε4+ group **(B)**. (PS: Jittering was used to avoid severe dot overlap).

TABLE 3 | Baseline associations of AD-RAI and APOE status with cognitive measures.

Independent Factors	Statistics	MMSE	CDR-SOB	ADNI-EF	ADNI-MEM
APOE Status, ε4 +	β	−0.37	0.10	−0.16	−0.27
	95% *CI*[1]	−0.62, -0.13	−0.02, 0.23	−0.28, -0.04	−0.36, -0.19
	P value	0.003*	0.112	0.008*	<0.001*
Baseline AD-RAI>0.5	β	−0.76	0.33	−0.39	−0.42
	95% *CI*	−1.20, -0.36	0.20, 0.46	−0.51, -0.27	−0.51, -0.34
	P value	<0.001*	<0.001*	<0.001*	<0.001*

MMSE, Mini-Mental State Examination; CDR-SOB, Clinical Dementia Rating Scale Sum of Boxes; MEM, Memory Function; EF, Executive Function.
**Statistically significant.*
All models were adjusted for age, gender and education. No significant interaction was found between AD-RAI and APOE status.

and clinical diagnosis (Jack et al., 2013a; Ruan et al., 2016). Hippocampal atrophy is a better predictor of progression in Aβ-positive MCI populations than CSF Aβ because there is a plateau in Aβ aggregation, whereas there is no plateau in the rate of hippocampal atrophy (Jack et al., 2010; Jack et al., 2013b). The amygdala, temporal lobe, and insula have also been used as early biomarkers to distinguish MCI from AD (Dubois et al., 2007; De Jong et al., 2008; Jack et al., 2013a). However, as a heterogeneous disease, there is heterogeneity in the atrophy of brain structures in AD (Poulakis et al., 2018). The AD-RAI is based on an atrophy of brain structures that is characteristic of AD in the whole brain, and is 92% accurate in differentiating healthy subjects from patients with AD, which is almost identical

TABLE 4 | Estimates of mean yearly rates of change in the cognitive measures of individuals with different APOE genotypes and AD-RAI levels.

Groups	MMSE	CDR-SOB	ADNI-EF	ADNI-MEM
APOE-ε4- AD-RAI-negative	–0.49	0.15	–0.06	–0.04
APOE-ε4- AD-RAI-positive	–0.70*	0.41*	–0.08*	–0.07*
APOE-ε4 + AD-RAI-negative	–0.64	0.38*	–0.10*	–0.08*
APOE-ε4 + AD-RAI-positive	–1.40*	1.00*	–0.15*	–0.12*

MMSE, Mini-Mental State Examination; CDR-SOB, Clinical Dementia Rating Scale Sum of Boxes; MEM, Memory Function; EF: Executive Function.
**Statistically significant when compared with the APOE-ε4- plus AD-RAI-negative group.*
The analyses were based on 15-year follow-up data and 10-year follow-up data respectively. There were no significant changes in the results. All models were adjusted for age, gender and education.

to the accuracy of CSF biomarkers (Mai et al., 2021). In this study, we found that the AD-RAI predicted the risk of progression to AD in those with MCI, and the time to conversion to AD in patients with MCI was significantly shorter when their AD-RAI was >0.5. Consistent with our previous study, the AD-RAI was able to assess and predict structural brain indicators of the progression from normal functioning to MCI, and from MCI to AD (Zhao et al., 2019).

In the present study, the AD-RAI was better able to predict the progression to AD in patients with MCI carrying the APOE-ε4 allele than in patients with MCI not carrying the APOE ε4-allele. Patients with MCI carrying APOE-ε4 converted to AD in a shorter time than those not carrying the allele. Many studies have shown that APOE-ε4 promotes Aβ deposition in the brain (including neocortical areas) and disrupts the cortico-hippocampal network, which indirectly causes hippocampal atrophy through cortical denervation, further affecting the rate of hippocampal volume loss and gray matter atrophy (Geroldi et al., 2000; Schuff et al., 2009; Hesse et al., 2019; Yan et al., 2020). In contrast, the APOE-ε4-positive MCI population already has significant pathological changes, such as structural brain atrophy or Aβ deposition, and the use of only single characteristic brain structures or CSF Aβ has been found to lead to a decreased sensitivity in predicting the progression of MCI to AD (Jack et al., 2010). In another study, the AD-RAI was more accurate than single hippocampal and temporal

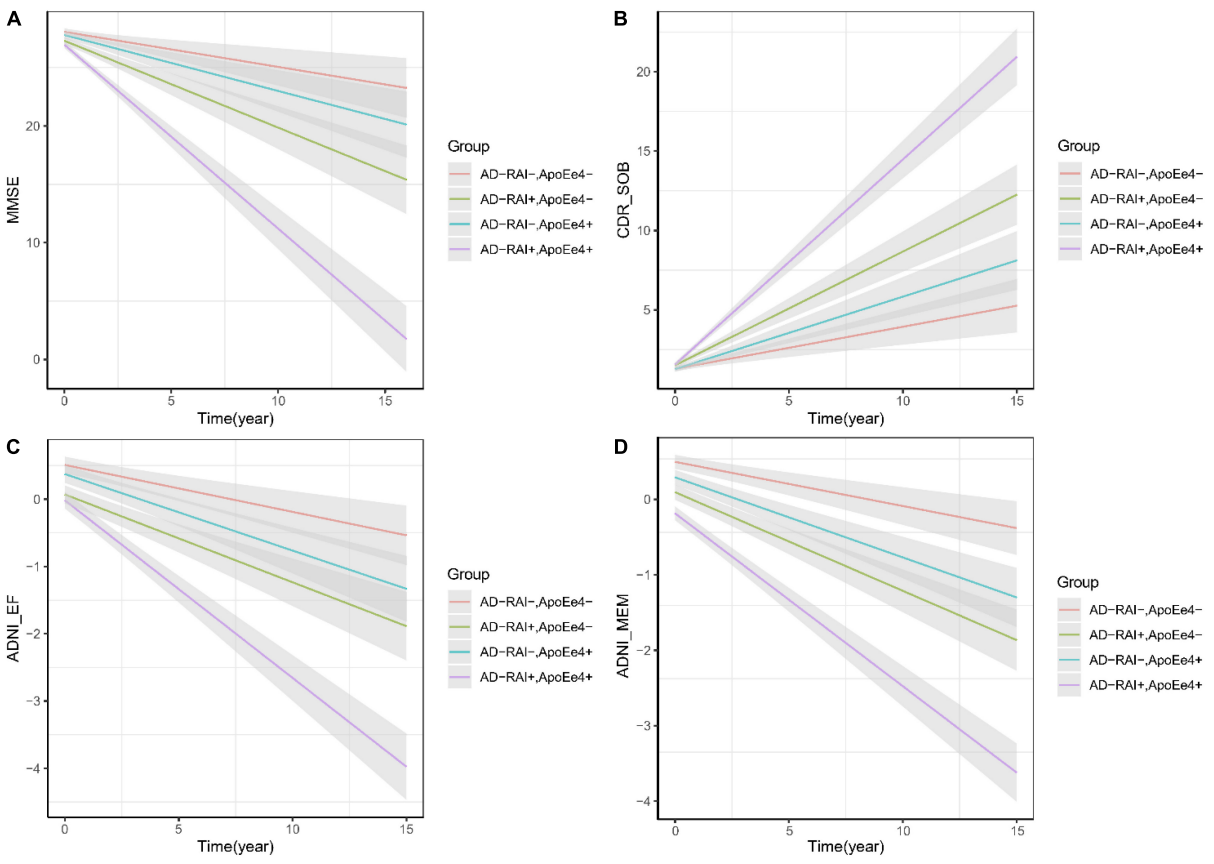

FIGURE 2 | AD-RAI and APOE-ε4 as predictors of cognitive decline of MCI patients. Both AD-RAI-positive groups and APOE-ε4 + groups showed faster decline of memory **(D)** and executive ability **(C)** than their corresponding control groups. In our analysis, APOE-ε4+ failed to predict a faster decline of MMSE scores **(A)** among MCI patients with AD-RAI < 0.5 at baseline, but it was found to further amplify the acceleration of cognitive decline **(A–D)** in those with AD-RAI > 0.5.

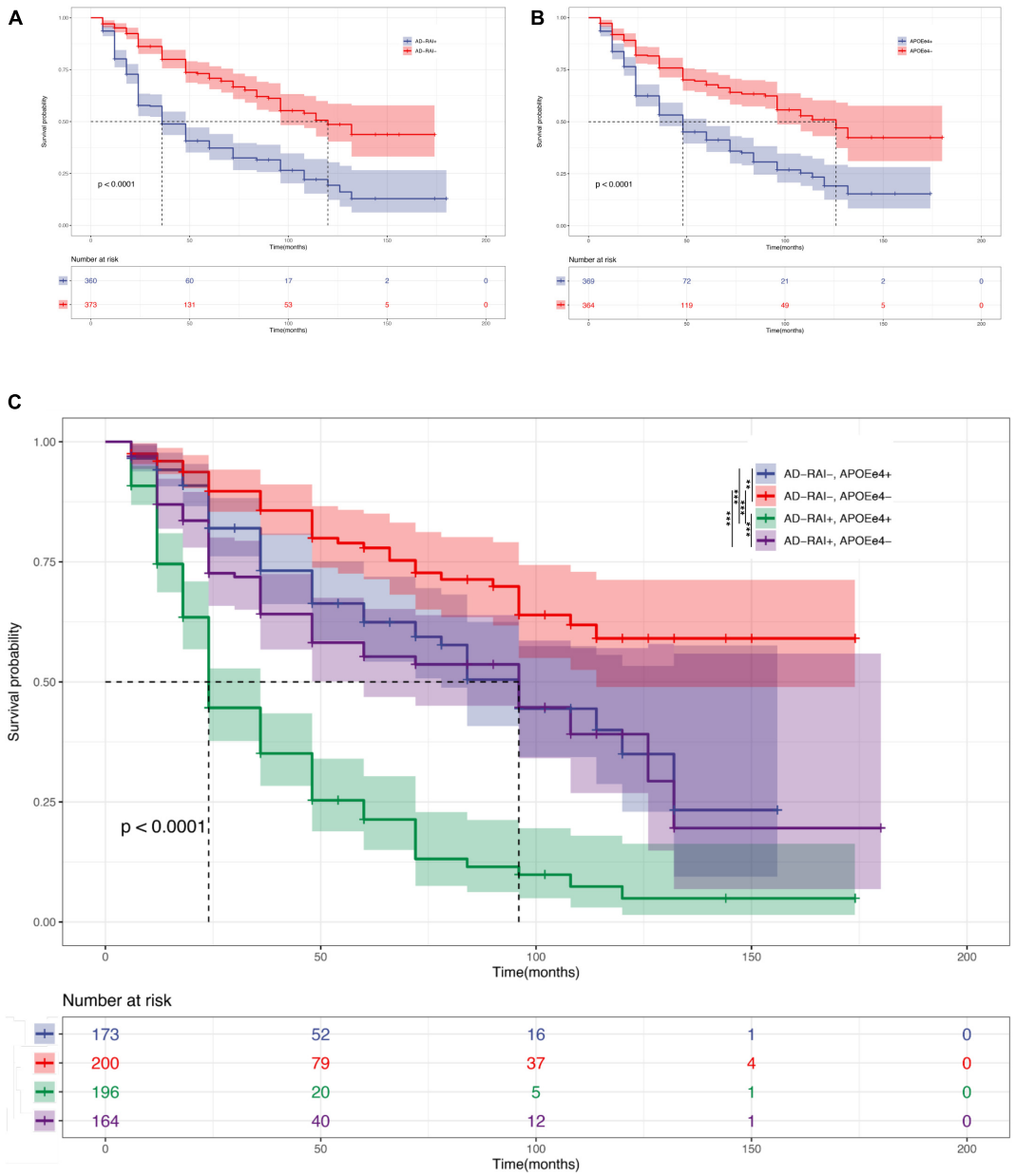

FIGURE 3 | AD-RAI and APOE-ε4 as predictors in MCI. Kaplan–Meier curves showing that AD-RAI+ **(A)** and APOE-ε4+ **(B)** increased the risk of MCI progression. AD-RAI+ together with APOE-ε4+ reached the highest speed of AD conversion **(C)**. *$P < 0.05$; **$P < 0.01$; ***$P < 0.001$.

brain structure characteristics in predicting and diagnosing AD (Mai et al., 2021). We performed a Cox-proportional risk analysis of the AD-RAI and APOE ε4, and found that the AD-RAI can independently predict the conversion of MCI to AD, independent of APOE. The APOE-ε4 allele is not only one of the strongest risk factors for AD but it is also a risk factor for Lewy body dementia (Mirza et al., 2019). Our previous study of the AD-RAI in differentiating AD from frontotemporal dementia revealed that the AD-RAI was more suitable for differentiating AD from healthy individuals and less accurate in frontotemporal dementia in terms of diagnostic accuracy (Yu et al., 2021). Therefore, the AD-RAI may be targeted to predict MCI progression to AD, and can accurately predict progression in patients with MCI with the APOE-ε4 allele.

The present study has some limitations. First, the population targeted in this study was patients with MCI; while our findings indicate that the AD-RAI can predict the risk of MCI progression to AD in those with the APOE-ε4 allele, the prediction of the risk of MCI or AD in APOE-ε4-positive healthy population is unknown, and it is possible that the AD-RAI differently predicts the risk of progression and cognitive decline in healthy

individuals. Second, we excluded those carrying the ε2/ε4 allele, given the protective role of the ε2 allele against AD and the lack of studies on the ε2/ε4 allele in AD. Therefore, future studies could include healthy participants and those carrying the ε2/ε4 allele to further confirm the ability of the AD-RAI to predict AD risk. Third, the present study was a cross-sectional study of the AD-RAI and did not explore longitudinal changes in the AD-RAI to assess its numerical stability in continuous testing. Finally, we only considered the conversion of MCI to AD, without considering MCI subtypes and biomarkers. Therefore, the next step could be to analyze longitudinal studies of the AD-RAI in different populations to examine the validity of the AD-RAI for clinical and community applications.

In conclusion, the AD-RAI can be used as a prognostic imaging marker in patients with MCI carrying the APOE-ε4 allele, and can accurately and effectively predict the risk of progression to AD in both patients with MCI carrying APOE-ε4 and those without APOE-ε4. The AD-RAI was strongly correlated with cognition and could predict cognitive decline. Therefore, this study supports the use of the AD-RAI as a non-invasive diagnostic and prognostic tool for AD; the AD-RAI can be objectively, economically, simply, and efficiently applied in the clinic or community to identify the onset of early AD.

DATA AVAILABILITY STATEMENT

The raw data supporting the conclusions of this article will be made available by the authors, without undue reservation.

ETHICS STATEMENT

The studies involving human participants were reviewed and approved by the Ludwig-Maximilians Universität München institutional review board (IRB). The patients/participants provided their written informed consent to participate in this study.

AUTHOR CONTRIBUTIONS

YM, ZC, JX, and JL designed the study. YM, ZC, and JX analyzed data, composition of figures and drafted the manuscript. QY, JT, WF, and LZ collected the data. VM, LS, and YL contributed to the MRI acquisition and processing. SY and ML interpreted data for the study. WL and JL contributed to the study supervision and critical review of manuscript for intellectual content. All authors gave their final approval of the version to be published and agreed to be accountable for all aspects of the work.

FUNDING

This study was supported by the grant provided by funding from the National Nature Science Foundation of China (grant numbers 82171178, 81801083, and 82101271), the Natural Science Foundation of Guangdong Province (grant numbers 2020A1515010210 and 2020A1515110317), and the Research and Development program in key areas of Science and Technology Program of Guangzhou, China (grant number 202007030010). Data collection and sharing for this project was funded by the Alzheimer's Disease Neuroimaging Initiative (ADNI; National Institutes of Health Grant U01 AG024904) and DOD ADNI (Department of Defense award number W81XWH-12-2-0012). ADNI was funded by the National Institute on Aging and the National Institute of Biomedical Imaging and Bioengineering and through generous contributions from the following: AbbVie, Alzheimer's Association; Alzheimer's Drug Discovery Foundation; Araclon Biotech; BioClinica, Inc.; Biogen; Bristol-Myers Squibb Company; CereSpir, Inc.; Cogstate; Eisai Inc.; Elan Pharmaceuticals, Inc.; Eli Lilly and Company; EuroImmun; F. Hoffmann-La Roche Ltd. and its affiliated company Genentech, Inc.; Fujirebio; GE Healthcare; IXICO Ltd.; Janssen Alzheimer Immunotherapy Research & Development, LLC.; Johnson & Johnson Pharmaceutical Research & Development LLC.; Lumosity; Lundbeck; Merck & Co., Inc.; Meso Scale Diagnostics, LLC.; NeuroRx Research; Neurotrack Technologies; Novartis Pharmaceuticals Corporation; Pfizer Inc.; Piramal Imaging; Servier; Takeda Pharmaceutical Company; and Transition Therapeutics. The Canadian Institutes of Health Research provided funds to support ADNI clinical sites in Canada. Private sector contributions are facilitated by the Foundation for the National Institutes of Health (www.fnih.org). The grantee organization is the Northern California Institute for Research and Education, and the study is coordinated by the Alzheimer's Therapeutic Research Institute at the University of Southern California. ADNI data are disseminated by the Laboratory for Neuro Imaging at the University of Southern California.

REFERENCES

Abrigo, J., Shi, L., Luo, Y., Chen, Q., Chu, W. C. W., and Mok, V. C. T. (2019). Standardization of hippocampus volumetry using automated brain structure volumetry tool for an initial Alzheimer's disease imaging biomarker. *Acta Radiol.* 60, 769–776. doi: 10.1177/0284185118795327

Anacker, C., and Hen, R. (2017). Adult hippocampal neurogenesis and cognitive flexibility - linking memory and mood. *Nat. Rev. Neurosci.* 18, 335–346. doi: 10.1038/nrn.2017.45

Caselli, R. J., Dueck, A. C., Osborne, D., Sabbagh, M. N., Connor, D. J., Ahern, G. L., et al. (2009). Longitudinal modeling of age-related memory decline and the APOE epsilon4 effect. *N. Engl. J. Med.* 361, 255–263. doi: 10.1056/NEJMoa0809437

Cho, H., Choi, J. Y., Hwang, M. S., Lee, J. H., Kim, Y. J., Lee, H. M., et al. (2016). Tau PET in Alzheimer disease and mild cognitive impairment. *Neurology* 87, 375–383. doi: 10.1212/wnl.0000000000002892

Corder, E. H., Saunders, A. M., Strittmatter, W. J., Schmechel, D. E., Gaskell, P. C., Small, G. W., et al. (1993). Gene dose of apolipoprotein E type 4 allele and the risk of Alzheimer's disease in late onset families. *Science* 261, 921–923. doi: 10.1126/science.8346443

Crane, P. K., Carle, A., Gibbons, L. E., Insel, P., Mackin, R. S., Gross, A., et al. (2012). Development and assessment of a composite score for memory in the Alzheimer's Disease Neuroimaging Initiative (ADNI). *Brain Imaging Behav.* 6, 502–516. doi: 10.1007/s11682-012-9186-z

De Jong, L. W., Van Der Hiele, K., Veer, I. M., Houwing, J. J., Westendorp, R. G., Bollen, E. L., et al. (2008). Strongly reduced volumes of putamen and thalamus

in Alzheimer's disease: an MRI study. *Brain* 131, 3277–3285. doi: 10.1093/brain/awn278

Den Heijer, T., Van Der Lijn, F., Koudstaal, P. J., Hofman, A., Van Der Lugt, A., Krestin, G. P., et al. (2010). A 10-year follow-up of hippocampal volume on magnetic resonance imaging in early dementia and cognitive decline. *Brain* 133, 1163–1172. doi: 10.1093/brain/awq048

Dubois, B., Feldman, H. H., Jacova, C., Dekosky, S. T., Barberger-Gateau, P., Cummings, J., et al. (2007). Research criteria for the diagnosis of Alzheimer's disease: revising the NINCDS-ADRDA criteria. *Lancet Neurol.* 6, 734–746. doi: 10.1016/S1474-4422(07)70178-3

Dubois, B., Villain, N., Frisoni, G. B., Rabinovici, G. D., Sabbagh, M., Cappa, S., et al. (2021). Clinical diagnosis of Alzheimer's disease: recommendations of the International Working Group. *Lancet Neurol.* 20, 484–496. doi: 10.1016/S1474-4422(21)00066-1

Farrer, L. A., Cupples, L. A., Haines, J. L., Hyman, B., Kukull, W. A., Mayeux, R., et al. (1997). Effects of age, sex, and ethnicity on the association between apolipoprotein E genotype and Alzheimer disease. a meta-analysis. APOE and alzheimer disease meta analysis consortium. *Jama* 278, 1349–1356. doi: 10.1001/jama.278.16.1349

Frisoni, G. B., Fox, N. C., Jack, C. R. Jr., Scheltens, P., and Thompson, P. M. (2010). The clinical use of structural MRI in Alzheimer disease. *Nat. Rev. Neurol.* 6, 67–77. doi: 10.1038/nrneurol.2009.215

Genin, E., Hannequin, D., Wallon, D., Sleegers, K., Hiltunen, M., Combarros, O., et al. (2011). APOE and Alzheimer disease: a major gene with semi-dominant inheritance. *Mol. Psychiatry* 16, 903–907. doi: 10.1038/mp.2011.52

Geroldi, C., Laakso, M. P., Decarli, C., Beltramello, A., Bianchetti, A., Soininen, H., et al. (2000). Apolipoprotein E genotype and hippocampal asymmetry in Alzheimer's disease: a volumetric MRI study. *J. Neurol. Neurosurg. Psychiatry* 68, 93–96. doi: 10.1136/jnnp.68.1.93

Guzmán-Vélez, E., Warren, D. E., Feinstein, J. S., Bruss, J., and Tranel, D. (2016). Dissociable contributions of amygdala and hippocampus to emotion and memory in patients with Alzheimer's disease. *Hippocampus* 26, 727–738. doi: 10.1002/hipo.22554

Hardy, J. A., and Higgins, G. A. (1992). Alzheimer's disease: the amyloid cascade hypothesis. *Science* 256, 184–185.

Hesse, R., Hurtado, M. L., Jackson, R. J., Eaton, S. L., Herrmann, A. G., Colom-Cadena, M., et al. (2019). Comparative profiling of the synaptic proteome from Alzheimer's disease patients with focus on the APOE genotype. *Acta Neuropathol. Commun.* 7:214. doi: 10.1186/s40478-019-0847-7

Hodson, R. (2018). Alzheimer's disease. *Nature* 559:S1.

Jack, C. R. Jr., Knopman, D. S., Jagust, W. J., Petersen, R. C., Weiner, M. W., Aisen, P. S., et al. (2013a). Tracking pathophysiological processes in Alzheimer's disease: an updated hypothetical model of dynamic biomarkers. *Lancet Neurol.* 12, 207–216. doi: 10.1016/S1474-4422(12)70291-0

Jack, C. R. Jr., Wiste, H. J., Lesnick, T. G., Weigand, S. D., Knopman, D. S., Vemuri, P., et al. (2013b). Brain β-amyloid load approaches a plateau. *Neurology* 80, 890–896. doi: 10.1212/wnl.0b013e3182840bbe

Jack, C. R. Jr., Wiste, H. J., Vemuri, P., Weigand, S. D., Senjem, M. L., Zeng, G., et al. (2010). Brain beta-amyloid measures and magnetic resonance imaging atrophy both predict time-to-progression from mild cognitive impairment to Alzheimer's disease. *Brain* 133, 3336–3348. doi: 10.1093/brain/awq277

Jiang, Q., Lee, C. Y., Mandrekar, S., Wilkinson, B., Cramer, P., Zelcer, N., et al. (2008). ApoE promotes the proteolytic degradation of Abeta. *Neuron* 58, 681–693. doi: 10.1016/j.neuron.2008.04.010

Knight, M. J., Mccann, B., Kauppinen, R. A., and Coulthard, E. J. (2016). Magnetic Resonance Imaging to Detect Early Molecular and Cellular Changes in Alzheimer's Disease. *Front. Aging Neurosci.* 8:139. doi: 10.3389/fnagi.2016.00139

Liu, W., Au, L. W. C., Abrigo, J., Luo, Y., Wong, A., Lam, B. Y. K., et al. (2021). MRI-based Alzheimer's disease-resemblance atrophy index in the detection of preclinical and prodromal Alzheimer's disease. *Aging (Albany NY)* 13, 13496–13514. doi: 10.18632/aging.203082

Liu, X., Chen, K., Wu, T., Weidman, D., Lure, F., and Li, J. (2018). Use of multimodality imaging and artificial intelligence for diagnosis and prognosis of early stages of Alzheimer's disease. *Transl. Res.* 194, 56–67. doi: 10.1016/j.trsl.2018.01.001

Liu, Y., Yu, J. T., Wang, H. F., Han, P. R., Tan, C. C., Wang, C., et al. (2015). APOE genotype and neuroimaging markers of Alzheimer's disease: systematic review and meta-analysis. *J. Neurol. Neurosurg. Psychiatry* 86, 127–134. doi: 10.1136/jnnp-2014-307719

Mai, Y., Yu, Q., Zhu, F., Luo, Y., Liao, W., Zhao, L., et al. (2021). AD Resemblance atrophy index as a diagnostic biomarker for alzheimer's disease: a retrospective clinical and biological validation. *J. Alzheimers Dis.* 79, 1023–1032. doi: 10.3233/JAD-201033

Mckhann, G. M., Knopman, D. S., Chertkow, H., Hyman, B. T., Jack, C. R. Jr., Kawas, C. H., et al. (2011). The diagnosis of dementia due to alzheimer's disease: recommendations from the national institute on aging-alzheimer's association workgroups on diagnostic guidelines for alzheimer's disease. *Alzheimers Dement.* 7, 263–269. doi: 10.1016/j.jalz.2011.03.005

Mirza, S. S., Saeed, U., Knight, J., Ramirez, J., Stuss, D. T., Keith, J., et al. (2019). APOE ε4, white matter hyperintensities, and cognition in Alzheimer and Lewy body dementia. *Neurology* 93, e1807–e1819. doi: 10.1212/WNL.0000000000008377

Molinuevo, J. L., Ayton, S., Batrla, R., Bednar, M. M., Bittner, T., Cummings, J., et al. (2018). Current state of Alzheimer's fluid biomarkers. *Acta Neuropathol.* 136, 821–853. doi: 10.1007/s00401-018-1932-x

Mueller, S. G., Weiner, M. W., Thal, L. J., Petersen, R. C., Jack, C. R., Jagust, W., et al. (2005). Ways toward an early diagnosis in Alzheimer's disease: the Alzheimer's Disease Neuroimaging Initiative (ADNI). *Alzheimers Dement.* 1, 55–66. doi: 10.1016/j.jalz.2005.06.003

Petersen, R. C. (2011). Clinical practice. Mild cognitive impairment. *N. Engl. J. Med.* 364, 2227–2234. doi: 10.1056/NEJMcp0910237

Petersen, R. C., Caracciolo, B., Brayne, C., Gauthier, S., Jelic, V., and Fratiglioni, L. (2014). Mild cognitive impairment: a concept in evolution. *J. Intern. Med.* 275, 214–228.

Petersen, R. C., Thomas, R. G., Grundman, M., Bennett, D., Doody, R., Ferris, S., et al. (2005). Vitamin E and donepezil for the treatment of mild cognitive impairment. *N. Engl. J. Med.* 352, 2379–2388.

Poulakis, K., Pereira, J. B., Mecocci, P., Vellas, B., Tsolaki, M., Kloszewska, I., et al. (2018). Heterogeneous patterns of brain atrophy in Alzheimer's disease. *Neurobiol. Aging* 65, 98–108. doi: 10.1016/j.neurobiolaging.2018.01.009

Rawle, M. J., Davis, D., Bendayan, R., Wong, A., Kuh, D., and Richards, M. (2018). Apolipoprotein-E (Apoe) ε4 and cognitive decline over the adult life course. *Transl. Psychiatry* 8:18. doi: 10.1038/s41398-017-0064-8

Ruan, Q., D'onofrio, G., Sancarlo, D., Bao, Z., Greco, A., and Yu, Z. (2016). Potential neuroimaging biomarkers of pathologic brain changes in Mild Cognitive Impairment and Alzheimer's disease: a systematic review. *BMC Geriatr.* 16:104. doi: 10.1186/s12877-016-0281-7

Scheltens, P., De Strooper, B., Kivipelto, M., Holstege, H., Chételat, G., Teunissen, C. E., et al. (2021). Alzheimer's disease. *Lancet* 397, 1577–1590.

Schuff, N., Woerner, N., Boreta, L., Kornfield, T., Shaw, L. M., Trojanowski, J. Q., et al. (2009). MRI of hippocampal volume loss in early Alzheimer's disease in relation to ApoE genotype and biomarkers. *Brain* 132, 1067–1077. doi: 10.1093/brain/awp007

Sluimer, J. D., Van Der Flier, W. M., Karas, G. B., Fox, N. C., Scheltens, P., Barkhof, F., et al. (2008). Whole-brain atrophy rate and cognitive decline: longitudinal MR study of memory clinic patients. *Radiology* 248, 590–598. doi: 10.1148/radiol.2482070938

Sperling, R. A., Jack, C. R. Jr., and Aisen, P. S. (2011). Testing the right target and right drug at the right stage. *Sci. Transl. Med.* 3:111cm133. doi: 10.1126/scitranslmed.3002609

Strittmatter, W. J., Weisgraber, K. H., Huang, D. Y., Dong, L. M., Salvesen, G. S., Pericak-Vance, M., et al. (1993). Binding of human apolipoprotein E to synthetic amyloid beta peptide: isoform-specific effects and implications for late-onset Alzheimer disease. *Proc. Natl. Acad. Sci. U.S.A.* 90, 8098–8102. doi: 10.1073/pnas.90.17.8098

The Alzheimer's Association (2021). 2021 Alzheimer's disease facts and figures. *Alzheimers Dement.* 17, 327–406. doi: 10.1002/alz.12328

Van Loenhoud, A. C., Van Der Flier, W. M., Wink, A. M., Dicks, E., Groot, C., Twisk, J., et al. (2019). Cognitive reserve and clinical progression in Alzheimer disease: a paradoxical relationship. *Neurology* 93, e334–e346. doi: 10.1212/WNL.0000000000007821

Verghese, P. B., Castellano, J. M., and Holtzman, D. M. (2011). Apolipoprotein e in Alzheimer's disease and other neurological disorders. *Lancet Neurol.* 10, 241–252. doi: 10.1016/S1474-4422(10)70325-2

Wei, M., Shi, J., Ni, J., Zhang, X., Li, T., Chen, Z., et al. (2019). A new age-related cutoff of medial temporal atrophy scale on MRI improving the diagnostic accuracy of neurodegeneration due to Alzheimer's disease in a Chinese population. *BMC Geriatr.* 19:59. doi: 10.1186/s12877-019-1072-8

Yan, S., Zheng, C., Paranjpe, M. D., Li, J., Benzinger, T. L. S., Lu, J., et al. (2020). Association of sex and APOE ε4 with brain tau deposition and atrophy in older adults with Alzheimer's disease. *Theranostics* 10, 10563–10572. doi: 10.7150/thno.48522

Yavuz, B. B., Ariogul, S., Cankurtaran, M., Oguz, K. K., Halil, M., Dagli, N., et al. (2007). Hippocampal atrophy correlates with the severity of cognitive decline. *Int. Psychogeriatr.* 19, 767–777. doi: 10.1017/S1041610206004303

Yu, Q., Mai, Y., Ruan, Y., Luo, Y., Zhao, L., Fang, W., et al. (2021). An MRI-based strategy for differentiation of frontotemporal dementia and Alzheimer's disease. *Alzheimers Res. Ther.* 13:23. doi: 10.1186/s13195-020-00757-5

Zalocusky, K. A., Nelson, M. R., and Huang, Y. (2019). An Alzheimer's-disease-protective APOE mutation. *Nat. Med.* 25, 1648–1649. doi: 10.1038/s41591-019-0634-9

Zhao, L., Luo, Y., Lew, D., Liu, W., Au, L., Mok, V., et al. (2019). Risk estimation before progression to mild cognitive impairment and Alzheimer's disease: an AD resemblance atrophy index. *Aging (Albany NY)* 11, 6217–6236. doi: 10.18632/aging.102184

Conflict of Interest: LS is the director of BrainNow Medical Technology Limited. VM is the chief medical consultant of BrainNow Medical Technology Limited. YL and LZ are employed by BrainNow Medical Technology Limited.

The remaining authors declare that the research was conducted in the absence of any commercial or financial relationships that could be construed as a potential conflict of interest.

Publisher's Note: All claims expressed in this article are solely those of the authors and do not necessarily represent those of their affiliated organizations, or those of the publisher, the editors and the reviewers. Any product that may be evaluated in this article, or claim that may be made by its manufacturer, is not guaranteed or endorsed by the publisher.

Citation: Mai Y, Cao Z, Xu J, Yu Q, Yang S, Tang J, Zhao L, Fang W, Luo Y, Lei M, Mok VCT, Shi L, Liao W, Liu J and The Alzheimer's Disease Neuroimaging Initiative (2022) AD Resemblance Atrophy Index of Brain Magnetic Resonance Imaging in Predicting the Progression of Mild Cognitive Impairment Carrying Apolipoprotein E-ε4 Allele. Front. Aging Neurosci. 14:859492. doi: 10.3389/fnagi.2022.859492

frontiers | Frontiers in Cellular Neuroscience

ORIGINAL RESEARCH
published: 28 April 2022
doi: 10.3389/fncel.2022.878673

TAT-HSP27 Peptide Improves Neurologic Deficits *via* Reducing Apoptosis After Experimental Subarachnoid Hemorrhage

Xiao-yan Zhou[1,2,3,4†], *Jing-yi Sun*[5†], *Wei-qi Wang*[6†], *Shu-xian Li*[7†], *Han-xia Li*[7], *Hui-juan Yang*[7], *Ming-feng Yang*[7], *Hui Yuan*[7], *Zong-yong Zhang*[6,7*], *Bao-liang Sun*[7*] and *Jin-Xiang Han*[2,3,4*]

[1] Department of Biochemistry and Molecular Biology, School of Basic Medical Sciences, Shandong University, Ji'nan, China, [2] Department of Neurosurgery, First Affiliated Hospital of Shandong First Medical University and Shandong Academy of Medical Sciences, Ji'nan, China, [3] Biomedical Sciences College and Shandong Medicinal Biotechnology Centre, Shandong First Medical University and Shandong Academy of Medical Sciences, Ji'nan, China, [4] Key Lab for Biotech-Drugs of National Health Commission, Shandong First Medical University and Shandong Academy of Medical Sciences, Ji'nan, China, [5] Department of Orthopedics, Shandong Provincial Hospital Affiliated to Shandong First Medical University and Shandong Academy of Medical Sciences, Jinan, China, [6] Department of Neurology, Shandong Provincial Hospital Affiliated to Shandong First Medical University and Shandong Academy of Medical Sciences, Jinan, China, [7] Department of Neurology, Key Laboratory of Cerebral Microcirculation, Second Affiliated Hospital of Shandong First Medical University and Shandong Academy of Medical Sciences, Taian, China

Cell apoptosis plays an important role in early brain injury (EBI) after subarachnoid hemorrhage (SAH). Heat shock protein 27 (HSP27), a member of the small heat shock protein (HSP) family, is induced by various stress factors and exerts protective role on cells. However, the role of HSP27 in brain injury after SAH needs to be further clarified. Here, we reported that HSP27 level of cerebrospinal fluid (CSF) is increased obviously at day 1 in patients with aneurysmal SAH (aSAH) and related to the grades of Hunt and Hess (HH), World Federation of Neurological Surgeons (WFNS), and Fisher score. In rat SAH model, HSP27 of CSF is first increased and then obviously declined; overexpression of HSP27, not knockdown of HSP27, attenuates SAH-induced neurological deficit and cell apoptosis in the basal cortex; and overexpression of HSP27 effectively suppresses SAH-elevated activation of mitogen-activated protein Kinase Kinase 4 (MKK4), the c-Jun N-terminal kinase (JNK), c-Jun, and caspase-3. In an *in vitro* hemolysate-damaged cortical neuron model, $HSP27_{65-90}$ peptide effectively inhibits hemolysate-induced neuron death. Furthermore, TAT-$HSP27_{65-90}$ peptide, a fusion peptide consisting of trans-activating regulatory protein (TAT) of HIV and $HSP27_{65-90}$ peptide, effectively attenuates SAH-induced neurological deficit and cell apoptosis in the basal cortex of rats. Altogether, our results suggest that TAT-HSP27 peptide improves neurologic deficits *via* reducing apoptosis.

Keywords: subarachnoid hemorrhage, HSP27, cell apoptosis, neurologic deficits, TAT-$HSP27_{65-90}$ peptide

OPEN ACCESS

Edited by:
Yuzhen Xu,
Tongji University, China

Reviewed by:
Lingjing Jin,
Tongji University, China
Sami Ridwan,
Klinikum Ibbenbueren, Germany
Wenhua Zhang,
Nanchang University, China

***Correspondence:**
Zong-yong Zhang
zyzhang@sdfmu.edu.cn
Bao-liang Sun
blsun88@163.com
Jin-Xiang Han
samshjx@sina.com

†These authors have contributed equally to this work

Specialty section:
This article was submitted to Cellular Neuropathology, a section of the journal Frontiers in Cellular Neuroscience

Received: *18 February 2022*
Accepted: *10 March 2022*
Published: *28 April 2022*

Citation:
Zhou X-y, Sun J-y, Wang W-q, Li S-x, Li H-x, Yang H-j, Yang M-f, Yuan H, Zhang Z-y, Sun B-l and Han J-X (2022) TAT-HSP27 Peptide Improves Neurologic Deficits via Reducing Apoptosis After Experimental Subarachnoid Hemorrhage. Front. Cell. Neurosci. 16:878673. doi: 10.3389/fncel.2022.878673

INTRODUCTION

Subarachnoid hemorrhage (SAH) is a subtype of stroke with high mortality and morbidity rate, which is mainly caused by the rupture of intracranial aneurysm (Chen et al., 2014). Although ruptured aneurysms are treated by clipping or coiling surgically, 67% of patients with SAH still have neurological sequelae due to early brain injury (EBI) and delayed brain injury (Sehba et al., 2012; Fujii et al., 2013). Cell apoptosis is the most important pathophysiological change underlying EBI, which initiates complex signaling pathways that lead to neuronal death (Sehba et al., 2012; Fujii et al., 2013; Zhang et al., 2015). Therefore, identifying critical pro-death signaling cascades and finding neuroprotective agents targeting this cascade have become an important strategy to against EBI after SAH.

Heat shock proteins are evolutionarily conserved molecular chaperones that consists HSP 40, HSP60, HSP70, HSP90, and small HSPs, which have critical role in stress response (Shan et al., 2020). HSP27 is a member of the small HSP family, has molecular chaperone activity (Kostenko and Moens, 2009), decreases protein aggregation and helps degradation by the proteasome, suppresses release of cytochrome c and caspase activation (Shan et al., 2021), and also exerts cytoprotective effect through cytoskeleton stabilization and antioxidant activity (Vendredy et al., 2020). Previous studies demonstrated that overexpression of HSP27 provides neuroprotection in multiple neurological disease models, include cerebral ischemia (An et al., 2008; Stetler et al., 2008; Shi et al., 2017), kainate-induced neuronal death, and Alzheimer's disease (Akbar et al., 2003; Toth et al., 2013), which were mainly credited to its anti-apoptotic effect. Under SAH pathology, the change of expression and phosphorylation of HSP27 in brainstem and cerebral vessels has been observed in the SAH model (Macomson et al., 2002; Satoh et al., 2003), suggesting that HSP27 is associated with brain injury. However, the potential neuroprotective role of HSP27 has not been illustrated in SAH.

In this study, we measured the concentration of HSP27 in cerebrospinal fluid (CSF) from patients with aneurysmal SAH (aSAH) and then assessed the expression of HSP27 and investigated the effect of knockdown or overexpression of HSP27 on neurological deficit in rat SAH model. We investigated the effect of small peptides from HSP27 on cell apoptosis in an *in vitro* hemolysate-damaged cortical neuron model. We next explored the effect of TAT-HSP27$_{65-90}$ peptide on neurological deficit and cell apoptosis in rat SAH model.

Abbreviations: EBI, early brain injury; SAH, subarachnoid hemorrhage; HSP27, Heat shock protein 27; aSAH, aneurysmal subarachnoid hemorrhage; CSF, cerebrospinal fluid; HH, Hunt and Hess; WFNS, World Federation of Neurological Surgeons; MKK4, mitogen-activated protein kinase kinase 4; JNK, c-Jun N-terminal kinase; TAT, transactivating regulatory protein; NPH, normal pressure hydrocephalus; ELISA, enzyme linked immunosorbent assay; AAV, adeno-associated virus; TUNEL, terminal deoxynucleotidyl transferase-mediated dUTP nick end labeling.

TABLE 1 | Behavior scores.

Category	Behavior	Score
Appetite	Finished meal	0
	Left meal unfinished	1
	Scarcely ate	2
Activity	Active, walking, barking, or standing	0
	Lying down, walk and stand with some stimulations	1
	Almost always lying down	2
Deficits	No deficits	0
	Unstable walk	1
	Impossible to walk and stand	2

MATERIALS AND METHODS

Patients and CSF Collection

After approval by the ethical committee of Shandong Provincial Hospital, an observational study of CSF from 73 patients with SAH (confirmed by a head computed tomography angiography) between May 2019 and May 2020 was performed. Inclusion criteria: (1) aneurysm treated endovascularly (aneurysm coiled and aneurysm clipped) <24-h post-rupture and (2) external ventricular drainage placed <48-h post-rupture. Exclusion criteria were as follows: (1) CNS disease history, (2) CNS infection, and (3) systemic disease (diabetes mellitus, malignancy, and cirrhosis). On admission, clinical and hemorrhage severity were assessed by the Hunt and Hess (HH) grade, World Federation of Neurological Surgeons (WFNS) grade, and Fisher score (Dong et al., 2019). Patients received intravenous infusion of nimodipine for at least 7 days. Euvolemia was maintained, and hypotension was avoided with vasopressors (Dong et al., 2019). The end point was assessed at day 8. CSF samples were collected in sterile tubes or catheter and stored at −80°C. CSF samples of patients with normal pressure hydrocephalus (NPH) were as the experimental control because CSF is difficult to obtain from healthy individuals (Kwan et al., 2019).

Rat SAH Model, Neurological Score, and CSF Collection

After approval by ethics committee of Shandong First Medical University, SAH models were produced in male Sprague–Dawley rats (12 weeks old, 320–350 g, Jinan Pengyue Laboratory Animal Center) by single blood injection model (Wu et al., 2017). Briefly, rats were deeply anesthetized (5% isoflurane) and then maintained (2% isoflurane) using a rodent ventilator (MatrixVMR). Non-heparinized autologous blood (0.3 ml) was injected into cisterna magna for 3 min using a 1-ml syringe with a 25-G needle under a stereotaxic apparatus. Sham-operated group underwent the same procedures except for injection of blood.

Three behavioral activity test of scoring system (**Table 1**) was performed at day 2 after SAH as previously described (Wu et al., 2017). Sequence of testing was randomized. Scoring was evaluated to record appetite, activity, and deficits blindly. About 50 μl of CSF was extracted from the cisterna magna (0.5 cm

depth) with 1-ml syringe under a stereotaxic apparatus and then stored at −80°C (Zhang et al., 2020).

Analysis of CSF HSP27 Concentration and Western Blot Analysis

The HSP27 of CSF was assayed using an enzyme linked immunosorbent assay (ELISA) Kit (ab108862, Abcam) according to the manufacturer's instruction and expressed in ng/ml. Western blot was conducted as previously described (Zhao et al., 2020). Briefly, total protein was extracted with a protein extraction kit (BC3710, Solarbio), which was supplemented with a protease inhibitor cocktail (P8340, Sigma), and analyzed by bicinchoninic acid (BCA) protein concentration kit (PC0020, Solarbio). About 20 μg of total protein was separated using sodium dodecyl sulfate (SDS) polyacrylamide gel electrophoresis and then electrotransferred onto nitrocellulose membrane. After blocking with 5% (w/v) non-fat milk, the membranes were incubated with anti-HSP27 (1:1,000, ab2790, Abcam), anti-active caspase-3 (1:1,000, ab2302, Abcam), anti-FLAG (1:1,000, F1804, Sigma), anti-phospho-MKK4 (Ser257/Thr261; 1:1,000, #9165, CST), anti-phospho-c-Jun N-terminal kinase (JNK) (Thr183/Tyr185; 1:1,000, #4688, CST), anti-phospho-c-Jun (Ser63; 1:1,000, #2361, CST), anti-MKK4 (1:1,000, #9152, CST), and β-actin (1:1,000, #4970, CST) at 4°C overnight and then incubated with anti-mouse immunoglobulin G-horseradish peroxidase (IgG-HRP; 1:3,000, #7076, CST) or anti-rabbit IgG-HRP (1:3,000, #7074, CST) linked antibody for 2 h at the room temperature. After washing with Tris-buffered saline with Tween 20 (TBST) buffer (T1081, Solarbio), the protein bands were visualized by using chemiluminescent substrate (#34577, Thermo Scientific) in a ChemiDoc^{TM} MP Imaging System (Bio-Rad) and quantified by Image J software.

TABLE 2 | Adeno-associated virus (AAV).

Product	Serotype	Titer (pfu/ml)	Company
pAAV-CAG-HSP27-3FLAG	AAV2/2	1.68×10^{12}	OBiO technology
pAAV-CAG-3FLAG	AAV2/2	1.18×10^{12}	
pAKD-CMV-EGFP-H1-shRNA-HSP27	AAV2/2	1.48×10^{12}	
pAKD-CMV-EGFP-H1-shRNA-NC	AAV2/2	1.64×10^{12}	

Adeno-Associated Virus, Peptides, and Intracerebroventricular Injection

The HSP27-overexpressing adeno-associated virus (AAV) and HSP27 shRNA (**Table 2**) were constructed by OBiO Technology (Shanghai, China). Full-length rat cDNA of HSP27 was cloned into the pAAV-CAG-3FLAG vector. AAV-HSP27-RNAi was constructed using the pAKD-CMV-EGFP-H1 vector, which contains a CMV promoter (driving EGFP) and a H1 promoter (driving shRNA expression). The sequence of HSP27 shRNA is 5′-GCTACATCTCTCGGTGCTTCA-3′ and 5′-GCCCAAAGCAGTCACACAATC-3′ as previously described (Stetler et al., 2008). AAV was produced by co-transfection (one AAV vector and two helper vectors) of HEK293T cells. At 72 h after transfection, cells were harvested and lysed using a freeze–thaw procedure. AAV of cell lysate was purified using a heparin-agarose column and concentrated using an ultrafiltration device. The virus titer was measured and shown in **Table 2**. The HSP27 peptides (**Table 3**) were synthesized by ChinaPeptides (Shanghai, China). For intracerebroventricular (i.c.v.) injection, rats received a single injection (0.8 mm posterior, 1.2 mm lateral, and 3.8 mm depth) of AAV (5 μl), TAT (0.3 mg, 10 μl), or TAT-HSP27$_{65-90}$ (0.3 mg, 10 μl) with a 30-G needle of a 10-μl Hamilton syringe under a stereotaxic apparatus.

Immunofluorescence and TUNEL Staining

Staining of slices was performed as previously described (Wang et al., 2019). Briefly, rats were deeply anesthetized and perfused transcardially with ice-cold 4% paraformaldehyde. Rat's brain was post-fixed with 4% paraformaldehyde for 12 h, dehydrated with 30% sucrose/phosphate-buffered saline (PBS) at 4°C for 3 days, and then cut into 10-μm thickness coronal slices (−2.5 to −5 mm from bregma) using a Leica cryostat microtome. Coronal slices were permeabilized with 0.5% Triton X-100 and blocked with 5% goat serum, incubated with anti-NeuN rabbit antibody (1:200, #12943, CST), anti-NeuN mouse antibody (1:200, #94403, CST), anti-HSP27 (1:200, ab2790, Abcam), anti-Iba-1 (1:200, #19741, Wako) primary antibody at 4°C overnight and then incubated with the Anti-Mouse IgG-TRITC (1:100, T5393, Sigma) or Anti-Rabbit IgG-FITC (1:100, F9887, Sigma) at room temperature for 2 h. Terminal deoxynucleotidyl transferase-mediated dUTP nick end labeling (TUNEL) staining was assayed using *in situ* Cell Death Detection Kit with Fluorescein (11684795910, Roche) according to the manufacturer's instruction. Images were captured using

TABLE 3 | HSP27 peptides.

Product	Sequence	Purity	Company
HSP27$_{1-30}$	MTERRVPFSLLRSPSWEPFRDWYPAHSRLF	96.04%	China peptides
HSP27$_{31-60}$	DQAFGVPRFPDEWSQWFSSAGWPGYVRPLP	96.28%	
HSP27$_{61-90}$	AATAEGPAAVTLARPAFSRALNRQLSSGVS	97.41%	
HSP27$_{91-120}$	EIRQTADRWRVSLDVNHFAPEELTVKTKEG	96.05%	
HSP27$_{65-90}$	EGPAAVTLARPAFSRALNRQLSSGVS	95.80%	
TAT	YGRKKRRQRRR	96.75%	
TAT-HSP27$_{65-90}$	YGRKKRRQRRREGPAAVTLARPAFSRALNRQLSSGVS	98.23%	

TABLE 4 | Characteristics for patients.

	aSAH ($n = 73$)	*NPH* ($n = 20$)
Demographics		
Age, years	56.5 ± 8.0	51.8 ± 9.0
Gender, female	47 (64.3)	12 (60)
Clinical status on admission		
Hunt and Hess grade	2.6 ± 1.0	–
WFNS grade	2.4 ± 1.5	–
Fisher score	2.9 ± 0.7	–
Aneurysm location		
Internal carotid artery	18 (24.6)	–
Middle cerebral artery	16 (21.9)	–
Anterior communicating artery	30 (41.1)	–
Others	9 (12.3)	–
Aneurysm treatment		
Coiling	61 (83.5)	–
Clipping	12 (16.5)	–

Values were expressed as mean ± SD or numbers (% of total).

a fluorescence microscope (BX51, Olympus) and analyzed with Image J software.

Hemolysate Treatment and TUNEL Assay on Primary Cortical Neurons

Primary cortical neurons were obtained from E18 rat embryos as previously described (Zhang et al., 2018). Briefly, the dissociated neurons (10^6 cells) were plated in 60 mm dish with neurobasal medium [2% B27 (Gibco), 1% L-glutamine (Gibco), 0.3% D-glucose (Sigma), and 1% fetal bovine serum (Gibco)] and fed with fresh medium every 3 days. Hemolysate-induced cortical neuron death model was produced as described previously (Li et al., 2017). Briefly, hemolysate was prepared from mouse arterial whole blood by freezing and stored at −80°C. In order to induce neuronal death, hemolysate in medium (1:50) was used to stimulate for 24 h. Neurons were treated with hemolysate in medium (1:50) or plus indicated HSP27 peptides (0.03 mg/ml, **Table 3**) for 24 h. Cell viability was measured with Cell Counting Kit-8 (CCK-8, Dojindo) according to the

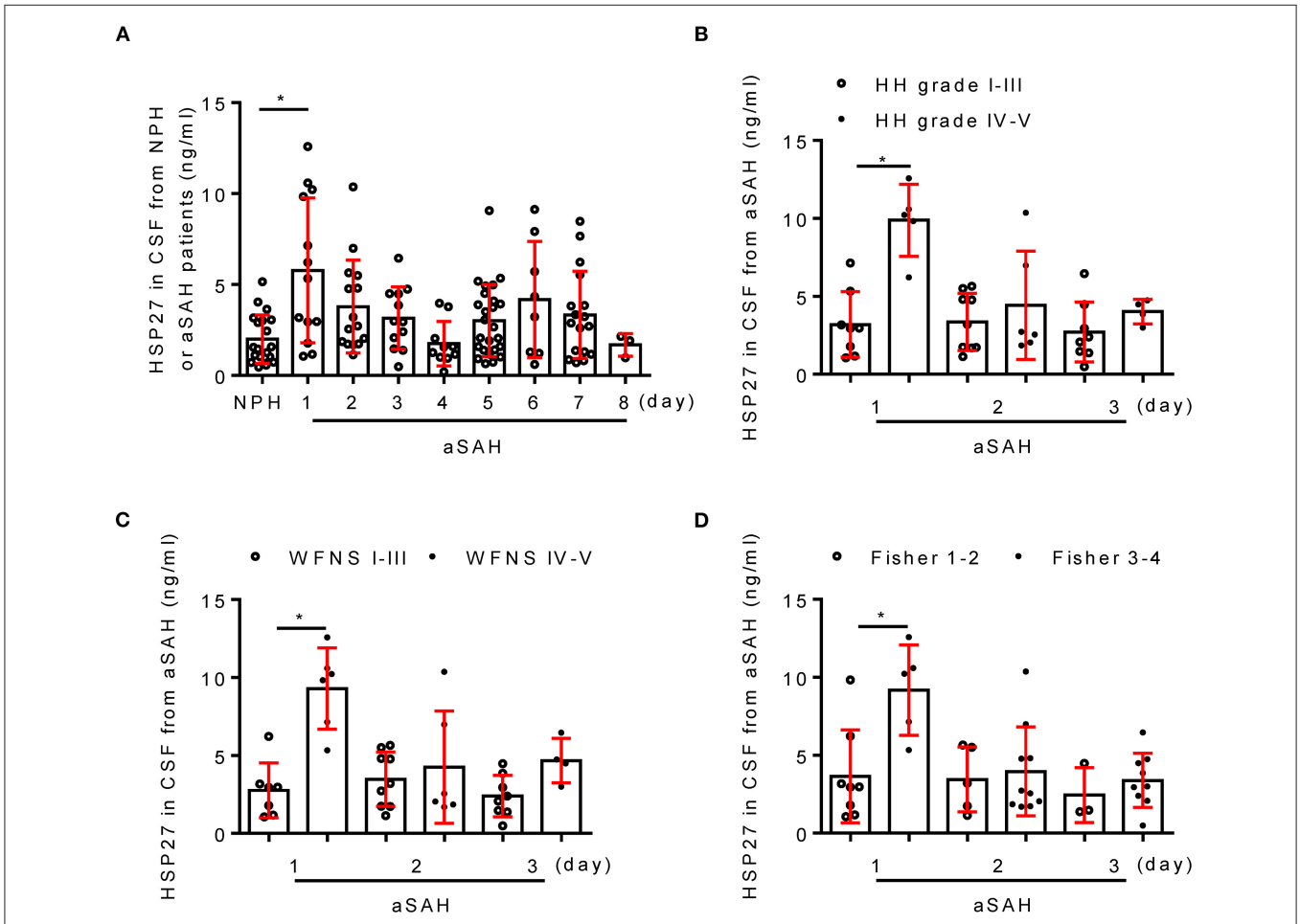

FIGURE 1 | Change of CSF HSP27 level in patients with aSAH. **(A)** Concentration of CSF HSP27 of patients with NPH and aSAH is measured at indicated time with HSP27 ELISA Kit. The histogram shows CSF HSP27 level of patients with aSAH with HH grades I–III and IV–V **(B)**, WFNS grades I–III and IV–V **(C)**, Fisher score 1–2 and 3–4 **(D).** The values are expressed in ng/ml. Data are mean ± SD, $^*p < 0.05$, ANOVA with Bonferroni's multiple comparisons test.

manufacturer's instruction. Cell apoptosis was assayed with TUNEL bright-red apoptosis kit (A113, Vazyme) according to the manufacturer's instruction. Images of cultured neurons were captured under a phase contrast microscope (phase contrast, ×200). Pictures of TUNEL staining were captured under a fluorescence microscope (red, ×200). In addition, the total protein of neurons was extracted and then analyzed by Western blot.

Statistical Analysis

GraphPad Prism 6 was used to perform statistical analyses. All results were expressed as means ± standard deviation (SD). Data of figure were analyzed using one-way analysis of variance (ANOVA) followed by the Bonferroni's multiple comparisons test and the two-tailed *t*-test. $p < 0.05$ considered statistically significant.

RESULTS

HSP27 Level of CSF in Patients With SAH

Table 4 shows the clinical characteristics of patients with aSAH and NPH. There was no significant difference in age and gender between two groups ($p > 0.05$). In patients with aSAH, HH grade, WFNS grade, and modified Fisher score (on admission) were 2.6 ± 1.0, 2.4 ± 1.5, and 2.9 ± 0.7, respectively. Next, the temporal course of HSP27 level (day 1 to 8) following aSAH is depicted in **Figure 1**. HSP27 level of CSF on day 1 was significantly increased in comparison to that in patients with NPH. HSP27 level of day 2 to 4 was gradually decreased in comparison to day 1 (**Figure 1A**). Furthermore, there was a significant difference in HSP27 level (day 1) between patients with aSAH with HH grade of I–III vs. IV–V (**Figure 1B**), WFNS grades of I–III vs. IV–V (**Figure 1C**), and Fisher scores of 1–2 vs. 3–4 (**Figure 1D**).

HSP27 Expression Is First Increased and Then Declined After Rat SAH

Next, we evaluated the expression of HSP27 in brain using the rat SAH model. The calculated mortality rate at 72 h is given in **Table 5**. Blood clots were observed on the circle of Willis in SAH groups (**Figure 2A**). ELISA showed that HSP27 level of CSF was obviously increased at 12 h in comparison to that in sham group and then declined significantly (**Figure 2B**). In immunofluorescence staining, HSP27 can be co-located with NeuN (a marker for neuron) (**Figure 2C**), whereas rarely co-located with Iba-1 (a marker for macrophages/microglia) (**Figure 2D**). Moreover, HSP27 staining was significantly increased at 12 h compared with that of the sham group, whereas obviously declined at 72 h (**Figures 2C,D**). These results indicate that expression of HSP27 is first increased and then declined in rat SAH.

Knockdown of HSP27 Deteriorates Neurological Deficit After Rat SAH

To confirm whether endogenous HSP27 has effect on neurological function, rat SAH was subjected to HSP27 knockdown using AAV-eGFP-shRNA (**Figure 3A**). The calculated mortality rate at 48 h is given in **Table 5**. After microinjection into the lateral ventricle of rat (**Figure 3A**), AAV-eGFP-shRNA effectively infected the basal cortex, produced considerable expression of eGFP (**Figure 3B**), and significantly decreased expression of HSP27 (**Figures 3C**, **4C**), suggesting an effective knockdown effect. Statistical results of TUNEL staining showed that numerous TUNEL positive cortical cells significantly increased in SAH + HSP27 shRNA group as compared with that of SAH + negative control of shRNA group on day 2 after SAH (**Figure 3D**). Moreover, the behavior scores in SAH + HSP27 shRNA group were significantly increased when compared to SAH + negative control of shRNA group (**Figures 4A,B**), suggesting that HSP27 shRNA worsens neurological function after SAH. Western blot analysis showed that the activation of caspase-3 was significantly increased in SAH + HSP27 shRNA group as compared to SAH + negative control of shRNA group (**Figure 4C**). These results indicate that knockdown of endogenous HSP27 increases cell apoptosis and deteriorates neurological deficit in rat SAH.

TABLE 5 | Mortality rate.

Groups	Endpoint	Mortality rate	Included (*n*)
Experiment 1 (ELISA, IF)	72 h		
Sham		0.0% (0/6)	6
6 h		0.0% (0/8)	6
12 h		0.0% (0/8)	6
24 h		12.5% (1/8)	7
72 h		25.0% (2/8)	6
Experiment 2 (Behavior, IF, WB, TUNEL)	48 h		
Sham		0.0% (0/12)	12
SAH + vehicle		25.0% (4/16)	12
SAH + NC		18.7% (3/16)	13
SAH + shRNA		31.3% (5/16)	11
Experiment 3 (Behavior, IF, WB, TUNEL)	48 h		
Sham		0.0% (0/12)	12
SAH + vehicle		25.0% (4/16)	12
SAH + Con		25.0% (4/16)	12
SAH + HSP27		12.5% (2/16)	14
Experiment 4 (Behavior, IF, WB, TUNEL)	48 h		
Sham		0.0% (0/12)	12
SAH + vehicle		31.25% (5/16)	11
SAH + TAT		18.7% (3/16)	13
SAH + TAT-HSP27		12.5% (2/16)	14

HSP27 Overexpression Attenuates Neurological Deficit and Cortical Apoptosis After Rat SAH

To test whether HSP27 overexpression has effect on neurological function, rat SAH was infected with AAV-HSP27-3FLAG

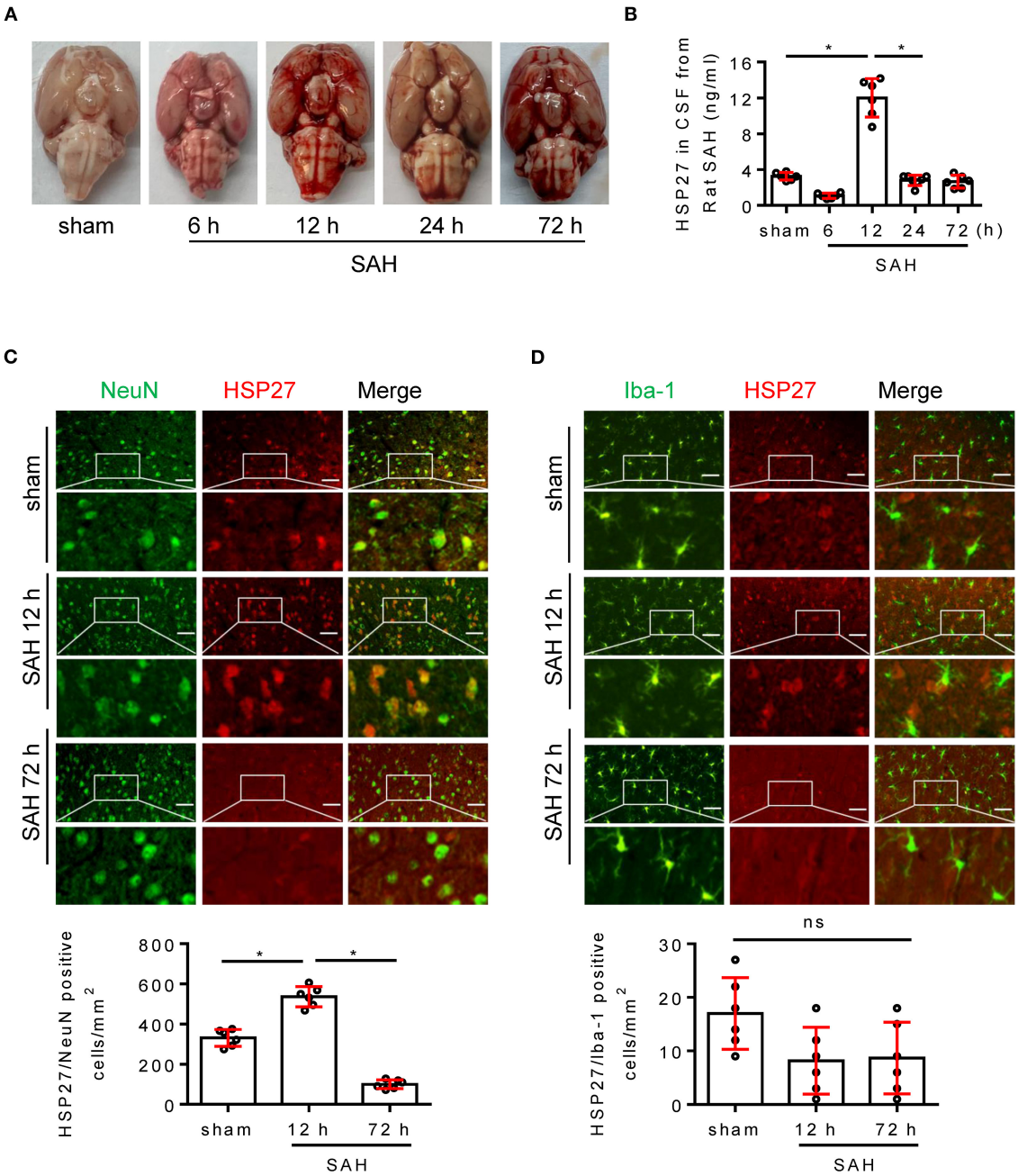

FIGURE 2 | Change of HSP27 level in rat SAH model. **(A)** Representative images of rat brain at indicated time from the sham and SAH groups. **(B)** Samples of CSF was collected (6, 12, 72 h, $n = 6$; 24 h, $n = 7$), HSP27 concentration was measured with HSP27 ELISA Kit and expressed in ng/ml. **(C,D)** Coronal sections from the sham and SAH group reperfusion (12 and 72 h) subjected to immunostaining for the neuronal marker NeuN (green) or macrophages/microglia marker Iba-1 (green) and HSP27 (red) in the basal cortex. Quantification was performed by counting the HSP27/NeuN or HSP27/Iba-1 positive cells per mm^2 region in the basal cortex, $n = 6$, scale bar = 50 μm. Data are mean ± SD, *$p < 0.05$, ANOVA with Bonferroni's multiple comparisons test.

(**Figure 5A**), which expresses full-length HSP27. The calculated mortality rate at 48 h is given in **Table 5**. The behavior score analysis showed that behavior scores in SAH + AAV vector encoding HSP27 group were significantly decreased when compared to SAH + AAV vector group (**Figure 5B**), suggesting an improvement effect. After microinjection into the lateral ventricle of rat, immunofluorescence staining showed that AAV-HSP27-3FLAG obviously increased expression of HSP27 in the basal cortex (**Figure 5C**). Western blot confirmed the increased HSP27 protein expression by detecting FLAG expression (**Figure 6**). Moreover, statistical results of TUNEL staining showed that numerous TUNEL positive cortical cells

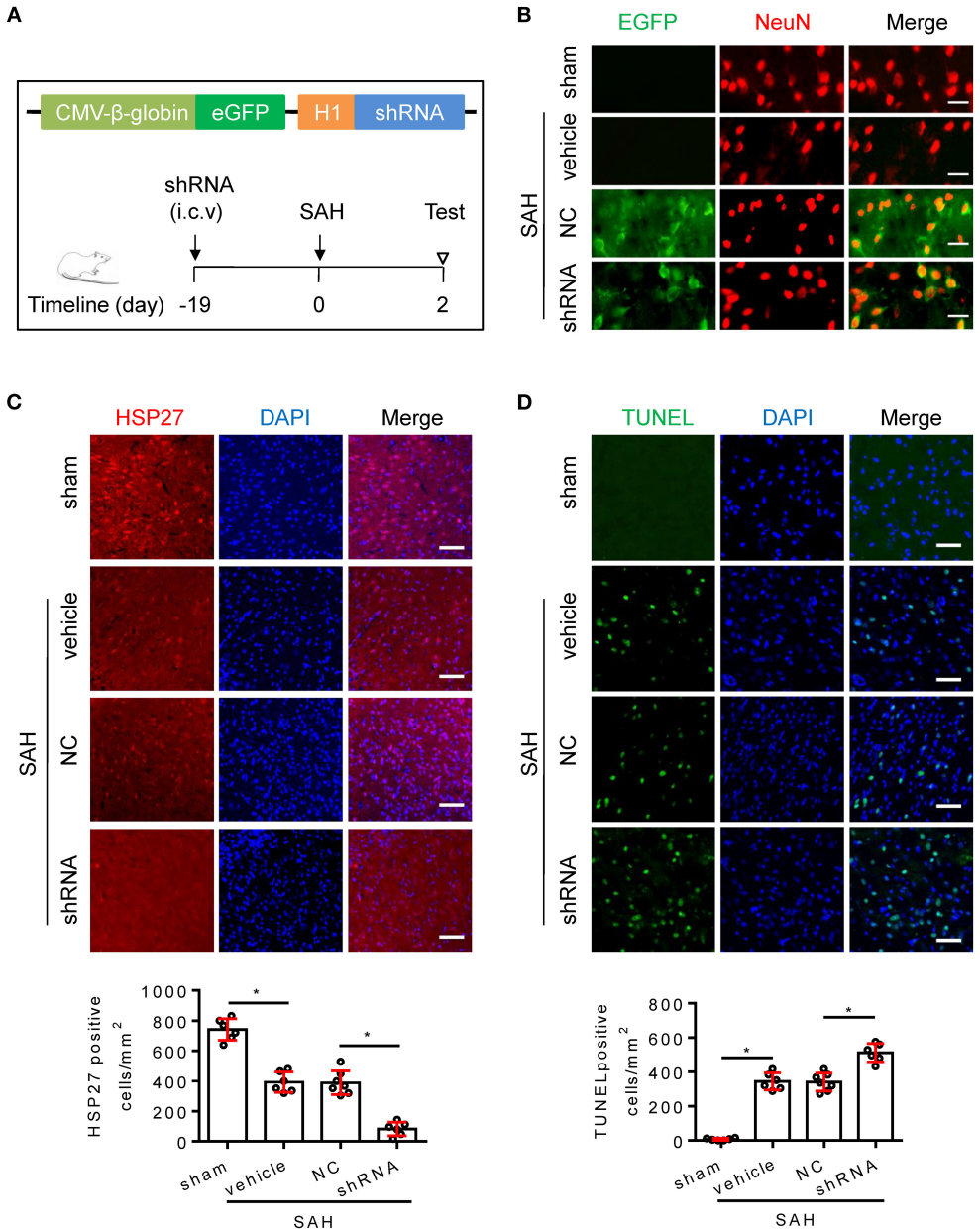

FIGURE 3 | AAV-shRNA targeting HSP27 increased cell apoptosis after SAH in rats. **(A)** Schematic of AAV vector encoding shRNA and experimental design. **(B–D)** Coronal sections from the sham ($n = 6$), SAH + vehicle ($n = 6$), SAH + negative control of shRNA (SAH + NC, $n = 7$), and SAH + HSP27 shRNA (SAH + shRNA, $n = 6$) group reperfusion on day 2 after SAH, subjected to immunostaining for the neuronal marker NeuN (red) or HSP27 (red) or TUNEL (green) in the basal cortex. **(B)** Representative images showing AAV-eGFP-shRNA expression (indicated by EGFP, green) in the neurons (NeuN staining, red) in the basal cortex, scale bar = 50 μm. **(C,D)** Quantification was performed by counting the HSP27 or TUNEL positive cells per mm^2 region in the basal cortex, scale bar = 50 μm. Data are mean ± SD, *$p < 0.05$, ANOVA with Bonferroni's multiple comparisons test.

significantly decreased in SAH + AAV vector encoding HSP27 group as compared with that of SAH + AAV vector group on day 2 after SAH (**Figure 5D**). Previous review showed that HSP27 exerts an anti-apoptosis role by inhibiting MKK/JNK cell death signal, and or mitochondria-related pro-apoptotic factors (Shan et al., 2021). Thus, we further examined the activity of MKK/JNK and caspase-3 by Western blot. Data showed that the phosphorylation of MKK4, JNK, and c-Jun and the activation of caspase-3 were obviously increased in SAH + vehicle and SAH + AAV vector group, whereas significantly decreased in SAH + AAV vector encoding HSP27 group (**Figure 6**). These results indicate that HSP27 overexpression

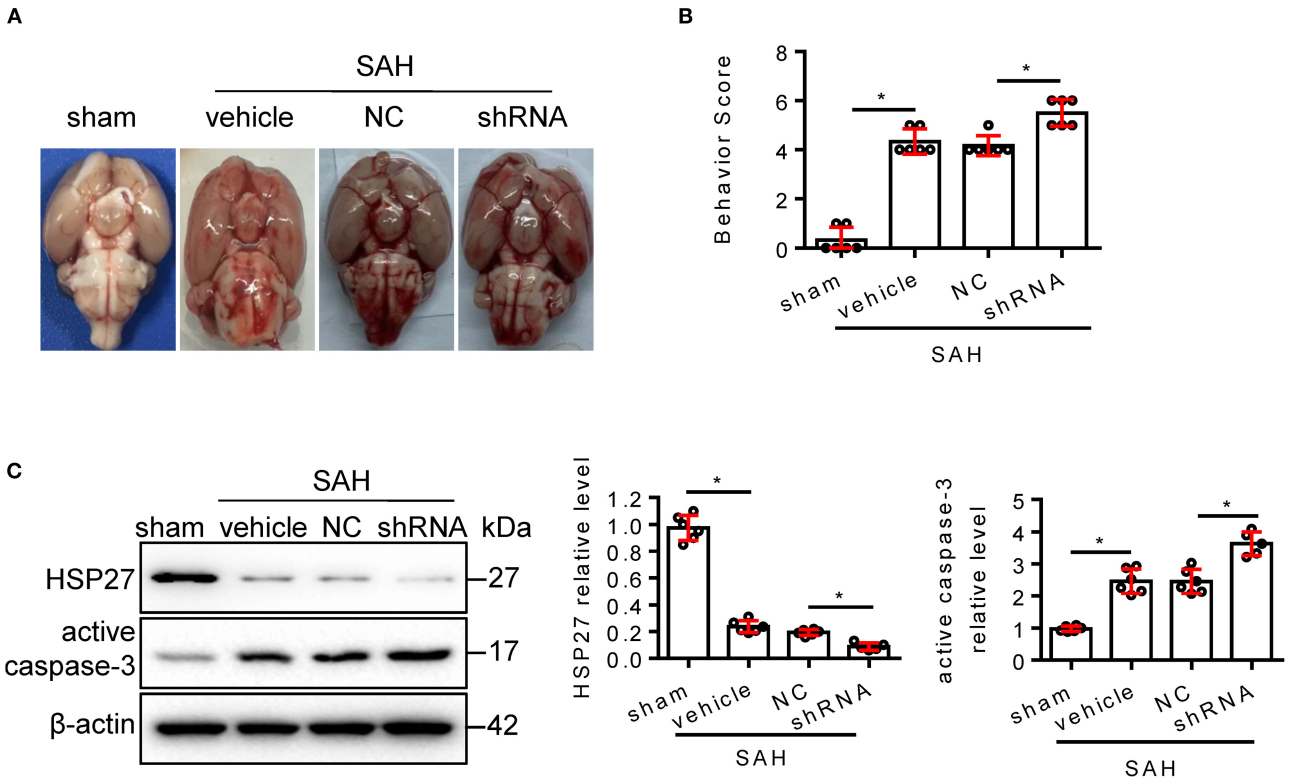

FIGURE 4 | AAV-shRNA targeting HSP27 deteriorated neurological deficit after SAH in rats. **(A)** Representative images of rat brain on day 2 after surgery for the sham, SAH + vehicle, SAH + NC, and SAH + shRNA groups. **(B)** Behavior scores of each group were assessed at 48 h, $n = 6$. **(C)** The basal cortex was collected on day 2 following SAH from the sham ($n = 6$), SAH + vehicle ($n = 6$), SAH + NC ($n = 6$), and SAH + shRNA ($n = 5$) groups; homogenates were blotted with anti-HSP27, anti-active caspase-3, and anti-β-actin, quantification of optical density was normalized to sham group. Data are mean ± SD, $^*p < 0.05$, ANOVA with Bonferroni's multiple comparisons test.

attenuated cortical cell apoptosis and neurological deficit in rat SAH.

Effect of HSP27 Peptides on Hemolysate-Induced Cell Apoptosis in Cultured Cortical Neurons

N-terminal region of HSP27 is composed of 1–120 amino acids and proved to be a necessary domain for neuroprotection (Stetler et al., 2008). So, we designed and synthesized peptides from the N-terminal 1–120 amino acids of HSP27 (**Figure 7A**), which had no effect on cell activity in cultured cortical neuron (**Figure 7B**), aiming to find the key peptide that affects cell apoptosis. Using a hemolysate-induced cortical neuron death model, Western blot and TUNEL staining showed that $HSP27_{61-90}$ and $HSP27_{65-90}$ peptides, but not $HSP27_{1-30}$, $HSP27_{31-60}$, and $HSP27_{91-120}$ peptides, can effectively inhibit hemolysate-induced the increased the activation of caspase-3 (**Figure 7C**) and reduce hemolysate-elevated the number of TUNEL positive cells (**Figure 7D**). These results suggest that the N-terminal 65–90 amino acids of HSP27 are the key area for affecting cell apoptosis.

TAT-$HSP27_{65-90}$ Peptide Attenuates Neurological Deficit and Cortical Apoptosis After Rat SAH

Furthermore, we investigated whether TAT-$HSP27_{65-90}$ peptide could improve neurological deficit in rat SAH. The calculated mortality rate at 48 h is given in **Table 5**. As expected, after microinjection into the lateral ventricle of rat SAH (**Figure 8A**), TAT-$HSP27_{65-90}$ significantly decreased the behavior score as compared with the TAT-treated SAH group (**Figure 8B**), suggesting that TAT-$HSP27_{65-90}$ treatment attenuates SAH-induced neurological deficits. In addition, Western blot analysis suggested that the vehicle or TAT-treated SAH group showed upregulation of active caspase-3, which was attenuated by TAT-$HSP27_{65-90}$ treatment (**Figure 8C**). Furthermore, TUNEL staining suggested that TUNEL-positive cells of the basal cortex were significantly decreased at 48 h in the TAT-$HSP27_{65-90}$-treated SAH group when compared to the TAT-treated SAH group (**Figure 8D**), indicating TAT-$HSP27_{65-90}$ reduced cortical cell apoptosis after SAH. There are two commonly used SAH models: blood injection model and endovascular puncture model (Kooijman et al., 2014). Later, we explored the effect of TAT-$HSP27_{65-90}$ on neurological deficit and cell apoptosis in the

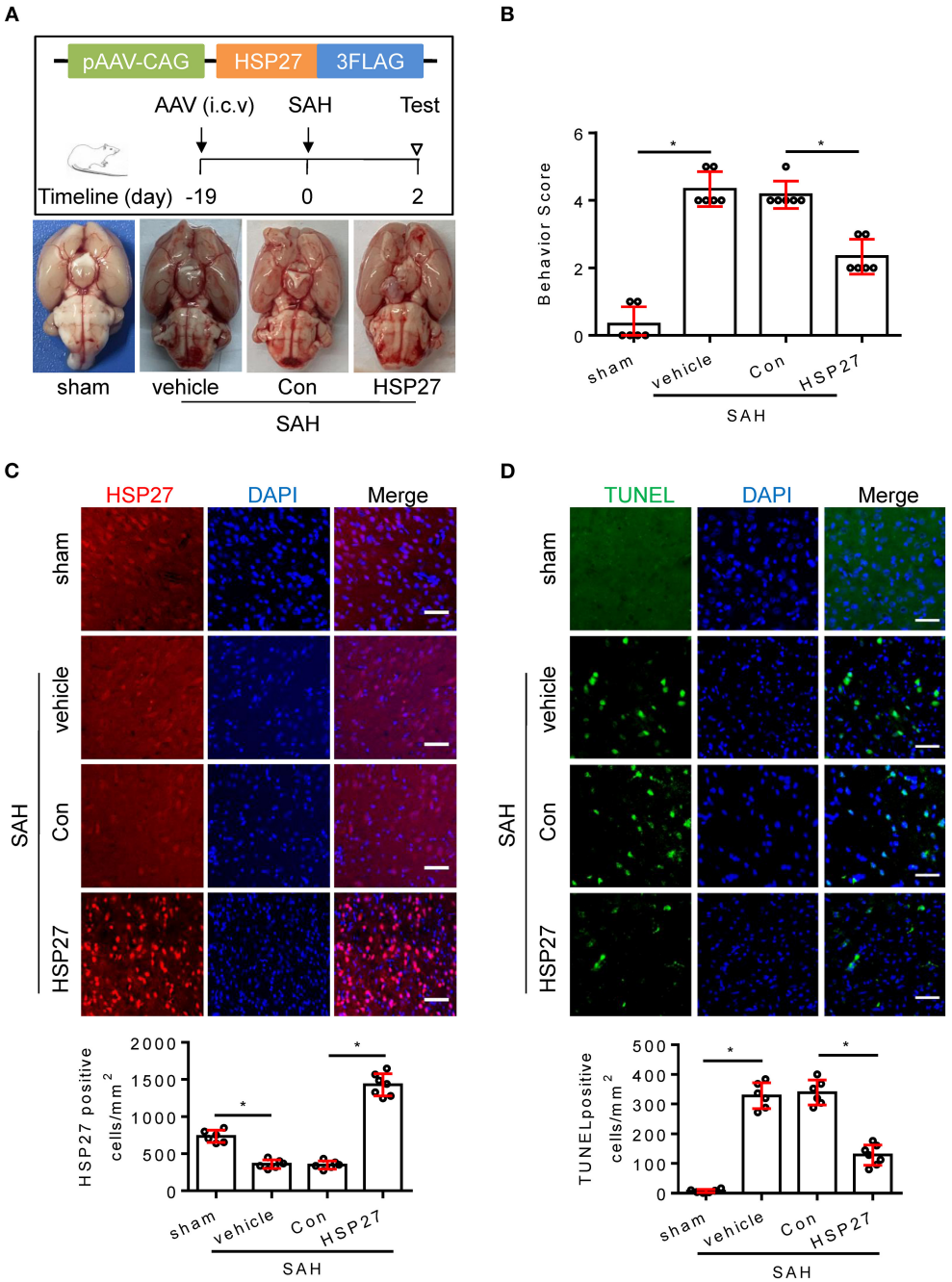

FIGURE 5 | HSP27 overexpression attenuated neurological deficit and cell apoptosis after SAH in rats. **(A)** Schematic of AAV vector encoding HSP27 and experimental design. Representative images of rat brain on day 2 after surgery for the sham, SAH + vehicle, SAH + AAV vector (SAH + Con), and SAH + AAV vector encoding HSP27 (SAH + HSP27) group. **(B)** Behavior scores of each group were assessed at 48 h, $n = 6$. **(C,D)** Coronal sections from the sham ($n = 6$), SAH + vehicle ($n = 6$), SAH + Con ($n = 6$), and SAH + HSP27 ($n = 7$) group reperfusion on day 2 after SAH, subjected to immunostaining for the HSP27 (red) or TUNEL (green) in the basal cortex. Quantification was performed by counting the HSP27 or TUNEL positive cells per mm^2 region in the basal cortex, scale bar = 50 μm. Data are mean ± SD, $^*p < 0.05$, ANOVA with Bonferroni's multiple comparisons test.

endovascular puncture rat SAH model. There was no statistical difference in SAH grading score among the vehicle, TAT, or TAT-$HSP27_{65-90}$-treated SAH group (**Supplementary Figure S1A**). TAT-$HSP27_{65-90}$ treatment significantly increased the average modified Garcia score as compared with the TAT-treated SAH group (**Supplementary Figure S1B**), suggesting that TAT-$HSP27_{65-90}$ treatment improved neurological deficits after SAH. Moreover, NeuN staining suggested that

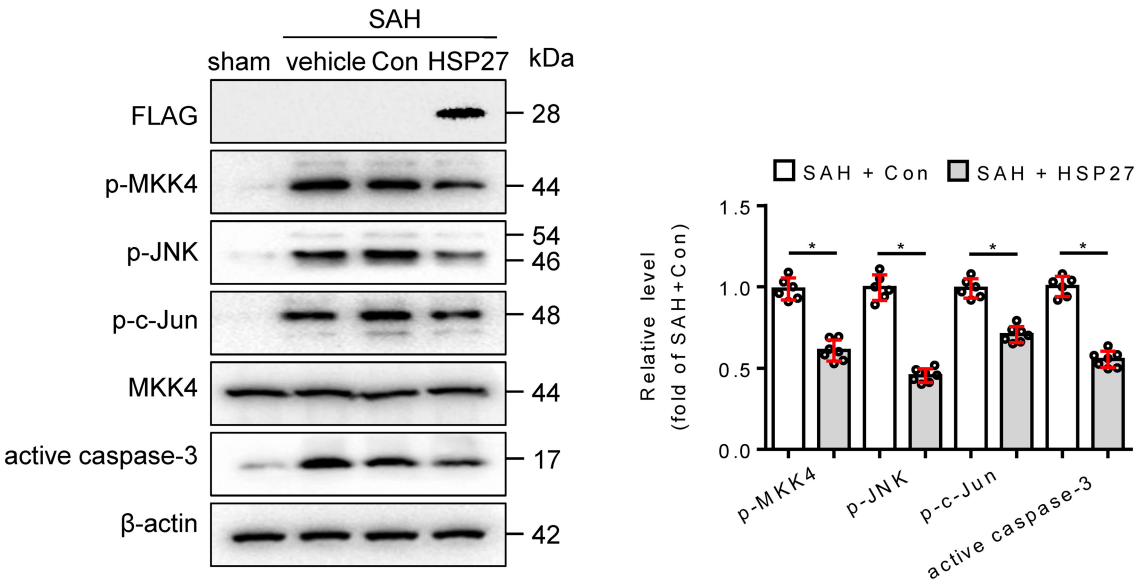

FIGURE 6 | Effect of HSP27 overexpression on the activation of MKK4, JNK, c-Jun, and caspase-3 on day 2 after SAH. The basal cortex was collected on day 2 following SAH from the sham ($n = 6$), SAH + vehicle ($n = 6$), SAH + Con ($n = 6$), and SAH + HSP27 ($n = 7$) groups; homogenates were blotted with anti-FLAG, anti-phospho-MKK4, anti-phospho-JNK, anti-phospho-c-Jun, anti-MKK4, anti-active caspase-3, and anti-β-actin; and quantification of optical density was normalized to sham group. Data are mean ± SD, $^*p < 0.05$, the two-tailed *t*-test.

NeuN-positive neurons of the hippocampal CA1 region were significantly increased at 24 h in the TAT-HSP27$_{65-90}$-treated SAH group in comparison with that of the TAT-treated SAH group (**Supplementary Figure S1C**). TUNEL staining suggested that TUNEL-positive cells of the basal cortex were significantly decreased at 24 h in the TAT-HSP27$_{65-90}$-treated SAH group when compared to the TAT-treated SAH group (**Supplementary Figure S1C**), indicating TAT-HSP27$_{65-90}$ reduced cortical cell death after SAH in the endovascular puncture model.

DISCUSSION

The main findings of this study are as follows: change of HSP27 level in CSF from patients with aSAH; expression of HSP27 is first increased and then declined after SAH in rats; and knockdown of HSP27 deteriorated neurological deficit, whereas overexpression of HSP27 confers neuroprotection after SAH in rats. TAT-HSP27$_{65-90}$ peptide effectively reduces hemolysate-induced cell apoptosis on cultured cortical neurons and attenuates neurological deficit after SAH in rats.

Since intracerebral microdialysis allows *in vivo* sampling of interstitial fluid, it is used to continuously monitor the neurochemical metabolism of the damaged brain after aSAH, but this method is limited to the injured tissue around the probe (Unterberg et al., 2001; Helbok et al., 2015). Physiologically, CSF is secreted in the choroid plexus and recirculates through the cerebral ventricles and subarachnoid space, interchanging with interstitial fluid, which is thought to play a role in clearance of solutes and metabolic waste products from the brain (Iliff et al., 2013; Xie et al., 2013). Compared to intracerebral microdialysis, CSF analysis may reflect a more general picture of brain injury. CSF analysis basing on lumbar puncture is cornerstone for aSAH diagnosis, which means that changes of proteins can be detected quickly and conveniently to clarify the correlation between these changes and SAH pathology (Wasik et al., 2017; Papa et al., 2018; Kwan et al., 2019). To our knowledge, this study is the first to report the change of CSF HSP27 in patients with aSAH as compared with patients with NPH, showing a trend of increasing first and then decreasing in the early days. Our findings show that CSF HSP27 is obviously increased on day 1, and related to the grades of HH, WFNS, and Fisher score, which means that early higher level of HSP27 is related to clinical and hematological severity. CSF HSP27 is increased second in about 6 days, whether it is related to the occurrence of complications after SAH needs further study. Using the rat SAH model, we observed that CSF HSP27 decreased at 6 h, increased significantly at 12 h, and then significantly decreased at 24 and 72 h. The change trend of CSF HSP27 in EBI is similar to that of patients with aSAH in the early days. There have been two previous studies relating to HSP27 expression in SAH. The first study involved a rat SAH model where HSP27 expression was observed in the cerebral arteries at 48 h post-ictus, the overall expression of HSP27 almost unchanged, whereas the phosphorylated isoforms of HSP27 increased (Macomson et al., 2002). In the second study, the protein level of HSP27 was markedly decreased at 0.5 h and significantly elevated in brain stem after rat SAH (Satoh et al., 2003). Interestingly, our immunofluorescence results showed that the change of HSP27 expression mainly occurred in neurons rather than

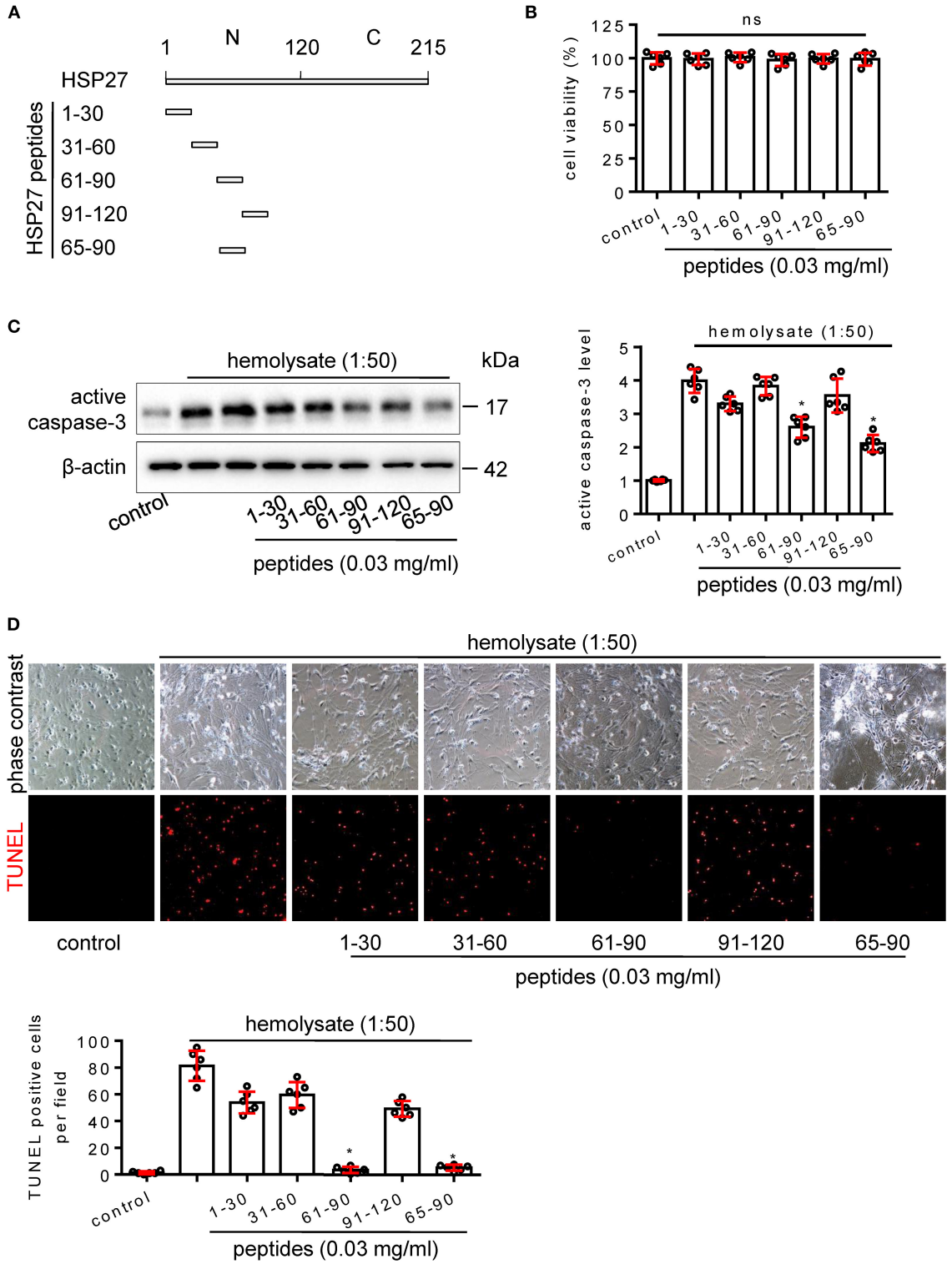

FIGURE 7 | Effect of HSP27 peptides on hemolysate-induced cell apoptosis in primary cortical neurons. **(A)** Schematic representation of various HSP27 peptides. **(B)** Hsp27 peptides have no effect on cell viability in primary cortical neurons; Cortical neurons were treated with indicated HSP27 peptides (0.03 mg/ml) in medium (1:50) for 24 h. Cell viability was measured with Cell Counting Kit-8 (CCK-8) and normalized to control. **(C,D)** Cortical neurons were treated with hemolysate in medium (1:50) or plus indicated HSP27 peptides (0.03 mg/ml) for 24 h. **(C)** Active caspase-3 levels in each group were detected by Western blot, β-actin serves as a control, and quantification of optical density was normalized to control. **(D)** Representative images of cortical neurons (phase contrast, ×200) and TUNEL staining (red, ×200), and quantification of TUNEL-positive cells from each group was performed. Data are mean ± SD, $n = 6$, $^*p < 0.05$ vs. hemolysate treatment, ANOVA with Bonferroni's multiple comparisons test.

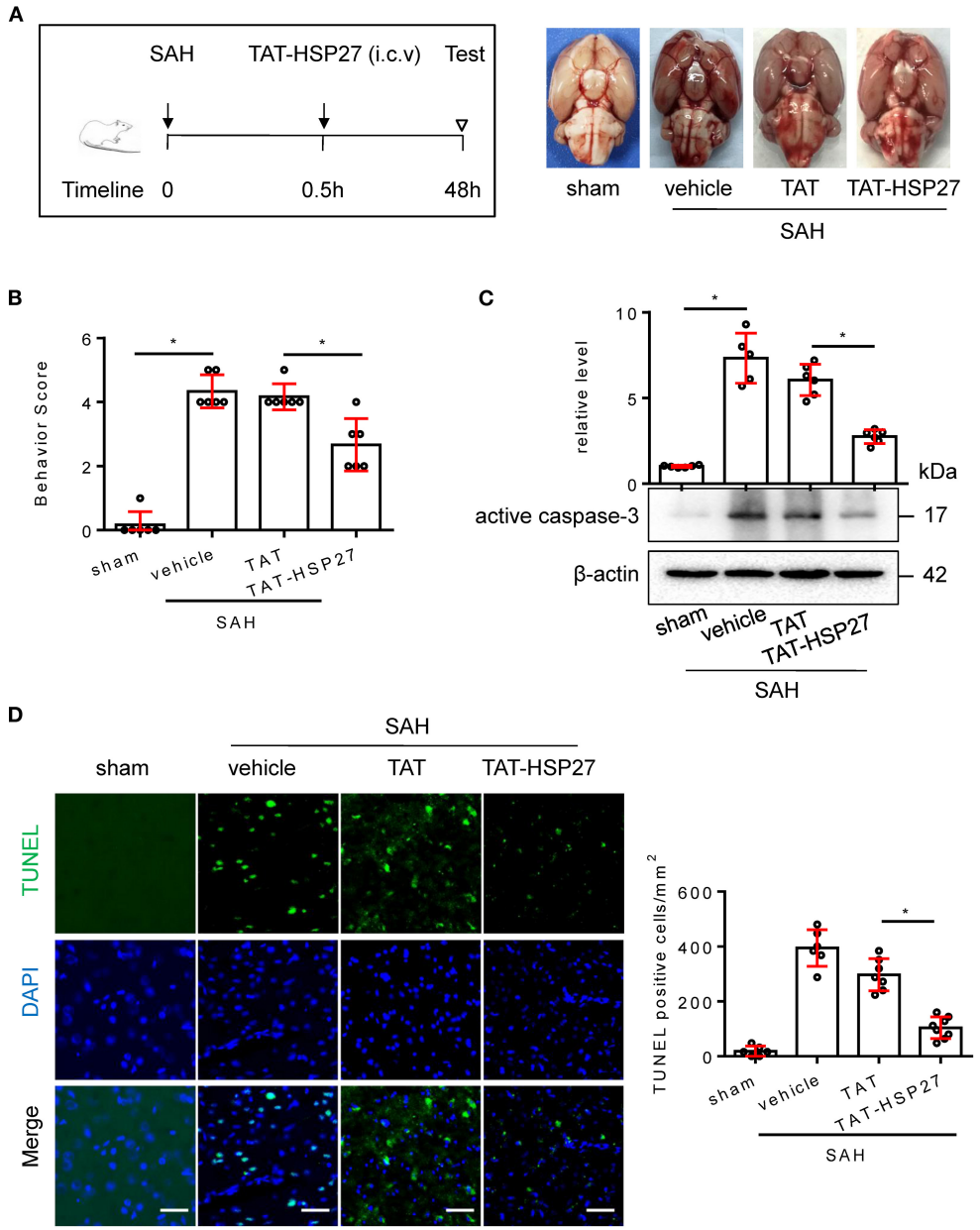

FIGURE 8 | TAT- HSP27$_{65-90}$ peptide attenuated neurological deficits and cell apoptosis after SAH in rats. **(A)** Experimental design; representative images of rat brain on day 2 after surgery for the sham, SAH + vehicle, SAH + TAT peptide (SAH + TAT), and SAH + TAT-HSP27$_{65-90}$ peptide (SAH + TAT-HSP27) groups. **(B)** Behavior scores of each group were assessed at 48 h, $n = 6$. **(C)** The basal cortex was collected on day 2 following SAH from the sham ($n = 6$), SAH + vehicle ($n = 5$), SAH + TAT ($n = 6$), and SAH + TAT-HSP27 ($n = 6$) groups; homogenates were blotted with anti-active caspase-3 and anti-β-actin, and quantification of optical density was normalized to sham group. **(D)** Coronal sections from the sham ($n = 6$), SAH + vehicle ($n = 6$), SAH + TAT ($n = 7$), and SAH + TAT-HSP27 ($n = 8$) group reperfusion on day 2 after SAH, subjected to immunostaining for the TUNEL (green) in the basal cortex. Quantification was performed by counting the TUNEL positive cells per mm^2 region in the basal cortex, scale bar = 50 μm. Data are mean ± SD, *$p < 0.05$ vs. hemolysate treatment, ANOVA with Bonferroni's multiple comparisons test.

in macrophages/microglia after SAH. Based on the results of animal experiments, the change trend of HSP27 in CSF and the basal cortex is similar. We speculate that the change trend of CSF HSP27 may reflect the change of HSP27 in human brain tissue after aSAH.

Although the change of HSP27 may be an endogenous response and a possible protective mechanism against brain injury following SAH, this has not been directly tested with HSP27 knockdown or overexpression. Our data showed that worsening neurological deficit was observed in rat SAH after

knockdown of endogenous HSP27 using the previously reported shRNA. However, AAV-mediated overexpression of HSP27 attenuated SAH-induced neurological deficits and cell apoptosis in the basal cortex of rats. It has been shown that overexpression of HSP27 provides neuroprotection in cerebral ischemia mice model, which indicated the mechanism involving the inhibition of mitochondrial cell death signaling (Stetler et al., 2008, 2012; Leak et al., 2013; Shi et al., 2017). We observed that the knockdown of endogenous HSP27 increased activation of pro-apoptotic molecular caspase-3, whereas virus-mediated overexpression of HSP27 inhibits activation of caspase-3 after SAH in rats. Indeed, HSP27 is reported to inhibit cell apoptosis by reducing cytochrome c release from mitochondria (Garrido et al., 1999) and consequently downregulating cleaved caspase-3 (Garrido et al., 1999; Bruey et al., 2000). Moreover, HSP27 can directly bind to the prodomain of caspase-3 and attenuates its proteolytic activation (Pandey et al., 2000; Voss et al., 2007). Our data also showed that overexpression of HSP27 attenuates SAH-elevated kinase phosphorylation of MKK4, JNK, and c-Jun in rats. Some reports have found that HSP27 inhibits cell apoptosis by hindering MKK/JNK cell death signal pathway induced by oxidative stress or ischemia (Stetler et al., 2008, 2012). Because oxidative stress and delayed cerebral ischemia are the key factors of cell apoptosis after SAH (Sabri et al., 2013; Yang et al., 2017), we speculate that overexpression of HSP27 maybe reduce cell apoptosis through inhibiting caspase activity and phosphorylation of MKK4 and JNK after SAH in rats. In non-phosphorylated form, HSP27 is an ATP-independent molecular chaperone and exists as the high molecular weight oligomeric; upon different stimuli, HSP27 is phosphorylated at Ser15, Ser78, and Ser82 by several protein kinases, and phosphorylation of HSP27 changes its conformation, which shifts from the large oligomers to dimers and monomers (Stetler et al., 2009; Sharp et al., 2013). Whether HSP27 phosphorylation occurs and subsequently mediates JNK phosphorylation in EBI after SAH needs to be verified in the following studies.

In addition to the overexpression of HSP27 that provides neuroprotection, the synthetic mimic peptide where transduced PEP-1-HSP27 peptide, a fusion peptide consisting of the PEP-1 peptide and human HSP27, can protect against ischemic injury in a gerbil animal model (An et al., 2008); intravenous injection of TAT-HSP27 peptide, a fusion peptide consisting of TAT and human HSP27 ameliorated ischemia/reperfusion-induced neurological deficits in mice (Shi et al., 2017). The structure of HSP27 includes the N-terminal domain containing three serine phosphorylation sites that regulates the reconfiguration of oligomeric function and structure, and the C-terminal domain containing β-pleated sheets that functions protein–protein interactions (Stetler et al., 2009; Sharp et al., 2013). The N-terminal region of HSP27 proved to be a necessary domain for neuroprotection *in vitro* ischemia (Stetler et al., 2008). So, we synthesized peptides from the N-terminal region of HSP27 and found that the $HSP27_{65-90}$ peptide reduces cortical neuronal death in an *in vitro* hemolysate-damaged cortical neuron model (Li et al., 2017), which contains multiple components and mimics the pathophysiological scenario of SAH observed *in vivo* (Zhou et al., 2007). Generally, it is believed that SAH causes neuronal death in the basal cortex exposed to bloody CSF (Park et al., 2004). TAT protein transduction domain can facilitate the delivery of proteins or peptides without cell type specificity, its fusion peptide can be delivered into the brain parenchyma after systemic injection (Cao et al., 2002; Wang et al., 2019). Similar to overexpression of HSP27, we observed that i.c.v. injection of TAT-$HSP27_{65-90}$ peptide provides neuroprotection, suppresses mitochondrial cell apoptosis signaling of active caspase-3, and attenuates cellular apoptosis in the basal cortex after SAH in rats. There are several limitations in this study. First, we utilized young male rats to make the SAH model, whereas aSAH mostly occurs in middle-aged and elderly women (Duan et al., 2018). Second, we studied the overexpression or knockdown of HSP27 on neurological deficit in blood injection SAH model, which is fairly reproducible mild SAH model developed by injecting a fixed amount of blood into the subarachnoid space (Prunell et al., 2003).

CONCLUSION

In conclusion, the present study shows that early CSF level of HSP27 is related to clinical and hematological severity in patients with aSAH. Expression of HSP27 is first increased and then declined; overexpression of HSP27, but not knockdown of HSP27, confers neuroprotection after SAH in rats. TAT-$HSP27_{65-90}$ peptide can effectively inhibit neuronal death in an *in vitro* hemolysate-damaged cortical neuron model, and thus attenuated neurological deficit after SAH in rats.

DATA AVAILABILITY STATEMENT

The original contributions presented in the study are included in the article/**Supplementary Material**, further inquiries can be directed to the corresponding author/s.

ETHICS STATEMENT

The studies involving human participants were reviewed and approved by Ethical Committee of Shandong Provincial Hospital. The patients/participants provided their written informed consent to participate in this study. The animal study was reviewed and approved by Ethics Committee of Shandong First Medical University.

AUTHOR CONTRIBUTIONS

J-XH, B-lS, and Z-yZ designed experiments, analyzed the results, and wrote the manuscript. X-yZ, J-yS, W-qW, S-xL, H-xL, M-fY, and HY performed experiments. All authors read and approved the final manuscript.

FUNDING

This study was financially supported by the National Natural Science Foundation of China (81870938 and 82071303),

the Natural Science Foundation of Shandong province (ZR2019ZD32 and ZR2020QH107), the Youth Innovation Team of Shandong Universities (2019KJK001), and the Taishan Scholar Project, Academic Promotion Program of Shandong First Medical University (2019LJ001 and 2019QL016).

SUPPLEMENTARY MATERIAL

The Supplementary Material for this article can be found online at: https://www.frontiersin.org/articles/10.3389/fncel.2022.878673/full#supplementary-material

REFERENCES

Akbar, M. T., Lundberg, A. M., Liu, K., Vidyadaran, S., Wells, K. E., Dolatshad, H., et al. (2003). The neuroprotective effects of heat shock protein 27 overexpression in transgenic animals against kainate-induced seizures and hippocampal cell death. *J. Biol. Chem.* 278, 19956–19965. doi: 10.1074/jbc.M207073200

An, J. J., Lee, Y. P., Kim, S. Y., Lee, S. H., Lee, M. J., Jeong, M. S., et al. (2008). Transduced human PEP-1-heat shock protein 27 efficiently protects against brain ischemic insult. *FEBS J.* 275, 1296–1308. doi: 10.1111/j.1742-4658.2008.06291.x

Bruey, J. M., Ducasse, C., Bonniaud, P., Ravagnan, L., Susin, S. A., Diaz-Latoud, C., et al. (2000). Hsp27 negatively regulates cell death by interacting with cytochrome c. *Nat. Cell Biol.* 2, 645–652. doi: 10.1038/35023595

Cao, G., Pei, W., Ge, H., Liang, Q., Luo, Y., Sharp, F. R., et al. (2002). In Vivo delivery of a Bcl-xL fusion protein containing the TAT protein transduction domain protects against ischemic brain injury and neuronal apoptosis. *J. Neurosci.* 22, 5423–5431. doi: 10.1523/JNEUROSCI.22-13-05423.2002

Chen, S., Feng, H., Sherchan, P., Klebe, D., Zhao, G., Sun, X., et al. (2014). Controversies and evolving new mechanisms in subarachnoid hemorrhage. *Prog. Neurobiol.* 115, 64–91. doi: 10.1016/j.pneurobio.2013.09.002

Dong, Y., Guo, Z. N., Li, Q., Ni, W., Gu, H., Gu, Y. X., et al. (2019). Chinese Stroke Association guidelines for clinical management of cerebrovascular disorders: executive summary and 2019 update of clinical management of spontaneous subarachnoid haemorrhage. *Stroke Vasc. Neurol.* 4, 176–181. doi: 10.1136/svn-2019-000296

Duan, W., Pan, Y., Wang, C., Wang, Y., Zhao, X., Wang, Y., et al. (2018). Risk factors and clinical impact of delayed cerebral ischemia after aneurysmal subarachnoid hemorrhage: analysis from the china national stroke registry. *Neuroepidemiology.* 50, 128–136. doi: 10.1159/000487325

Fujii, M., Yan, J., Rolland, W. B., Soejima, Y., Caner, B., and Zhang, J. H. (2013). Early brain injury, an evolving frontier in subarachnoid hemorrhage research. *Transl. Stroke Res.* 4, 432–446. doi: 10.1007/s12975-013-0257-2

Garrido, C., Bruey, J. M., Fromentin, A., Hammann, A., Arrigo, A. P., and Solary, E. (1999). HSP27 inhibits cytochrome c-dependent activation of procaspase-9. *FASEB J.* 13, 2061–2070. doi: 10.1096/fasebj.13.14.2061

Helbok, R., Schiefecker, A. J., Beer, R., Dietmann, A., Antunes, A. P., Sohm, F., et al. (2015). Early brain injury after aneurysmal subarachnoid hemorrhage: a multimodal neuromonitoring study. *Crit. Care.* 19, 75. doi: 10.1186/s13054-015-0809-9

Iliff, J. J., Lee, H., Yu, M., Feng, T., Logan, J., Nedergaard, M., et al. (2013). Brain-wide pathway for waste clearance captured by contrast-enhanced MRI. *J. Clin. Invest.* 123, 1299–1309. doi: 10.1172/JCI67677

Kooijman, E., Nijboer, C. H., Van Velthoven, C. T., Kavelaars, A., Kesecioglu, J., and Heijnen, C. J. (2014). The rodent endovascular puncture model of subarachnoid hemorrhage: mechanisms of brain damage and therapeutic strategies. *J. Neuroinflam.* 11, 2. doi: 10.1186/1742-2094-11-2

Kostenko, S., and Moens, U. (2009). Heat shock protein 27 phosphorylation: kinases, phosphatases, functions and pathology. *Cell Mol. Life Sci.* 66, 3289–3307. doi: 10.1007/s00018-009-0086-3

Kwan, K., Arapi, O., Wagner, K. E., Schneider, J., Sy, H. L., Ward, M. F., et al. (2019). Cerebrospinal fluid macrophage migration inhibitory factor: a potential predictor of cerebral vasospasm and clinical outcome after aneurysmal subarachnoid hemorrhage. *J. Neurosurg.* 1, 1–6. doi: 10.3171/2019.6.JNS19613

Leak, R. K., Zhang, L., Stetler, R. A., Weng, Z., Li, P., Atkins, G. B., et al. (2013). HSP27 protects the blood-brain barrier against ischemia-induced loss of integrity. *CNS Neurol. Disord. Drug Target.* 12, 325–337. doi: 10.2174/18715273113120300006

Li, M., Wang, Y., Wang, W., Zou, C., Wang, X., and Chen, Q. (2017). Recombinant human brain-derived neurotrophic factor prevents neuronal apoptosis in a novel in vitro model of subarachnoid hemorrhage. *Neuropsychiatr. Dis. Treat* 13, 1013–1021. doi: 10.2147/NDT.S128442

Macomson, S. D., Brophy, C. M., Miller, W., Harris, V. A., and Shaver, E. G. (2002). Heat shock protein expression in cerebral vessels after subarachnoid hemorrhage. *Neurosurgery* 51, 204–210; discussion 210–201. doi: 10.1097/00006123-200207000-00029

Pandey, P., Farber, R., Nakazawa, A., Kumar, S., Bharti, A., Nalin, C., et al. (2000). Hsp27 functions as a negative regulator of cytochrome c-dependent activation of procaspase-3. *Oncogene.* 19, 1975–1981. doi: 10.1038/sj.onc.1203531

Papa, L., Rosenthal, K., Silvestri, F., Axley, J. C., Kelly, J. M., and Lewis, S. B. (2018). Evaluation of alpha-II-spectrin breakdown products as potential biomarkers for early recognition and severity of aneurysmal subarachnoid hemorrhage. *Sci. Rep.* 8, 13308. doi: 10.1038/s41598-018-31631-y

Park, S., Yamaguchi, M., Zhou, C., Calvert, J. W., Tang, J., and Zhang, J. H. (2004). Neurovascular protection reduces early brain injury after subarachnoid hemorrhage. *Stroke.* 35, 2412–2417. doi: 10.1161/01.STR.0000141162.29864.e9

Prunell, G. F., Mathiesen, T., Diemer, N. H., and Svendgaard, N. A. (2003). Experimental subarachnoid hemorrhage: subarachnoid blood volume, mortality rate, neuronal death, cerebral blood flow, and perfusion pressure in three different rat models. *Neurosurgery* 52, 165–175; discussion 175–166. doi: 10.1097/00006123-200301000-00022

Sabri, M., Lass, E., and Macdonald, R. L. (2013). Early brain injury: a common mechanism in subarachnoid hemorrhage and global cerebral ischemia. *Stroke Res. Treat.* 2013, 394036. doi: 10.1155/2013/394036

Satoh, M., Tang, J., Nanda, A., and Zhang, J. H. (2003). Heat shock proteins expression in brain stem after subarachnoid hemorrhage in rats. *Acta Neurochir. Suppl.* 86, 477–482. doi: 10.1007/978-3-7091-0651-8_98

Sehba, F. A., Hou, J., Pluta, R. M., and Zhang, J. H. (2012). The importance of early brain injury after subarachnoid hemorrhage. *Prog Neurobiol.* 97, 14–37. doi: 10.1016/j.pneurobio.2012.02.003

Shan, Q., Ma, F., Wei, J., Li, H., Ma, H., and Sun, P. (2020). Physiological functions of heat shock proteins. *Curr. Protein Pept. Sci.* 21, 751–760. doi: 10.2174/1389203720666191111113726

Shan, R., Liu, N., Yan, Y., and Liu, B. (2021). Apoptosis, autophagy and atherosclerosis: relationships and the role of Hsp27. *Pharmacol. Res.* 166, 105169. doi: 10.1016/j.phrs.2020.105169

Sharp, F. R., Zhan, X., and Liu, D. Z. (2013). Heat shock proteins in the brain: role of Hsp70, Hsp 27, and HO-1 (Hsp32) and their therapeutic potential. *Transl. Stroke Res.* 4, 685–692. doi: 10.1007/s12975-013-0271-4

Shi, Y., Jiang, X., Zhang, L., Pu, H., Hu, X., Zhang, W., et al. (2017). Endothelium-targeted overexpression of heat shock protein 27 ameliorates blood-brain barrier disruption after ischemic brain injury. *Proc. Natl. Acad Sci. U S A.* 114, E1243–E1252. doi: 10.1073/pnas.1621174114

Stetler, R. A., Cao, G., Gao, Y., Zhang, F., Wang, S., Weng, Z., et al. (2008). Hsp27 protects against ischemic brain injury via attenuation of a novel stress-response cascade upstream of mitochondrial cell death signaling. *J. Neurosci.* 28, 13038–13055. doi: 10.1523/JNEUROSCI.4407-08.2008

Stetler, R. A., Gao, Y., Signore, A. P., Cao, G., and Chen, J. (2009). HSP27: mechanisms of cellular protection against neuronal injury. *Curr. Mol. Med.* 9, 863–872. doi: 10.2174/156652409789105561

Stetler, R. A., Gao, Y., Zhang, L., Weng, Z., Zhang, F., Hu, X., et al. (2012). Phosphorylation of HSP27 by protein kinase D is essential for mediating neuroprotection against ischemic neuronal injury. *J. Neurosci.* 32, 2667–2682. doi: 10.1523/JNEUROSCI.5169-11.2012

Toth, M. E., Szegedi, V., Varga, E., Juhasz, G., Horvath, J., Borbely, E., et al. (2013). Overexpression of Hsp27 ameliorates symptoms of

Alzheimer's disease in APP/PS1 mice. *Cell Stress Chaper.* 18, 759–771. doi: 10.1007/s12192-013-0428-9

Unterberg, A. W., Sakowitz, O. W., Sarrafzadeh, A. S., Benndorf, G., and Lanksch, W. R. (2001). Role of bedside microdialysis in the diagnosis of cerebral vasospasm following aneurysmal subarachnoid hemorrhage. *J. Neurosurg.* 94, 740–749. doi: 10.3171/jns.2001.94.5.0740

Vendredy, L., Adriaenssens, E., and Timmerman, V. (2020). Small heat shock proteins in neurodegenerative diseases. *Cell Stress Chaperones* 25, 679–699. doi: 10.1007/s12192-020-01101-4

Voss, O. H., Batra, S., Kolattukudy, S. J., Gonzalez-Mejia, M. E., Smith, J. B., and Doseff, A. I. (2007). Binding of caspase-3 prodomain to heat shock protein 27 regulates monocyte apoptosis by inhibiting caspase-3 proteolytic activation. *J. Biol. Chem.* 282, 25088–25099. doi: 10.1074/jbc.M701740200

Wang, W., Han, P., Xie, R., Yang, M., Zhang, C., Mi, Q., et al. (2019). TAT-mGluR1 attenuation of neuronal apoptosis through prevention of MGluR1alpha truncation after experimental subarachnoid hemorrhage. *ACS Chem. Neurosci.* 10, 746–756. doi: 10.1021/acschemneuro.8b00531

Wasik, N., Sokol, B., Holysz, M., Manko, W., Juszkat, R., Jagodzinski, P. P., et al. (2017). Clusterin, a new cerebrospinal fluid biomarker in severe subarachnoid hemorrhage: a pilot study. *World Neurosurg.* 107, 424–428. doi: 10.1016/j.wneu.2017.08.006

Wu, Q., Qi, L., Li, H., Mao, L., Yang, M., Xie, R., et al. (2017). Roflumilast reduces cerebral inflammation in a rat model of experimental subarachnoid hemorrhage. *Inflammation* 40, 1245–1253. doi: 10.1007/s10753-017-0567-8

Xie, L., Kang, H., Xu, Q., Chen, M. J., Liao, Y., Thiyagarajan, M., et al. (2013). Sleep drives metabolite clearance from the adult brain. *Science.* 342, 373–377. doi: 10.1126/science.1241224

Yang, Y., Chen, S., and Zhang, J. M. (2017). The updated role of oxidative stress in subarachnoid hemorrhage. *Curr. Drug. Deliv.* 14, 832–842. doi: 10.2174/1567201813666161025115531

Zhang, C., Jiang, M., Wang, W. Q., Zhao, S. J., Yin, Y. X., Mi, Q. J., et al. (2020). Selective mGluR1 negative allosteric modulator reduces blood-brain barrier permeability and cerebral edema after experimental subarachnoid hemorrhage. *Transl. Stroke Res.* 11, 799–811. doi: 10.1007/s12975-019-00758-z

Zhang, Z., Liu, J., Fan, C., Mao, L., Xie, R., Wang, S., et al. (2018). The GluN1/GluN2B NMDA receptor and metabotropic glutamate receptor 1 negative allosteric modulator has enhanced neuroprotection in a rat subarachnoid hemorrhage model. *Exp. Neurol.* 301, 13–25. doi: 10.1016/j.expneurol.2017.12.005

Zhang, Z. Y., Sun, B. L., Yang, M. F., Li, D. W., Fang, J., and Zhang, S. (2015). Carnosine attenuates early brain injury through its antioxidative and anti-apoptotic effects in a rat experimental subarachnoid hemorrhage model. *Cell Mol. Neurobiol.* 35, 147–157. doi: 10.1007/s10571-014-0106-1

Zhao, C., Ma, J., Wang, Z., Li, H., Shen, H., Li, X., et al. (2020). Mfsd2a attenuates blood-brain barrier disruption after sub-arachnoid hemorrhage by inhibiting caveolae-mediated transcellular transport in rats. *Transl. Stroke Res.* 11, 1012–1027. doi: 10.1007/s12975-019-00775-y

Zhou, M. L., Shi, J. X., Hang, C. H., Cheng, H. L., Qi, X. P., Mao, L., et al. (2007). Potential contribution of nuclear factor-kappaB to cerebral vasospasm after experimental subarachnoid hemorrhage in rabbits. *J. Cereb. Blood Flow Metab.* 27, 1583–1592. doi: 10.1038/sj.jcbfm.9600456

Conflict of Interest: The authors declare that the research was conducted in the absence of any commercial or financial relationships that could be construed as a potential conflict of interest.

Publisher's Note: All claims expressed in this article are solely those of the authors and do not necessarily represent those of their affiliated organizations, or those of the publisher, the editors and the reviewers. Any product that may be evaluated in this article, or claim that may be made by its manufacturer, is not guaranteed or endorsed by the publisher.

frontiers | Frontiers in Aging Neuroscience

ORIGINAL RESEARCH
published: 06 May 2022
doi: 10.3389/fnagi.2022.851929

Altered Spontaneous Brain Activity in Patients With Diabetic Osteoporosis Using Regional Homogeneity: A Resting-State Functional Magnetic Resonance Imaging Study

Min Liu, Jiang Li, Juan Li, Hui Yang, Qianqian Yao, Xiuzhu Zheng, Zheng Zhang and Jian Qin*

Department of Radiology, The Second Affiliated Hospital of Shandong First Medical University, Taian, China

OPEN ACCESS

Edited by:
Ulises Gomez-Pinedo, Health Research Institute of Hospital Clínico San Carlos, Spain

Reviewed by:
Han Lv, Capital Medical University, China
Alejandro A. Canales-Aguirre, CONACYT Centro de Investigación y Asistencia en Tecnología y Diseño del Estado de Jalisco (CIATEJ), Mexico

****Correspondence:***
Jiang Li
siyany@163.com

Specialty section:
This article was submitted to Neurocognitive Aging and Behavior, a section of the journal Frontiers in Aging Neuroscience

Received: *10 January 2022*
Accepted: *06 April 2022*
Published: *06 May 2022*

Citation:
Liu M, Li J, Li J, Yang H, Yao Q, Zheng X, Zhang Z and Qin J (2022) Altered Spontaneous Brain Activity in Patients With Diabetic Osteoporosis Using Regional Homogeneity: A Resting-State Functional Magnetic Resonance Imaging Study. Front. Aging Neurosci. 14:851929. doi: 10.3389/fnagi.2022.851929

Background: The pathophysiological mechanism of cognitive impairment by osteoporosis in type 2 diabetes mellitus (T2DM) remains unclear. This study aims to further investigate the regional spontaneous brain activity changes of patients with diabetic osteoporosis (DOP), and the correlation between abnormal brain regions and bone metabolites.

Methods: A total of 29 subjects with T2DM were recruited, including fourteen patients with DOP and thirteen patients without osteoporosis (Control group). Based on the resting-state functional magnetic resonance imaging (rs-fMRI) datasets acquired from all the subjects, a two-sample *t*-test was performed on individual normalized regional homogeneity (ReHo) maps. Spearman correlation analysis was performed between the abnormal ReHo regions with the clinical parameters and Montreal Cognitive Assessment (MOCA) scores.

Results: In the DOP group, we demonstrated the significantly increased ReHo values in the left middle temporal gyrus (MTG), right superior occipital gyrus (SOG), aright superior parietal lobule (SPL), right angular gyrus (AG), and left precuneus (PE). Additionally, we also found a significant positive correlation between increased ReHo values in the left MTG and the average bone mineral density (BMD AVG), and average T scores (T AVG). The ReHo values of the right SOG and right SPL showed a negative correlation with MOCA scores, as well as a negative correlation between increased ReHo values in the right SPL and osteocalcin (OC) level.

Conclusion: Patients with DOP showed increased spontaneous activity in multiple brain regions. The results indicated that osteoporosis exacerbated cognitive impairment and brain damage. Also, the OC might be considered as a bone marker to track the progression of cognitive impairment.

Keywords: diabetic osteoporosis (DOP), type 2 diabetes mellitus, regional homogeneity, resting-state functional magnetic resonance imaging, cognitive impairment

INTRODUCTION

The International Diabetes Federation has released new estimates on the prevalence of diabetes worldwide, indicating that the number of diabetes patients was about 415 million and predicted that it would reach up to 642 million by 2040 (Ogurtsova et al., 2017). Diabetes can cause a variety of complications, such as microvascular disease, retinopathy, kidney disease, peripheral neuropathy, osteoporosis, and cognitive impairment (Tiehuis et al., 2010; Macpherson et al., 2017; Cho et al., 2018). Especially, diabetic osteoporosis (DOP) is a serious complications of diabetes mellitus, which is characterized by a reduction of bone mineral density (BMD), destruction of bone microstructural, and a high risk of fractures (Saito and Marumo, 2010; Hamann et al., 2012). Kostev et al. (2018) showed that osteoporosis was a risk factor for dementia. Lee et al. (2012) found that reduced BMD was associated with cognitive impairment and proposed that there was a correlation between cognitive status and BMD in postmenopausal women. However, it is unknown whether osteoporosis will exacerbate cognitive impairment and brain damage in patients with diabetes. The pathophysiological mechanism of cognitive impairment by osteoporosis in diabetes mellitus remains unclear. And whether some markers of bone metabolism may be key factors affecting cognitive ability.

A variety of bone-related peptides are secreted into the circulation, and whether they affect the central nervous system has attracted the attention of researchers (Chamouni et al., 2015). Revealing the spontaneous brain activity induced by osteoporosis helps to elucidate the neuropathological mechanism of cognitive dysfunction. In the present research, we compared the altered spontaneous brain activity between osteoporosis and non-osteoporosis patients with type 2 diabetes mellitus (T2DM) by regional homogeneity (ReHo) of resting-state functional magnetic resonance imaging (rs-fMRI), to explore the correlation of altered ReHo values with BMD, OC, and the neurocognitive scale, and to discuss the influence mechanism of osteoporosis. The findings may provide insight into the neurological underpinnings of osteoporosis-related brain dysfunction.

METHODS

Subjects

The present study was approved by the ethics review committee of the second affiliated hospital of Shandong's first medical university. Informed written consent was obtained from each participant. The subjects who met the inclusion criteria in this study were recruited from June 2020 to September 2021 in the surrounding community by posting a recruitment notice. Twenty-nine right-handed Patients with T2DM participated in this study. Fifteen patients (5 male and 10 female, mean age 58.33 $\pm$ 4.63) were included in the DOP group, and fourteen non-osteoporosis patients (6 male and 8 female, mean age 56.00 $\pm$ 4.22) with matching gender, age, duration, and education were enrolled as the Control group. All patients maintained stable blood glucose by using oral drugs or insulin. The diagnosis of T2DM was based on standard criteria from the American Diabetes Association (2018). The criteria for the diagnosis of diabetes: The fasting plasma glucose (FPG) $\geq$126 mg/dL (7.0 mmol/L), fasting is defined as no caloric intake for at least 8 h or 2-h Plasma Glucose (PG) $\geq$ 200 mg/dL (11.1 mmol/L) during a 75-g oral glucose tolerance test (OGTT), the test should be performed as described by the WHO, using a glucose load containing the equivalent of 75-g anhydrous glucose dissolved in water or A1C $\geq$ 6.5% (48 mmol/mol), the test should be performed in a laboratory using a method that is NGSP certified and standardized to the DCCT assay or In a patient with classic symptoms of hyperglycemia or hyperglycemic crisis, random plasma glucose $\geq$200 mg/dL(11.1 mmol/L). The exclusion criteria included the following: (1) Patients with other complications of diabetes, such as severe liver and kidney dysfunction, diabetic retinopathy, diabetic peripheral neuropathy, etc; (2) diseases affecting bone metabolisms, such as hyperthyroidism, hypercortisolism, connective tissue disease, and glucocorticoid administration; (3) lesions in the brain, such as tumors, cerebral infarction, hemorrhage, or vascular malformation; (4) contraindication to MRI examination, such as the presence of metallic implants or claustrophobia; (5) a history of neurological or psychiatric disorders; (6) used bisphosphonates, calcium, vitamin D and other osteoporosis drugs in the last 3 months; (7) used hormone drugs; (8) other types of diabetes. People with one of the above conditions will be excluded from this experiment.

General Information and Cognitive Assessment

Clinical examinations including measurements of height, weight, body mass index (BMI), glycosylated hemoglobin A1C (HbA1c), duration, and serum OC were carefully performed by specialists. All subjects underwent the Montreal Cognitive Assessment (MoCA). The MoCA is commonly used to screen for Mild Cognitive Impairment (MCI), for which it displays high-sensitivity (Hobson, 2015), with a final score $\geq$ 26 considered normal. Subjects with less than 12 years of education receive an extra point. MoCA testing took place in a quiet room by trained professionals.

Bone Mineral Density (BMD)

The BMD was measured by dual-energy X-ray absorptiometry (Horizon W, Hologic Inc, US). The criteria for diagnosing osteoporosis using DXA are the following: scans of the lumbar spine and hip, selecting the L1 to L4 vertebral bodies and the femoral neck and total hip as a region of interest (ROI), and using the lowest T-score amongst the 3 ROIs to make the diagnosis (Cheng et al., 2020). According to diagnostic criteria of osteoporosis (Camacho et al., 2020): a T-score ≥ -1 indicated normal; T-score between -1 and -2.5 indicated osteopenia; and T-score was -2.5 or below indicated osteoporosis. The patients with DOP included met the diagnostic criteria for osteoporosis.

MRI Data Acquisition

Images were acquired on a 3.0T MRI scanner (Discovery MR750, GE Healthcare, Waukesha, WI, USA) using a commercial eight-channel head coil. Foam padding was used to restrict head movement and earplugs were used to minimize scanner noise.

Subjects were asked to lie with their eyes closed, not to fall asleep, and not to think of anything in particular. Routine sequence scanning was performed to exclude brain tumors, cerebral infarction, cerebral hemorrhage, and other brain abnormalities. High-resolution anatomical images were obtained with a sagittal T1-3D brain volume imaging sequence (TE = 3.2 ms, TR = 8.2 ms, TI = 450 ms, FOV = 256 × 256 mm, matrix = 256 × 256, layer spacing = 0 mm, layer thickness = 1 mm, layer number = 176, NEX = 1). Functional images were obtained axially using a gradient-echo planar imaging sequence with the following parameters: TR = 2,000 ms, TE = 30 ms, Slice = 41, Slice thickness = 3 mm, FA = 90°, matrix = 64 × 64, FOV = 224 × 224 mm, NEX = 1, time point is 240, number of slices: 41, scanning time = 8 min.

Data Preprocessing and ReHo Analysis

Functional image preprocessing was performed using the data processing assistant in the rs-fMRI toolbox (Yan et al., 2016) (DPABI, http://rfmri.org/dpabi V6.0_210501). The first 10 time points were discarded, and the subjects with more than 2 mm maximum displacement in any dimension and 2 degrees of angular motion during the entire fMRI were excluded (one subject from each group was eliminated in this step). The functional images were then spatially normalized to standard coordinates and resampled to 3 × 3 × 3 mm^3. After that, the linear trend of the time series was removed and a temporal filter (0.01 Hz < f < 0.08 Hz) was conducted to reduce the effects of low-frequency drift and physiological high-frequency noise.

Individual ReHo maps were generated by calculating Kendall's coefficient of concordance (KCC) of the time series of a given voxel to its nearest 26 voxels (Zang et al., 2004). The average ReHo values of all voxels in the significant region were extracted using the rs-fMRI data analysis tool (Song et al., 2011) (REST, http://www.restfmri.net/forum/REST_V1.8) in the mask generated by the standardized step. Then, the resulting data were spatially smoothed with a Gaussian kernel (fullwidth at half-maximum, FWHM = 6 mm). Finally, a z-transformation was conducted on the individual ReHo maps to generate normally distributed szReHo maps.

Statistical Analysis

SPSS Statistics version 23.0 was used for statistical analysis. The inter-group comparison of nominal variables (sex) was performed using the *Chi-square* (χ^2) test. Then, the *Kolmogorov-Smirnov* test was applied in each group to verify the normality of the other numerical data distribution. According to the normality or non-normality, the two-sample *t*-test and the *Mann–Whitney U* test were applied to reveal significant differences between the DOP group and the control group. To explore the inter-group ReHo differences, a two-sample *t*-test was performed on the individual normalized ReHo maps. And We used the false discovery rate (*FDR, p<0.01*) to correct the multiple comparisons for the *p-value*. *Spearman* correlation analysis was performed between the abnormal ReHo regions with the clinical parameters, such as BMD AVG, T AVG, MOCA, OC, and HbA1c, $p < 0.05$ was considered statistically significant.

TABLE 1 | Demographic, clinical, and cognitive data.

	DOP group ($n = 14$)	Control group ($n = 13$)	*P* value
Age (years)	58.33 ± 4.63	56.00 ± 4.22	0.169
Sex (male/female)	5/10	6/8	0.597[a]
HbA1c (%)	8.24 ± 1.21	8.64 ± 1.63	0.463
duration (month)	49.60 ± 6.51	50.00 ± 6.56	0.870
Education (years)	9.93 ± 2.40	11.86 ± 3.21	0.077
BMI (kg/m^2)	23.90 ± 3.42	26.21 ± 3.34	0.077
Weight (Kg)	62.46 ± 9.83	68.32 ± 5.35	0.059
Height (CM)	161.60 ± 6.10	163.43 ± 5.14	0.392
BMD AVG (g/cm^2)	0.77 (0.70,0.83)	1.04 (1.02,1.12)	0.000*[b]
T AVG	−2.80 (−3.30,−2.60)	−0.05 (−0.50,0.35)	0.000*[b]
MOCA	21.67 ± 2.47	25.64 ± 2.65	0.000*
OC (ng/ml)	23.53 (22.05,24.81)	29.94 (26.97,32.79)	0.000*[b]

*$p < 0.05$. Data are presented as n for proportions, means ± SD for normally distributed continuous data, and median (QR) for non-normally distributed data; [a] The p-value for sex was obtained using the $\chi 2$ test; [b] The p-value was obtained using the Mann–Whitney U test; DOP, T2DM with osteoporosis;T2DM with non-osteoporosis as controls; BMI, body mass index; BMD, Bone Mineral Density; MOCA, Montreal Cognitive Assessment; OC, osteocalcin.

RESULTS

Demographics

According to the two-sample *t*-test, significantly decreased levels of BMD AVG, T AVG, MOCA scores, and OC were observed in the DOP group compared to the Control group ($p < 0.05$). There were no significant differences between the DOP group and the Control group in terms of age, sex, height, weight, BMI, HbA1c, duration, and education years ($p > 0.05$, **Table 1**).

ReHo Differences and Correlation Analysis

Compared to the control group, patients with DOP had significantly higher ReHo values in the left middle temporal gyrus (MTG), right superior occipital gyrus (SOG), right superior parietal lobule (SPL), right angular gyrus (AG) and left precuneus (PE),as shown in **Figure 1**, **Table 2**. In the DOP group, the ReHo values of the left MTG showed positive correlation with the average BMD (BMD AVG) and average T scores (T AVG) (separately, $r = 0.601$, $P = 0.023$; $r = 0.658$, $P = 0.011$) (**Figures 2**, **3**). The ReHo values of the right SOG and right SPL showed negative correlation with MOCA scores (separately, $r = -0.686$, $P = 0.01$; $r = -0.734$, $P = 0.004$) (**Figures 4**, **5**). The ReHo values of right SPL showed negative correlation with OC ($r = -0.705$, $P = 0.007$) (**Figure 6**).

DISCUSSION

In the present study, we demonstrated that patients with DOP showed significantly higher ReHo values in the left MTG, right SOG, right SPL, right AG, and left PE. In the DOP group, the ReHo values of the left MTG showed a positive correlation with the BMD AVG and T AVG, and the ReHo values of the right SOG

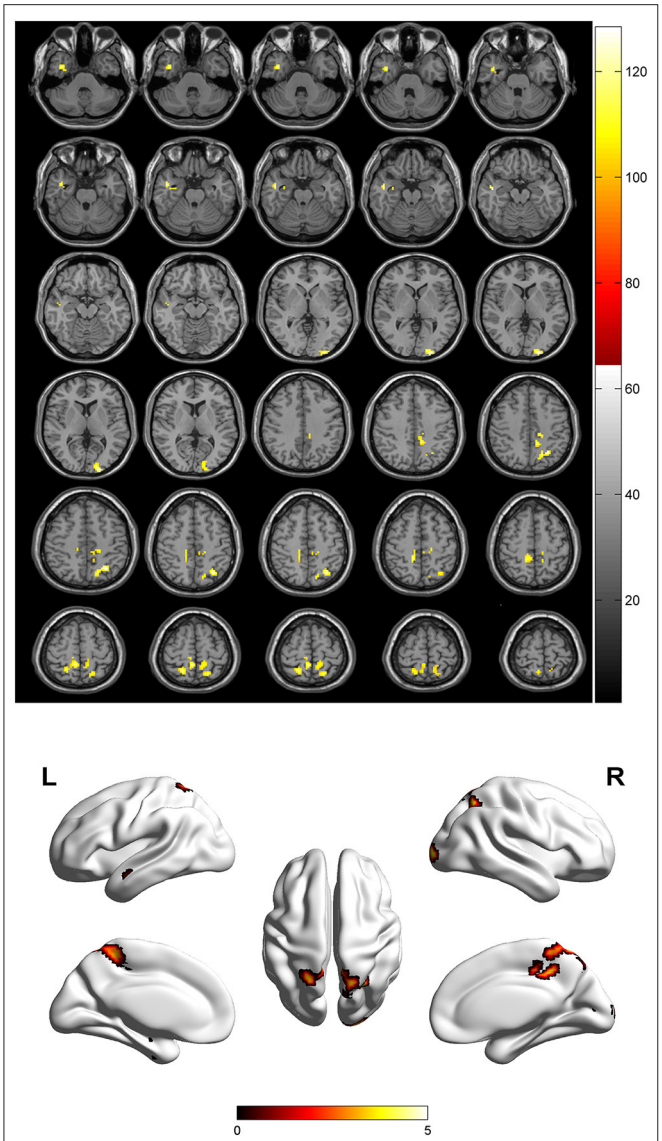

FIGURE 1 | Spontaneous brain activity in patients with DOP group vs. Control group. The threshold was set $p < 0.01$(FDR correction).

TABLE 2 | Brain areas with significantly different regional homogeneity (ReHo) values between groups.

Brain region	MNI coordinates			T value	Cluster Size
	X	Y	Z		
Temporal_Mid_L (aal)	−48	−6	−21	4.4099	56
Occipital_Sup_R (aal)	24	−99	3	4.3332	62
Parietal_Sup_R (aal)	18	−60	63	3.4653	113
Angular_R (aal)	27	−60	48	4.3883	60
Precuneus_L (aal)	−15	−39	54	3.7383	118

L, left; R, right; AAL, Anatomical Automatic Labeling; MNI, Montreal Neurological Institute; cluster_size > 50.

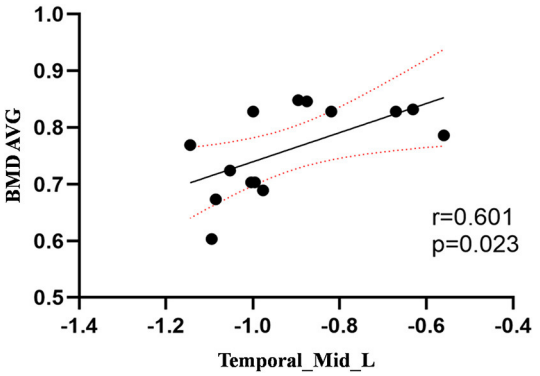

FIGURE 2 | Correlation between ReHo values of the left MTG and the BMD AVG. The ReHo values of the left MTG showed a positive correlation with the BMD AVG ($r = 0.601$; $P = 0.023$).

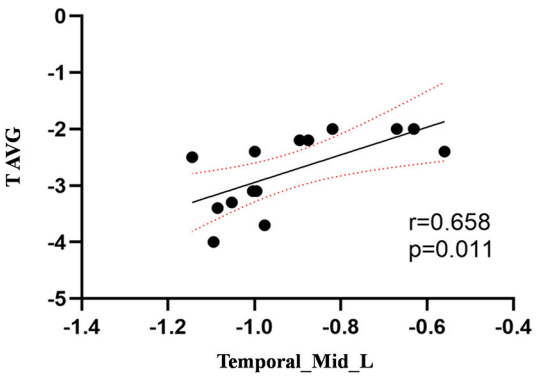

FIGURE 3 | Correlation between ReHo values of the left MTG and the T AVG. The ReHo values of the left MTG showed a positive correlation with the T AVG ($r = 0.658$; $P = 0.011$).

and right SPL showed a negative correlation with MOCA scores, the ReHo values of right SPL showed negative correlation with OC level.

The temporal lobe is involved in audiovisual language integration and is considered a key component of the midline cortex (Ye et al., 2017). Impairment of the temporal lobe is considered to cause a defect in self-awareness (Chavoix and Insausti, 2017). Deletion of temporal lobe neurons and abnormal connections in the frontotemporal gyrus is thought to be closely related to dementia (Sato and Morishita, 2014). This study demonstrated that the ReHo values in the left MTG were increased in the DOP group, suggesting a decrease in the presence of cognitive function in patients with DOP. Furthermore, Zhou et al. (2014b) revealed that the regional function of the inferior and middle temporal gyrus was increased in mild cognitive impairment in patients with T2DM, which was linked to the functional compensation for cognitive decline. Therefore, we considered that osteoporosis exacerbated cognitive impairment, and the increased ReHo

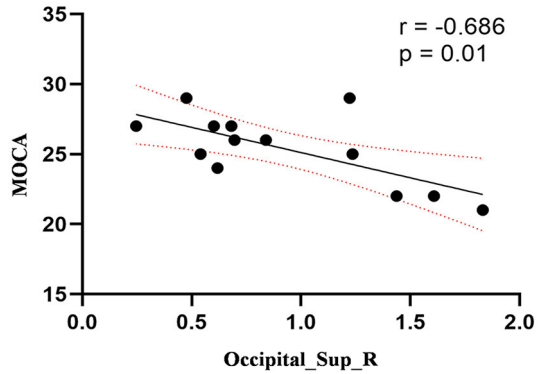

FIGURE 4 | Correlation between ReHo values of the right SOG and the MOCA scores. The ReHo values of right SOG showed a negnative correlation with MOCA scores ($r = -0.686$; $P = 0.01$).

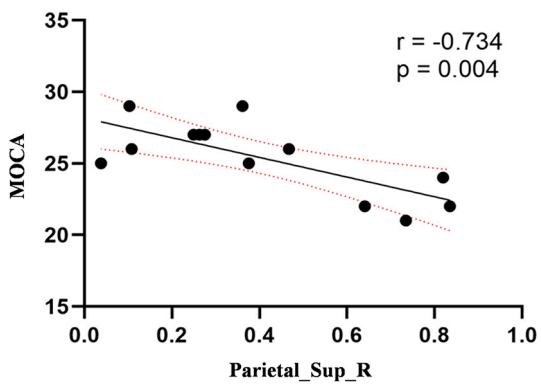

FIGURE 5 | Correlation between ReHo values of the right SPL and the MOCA scores. The ReHo values of right SPL showed a negnative correlation with MOCA scores ($r = -0.734$; $P = 0.004$).

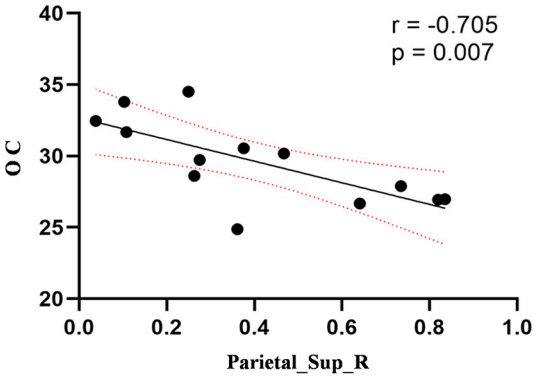

FIGURE 6 | Correlation between ReHo values of the right SPL and OC. The ReHo values of right SPL showed a negnative correlation with OC ($r = -0.705$; $P = 0.007$).

values in the left MTG were compensation mechanisms for cognitive impairment. In this study, we also discovered that the ReHo values of the left MTG showed a positive correlation with the BMD AVG and T AVG and confirmed that osteoporosis aggravated cognitive impairment based on T2DM. Lee et al. (2012) confirmed that cognitive impairment was associated with lower BMD, which was consistent with our findings.

The occipital cortex is usually considered to be the visual area, especially the primary visual cortex (Wandell, 1999), responsible for visual memory and vision processing (Rehman and Al Khalili, 2021). The occipital visual areas and frontal/parietal sensorimotor areas are activated concurrently during the visuospatial working memory task (Kwon et al., 2002). Functional impairment of the occipital lobe can lead to defects in the visual pathway, which affects the processing of visual information and recognition of the outside world (Tohid et al., 2015). This study demonstrated that the ReHo value in the right SOG was increased in the DOP group, and we held that the increased ReHo in the occipital cortex might be an important factor and early indicator of cognitive deficits and visual impairment in patients with DOP. Moreover, multiple studies have confirmed that the visual processing area of the occipital lobe was the most vulnerable region of the brain to T2DM (Cui et al., 2014; Wang et al., 2017). Therefore, we speculated that osteoporosis exacerbated visual impairment based on T2DM. We also found the ReHo values of the right SOG showed a negative correlation with MOCA scores, which represented an early compensatory mechanism for neuroplasticity induced by osteoporosis to counteract the effects of cognitive deficits and maintain normal cognitive functions probably, namely the greater the cognitive decline, the stronger the compensation (Wang et al., 2014).

In addition, we discovered that abnormities also occurred in the right AG and right SPL of the DOP group. As the important regions of the middle longitudinal fascicle (M dLF), AG and SPL encompassed numerous and specialized subdivisions that subserved a vast array of functions, which involved linguistic, attentive, visuospatial, and integrative audiovisual parts (Makris et al., 2013). According to a study of causal connectivity regarding subjective cognitive decline (SCD) (Cai et al., 2020), the right AG and SPL both had exhibited significant aberrant connections, which might reflect the impairments in cognitive functions. Tan et al. (2019) found the aberrant functional connectivity of the posterior cingulate cortex (PCC) to AG (associated with short-term memory functional decline) and SPL (associated with attention and spatial orientation) in patients with T2DM, thus causing the cognitive dysfunction. The AG is involved in a variety of cognitive processes, especially episodic memory retrieval and semantic processing, which has been found in human beings (Seghier, 2013; Ramanan et al., 2018; Qi et al., 2021). Therefore, we held that an increased ReHo in the right AG might be the important factors and indicator of episodic memory impairment and semantic processing disorder in the DOP group. Furthermore, we also discovered abnormities that occurred in the right SPL of the DOP group. It has been well

established that SPL has mostly positive connections with the regions defining the default mode network, which could be their involvement in higher order of cognitive and attentional tasks (Alahmadi, 2021). Gu and Zhang (2019) reported that patients with MCI showed hyperactive resting-state activity in the SPL, which was consistent with our study. For the DOP group, increased ReHo values of SPL showed significant correlation with OC in the follow-up research. Oury et al. (2013) showed that OC crossed the placenta and the blood-brain barrier to influence fetal development and cognitive function in mice. Puig et al. (2016) indicated that lower serum OC concentrations were associated with brain microstructural changes and worse cognitive performance. Therefore, we speculated that OC as an intermediate of bone metabolism might be the key factor leading to cognitive impairment in osteoporotic patients, and the SPL might be the specific target and functional site.

The PE has important roles in cognitive function, including visuospatial imagery and episodic memory retrieval (Cavanna and Trimble, 2006). Histopathological deposition of amyloid in the PE occurs in the early stage of MCI (Wu et al., 2012), and its resulting damage leads to atrophy of the PE, as seen in early-stage of Alzheimer's disease (AD) (He et al., 2007). The PCC, PE, and parietal lobe were considered to be deeply implicated in the pathophysiology of AD since these regions showed reduced glucose metabolism (Del Sole et al., 2008) and regional cerebral blood flow (rCBF) (Borroni et al., 2006) from an early stage of the disease. In our study, we found the ReHo values in the left PE increased in the DOP group, which suggested that osteoporosis, as a metabolic disease, tended to exacerbate the progression of AD, which could be a predisposing factor for AD progression. A prospective cohort study found that women with faster bone loss were more likely to have cognitive decline (Zhou et al., 2014a), which was consistent with our results.

Interestingly, the multiple abnormal brain regions identified in our study are affiliated with the default mode network (DMN). As a functionally homogeneous system, the DMN involves the posterior cingulate cortex, precuneus, medial prefrontal cortex, and temporal regions, which are the most active at rest and suspended during cognitive activity (McCormick et al., 2014), and are suggested as a major contributor to the normal cognitive functioning (Smucny et al., 2014). Reduction of intrinsic connectivity of the DMN has been observed in several mental disorders, such as AD, autism, schizophrenia, and hepatic encephalopathy (Buckner et al., 2008; Zhang et al., 2012; Zhou et al., 2012; Adriaanse et al., 2014). Our results furtherly confirmed that the default network was the most active network in the resting state. The brain damage caused by osteoporosis firstly affected the DMN, an osteoporosis-exacerbated cognitive impairment based on T2DM.

The preliminary study has some limitations. Firstly, this study had a relatively small sample size. Due to strict inclusion criteria, relatively few patients with DOP were enrolled. Further study with more participants and follow-up on these patients are great importance to evaluate whether the OC could be markers for tracking the very early changes of brain function associated with patients with DOP. Secondly, this study was inadequate to examine the spontaneous activity of DOP by using ReHo without studying structural image data at the same time in resting-state. We should combine multi-modal imaging data to establish these relationships in the future, which would provide more accurate interpretation of the neural mechanisms of cognitive impairment by osteoporosis in T2DM. Moreover, we did not include a completely healthy control group, because the purpose of this study was to observe the effect of osteoporosis on altered spontaneous brain activity in patients with T2DM, rather than the influence of T2DM itself.

CONCLUSION

Based on ReHo analysis on rs-fMRI, this study suggested that activities of multiple brain regions were altered in patients with DOP, which indicated that osteoporosis exacerbated cognitive impairment and brain damage. Also, the OC might be considered as a bone marker to track the progression of cognitive impairment.

DATA AVAILABILITY STATEMENT

The original contributions presented in the study are included in the article/supplementary material, further inquiries can be directed to the corresponding author/s.

ETHICS STATEMENT

The studies involving human participants were reviewed and approved by The Second Affiliated Hospital of Shandong First Medical University. The patients/participants provided their written informed consent to participate in this study.

AUTHOR CONTRIBUTIONS

ML: writing—original draft preparation. HY: formal analysis and writing—reviewing and editing. JQ: conceptualization and methodology. XZ: data curation and methodology. QY: visualization and resources. GY: formal analysis, data curation, and software. JuL: visualization and software. JiL: resources, supervision, and project administration. All authors contributed to the article and approved the submitted version.

FUNDING

This study was supported by the Medical Health Science and Technology Development Plan Project of Shandong Province (202009041141), the Academic promotion programme of Shandong Frist Medical University (2019QL017), the Medical Health Science and Technology Development Plan Project of Shandong Province (202109010477), and the Science and Technology innovation development project of Tai'an city (2021NS127).

REFERENCES

Adriaanse, S. M., Sanz-Arigita, E. J., Binnewijzend, M. A., Ossenkoppele, R., Tolboom, N., van Assema, D. M., et al. (2014). Amyloid and its association with default network integrity in Alzheimer's disease. *Human Brain Map.* 35, 779–791. doi: 10.1002/hbm.22213

Alahmadi, A. (2021). Investigating the sub-regions of the superior parietal cortex using functional magnetic resonance imaging connectivity. *Insights Into Imag.* 12, 47. doi: 10.1186/s13244-021-00993-9

American Diabetes Association (2018). Classification and diagnosis of diabetes: standards of medical care in diabetes-2018. *Diabetes Care.* 41, S13–S27. doi: 10.2337/dc18-S002

Borroni, B., Anchisi, D., Paghera, B., Vicini, B., Kerrouche, N., Garibotto, V., et al. (2006). Combined 99mTc-ECD SPECT and neuropsychological studies in MCI for the assessment of conversion to AD. *Neurobiol. Aging.* 27, 24–31. doi: 10.1016/j.neurobiolaging.2004.12.010

Buckner, R. L., Andrews-Hanna, J. R., and Schacter, D. L. (2008). The brain's default network: anatomy, function, and relevance to disease. *Ann. New York Acad. Sci.* 1124, 1–38. doi: 10.1196/annals.1440.011

Cai, C., Huang, C., Yang, C., Lu, H., Hong, X., Ren, F., et al. (2020). Altered patterns of functional connectivity and causal connectivity in salience subnetwork of subjective cognitive decline and amnestic mild cognitive impairment. *Front. Neurosci.* 14, 288. doi: 10.3389/fnins.2020.00288

Camacho, P. M., Petak, S. M., Binkley, N., Diab, D. L., Eldeiry, L. S., Farooki, A., et al. (2020). American association of clinical endocrinologists/American college of endocrinology clinical practice guidelines for the diagnosis and treatment of postmenopausal osteoporosis-2020 update. *Endocrine Pract.* 26, 1–46. doi: 10.4158/GL-2020-0524SUPPL

Cavanna, A. E., and Trimble, M. R. (2006). The precuneus: a review of its functional anatomy and behavioural correlates. *Brain J. Neurol.* 129, 564–583. doi: 10.1093/brain/awl004

Chamouni, A., Schreiweis, C., and Oury, F. (2015). Bone, brain and beyond. *Rev. Endocr. Metab. Diso.* 16, 99–113. doi: 10.1007/s11154-015-9312-5

Chavoix, C., and Insausti, R. (2017). Self-awareness and the medial temporal lobe in neurodegenerative diseases. *Neurosci. Biobehav. Rev.* 78, 1–12. doi: 10.1016/j.neubiorev.2017.04.015

Cheng, X., Yuan, H., Cheng, J., Weng, X., Xu, H., Gao, J., et al. (2020). Chinese expert consensus on the diagnosis of osteoporosis by imaging and bone mineral density. *Quantit. Imag. Med. Surg.* 10, 2066–2077. doi: 10.21037/qims-2020-16

Cho, N. H., Shaw, J. E., Karuranga, S., Huang, Y., da Rocha Fernandes, J. D., Ohlrogge, A. W., et al. (2018). IDF Diabetes Atlas: Global estimates of diabetes prevalence for 2017 and projections for 2045. *Diab. Res. Clin. Pract.* 138, 271–281. doi: 10.1016/j.diabres.2018.02.023

Cui, Y., Jiao, Y., Chen, Y. C., Wang, K., Gao, B., Wen, S., et al. (2014). Altered spontaneous brain activity in type 2 diabetes: a resting-state functional MRI study. *Diabetes.* 63, 749–760. doi: 10.2337/db13-0519

Del Sole, A., Clerici, F., Chiti, A., Lecchi, M., Mariani, C., Maggiore, L., et al. (2008). Individual cerebral metabolic deficits in Alzheimer's disease and amnestic mild cognitive impairment: an FDG PET study. *Eur. J. Nucl. Med. Molec. Imag.* 35, 1357–1366. doi: 10.1007/s00259-008-0773-6

Gu, L., and Zhang, Z. (2019). Exploring structural and functional brain changes in mild cognitive impairment: a whole brain ALE meta-analysis for multimodal MRI. *ACS Chem. Neurosci.* 10, 2823–2829. doi: 10.1021/acschemneuro.9b00045

Hamann, C., Kirschner, S., Günther, K. P., and Hofbauer, L. C. (2012). Bone, sweet bone–osteoporotic fractures in diabetes mellitus. *Nat. Rev. Endocrinol.* 8, 297–305. doi: 10.1038/nrendo.2011.233

He, Y., Wang, L., Zang, Y., Tian, L., Zhang, X., Li, K., et al. (2007). Regional coherence changes in the early stages of Alzheimer's disease: a combined structural and resting-state functional MRI study. *NeuroImage.* 35, 488–500. doi: 10.1016/j.neuroimage.2006.11.042

Hobson, J. (2015). The montreal cognitive assessment (MoCA). *Occupat. Med.* 65, 764–765. doi: 10.1093/occmed/kqv078

Kostev, K., Hadji, P., and Jacob, L. (2018). Impact of osteoporosis on the risk of dementia in almost 60,000 patients followed in general practices in Germany. *J. Alzheimer's Dis.* 65, 401–407. doi: 10.3233/JAD-180569

Kwon, H., Reiss, A. L., and Menon, V. (2002). Neural basis of protracted developmental changes in visuo-spatial working memory. *Proc. Nat. Acad. Sci. U. S. A.* 99, 13336–13341. *doi: 10.1073/pnas.162486399*

Lee, D. Y., Na, D. L., Seo, S. W., Chin, J., Lim, S. J., Choi, D., et al. (2012). Association between cognitive impairment and bone mineral density in postmenopausal women. *Menopause.* 19, 636–641. doi: 10.1097/gme.0b013e31823dbec7

Macpherson, H., Formica, M., Harris, E., and Daly, R. M. (2017). Brain functional alterations in Type 2 Diabetes - A systematic review of fMRI studies. *Front. Neuroendocrinol.* 47, 34–46. doi: 10.1016/j.yfrne.2017.07.001

Makris, N., Preti, M. G., Wassermann, D., Rathi, Y., Papadimitriou, G. M., Yergatian, C., et al. (2013). Human middle longitudinal fascicle: segregation and behavioral-clinical implications of two distinct fiber connections linking temporal pole and superior temporal gyrus with the angular gyrus or superior parietal lobule using multi-tensor tractography. *Brain Imag. Behav.* 7, 335–352. doi: 10.1007/s11682-013-9235-2

McCormick, C., Protzner, A. B., Barnett, A. J., Cohn, M., Valiante, T. A., and McAndrews, M. P. (2014). Linking DMN connectivity to episodic memory capacity: what can we learn from patients with medial temporal lobe damage? *NeuroImage. Clin.* 5, 188–196. doi: 10.1016/j.nicl.2014.05.008

Ogurtsova, K., da Rocha Fernandes, J. D., Huang, Y., Linnenkamp, U., Guariguata, L., Cho, N. H., et al. (2017). IDF Diabetes Atlas: Global estimates for the prevalence of diabetes for 2015 and 2040. *Diab. Res. Clin. Pract.* 128, 40–50. doi: 10.1016/j.diabres.2017.03.024

Oury, F., Khrimian, L., Denny, C. A., Gardin, A., Chamouni, A., Goeden, N., et al. (2013). Maternal and offspring pools of osteocalcin influence brain development and functions. *Cell.* 155, 228–241. doi: 10.1016/j.cell.2013.08.042

Puig, J., Blasco, G., Daunis-i-Estadella, J., Moreno, M., Molina, X., Alberich-Bayarri, A., et al. (2016). Lower serum osteocalcin concentrations are associated with brain microstructural changes and worse cognitive performance. *Clin. Endocrinol.* 84, 756–763. doi: 10.1111/cen.12954

Qi, F., Zhang, D., Gao, J., Tang, M., Wang, M., Su, Y., et al. (2021). Functional disconnection of the angular gyrus related to cognitive impairment in patients with type 2 diabetes mellitus. *Front. Human Neurosci.* 15, 621080. doi: 10.3389/fnhum.2021.621080

Ramanan, S., Piguet, O., and Irish, M. (2018). Rethinking the role of the angular gyrus in remembering the past and imagining the future: the contextual integration model. *Neurosci.* 24, 342–352. doi: 10.1177/1073858417735514

Rehman, A., and Al Khalili, Y. (2021). "*Neuroanatomy, Occipital Lobe*", in StatPearls. StatPearls Publishing.

Saito, M., and Marumo, K. (2010). Collagen cross-links as a determinant of bone quality: a possible explanation for bone fragility in aging, osteoporosis, and diabetes mellitus. *Osteopor. Int.* 21, 195–214. doi: 10.1007/s00198-009-1066-z

Sato, N., and Morishita, R. (2014). Brain alterations and clinical symptoms of dementia in diabetes: aβ/tau-dependent and independent mechanisms. *Front. Endocrinol.* 5, 143. doi: 10.3389/fendo.2014.00143

Seghier, M. L. (2013). The angular gyrus: multiple functions and multiple subdivisions. *Neuroscientist* 19, 43–61. doi: 10.1177/1073858412440596

Smucny, J., Wylie, K. P., and Tregellas, J. R. (2014). Functional magnetic resonance imaging of intrinsic brain networks for translational drug discovery. *Trends Pharmacol. Sci.* 35, 397–403. doi: 10.1016/j.tips.2014.05.001

Song, X. W., Dong, Z. Y., Long, X. Y., Li, S. F., Zuo, X. N., Zhu, C. Z., et al. (2011). REST: a toolkit for resting-state functional magnetic resonance imaging data processing. *PLoS ONE.* 6, e25031. doi: 10.1371/journal.pone.0025031

Tan, X., Liang, Y., Zeng, H., Qin, C., Li, Y., Yang, J., et al. (2019). Altered functional connectivity of the posterior cingulate cortex in type 2 diabetes with cognitive impairment. *Brain Imag. Behav.* 13, 1699–1707. doi: 10.1007/s11682-018-0017-8

Tiehuis, A., van der Meer, F., Mali, W., Pleizier, M., Biessels, G. J., Kappelle, J., et al. (2010). MR spectroscopy of cerebral white matter in type 2 diabetes; no association with clinical variables and cognitive performance. *Neuroradiology.* 52, 155–161. doi: 10.1007/s00234-009-0598-4

Tohid, H., Faizan, M., and Faizan, U. (2015). Alterations of the occipital lobe in schizophrenia. *Neurosciences.* 20, 213–224. doi: 10.17712/nsj.2015.3.20140757

Wandell, B. A. (1999). Computational neuroimaging of human visual cortex. *Ann. Rev. Neurosci.* 22, 145–173. doi: 10.1146/annurev.neuro.22.1.145

Wang, C. X., Fu, K. L., Liu, H. J., Xing, F., and Zhang, S. Y. (2014). Spontaneous brain activity in type 2 diabetics revealed by amplitude of low-frequency fluctuations and its association with diabetic vascular disease: a resting-state FMRI study. *PLoS ONE.* 9, e108883. doi: 10.1371/journal.pone.0108883

Wang, Z. L., Zou, L., Lu, Z. W., Xie, X. Q., Jia, Z. Z., Pan, C. J., et al. (2017). Abnormal spontaneous brain activity in type 2 diabetic retinopathy revealed by amplitude of low-frequency fluctuations: a resting-state fMRI study. *Clin. Radiol.* 72, 340.e1–340.e7. doi: 10.1016/j.crad.2016.11.012

Wu, L., Rowley, J., Mohades, S., Leuzy, A., Dauar, M. T., Shin, M., et al.(2012). Dissociation between brain amyloid deposition and metabolism in early mild cognitive impairment. *PLoS ONE.* 7, e47905. doi: 10.1371/journal.pone.0047905

Yan, C. G., Wang, X. D., Zuo, X. N., and Zang, Y. F. (2016). DPABI: data processing and analysis for (resting-state) brain imaging. *Neuroinformatics.* 14, 339–351. doi: 10.1007/s12021-016-9299-4

Ye, Z., Rüsseler, J., Gerth, I., and Münte, T. F. (2017). Audiovisual speech integration in the superior temporal region is dysfunctional in dyslexia. *Neuroscience.* 356, 1–10. doi: 10.1016/j.neuroscience.2017.05.017

Zang, Y., Jiang, T., Lu, Y., He, Y., and Tian, L. (2004). Regional homogeneity approach to fMRI data analysis. *NeuroImage.* 22, 394–400. doi: 10.1016/j.neuroimage.2003.12.030

Zhang, L., Qi, R., Wu, S., Zhong, J., Zhong, Y., Zhang, Z., et al. (2012). Brain default-mode network abnormalities in hepatic encephalopathy: a resting-state functional MRI study. *Human Brain Mapp.* 33, 1384–1392. doi: 10.1002/hbm.21295

Zhou, R., Zhou, H., Rui, L., and Xu, J. (2014a). Bone loss and osteoporosis are associated with conversion from mild cognitive impairment to Alzheimer's disease. *Cur. Alzheimer Res.* 11, 706–713. doi: 10.2174/1567205011666140812115818

Zhou, X., Zhang, J., Chen, Y., Ma, T., Wang, Y., Wang, J., et al. (2014b). Aggravated cognitive and brain functional impairment in mild cognitive impairment patients with type 2 diabetes: a resting-state functional MRI study. *J. Alzheimer's Dis.* 41, 925–935. doi: 10.3233/JAD-132354

Zhou, Y., Milham, M. P., Lui, Y. W., Miles, L., Reaume, J., Sodickson, D. K., et al. (2012). Default-mode network disruption in mild traumatic brain injury. *Radiology.* 265, 882–892. doi: 10.1148/radiol.12120748

Conflict of Interest: The authors declare that the research was conducted in the absence of any commercial or financial relationships that could be construed as a potential conflict of interest.

Publisher's Note: All claims expressed in this article are solely those of the authors and do not necessarily represent those of their affiliated organizations, or those of the publisher, the editors and the reviewers. Any product that may be evaluated in this article, or claim that may be made by its manufacturer, is not guaranteed or endorsed by the publisher.

frontiers | Frontiers in Aging Neuroscience

ORIGINAL RESEARCH
published: 09 May 2022
doi: 10.3389/fnagi.2022.865430

Brain Activity in Age-Related Macular Degeneration Patients From the Perspective of Regional Homogeneity: A Resting-State Functional Magnetic Resonance Imaging Study

Qi-Ying Liu†, Yi-Cong Pan†, Hui-Ye Shu†, Li-Juan Zhang, Qiu-Yu Li, Qian-Min Ge, Yi Shao and Qiong Zhou**

Department of Ophthalmology, Jiangxi Center of National Ocular Disease Clinical Research Center, The First Affiliated Hospital of Nanchang University, Nanchang, China

OPEN ACCESS

Edited by:
Yuzhen Xu,
Tongji University, China

Reviewed by:
Yuan Liu,
University of Miami Health System, United States
Wensi Tao,
University of Miami Health System, United States

***Correspondence:**
Yi Shao
freebee99@163.com
Qiong Zhou
qiongzD06@126.com

† These authors have contributed equally to this work

Specialty section:
This article was submitted to Parkinson's Disease and Aging-related Movement Disorders, a section of the journal Frontiers in Aging Neuroscience

Received: *29 January 2022*
Accepted: *30 March 2022*
Published: *09 May 2022*

Citation:
Liu Q-Y, Pan Y-C, Shu H-Y, Zhang L-J, Li Q-Y, Ge Q-M, Shao Y and Zhou Q (2022) Brain Activity in Age-Related Macular Degeneration Patients From the Perspective of Regional Homogeneity: A Resting-State Functional Magnetic Resonance Imaging Study. Front. Aging Neurosci. 14:865430. doi: 10.3389/fnagi.2022.865430

Objective: In this study, the regional homogeneity (ReHo) method was used to investigate levels of cerebral homogeneity in individuals with age-related macular degeneration (AMD), with the aim of exploring whether these measures are associated with clinical characteristics.

Materials and Methods: Patients with AMD and healthy controls attending the First Affiliated Hospital of Nanchang University were invited to participate. Resting state functional magnetic resonance images were recorded in each participant and levels of synchronous neural activity were evaluated using ReHo. Receiver operating characteristic (ROC) curves were used to evaluate the sensitivity and specificity of this method.

Results: Eighteen patients with AMD (9 males and 9 females) and 15 healthy controls (HCs) were recruited. The two groups were approximately matched in age, gender and weight. Compared with controls, the ReHo values were significantly higher in the AMD group at the limbic lobe and parahippocampal gyrus, and were significantly reduced at the cingulate gyrus, superior frontal gyrus, middle frontal gyrus, inferior parietal lobule, and precentral gyrus. Mean ReHo values at the cingulate gyrus and the superior frontal gyrus were negatively correlated with clinical symptoms.

Conclusion: Brain neural homogeneity dysfunction is a manifestation of visual pathways in AMD patients, and may be one of the pathological mechanisms of chronic vision loss, anxiety and depression in AMD patients. In addition, the ReHo data may be useful for early screening for AMD.

Keywords: neural regional homogeneity, resting state, functional magnetic resonance imaging, age-related macular degeneration (AMD), pathogenesis

INTRODUCTION

Age-related macular degeneration (AMD) is a significant cause of irreversible blindness in the elderly (VanNewkirk et al., 2000). AMD affects over one-quarter of those who aged over 75 and is the world's third most common blinding eye disease, as well as the most common reason for irreversible blindness among the elderly in Western countries (Pennington and DeAngelis, 2016). Asia has recently witnessed an increase in the incidence of AMD and it has been predicted to evolve into a global disease, with the total number of people affected worldwide reaching 196 million by 2020 and increasing to 288 million in 2040 (Wong et al., 2014). The treatment of retinal angiogenesis and fluid leakage in neovascular AMD is currently treated by blocking vascular endothelial growth factor A (Bakri et al., 2019). The mechanisms by which AMD exerts long-term effects on the human brain and behavior are not clear, and there is no cure for this disease. Few researchers have explored the relationship between AMD and spontaneous brain activity. Previous studies using functional magnetic resonance imaging (fMRI) and electroencephalography (EEG) have suggested that synchronous neuronal activity may also make a difference in numerous neurophysiological events (Ward, 2003; Spencer et al., 2004; Li et al., 2015). Resting state fMRI (rs-fMRI) is one of the most effective ways to detect changes in brain activity. Regional homogeneity (ReHo) is a measurement technique used in rs-fMRI to estimate the consistency of signals related to blood oxygen levels between adjacent voxels throughout the brain at rest (Tononi et al., 1998; Zang et al., 2004). ReHo is a method to evaluate brain activity in its resting state, as well as one of the methods currently available to study the partial synchronization of idiopathic fMRI signs. Our previous research using the ReHo method has assessed neurological status in eye diseases including corneal ulcer (Xu et al., 2019), diabetic retinopathy (Liao et al., 2019), optical neuritis (Shao et al., 2015) and others (Dai et al., 2012; Song et al., 2014; Huang et al., 2016a,b, 2017a,b; Li et al., 2016, 2020; Tan et al., 2016a,b; Tang et al., 2018; Ye et al., 2018; Zhu et al., 2018; Shao et al., 2019; Xiang et al., 2019; Zhang et al., 2020).

Resting-state fMRI and ReHo values may be useful indicators of macular degeneration at an early stage. In the present study, correlation analysis was used to calculate the average ReHo signal in different brain regions to explore the relationship between the signal and clinical symptoms in AMD patients.

MATERIALS AND METHODS

Subjects

Patients with AMD who regularly visited the ophthalmology department of the First Affiliated Hospital of Nanchang University were invited to participate in this study. Inclusion criteria for AMD patients were: (1) age-related macular degeneration diagnosed using fundus fluorescein angiography and confirmed by indocyanine green angiography (Spectralis HRA-OCT; Heidelberg Engineering, Heidelberg, Germany; **Figure 1**); (2) no eye disease other than AMD; (3) no anti-vascular endothelial growth factor treatment; (4) no dementia (based on an existing diagnosis, or five or more errors in the Short Portable Mental Status Questionnaire); and (5) no history of brain surgery.

In addition, patients with a history or diagnosis of mild cognitive impairment, Alzheimer's disease, generalized anxiety disorder, depressive disorder, Parkinson's disease, proliferative retinopathy, other retinopathy, retinal vein occlusion, neovascular glaucoma, chronic myeloproliferative disease, macular or cystic macular edema were excluded since these conditions may alter the value of the ReHo signals in the brain region associated with macular degeneration.

Healthy controls who met the following criteria were eligible for inclusion: (1) no contraindications to MRI scan (such as implanted metal device); (2) no neurological diseases or psychiatric diseases (such as mania or depression); (3)no prior or present age-related macular degeneration or other retinal or fundus lesions.

The methods used in this study were consistent with the Declaration of Helsinki. The study was approved by the Ethics Committee of the First Affiliated Hospital of Nanchang University. Research protocols and procedures were fully explained to each subject before obtaining written informed consent.

MRI Parameters

MRI scanning was performed on a 3-Tesla MR scanner (Trio, Siemens, Munich, Germany). T1-weighted images with high resolution were acquired using a tridimensional destruction gradient echo sequence, with repetition time = 190 ms, echo time = 2.26 ms, thickness = 3.0 mm, gap = 0.5 mm, acquisition matrix = 256 × 256, field of view = 250 mm × 250 mm, and flip angle = 9o. Some functional images needed to be corrected at thickness = 4.0 mm, repetition time = 2,000 ms, echo time = 30 ms, gap = 1.2 mm, and field of view = 220 mm × 220 mm, 29 axial.

Data Analysis From Functional Magnetic Resonance Imaging

Using MRIcro1 software [MRIcro software (McCausland Center for Brain Imaging, Columbia, SC, United States)],[1] all images were checked and any defective images removed. The first 10 volumes recorded from each subject were discarded to remove any noise associated with movement at the beginning of the procedure. The valid images were processed using SPM82 and Data Processing Assistant for rs-fMRI DPARSFA (Institute of Psychology, CAS., Beijing, People's Republic of China) software. Following this, slice timing, head motion correction (any of the six parameters within 1.5 mm or 1.5), and spatial normalization were performed on the digital data. The data were then smoothed using a 6 mm full-width at half-maximum Gaussian. Finally, the fMRI image space was normalized to the Montreal Neurological Institute space employing an echo plane imaging template and was resampled at a resolution of 3 mm × 3 mm × 3 mm. To optimize reliability, the data were de-trended and bandpass

[1] www.mricro.com

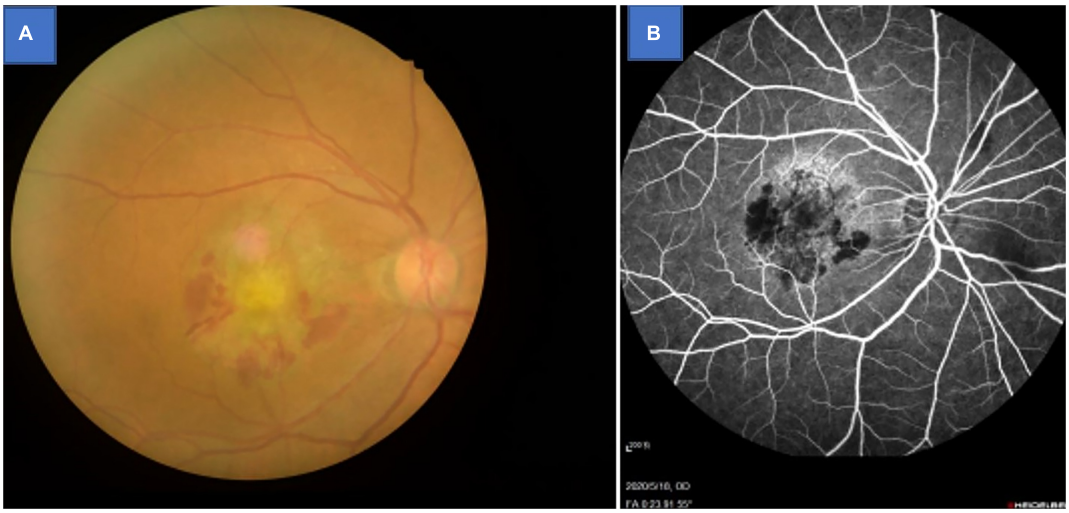

FIGURE 1 | Example of age-related macular degeneration seen on fundus camera **(A)** and fluorescence fundus angiography **(B)**.

filtered (0.01–0.08 Hz) to remove low-frequency drift and physiological high-frequency respiratory and cardiac noise.

Statistical Analysis

To compare ReHo values between AMD and HC groups, SPM8 software was used to conduct an independent-samples test after excluding other influencing factors such as age and gender (two-tail, voxel level: $P < 0.005$ Gaussian random field correction, cluster-level: $P < 0.05$, cluster: 162).

Brain–Behavior Correlation Analysis

Regions of interest were defined on images from each group using REST software.[2] Within each region, the average ReHo value was obtained from the ReHo values of all voxels. Correlation analysis were used to determine whether the ReHo values were associated with clinical manifestations ($P < 0.05$ was considered statistically significant).

Clinical Data Analysis

Intraocular pressure, best-corrected visual acuity and body weight were measured in each participant, and these plus disease duration were recorded. Demographic and clinical variables were compared between the two groups using SPSS version 20.0 software, and *P*-values < 0.05 were again considered significant. Receiver operating characteristic (ROC) curves were used to test stability, sensitivity and specificity.

RESULTS

Demographics and Behavioral Results

The two groups were statistically similar in weight ($P = 0.542$) and age ($P = 0.785$), but significantly poorer monocular visual acuities were found in the AMD than HC group (right $P = 0.003$; left $P = 0.004$) (**Table 1**).

Regional Homogeneity Value Comparisons Between Groups

ReHo values in the AMD group were significantly higher than controls at the limbic lobe and parahippocampal gyrus ($P < 0.05$), and significantly lower at the cingulate gyrus, superior frontal gyrus, middle frontal gyrus, inferior parietal lobule and precentral gyrus ($P < 0.05$) (**Figures 2**, **3** and **Table 2**).

Receiver Operating Characteristic Curve

Since ReHo values differed between groups, as explained above, they were further analyzed using ROC curves to assess how well these values distinguish between the two groups. AUC (Area Under Curve) is defined as the area under the ROC curve enclosed by the coordinate axis, The closer the AUC is to 1.0,

TABLE 1 | Demographics and clinical measurements of AMD and HC Groups.

Condition	AMD	HC	*t*	*P*-value*
Male/female	10/8	10/8	N/A	>0.99
Age (years)	55.25 ± 4.04	53.87 ± 5.16	0.375	0.785
Weight (kg)	61.58 ± 11.84	69.36 ± 12.78	0.542	0.542
Handedness	18R	18R	N/A	>0.99
Best-corrected VA-L	0.15 ± 0.10	1.05 ± 0.10	−4.836	0.004
Best-corrected VA-R	0.10 ± 0.05	1.05 ± 0.15	−4.736	0.003
Duration of AMD (months)	3.34 ± 2.88	N/A	N/A	N/A
IOP-L	12.14 ± 3.64	14.36 ± 3.76	0.312	0.898
IOP-R	14.26 ± 3.97	15.95 ± 4.12	0.336	0.802

Independent t-tests comparing the two groups ($p < 0.05$ represented statistically significant differences). Data shown as mean standard deviation or n.
*AMD, age-related macular degeneration; HC, healthy control; L, left; R, right; N/A, not applicable; VA, visual acuity; IOP, intraocular pressure. *$p < 0.05$ represented statistically significant differences.*

[2]http://www.restfmri.net

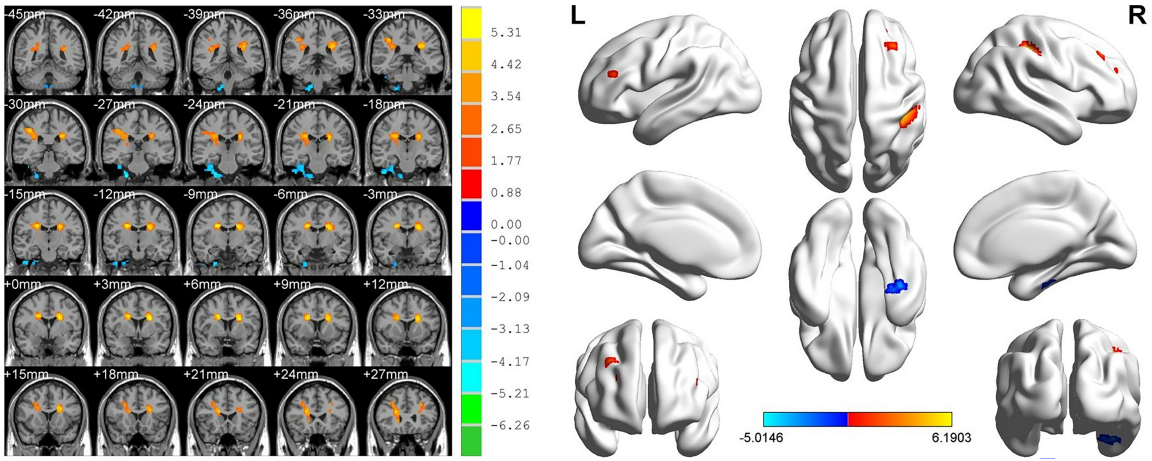

FIGURE 2 | Significant differences in ReHo values between the AMD group and HCs. Blue areas denote significantly reduced ReHo values in the cingulate gyrus, superior frontal gyrus, middle frontal gyrus, inferior parietal lobule, and precentral gyrus, red areas denote significantly increased ReHo values in the limbic lobe and parahippocampal gyrus.

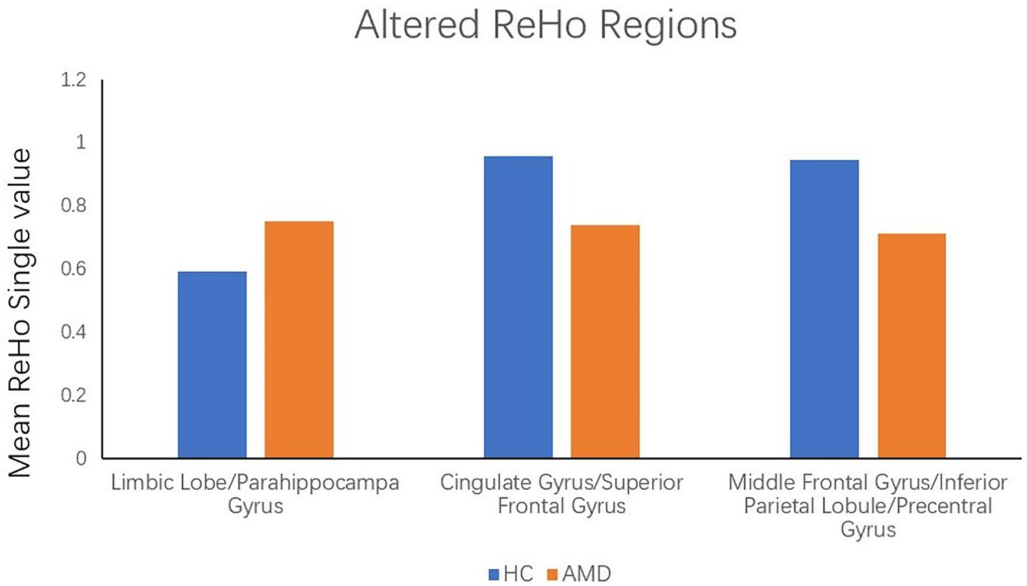

FIGURE 3 | The mean single ReHo value between the AMDs group and HCs. Data presented as mean ± standard deviation. ReHo, regional homogeneity; HCs, healthy controls; N/A, not applicable; AMD, age-related macular degeneration.

TABLE 2 | Brain regions with significantly different ReHo values between the AMDs and HCs.

Brain areas	MNI coordinates			Number of voxels	*T*-value	ROI顺序()
	X	Y	Z			
HC < AMD						
Limbic Lobe/Parahippocampal Gyrus	27	−27	−48	541	−5.0146	1
HC > AMD						
Cingulate Gyrus/Superior Frontal Gyrus	21	6	27	832	6.1903	2
Middle Frontal Gyrus/Inferior Parietal Lobule/Precentral Gyrus	−21	6	24	661	5.9303	3

Voxel-level: P < 0.005, GRF correction, cluster-level: 162. P < 0.05. CU, corneal ulcer; HCs, healthy controls; BA, Brodmann area.

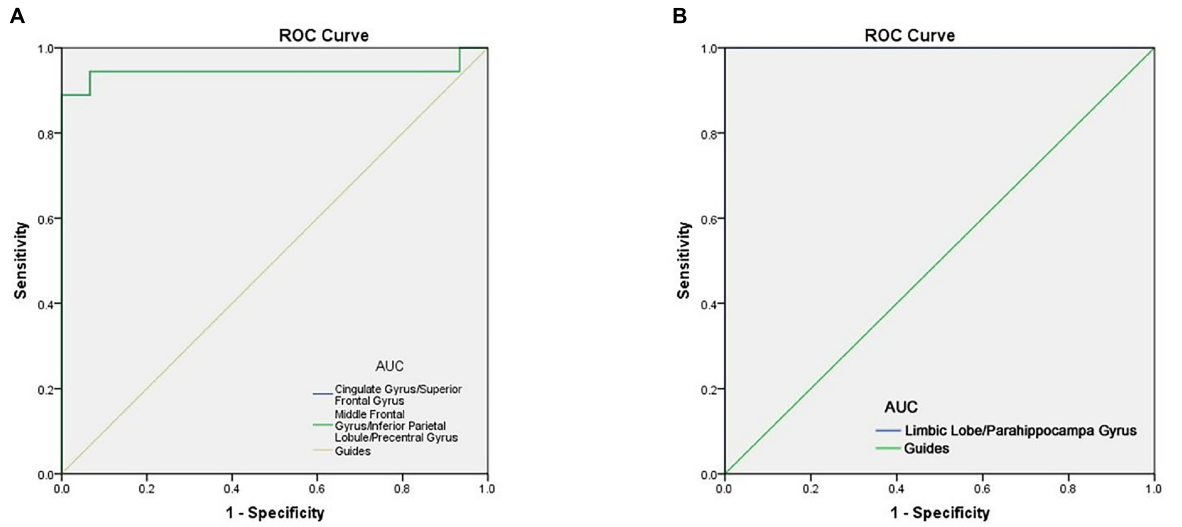

FIGURE 4 | ROC curve analysis of the mean ReHo values for altered brain regions. **(A)** The area under the ROC curve were 0.944 ($p < 0.0001$; 95% CI: 0.845–1.000), for Cingulate Gyrus/Superior Frontal Gyrus, Middle Frontal Gyrus/Inferior Parietal Lobule/Precentral Gyrus 0.944 ($p < 0.0001$; 95% CI: 0.845–1.000). **(B)** The area under the ROC curve were 1.000 ($p < 0.0001$; 95% CI: 1.000–1.000), for Limbic Lobe/Parahippocampal Gyrus. AUC, area under the curve; ROC, receiver operating characteristic.

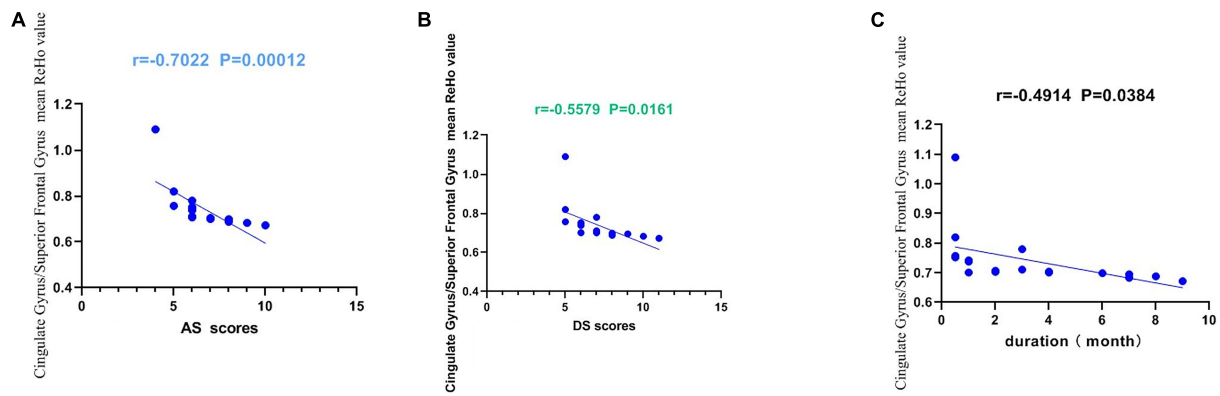

FIGURE 5 | Correlations between the mean ReHo values of the Cingulate Gyrus/Superior Frontal Gyrus and the clinical behaviors. **(A)** The AS showed a negative correlation with the mean ReHo values of the Cingulate Gyrus/Superior Frontal Gyrus ($r = -0.702$, $p = 0.0001 < 0.001$), **(B)** the DS showed a negative correlation with the mean ReHo values of the Cingulate Gyrus/Superior Frontal Gyrus ($r = -0.5579$, $p = 0.0161 < 0.05$). **(C)** The duration showed a negative correlation with the mean ReHo values of the Cingulate Gyrus/Superior Frontal Gyrus ($r = 0.4914$, $p = 0.0384 < 0.05$). AS, anxiety scores; DS, depression scores.

the higher the authenticity of the detection method AUCfor ReHo values at the cingulate gyrus, superior frontal gyrus, middle frontal gyrus, inferior parietal lobule and precentral gyrus was 0.944 in each case (AMDs > HCs) (**Figure 4B**). ROC curve can also reflect to some extent that ReHo values have certain advantages in diagnosing AMD (**Figure 4A**).

Correlation Analysis

The present study used the Chinese version of the Hospital Anxiety and Depression Scale (HADS). The HADS questionnaire, 10 which involves self-assessment, has been found to be a reliable instrument for determining depression and anxiety status in a hospital outpatient clinic setting. The anxiety and depressive subscales are also valid measures of the severity of emotional disorder. We defined that a score greater than or equal to 8 points was positive. The higher the score, the more serious the depression and anxiety. Within the AMD group, anxiety scores, depression scores and disease duration were all inversely correlated with the ReHo values at the cingulate gyrus and at the superior frontal gyrus ($P < 0.05$). These data indicate that AMD is associated with all three factors (**Figure 5**).

DISCUSSION

Our previous studies on the ReHo method have demonstrated that it can be applied to a variety of ophthalmic diseases and

TABLE 3 | Regional homogeneity method applied in ophthalmological diseases.

References	Year	Disease
Xu et al. (2019)	2019	Corneal ulcer
Liao et al. (2019)	2019	Diabetic retinopathy
Huang et al. (2017a)	2017	Late monocular blindness
Xiang et al. (2019)	2019	Classic trigeminal neuralgia
Tang et al. (2018)	2018	Acute eye pain
Huang et al. (2017b)	2017	Retinal detachment
Huang et al. (2016a)	2016	Universal acute open-globe injury
Zhang et al. (2020)	2020	Diabetic vital pathogenesis
Shao et al. (2015)	2015	Optical neuritis
Huang et al. (2016b)	2016	Comitant strabismus
Shao et al. (2019)	2019	Strabismus and amblyopia
Song et al. (2014)	2014	Glaucoma
Dai et al. (2012)	2012	Sleep disorders
Li et al. (2016)	2016	Parkinson's disease

TABLE 4 | Brain regions alternation and its potential impact.

Brain regions	Experimental result	Brain function	Anticipated results
Limbic Lobe	HC < AMD	Processing of memory, decision-making and emotional responses	Depression, epilepsy, affective cognitive impairment
Parahippocampal Gyrus	HC < AMD	Associative memory, source memory and processing of emotional stimuli	The problems of memory, sleep
Cingulate Gyrus	HC > AMD	The integration of attention and emotional information	Disorders of emotion regulation
Superior Frontal Gyrus	HC > AMD	Part of the default model network	Depression and anxiety
Middle Frontal Gyrus	HC > AMD	Part of the default model network	Depression and anxiety
Inferior Parietal Lobule	HC > AMD	Part of the default model network	Depression and anxiety
Precentral Gyrus	HC > AMD	Control voluntary movement	Depressive disorder and memory performance

has broad scope for further development (**Table 3**). The studies have highlighted regional disease-related changes in brain activity and their potential effects that needed to be further examined (**Table 4**). So far, there is no consensus on the relationship between ReHo value and resting state of AMD patients, and the present study aimed to fill this gap.

We found that ReHo values were significantly different between AMD patients and controls, being higher in AMD at the limbic lobe and parahippocampal gyrus and lower at the cingulate gyrus, superior frontal gyrus, middle frontal gyrus, inferior parietal lobule and the precentral gyrus (**Figure 6**).

Implications of Increased Regional Homogeneity Values in Age-Related Macular Degeneration

The limbic system plays a major part in memory, decision making and emotional feedback. Research has shown that its damage interferes with memories that are enhanced by emotion (Amunts et al., 2005) and that the limbic system is associated with depression and anxiety in the epilepsies (Krishnan, 2020). The brain combines emotion with cognition to produce flexible behavioral output based on its judgments of the environment (Rusbridge, 2020). In addition, the parahippocampal gyrus is associated with episodic memory relating to source memory, associative memory and processing of emotional stimuli (Suthana et al., 2012). For example, Mankin found that deep brain stimulation of hippocampal circuits can modulate human memory (Mankin and Fried, 2020). In addition to its role in memory, the parahippocampal cortex is involved in visuospatial processing related to scene perception and spatial representation of navigation (Aminoff et al., 2013). However, further study is needed to confirm whether an increase in the value of ReHo in the parahippocampal gyrus in AMD has an effect on memory enhancement (**Figure 7**).

Implications of Decreased Regional Homogeneity Values in Age-Related Macular Degeneration

Anatomically, the anterior central gyrus, also called precentral gyrus, is divided into four parts by three contours in the paracentral lobule and gyrus. It is bounded above by the anterior central sulcus and below by the lateral fissure, which is mainly located on the lateral side of the cerebral hemisphere. Study has shown that abnormal or weak connections between them may be risk factors for disease (Nebel et al., 2014). According to previous studies, the paracentral gyrus has also been associated with memory ability and depression disorders (Nebel et al., 2014; Li et al., 2018; Shang et al., 2018).

The structure on the medial side of the cerebral hemisphere between the cingulate sulcus and the corpus callosum sulcus is called the cingulate gyrus. It belongs to the cortical part of the limbic system and is an important region connecting the orbitofrontal cortex, amygdala, insular lobe, septal nucleus, and hypothalamus. The cingulate gyrus is the bridge between attention and emotional processing and is responsible for the integration of attention and emotional information. Burger's research points out that cingulate gyrus activation was sharply reduced in major depressive disorders (Nebel et al., 2014) potentially indicating impaired bottom-up emotional processing and abnormal automatic emotional regulation. The Fischer's study suggested that parietal activity may be particularly important for linking long-term memory representation and attention components (Bürger et al., 2017). In other fMRI study, frontal and parietal activation was found in spatial memory-guided attention tasks (Fischer et al., 2021).

To some extent, the decline of memory and depression in AMD patients can be traced to the changes in brain

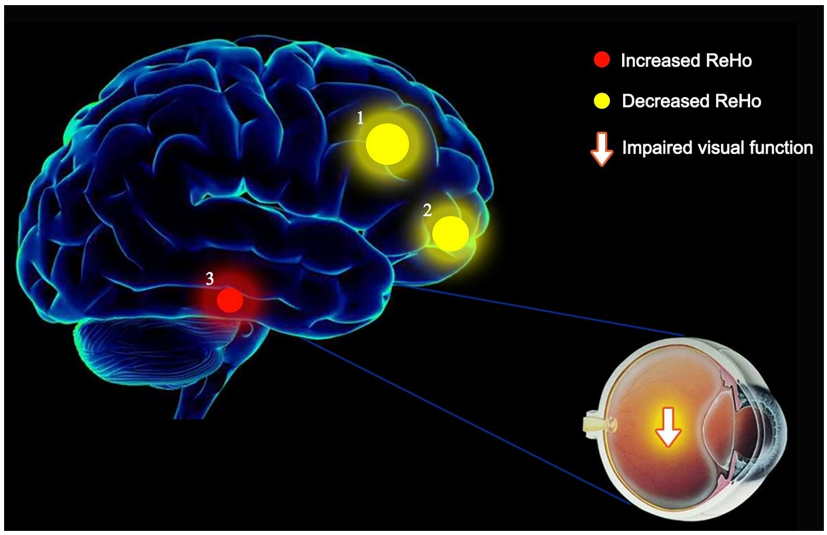

FIGURE 6 | The ReHo results of brain activity in the AMD group. Compared with the HCs, the ReHo values of the following regions were decreased to various extents: 1- Cingulate Gyrus/Superior Frontal Gyrus (BA 32, t = 6.1903), 2- Middle Frontal Gyrus/Inferior Parietal Lobule/Precentral Gyrus (t = 5.9303). Compared with the HCs, the ReHo values of the following regions were increased to various extents: 3- Limbic Lobe/Parahippocampal Gyrus (t = −5.0146). HCs, healthy controls; BA, Brodmann's area.

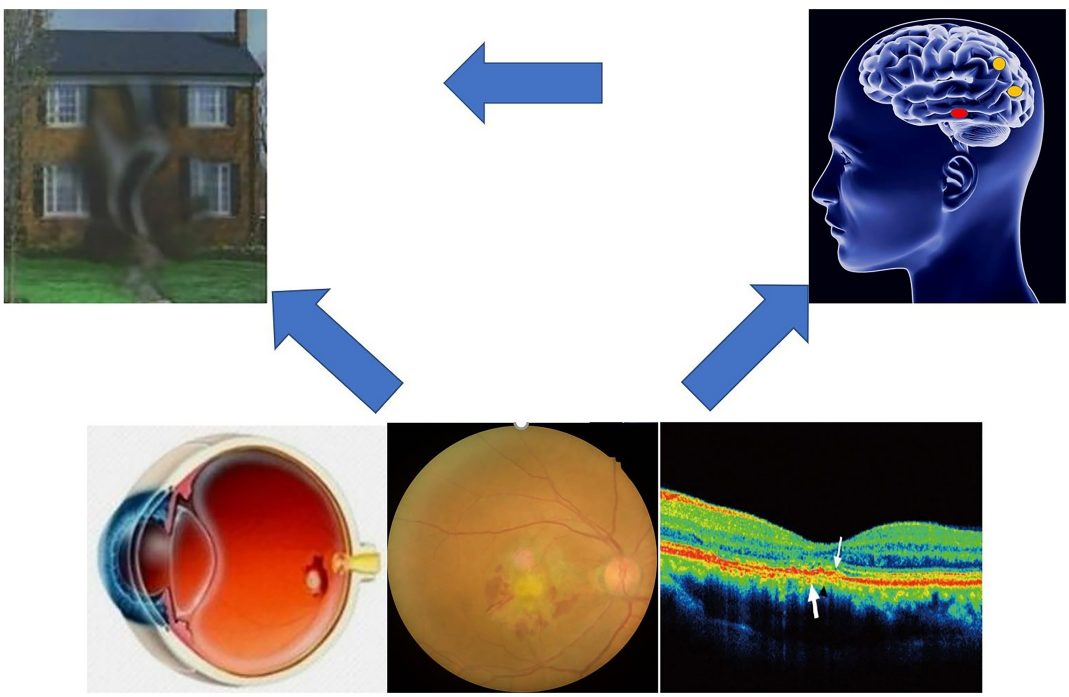

FIGURE 7 | Correlations between AMDs ReHo and behavioral performance, compare with HCs, AMDs may suffer more problems with dealing with emotion, memory and visual disturbances.

activity (Giesbrecht et al., 2013). The present results showed that the ReHo value of five brain regions were decreased in AMD, with reliability verified by the ROC curve analysis results. AUC values of over 0.7 are considered high, and our analysis showed that the AUC values of ReHo values in the above brain regions were all greater than 0.9, indicating very high accuracy. The abnormality of ReHo values in some brain regions is an important finding relating to the diagnosis of AMD based on imaging data. The results suggest that the ReHo

method may be a non-invasive, rapid and sensitive method for early diagnosis of AMD patients in the future.

CONCLUSION

The present findings suggest that AMD patients have abnormal spontaneous brain activity, which may prove useful for early disease detection. Activity in the cingulate gyrus and superior frontal gyrus was inversely associated with anxiety, depression and disease duration. These findings provide powerful information for further research. However, there are still some limitations in our study. Such as larger sample sizes and detailed grouping of different types of AMDs are needed. Moreover, our study only demonstrated the existence of the correlation between changes of ReHo values in specific brain regions and RVO. But It is unclear whether AMD will cause changes in brain activity or whether patients with brain dysfunction are susceptible to AMD.

DATA AVAILABILITY STATEMENT

The original contributions presented in the study are included in the article/supplementary material, further inquiries can be directed to the corresponding author/s.

ETHICS STATEMENT

The studies involving human participants were reviewed and approved by the First Affiliated Hospital of Nanchang University. The patients/participants provided their written informed consent to participate in this study.

AUTHOR CONTRIBUTIONS

Q-YiL, Y-CP, H-YS, YS, and QZ: study design and manuscript preparation. Q-YiL, Y-CP, H-YS, L-JZ, YS, and QZ: data collection. Q-YiL, Y-CP, H-YS, Q-YuL, YS, and QZ: statistical analysis. Q-YiL, Y-CP, H-YS, Q-MG, YS, and QZ: data interpretation and literature search. All authors read and approved the final manuscript.

FUNDING

This work was supported by the Central Government Guides Local Science and Technology Development Foundation (No. 20211ZDG02003), the Key Research Foundation of Jiangxi Province (Nos. 20181BBG70004 and 20203BBG73059), the Excellent Talents Development Project of Jiangxi Province (No. 20192BCBL23020), the Natural Science Foundation of Jiangxi Province (No. 20181BAB205034), the Grassroots Health Appropriate Technology "Spark Promotion Plan" Project of Jiangxi Province (No. 20188003), the Health Development Planning Commission Science Foundation of Jiangxi Province (Nos. 20201032 and 202130210), the Health Development Planning Commission Science TCM Foundation of Jiangxi Province (Nos. 2018A060 and 2020A0087), and the Education Department Foundation of Jiangxi Province (Nos. GJJ200157, GJJ200159, and GJJ200169).

REFERENCES

Aminoff, E. M., Kveraga, K., and Bar, M. (2013). The role of the parahippocampal cortex in cognition. *Trends Cogn. Sci.* 17, 379–390. doi: 10.1016/j.tics.2013.06.009

Amunts, K., Kedo, O., Kindler, M., Pieperhoff, P., Mohlberg, H., Shah, N. J., et al. (2005). Cytoarchitectonic mapping of the human amygdala, hippocampal region and entorhinal cortex: intersubject variability and probability maps. *Anat. Embryol. (Berl).* 210, 343–352. doi: 10.1007/s00429-005-0025-5

Bakri, S. J., Thorne, J. E., Ho, A. C., Ehlers, J. P., Schoenberger, S. D., Yeh, S., et al. (2019). Safety and efficacy of anti-vascular endothelial growth factor therapies for neovascular age-related macular degeneration: a report by the American academy of ophthalmology. *Ophthalmology* 126, 55–63. doi: 10.1016/j.ophtha.2018.07.028

Bürger, C., Redlich, R., Grotegerd, D., Meinert, S., Dohm, K., Schneider, I., et al. (2017). Differential abnormal pattern of anterior cingulate gyrus activation in unipolar and bipolar depression: an fMRI and pattern classification approach. *Neuropsychopharmacology* 42, 1399–1408. doi: 10.1038/npp.2017.36

Dai, X. J., Gong, H. H., Wang, Y. X., Zhou, F. Q., Min, Y. J., Zhao, F., et al. (2012). Gender differences in brain regional homogeneity of healthy subjects after normal sleep and after sleep deprivation: a resting-state fMRI study. *Sleep Med.* 13, 720–727. doi: 10.1016/j.sleep.2011.09.019

Fischer, M., Moscovitch, M., and Alain, C. (2021). A systematic review and meta-analysis of memory-guided attention: frontal and parietal activation suggests involvement of fronto-parietal networks. *Wiley Interdiscip. Rev. Cogn. Sci.* 12:e1546. doi: 10.1002/wcs.1546

Giesbrecht, B., Sy, J. L., and Guerin, S. A. (2013). Both memory and attention systems contribute to visual search for targets cued by implicitly learned context. *Vis. Res.* 85, 80–89. doi: 10.1016/j.visres.2012.10.006

Huang, X., Li, H. J., Ye, L., Zhang, Y., Wei, R., Zhong, Y. L., et al. (2016a). Altered regional homogeneity in patients with unilateral acute open-globe injury: a resting-state functional MRI study. *Neuropsychiatr. Dis. Treat.* 12, 1901–1906. doi: 10.2147/NDT.S110541

Huang, X., Li, S. H., Zhou, F. Q., Zhang, Y., Zhong, Y. L., Cai, F. Q., et al. (2016b). Altered intrinsic regional brain spontaneous activity in patients with comitant strabismus: a resting-state functional MRI study. *Neuropsychiatr. Dis. Treat.* 12, 1303–1308. doi: 10.2147/NDT.S105478

Huang, X., Li, D., Li, H. J., Zhong, Y. L., Freeberg, S., Bao, J., et al. (2017a). Abnormal regional spontaneous neural activity in visual pathway in retinal detachment patients: a resting-state functional MRI study. *Neuropsychiatr. Dis. Treat.* 13, 2849–2854. doi: 10.2147/NDT.S147645

Huang, X., Ye, C. L., Zhong, Y. L., Ye, L., Yang, Q. C., Li, H. J., et al. (2017b). Altered regional homogeneity in patients with late monocular blindness: a resting-state functional MRI study. *Neuroreport* 28, 1085–1091. doi: 10.1097/WNR.0000000000000855

Krishnan, V. (2020). Depression and anxiety in the epilepsies: from bench to bedside. *Curr. Neurol. Neurosci. Rep.* 20:41. doi: 10.1007/s11910-020-01065-z

Li, C., Dong, M., Yin, Y., Hua, K., Fu, S., and Jiang, G. (2018). Aberrant effective connectivity of the right anterior insula in primary insomnia. *Front. Neurol.* 9:317. doi: 10.3389/fneur.2018.00317

Li, H., Li, L., Shao, Y., Gong, H., Zhang, W., Zeng, X., et al. (2016). Abnormal intrinsic functional hubs in severe male obstructive sleep apnea: evidence from a voxel-wise degree centrality analysis. *PLoS One.* 11:e0164031. doi: 10.1371/journal.pone.0164031

Li, M. G., Liu, T. F., Zhang, T. H., Chen, Z. Y., Nie, B. B., Lou, X., et al. (2020). Alterations of regional homogeneity in Parkinson's disease with mild cognitive impairment: a preliminary resting-state fMRI study. *Neuroradiology* 62, 327–334. doi: 10.1007/s00234-019-02333-7

Li, R., Li, Y., An, D., Gong, Q., Zhou, D., and Chen, H. (2015). Altered regional activity and inter-regional functional connectivity in psychogenic non-epileptic seizures. *Sci. Rep.* 5:11635. doi: 10.1038/srep11635

Liao, X. L., Yuan, Q., Shi, W. Q., Li, B., Su, T., Lin, Q., et al. (2019). Altered brain activity in patients with diabetic retinopathy using regional homogeneity: a resting-state fMRI study. *Endocr. Pract.* 25, 320–327. doi: 10.4158/EP-2018-0517

Mankin, E. A., and Fried, I. (2020). Modulation of human memory by deep brain stimulation of the entorhinal-hippocampal circuitry. *Neuron* 106, 218–235. doi: 10.1016/j.neuron.2020.02.024

Nebel, M. B., Eloyan, A., Barber, A. D., and Mostofsky, S. H. (2014). Precentral gyrus functional connectivity signatures of autism. *Front. Syst. Neurosci.* 8:80. doi: 10.3389/fnsys.2014.00080

Pennington, K. L., and DeAngelis, M. M. (2016). Epidemiology of age-related macular degeneration (AMD): associations with cardiovascular disease phenotypes and lipid factors. *Eye Vis. (Lond).* 3:34. doi: 10.1186/s40662-016-0063-5

Rusbridge, C. (2020). Neurobehavioral disorders: the corticolimbic system in health and disease. *Vet. Clin. North Am. Small Anim. Pract.* 50, 1157–1181. doi: 10.1016/j.cvsm.2020.06.009

Shang, C. Y., Lin, H. Y., Tseng, W. Y., and Gau, S. S. (2018). A haplotype of the dopamine transporter gene modulates regional homogeneity, gray matter volume, and visual memory in children with attention-deficit/hyperactivity disorder. *Psychol. Med.* 48, 2530–2540. doi: 10.1017/S0033291718000144

Shao, Y., Cai, F. Q., Zhong, Y. L., Huang, X., Zhang, Y., Hu, P. H., et al. (2015). Altered intrinsic regional spontaneous brain activity in patients with optic neuritis: a resting-state functional magnetic resonance imaging study. *Neuropsychiatr. Dis. Treat.* 11, 3065–3073. doi: 10.2147/NDT.S92968

Shao, Y., Li, Q. H., Li, B., Lin, Q., Su, T., Shi, W. Q., et al. (2019). Altered brain activity in patients with strabismus and amblyopia detected by analysis of regional homogeneity: a resting-state functional magnetic resonance imaging study. *Mol. Med. Rep.* 19, 4832–4840. doi: 10.3892/mmr.2019.10147

Song, Y., Mu, K., Wang, J., Lin, F., Chen, Z., Yan, X., et al. (2014). Altered spontaneous brain activity in primary open angle glaucoma: a resting-state functional magnetic resonance imaging study. *PLoS One.* 9:e89493. doi: 10.1371/journal.pone.0089493

Spencer, K. M., Nestor, P. G., Perlmutter, R., Niznikiewicz, M. A., Klump, M. C., Frumin, M., et al. (2004). Neural synchrony indexes disordered perception and cognition in schizophrenia. *Proc. Natl. Acad. Sci. U. S. A.* 101, 17288–17293. doi: 10.1073/pnas.0406074101

Suthana, N., Haneef, Z., Stern, J., Mukamel, R., Behnke, E., Knowlton, B., et al. (2012). Memory enhancement and deep-brain stimulation of the entorhinal area. *N. Engl. J. Med.* 366, 502–510. doi: 10.1056/NEJMoa1107212

Tan, G., Huang, X., Ye, L., Wu, A. H., He, L. X., Zhong, Y. L., et al. (2016a). Altered spontaneous brain activity patterns in patients with unilateral acute open globe injury using amplitude of low-frequency fluctuation: a functional magnetic resonance imaging study. *Neuropsychiatr. Dis. Treat.* 12, 2015–2020. doi: 10.2147/NDT.S110539

Tan, G., Huang, X., Zhang, Y., Wu, A. H., Zhong, Y. L., Wu, K., et al. (2016b). A functional MRI study of altered spontaneous brain activity pattern in patients with congenital comitant strabismus using amplitude of low-frequency fluctuation. *Neuropsychiatr. Dis. Treat.* 12, 1243–1250. doi: 10.2147/NDT.S104756

Tang, L. Y., Li, H. J., Huang, X., Bao, J., Sethi, Z., Ye, L., et al. (2018). Assessment of synchronous neural activities revealed by regional homogeneity in individuals with acute eye pain: a resting-state functional magnetic resonance imaging study. *J. Pain Res.* 11, 843–850. doi: 10.2147/JPR.S156634

Tononi, G., McIntosh, A. R., Russell, D. P., and Edelman, G. M. (1998). Functional clustering: identifying strongly interactive brain regions in neuroimaging data. *Neuroimage* 7, 133–149. doi: 10.1006/nimg.1997.0313

VanNewkirk, M. R., Nanjan, M. B., Wang, J. J., Mitchell, P., Taylor, H. R., and McCarty, C. A. (2000). The prevalence of age-related maculopathy: the visual impairment project. *Ophthalmology* 107, 1593–1600. doi: 10.1016/s0161-6420(00)00175-5

Ward, L. M. (2003). Synchronous neural oscillations and cognitive processes. *Trends Cogn. Sci.* 7, 553–559. doi: 10.1016/j.tics.2003.10.012

Wong, W. L., Su, X., Li, X., Cheung, C. M., Klein, R., Cheng, C. Y., et al. (2014). Global prevalence of age-related macular degeneration and disease burden projection for 2020 and 2040: a systematic review and meta-analysis. *Lancet Glob, Health* 2, e106–e116. doi: 10.1016/S2214-109X(13)70145-1

Xiang, C. Q., Liu, W. F., Xu, Q. H., Su, T., Yong-Qiang, S., Min, Y. L., et al. (2019). Altered spontaneous brain activity in patients with classical trigeminal neuralgia using regional homogeneity: a resting-state functional MRI study. *Pain Pract.* 19, 397–406. doi: 10.1111/papr.12753

Xu, M. W., Liu, H. M., Tan, G., Su, T., Xiang, C. Q., Wu, W., et al. (2019). Altered regional homogeneity in patients with corneal ulcer: a resting-state functional MRI study. *Front. Neurosci.* 13:743. doi: 10.3389/fnins.2019.00743

Ye, L., Wei, R., Huang, X., Shi, W. Q., Yang, Q. C., Yuan, Q., et al. (2018). Reduction in interhemispheric functional connectivity in the dorsal visual pathway in unilateral acute open globe injury patients: a resting-state fMRI study. *Int. J. Ophthalmol.* 11, 1056–1060. doi: 10.18240/ijo.2018.06.26

Zang, Y., Jiang, T., Lu, Y., He, Y., and Tian, L. (2004). Regional homogeneity approach to fMRI data analysis. *Neuroimage* 22, 394–400. doi: 10.1016/j.neuroimage.2003.12.030

Zhang, B., Li, B., Liu, R. Q., Shu, Y. Q., Min, Y. L., Yuan, Q., et al. (2020). Altered spontaneous brain activity pattern in patients with ophthalmectomy: an resting-state fMRI study. *Int. J. Ophthalmol.* 13, 263–270. doi: 10.18240/ijo.2020.02.10

Zhu, P. W., Huang, X., Ye, L., Jiang, N., Zhong, Y. L., Yuan, Q., et al. (2018). Altered intrinsic functional connectivity of the primary visual cortex in youth patients with comitant exotropia: a resting state fMRI study. *Int. J. Ophthalmol.* 11, 668–673. doi: 10.18240/ijo.2018.04.22

Conflict of Interest: The authors declare that the research was conducted in the absence of any commercial or financial relationships that could be construed as a potential conflict of interest.

Publisher's Note: All claims expressed in this article are solely those of the authors and do not necessarily represent those of their affiliated organizations, or those of the publisher, the editors and the reviewers. Any product that may be evaluated in this article, or claim that may be made by its manufacturer, is not guaranteed or endorsed by the publisher.

frontiers | Frontiers in Aging Neuroscience

ORIGINAL RESEARCH
published: 09 May 2022
doi: 10.3389/fnagi.2022.860364

Potential Mechanism Underlying Exercise Upregulated Circulating Blood Exosome miR-215-5p to Prevent Necroptosis of Neuronal Cells and a Model for Early Diagnosis of Alzheimer's Disease

Yisheng Chen[1†], Yaying Sun[1†], Zhiwen Luo[1†], Jinrong Lin[1†], Beijie Qi[1†], Xueran Kang[2], Chenting Ying[3], Chenyang Guo[4], Mengxuan Yao[5,6], Xiangjun Chen[7], Yi Wang[7], Qian Wang[8], Jiwu Chen[4]* and Shiyi Chen[1]**

[1] Department of Sports Medicine, Huashan Hospital, Fudan University, Shanghai, China, [2] Shanghai Jiao Tong University School of Medicine, Shanghai Jiao Tong University, Shanghai, China, [3] Department of Orthopaedics, The Second Affiliated Hospital, Zhejiang University School of Medicine, Hangzhou, China, [4] Department of Orthopedics, Shanghai General Hospital, Shanghai Jiao Tong University School of Medicine, Shanghai Jiao Tong University, Shanghai, China, [5] Department of Orthopaedic Surgery, The Third Hospital of Hebei Medical University, Shijiazhuang, China, [6] Key Laboratory of Biomechanics of Hebei Province, Orthopaedic Research Institution of Hebei Province, Shijiazhuang, China, [7] Huashan Hospital, Fudan University, Shanghai, China, [8] Department of Central Laboratory, The Affiliated Taian City Central Hospital of Qingdao University, Tai'an, China

Exercise is crucial for preventing Alzheimer's disease (AD), although the exact underlying mechanism remains unclear. The construction of an accurate AD risk prediction model is beneficial as it can provide a theoretical basis for preventive exercise prescription. In recent years, necroptosis has been confirmed as an important manifestation of AD, and exercise is known to inhibit necroptosis of neuronal cells. In this study, we extracted 67 necroptosis-related genes and 32 necroptosis-related lncRNAs and screened for key predictive AD risk genes through a random forest analysis. Based on the neural network Prediction model, we constructed a new logistic regression-based AD risk prediction model in order to provide a visual basis for the formulation of exercise prescription. The prediction model had an area under the curve (AUC) value of 0.979, indicative of strong predictive power and a robust clinical application prospect. In the exercise group, the expression of exosomal miR-215-5p was found to be upregulated; miR-215-5p could potentially inhibit the expressions of *IDH1*, *BCL2L11*, and *SIRT1*. The single-cell SCENIC assay was used to identify key transcriptional regulators in skeletal muscle. Among them, *CEBPB* and *GATA6* were identified as putative transcriptional regulators of miR-215. After "skeletal muscle removal of load," the expressions of *CEBPB* and *GATA6* increased substantially, which in turn led to the elevation of miR-215 expression, thereby suggesting a putative mechanism for negative feedback regulation of exosomal homeostasis.

Keywords: Alzheimer's disease, exercise, necroptosis, exosomes, miR-215-5p, neural network prediction model

OPEN ACCESS

Edited by:
Jun Xu,
Capital Medical University, China

Reviewed by:
Xiaomeng Sun,
GloriousMed Clinical Laboratory Co., Ltd., China
Carmen Picon,
Imperial College London, United Kingdom
Huilin Xu,
Shanghai Medical College of Fudan University, China

***Correspondence:**
Qian Wang
qianqianwangxi@163.com
Jiwu Chen
jeevechen@gmail.com
Shiyi Chen
cshiyi@163.com

† These authors have contributed equally to this work

Specialty section:
This article was submitted to Alzheimer's Disease and Related Dementias, a section of the journal Frontiers in Aging Neuroscience

Received: *22 January 2022*
Accepted: *21 March 2022*
Published: *09 May 2022*

Citation:
Chen Y, Sun Y, Luo Z, Lin J, Qi B, Kang X, Ying C, Guo C, Yao M, Chen X, Wang Y, Wang Q, Chen J and Chen S (2022) Potential Mechanism Underlying Exercise Upregulated Circulating Blood Exosome miR-215-5p to Prevent Necroptosis of Neuronal Cells and a Model for Early Diagnosis of Alzheimer's Disease. Front. Aging Neurosci. 14:860364. doi: 10.3389/fnagi.2022.860364

INTRODUCTION

Alzheimer's disease (AD), a global health concern, is a neurodegenerative disease whose pathology is thought to be characterized by neurofibrillary tangles due to extracellular β-amyloid deposition and tau hyperphosphorylation (p-tau). At present, as the pathogenesis of AD remains unclear, no effective treatment is available (Lei et al., 2021). Recent studies suggest that physical activity is an important preventative method for AD and can greatly improve the quality of life of the patient (Dimities et al., 2021). Exercise prescription has now been included in the agenda (Luan et al., 2019). However, further research is needed to determine and identify patients at risk for AD who may require early exercise prescription. The specific mechanisms underlying exercise-related prevention of AD are complex and remain largely unclear (De la Rosa et al., 2020). Therefore, the construction of an accurate AD risk prediction model may serve as the basis for early implementation of the exercise prescription therapy (Li et al., 2016).

In recent years, necroptosis has been identified as an important player in neurodegenerative diseases, including AD (Caccamo et al., 2017; Yuan et al., 2019). Necroptosis, also called programmed necrosis, is a regulated mode of necrotic cell death mediated by RIP1 and RIP3 kinases. In 2021, Fu et al. (2021) reported that exercise could help prevent necroptosis of cardiomyocytes. Accumulating evidence indicates that exercise can prevent necroptosis through various pathways (Zhang et al., 2022). However, to the best of our knowledge, at present, the number of mechanistic studies on exercise-based prevention of necroptosis in AD is scarce. The study of necroptosis-related expression epistasis may help in constructing a new exercise prescription-sensitive AD risk prediction model.

In what ways might exercise prevent necroptosis in AD patients? Recent findings suggest that exosomes are mediators of systemic adaptation to endurance exercise, that is, they are important channels through which exercise may regulate other tissues (Safdar and Tarnopolsky, 2018). Exosomes can cross the blood–brain barrier and influence the development and progression of AD (Jiang et al., 2019; Soares Martins et al., 2021). Exercise has the potential to prevent the onset of neurodegeneration by modulating changes in exosome levels in the plasma (Fuller et al., 2020). We hypothesized that miRNAs carried by the exercise-regulated exosomes may affect AD development by inhibiting the necroptosis-related pathways, while lncRNAs exert a competitive effect by repressing these miRNAs (Tay et al., 2014). Recent studies show that lncRNAs play an important role in the process of necroptosis (Su et al., 2016; Jiang et al., 2021). Therefore, evaluating necroptosis-associated lncRNAs is necessary. Analysis of single-cell sequencing data yields transcriptional regulatory relationships in the organization of the locomotor system at single-cell resolution, thereby providing a plausible explanation for the differential expression of miRNAs in blood as a result of the exercise (Holland et al., 2020; Chen Y. et al., 2021; Wen-Jin et al., 2021). Therefore, analysis of scRNA transcriptional features of skeletal muscles is beneficial to understand the potential mechanisms and regulatory networks of miRNA upregulation in exosomes after exercise. This study aimed to construct a predictive model for the risk of AD associated with necroptosis in an effect to provide a theoretical basis for early administration of exercise prescription. We also examined the potential mechanisms underlying exosomal miRNA expression and regulation after exercise; these findings are expected to provide a potential biological basis for preventative exercise prescription for pre-AD patients.

MATERIALS AND METHODS

Data Acquisition and Variance Analysis

A total of five datasets were downloaded from the GEO database[1], namely, two AD datasets (GSE33000 and GSE44770), a dataset consisting of altered microRNA expressions in circulating blood after exercise (GSE144627), a skeletal muscle load-related dataset (GSE155933), and a single-cell transcriptome dataset of the skeletal muscle (GSE138826) (**Supplementary Table 3**). The GSE33000 dataset is based on the GPL4372 platform. This was examined on the Rosetta/Merck Human 44k 1.1 microarray. In this study, 467 human brain tissues were selected; among them, 310 were specimens from AD patients and 157 were specimens from non-demented controls. All brain tissue samples were obtained from the Harvard Brain Tissue Resource Center (HBTRC) (Narayanan et al., 2014). The GSE44770 dataset is also based on the GPL4372 platform. This was examined on the Rosetta/Merck Human 44k 1.1 microarray. A total of 230 human brain tissues were included; among them, 129 specimens were obtained from AD patients and 101 specimens were obtained from non-demented controls (Zhang et al., 2013). The GSE144627 dataset is based on the GPL15520 platform. The miRNA samples of circulating exosomes from 10 older adults (five endurance trainers and five sedentary individuals) were analyzed using the Illumina MiSeq (Homo sapiens) system (Nair et al., 2020). The GSE155933 dataset is based on the GPL24047 platform. This was assayed using the Affymetrix Human Transcriptome Array 2.0. A total of 230 skeletal muscle samples were included and the dataset comprised information on muscle conditions before and after muscle resistance training/unloading (Timmons et al., 2019). The GSE138826 dataset, based on the GPL24247 platform, was screened using Illumina NovaSeq 6000. It is a single-cell dataset from the mouse tibialis anterior muscle tissue (Oprescu et al., 2020). Differential expression analysis was performed using the limma package in R software; the fold change (FC) and false discovery rate (FDR) of all differential genes were noted, and a p-value < 0.05 was the criterion for statistical significance (Costa-Silva et al., 2017).

Correlation Analysis for Genes and Long Non-coding RNA Associated With Alzheimer's Disease and Necroptosis

The necroptosis gene set, M24779.gmt, consists of eight necroptosis genes, all of which were downloaded from the

[1]https://www.ncbi.nlm.nih.gov/pubmed/

Gene Set Enrichment Analysis (GSEA)[2] database. Finally, 67 necroptosis-related genes were included in the study (Zhao et al., 2021). After Pearson correlation analysis for all lncRNAs and the 67 necroptosis-related genes in the gene expression matrix, a total of 32 lncRNAs were identified and defined as significant necroptosis-related lncRNAs in AD (Pearson correlation coefficients > 0.4 and $p < 0.001$).

Random Forest Analysis and Neural Network Model

To ensure the reproducibility of the results, we set the seed at "123456." The random forest analysis was performed using the "randomForest" package in the R software. The parameters were set using the default function with 500 "trees." Since the error of the random forest model was minimized when 324 trees were used, accordingly, the importance of each gene was defined. The neural network model was constructed using the "neuralnet" and "NeuralNetTools" packages, with the seed set to "12345678" and the parameter to "hidden = 5." The GSE33000 dataset was used as the training group, and the GSE44770 dataset was used as the test group. The "pROC" package was used to plot the receiver operating characteristic (ROC) curve for the model.

Intersection Analysis and the Construction of the miRNA–mRNA Regulatory Network

The visualization function in R software was used to draw the Venn diagram. Prediction of mRNA targets for corresponding miRNAs was based on the database results. miRNA/mRNA interactions were identified using the miRWalk database[3]; subsequently, the miRNA–mRNA regulatory networks were constructed.

SCENIC Data Analysis and Regulatory Gene Network Based on the scRNA-Seq Analysis

The scRNA-seq analysis was performed using the "Seurat" package. Briefly, the cell clustering and clustering for the GSE138826 dataset followed the methods described previously by Oprescu et al. (2020). SCENIC supports the analysis of positive transcriptional regulation, which implies that it can screen transcription factors that regulate miRNAs during positive transcription. An improved version of the SCENIC method was used to screen the key transcription factors in skeletal muscles, as described previously (Suo et al., 2018; Chen Y. et al., 2021; Lin et al., 2021a,b). Moreover, to quantify the cell-type specificity of a regulon, we adapted an entropy-based strategy that was previously used for the analysis of gene expression data (Cabili et al., 2011).

[2]http://www.gsea-msigdb.org/gsea/index.jsp

[3]http://mirwalk.umm.uni-heidelberg.de/

Immune Infiltration and Immune Checkpoint Analysis

As an extension of the GSEA, a single sample gene set enrichment analysis (ssGSEA) allows for defining an enrichment score corresponding to the absolute enrichment of a gene set for each sample within a given dataset. This was published in 2009 (Barbie et al., 2009). The "GSVA" and "GSEABase" packages in the R software were used for immuno-infiltration analysis; the "limma" package was used for differential analysis, and the results of the final analyses were visualized using the "ggpubr" package. Immune checkpoint-related genes were extracted to screen the differentially expressed immune checkpoint genes in AD.

Gene Set Enrichment Analysis

The R (version 3.6.3) software was used for GSEA and visualization, as described in previous studies (Wang et al., 2020). The reference gene collection "c2.cp.v7.2.symbols.gmt" and the species *Homo sapiens* were chosen for this study, and the analysis was carried out according to the clusterProfiler package's instructions. Pathways meeting a FDR < 0.25 and p.adjust < 0.05 were considered significantly enriched.

Protein–Protein Interaction Network and Drug Sensitivity Analysis

The STRING database[4] was used to calculate the level of interaction likelihood and construct the network of interactions between known and predicted proteins. The more complex was the protein-protein relationship network encoded by a gene, the more was its importance for the gene function. The protein–protein interaction (PPI) network encoded by DEGs was constructed using STRING, and the key genes were screened. Drug sensitivity analysis was based on the results of the "pRRophetic" package; the "limma" package was used for variance analysis. The "pRRophetic" package uses the expression matrix and drug handling information from the Cancer Genome Project (CGP), a database comprising 138 anticancer drugs tested against 727 cell lines. The "cgp2016" dataset was used for the bulk prediction of drug data.

Statistical Methods and Neural Network-Based Clinical Prediction Model

Based on the neural network prediction model, we constructed a new logistic regression-based AD risk prediction model in order to provide a visual basis for the formulation of exercise prescription. Factors with p-values < 0.05 were further screened and used to construct a column line graph prediction model, as described previously (Chen et al., 2020; Ying et al., 2021; Zhou et al., 2021). The GSE44770 dataset was used as an external dataset to validate the findings. These data were used for principal component analysis (PCA) to assess their ability to discriminate between different outcomes as our previous research (Ying et al., 2021). Calibration curves were plotted to evaluate the accuracy of the nomogram. Moreover, the C-index and AUC values

[4]https://www.string-db.org/

were also calculated for further verification of the prediction accuracy. Besides, accuracy, *F*-value, precision, and recall of each dataset and proposed nomogram were also described as our previous research (Wang et al., 2020). Finally, decision curves were used to evaluate the clinical applicability of the nomogram (Kang et al., 2020).

RESULTS

Screening Necroptosis-Associated Messenger RNA and Long Non-coding RNA in Brain Tissue From Alzheimer's Disease Patients

The research flow schema of this study is shown in **Figure 1**. Sixty-seven necroptosis-related genes were initially included (Zhao et al., 2021). After Pearson correlation analysis for all lncRNAs in the GSE33000 gene expression matrix and 67 necroptosis-related genes, a total of 32 lncRNAs were identified for subsequent analysis. These lncRNAs were considered as significant necroptosis-associated lncRNAs (Pearson correlation coefficients > 0.4 and $p < 0.001$) in AD. The PPI network for these lncRNAs is positively associated with mRNAs as shown in **Supplementary Figure 1**. Our main objective was to screen lncRNAs that may regulate exosomal microRNAs. MicroRNAs negatively regulate mRNAs. Therefore, based on the ceRNA theory, we only screened the lncRNAs–mRNA pairs, wherein the lncRNAs were positively associated with mRNAs. **Figure 2A** presents a circle diagram of necroptosis-related lncRNAs–mRNAs relationship pairs. The lncRNAs are in the middle of the circle; mRNAs are in the outer periphery of the circle, and the linkage of the outer circle origin with the inner circle origin indicates a significant correlation. To determine whether these lncRNAs–mRNAs relationship pairs are differentially expressed in AD patients and normal patients, we performed the difference analysis. Red connecting lines indicate that these mRNAs are highly expressed in AD, and purple indicates that these mRNAs are lowly expressed in AD. Volcano maps were used to visualize the significantly different lncRNAs and mRNAs. Since data on microRNAs in the GSE33000 dataset are lacking, the dataset of microRNAs is not shown in the volcano plot. The volcano plots for the differentially expressed genes between AD and normal brain tissues are shown in **Figures 2B,C**. *GATA3*, *ALK*, *TRAF2*, *HSPA4*, *HDAC9*, *BCL2L11*, *FASLG,* and *IDH1* are significantly overexpressed in AD patients. Also, the EGFR expression is downregulated in AD patients. *DLEU2*, *DKFZP434H168*, *MYCNOS*, *C22or24*, *C8orf49*, *FLJ13224*, *DGOR5,* and *HPYR1* are lncRNAs that are also overexpressed in AD.

Neural Network Model Based on Random Forest Analysis to Evaluate the Alzheimer's Disease Risk Score

Genes showing significant differences were used for analysis using the random forest model. In **Figure 2D**, the green line indicates the training group error; the red line indicates the test group error, and the black line indicates the overall group error. We found that the random forest model exhibited the lowest error at 324 "trees," and all genes with scores less than 2 were excluded (**Figure 2E**). Due to the large error, it was necessary to further optimize the random forest model. The ROC curves for the AD neural network prediction model (**Figure 2F**) are shown in **Figures 2G,H**; the AUC of the training group was 0.948 (95% CI: 0.928–0.967) and that of the test group was 0.932 (95% CI: 0.896–0.961). This result suggested that mRNAs and lncRNAs based on necroptosis-related genes show good predictive ability.

Alzheimer's Disease Risk Assessment Model Based on the Neural Network

Since this neural network model did not include basic clinical features such as age and gender, we constructed a forest plot using the age, gender, and neural network risk score (**Figure 3A**). A forest plot for the multifactor logistical analysis based on age, gender, and neural network risk scores is shown in **Figure 3A**. The *p*-values for multifactor regression analysis of age and neural network risk score were significant and were subsequently used to construct the nomogram prediction model (**Figure 3B**). A PCA suggested that the model could better distinguish AD from normal patients (**Figure 3C**). The calibration curve was plotted using data from the entire group (**Figure 3D**). The mean absolute error of this calibration curve was 0.016, while the mean squared error was 0.0049 (**Figure 3D**). To determine the prediction accuracy of this neural network model, we calculated the AUC for the ROC curve (**Figure 3E**). The AUC value of the training group was 0.979, while that of the test group was 0.957. In addition, the C-index was calculated and reached 0.979 [95% credibility interval (95% CI; 0.959–0.983)] in the training set and 0.957 (95% CI; 0.968–0.990) in the validation set (**Table 1**). Besides, we also described the accuracy, *F*-value, precision, and recall of each dataset and proposed nomogram in **Table 2**. This indicated that the prediction model was capable of accurately representing the transcriptomic aspects of the brains of AD patients and had high predictive potential. The DCA curve for this nomogram prediction model is shown in **Figure 3F**, which suggests that the model has a very high predictive power.

Correlation Analysis for Alzheimer's Disease Risk Assessment Models With Local Immune Microenvironment and Drug Sensitivity

Previous studies show that microenvironmental alterations characterized by an imbalance in the immune microenvironment of the brain induced upon damage to the blood–brain barrier are closely related to the AD pathogenesis (Lu et al., 2021). In our investigation, using ssGSEA, we determined the degree of immune cell infiltration. Cytolytic activity, MHC class I, neutrophils, para-inflammation, T cell co-inhibition, Tfh, TIL, Type I, and Type II IFN responses were all found to be significantly associated with the AD risk assessment model (**Figure 4A**). ICOSLG, PDCD1, and TNFRSF25 were found to be overexpressed in patients in the high-risk group. In the high-risk group, the expressions of TNFRSF18, HAVCR2, and CD276, were found to be downregulated (**Figure 4B**). Findings

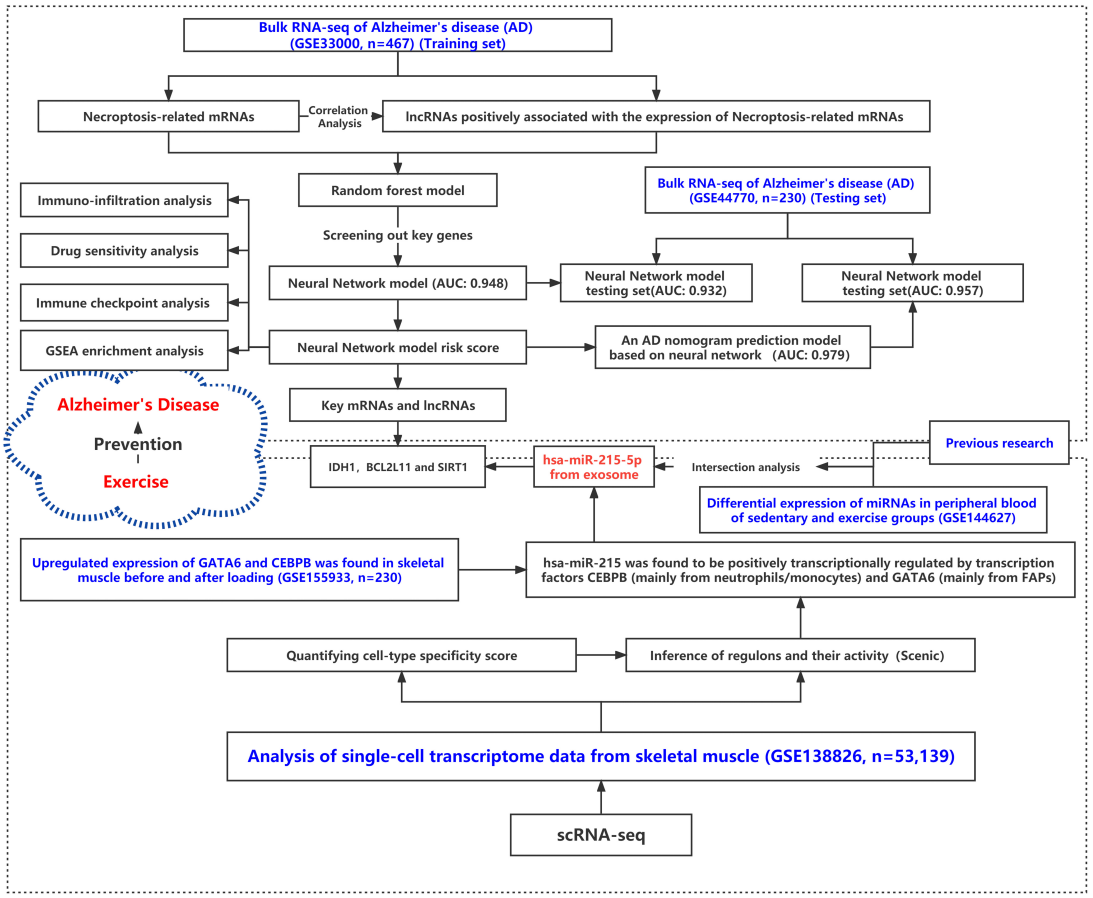

FIGURE 1 | Research roadmap for this study.

from GSEA revealed a substantial association between the gut immune network for IgA production and the AD risk score (**Figure 4C**). The aforementioned results indicated that this model of AD risk assessment was intimately connected to the local immunological microenvironment. Imbalances in the circulatory system and intracerebral immune microenvironment were found to be strongly related to neuronal necroptosis. Additionally, **Supplementary Figure 2** illustrates the differential susceptibility of neuronal cells to medicines in individuals at high and low risk of developing AD. Thus, those medicines may contribute to AD by impairing neuronal necroptosis.

Upregulation of Exosomal hsa-miR-215 Expression in Circulating Blood After Exercise May Contribute to the Inhibition of Alzheimer's Disease Necroptosis-Related Genes

Previous studies suggest that regular exercise leads to the upregulation of three microRNAs, namely, miR-486-5p, miR-215-5p, and miR-941, in the peripheral blood, while that of the exosomal miR-151b is downregulated (Nair et al., 2020). We performed a differential analysis using the GSE144627 dataset and found that miR-1306-3p, miR-215-5p, miR-432-5p, miR-129-5p, miR-370-3p, and miR-197-3p were all upregulated in the exercise group (**Supplementary Table 1**). The logFC values for miR-215-5p and miR-197-3p expressions were greater than 2. The Venn diagram demonstrated that the microRNA, miR-215-5p, was co-significantly differentially expressed in both previous studies and the GSE144627 dataset (**Figure 5A**). The miRWalk database was used to construct a miRNA–mRNA regulatory network (**Supplementary Table 2**). We reasonably hypothesized that the upregulation of exosomal hsa-miR-215 expression in circulating blood after exercise may contribute to the inhibition of AD necroptosis-related genes (e.g., *IDH1*, *SIRT1*, and *BCL2L11*). Among them, *SIRT1* and *BCL2L11* have been previously validated as the target genes of miR-215-5p.

CEBPE and *GATA6* Were Defined as Potential Transcriptional Regulators Leading to the Upregulation of hsa-miR-215 Expression

Based on the TransmiR v2.0 database, a total of 44 TFs, the possible upstream transcriptional regulators regulating hsa-miR-215 transcription, were predicted (**Figure 5B**). Cell clustering in

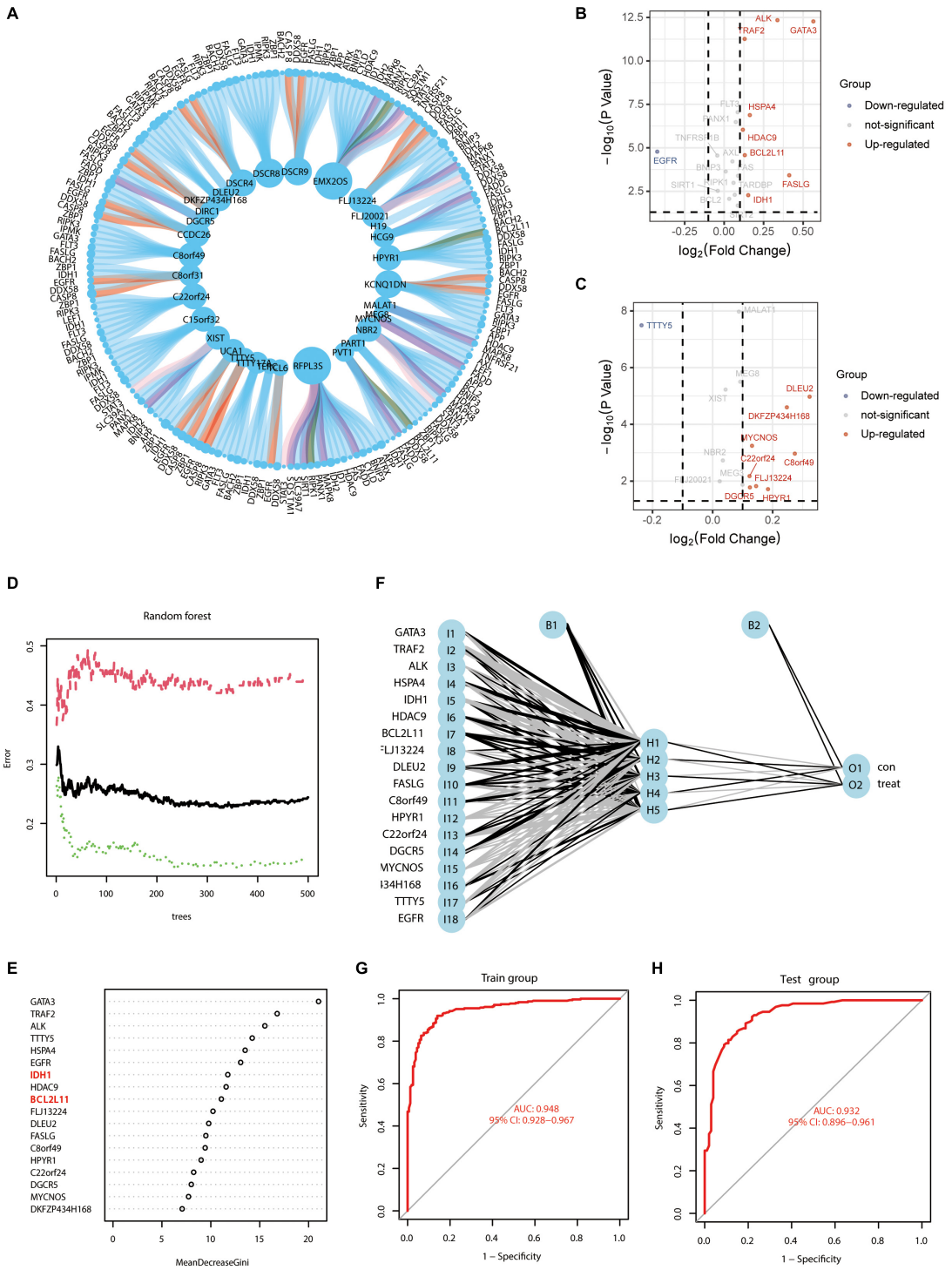

FIGURE 2 | Screening of necroptosis-associated mRNAs and lncRNAs in AD brain tissue to construct AD risk score scores. **(A)** Circle diagram of necroptosis-related lncRNAs–mRNAs correlation analysis; lncRNAs are in the middle of the circle, and mRNAs are in the outer periphery of the circle. Linkage of peripheral circle origin to inner circle origin indicates a significant correlation. Red connecting lines indicate that these mRNAs are highly expressed in AD, and purple indicates that these mRNAs are lowly expressed in AD. **(B)** Volcano map of necroptosis-related mRNAs differentially expressed in AD. **(C)** Volcano map of necroptosis-related lncRNAs differentially expressed in AD. **(D)** Prediction error diagram of random forest model; green line indicates training group error, red line indicates test group error and black line indicates overall group error. **(E)** Importance analysis of genes in predicting AD in random forest, filtering all genes with scores greater than 2 according to the model with the lowest error point in panel **(D)**. **(F)** Schematic diagram of a neural network model for AD diagnosis prediction based on gene expression features. **(G,H)** ROC curves of the AD neural network prediction model for the training group (AUC = 0.948; 95% CI: 0.928–0.967) and the test group (AUC = 0.932; 95% CI: 0.896–0.961).

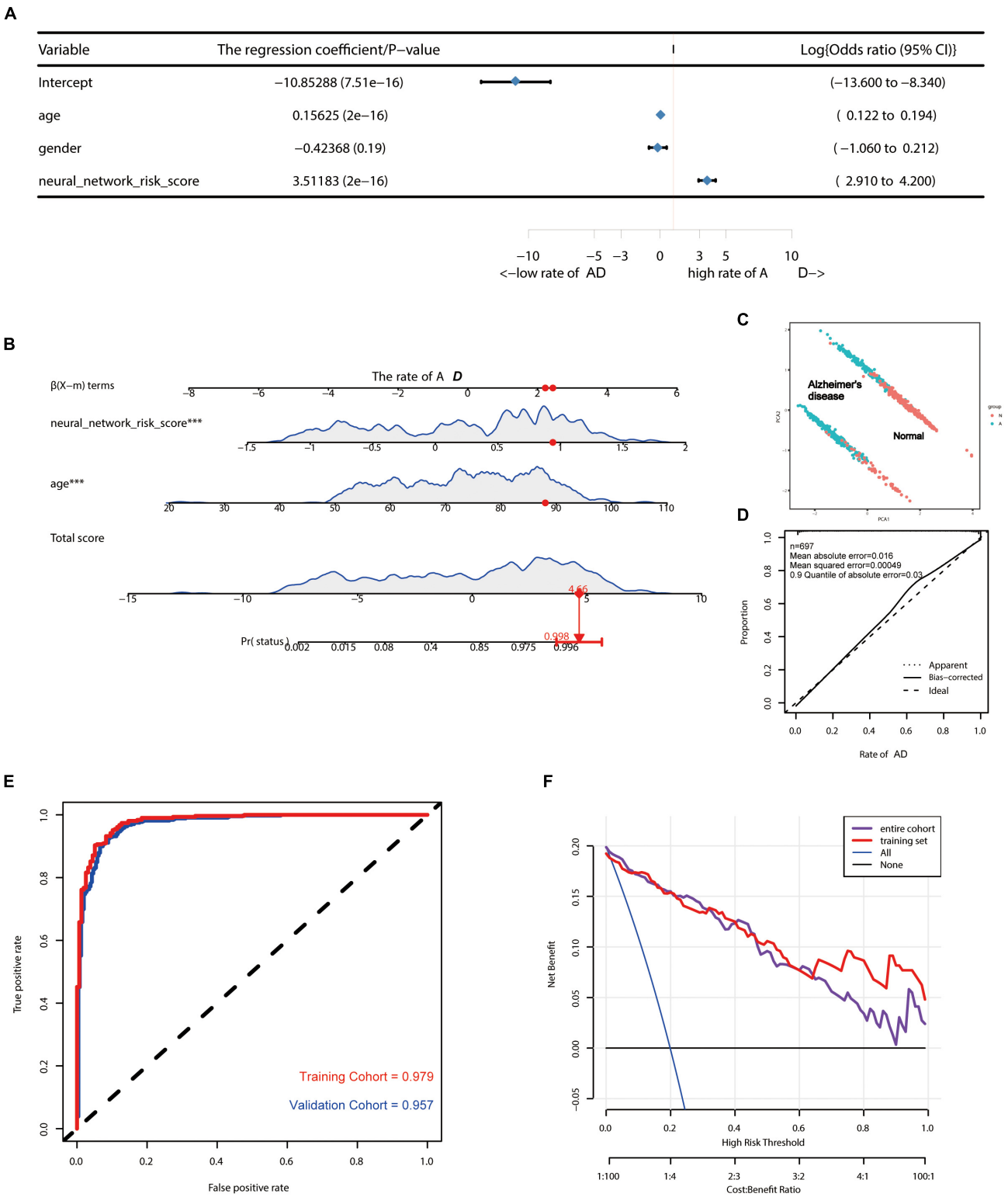

FIGURE 3 | Construction of AD risk nomogram model based on neural network model. **(A)** A forest plot for multifactor logistical analysis based on age, gender, and neural network risk score. **(B)** A nomogram prediction model was constructed using neural network risk score and age. **(C)** PCA suggests that the model is better able to distinguish AD from normal patients. **(D)** The calibration curve of this nomogram prediction model after including a sample of 697 cases. **(E)** ROC curves of the AD risk nomogram prediction model constructed based on the neural network model for the training group (AUC = 0.979) and the test group (AUC = 0.957). **(F)** DCA curves of this nomogram prediction model.

TABLE 1 | C-index of the prediction model.

Dataset group	C-index of the prediction model	
	C-index	The C-index (95% CI)
Training set	0.979	0.959–0.983
Validation set	0.957	0.968–0.990
Entire cohort	0.97	0.930–0.984

TABLE 2 | Accuracy, *F*-value, precision, and recall of each dataset.

	Dataset group		
	Entire cohort	Training set	Validation set
Accuracy	0.9283	0.9358	0.9087
F-value ($\alpha = 1$)	0.9433	0.9518	0.9195
Precision	0.9391	0.9487	0.9091
Recall	0.9476	0.9548	0.9302

the GSE138826 dataset was performed based on the findings of Oprescu et al. (2020; **Figure 5C**). Subsequently, the connection specificity index (CSI) matrix was constructed using the SCENIC method, and a total of ten modules were obtained (**Figure 5D**). In these modules, 316 key TFs were included. The Venn diagram shows the intersection of key TFs from skeletal muscle scRNA-seq data with those predicted to potentially regulate miR-215 using the TransmiR database (**Figure 5E**). The regulator rankings for FAPs and skeletal muscle based on the Regulon specificity score (RSS) are shown in **Figure 5F**. Thus, Cebpe and GATA6 were identified as key TF in FAPs and skeletal muscle cells, respectively. Since Cebpe and GATA6 could potentially regulate miR-215, we speculated that the upregulation of Cebpe and GATA6 expressions in skeletal muscles could elevate miR-215 levels in exosomes.

Upregulation of *CEBPE* and *GATA6* Expression After Unloading Muscle Load May Help Prevent the Excessive Downregulation of miR-215

The tSNE plot was used to demonstrate the expression characteristics of the regulon, *CEBPB*, and *GATA6* from the scRNA-seq data (**Figures 6A,B**). *GATA6* and *CEBPB* were found to be significantly upregulated in the de-load group (**Figure 6C**). The tSNE plot shows the average expression characteristics of each gene module (**Figure 6D**). The distribution of the rankings of each cell type in each module according to the regulon activity score is also shown (**Figure 6E**). This suggested that *CEBPB* may exert an important transcriptional regulatory effect in the M2 and M3 cell clusters, while *GATA6* may play a critical transcriptional regulatory role in the M4 and M5 cell clusters. *CEBPB* and *GATA6* were found to be significantly upregulated after muscle exercise and de-loading. In a previous study, we found that regular exercise resulted in a significant increase in baseline expression of exosomal microRNA-215. However, acute exercise did not elicit the same effect on exosomal miRNA-215 expression (**Figure 7**). These suggest that the upregulation of miR-215 expression is not transient, rather it is the result of longterm exercise treatment. Although further validation is needed, we hypothesize that the transcriptional activity of CEBPB and GATA6 in upregulating miR-215 may be a potential negative regulatory feedback mechanism in exosome homeostasis after skeletal muscle unloading.

DISCUSSION

Exercise promotes longevity and fitness. It is also used therapeutically to prevent and treat several physical disorders, including cardiovascular diseases and diabetes. Although exercise offers numerous benefits for mood, learning ability, spatial and verbal memory, and cognition, the molecular mechanisms underlying these benefits remain unclear. Exercise helps in the prevention and treatment of disorders associated with age-related cognitive loss, such as AD and dementia (Lautenschlager et al., 2019).

Based on necroptosis-related genes, we constructed an AD risk prediction model with high predictive accuracy, excellent predictive power, and good prospects for clinical application. In exosomes, miR-215-5p could potentially target some genes involved in necroptosis (e.g., *IDH1*, *BCL2L11*, and *SIRT1*). Additionally, the expressions of *CEBPB* and *GATA6* were highly upregulated following exercise and load decrease. We postulated that the elevation in miR-215 expression through the overexpression of *CEBPB* and *GATA6* may serve as a negative feedback loop for the regulation of exosomal homeostasis following a decrease in the skeletal muscle load.

First, we screened the AD brain tissue data for necroptosis-associated mRNAs and lncRNAs. This is the first study to test a neural network model for predicting AD risk using necroptosis-associated miRNAs and lncRNAs. This prediction model exhibited greater predictive power than some previously described models. For instance, the prediction model of Chen W. et al. (2021) has an AUC of 0.872, while that proposed by Wang et al. (2021) has an AUC of 0.822. The C-index of the AD prediction model combining radiomic-clinical-laboratory data in the study by Tang et al. (2021) was also lower than that predicted using the model constructed in this study (0.979; 95% CI, 0.959–0.983); the maximum was at 0.950 (95% CI, 0.929–0.971). This suggested that the clinical features of AD patients could be well predicted based on necroptosis-related genes.

DLEU2, DKFZP434H168, MYCNOS, C22or24, C8orf49, FLJ13224, and *DGOR5* are also overexpressed in AD. They have all been incorporated into neural network models as risk predictors of AD. To the best of our knowledge, this study is the first to reveal a potential relationship between these lncRNAs and AD. Interestingly, in our previous study, lncRNA DLEU2 acts as a miR-181a sponge to regulate SEPP1 and inhibit skeletal muscle differentiation and regeneration (Wang et al., 2020). Combining the results of the previous study and this study, we suggested that DLEU2 is a potential common risk factor for the development of sarcopenia and Alzheimer's disease. Therefore, DLEU2 was proposed as a risk marker for sarcopenia and Alzheimer's disease in this study.

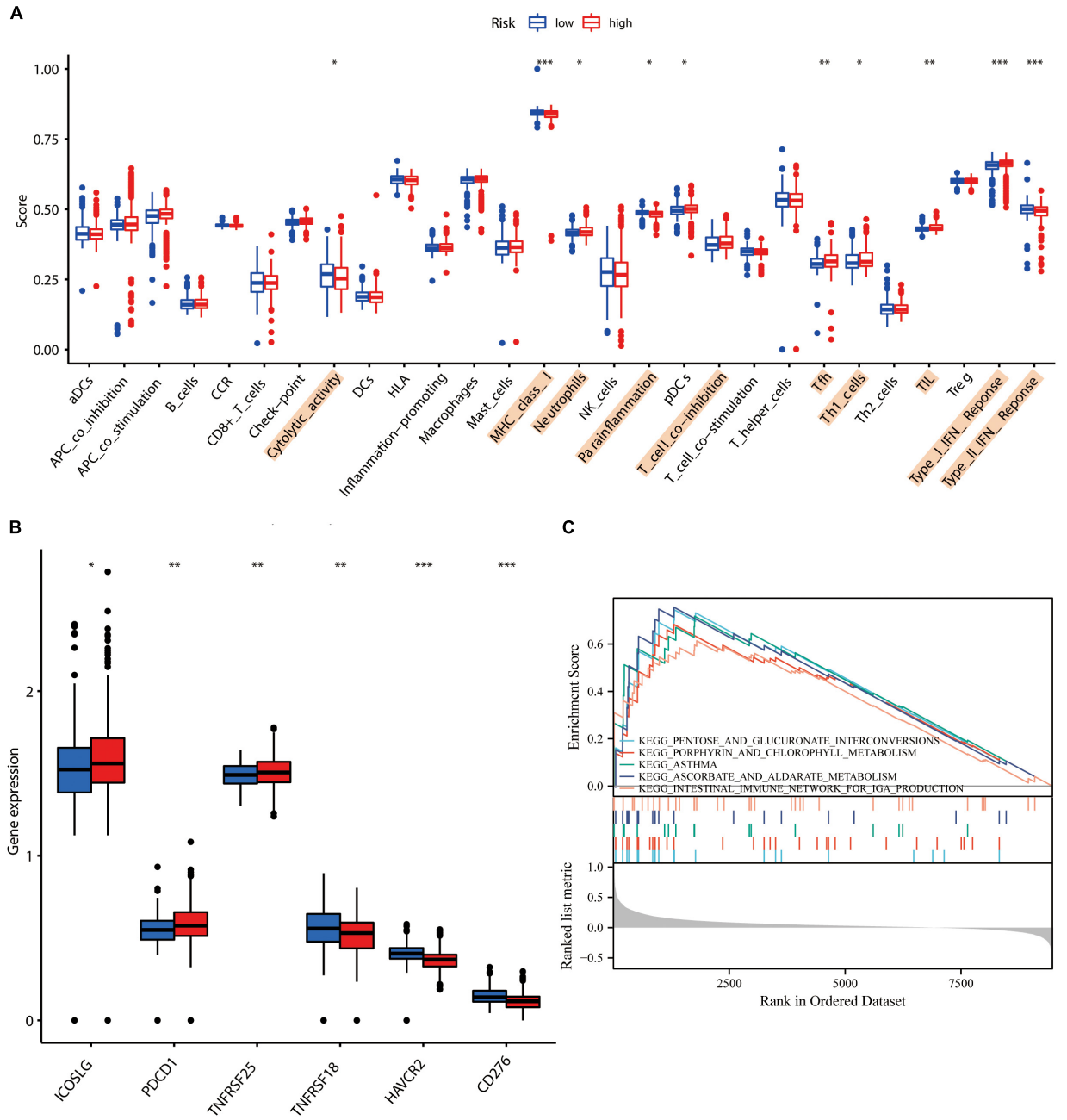

FIGURE 4 | Correlation study of AD risk score scores with local immune characteristics. **(A)** Immune cell infiltration analysis based on ssGSEA. **(B)** Correlation of high and low AD risk scores with immune checkpoints. **(C)** GSEA enrichment analysis based on AD scores. * represents p-value < 0.05, ** represents p-value < 0.01, and *** represents p-value < 0.001.

In addition, the AD risk assessment model was closely associated with the local immune microenvironment and the pathways in this study, consistent with previous findings. Cytolytic activity-related proteins are associated with neurodegenerative diseases (Tampio et al., 2020). Higher neutrophil counts are associated with AD (Ramos-Cejudo et al., 2021). The IFN pathway is significantly upregulated in AD and correlates significantly with disease severity and complement activation pathway (Roy et al., 2020). Immune checkpoints are also associated with the development of AD. In this study, the immune checkpoints, such as ICOSLG, PDCD1, TNFRSF25, TNFRSF18, HAVCR2, and CD276, were found to be significantly associated with AD risk scores (Baruch et al., 2016). Moreover, GSEA showed that immune-related pathways were closely associated with the AD risk assessment model. Therefore, the regulation of the

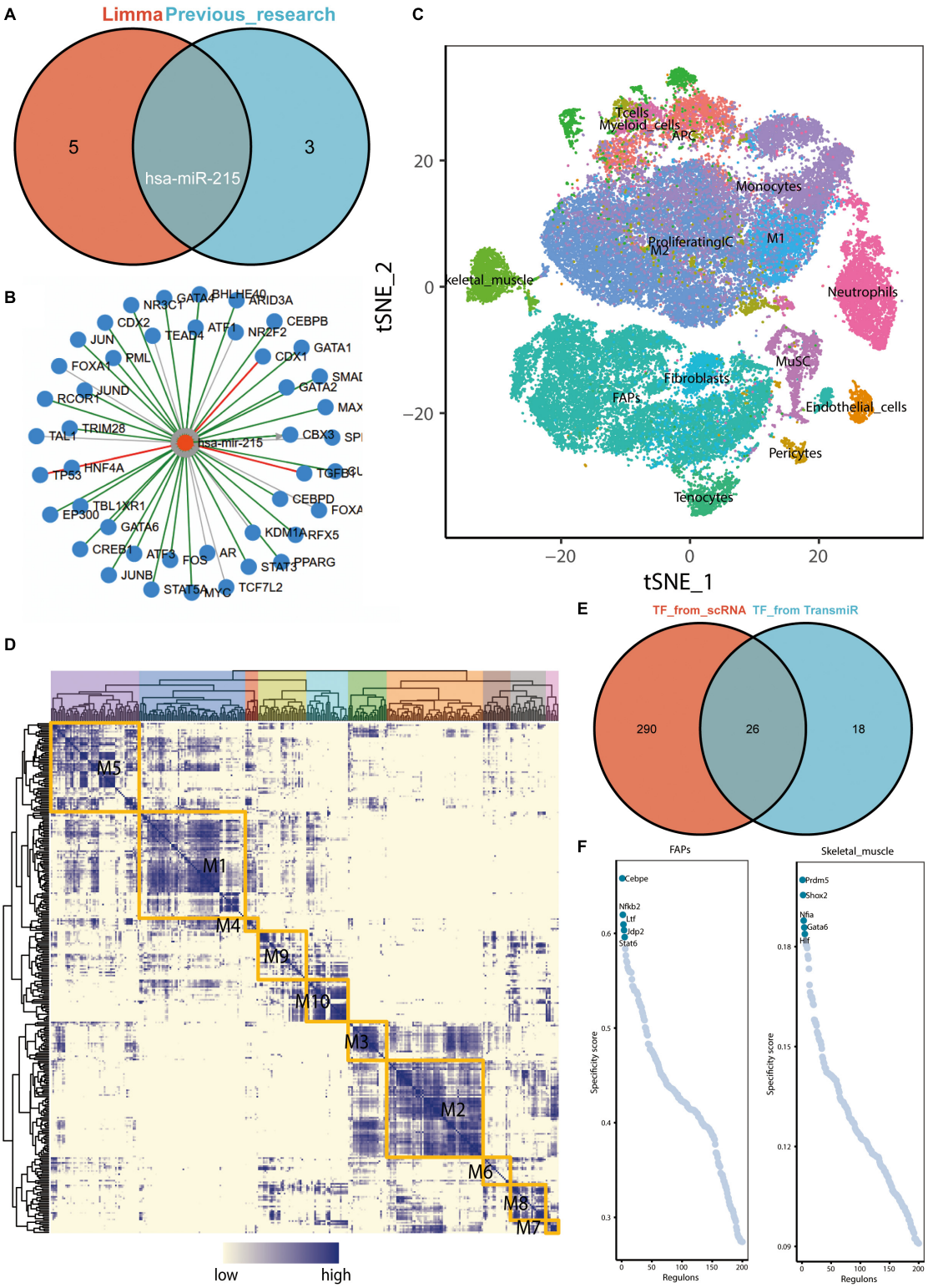

FIGURE 5 | Upregulation of exosome hsa-miR-215 expression in circulating blood after exercise and analysis of key transcription factors in skeletal muscle. **(A)** Venn diagram demonstrating that miR-215 is the microRNA found to be co-differentially expressed in previous studies and in the GSE144627 dataset. The "limma" here refers to the difference analysis for the GSE144627 dataset. **(B)** Prediction of upstream transcription factors that may regulate hsa-miR-215 transcription based on TransmiR v2.0. **(C)** tSNE distribution map of GSE138826 single cell dataset. **(D)** Regulatory modules identified based on the connection specificity index (CSI) matrix. **(E)** Venn diagram showing key transcription factors from skeletal muscle single cells ($n = 316$) with possible common transcription factors predicted to regulate miR-215 based on the TransmiR database ($n = 44$). **(F)** Ranking of regulators of FAPs and skeletal muscle based on regulatory specificity score (RSS).

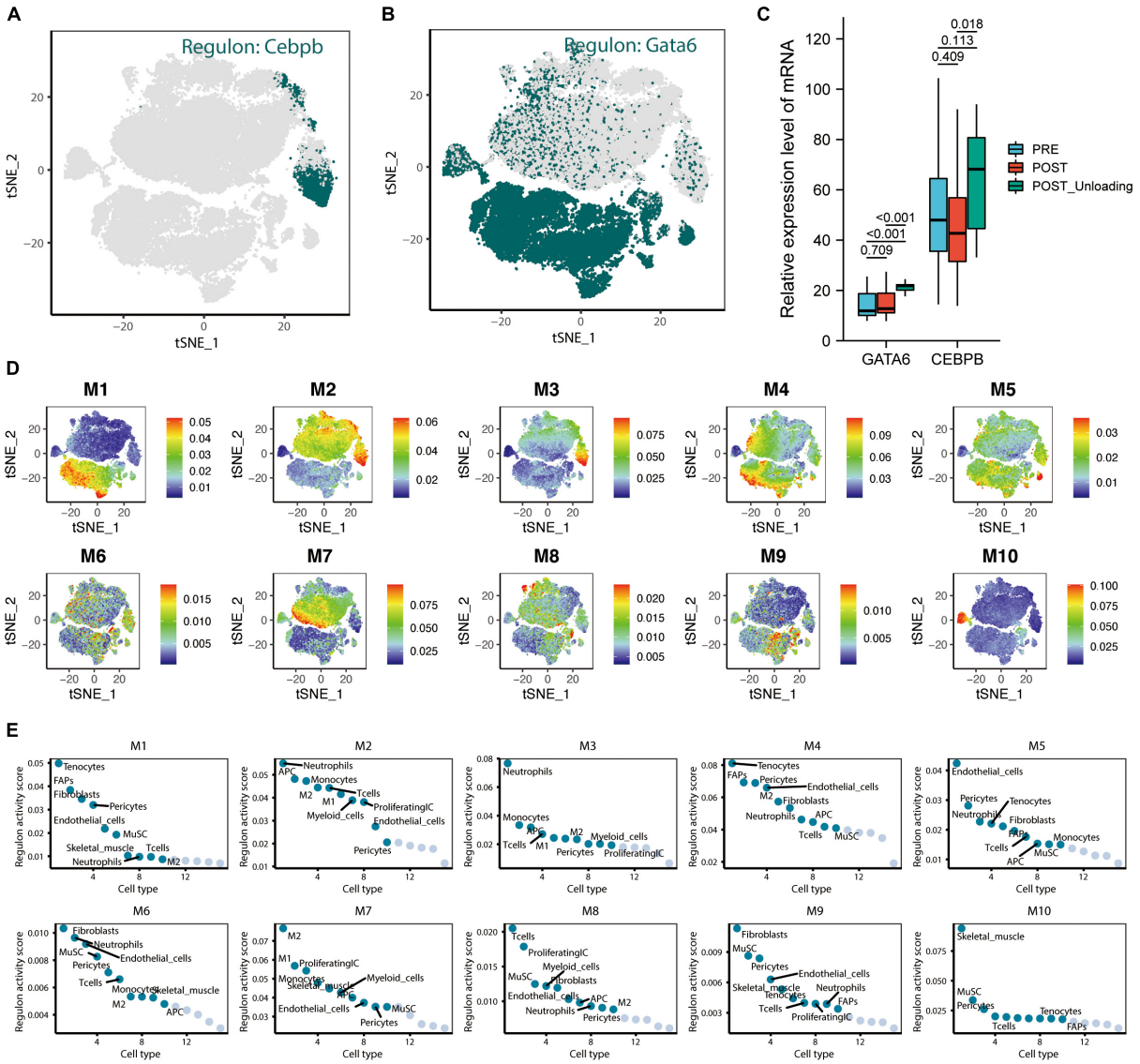

FIGURE 6 | CEBPE and *GATA6* were defined as potential transcriptional regulators leading to the upregulation of hsa-miR-215 expression and analysis of skeletal muscle single-cell transcriptional regulatory module. **(A)** tSNE plot demonstrating the expression characteristics of regulon *CEBPB* in single cells. **(B)** The tSNE plot demonstrates the expression characteristics of regulon *GATA6* in single cells. **(C)** Expression characteristics of *GATA6* and *CEBPB* in the pre-loading (PRE), post-loading (POST), and de-loading groups (POST Unloading) in the GSE155933 dataset, with p-values < 0.05 defined as significant differences. **(D)** The average expression characteristics of genes in each module are shown on the tSNE plot. **(E)** Plot of ranking distribution of individual cells in each module according to the regulon activity score.

immune system on exercising may be an important mechanism underlying its preventative effects against the development of AD (Madore et al., 2020).

Overall, changes in the expression of miRNAs enriched in muscle exosomes after exercise are consistent with changes in expression produced due to long-term regular muscle exercise (Nair et al., 2020). Exosomal miR-215-5p was upregulated in the exercise group, consistent with the results of a previous study (Nair et al., 2020). However, acute exercise was not found to have a significant effect on the expression of exosomal microRNA-215-5p. In this research, the miRWalk database was used to construct a miRNA–mRNA regulatory network. Based on the regulation principle of ceRNA, the upregulation of exosomal hsa-miR-215 expression in circulating blood after exercise was found to potentially contribute to the inhibition of AD necroptosis-related genes such as *IDH1*, *SIRT1*, and *BCL2L11*. According to miRWalk database, *SIRT1* and *BCL2L11* have been previously validated as the target genes of miR-215-5p. Therefore, miR-215-5p may target and bind *IDH1*, *BCL2L11*, and *SIRT1* mRNAs, thereby inhibiting their protein synthesis. *IDH1*, *BCL2L11*, and *SIRT1* have been revealed to be necroptosis-related genes in previous studies, and they play important functions in

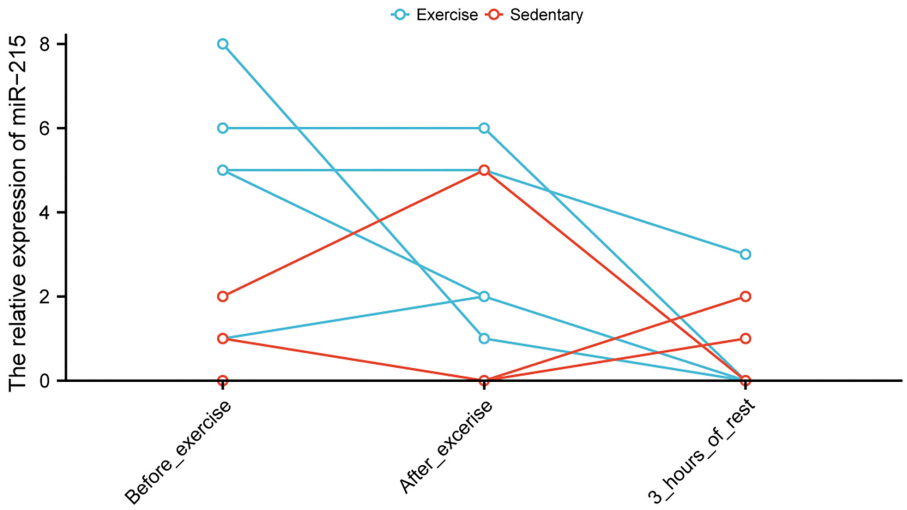

FIGURE 7 | Altered levels of miR-215 in circulating blood exosomes before and after exercise.

the development of necroptosis (Zhao et al., 2021). For example, IDH1/2-driven tumorigenesis was found to be associated with necroptosis (Schmauss et al., 2017). Targeted inhibitors of SIRT1 can downregulate necroptosis pathway activity by inhibiting the function of SIRT1 (Nikseresht et al., 2019). In skeletal muscle, the myoprotective effects of unacylated ghrelin on pressure-induced tissue injury were associated with SIRT1 and necroptosis signaling (Ugwu et al., 2017). Furthermore, BCL2L11 was also found to play an important function in the necroptosis pathway (Bohgaki et al., 2011; Cabon et al., 2012; Locatelli et al., 2014). However, to the best of our knowledge, the effect of exercise on *IDH1* and *BCL2L11* expression has not been studied in detail. In AD patients, high *SIRT1* expression has been suggested to exert neuroprotective effects for preventing the occurrence of neuronal apoptosis (Gomes et al., 2018). Exercise can upregulate the AMPK-SIRT1-TFEB signaling pathway, thereby activating the lysosomal functions in the brain (Huang et al., 2019). Immune checkpoints are associated with the development of AD. In this study, the immune checkpoints, such as ICOSLG, PDCD1, TNFRSF25, TNFRSF18, HAVCR2, and CD276, were found to be significantly associated with AD risk scores. The result from the miRWalk database analysis suggested that miR-215-5p could target and inhibit *BCL2L11* expression to a certain extent. Downregulation of *BCL2L11* expression can prevent the development of AD (Shi et al., 2016; Li et al., 2020). Therefore, "miR-215-5p targeting *BCL2L11*" may be an important potential mechanism underlying the prevention of AD occurrence.

The levels of expression of *CEBPB* and *GATA6* were considerably elevated following muscle load decrease. To date, no study reports the association between exercise and *GATA6* expression. *CEBPB* is implicated in myocardial protection, and its deficiency results in cardiomyocyte hypertrophy and proliferation (Boström et al., 2010). In addition, endurance exercise training can affect the expression of *CEBPB* (Walton et al., 2019). Interestingly, *CEBPB* expression in blood is consistent with the CEBPB-dependent muscle repair process, suggesting that *CEBPB* may be a potential marker for muscle repair (Blackwell et al., 2015). The upregulation of miR-215 expression brought about by the elevated expressions of *CEBPB* and *GATA6* after muscle loss of load may be the potential mechanism underlying the negative feedback regulation of exosomal homeostasis after skeletal muscle loss of load. However, the mechanisms involved need to be further investigated.

This study elucidated a possible mechanism by which exercise protects against the development of AD by modifying the aspects of circulating blood exosomes. miR-215-5p in exosomes may exert protective effects against the development of AD by targeting *BCL2L11*. In this study, a training group of more than 400 cases and a test group of more than 200 cases were obtained using two different datasets, thus, potentially making the results of this study highly reliable. The high AUC may be attributed to the role of necroptosis in the development of AD. In addition, the construction of the logistic prediction model based on the neural network model may have helped in improving the prediction accuracy of this study. Although the sample size used for this investigation was sufficient, the findings must be validated in clinical trials. Additionally, the contradictory outcomes of the data analysis, while interpretable, require further verification using clinical data. We proposed some necrotizing apoptosis-related biomarkers associated with AD. However, we did not analyse the association of these markers with exercise due to objective constraints. In the future, single-cell transcriptome sequencing data before and after exercise should also be made available. Although the predictive effect of the model was high, the prediction results still seemed to be somewhat biased from the PCA. This study was focused on constructing a prediction model based on necroptosis-related characteristics. However, the occurrence of AD is influenced by several other factors, which may affect the prediction results to some extent. Furthermore, the prediction model in this study is more similar to a diagnostic model. The progressive nature of the disease leads to a progressive change in the disease marker as well. This feature permits the

potential diagnostic use of the markers in the discriminant model as tools for staging or evaluating prognosis. This means that the higher the risk score, the higher the risk for future diseases. Therefore, it follows that patients with higher risk scores are more likely to benefit from exercise prescription.

Based on the neural network prediction model, we constructed a new logistic regression-based AD risk prediction model in order to provide a visual basis for the formulation of exercise prescription. This study provides a predictive model related to necroptosis that can be useful for clinical practitioners to assess the risk of patients suffering from AD. Further studies on the regulatory function of miR-215-5p in exosomes by *CEBPB* and *GATA6* are still needed. Based on these key predictors, we revealed miRNAs that may regulate necroptosis and whose expression may be upregulated after exercise. Analysis of the transcriptional profile of skeletal muscle scRNAs helps to understand the potential mechanisms and regulatory networks underlying the upregulation of miRNAs in exosomes after exercise. Based on these mechanisms, more in-depth studies can be conducted in the future to identify specific mechanisms of exercise for AD prevention, which can provide prospective input for the development of new bionic drugs.

CONCLUSION

In conclusion, exercise may help avoid necroptosis. The purpose of this study was to develop a novel AD-risk prediction model having high predictive accuracy. Exercise-induced upregulation of circulating blood exosome miR-215 expression may underlie its preventative effect on AD. miR-215 expression increases by negative feedback following a decrease in the load.

DATA AVAILABILITY STATEMENT

The original contributions presented in the study are included in the article/**Supplementary Material**, further inquiries can be directed to the corresponding authors.

AUTHOR CONTRIBUTIONS

YC contributed to the methodology, conceptualization, software, validation, formal analysis, data curation, and writing (original draft). YS contributed to the conceptualization, methodology, and supervision. ZL contributed to the methodology and conceptualization. JL contributed to the data curation and methodology. BQ and XK contributed to the data curation and writing (review and editing). CY and CG contributed to the software and validation. MY contributed to the formal analysis and data curation. XC and YW contributed to the supervision and project administration. QW contributed to the writing (original draft), conceptualization, supervision, methodology, and funding acquisition. JW and SC contributed to the conceptualization, supervision, project administration, and funding acquisition. All authors contributed to the article and approved the submitted version.

FUNDING

This study was supported by grants from the National Natural Science Foundation of China (Grant Nos. 82102634, 81972062, and 81772419) and the Medical and Health Science and Technology Development Project of Shandong Province (Grant No. 2018WS147). This work was also supported by the Project of the Key Clinical Medicine Center of Shanghai (Grant No. 2017ZZ01006), Sanming Project of Medicine in Shenzhen (Grant No. SZSM201612078), Development Project of Shanghai Peak Disciplines-Integrative Medicine (Grant No. 20180101), and Shanghai Committee of Science and Technology (Grant No. 19441901600).

ACKNOWLEDGMENTS

We thank the reviewers for their contribution to the successful publication of this study. We also thank Bullet Edits Limited for the linguistic editing and proofreading of the manuscript, and XC and YW for their constructive comments on the revision of this study.

SUPPLEMENTARY MATERIAL

The Supplementary Material for this article can be found online at: https://www.frontiersin.org/articles/10.3389/fnagi.2022.860364/full#supplementary-material

Supplementary Figure 1 | PPI network of mRNAs in the analysis of necroptosis-related lncRNAs–mRNAs correlation.

Supplementary Figure 2 | Differential analysis of neuronal cell sensitivity to drugs in high and low AD risk.

REFERENCES

Barbie, D. A., Tamayo, P., Boehm, J. S., Kim, S. Y., Moody, S. E., Dunn, I. F., et al. (2009). Systematic RNA interference reveals that oncogenic KRAS-driven cancers require TBK1. *Nature* 462, 108–112. doi: 10.1038/nature08460

Baruch, K., Deczkowska, A., Rosenzweig, N., Tsitsou-Kampeli, A., Sharif, A. M., Matcovitch-Natan, O., et al. (2016). PD-1 immune checkpoint blockade reduces pathology and improves memory in mouse models of Alzheimer's disease. *Nat. Med.* 22, 135–137. doi: 10.1038/nm.4022

Blackwell, J., Harries, L. W., Pilling, L. C., Ferrucci, L., Jones, A., and Melzer, D. (2015). Changes in CEBPB expression in circulating leukocytes following eccentric elbow-flexion exercise. *J. Physiol. Sci.* 65, 145–150. doi: 10.1007/s12576-014-0350-7

Bohgaki, T., Mozo, J., Salmena, L., Matysiak-Zablocki, E., Bohgaki, M., Sanchez, O., et al. (2011). Caspase-8 inactivation in T cells increases necroptosis and suppresses autoimmunity in $Bim^{-/-}$ mice. *J. Cell Biol.* 195, 277–291. doi: 10.1083/jcb.201103053

Boström, P., Mann, N., Wu, J., Quintero, P. A., Plovie, E. R., Panáková, D., et al. (2010). C/EBPβ controls exercise-induced cardiac growth and protects against

pathological cardiac remodeling. *Cell* 143, 1072–1083. doi: 10.1016/j.cell.2010.11.036

Cabili, M. N., Trapnell, C., Goff, L., Koziol, M., Tazon-Vega, B., Regev, A., et al. (2011). Integrative annotation of human large intergenic noncoding RNAs reveals global properties and specific subclasses. *Genes Dev.* 25, 1915–1927. doi: 10.1101/gad.17446611

Cabon, L., Galán-Malo, P., Bouharrour, A., Delavallée, L., Brunelle-Navas, M.-N., Lorenzo, H. K., et al. (2012). BID regulates AIF-mediated caspase-independent necroptosis by promoting BAX activation. *Cell Death Differ.* 19, 245–256. doi: 10.1038/cdd.2011.91

Caccamo, A., Branca, C., Piras, I. S., Ferreira, E., Huentelman, M. J., Liang, W. S., et al. (2017). Necroptosis activation in Alzheimer's disease. *Nat. Neurosci.* 20, 1236–1246. doi: 10.1038/nn.4608

Chen, W., Li, S., Ma, Y., Lv, S., Wu, F., Du, J., et al. (2021). A simple nomogram prediction model to identify relatively young patients with mild cognitive impairment who may progress to Alzheimer's disease. *J. Clin. Neurosci.* 91, 62–68. doi: 10.1016/j.jocn.2021.06.026

Chen, Y., Cai, Y., Kang, X., Zhou, Z., Qi, X., Ying, C., et al. (2020). Predicting the risk of sarcopenia in elderly patients with patellar fracture: development and assessment of a new predictive nomogram. *PeerJ* 8:e8793. doi: 10.7717/peerj.8793

Chen, Y., Sun, Y., Xu, Y., Lin, W.-W., Luo, Z., Han, Z., et al. (2021). Single-cell integration analysis of heterotopic ossification and fibrocartilage developmental lineage: endoplasmic reticulum stress effector Xbp1 transcriptionally regulates the notch signaling pathway to mediate fibrocartilage differentiation. *Oxid. Med. Cell. Longev.* 2021, 1–29. doi: 10.1155/2021/7663366

Costa-Silva, J., Domingues, D., and Lopes, F. M. (2017). RNA-Seq differential expression analysis: an extended review and a software tool. *PLoS One* 12:e0190152. doi: 10.1371/journal.pone.0190152

De la Rosa, A., Olaso-Gonzalez, G., Arc-Chagnaud, C., Millan, F., Salvador-Pascual, A., García-Lucerga, C., et al. (2020). Physical exercise in the prevention and treatment of Alzheimer's disease. *J. Sport Health Sci.* 9, 394–404. doi: 10.1016/j.jshs.2020.01.004

Dimities, M., Xristina, F., Theodora-Elesa, K., and Maria, C. (2021). The impact of exercising in the quality of life of people with dementia-Alzheimer's disease. *Adv. Exp. Med. Biol.* 1339, 309–315. doi: 10.1007/978-3-030-78787-5_36

Fu, Y., Jiang, T., Sun, H., Li, T., Gao, F., Fan, B., et al. (2021). Necroptosis is required for atrial fibrillation and involved in aerobic exercise-conferred cardioprotection. *J. Cell Mol. Med.* 25, 8363–8375. doi: 10.1111/jcmm.16796

Fuller, O. K., Whitham, M., Mathivanan, S., and Febbraio, M. A. (2020). The protective effect of exercise in neurodegenerative diseases: the potential role of extracellular vesicles. *Cells* 9:E2182. doi: 10.3390/cells9102182

Gomes, B. A. Q., Silva, J. P. B., Romeiro, C. F. R., Dos Santos, S. M., Rodrigues, C. A., Gonçalves, P. R., et al. (2018). Neuroprotective mechanisms of resveratrol in Alzheimer's disease: role of SIRT1. *Oxid. Med. Cell. Longev.* 2018, 8152373. doi: 10.1155/2018/8152373

Holland, C. H., Tanevski, J., Perales-Patón, J., Gleixner, J., Kumar, M. P., Mereu, E., et al. (2020). Robustness and applicability of transcription factor and pathway analysis tools on single-cell RNA-seq data. *Genome Biol.* 21:36. doi: 10.1186/s13059-020-1949-z

Huang, J., Wang, X., Zhu, Y., Li, Z., Zhu, Y.-T., Wu, J.-C., et al. (2019). Exercise activates lysosomal function in the brain through AMPK-SIRT1-TFEB pathway. *CNS Neurosci. Ther.* 25, 796–807. doi: 10.1111/cns.13114

Jiang, L., Dong, H., Cao, H., Ji, X., Luan, S., and Liu, J. (2019). Exosomes in pathogenesis, diagnosis, and treatment of Alzheimer's disease. *Med. Sci. Monit.* 25, 3329–3335. doi: 10.12659/MSM.914027

Jiang, N., Zhang, X., Gu, X., Li, X., and Shang, L. (2021). Progress in understanding the role of lncRNA in programmed cell death. *Cell Death Discov.* 7:30. doi: 10.1038/s41420-021-00407-1

Kang, X., Chen, B., Chen, Y., Yi, B., Yan, X., Jiang, C., et al. (2020). A prediction modeling based on SNOT-22 score for endoscopic nasal septoplasty: a retrospective study. *PeerJ* 8:e9890. doi: 10.7717/peerj.9890

Lautenschlager, N. T., Cox, K. L., and Ellis, K. A. (2019). Physical activity for cognitive health: what advice can we give to older adults with subjective cognitive decline and mild cognitive impairment? *Dialogues Clin. Neurosci.* 21, 61–68. doi: 10.31887/DCNS.2019.21.1/nlautenschlager

Lei, P., Ayton, S., and Bush, A. I. (2021). The essential elements of Alzheimer's disease. *J. Biol. Chem.* 296:100105. doi: 10.1074/jbc.REV120.008207

Li, D., Thomas, R., Tsai, M. Y., Li, L., Vock, D. M., Greimel, S., et al. (2016). Vascular biomarkers to predict response to exercise in Alzheimer's disease: the study protocol. *BMJ Open* 6:e011054. doi: 10.1136/bmjopen-2016-011054

Li, J., Li, D., Zhou, H., Wu, G., He, Z., Liao, W., et al. (2020). MicroRNA-338-5p alleviates neuronal apoptosis via directly targeting BCL2L11 in APP/PS1 mice. *Aging (Albany NY)* 12, 20728–20742. doi: 10.18632/aging.104005

Lin, W. W., Wang, Y., Chen, Y., Wang, Q., Gu, Z., and Zhu, Y. (2021a). Role of calcium signaling pathway-related gene regulatory networks in ischemic stroke based on multiple WGCNA and single-cell analysis. *Oxid. Med. Cell. Longev.* 2021, 1–35. doi: 10.1155/2021/8060477

Lin, W. W., Xu, L.-T., Chen, Y.-S., Go, K., Sun, C., and Zhu, Y.-J. (2021b). Single-cell transcriptomics-based study of transcriptional regulatory features in the mouse brain vasculature. *Biomed Res. Int.* 2021, 1–15. doi: 10.1155/2021/7643209

Locatelli, S. L., Cleris, L., Stirparo, G. G., Tartari, S., Saba, E., Pierdominici, M., et al. (2014). BIM upregulation and ROS-dependent necroptosis mediate the antitumor effects of the HDACi Givinostat and Sorafenib in Hodgkin lymphoma cell line xenografts. *Leukemia* 28, 1861–1871. doi: 10.1038/leu.2014.81

Lu, S., Kong, W., and Wang, S. (2021). Exploring the changes of brain immune microenvironment in Alzheimer's disease based on PANDA algorithm combined with blood brain barrier injury-related genes. *Biochem. Biophys. Res. Commun.* 557, 159–165. doi: 10.1016/j.bbrc.2021.04.014

Luan, X., Tian, X., Zhang, H., Huang, R., Li, N., Chen, P., et al. (2019). Exercise as a prescription for patients with various diseases. *J. Sport Health Sci.* 8, 422–441. doi: 10.1016/j.jshs.2019.04.002

Madore, C., Yin, Z., Leibowitz, J., and Butovsky, O. (2020). Microglia, lifestyle stress, and neurodegeneration. *Immunity* 52, 222–240. doi: 10.1016/j.immuni.2019.12.003

Nair, V. D., Ge, Y., Li, S., Pincas, H., Jain, N., Seenarine, N., et al. (2020). Sedentary and trained older men have distinct circulating exosomal microRNA profiles at baseline and in response to acute exercise. *Front. Physiol.* 11:605. doi: 10.3389/fphys.2020.00605

Narayanan, M., Huynh, J. L., Wang, K., Yang, X., Yoo, S., McElwee, J., et al. (2014). Common dysregulation network in the human prefrontal cortex underlies two neurodegenerative diseases. *Mol. Syst. Biol.* 10:743. doi: 10.15252/msb.20145304

Nikseresht, S., Khodagholi, F., and Ahmadiani, A. (2019). Protective effects of ex-527 on cerebral ischemia–reperfusion injury through necroptosis signaling pathway attenuation. *J. Cell. Physiol.* 234, 1816–1826. doi: 10.1002/jcp.27055

Oprescu, S. N., Yue, F., Qiu, J., Brito, L. F., and Kuang, S. (2020). Temporal dynamics and heterogeneity of cell populations during skeletal muscle regeneration. *iScience* 23:100993. doi: 10.1016/j.isci.2020.100993

Ramos-Cejudo, J., Johnson, A. D., Beiser, A., Seshadri, S., Salinas, J., Berger, J. S., et al. (2021). The neutrophil to lymphocyte ratio is associated with the risk of subsequent dementia in the framingham heart study. *Front. Aging Neurosci.* 13:773984. doi: 10.3389/fnagi.2021.773984

Roy, E. R., Wang, B., Wan, Y.-W., Chiu, G., Cole, A., Yin, Z., et al. (2020). Type I interferon response drives neuroinflammation and synapse loss in Alzheimer disease. *J. Clin. Invest.* 130, 1912–1930. doi: 10.1172/JCI133737

Safdar, A., and Tarnopolsky, M. A. (2018). Exosomes as mediators of the systemic adaptations to endurance exercise. *Cold Spring Harb. Perspect. Med.* 8:a029827. doi: 10.1101/cshperspect.a029827

Schmauss, D., Bigdeli, A. K., Hellmich, S., Barreiros, A. P., Kremer, T., Germann, G., et al. (2017). Long-term results of organ procurement from burn victims. *Burns* 43, 1163–1167. doi: 10.1016/j.burns.2017.05.012

Shi, C., Viccaro, K., Lee, H.-G., and Shah, K. (2016). Cdk5-Foxo3 axis: initially neuroprotective, eventually neurodegenerative in Alzheimer's disease models. *J. Cell Sci.* 129, 1815–1830. doi: 10.1242/jcs.185009

Soares Martins, T., Trindade, D., Vaz, M., Campelo, I., Almeida, M., Trigo, G., et al. (2021). Diagnostic and therapeutic potential of exosomes in Alzheimer's disease. *J. Neurochem.* 156, 162–181. doi: 10.1111/jnc.15112

Su, Y., Wu, H., Pavlosky, A., Zou, L.-L., Deng, X., Zhang, Z.-X., et al. (2016). Regulatory non-coding RNA: new instruments in the orchestration of cell death. *Cell Death Dis.* 7:e2333. doi: 10.1038/cddis.2016.210

Suo, S., Zhu, Q., Saadatpour, A., Fei, L., Guo, G., and Yuan, G.-C. (2018). Revealing the critical regulators of cell identity in the mouse cell atlas. *Cell Rep.* 25, 1436.e–1445.e. doi: 10.1016/j.celrep.2018.10.045

Tampio, J., Huttunen, J., Montaser, A., and Huttunen, K. M. (2020). Targeting of perforin inhibitor into the brain parenchyma via a prodrug approach can decrease oxidative stress and neuroinflammation and improve cell survival. *Mol. Neurobiol.* 57, 4563–4577. doi: 10.1007/s12035-020-02045-7

Tang, L., Wu, X., Liu, H., Wu, F., Song, R., Zhang, W., et al. (2021). Individualized prediction of early Alzheimer's disease based on magnetic resonance imaging radiomics, clinical, and laboratory examinations: a 60-month follow-up study. *J. Magn. Reson. Imaging* 54, 1647–1657. doi: 10.1002/jmri.27689

Tay, Y., Rinn, J., and Pandolfi, P. P. (2014). The multilayered complexity of ceRNA crosstalk and competition. *Nature* 505, 344–352. doi: 10.1038/nature12986

Timmons, J. A., Volmar, C.-H., Crossland, H., Phillips, B. E., Sood, S., Janczura, K. J., et al. (2019). Longevity-related molecular pathways are subject to midlife "switch" in humans. *Aging Cell* 18:e12970. doi: 10.1111/acel.12970

Ugwu, F. N., Yu, A. P., Sin, T. K., Tam, B. T., Lai, C. W., Wong, S. C., et al. (2017). Protective effect of unacylated ghrelin on compression-induced skeletal muscle injury mediated by SIRT1-signaling. *Front. Physiol.* 8:962. doi: 10.3389/fphys.2017.00962

Walton, R. G., Kosmac, K., Mula, J., Fry, C. S., Peck, B. D., Groshong, J. S., et al. (2019). Human skeletal muscle macrophages increase following cycle training and are associated with adaptations that may facilitate growth. *Sci. Rep.* 9:969. doi: 10.1038/s41598-018-37187-1

Wang, L., Li, P., Hou, M., Zhang, X., Cao, X., and Li, H. (2021). Construction of a risk prediction model for Alzheimer's disease in the elderly population. *BMC Neurol.* 21:271. doi: 10.1186/s12883-021-02276-8

Wang, Y., Zhao, Z.-J., Kang, X.-R., Bian, T., Shen, Z.-M., Jiang, Y., et al. (2020). lncRNA DLEU2 acts as a miR-181a sponge to regulate SEPP1 and inhibit skeletal muscle differentiation and regeneration. *Aging* 12, 24033–24056. doi: 10.18632/aging.104095

Wen-Jin, C., Xiu-Wu, P., Jian, C., Da, X., Jia-Xin, C., Wei-Jie, C., et al. (2021). Study of cellular heterogeneity and differential dynamics of autophagy in human embryonic kidney development by single-cell RNA sequencing. *Cancer Cell Int.* 21:460. doi: 10.1186/s12935-021-02154-w

Ying, C., Guo, C., Wang, Z., Chen, Y., Sun, J., Qi, X., et al. (2021). Prediction modeling based on the hospital for special surgery (HSS) knee score for poor postoperative functional prognosis of elderly patients with patellar fractures. *Biomed Res. Int.* 2021, 1–10. doi: 10.1155/2021/6620504

Yuan, J., Amin, P., and Ofengeim, D. (2019). Necroptosis and RIPK1-mediated neuroinflammation in CNS diseases. *Nat. Rev. Neurosci.* 20, 19–33. doi: 10.1038/s41583-018-0093-1

Zhang, B., Gaiteri, C., Bodea, L.-G., Wang, Z., McElwee, J., Podtelezhnikov, A. A., et al. (2013). Integrated systems approach identifies genetic nodes and networks in late-onset Alzheimer's disease. *Cell* 153, 707–720. doi: 10.1016/j.cell.2013.03.030

Zhang, T., Feng, X., Dong, J., Xu, Z., Feng, B., Haas, K. M., et al. (2022). Cardiac troponin T and autoimmunity in skeletal muscle aging. Geroscience. doi: 10.1007/s11357-022-00513-7 [Epub ahead of print].

Zhao, Z., Liu, H., Zhou, X., Fang, D., Ou, X., Ye, J., et al. (2021). Necroptosis-related lncRNAs: predicting prognosis and the distinction between the cold and hot tumors in gastric cancer. *J. Oncol.* 2021:6718443. doi: 10.1155/2021/6718443

Zhou, S.-P., Fei, S.-D., Han, H.-H., Li, J.-J., Yang, S., and Zhao, C.-Y. A. (2021). Prediction model for cognitive impairment risk in colorectal cancer after chemotherapy treatment. *Biomed Res. Int.* 2021:6666453. doi: 10.1155/2021/6666453

Conflict of Interest: The authors declare that the research was conducted in the absence of any commercial or financial relationships that could be construed as a potential conflict of interest.

The reviewer HX declared a shared parent affiliation with the authors YC, YS, ZL, JL, BQ, and SC to the handling editor at the time of review.

Publisher's Note: All claims expressed in this article are solely those of the authors and do not necessarily represent those of their affiliated organizations, or those of the publisher, the editors and the reviewers. Any product that may be evaluated in this article, or claim that may be made by its manufacturer, is not guaranteed or endorsed by the publisher.

frontiers | Frontiers in Aging Neuroscience

ORIGINAL RESEARCH
published: 10 May 2022
doi: 10.3389/fnagi.2022.887168

Identification of Immune Hub Genes Associated With Braak Stages in Alzheimer's Disease and Their Correlation of Immune Infiltration

Xiao-hang Qian[1†], Xiao-li Liu[2†], Sheng-di Chen[1] and Hui-dong Tang[1*]*

[1] Department of Neurology and Institute of Neurology, Ruijin Hospital, Shanghai Jiao Tong University School of Medicine, Shanghai, China, [2] Department of Neurology, Shanghai Fengxian District Central Hospital, Shanghai Jiao Tong University Affiliated Sixth People's Hospital South Campus, Shanghai, China

OPEN ACCESS

Edited by:
Yuzhen Xu,
Tongji University, China

Reviewed by:
Wenshi Wei,
Fudan University, China
Xinying Guo,
Guangzhou Women and Children's Medical Center, China

****Correspondence:***
Sheng-di Chen
ruijincsd@126.com
Hui-dong Tang
thd10495@rjh.com.cn

[†] These authors have contributed equally to this work

Specialty section:
This article was submitted to Alzheimer's Disease and Related Dementias, a section of the journal Frontiers in Aging Neuroscience

Received: *01 March 2022*
Accepted: *31 March 2022*
Published: *10 May 2022*

Citation:
Qian X-h, Liu X-l, Chen S-d and Tang H-d (2022) Identification of Immune Hub Genes Associated With Braak Stages in Alzheimer's Disease and Their Correlation of Immune Infiltration. Front. Aging Neurosci. 14:887168. doi: 10.3389/fnagi.2022.887168

Background: Alzheimer's disease (AD) is the most common type of neurodegenerative disease. Tau pathology is one of the pathological features of AD, and its progression is closely related to the progress of AD. Immune system dysfunction is an important mediator of Tau pathological progression, but the specific molecular mechanism is still unclear. The purpose of this study is to determine the immune hub genes and peripheral immune cell infiltration associated with the Braak stages, and the molecular mechanisms between them.

Methods: In this study, 60 samples with different Braak stages in the GSE106241 dataset were used to screen Braak stages-related immune hub genes by using the WGCNA package in R and cytoHubba plugin. The temporal lobe expression data in the Alzdata database were used to verify the results. The correlation between the expression level of immune core genes and the pathological features of AD was analyzed to evaluate the abundance of peripheral immune cell infiltration and screened Braak stages-related cells. Finally, we used correlation analysis of immune hub genes and immune cells and Gene Set Enrichment Analysis (GSEA) of them.

Results: Seven genes (GRB2, HSP90AA1, HSPA4, IGF1, KRAS, PIK3R1, and PTPN11) were identified as immune core genes after the screening of the test datasets and validation of independent data. Among them, Kirsten rat sarcoma viral oncogene homolog (KRAS) and Phosphoinositide-3-Kinase Regulatory Subunit 1 (PIK3R1) were the most closely related to Tau and Aβ pathology in AD. In addition, the ImmuneScore increased gradually with the increase of Braak stages. Five types of immune cells (plasma cells, T follicular helper cells, M2 macrophage, activated NK cells, and eosinophils) were correlated with Braak stages. KRAS and PIK3R1 were the immune core genes most related to the abnormal infiltration of peripheral immune cells. They participated in the regulation of the pathological process of AD through axon guidance, long-term potentiation, cytokine–cytokine receptor interaction, RNA polymerase, etc.

Conclusion: The KRAS and PIK3R1 genes were identified as the immune hub genes most associated with Tau pathological progress in AD. The abnormal infiltration of peripheral immune cells mediated by these cells was involved in the Tau pathological process. This provides new insights for AD.

Keywords: Alzheimer's disease, Braak stage, immune hub gene, immune cell infiltration, Tau pathology

INTRODUCTION

Alzheimer's disease (AD), the most commontype of dementia, is a progressive neurodegenerative disease that is characterized by impairment in multiple cognitive domains, executive functioning disorders, and a range of neuropsychiatric symptoms (Cummings, 2021; Seto et al., 2021). Extracellular amyloid-β (Aβ) plaques and intracellular neurofibrillary tangles are the neuropathological hallmarks of AD (Busche and Hyman, 2020; Kent et al., 2020). However, the classical amyloid cascade hypothesis cannot explain all the pathological processes of AD, and there is no significant correlation between the Aβ compliance level and the cognitive level of patients with AD (Giacobini and Gold, 2013; Roda et al., 2022). More importantly, most therapeutic strategies that target different stages of the amyloid pathway have failed to achieve expected efficacy (Long and Holtzman, 2019; Mecocci and Boccardi, 2021). Another important pathological feature of AD is neurofibrillary tangles formed by the misfolding of intracellular Tau protein. This abnormal folding of Tau protein is associated with neuronal loss and synaptic dysfunction (Malpetti et al., 2020). As the disease progresses, Tau pathology spreads in a relatively stereotypic progressive pattern. According to the distribution stage, Braak et al. proposed that Tau pathology to be divided into six different stages, which are closely related to the severity of cognitive impairment and neuronal loss of patients with AD (Chung et al., 2021; Roda et al., 2022). Therefore, exploring the pathogenesis of Tau pathologic progression may provide important targets for preventing or delaying AD progression.

Recently, the important role of immune system dysfunction in aging or neurodegenerative diseases has attracted extensive attention (Passaro et al., 2021). In the central nervous system (CNS), microglia are the most important innate immune cells. They originate from myeloid progenitors in the yolk sac and play a physiological role in the clearance of abnormal aggregates, signal transduction, maintenance of homeostasis, and synaptic plasticity (Cisbani and Rivest, 2021). In AD, microglia can be activated by misfolded proteins and participate in a series of pathological processes, such as neuroinflammatory initiation, Aβ aggregation, and neuron loss (Ennerfelt and Lukens, 2020; Qian et al., 2021). Recent studies on patients with AD and animal models have proved that microglia are important vectors in the transmission of Tau pathology (Hopp et al., 2018; Pascoal et al., 2021). What's more, the interaction between the peripheral immune system and the CNS also exists in AD (Passaro et al., 2021). In a healthy state, peripheral immune cells are restricted to enter the CNS by the presence of structures, such as blood-brain barrier (Greenhalgh et al., 2020). When the barrier permeability increases due to aging, trauma, infection, neurodegeneration, etc., peripheral immune cells, such as monocytes, macrophages, neutrophils, and T cells can infiltrate into the brain and affect glial and neuronal function (Greenhalgh et al., 2020). In the brain of patients with AD, extravascular T cells were detected, specifically in the hippocampus, and the abundance of T cells was correlated with tau pathology without Aβ pathology (Merlini et al., 2018). Another study confirmed that T cells infiltration abundance in the brain of patients with AD was positively correlated with *p*-Tau levels (Zotova et al., 2013). These data strongly suggest a close relationship between immune system dysfunction and AD-associated Tau pathological process. However, understanding the molecular biological mechanism of immune system-driven abnormal Tau propagation accelerates AD progression remains unclear.

In this study, we used weighted gene co-expression network analysis to identify immune hub genes closely associated with Braak stages in AD and then validated by using independent datasets. In addition, we analyzed the abundance of peripheral immune cell infiltration in the brain associated with Braak stages in AD through the CIBERSORT algorithm. Finally, the correlation between immune hub genes and the abundance of peripheral immune cell infiltration was analyzed. This study will provide an important basis for exploring the cellular and molecular mechanisms related to the Tau pathological process of AD from the perspective of immunology.

MATERIALS AND METHODS

Data Collection and Processing

The GSE106241 data file was downloaded from the NCBI Gene Expression Omnibus public database (GEO, https://www.ncbi.nlm.nih.gov/geo/) annotated by GPL24170 as a Series Matrix File. The dataset included data on gene expression profiles from 60 human temporal cortical tissue samples with varying degrees of AD-related neurofibrillary pathology. The AD pathological features, such as Braak stages, α, β, and γ—secretase activity, and $A\beta_{1-42}$ levels of each sample were downloaded from the GEO database to perform Pearson's correlation analysis with Braak stages-related immune hub genes (https://ncbi.nlm.nih.gov/geo/geo2r/?acc=GSE106241). The AlzData database was a full collection of current high-throughput omics databases, such as genomics (GWAS and Whole Exome Sequencing), Proteomics, Functional genomics, and Transcriptomes data (Xu et al., 2018). In this study, we selected transcriptome expression data of temporal cortical from AlzData as a validation dataset, including 39 healthy controls and 52 patients with AD. In addition, the expression level of the Braak stages-related immune

hub gene at the single-cell level in the brain was analyzed and visualized through the AlzData database.

Construction of WGCNA

Based on the genetic and clinical data in GSE106241, a weighted messenger RNA (mRNA) co-expression network was constructed using the WGCNA package in R. First of all, we used the gene expression spectrum to calculate the Median Absolute Deviation (MAD) of each gene, and removed the first 50% of the smallest MAD genes. Then, we used the goodSamplesGenes method of R software package WGCNA to remove outlier genes and samples. WGCNA was further used to build a scale-free co-expression network. After the acquisition of an appropriate power ($\beta = 6$), the adjacency matrix was transformed into the topological overlap matrix (TOM). Third, hierarchical clustering was performed to identify modules, and the eigengene was calculated. Finally, we calculated the correlation between Braak stages and each module through Pearson's correlation analysis.

Gene Ontology Functional, Kyoto Encyclopedia of Genes and Genomes Pathway Enrichment, and Protein-Protein Interaction Network Analysis

Functional enrichment was analyzed through the STRING online tool to investigate GO cellular components (CC), biological process (BP), molecular function (MF), and Kyoto Encyclopedia of Genes and Genomes (KEGG) pathways related to potential immune-related pathogenesis of Braak stages in AD. The interaction score was 0.4. The false discovery rate (FDR) was < 0.05. The protein-protein interaction (PPI) network was constructed through the NetworkAnalyst based on the STRING interactome with a 900 confidence score (https://www.networkanalyst.ca/) (Xia et al., 2015).

Immune-Related Hub Genes Selection and Validation

Then, the total of 2,483 immune-related genes list was download from the Immunology Database and Analysis Portal (ImmPort) (https://www.immport.org/home) to screen out the DEIRGs (Bhattacharya et al., 2014). The cytoHubba plugin was adopted to screen out immune-related hub genes through three different algorithms [Edge Percolated Component (EPC), Maximum Neighborhood Component (MNC), and Degree]. In total, 91 temporal lobe transcriptomic data (39 healthy controls and 52 patients with AD) from the AlzData database were used as a validation dataset to analyze the difference in immune hub genes between the AD and HC groups.

Immune Cell Infiltration Abundance Analysis

In this study, CIBERSORT was used to assess the abundance of 22 types of immune cells in 60 samples with different Braak stages. CIBERSORT is an analytical algorithm that uses normalized gene expression profiles to assess the abundance of specific cells in complex tissues (Newman et al., 2015). After evaluating the abundance of 22 types of immune cells in each sample, we performed differential analysis and correlation analysis according to the Braak stages of the samples.

Gene Set Enrichment Analysis

The Gene Set Enrichment Analysis (GSEA) was used to identify the different signal pathways between the high and low levels of immune hub genes in GSE106251. The annotated gene set c2.cp.kegg.v7.1.symbols.gmt was chosen as the reference gene list. The cut-off value for the GSEA was set as $p < 0.05$.

Statistical Analysis

Statistical analysis and graphs were performed using Sangerbox online software (http://sangerbox.com/) and GraphPad Prism 5.0 software. A value of p less than 0.05 was considered statistically significant. Multiple testing corrections were made using the Bonferroni correction and Duncan's multiple range test.

RESULTS

WGCNA Was Established to Screen Genes Associated With Braak Stages

The WGCNA method was used to identify genes associated with Braak stages. First of all, we screened the top 50% highest variance of the expression profile (a total of 9,386 genes) from 60 samples for WGCNA analysis. Then, the scale-free network was constructed with a β value equal to 6 ($R^2 = 0.74$) (**Figures 1A,B**). Finally, a total of 14 co-expression modules were identified (**Figure 1C**). The connectivity was calculated and cluster analysis was performed among the 14 modules (**Figure 1D**). To further analyze the association between the models and phenotype, we calculated the correlation coefficients of each model with Braak stages. The results showed that the blue module ($r = -0.32$, $p = 0.01$) was the most negatively and the dark gray module ($r = 0.31$, $p = 0.02$) was the most positively associated with the Braak stage (**Figures 1E–G**). In total, 5,374 genes from these two modules were selected for the next analysis.

Enrichment Analysis of Braak Stages-Related Immune Gene in AD and PPI Network Analysis

We intersected the above Braak stages-related immune genes screened by WGCNA with immune gene in the ImmPort database to screen out Braak stages-related immune genes. Among them, there were 260 Braak stages-related immune genes (**Figure 2A** and **Supplementary Table 1**). The enrichment analysis of GO cellular components revealed that these genes were mainly located at the extracellular region, cell surface, proteasome complex, MHC protein complex, etc. (**Figure 2B**). The biological processes of each of them were associated with signal transduction, cytokine-mediated signaling pathway, response to cytokine, cellular response to cytokine stimulus, etc. (**Figure 2C**). The enrichment analysis of GO molecular function showed that Braak stage-related immune

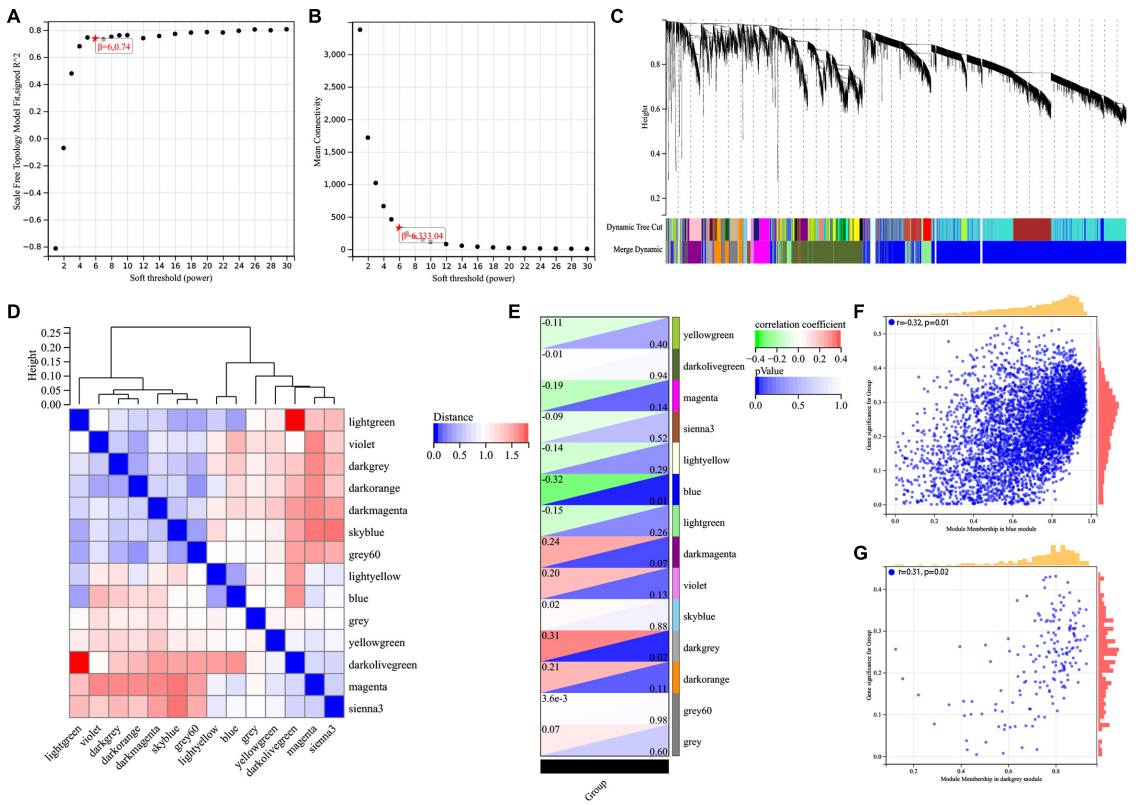

FIGURE 1 | Screening for BRAAK staging related genes by WGCNA. **(A)** Analysis of the scale-free index for various soft-threshold powers (β). **(B)** Analysis of the mean connectivity for various soft-threshold powers. **(C)** Recognition module, each module was given an individual color as identifier, such as 14 different modules. **(D)** Co-expression similarity of entire modules based on the hierarchical clustering of module eigengenes and the correlation between different modules, red indicates high adjacency (positive correlation) and blue low adjacency (negative correlation). **(E)** In the correlation heat map of gene modules and phenotypes, red is positively correlated with the phenotype; green is negatively correlated with the phenotype. **(F,G)** Scatter plots for correlations between gene significance and module membership in blue and darkgrey module.

genes were involved in signaling receptor binding, growth factor activity, cytokine activity, peptide antigen binding, etc. (**Figure 2D**). The KEGG enrichment analysis revealed that these genes were involved in AD, antigen processing and presentation, natural killer cell-mediated cytotoxicity, B-cell receptor signaling pathway, etc. (**Figure 2E**). The PPI network of the 260 Braak stages-related immune genes was constructed (**Figures 2F,G**). These results strongly suggest the role of immune-related genes in the pathological progression of Braak stages in AD.

Screening of Braak Stages-Related and Validation in Database

The cytoHubba plugin was adopted to screen out Braak stages-related immune hub genes through three different algorithms (EPC, MNC, and Degree). The top 15 hub genes, filtered by the EPC algorithm, were CD86, HSPA4, FOS, GRB2, PTPN11, Kirsten rat sarcoma viral oncogene homolog (KRAS), PTPRC, CXCL12, TLR2, Phosphoinositide-3-Kinase Regulatory Subunit 1 (PIK3R1), IGF1, JUN, HSP90AA1, STAT3, and SOCS3 (**Figure 3A**). The DEGREE screened out TLR2, FOS, GRB2, HSPA8, IGF1, PTPRC, STAT3, HSP90AA1, JUN, CD86, PIK3R1, PTPN11, KRAS, HSPA4, and SOD1 (**Figure 3B**). TLR2, FOS, GRB2, HSPA8, IGF1, PTPRC, STAT3, HSP90AA1, JUN, CD86, PIK3R1, PTPN11, KRAS, HSPA4, and SOD1were found out by the MNC (**Figure 3C**). Finally, the co-existing gene of the three algorithms was selected as the hub gene, such as CD86, HSPA4, FOS, GRB2, KRAS, PTPN11, PTPRC, TLR2, PIK3R1, IGF1, JUN, HSP90AA1, and STAT3 (**Figure 3D**). After that, we then validated these Braak stages-related immune hub genes by using the temporal lobe transcriptome data of 39 healthy controls and 52 patients with AD from the Alzdata database. The results showed that the expression levels of GRB2, HSP90AA1, HSPA4, IGF1, KARS, PIK3R1, and PTPN11 were significantly decreased in the AD group compared with the HC group (**Figures 3G–J,L–N**), and the expression levels of CD86, FOS, JUN, PTPRC, STAT3, and TLR2 were not statistically different between the AD and HC groups (**Figures 3E,F,K,O–Q**).

Correlation Analysis of Braak Stages-Related Immune Hub Genes With Pathological Features of AD

We further analyzed the correlation between Braak stages-related immune core genes and AD pathological features, such as Braak stages, α, β, γ-secretase activity, and $A\beta_{1-42}$ levels.

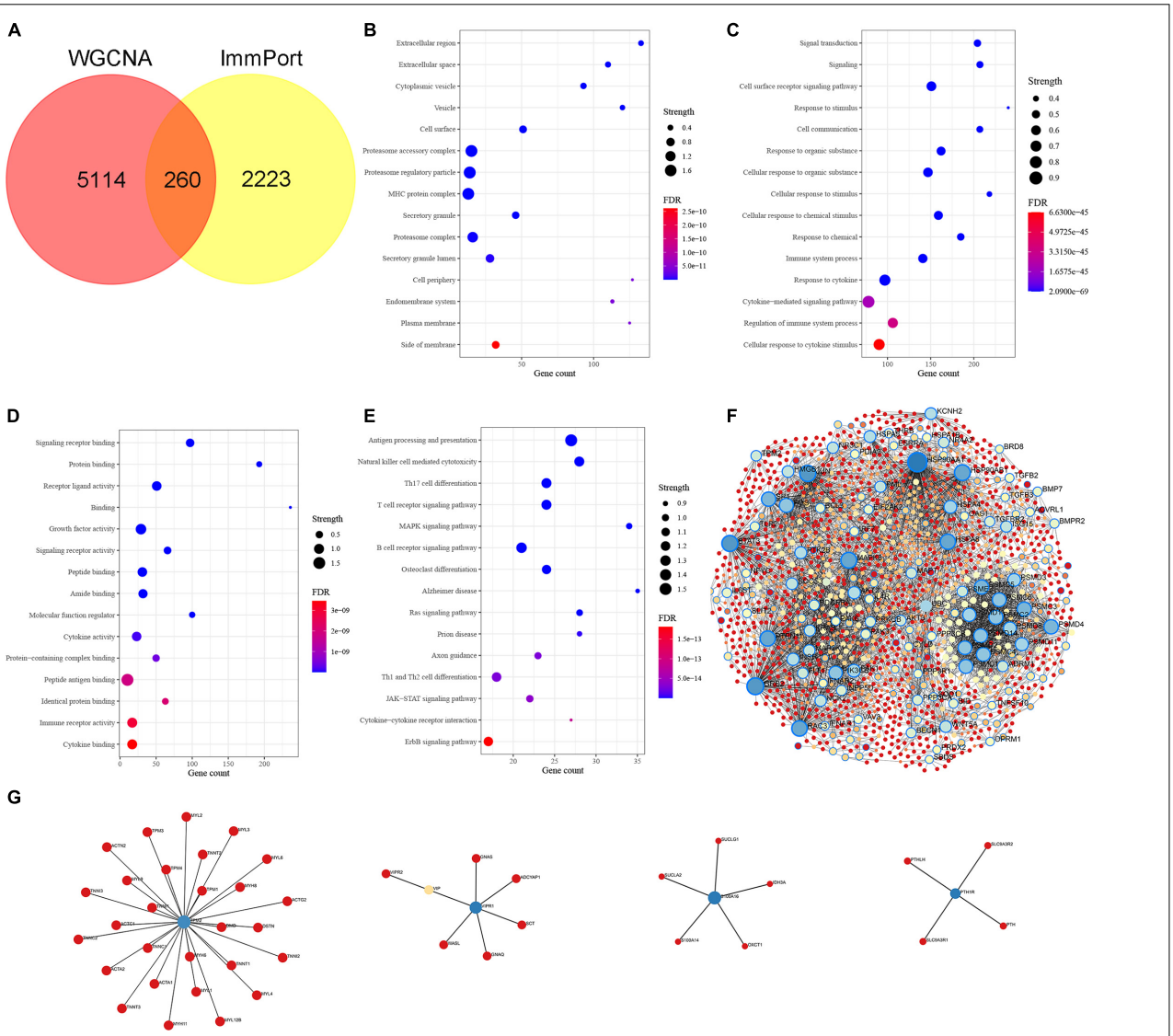

FIGURE 2 | Identification of Braak stages associated immune genes and enrichment analysis of Gene Ontology (GO) and Kyoto Encyclopedia of Genes and Genomes (KEGG). **(A)** The Venn diagram shows the common Braak stages associated immune genes between the Braak stages associated genes and the ImmPort dataset. **(B–D)** GO biological function enrichment analysis. **(E)** KEGG pathway enrichment analysis. **(F,G)** Protein-protein interaction (PPI) network of Braak stages associated immune genes. FDR, false discovery rate.

The expression levels of GRB2 ($r = -0.321$, $p = 0.002$), HSP90AA1 ($r = -0.359$, $p < 0.001$), IGF1 ($r = -0.191$, $p = 0.07$), KRAS ($r = -0.344$, $p < 0.001$), PIK3R1 ($r = -0.467$, $p < 0.001$), and PTPN11 ($r = -0.291$, $p = 0.005$) were negatively correlated with the grade of Braak stages (**Figures 4A–G**). The expression level of STAT3 was positively correlated with Braak stages ($r = 0.264$, $p = 0.012$) (**Figure 4H**). In amyloidogenic APP processing, we found that the γ-secretase activity was negatively correlated with the expression level of KARS ($r = -0.40$, $p = 0.002$) and PIK3R1 ($r = -0.35$, $p = 0.009$). The β-secretase activity was negatively correlated with the expression level of GRB2 ($r = -0.36$, $p = 0.006$), KRAS ($r = -0.63$, $p < 0.001$), PIK3R1 ($r = -0.49$, $p < 0.001$), and was positively correlated with PTPN11 expression level ($r = 0.44$, $p < 0.001$). In addition, the $A\beta_{1-42}$ levels were negatively correlated with KRAS ($r = -0.29$, $p = 0.029$) and PIK3R1 ($r = -0.31$, $p = 0.019$). However, the expression level of KRAS ($r = -0.34$, $p = 0.011$) was negatively correlated with the α-secretase activity in non-amyloidogenic APP processing (**Figure 4I**). Accordingly, we found that KRAS and PIK3R1 were not only involved in the Tau pathologically related Braak stages, but also closely related to the regulation of Aβ pathology.

Abundance of Immune Cell Infiltration in Patients With AD With Different Braak Stages

Subsequently, we estimated the abundance of 22 kinds of immune cell infiltration in the GSE106241 samples by CIBERSORT

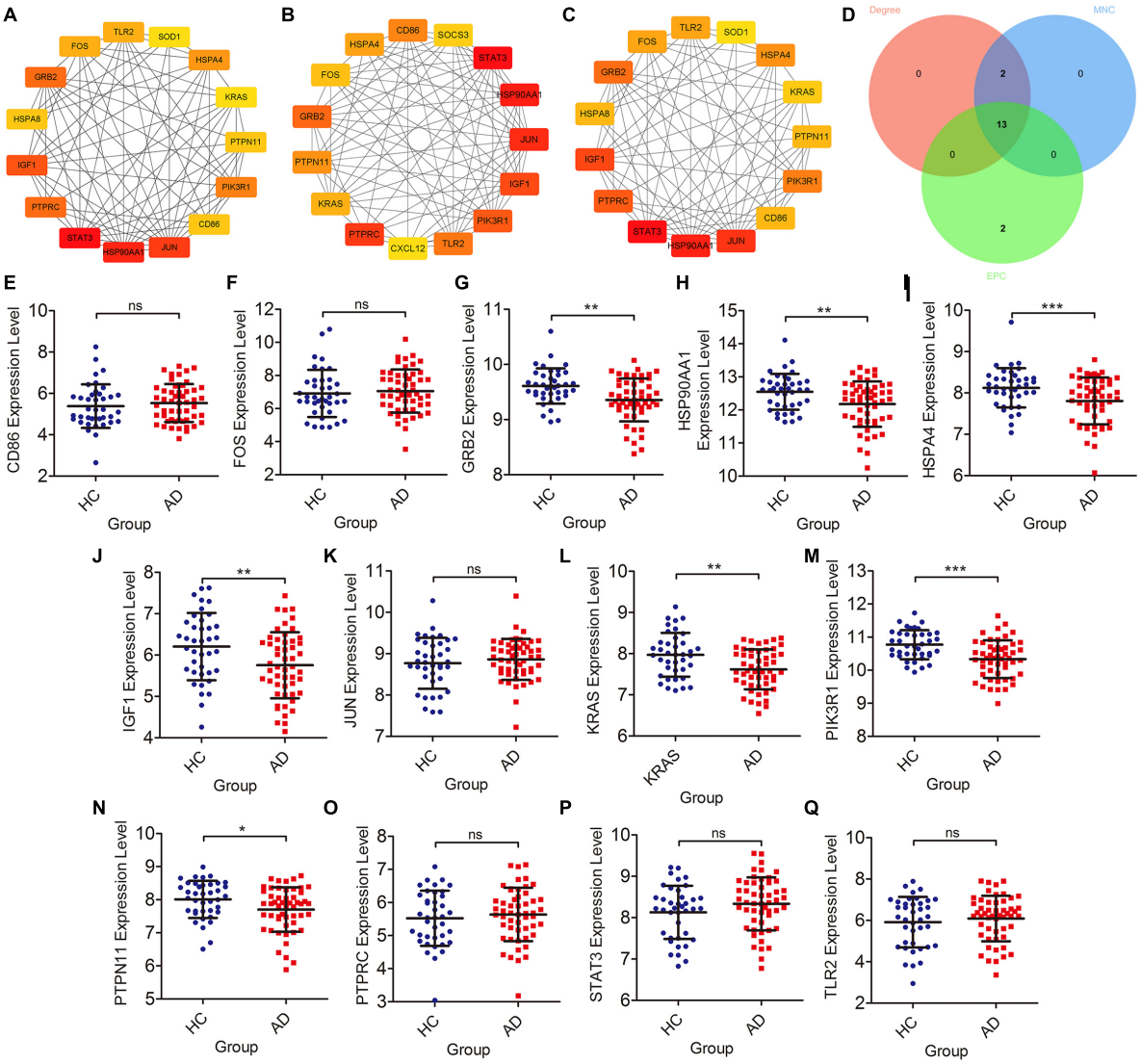

FIGURE 3 | Screening of immune hub genes and database validation of their expression levels. **(A–C)** The top 15 immune hub genes identified by MNC, EPC, and Degree algorithms in cytoHubba plugin. **(D)** Venn diagram showing the intersection of immune hub genes obtained by the three algorithms. **(E–Q)** The different expression levels of immune hub genes in the temporal cortex between the AD and HC groups were validated in the Alzdata database. *$p < 0.05$, **$p < 0.01$, ***$p < 0.001$, and ns, no sense.

to explore the role of the peripheral immune system in the progression of Braak stages in AD. We found that the ImmuneScore, which represents the total level of immune cells infiltration, increased with the increase of Braak stages (**Figures 5B,C**). In immune cell subtype analysis, four kinds of immune cells were significantly different in different Braak stages (**Figure 5A**). Among them, the Braak stages were negatively correlated with the abundance of follicular helper T cells ($r = -0.337$, $p = 0.008$), activated NK cells ($r = -0.226$, $p = 0.082$), and eosinophils ($r = -0.348$, $p = 0.008$) (**Figures 5E,G,H**). The abundance of M2 macrophages was positively correlated with Braak stages (**Figure 5F**). In addition, the abundance of plasma cells was negatively correlated with Braak stages (**Figure 5D**). Therefore, we speculated that peripheral immune cells play an important role in the pathological process of AD.

Correlation Analysis of Braak Stages-Related Immune Hub Genes and Immune Cells

To explore whether these two core genes were involved in regulating abnormal infiltration of peripheral immune cells, we conducted a correlation analysis between immune hub genes and differentially infiltrated immune cells (**Figures 6A,B**). The ImmuneScore was negatively correlated with GRB2 ($r = -0.31$, $p = 0.014$), HSP90AA1 ($r = -0.44$, $p < 0.001$), HSPA4 ($r = -0.36$, $p = 0.005$), KRAS ($r = -0.66$, $p < 0.001$), and PIK3R1 ($r = -0.73$,

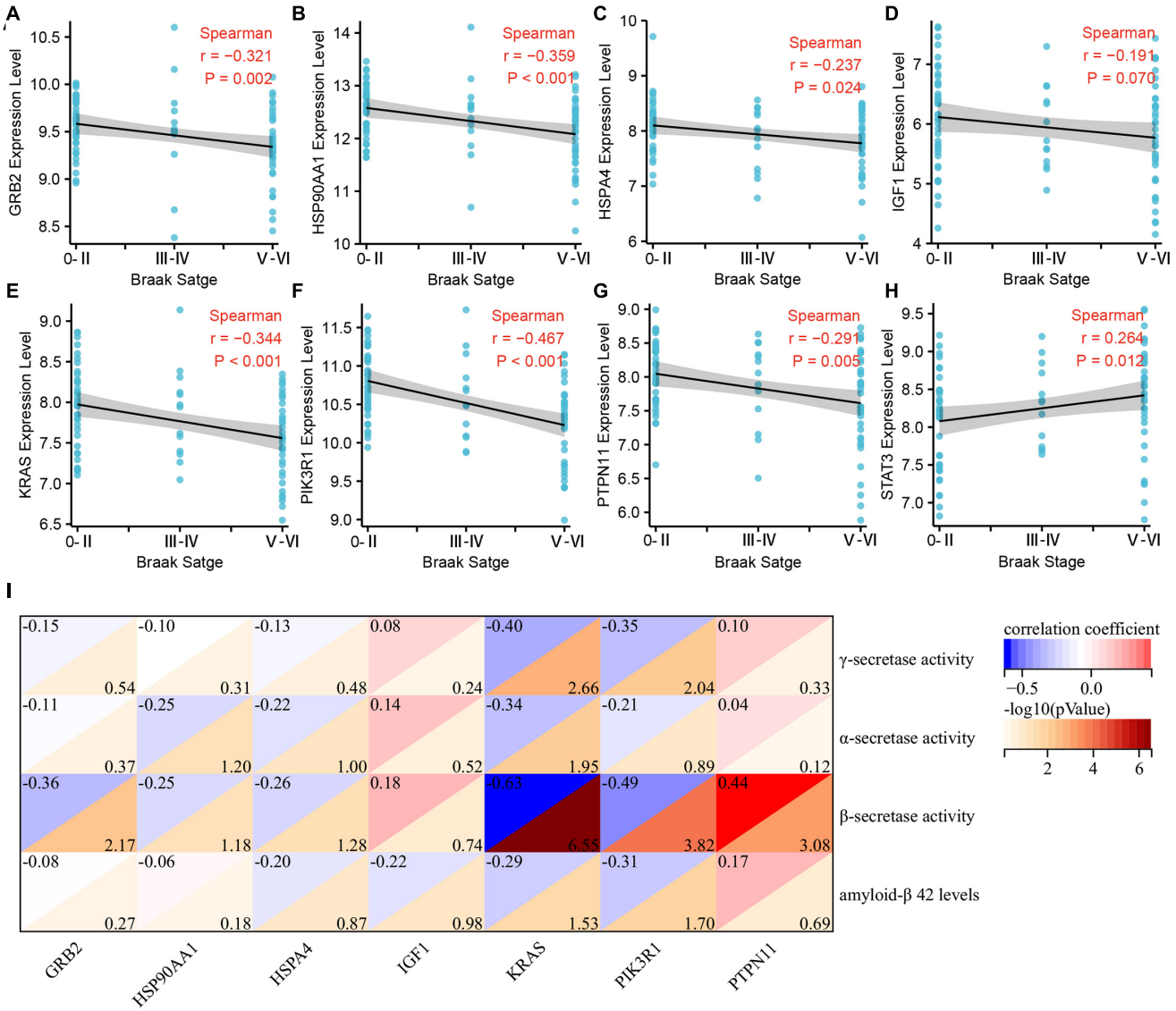

FIGURE 4 | Correlation analysis of Braak stages-related immune hub genes with pathological features of Alzheimer's disease (AD). **(A–H)** Correlation analysis between the expression level of immune hub genes and Braak stages. **(I)** Correlation analysis between the expression level of immune hub genes and α, β, γ-secretase activity, and $A\beta_{1-42}$.

$p < 0.001$) expression level, and was positively correlated with the PTPN11 ($r = 0.29$, $p = 0.025$). The abundance of plasma cells was positively correlated with GRB2 ($r = 0.43$, $p < 0.001$), HSP90AA1 ($r = 0.45$, $p < 0.001$), HSPA4 ($r = 0.32$, $p = 0.013$), KRAS ($r = 0.54$, $p < 0.001$), and PIK3R1 ($r = 45$, $p < 0.001$) expression levels. The abundance of follicular helper T cells was positively correlated with GRB2 ($r = 0.32$, $p = 0.011$), HSP90AA1 ($r = 0.27$, $p = 0.034$), KRAS ($r = 0.37$, $p = 0.004$), and PIK3R1 ($r = 43$, $p < 0.001$) expression levels. The abundance of activated NK cells was positively correlated with KRAS ($r = 0.34$, $p = 0.008$) and PIK3R1 ($r = 0.43$, $p = 0.002$). The abundance of M2 macrophage was negatively correlated with HSPA4 ($r = -0.27$, $p = 0.038$), KRAS ($r = -0.26$, $p = 0.045$), and PIK3R1 ($r = -0.45$, $p < 0.001$). Among them, we found that KRAS and PI3KR1 were the two most important hub genes in Braak stages-related immune regulation (**Figure 6B**).

Single Cell Expression Level Detection and GSEA for Braak Stages Related Immune Hub Gene

To explore the function of Braak stages-related immune hub genes, we analyzed the expression level at the single-cell level of brain tissue. The results showed that the expression level of KRAS was the highest in neurons, but was limited in the other five cell types (endothelial, astrocytes, microglia, oligodendrocytes, and oligodendrocyte precursor cell) (**Supplementary Figure 1A**). The expression level of PIK3R1 was relatively high in six

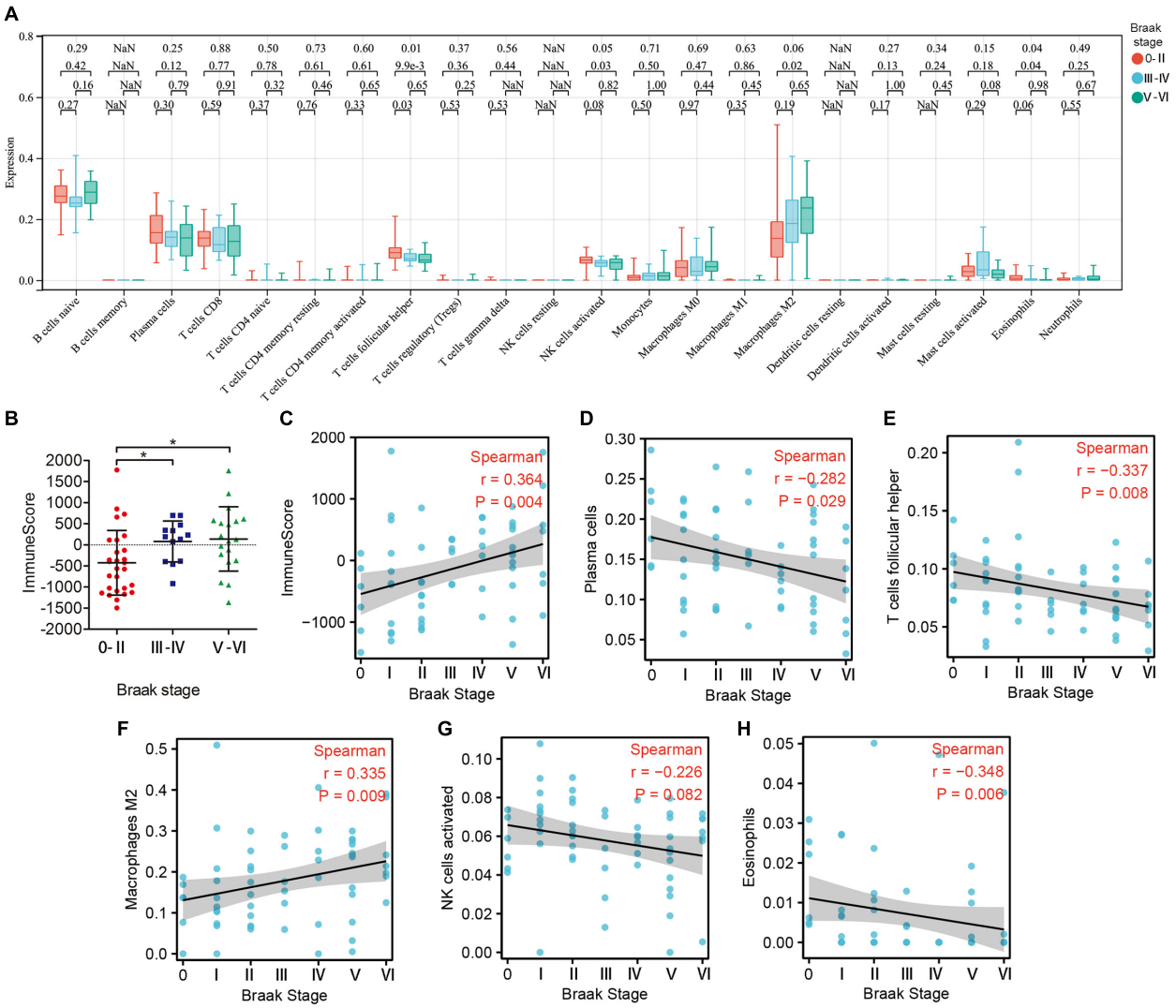

FIGURE 5 | The landscape of immune cell infiltration in different Braak stages. **(A)** The box plot shows the difference of 24 immune cell proportions between different Braak stages. Red color represents Braak 0-II, blue color represents Braak III-IV, and green color represents Braak V-VI. The values of *p* between each group were shown at the top of the panel **(A)**. **(B)** Differences in ImmuneScores between Braak stages. **(C–H)** Correlation analysis between differential immune cell abundance and Braak stages.

kinds of cells, among which the expression level was highest in neurons and astrocytes (**Supplementary Figure 1B**). After that, we explored the potential molecular mechanisms of KRAS and PI3KR1 associated with Braak stages in AD through GSEA. The results showed that axon guidance, long-term potentiation, inositol phosphate metabolism, and GnRH signaling pathway were significantly enriched in groups with high KRAS expression (**Figure 7A**). In addition, the high expression of PI3KR1 is involved in AD and Ubiquitin mediated proteolysis (**Figure 7B**). The PI3KR1 low expression group was related to cytokine–cytokine receptor interaction and RNA polymerase (**Figure 7B**). These results suggested that both KRAS and PI3KR1 were involved in the pathway of AD-related pathological mechanisms.

DISCUSSION

Alzheimer's disease, the most common form of dementia, currently has limited therapeutic options. Aβ and Tau are two typical pathological features of AD. Most previous studies on therapeutic strategies for AD have focused on the amyloid pathway. But almost all these studies ended in failure. In addition, the Tau pathological degree is closely related to the cognitive impairment level of patients with AD, while Aβ pathology cannot reflect the severity of patients with AD (Chung et al., 2021; Roda et al., 2022). In recent years, the role of the immune system in regulating the progress of AD was the latest hotspot. Pascoal et al. (2021) first confirmed the role of activated microglia in the spatial transmission of Tau

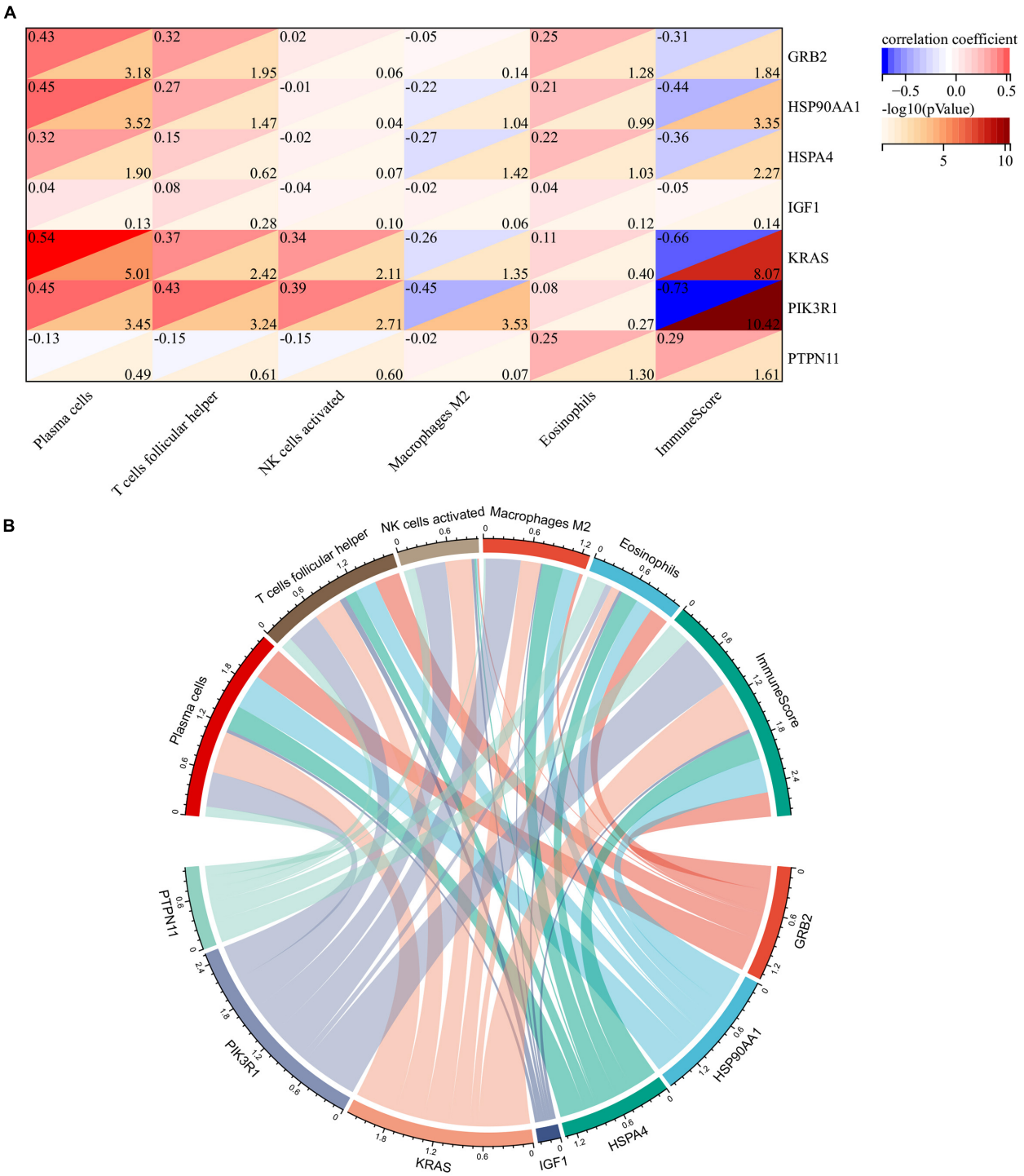

FIGURE 6 | Correlation analysis of immune hub genes with different infiltrating immune cells. **(A)** Heatmap of correlation between immune hub genes and different infiltrating immune cells. **(B)** Network diagram of interactions between immune hub genes and different infiltrating immune cells. The larger the circle represents the greater interaction with other.

protein in the brain of patients with AD by positron emission tomography (PET). However, it is not only the central innate immune cells but also the peripheral immune system that are critical for the maintenance of the CNS homeostasis and the progress of AD (Jevtic et al., 2017; Castellani and Schwartz, 2020). Therefore, exploring the molecular mechanism of immune

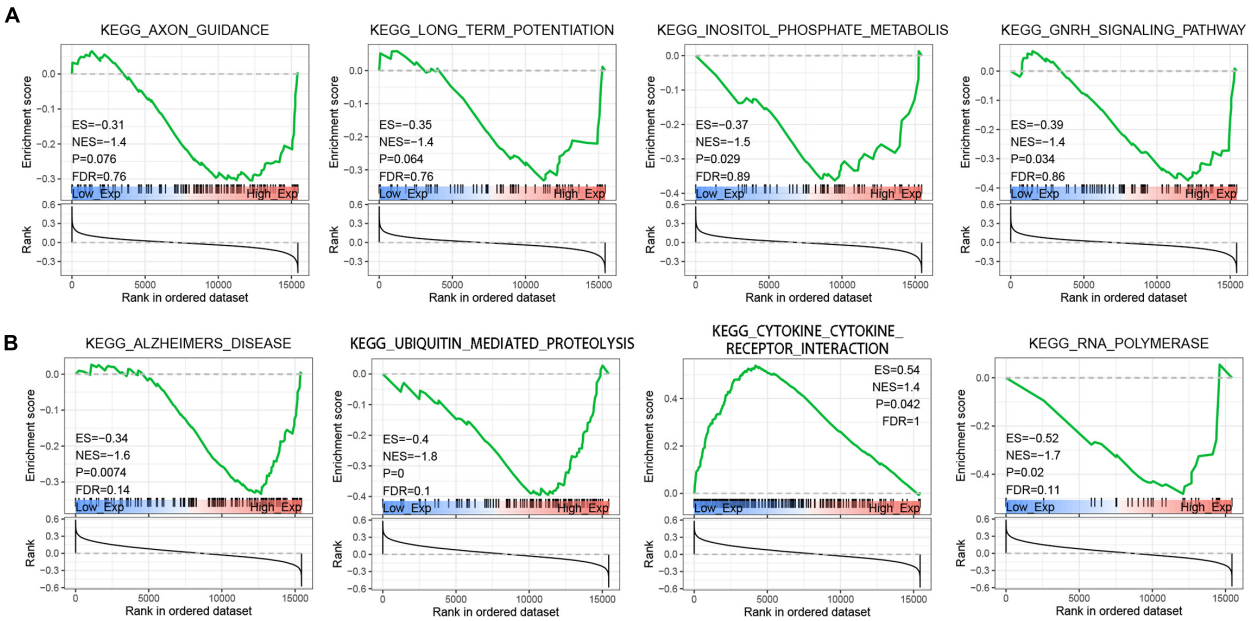

FIGURE 7 | Gene Set Enrichment Analysis (GSEA) screened the potential molecular mechanism of immune core genes. **(A)** GSEA of Kirsten rat sarcoma viral oncogene homolog (KRAS). **(B)** GSEA of Phosphoinositide-3-Kinase Regulatory Subunit 1 (PIK3R1). ES, Enrichment Score; NES, Normalized Enrichment Score; and FDR, false discovery rate.

system progression in Tau pathology in patients with AD will provide new strategies for treatment.

In the present study, we identified thirteen immune hub genes (CD86, HSPA4, FOS, GRB2, KRAS, PTPN11, PTPRC, TLR2, PIK3R1, IGF1, JUN, HSP90AA1, and STAT3) associated with Braak stages in AD through WGCNA and the cytoHubba plugin. After verifying the expression level in independent datasets and correlation analysis of AD pathological features, KRAS and PI3KR1b were finally identified as the most reliable Braak stages-associated immune hub genes. KRAS was the most common oncogene. The mutations of the KRAS gene can accelerate and maintain tumorigenesis (Mustachio et al., 2021). However, its role in neurodegenerative diseases has been limited. In our results, the expression level of KRAS was significantly decreased in patients with AD, and was negatively correlated with Braak stages and Aβ pathology. In APP/PS1 mice, the expression level of Kras was also decreased (Xiao et al., 2021). The GSEA showed that the axon guidance and long-term potentiation were enriched in the high expression level of KRAS. This was consistent with the result that KRAS was highly expressed in neurons. A previous study reported that KRAS was selected as putative neuronal cell cycle re-entry related factor in AD (Yuen et al., 2022). In BV-2 cells, Aβ can induce cell apoptosis by decreasing KRAS expression levels (Xiao et al., 2021). These results suggested the function of KRAS in regulating the cell cycle and promoting cell proliferation in the brain. However, there was no significant correlation between the immune signaling pathway and KRAS in GSEA analysis, which may be related to the dataset selected in this study. PIK3R1 was a member of the class IA in the PI3K family, which took part in the regulation of cell proliferation, differentiation, survival, etc. (Huang et al., 2020). Genome-wide network analysis has reported that the PIK3R1 was associated with Aβ production in AD (Cong et al., 2017). Moreover, the PIK3R1 polymorphism (Met326Ile) was closely associated with the genetic susceptibility of female patients with AD patients, which may be related to interference with insulin signals in the brains of patients with AD (Liolitsa et al., 2002). In this study, we identified PIK3R1 as a BRAAK stage-associated immune hub gene. Its expression level was decreased in patients with AD and negatively correlated with BRAAK stage and Aβ pathology. In the brain, PIK3R1 was widely expressed, such as endothelial, astrocyte, microglia, oligodendrocyte, OPC, and neuron. The GSEA showed that AD, ubiquitin-mediated proteolysis, and RNA polymerase were enriched in the high PIK3R1 expression level AD group. In addition, our result showed that PIK3R1was involved in the regulation of immunity through cytokine–cytokine receptor interaction. More importantly, previous studies have reported that heterozygous mutation in PIK3R1 lead to activated phosphoinositide 3-kinase delta syndrome (APDS), which is a primary immunodeficiency and immune dysregulation (Nunes-Santos et al., 2019). It is speculated that the low expression level of PIK3R1 in AD may affect the function of immune cells, such as microglia. However, the specific mechanisms of KRAS and PIK3R1 in AD need to be further verified *in vivo* or *in vitro*.

However, due to the limitations of previous research techniques, it is difficult to conduct a relative quantitative analysis of peripheral immune cells in the CNS of AD and further study their mechanism of action. In this study, the CIBERSORT was used to evaluate the relative abundance of

immune cell infiltration associated with Braak stages in patients with AD. Our results showed that the ImmuneScore increased with Braak stages, which suggested the chronic activation of the immune system in patients with AD. Among the 22 immune cell subtypes, we found that five types of immune cell abundance were associated with Braak stages, such as plasma cells, T follicular helper cells, M2 macrophage, activated NK cells, and eosinophils. T follicular helper cells and plasma cells were adaptive immune cells. Previous studies have shown that T follicular helper cells can assist B cells to perform effector humoral immunity (Gowthaman et al., 2021). This may explain the reduced consistency of T follicular helper cells and plasma cells with high Braak stages group in our results. In addition, the abundance of activated NK cells was also decreased in the high Braak stages group. In the 5XFAD model, the absence of B cells, T cells, and NK cells can accelerate the disease progression (Marsh et al., 2016). As for eosinophils, our results confirmed that eosinophil abundance was inversely associated with the Braak stage. Järemo et al. (2013) reported a reduction in the number of eosinophils in the peripheral blood of patients with AD, which was consistent with our results in the brain. A recent study reported that the eosinophils have a protective effect on maintaining normal physiological function and immune homeostasis in old age reported recently (Brigger et al., 2020). However, our study only analyzed the correlation between these different peripheral immune cells and the pathological characteristics of AD, and the specific role and potential mechanism of each immune cell in AD need further study. Furthermore, we found that KRAS and PIK3R1 were the genes most closely associated with peripheral immune cell infiltration. KRAS and PIK3R1 were negatively correlated with ImmuneScore and M2- macrophage abundance but positively correlated with plasma cells, T follicular helper cells, activated NK cells, and eosinophils. However, in this study, we did not detect the expression levels of KRAS and PIK3R1 in peripheral immune cells in the brain. This may be related to the low abundance of peripheral infiltrating immune cells in the brain. Further studies are needed to explore the molecular mechanisms by which they regulate immune cells in AD.

In summary, we identified KRAS and PIK3R1 as Braak stages-associated immune hub genes in AD. They were also correlated with Aβ pathology. In addition, this study indicated that the abundance of plasma cells, T follicular helper cells, M2 macrophage, activated NK cells, and eosinophils were related to the progression of Braak stages in AD. Besides, KRAS and PIK3R1 were negatively correlated with ImmuneScore and M2-macrophage abundance but positively correlated with plasma cells, T follicular helper cells, activated NK cells, and eosinophils. Further exploration of Braak stages-related immune genes and the role of differential infiltrating immune cells in the progression of AD will provide new targets for the pathogenesis and treatment of AD.

DATA AVAILABILITY STATEMENT

Publicly available datasets were analyzed in this study. This data can be found here: https://ncbi.nlm.nih.gov/geo/query/acc.cgi?acc=GSE106241.

AUTHOR CONTRIBUTIONS

H-DT and S-DC designed the study and prepared the manuscript. X-HQ and X-LL developed the methodology and analyzed the data. All authors discussed the results and approved the manuscript.

FUNDING

This work was supported by the National Natural Science Foundation of China (Grant No. 81971014) and the Shanghai Municipal Commission of Health and Family Planning (20184Y0056).

ACKNOWLEDGMENTS

We sincerely appreciated the high-quality data provided by the GEO database.

SUPPLEMENTARY MATERIAL

The Supplementary Material for this article can be found online at: https://www.frontiersin.org/articles/10.3389/fnagi.2022.887168/full#supplementary-material

Supplementary Figure 1 | Single-cell expression level of Kirsten rat sarcoma viral oncogene homolog (KRAS) and Phosphoinositide-3-Kinase Regulatory Subunit 1 (PIK3R1) in the healthy brain. **(A,B)** KRAS and PIK3R1 expression level in endothelial, astrocytes, microglia, oligodendrocytes, oligodendrocyte precursor cell (OPC), and neuron.

REFERENCES

Bhattacharya, S., Andorf, S., Gomes, L., Dunn, P., Schaefer, H., Pontius, J., et al. (2014). ImmPort: disseminating data to the public for the future of immunology. *Immunol. Res.* 58, 234–239. doi: 10.1007/s12026-014-8516-1

Brigger, D., Riether, C., van Brummelen, R., Mosher, K. I., Shiu, A., Ding, Z., et al. (2020). Eosinophils regulate adipose tissue inflammation and sustain physical and immunological fitness in old age. *Nat. Metab.* 2, 688–702. doi: 10.1038/s42255-020-0228-3

Busche, M. A., and Hyman, B. T. (2020). Synergy between amyloid-β and tau in Alzheimer's disease. *Nat. Neurosci.* 23, 1183–1193. doi: 10.1038/s41593-020-0687-6

Castellani, G., and Schwartz, M. (2020). Immunological features of non-neuronal brain cells: implications for Alzheimer's disease immunotherapy. *Trends Immunol.* 41, 794–804. doi: 10.1016/j.it.2020.07.005

Chung, D. C., Roemer, S., Petrucelli, L., and Dickson, D. W. (2021). Cellular and pathological heterogeneity of primary tauopathies. *Mol. Neurodegener.* 16:57. doi: 10.1186/s13024-021-00476-x

Cisbani, G., and Rivest, S. (2021). Targeting innate immunity to protect and cure Alzheimer's disease: opportunities and pitfalls. *Mol. Psychiatry* 26, 5504–5515. doi: 10.1038/s41380-021-01083-4

Cong, W., Meng, X., Li, J., Zhang, Q., Chen, F., Liu, W., et al. (2017). Genome-wide network-based pathway analysis of CSF t-tau/Aβ1-42 ratio in the ADNI cohort. *BMC Genomics* 18:421. doi: 10.1186/s12864-017-3798-z

Cummings, J. (2021). New approaches to symptomatic treatments for Alzheimer's disease. *Mol. Neurodegener.* 16:2. doi: 10.1186/s13024-021-00424-9

Ennerfelt, H. E., and Lukens, J. R. (2020). The role of innate immunity in Alzheimer's disease. *Immunol. Rev.* 297, 225–246. doi: 10.1111/imr.12896

Giacobini, E., and Gold, G. (2013). Alzheimer disease therapy–moving from amyloid-β to tau. *Nat. Rev. Neurol.* 9, 677–686. doi: 10.1038/nrneurol.2013.223

Gowthaman, U., Sikder, S., Lee, D., and Fisher, C. (2021). T follicular helper cells in IgE-mediated pathologies. *Curr. Opin. Immunol.* 74, 133–139. doi: 10.1016/j.coi.2021.12.001

Greenhalgh, A. D., David, S., and Bennett, F. C. (2020). Immune cell regulation of glia during CNS injury and disease. *Nat. Rev. Neurosci.* 21, 139–152. doi: 10.1038/s41583-020-0263-9

Hopp, S. C., Lin, Y., Oakley, D., Roe, A. D., DeVos, S. L., Hanlon, D., et al. (2018). The role of microglia in processing and spreading of bioactive tau seeds in Alzheimer's disease. *J. Neuroinflammation* 15:269. doi: 10.1186/s12974-018-1309-z

Huang, J., Chen, Z., Zhu, L., Wu, X., Guo, X., Yang, J., et al. (2020). Phosphoinositide-3-kinase regulatory subunit 1 gene polymorphisms are associated with schizophrenia and bipolar disorder in the Han Chinese population. *Metab. Brain Dis.* 35, 785–792. doi: 10.1007/s11011-020-00552-z

Järemo, P., Milovanovic, M., Buller, C., Nilsson, S., and Winblad, B. (2013). Alzheimer's disease and granulocyte density diversity. *Eur. J. Clin. Invest.* 43, 545–548. doi: 10.1111/eci.12072

Jevtic, S., Sengar, A. S., Salter, M. W., and McLaurin, J. (2017). The role of the immune system in Alzheimer disease: etiology and treatment. *Ageing Res. Rev.* 40, 84–94. doi: 10.1016/j.arr.2017.08.005

Kent, S. A., Spires-Jones, T. L., and Durrant, C. S. (2020). The physiological roles of tau and Aβ: implications for Alzheimer's disease pathology and therapeutics. *Acta Neuropathol.* 140, 417–447. doi: 10.1007/s00401-020-02196-w

Liolitsa, D., Powell, J., and Lovestone, S. (2002). Genetic variability in the insulin signalling pathway may contribute to the risk of late onset Alzheimer's disease. *J. Neurol. Neurosurg. Psychiatry* 73, 261–266. doi: 10.1136/jnnp.73.3.261

Long, J. M., and Holtzman, D. M. (2019). Alzheimer disease: an update on pathobiology and treatment strategies. *Cell* 179, 312–339. doi: 10.1016/j.cell.2019.09.001

Malpetti, M., Kievit, R. A., Passamonti, L., Jones, P. S., Tsvetanov, K. A., Rittman, T., et al. (2020). Microglial activation and tau burden predict cognitive decline in Alzheimer's disease. *Brain* 143, 1588–1602. doi: 10.1093/brain/awaa088

Marsh, S. E., Abud, E. M., Lakatos, A., Karimzadeh, A., Yeung, S. T., Davtyan, H., et al. (2016). The adaptive immune system restrains Alzheimer's disease pathogenesis by modulating microglial function. *Proc. Natl. Acad. Sci. U.S.A.* 113, E1316–E1325. doi: 10.1073/pnas.1525466113

Mecocci, P., and Boccardi, V. (2021). The impact of aging in dementia: it is time to refocus attention on the main risk factor of dementia. *Ageing Res. Rev.* 65:101210. doi: 10.1016/j.arr.2020.101210

Merlini, M., Kirabali, T., Kulic, L., Nitsch, R. M., and Ferretti, M. T. (2018). Extravascular CD3+ T cells in brains of Alzheimer disease patients correlate with tau but not with amyloid pathology: an immunohistochemical study. *Neurodegener. Dis.* 18, 49–56. doi: 10.1159/000486200

Mustachio, L. M., Chelariu-Raicu, A., Szekvolgyi, L., and Roszik, J. (2021). Targeting KRAS in cancer: promising therapeutic strategies. *Cancers (Basel).* 13:1204. doi: 10.3390/cancers13061204

Newman, A. M., Liu, C. L., Green, M. R., Gentles, A. J., Feng, W., Xu, Y., et al. (2015). Robust enumeration of cell subsets from tissue expression profiles. *Nat. Methods* 12, 453–457. doi: 10.1038/nmeth.3337

Nunes-Santos, C. J., Uzel, G., and Rosenzweig, S. D. (2019). PI3K pathway defects leading to immunodeficiency and immune dysregulation. *J. Allergy Clin. Immunol.* 143, 1676–1687. doi: 10.1016/j.jaci.2019.03.017

Pascoal, T. A., Benedet, A. L., Ashton, N. J., Kang, M. S., Therriault, J., Chamoun, M., et al. (2021). Microglial activation and tau propagate jointly across Braak stages. *Nat. Med.* 27, 1592–1599. doi: 10.1038/s41591-021-01456-w

Passaro, A. P., Lebos, A. L., Yao, Y., and Stice, S. L. (2021). Immune response in neurological pathology: emerging role of central and peripheral immune crosstalk. *Front. Immunol.* 12:676621. doi: 10.3389/fimmu.2021.676621

Qian, X. H., Song, X. X., Liu, X. L., Chen, S. D., and Tang, H. D. (2021). Inflammatory pathways in Alzheimer's disease mediated by gut microbiota. *Ageing Res. Rev.* 68:101317. doi: 10.1016/j.arr.2021.101317

Roda, A. R., Serra-Mir, G., Montoliu-Gaya, L., Tiessler, L., and Villegas, S. (2022). Amyloid-beta peptide and tau protein crosstalk in Alzheimer's disease. *Neural Regen. Res.* 17, 1666–1674. doi: 10.4103/1673-5374.332127

Seto, M., Weiner, R. L., Dumitrescu, L., and Hohman, T. J. (2021). Protective genes and pathways in Alzheimer's disease: moving towards precision interventions. *Mol. Neurodegener.* 16:29. doi: 10.1186/s13024-021-00452-5

Xia, J., Gill, E. E., and Hancock, R. E. (2015). NetworkAnalyst for statistical, visual and network-based meta-analysis of gene expression data. *Nat. Protoc.* 10, 823–844. doi: 10.1038/nprot.2015.052

Xiao, Y., Dai, Y., Li, L., Geng, F., Xu, Y., Wang, J., et al. (2021). Tetrahydrocurcumin ameliorates Alzheimer's pathological phenotypes by inhibition of microglial cell cycle arrest and apoptosis via Ras/ERK signaling. *Biomed. Pharmacother.* 139:111651. doi: 10.1016/j.biopha.2021.111651

Xu, M., Zhang, D. F., Luo, R., Wu, Y., Zhou, H., Kong, L. L., et al. (2018). A systematic integrated analysis of brain expression profiles reveals YAP1 and other prioritized hub genes as important upstream regulators in Alzheimer's disease. *Alzheimers Dement.* 14, 215–229. doi: 10.1016/j.jalz.2017.08.012

Yuen, S. C., Lee, S. M., and Leung, S. W. (2022). putative factors interfering cell cycle re-entry in Alzheimer's disease: an omics study with differential expression meta-analytics and co-expression profiling. *J. Alzheimers Dis.* 85, 1373–1398. doi: 10.3233/jad-215349

Zotova, E., Bharambe, V., Cheaveau, M., Morgan, W., Holmes, C., Harris, S., et al. (2013). Inflammatory components in human Alzheimer's disease and after active amyloid-β42 immunization. *Brain* 136, 2677–2696. doi: 10.1093/brain/awt210

Conflict of Interest: The authors declare that the research was conducted in the absence of any commercial or financial relationships that could be construed as a potential conflict of interest.

Publisher's Note: All claims expressed in this article are solely those of the authors and do not necessarily represent those of their affiliated organizations, or those of the publisher, the editors and the reviewers. Any product that may be evaluated in this article, or claim that may be made by its manufacturer, is not guaranteed or endorsed by the publisher.

frontiers | Frontiers in Aging Neuroscience

ORIGINAL RESEARCH
published: 10 June 2022
doi: 10.3389/fnagi.2022.880794

Based on Network Pharmacology and Molecular Dynamics Simulations, Baicalein, an Active Ingredient of Yiqi Qingre Ziyin Method, Potentially Protects Patients With Atrophic Rhinitis From Cognitive Impairment

Xueran Kang[1†], Yuxing Sun[1†], Bin Yi[1], Chenyan Jiang[1], Xiaojun Yan[1], Bin Chen[1], Lixing Lu[1], Fangze Shi[2], Yuanbo Luo[1], Yisheng Chen[3], Qian Wang[4] and Runjie Shi[1,2*]*

[1] Department of Otorhinolaryngology Head and Neck Surgery, Shanghai Ninth People's Hospital, Shanghai Jiao Tong University School of Medicine, Shanghai, China, [2] Shanghai Key Laboratory of Translational Medicine on Ear and Nose Diseases, Ear Institute Shanghai Jiao Tong University School of Medicine, Shanghai, China, [3] Department of Sports Medicine, Huashan Hospital, Fudan University, Shanghai, China, [4] Department of Central Laboratory, Taian City Central Hospital, Shandong First Medical University and Shandong Academy of Medical Sciences, Taian, China

OPEN ACCESS

Edited by:
Jun Xu,
Capital Medical University, China

Reviewed by:
Qingyuan Shi,
University of Chinese Academy of Sciences, China
Ashok Iyaswamy,
Hong Kong Baptist University, Hong Kong SAR, China

***Correspondence:**
Runjie Shi
runjieshi@hotmail.com
Qian Wang
qianqianwangxi@163.com

[†] These authors have contributed equally to this work

Specialty section:
This article was submitted to Neuroinflammation and Neuropathy, a section of the journal Frontiers in Aging Neuroscience

Received: *21 February 2022*
Accepted: *06 May 2022*
Published: *10 June 2022*

Citation:
Kang X, Sun Y, Yi B, Jiang C, Yan X, Chen B, Lu L, Shi F, Luo Y, Chen Y, Wang Q and Shi R (2022) Based on Network Pharmacology and Molecular Dynamics Simulations, Baicalein, an Active Ingredient of Yiqi Qingre Ziyin Method, Potentially Protects Patients With Atrophic Rhinitis From Cognitive Impairment. Front. Aging Neurosci. 14:880794. doi: 10.3389/fnagi.2022.880794

Cognition may be improved by the active ingredients of the Yiqi Qingre Ziyin method in patients with atrophic rhinitis (AR). This study aimed to identify potential targets of the Yiqi Qingre Ziyin method for the treatment of patients with cognitive impairment. Nasal mucosal tissue samples from patients with AR were subjected to proteomic assays, and differentially expressed proteins were obtained. To explore the mechanism of AR leading to mild cognitive impairment (MCI), a differential analysis of AR related differential proteins in the MCI related GSE140831 dataset was performed. Most AR-related differential proteins are also differentially expressed in peripheral blood tissues of MCI, have similar biological functions and are enriched in similar pathways. These co-expressed differential factors in AR and MCI are known as common differential proteins of AR and MCI (CDPAM). Based on the analysis and validation of the random forest, support vector machine and neural network models, CDPAM acted as a diagnostic marker for MCI risk. Cytochrome C (CYCS) was significantly upregulated in the peripheral blood of patients with MCI. The active ingredients in the Yiqi Qingre Ziqin method were obtained and targeted 137 proteins. Among these targeted proteins, *CYCS* belong to the CDPAM set. Molecular docking and molecular dynamics analysis revealed that baicalein, an active ingredient in the Yiqi Qingre Ziyin method, stably targeted the CYCS protein. Results of the enrichment analysis revealed that the up-regulation of *CYCS* expression may have a defensive effect on the cells to resist foreign stimuli. Therefore, baicalein, an active ingredient in the Yiqi Qingre Ziyin method, may prevent the development and progression of MCI by targeting the CYCS protein.

Keywords: atrophic rhinitis (AR), mild cognitive impairment (MCI), common differential proteins of AR and MCI (CDPAM), cytochrome C (CYCS), Yiqi Qingre Ziyin method, molecular dynamics simulation (MDS)

INTRODUCTION

Despite the relatively minor physical damages to the patients, symptoms such as nasal congestion and headache have a greater impact on their daily performance, including work and study, even regular sleep at night, which profoundly disturb some patients. Recent studies show that patients with chronic nasal cavity inflammation had decreased brain connectivity at one of the main functional centers, which plays a central role in cognitive regulation (Jafari et al., 2021). The pathology and pathogenesis of rhinitis sicca are less studied in modern medicine. Rhinitis sicca (RS) and atrophic rhinitis (AR) show similar mucosal ultrastructural changes, whereas the former's pathological manifestations and symptoms are mild and reversible. Both of them are often considered the same and treated as one disease. Some authors believe that rhinitis sicca, to a certain severity, can develop into AR; thus, these two types of rhinitis are discussed together during this study. Some studies have reported changes in patients' cognitive levels caused by negative emotions, consequently severely affecting their quality of life (Haug et al., 2009). The more serious the negative emotions are, the more severe the corresponding cognitive impairment gets. Both are positively correlated, showing that breakthroughs in relieving anxiety and depressive symptoms are keys to improving cognitive function in this group of patients (Zufferey et al., 2017), although no systematic studies have revealed the mechanisms of AS and AR affecting the cognitive function of patients.

Cognitive function is an important part of higher cortical functions of the brain, as reflected in various aspects of mental and intellectual activities, such as memory, behavior, attention, speech, abstract thinking, judgment and spatial relations. Numerous clinical trials were observed for the treatment of cognitive function disorders; however, no drugs have been found effective for their treatment (Pei et al., 2020). Mild cognitive impairment (MCI) is an early stage of cognitive decline, where mild cognitive function impairment has occurred but has not yet caused a decline in daily living skills. According to recent epidemiological studies, children with pollen allergies who suffer from rhinitis experience cognitive impairment and have impaired cognitive function (Blaiss and Allergic Rhinitis in Schoolchildren Consensus Group., 2004; Papapostolou et al., 2021). However, it is not well-known that rhinitis is associated with cognitive impairment.

Changes in serum concentrations of specific proteins may serve as predictive markers for impairment or deterioration of cognitive function. Studies showed a cognitive decline in patients with leukoaraiosis is remarkably correlated with S100B/asymmetric DMA (ADMA) levels (Gao et al., 2015), in which S100B (calcium-binding protein B) is responsible for stimulating the expression of pro-inflammatory cytokines, with DMA, asymmetric DMA (ADMA), and arginine/ADMA ratio as remarkable independent predictors of the variability in Mini-Mental State Examination (MMSE) score and Hachinski Ischemic Scale score, two valuable scales for the early screening of Alzheimer's disease (Fleszar et al., 2019). Therefore, we suggest that the effects of AR and AS on cognitive impairment may be reflected in blood markers that are potential therapeutic targets for preventing cognitive impairment related to rhinitis.

Traditional Chinese medicine (TCM) and its role in the prevention and treatment of cognitive impairment are gaining increasingly widespread attention, which has the advantages of multi-targeting and fewer side effects, thus, is more suitable for long-term use (Cheng et al., 2020; Pei et al., 2020; Li et al., 2022; Liu et al., 2022). For the treatment of cognitive dysfunction, TCM adheres to the principles of "diagnosis and treatment" and "holistic view." In recent years, certain progress has been made in the exploration of etiology and pathogenesis, disease prevention and drug treatment. Our literature review showed that although many clinical trials have tentatively demonstrated the effectiveness of TCM in improving the clinical symptoms of cognitive dysfunction in elderly people, more reliable and objective evidence-based medical evidence is still needed (May et al., 2009; Wang et al., 2020, 2021). Flavonoids, alkaloids, phenylpropanoids, triterpenoid saponins and polysaccharides, extracted from natural herbs, which often function as antioxidants, anti-inflammatory agents, anti-apoptotic agents and neural regulators, have proven to be effective treatments for dementia. Some of these pharmacological activities are associated with the regulation of nerve growth factor expression, brain-derived neurotrophic factor and glial-cell-derived neurotrophic factor and their related receptors (Oishi et al., 1998; Pang et al., 2016; Jarrell et al., 2018). Ginseng, *Atractylodes macrocephala*, Poria and Licorice, with anti-inflammatory and antioxidant bioactivities, can improve fatigue and reduce nerve function damage (Chen et al., 2016; Shimato et al., 2018; Jin et al., 2019; Yue et al., 2020). Meanwhile, our preliminary study showed that the Yiqi Qingre Ziyin method can effectively relieve AR symptoms, probably through the targeted modulation of neuropeptide-related genes (including DPP4, OPRD1, and OPRM1) (Lu et al., 2022). Therefore, the active ingredient of the Yiqi Qingre Ziyin method may greatly improve the cognitive level of patients with AS and AR.

This study aimed to identify potential targets of the Yiqi Qingre Ziyin method for treating cognitive impairment in patients with AR, providing a strong basis for traditional Chinese medicine for the clinical treatment of AS and AR.

MATERIALS AND METHODS

Participants

This study recruited patients who underwent surgical treatment at the Ninth People's Hospital in Shanghai, China. Case samples for proteomics in this study were collected from patients clinically diagnosed with AR (three patients) and uncinate process samples from patients clinically treated with nasal polypectomy (three patients) as a control group. Since uncinate process is routinely removed to expose the maxillary sinus intra-operatively, obtaining a sample of uncinate process does not cause additional damage to the patient. All samples included in the case group were confirmed to have AR. Strict information matching is ensured between samples. Specific clinical manifestations are dry nasal cavity, little or no snot, with

nasal itching, nasal congestion, nasal burning, nasal bleeding, blood in the snot, throat dryness and other symptoms; dry, congested and loss of normal luster in the nasal mucosa during the examination of the nasal cavity; and mucosal erosion or ulceration, accompanied by atrophy of nasal mucosa and turbinate. All patients were Chinese residents and voluntarily underwent nasal endoscopy by the same surgeon who conducted the study. All patients signed an informed consent form for study participation. The Ethics Committee of Shanghai Ninth People's Hospital approved this study (approval no. 2017-323-T243) following the Kissinger Declaration.

Protein Extraction

Nasal uncinate process tissues from patients with AR nasal mucosa or normal nasal polyps were precipitated and added to an appropriate amount of SDT lysis solution, transferred to a Lysing Matrix A tube and homogenized and broken up using an MP homogenizer. Then, the steps of boiling water bath for 10 min, centrifugation at 14,000 *g* for 15 min, supernatant filtration and filtrate collection were completed, respectively. Finally, the BCA method was used for protein quantification. The quality control procedures of the samples were as follows: 20 μg protein was extracted from each sample and added into 6X loading buffer, then bathed in boiling water for 5 min, followed by 12% SDS-PAGE electrophoresis (250 V, 40 min) and Coomassie blue staining.

Filter Aided Sample Preparation Enzymatic Digestion and Mass Spectrometry

Filter aided sample preparation (FASP) enzymatic digestion was carried out following the steps reported in a previous study (Zhu et al., 2014). Briefly, each sample was obtained from the protein solution, added separately to dithiothreitol, boiled in a water bath and then cooled to room temperature. About 200 μL of UA buffer was added, mixed and centrifuged; 100 μL of IAA buffer (100-mM IAA in UA) was added, shaken and reacted at room temperature; protected from light and centrifuged for 15 min, and the procedure was repeated twice. An NH4HCO3 solution was added and centrifuged, and the procedure was repeated twice. A new collection tube was changed, added with 40 μL Trypsin buffer (4 μg Trypsin in 40 μL and 40 mM NH4HCO3 solution), shaken for 1 min, placed at 37°C and centrifuged, and the filtrate was collected. Peptides were desalted using a C18 Cartridge, lyophilized and re-solubilized by adding 40 μL of 0.1% formic acid solution and were subsequently quantified (OD280). Mass spectrometric analysis was completed by NanoElute chromatography, and samples were separated using a NanoElute system (Bruker, Bremen, Germany) with a nanoliter flow rate. Samples were separated by chromatography and analyzed by mass spectrometry using a timsTOF Pro mass spectrometer (Bruker, Bremen, Germany). The mass spectrometry raw files were processed using Maxquant's algorithm. The protein sequence database used for this project is Uniprot_HomoSapiens_20387_20210928_9606_swissprot (download link: http://www.uniprot.org). The raw data were saved in text form.

Subcellular Localization Analysis

Because proteins can only function successfully if they are in the right place, their subcellular localization is important information in investigating protein function. Protein subcellular localization was determined using a prediction software with WoLF PSORT, converting protein sequences into digital localization features and predicting the subcellular localization of proteins using a K-nearest neighbor classifier (Wiśniewski et al., 2009).

Gene Ontology and Kyoto Encyclopedia of Genes and Genomes Enrichment Analysis

Enrichment analysis of screened proteins was performed using the Kyoto Encyclopedia of Genes and Genomes (KEGG) and Gene Ontology (GO) (Yu et al., 2012; Chen et al., 2021). The top-ranked genes and those with a p-value of <0.05 were visualized using R software similarly to previous studies. Enrichment analysis was performed using Fisher's exact test (FET) to determine whether differentially expressed proteins tended to be significantly enriched in certain functions (p-value < 0.05).

Data Set Acquisition

The MCI dataset is obtained from the GEO database's GSE140831 dataset and derived from the GPL15988 dataset annotated with HumanHT-12 v4 Expression BeadChip. The GSE140831 dataset contains 1,129 RNA-seq data from the whole blood of 530 healthy participants and 134 patients diagnosed with MCI.

Composite Compounds and Drug Targets of the Yiqi Qingre Ziyin Method

In this study, chemical compositions of the Yiqi Qingre Ziyin method were determined through the pharmacology platform of the Chinese Medicine Network [including Traditional Chinese Medicine Database, Traditional Chinese Medicine Systems Pharmacology (TCMSP) database and Bioinformatics Analysis Tool for Molecular Mechanism of Traditional Chinese Medicine (BATMAN-TCM)] (Chen et al., 2014; Ru et al., 2014; Liu et al., 2016). The main active ingredients of each drug were extracted under the following screening conditions: oral bioavailability of ≥30% and drug similarity of ≥0.18 (Di et al., 2021). The active ingredient targets of the Yiqi Qingre Ziyin method were obtained from the TCMSP database.

Molecular Docking and Molecular Dynamics Simulation

Protein structures were obtained from the alphafold2 database (Cramer, 2021). Target proteins were sequentially hydrogenated, charge-added and ligand-root detected using AutoDock. The structures of active ingredients were obtained from the PubChem database and docked with the corresponding proteins using AutoDock 4.2 software after energy minimization (Trott and Olson, 2009; Kim et al., 2021). The above molecular

docking pair structures were used as initial structures for molecular dynamics simulations. The ACPYPE server was used to create small-molecular force fields (Sousa da Silva and Vranken, 2012; Kastritis et al., 2014; Kagami et al., 2017). CHARMM was used to describe protein force fields (Van Der Spoel et al., 2005; Nava, 2018). The solvent model in the system is TIP3P, followed by Na+/Cl- used to balance the system charge (dos Santos et al., 2019) NVT and NPT simulations were performed after a slight increase in a system temperature from 0 to 307 K. Finally, molecular dynamics simulations of the complex object system were performed. Finally, a 20-ns MD simulation of the protein-small molecular complex system was performed, with conformations saved every 1 ps and visualization completed with pymol (Seeliger and de Groot, 2010).

Gene Set Enrichment Analysis

Gene set enrichment analysis enrichment analysis was performed with the clusterProfiler package of R software using "c2.cp.v7.2.symbols.gmt" from the MSigDB Collections dataset, with *Homo sapiens* species (Hung et al., 2012; Yu et al., 2012). Significant differences for GSEA enrichment analysis were defined as adjusted p of <0.05 and false discovery rate (FDR) of <0.25.

Statistical Analysis

Statistical analyzes and plots were performed using R software (version 3.6.3). Data for prediction models were obtained from the GSE140831 dataset. The prediction model for this study was constructed based on that of previous studies. The random forest (RF) model and support vector machine (SVM) were constructed using R software packages "caret," "DALEX," "randomForest," and "kernlab". Furthermore, the neural network models were constructed using "neuralnet" and "NeuralNetTools" packages. Their receiver operating characteristic (ROC) curves are drawn, and area under the curve (AUC) values are calculated using the "pROC" package, including "pheatmap" and "ggplot2" used for plotting. Statistical results were expressed as mean ± standard deviation, and two-tailed *t*-tests or analysis of variance was used to analyze differences in two samples, with *p*-values of <0.05 considered statistically different.

RESULTS

Distribution and Enrichment Characteristics of Differential Proteins in Atrophic Rhinitis Proteomics

In this study, a total of three samples from nasal mucosal tissues of patients with AR and three from unciform processes of patients with nasal polyp were sent for testing. To analyze significant differences in quantitative results, data were screened with at least half of the repeated experimental data within the sample group with non-null values for statistical analysis. Proteins that meet the expression difference ploidy of greater than twofold (up- and down-regulation) and *t*-test of <0.05 screening criteria are considered differentially expressed proteins. In total, 25 genes were obtained with up-regulated expression and 126 genes with down-regulated expression in the nasal mucosa tissue of patients with AR. Subcellular localization analysis showed that their proportion in the subcellular was cytosol (31.1%), nucleus (21.9%), plasma membrane (12.6%), mitochondria (13.9%), endoplasmic reticulum (4.0%), peroxisome (1.3%), and Golgi apparatus (0.7%). Differential genes are enriched in the cytosol, nucleus, plasma membrane and mitochondria (**Figure 1A**). Heat map analyzes were performed to identify the expression characteristics of all differentially expressed proteins (**Figure 1B**). Then, the main results of GO and KEGG enrichment were shown in a histogram (**Figures 1C,D**). During the biological process (BP), functions of enrichment included intra-Golgi vesicle-mediated transport, cytoplasmic translation, ribosomal small subunit assembly, protein transport, endosome to melanosome transport and amine transport. In molecular function (MF), functions of enrichment included protein tyrosine phosphatase activity, structural constituent of the ribosome and thiol oxidase activity. In the cellular component (CC), functions of enrichment included cytosolic large ribosomal subunit, Golgi membrane, *cis*-Golgi network Golgi transport complex, small-subunit processome, Scrib-APC-beta-catenin complex, TORC1 complex, the bounding membrane of the organelle and presynaptic membrane, indicating that AR proteomics differential genes are mainly enriched in protein transfer, DNA transcriptional regulation and Golgi-related functions. Moreover, differential genes have been enriched in the ribosomes, protein processing in the endoplasmic reticulum, coronavirus disease 2019, human immunodeficiency virus 1 infection, protein export and other related pathways, indicating disease progression in AR may be associated with ribosome-mediated protein processing caused by a viral infection, over-activation of export-related functions, and atrophy following functional depletion.

Atrophic Rhinitis Differential Proteins Are Differentially Co-expressed in the Mild Cognitive Impairment Peripheral Blood

To explore the mechanism of AR that may lead to MCI, further differential analysis of AR differential proteins in the GSE140831 dataset was performed. As shown in the bar chart, most AR differential proteins were found to be differentially expressed in the GSE140831 dataset (**Figure 2A**). The top-ranked differential genes were enriched and clustered analyzed in the heat map (**Figure 2B**). To understand the distribution of these genes on the chromosomes, their expression information was plotted on the chromosomes using the circle diagram (**Figure 2C**). We referred to these differentially expressed genes (DEGs) co-expressed as common differential proteins of AR and MCI (CDPAM). Enrichment analysis suggests that CDPAM genes are also mainly enriched in the endoplasmic reticulum, ribosome, and vesicle membrane for protein transcription translation and transmembrane transport-related functions and structures; in MF, CDPAM-related genes are mainly enriched in the structural constituent of ribosomes and other related functions, suggesting that disease progression in both AR and MCI is associated with

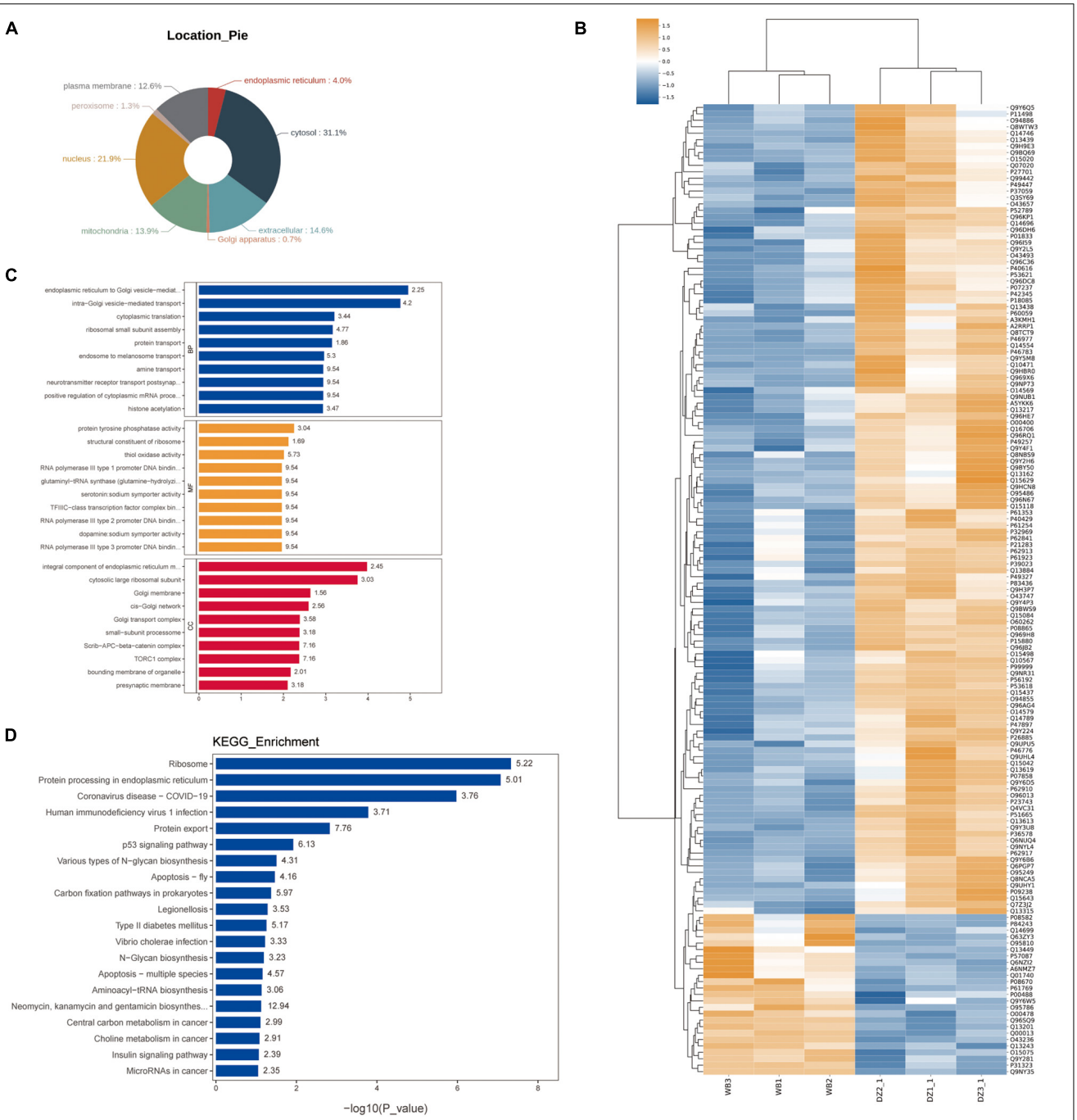

FIGURE 1 | Distribution and enrichment characteristics of differential proteins in atrophic rhinitis (AR) proteomics. **(A)** The pie chart demonstrates tissue distribution of differentially expressed proteins in AR; **(B)** heat map analyzing expression characteristics of all differentially expressed proteins; **(C)** gene Ontology (GO) enrichment analysis of AR-related differentially expressed proteins; and **(D)** Kyoto Encyclopedia of Genes and Genomes (KEGG) enrichment characteristics of AR-related differentially expressed proteins.

organelle-mediated protein processing, export-related functional hyper-activation, and atrophy after a functional depletion (**Figure 3A**). In the KEGG enrichment analysis, CDPAM-related genes were enriched during protein processing in the endoplasmic reticulum, ribosome, coronavirus disease 2019, human immunodeficiency virus 1 infection and various types of N-glycan biosynthesis-related pathways (**Figure 3B**). Here, we found that most AR-related differential proteins were also differentially expressed in the peripheral blood tissues of MCI, and these differential genes have similar biological functions and are enriched in similar pathways, revealing a potential association between AR and MCI.

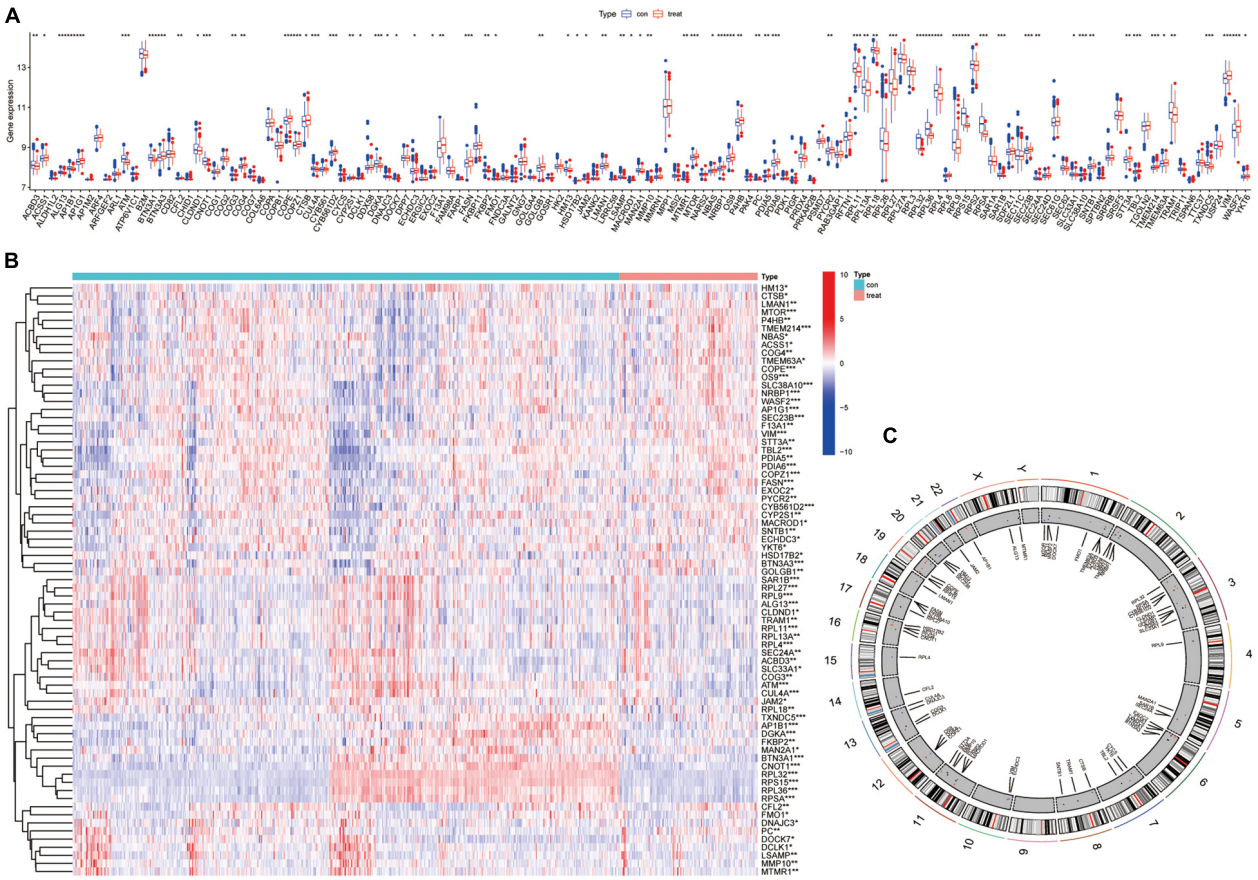

FIGURE 2 | Differential expression and gene distribution in peripheral blood of mild cognitive impairment (MCI) patients. **(A)** An expression box plot shows the AR differential protein-related genes in GSE140831 data; **(B)** heat map demonstrating AR differential protein expressing in the peripheral blood of patients with MCI; and **(C)** circle map demonstrating gene distribution corresponding to AR differential proteins on chromosomes.

Neural Network Model Validating Common Differential Proteins of Atrophic Rhinitis and Mild Cognitive Impairment as Diagnostic Markers for Mild Cognitive Impairment Risk

To further evaluate the predictive effects of the CDPAM gene on MCI, MCI prediction models were constructed using RF models and SVM. Box plots and reverse cumulative distribution of RF and SVM CDPAM models corresponding genes predicting the MCI indicate that RF model residual is lesser than that of SVM models (**Figures 4A,B**). The AUC value of 1 for the RF model of CDPAM corresponding to the gene prediction MCI is slightly higher than that of the SVM model (0.968) (**Figure 4C**). The relationship between RF model "trees" and "error" is shown in **Supplementary Figure 1A**. RPSA, RPS15, RPL32, and CNOT1 are among the highest predicted weights in RF models, suggesting that these genes are more closely associated with the MCI risk (**Figure 4D**). Next, neural network models were used to further validate whether the genes of interest in CDPAM could be used as diagnostic markers for MCI risk with a heat map demonstrating expression characteristics of genes building neural network models in the healthy group and patients with MCI (**Figure 5A**). **Figure 5B** shows how to use the model diagram of CDPAM building neural network model for predicting the MCI risk, the AUC value was 0.990 (95% confidence interval: 0.982–0.996) (**Figure 5C**). Based on the analysis and validation of the RF, SVM and neural network models, CDPAM was found to be a diagnostic marker for MCI risk.

Molecular Dynamics Simulations Reveal That Baicalein, an Active Ingredient of the Yiqi Qingre Ziyin Method, Can Target and Bind the CYCS Protein

Based on traditional Chinese medicine theories, the Yiqi Qingre Ziyin method has been found to control disease progression in AR to some extent in clinical applications. All active ingredients in the Yiqi Qingre Ziyin method were obtained, which targeted 137 proteins, among which the CYCS protein was found to be a protein belonging to the CDPAM set (**Figure 6A**). A molecular docking analysis was carried out and it was discovered that baicalein, the active ingredient of Yiqi Qinghe method, targets CYCS protein binding (**Figures 6B,C**). The OB and drug

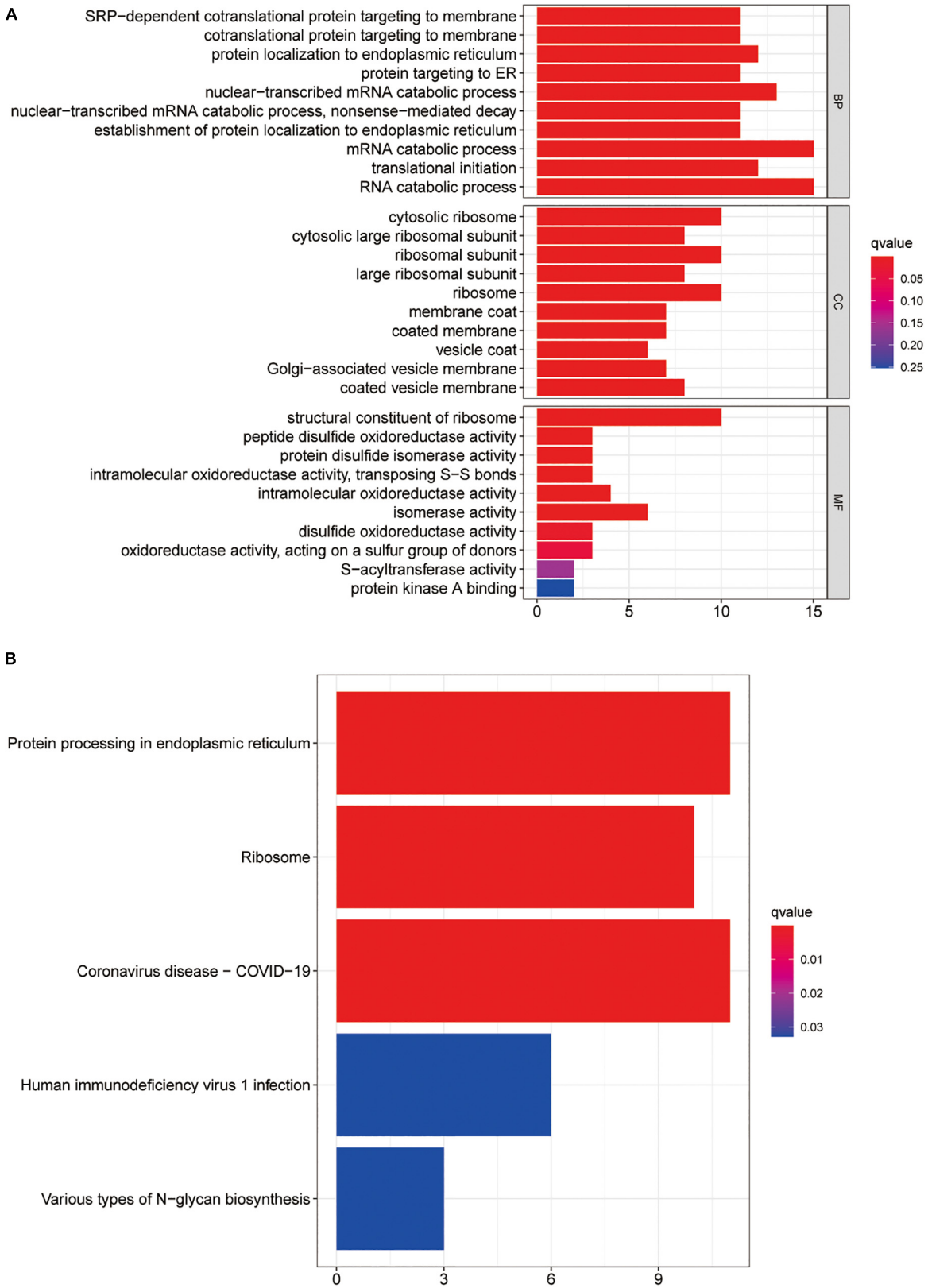

FIGURE 3 | Enrichment analysis of common differential protein of AR and MCI (CDPAM), GO functional enrichment analysis **(A)**, and KEGG pathway enrichment analysis **(B)**.

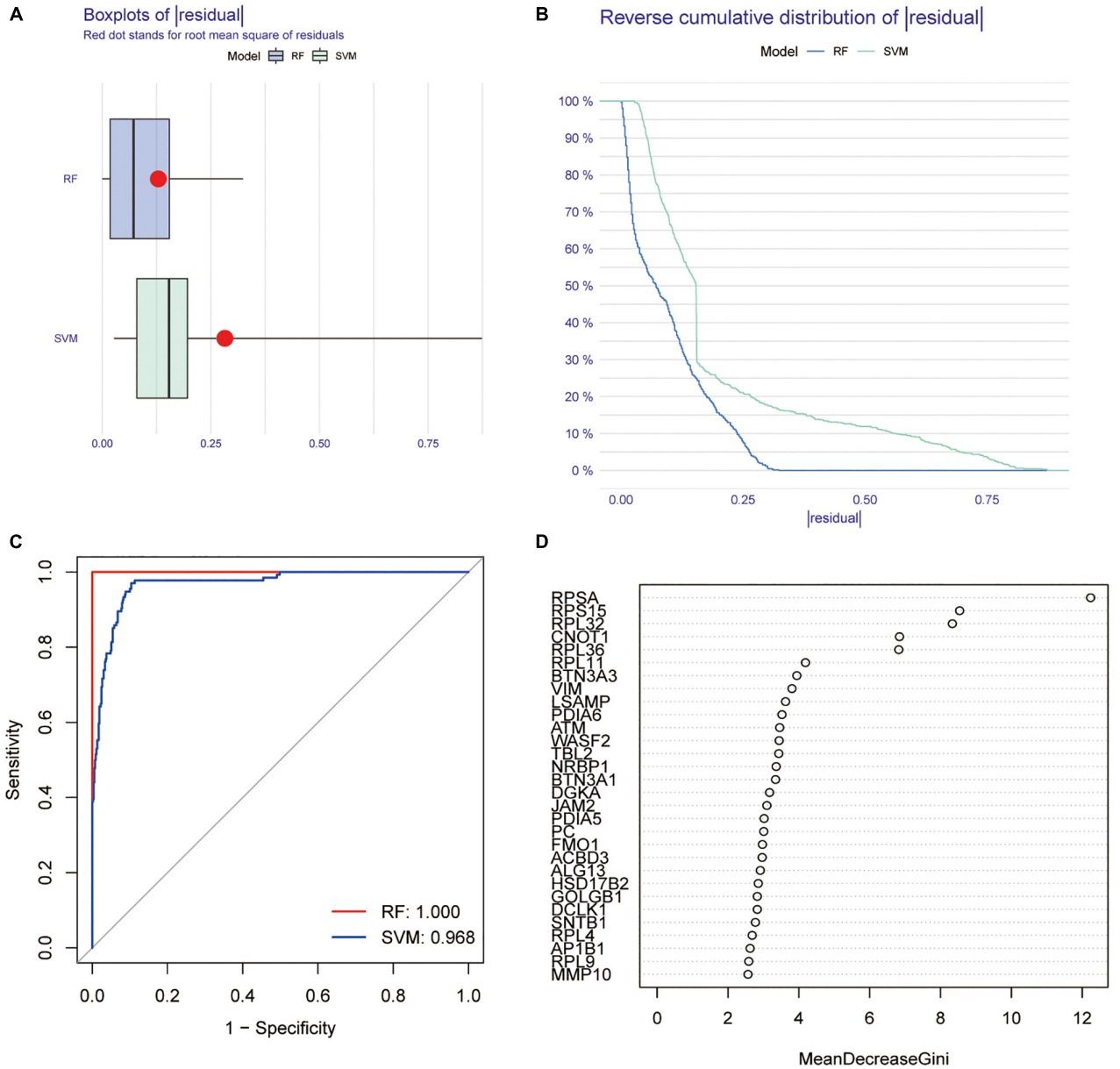

FIGURE 4 | The predictive power of CDPAM. **(A)** Box plots of RF and SVM models in the CDPAM corresponding genes predicting MCI; **(B)** reverse cumulative distribution of RF and SVM models in predicting CDPAM corresponding genes; **(C)** ROC curves of RF and SVM models in CDPAM corresponding genes predicting MCI; and **(D)** weights of each gene in the RF model of CDPAM predicting MCI.

similarity of baicalein, which binds to CYCS protein, can be seen in **Figure 6C**. Baicalein's structural diagram is shown in **Supplementary Figure 1B**. In the Yiqi Qingre Ziyin method, baicalein is the active ingredient of Chishao (Radix Paeoniae Rubra) (**Figure 6C**). We found that alphafold2 well-predicted the protein structure of CYCS, and the pattern map of the CYCS protein structure is shown (**Supplementary Figures 2A,B**). Analyzing the binding conformation of baicalein and CYCS protein shows that CYCS forms a hydrogen bond with baicalein at a hydrogen bond distance of 2.8 A (**Figure 6B**) with a free binding energy of –8.2 (kcal/mol).

Analysis of ligand–protein interactions before and after MDS revealed that protein conformation contracted to some extent while the binding between CYCS and baicalein was stable (**Figures 6D,E**). The variation of RMSD values in the CYCS protein-baicalein ligand system with time is shown in **Figure 7A**. During 0–10 ns, the RMSD values of the system increase due to interactions between the CYCS complex and the solvent; later during 10–20 ns, the RMSD values stabilize due to the interaction between the CYCS protein and the baicalein ligand maintenance. The radius of gyration (Rg) is frequently used to describe variations of the overall structure and can show a relatively stable

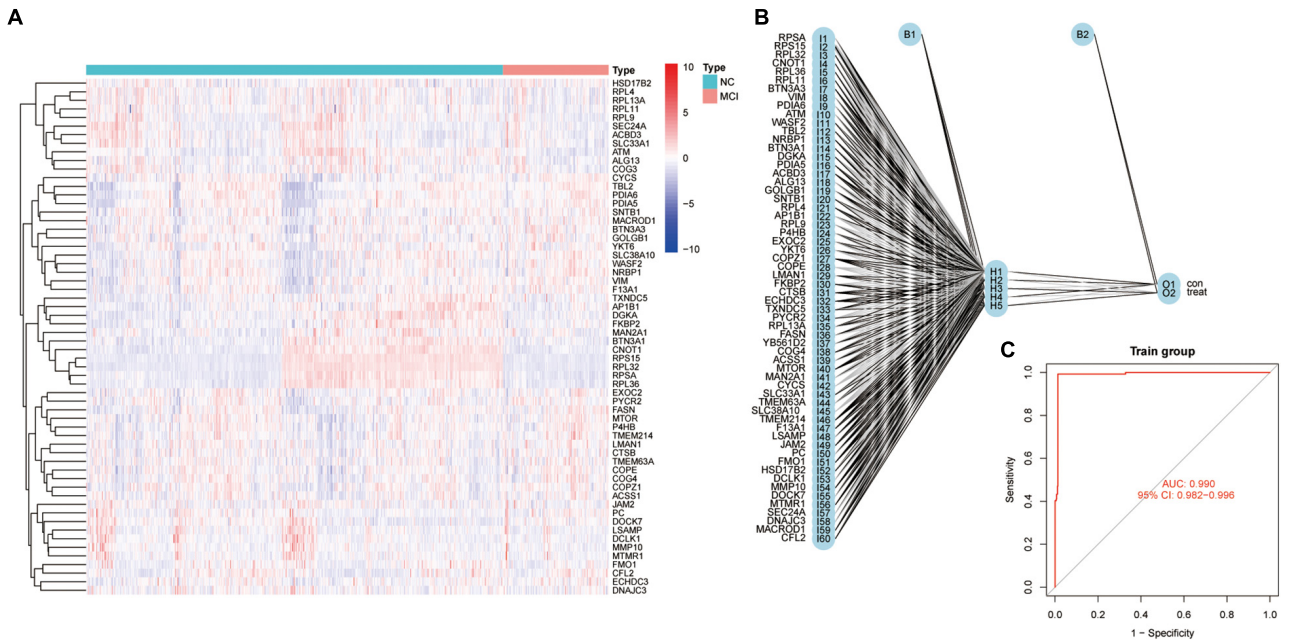

FIGURE 5 | Neural network model validating CDPAM as diagnostic markers for MCI risk. **(A)** Heat map demonstrating gene expression characteristics of building neural network models in the healthy group and patients with MCI; **(B)** model diagram of the CDPAM building neural network models for predicting MCI risk; and **(C)** receiver operating characteristic (ROC) curves of CDPAM corresponding genes predicting the MCI neural network models.

overall Rg value of the protein (**Figure 7B**), indicating that the CYCS protein-baicalein ligand system is relatively stable in the structure. **Figure 7C** shows the relationship between molecular hydrogen bonding and time. Proteins and water molecules form hydrogen bonds, and the figure showed a greater number of hydrogen bonds between water molecules and the protein, with an average of 59.6 hydrogen bonds throughout the simulation. Furthermore, the overall free energy in this system is relatively stable (**Figure 7D**), suggesting that baicalein stably targets and binds with CYCS protein. By targeting or binding with CYCS protein, baicalein, an active ingredient in Yiqi Qingre Ziyin, may prevent MCI onset and progression.

Functional Analysis of the Cytochrome C Protein

To further evaluate the *CYCS* expression in MCI, the GSE140831 dataset was used to extract CYSC expression data. The *CYCS* expression was significantly upregulated in the peripheral blood of patients with MCI (**Figure 8A**), indicating a high *CYCS* expression may be associated with the pathogenic process of MCI. The single-cell transcriptome showed that *CYCS* protein was significantly enriched in mouse immune cells (**Supplementary Figures 2C,D**), suggesting that *CYCS* may be related to the immune cell function. We then analyzed protein interactions associated with *CYCS* through the OncoBinder model to assess the potential function of *CYCS* (**Figure 8B**), indicating that many proteins interact with *CYCS* in the cytosol, extracellular, membrane, mitochondrion, nucleus and secretory pathway widely enriched in prion disease, Parkinson's disease, measles, flavin adenine dinucleotide binding, electron transfer activity, organelle outer membrane, mitochondrial outer membrane, mitochondrial inner membrane, intrinsic apoptotic signaling pathway, cellular respiration and electron transport chain (**Figure 8C**). Moreover, proteins that interact with *CYCS* are associated with the response to and occurrence of viral infections and neurodegenerative diseases. Consequently, these proteins play an important role in membrane function and transmission of the organelle's oxidative respiratory chain. To assess the relationship between *CYCS* expression changes and cellular pathways and functions, the GSEA was used to map the CYCS-related GO functional enrichment and KEGG pathway enrichment in the peripheral blood (**Figures 8D,E**). The *CYCS* expression relates to GO function enrichment, such as eukaryotic 43S preinitiation complex, molecular carrier activity, NADH dehydrogenase activity, positive regulation of B-cell differentiation, protein de-neddylation and translation preinitiation complex. GSEA analysis explained the correlation between the *CYCS* and KEGG pathway, including antigen processing and presentation, fatty acid elongation pathway, oxidative phosphorylation, proteasome, protein export, and ribosome pathway. Therefore, *CYCS* expression may be associated with the differentiation and antigen delivery of immune cells, protein export and synthesis and energy metabolism of mitochondria. Based on these results, we suggest that the up-regulation of *CYCS* expression may be a defensive effect made by the cells to resist foreign stimuli, whereas the *CYCS* expression down-regulation may follow the cells that undergo apoptosis. Based on the results of the study, a schematic diagram of the potential mechanism by which baicalein, the

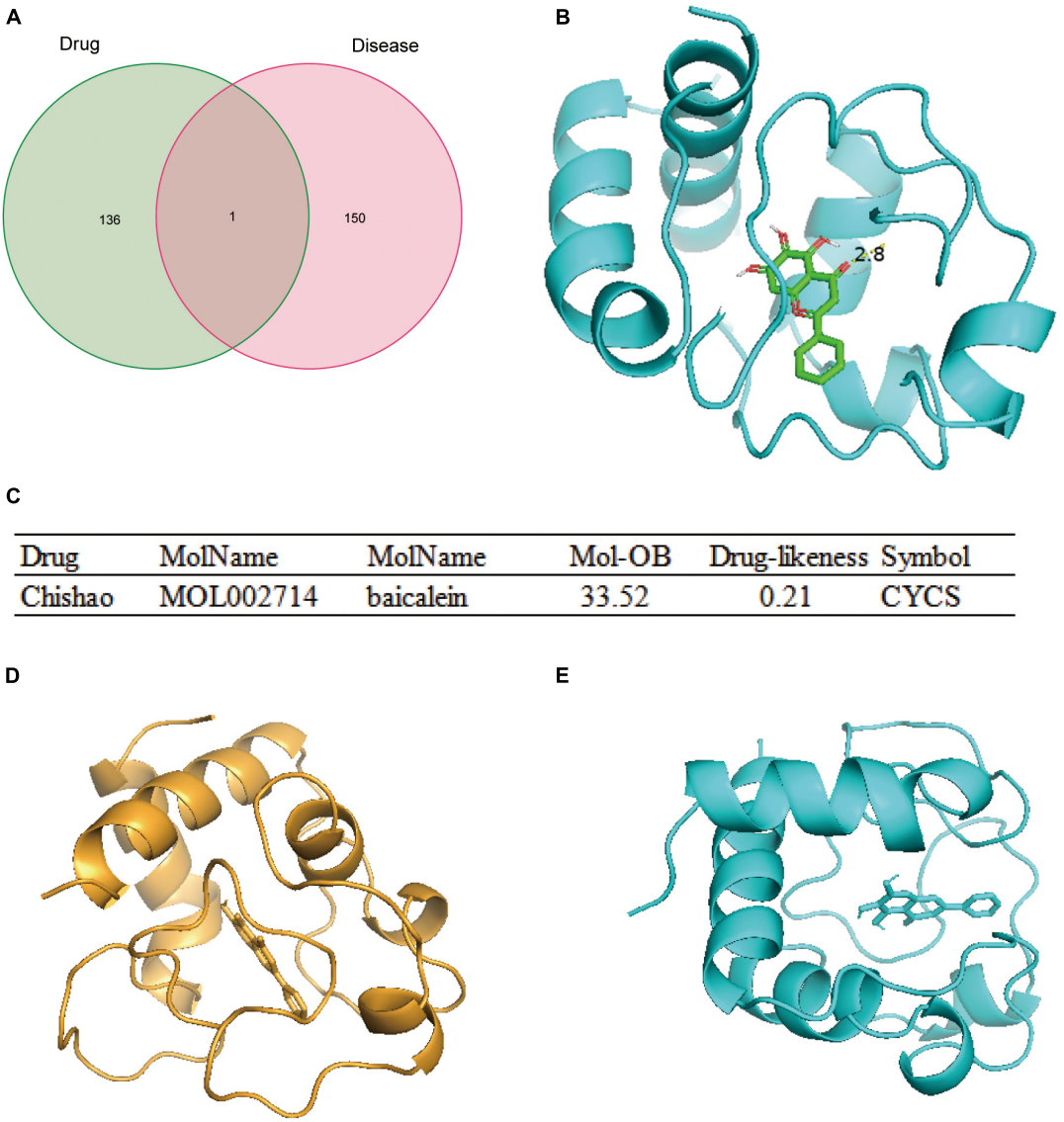

FIGURE 6 | The active ingredient of the Yiqi Qingre Ziyin method – baicalein targeted binding CYCS protein. **(A)** Wayne diagram intersection analysis showing CYCS targeted by the active ingredient of the Yiqi Qingre Ziyin method; **(B)** model diagram of the active ingredient in the Yiqi Qingre Ziyin method – baicalein target-binding *CYCS* protein; **(C)** OB and drug-likeness of the CYCS protein-binding baicalein; **(D)** model diagram of the molecular dynamics simulation in baicalein target binding CYCS protein at 0 ns; and **(E)** model diagram of molecular dynamics simulation in the baicalein target-binding CYCS protein at 20 ns.

active ingredient in Yiqi Qingre Ziyin method, inhibits the process of apoptosis by targeting the binding of CYCS, was drawn (**Figure 9**).

DISCUSSION

The cause of AR is complex, and no recognized or effective treatment options in Western medicine currently; therefore, its treatment is mostly local or systemic combination therapy to improve symptoms, which are not satisfactory or prone to recurrence. AR is also likely to results in depression, headache, insomnia, and other symptoms of emotional disorders, causing patients to gradually develop symptoms associated with cognitive impairment. Based on bioinformatics and proteomics analyzes, this study found that most AR-related differential proteins were also differentially expressed in the peripheral blood tissues of MCI, and these differential genes had similar biological functions and were enriched in similar pathways. These findings suggest a potential association between MCI and AR. Furthermore, baicalein, an active ingredient of the Yiqi Qingre Ziyin method, may prevent the development and progression of MCI by targeting the CYCS protein.

The Yiqi Qingre Ziyin method, based on traditional Chinese medicine theory, has been found to control the disease progression of AR to some extent in clinical applications.

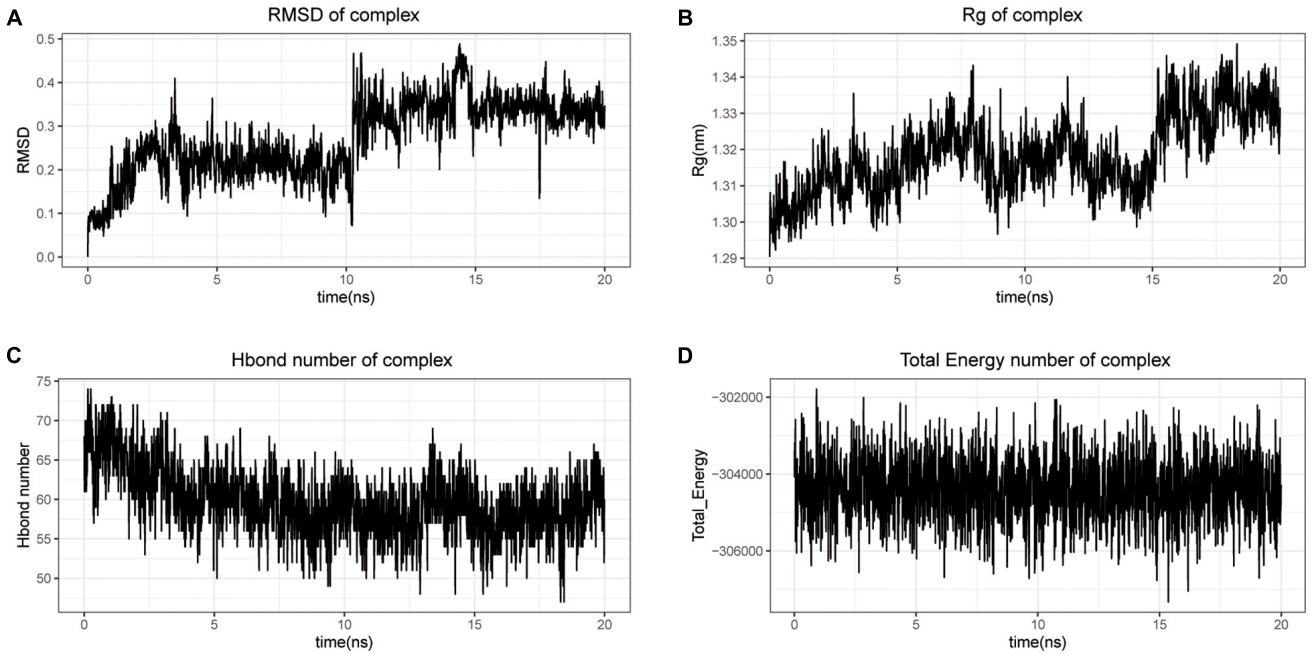

FIGURE 7 | Basic parameters of molecular dynamics simulation. Baicalein-binding CYCS complex RMSD; **(A)** Rg; **(B)** H-bond number; **(C)** total energy; and **(D)** parameter property.

Baicalein in the Yiqi Qingre Ziyin method may prevent the onset and progression of MCI by targeting and binding with the CYCS protein as our molecular docking analysis revealed. As an active ingredient of Chishao (Radix Paeoniae Rubra), baicalein is derived from the Yiqi Qingre Ziyin method to promote cell proliferation and differentiation, reduce expression of inflammatory factors, protect neuronal cells from death and resist neuronal cell apoptosis. It also reduces apoptotic damage in the brain tissue by upregulating Bax and downregulating Bcl-2 levels (Gu et al., 2016). Modern pharmacological studies have shown that baicalein significantly inhibits NO production and suppresses iNOS and NF-κB protein expressions in LPS-induced BV-2 microglia and primary microglia, thereby suppressing the inflammatory response of glial cells (Suk et al., 2003). Baicalein also blocks NF-κB and MAPK signaling pathways to inhibit the release of inflammatory factors, such as TNF-α, IL-6, and IL-1β, which in turn produces anti-inflammatory activities (Fan et al., 2013). Therefore, the effects of baicalein are suspected to be mediated by targeting CYCS.

Cytochrome C is a protein loosely attached to the surface of the inner mitochondrial membrane and is an important electron transfer chain component. It transfers electrons in the intermembrane space between the adjacent mitochondria. An early event in apoptosis is the release of CYCS from the mitochondria into the cytoplasm. Other proteins involved in the apoptotic process also interact with CYCS. A trend toward an increased percentage of CYCS immunoreactive dystrophic neuropil was observed in pathologically aged control cases compared with AD cases (Woodhouse et al., 2006). Elevated CYCS levels were observed in neuronal bodies and proximal protrusions after multiple *in vivo* experimental injuries (Martin and Liu, 2002; Benjelloun et al., 2003; Page et al., 2003). In a transgenic mouse model of AD, CYCS-positive dystrophic neuron density gradually increased with age until a late disease progression stage when CYCS-positive dystrophic neuron density decreased (Blanchard et al., 2003), suggesting that CYCS upregulation may be a sign that neurons are at an early stage of the apoptotic process. There are two classical apoptotic pathways, the cell surface death receptor pathway (or extracellular pathway) and the mitochondrial-initiated pathway (or intracellular pathway). During apoptosis, the mitochondrial permeability transition pore, MPTP, is overly open and the mitochondrial transmembrane potential is reduced, leading to the release of pro-apoptotic factors such as CYCS from the mitochondria into the cytoplasm. CYCS has been shown to be a key regulator of the mitochondrial apoptotic signaling pathway. Experimental studies have shown that CYCS cannot only directly mediate apoptosis, but also indirectly participate in the apoptotic process by interfering with respiratory chain electron transfer, promoting the production of reactive oxygen radicals, and blocking energy synthesis. CYCS is released from the respiratory chain before being released into the cytosol, and CYCS binds to the WD repeat at the carboxy terminus of Apaf-1, inducing Apaf-1 metamorphosis and further binding to the Caspase-9 precursor, resulting in spontaneous activation of the Caspase-9 complex. The apoptosome continues to activate downstream Caspase-3, triggering a cascade reaction that leads to apoptosis. These results are consistent with those of the current study, in which proteomic results showed reduced CYCS levels in the nasal mucosa of patients with AR, suggesting that

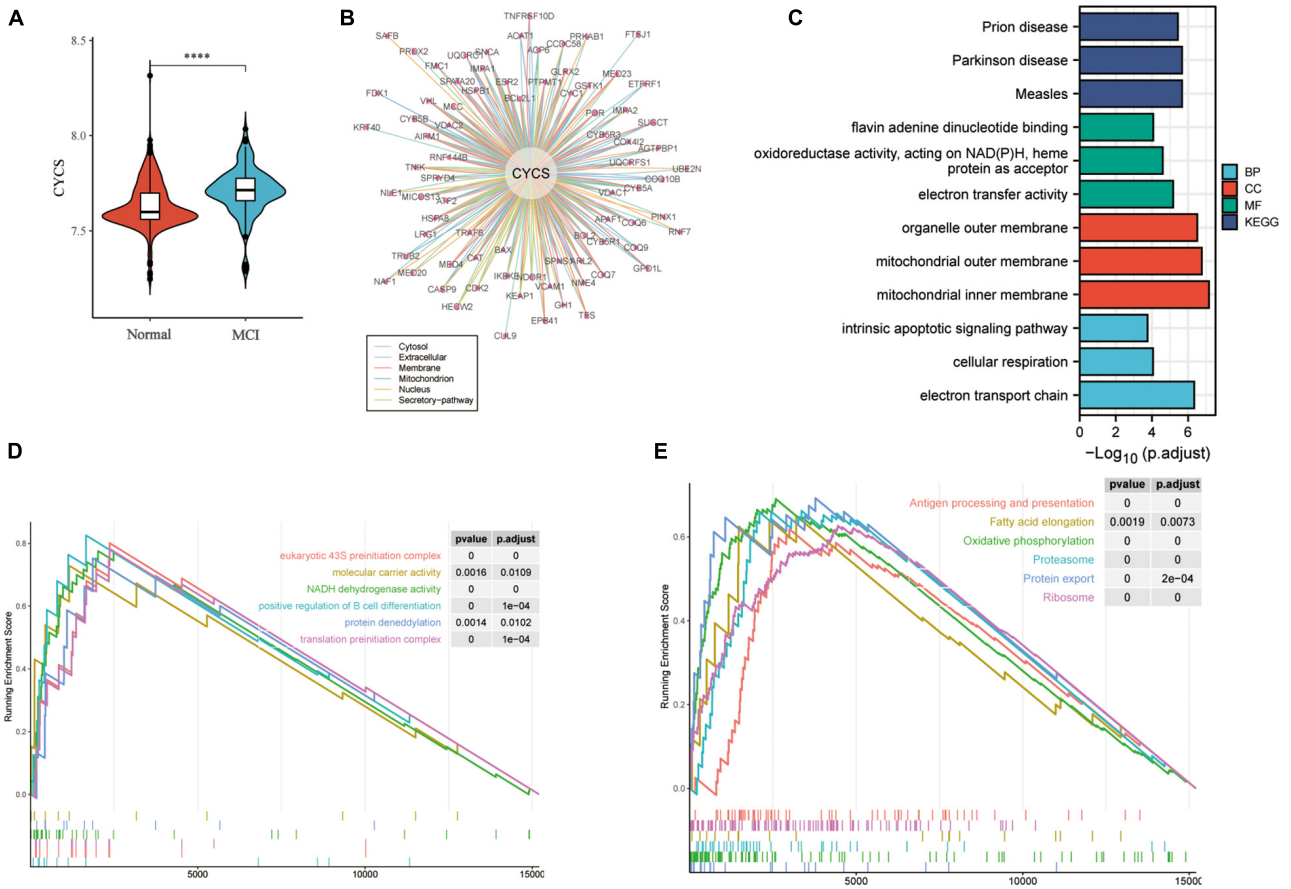

FIGURE 8 | Expression and function analysis of the *CYCS* protein. **(A)** Box plots of *CYCS* differential proteins in the peripheral blood of patients with MCI; **(B)** analysis of *CYCS*-related protein interactions through the OncoBinder model analysis to evaluate the potential function of CYCS; Lower left panel indicates subcellular localization of these protein interactions ($P < 0.01$, Pearson correlation, two-sided); **(C)** GO and KEGG enrichment analysis of proteins interacting with *CYCS*; and **(D,E)** mapping CYCS-related GO functional enrichment in the peripheral blood with GSEA **(D)** and KEGG pathway **(E)** enrichment.

their nasal mucosal peripheral nerves are atrophied and in an advanced stage, the reasons for the poor effects of neurotrophic drug therapy. We can speculate that high *CYCS* expression is an early neuronal apoptotic marker and early application of CYCS-targeted drugs for patients with dry rhinitis and AR can effectively inhibit nasal peripheral nerve atrophy and prevent the occurrence of cognitive impairment.

One of the most important elements in the preclinical drug discovery process today is computer-aided drug design (CADD), which facilitates the screening of potential drugs efficiently (Sabe et al., 2021). Out of over 600 relevant studies, there are currently over 70 approved CADD drugs, and this number is steadily increasing (Sabe et al., 2021). To predict the interactions between drugs and proteins, molecular dynamics simulation (MDS) is a reliable method (Honarparvar et al., 2014). Therefore, the binding affinity results obtained by MDS are reliable, and researchers can use this technique to check the validity of molecular docking results (Honarparvar et al., 2014). A number of studies have explored ways to combat cognitive decline using MDS recently. Huperzine A, for example, has been proven to be anti-Alzheimer's disease, and the study was based on MDS. Moreover, MDS has also been found to have great potential in the treatment of Ebola virus (EBOV) (Darko et al., 2021). As in our study using MDS, DPGS analogs were also able to block interleukin-6 (IL-6) and influence the course of inflammatory diseases (Sanader Maršić et al., 2021). The study identified molecular markers for MCI and identified potential targets for Yiqi Qingre Ziyin formula, which has provided a new example of pharmacological mechanism for MCI and AR treatment in TCM.

This study, based on a neural network model, found that CDPAM can be used as a diagnostic marker for MCI risk. Molecular markers of AR may predict the occurrence of MCI, indicating that MCI and AR may be related. Additionally, molecular dynamics and molecular docking studies indicated that baicalein was capable of stably targeting and binding CYCS protein in CDPAM. CYCS may serve as an intermediate mediator of AR that leads to MCI. However, there are also some limitations to the study. Firstly, a protein sample or blood sample is required for future studies to demonstrate the results of the expression of the target gene or protein. Secondly, considering that the present study is based on a database of clinical proteomic samples,

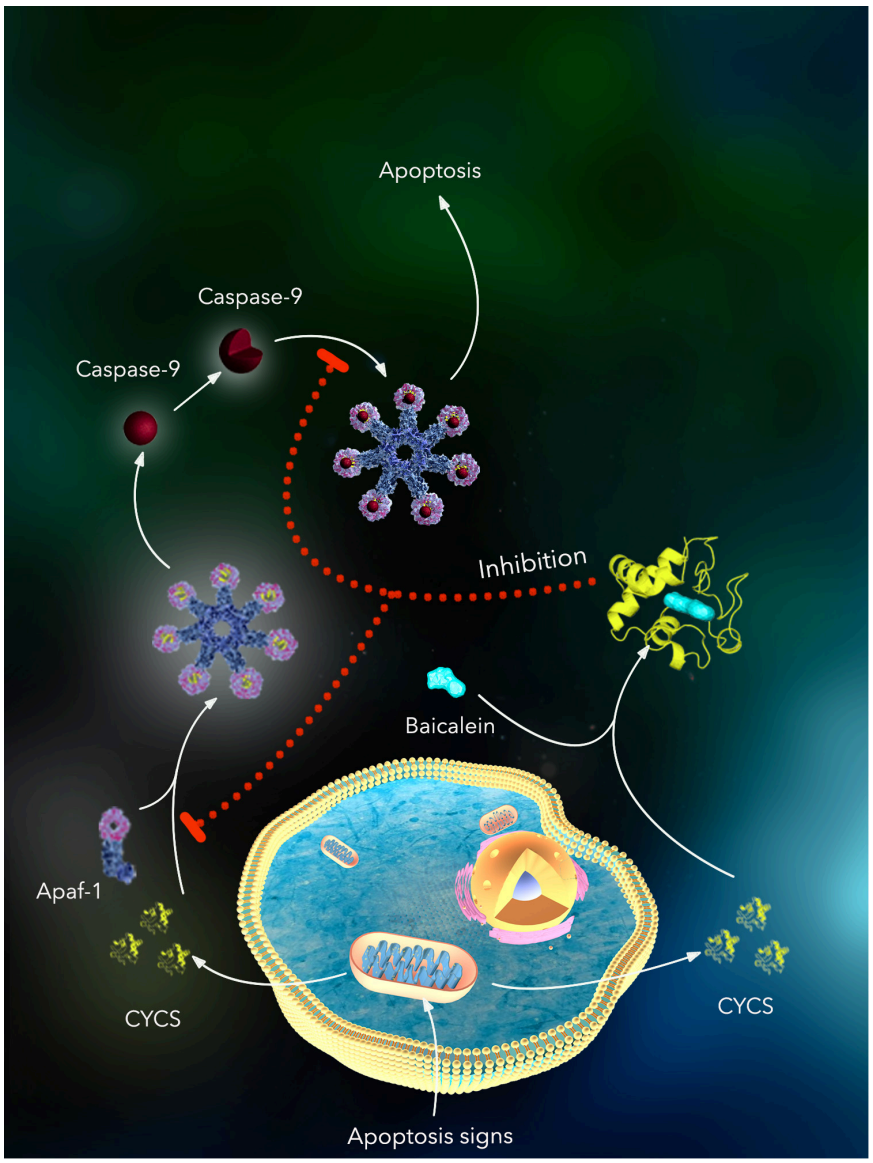

FIGURE 9 | The potential mechanism by which baicalein, the active ingredient in Yiqi Qingre Ziyin method, inhibits the process of apoptosis by targeting the binding of CYCS.

further exploration of the specific mechanisms underlying CYCS preventing MCI occurrence is required. Thirdly, *in vitro* evidence is pending to demonstrate the results of molecular docking and MDS analysis. And there may be a correlation between MCI and AR according to the bioinformatics analysis of this study, though it needs to be investigated clinically. In this process, questionnaire surveys or experimental studies are recommended. Furthermore, the effects of TCM are generally mild and slow (Tomioka, 2017; Pei et al., 2020). Accordingly, if our hypothesis holds true, it is necessary to conduct long-term cohort studies to investigate herbal medicine to prevent the occurrence of AR patients. It is important to note that patients with AS or AR should be guided patiently and informed that their disease is difficult to heal and prone to recurrence, and the efficacy of treatment should not be exaggerated to increase patients' trust, so as not to cause doctor–patient conflicts due to patients' eagerness to heal and intolerance to the pain caused by the disease. Simultaneously, a light diet, avoiding spicy and stimulating products, should be considered, and patients should adhere to the medication to obtain better and long-term sustainable results. The current study is limited by objective conditions and further clinical and biological studies are needed in order to further explore the mechanism of MCI prevention after baicalein targeting CYCS. A major contribution of this study was the comprehensive exploration of the mechanism of Yiqi Qingre Ziyin method against MCI, in which the potential link between AR and MCI was also examined. We also explored the potential value of MDS for identifying herbal medicines against MCI and AR.

CONCLUSION

Based on differential expression findings of proteomics in AR, this study used neural network models to validate that CDPAM can serve as a diagnostic marker for MCI risk. Molecular dynamics and molecular docking studies finally revealed that baicalein, an active ingredient of the Yiqi Qingre Ziyin method, can stably target and bind with the CYCS protein from CDPAM.

DATA AVAILABILITY STATEMENT

The datasets presented in this study can be found in online repositories. The names of the repository/repositories and accession number(s) can be found in the article/ **Supplementary Material**.

ETHICS STATEMENT

The studies involving human participants were reviewed and approved by 2017-323-T243. The patients/participants provided their written informed consent to participate in this study.

AUTHOR CONTRIBUTIONS

XK conceived and designed the study. RS and YS analyzed the data. All authors were involved to wrote the manuscript and approved the submitted version.

FUNDING

This work was supported by the Medical and Industrial Project, Shanghai Jiao Tong University School of Medicine (YG2021ZD16) and Clinical Research Program of 9th people's hospital, Shanghai Jiao Tong university school of medicine (JYLJ028).

ACKNOWLEDGMENTS

We thank all reviewers for their very valuable comments, which were a great contribution to improve the manuscript, and also for their appreciation of this work. We also thank Bullet Edits Limited for the linguistic editing and proofreading of the manuscript.

SUPPLEMENTARY MATERIAL

The Supplementary Material for this article can be found online at: https://www.frontiersin.org/articles/10.3389/fnagi.2022.880794/full#supplementary-material

Supplementary Figure 1 | The relationship between "trees" and "errors" in the random forest model. **(A)** Two-dimensional structure diagram with baicalein **(B)**.

Supplementary Figure 2 | Prediction and expression characteristics of CYCS protein in single-cell profiles. **(A)** Structure of the CYCS protein-aligned residue; **(B)** structure forecast of the CYCS protein based on alphafold2; **(C)** annotated single-cell transcript profiles of immune cells in the mouse spleen; **(D)** single-cell annotation map reflecting expression characteristics of CYCS protein in immune cells.

REFERENCES

Benjelloun, N., Joly, L.-M., Palmier, B., Plotkine, M., and Charriaut-Marlangue, C. (2003). Apoptotic mitochondrial pathway in neurones and astrocytes after neonatal hypoxia-ischaemia in the rat brain. *Neuropathol. Appl. Neurobiol.* 29, 350–360. doi: 10.1046/j.1365-2990.2003.00467.x

Blaiss, M. S., and Allergic Rhinitis in Schoolchildren Consensus Group. (2004). Allergic rhinitis and impairment issues in schoolchildren: a consensus report. *Curr. Med. Res. Opin.* 20, 1937–1952. doi: 10.1185/030079904X13266

Blanchard, V., Moussaoui, S., Czech, C., Touchet, N., Bonici, B., Planche, M., et al. (2003). Time sequence of maturation of dystrophic neurites associated with Abeta deposits in APP/PS1 transgenic mice. *Exp. Neurol.* 184, 247–263. doi: 10.1016/s0014-4886(03)00252-8

Chen, F.-P., Chang, C.-M., Hwang, S.-J., Chen, Y.-C., and Chen, F.-J. (2014). Chinese herbal prescriptions for osteoarthritis in Taiwan: analysis of national health insurance dataset. *BMC Complement. Altern. Med.* 14:91. doi: 10.1186/1472-6882-14-91

Chen, L.-G., Jan, Y.-S., Tsai, P.-W., Norimoto, H., Michihara, S., Murayama, C., et al. (2016). Anti-inflammatory and Antinociceptive Constituents of Atractylodes japonica Koidzumi. *J. Agric. Food Chem.* 64, 2254–2262. doi: 10.1021/acs.jafc.5b05841

Chen, Y., Sun, Y., Xu, Y., Lin, W.-W., Luo, Z., Han, Z., et al. (2021). Single-Cell Integration Analysis of Heterotopic Ossification and Fibrocartilage Developmental Lineage: endoplasmic Reticulum Stress Effector Xbp1 Transcriptionally Regulates the Notch Signaling Pathway to Mediate Fibrocartilage Differentiation. *Oxid. Med. Cell. Longev.* 2021:7663366. doi: 10.1155/2021/7663366

Cheng, X., Huang, Y., Zhang, Y., and Zhou, W. (2020). LW-AFC, a new formula from the traditional Chinese medicine Liuwei Dihuang decoction, as a promising therapy for Alzheimer's disease: pharmacological effects and mechanisms. *Adv. Pharmacol. Elsevier* 87, 159–177. doi: 10.1016/bs.apha.2019.10.005

Cramer, P. (2021). AlphaFold2 and the future of structural biology. *Nat. Struct. Mol. Biol.* 28, 704–705. doi: 10.1038/s41594-021-00650-1

Darko, L. K. S., Broni, E., Amuzu, D. S. Y., Wilson, M. D., Parry, C. S., and Kwofie, S. K. (2021). Computational Study on Potential Novel Anti-Ebola Virus Protein VP35 Natural Compounds. *Biomedicines* 9:1796. doi: 10.3390/biomedicines9121796

Di, S., Han, L., An, X., Kong, R., Gao, Z., Yang, Y., et al. (2021). In silico network pharmacology and in vivo analysis of berberine-related mechanisms against type 2 diabetes mellitus and its complications. *J. Ethnopharmacol.* 276:114180. doi: 10.1016/j.jep.2021.114180

dos Santos, M. A. F., Habitzreuter, M. A., Schwade, M. H., Borrasca, R., Antonacci, M., Gonzatti, G. K., et al. (2019). Dynamical aspects of supercooled TIP3P–water in the grooves of DNA. *J. Chem. Phys.* 150:235101. doi: 10.1063/1.5100601

Fan, G.-W., Zhang, Y., Jiang, X., Zhu, Y., Wang, B., Su, L., et al. (2013). Anti-inflammatory activity of baicalein in LPS-stimulated RAW264.7 macrophages via estrogen receptor and NF-κB-dependent pathways. *Inflammation* 36, 1584–1591. doi: 10.1007/s10753-013-9703-2

Fleszar, M. G., Wiśniewski, J., Zboch, M., Diakowska, D., Gamian, A., and Krzystek-Korpacka, M. (2019). Targeted metabolomic analysis of nitric oxide/L-arginine pathway metabolites in dementia: association with pathology, severity, and structural brain changes. *Sci. Rep.* 9:13764. doi: 10.1038/s41598-019-50205-0

Gao, Q., Fan, Y., Mu, L.-Y., Ma, L., Song, Z.-Q., and Zhang, Y.-N. (2015). S100B and ADMA in cerebral small vessel disease and cognitive dysfunction. *J. Neurol. Sci.* 354, 27–32. doi: 10.1016/j.jns.2015.04.031

Gu, J., Chen, J., Yang, N., Hou, X., Wang, J., Tan, X., et al. (2016). Combination of Ligusticum chuanxiong and Radix Paeoniae ameliorate focal cerebral ischemic in MCAO rats via endoplasmic reticulum stress-dependent apoptotic signaling pathway. *J. Ethnopharmacol.* 187, 313–324. doi: 10.1016/j.jep.2016.04.024

Haug, T., Sorteberg, A., Sorteberg, W., Lindegaard, K.-F., Lundar, T., and Finset, A. (2009). Surgical Repair Of Unruptured And Ruptured Middle Cerebral Artery Aneurysms. *Neurosurgery* 64, 412–422. doi: 10.1227/01.NEU.0000338952.13880.4E

Honarparvar, B., Govender, T., Maguire, G. E. M., Soliman, M. E. S., and Kruger, H. G. (2014). Integrated Approach to Structure-Based Enzymatic Drug Design: molecular Modeling. *Chem. Rev.* 114, 493–537. doi: 10.1021/cr300314q

Hung, J.-H., Yang, T.-H., Hu, Z., Weng, Z., and DeLisi, C. (2012). Gene set enrichment analysis: performance evaluation and usage guidelines. *Brief. Bioinform.* 13, 281–291. doi: 10.1093/bib/bbr049

Jafari, A., de Lima Xavier, L., Bernstein, J. D., Simonyan, K., and Bleier, B. S. (2021). Association of Sinonasal Inflammation With Functional Brain Connectivity. *JAMA Otolaryngol. Head Neck Surg.* 147:534. doi: 10.1001/jamaoto.2021.0204

Jarrell, J., Gao, L., Cohen, D., and Huang, X. (2018). Network Medicine for Alzheimer's Disease and Traditional Chinese Medicine. *Molecules* 23:1143. doi: 10.3390/molecules23051143

Jin, Y., Cui, R., Zhao, L., Fan, J., and Li, B. (2019). Mechanisms of Panax ginseng action as an antidepressant. *Cell Prolif.* 52:e12696. doi: 10.1111/cpr.12696

Kagami, L. P., das Neves, G. M., da Silva, A. W. S., Caceres, R. A., Kawano, D. F., and Eifler-Lima, V. L. (2017). LiGRO: a graphical user interface for protein–ligand molecular dynamics. *J. Mol. Model.* 23:304. doi: 10.1007/s00894-017-3475-9

Kastritis, P. L., Rodrigues, J. P. G. L. M., and Bonvin, A. M. (2014). HADDOCK(2P21): a Biophysical Model for Predicting the Binding Affinity of Protein–Protein Interaction Inhibitors. *J. Chem. Inf. Model.* 54, 826–836. doi: 10.1021/ci4005332

Kim, S., Gindulyte, A., Zhang, J., Thiessen, P. A., and Bolton, E. E. (2021). PubChem Periodic Table and Element pages: improving access to information on chemical elements from authoritative sources. *Chem. Teach. Int.* 3, 57–65. doi: 10.1515/cti-2020-0006

Li, Z., Liu, Y., Li, H., Li, W., Wu, X., and Li, Z. (2022). Application of network pharmacology in the prevention and treatment of COVID-19 by traditional Chinese medicine. *Tradit. Med. Res.* 7:21. doi: 10.53388/TMR20220225266

Liu, Y., Cui, N., Liu, X., Lin, P., Pecoraro, L., Venturella, G., et al. (2022). Anti-asthmatic mechanism of the Huashanshen dripping pill via suppressing contraction of the airway smooth muscle. *Tradit. Med. Res.* 7:20. doi: 10.53388/TMR20211124252

Liu, Z., Guo, F., Wang, Y., Li, C., Zhang, X., Li, H., et al. (2016). BATMAN-TCM: a Bioinformatics Analysis Tool for Molecular mechANism of Traditional Chinese Medicine. *Sci. Rep.* 6:21146. doi: 10.1038/srep21146

Lu, L., Kang, X., Yi, B., Jiang, C., Yan, X., Chen, B., et al. (2022). Exploring the Mechanism of Yiqi Qingre Ziyin Method in Regulating Neuropeptide Expression for the Treatment of Atrophic Rhinitis. *Dis. Markers* 2022:4416637. doi: 10.1155/2022/4416637

Martin, L. J., and Liu, Z. (2002). Injury-induced spinal motor neuron apoptosis is preceded by DNA single-strand breaks and is p53- and Bax-dependent. *J. Neurobiol.* 50, 181–197. doi: 10.1002/neu.10026

May, B. H., Yang, A. W. H., Zhang, A. L., Owens, M. D., Bennett, L., Head, R., et al. (2009). Chinese herbal medicine for Mild Cognitive Impairment and Age Associated Memory Impairment: a review of randomised controlled trials. *Biogerontology* 10, 109–123. doi: 10.1007/s10522-008-9163-5

Nava, M. (2018). Implementing dimer metadynamics using gromacs: implementing Dimer Metadynamics Using Gromacs. *J. Comput. Chem.* 39, 2126–2132. doi: 10.1002/jcc.25386

Oishi, M., Mochizuki, Y., Takasu, T., Chao, E., and Nakamura, S. (1998). Effectiveness of Traditional Chinese Medicine in Alzheimer Disease. *Alzheimer Dis. Assoc. Disord.* 12, 247–253. doi: 10.1097/00002093-199809000-00019

Page, A. B., Owen, C. R., Kumar, R., Miller, J. M., Rafols, J. A., White, B. C., et al. (2003). Persistent eIF2α(P) is colocalized with cytoplasmic cytochrome c in vulnerable hippocampal neurons after 4 hours of reperfusion following 10-minute complete brain ischemia. *Acta. Neuropathol.* 106, 8–16. doi: 10.1007/s00401-003-0693-2

Pang, X., Wang, Z., Fang, J., Lian, W., Zhao, Y., Kang, D., et al. (2016). [Network pharmacology study of effective constituents of traditional Chinese medicine for Alzheimer's disease treatment]. *Yao. Xue. Xue. Bao.* 51, 725–731.

Papapostolou, G., Kiotseridis, H., Romberg, K., Dahl, Å, Bjermer, L., Lindgren, M., et al. (2021). Cognitive dysfunction and quality of life during pollen season in children with seasonal allergic rhinitis. *Pediatr. Allergy. Immunol.* 32, 67–76. doi: 10.1111/pai.13328

Pei, H., Ma, L., Cao, Y., Wang, F., Li, Z., Liu, N., et al. (2020). Traditional Chinese Medicine for Alzheimer's Disease and Other Cognitive Impairment: a Review. *Am. J. Chin. Med.* 48, 487–511. doi: 10.1142/S0192415X20500251

Ru, J., Li, P., Wang, J., Zhou, W., Li, B., Huang, C., et al. (2014). TCMSP: a database of systems pharmacology for drug discovery from herbal medicines. *J. Cheminform.* 6:13. doi: 10.1186/1758-2946-6-13

Sabe, V. T., Ntombela, T., Jhamba, L. A., Maguire, G. E. M., Govender, T., Naicker, T., et al. (2021). Current trends in computer aided drug design and a highlight of drugs discovered via computational techniques: a review. *Eur. J. Med. Chem.* 224:113705. doi: 10.1016/j.ejmech.2021.113705

Sanader Maršić, Ž, Maysinger, D., and Bonaèić-Koutecký, V. (2021). Insights into Interactions between Interleukin-6 and Dendritic Polyglycerols. *IJMS* 22:2415. doi: 10.3390/ijms22052415

Seeliger, D., and de Groot, B. L. (2010). Ligand docking and binding site analysis with PyMOL and Autodock/Vina. *J. Comput. Aided Mol. Des.* 24, 417–422. doi: 10.1007/s10822-010-9352-6

Shimato, Y., Ota, M., Asai, K., Atsumi, T., Tabuchi, Y., and Makino, T. (2018). Comparison of byakujutsu (Atractylodes rhizome) and sojutsu (Atractylodes lancea rhizome) on anti-inflammatory and immunostimulative effects in vitro. *J. Nat. Med.* 72, 192–201. doi: 10.1007/s11418-017-1131-4

Sousa da Silva, A. W., and Vranken, W. F. (2012). ACPYPE - AnteChamber PYthon Parser interfacE. *BMC Res. Notes* 5:367. doi: 10.1186/1756-0500-5-367

Suk, K., Lee, H., Kang, S. S., Cho, G. J., and Choi, W. S. (2003). Flavonoid baicalein attenuates activation-induced cell death of brain microglia. *J. Pharmacol. Exp. Ther.* 305, 638–645. doi: 10.1124/jpet.102.047373

Tomioka, H. (2017). Usefulness of Chinese Herbal Medicines as Host-Directed Therapeutics against Mycobacterial Infections: a Review. *Am. J. Chin. Med.* 45, 1597–1611. doi: 10.1142/S0192415X17500860

Trott, O., and Olson, A. J. (2009). AutoDock Vina: improving the speed and accuracy of docking with a new scoring function, efficient optimization, and multithreading. *J. Comput. Chem.* 31, 455–461. doi: 10.1002/jcc.21334

Van Der Spoel, D., Lindahl, E., Hess, B., Groenhof, G., Mark, A. E., and Berendsen, H. J. (2005). GROMACS: fast, flexible, and free. *J. Comput. Chem.* 26, 1701–1718. doi: 10.1002/jcc.20291

Wang, H., Yu, H., Song, K., Xiong, F., and Zhang, H. (2020). Traditional Chinese medicine for mild cognitive impairment: a protocol for systematic review and network meta-analysis. *Medicine* 99:e22187. doi: 10.1097/MD.0000000000022187

Wang, W., Diwu, Y., Liu, Q., Zhou, Y., Sayed, T. I., Wang, D., et al. (2021). Chinese herbal medicine for mild cognitive impairment using mini-mental state examination: a systematic review and meta-analysis. *Medicine* 100:e27034. doi: 10.1097/MD.0000000000027034

Wiśniewski, J. R., Zougman, A., Nagaraj, N., and Mann, M. (2009). Universal sample preparation method for proteome analysis. *Nat. Methods* 6, 359–362. doi: 10.1038/nmeth.1322

Woodhouse, A., Vickers, J. C., and Dickson, T. C. (2006). Cytoplasmic cytochrome c immunolabelling in dystrophic neurites in Alzheimer's disease. *Acta. Neuropathol.* 112, 429–437. doi: 10.1007/s00401-006-0107-3

Yu, G., Wang, L.-G., Han, Y., and He, Q.-Y. (2012). clusterProfiler: an R Package for Comparing Biological Themes Among Gene Clusters. *OMICS* 16, 284–287. doi: 10.1089/omi.2011.0118

Yue, C., Ze-Xian, D., Yue, Z., Yue-Hang, J., Lei, W., Jian-Ping, L., et al. (2020). [Research progress on chemical structures and pharmacological activities of

Poria cocos polysaccharide and its derivatives]. *Zhongguo Zhong. Yao. Za. Zhi.* 45, 4332–4340. doi: 10.19540/j.cnki.cjcmm.20200624.601

Zhu, Y., Xu, H., Chen, H., Xie, J., Shi, M., Shen, B., et al. (2014). Proteomic Analysis of Solid Pseudopapillary Tumor of the Pancreas Reveals Dysfunction of the Endoplasmic Reticulum Protein Processing Pathway. *Mol. Cell. Proteom.* 13, 2593–2603. doi: 10.1074/mcp.M114.038786

Zufferey, V., Donati, A., Popp, J., Meuli, R., Rossier, J., Frackowiak, R., et al. (2017). Neuroticism, depression, and anxiety traits exacerbate the state of cognitive impairment and hippocampal vulnerability to Alzheimer's disease. *Alzheimers Dement. (Amst).* 7, 107–114. doi: 10.1016/j.dadm.2017.05.002

Conflict of Interest: The authors declare that the research was conducted in the absence of any commercial or financial relationships that could be construed as a potential conflict of interest.

Publisher's Note: All claims expressed in this article are solely those of the authors and do not necessarily represent those of their affiliated organizations, or those of the publisher, the editors and the reviewers. Any product that may be evaluated in this article, or claim that may be made by its manufacturer, is not guaranteed or endorsed by the publisher.

frontiers | Frontiers in Cellular Neuroscience

ORIGINAL RESEARCH
published: 17 June 2022
doi: 10.3389/fncel.2022.906270

Alzheimer's Amyloid-β Accelerates Human Neuronal Cell Senescence Which Could Be Rescued by Sirtuin-1 and Aspirin

Yi Li[1,2], Juan Lu[2], Yujun Hou[3], Shichao Huang[2] and Gang Pei[1,2,4,5]**

[1] School of Life Science and Technology, ShanghaiTech University, Shanghai, China, [2] State Key Laboratory of Cell Biology, CAS Center for Excellence in Molecular Cell Science, Shanghai Institute of Biochemistry and Cell Biology, Chinese Academy of Sciences, University of Chinese Academy of Sciences, Shanghai, China, [3] Institute for Regenerative Medicine, Shanghai East Hospital, Shanghai Key Laboratory of Signaling and Disease Research, School of Life Sciences and Technology, Tongji University, Shanghai, China, [4] Shanghai Key Laboratory of Signaling and Disease Research, Collaborative Innovation Center for Brain Science, School of Life Sciences and Technology, Tongji University, Shanghai, China, [5] Institute for Stem Cell and Regeneration, Chinese Academy of Sciences, Beijing, China

OPEN ACCESS

Edited by:
Yuzhen Xu,
Tongji University, China

Reviewed by:
Bo Jin,
Zhejiang Chinese Medical University, China
Javier Francisco-Morcillo, University of Extremadura, Spain

***Correspondence:**
Shichao Huang
huangshichao@sibcb.ac.cn
Gang Pei
gpei@sibs.ac.cn

Specialty section:
This article was submitted to Cellular Neuropathology, a section of the journal Frontiers in Cellular Neuroscience

Received: *28 March 2022*
Accepted: *24 May 2022*
Published: *17 June 2022*

Citation:
Li Y, Lu J, Hou Y, Huang S and Pei G (2022) Alzheimer's Amyloid-β Accelerates Human Neuronal Cell Senescence Which Could Be Rescued by Sirtuin-1 and Aspirin. Front. Cell. Neurosci. 16:906270. doi: 10.3389/fncel.2022.906270

Cellular senescence is a major biological process related to aging. Neuronal cell senescence contributes to the pathogenesis of many aging-related neurodegenerative diseases including Alzheimer's disease (AD). In this study, we showed that amyloid-β_{42} oligomers (Aβ), one of the core pathological players of AD, significantly upregulated the expression of senescence markers, p21, plasminogen activator inhibitor-1 (PAI-1), and SA-β-gal (senescence-associated β-galactosidase) in multiple human neuronal cells, including SK-N-SH cells, SH-SY5Y cells, and neural stem cell (NSC)-derived neuronal cells. Moreover, it was consistently observed among the cells that Aβ promoted senescence-associated DNA damage as the levels of 8-OHdG staining, histone variant H2AX phosphorylation (γ-H2AX), and genomic DNA lesion increased. Mechanism study revealed that the exposure of Aβ markedly suppressed the expression of sirtuin-1 (SIRT1), a critical regulator of aging, and the exogenous expression of SIRT1 alleviated Aβ-induced cell senescence phenotypes. To our surprise, a widely used cardiovascular drug aspirin considerably rescued Aβ-induced cellular senescence at least partially through its regulation of SIRT1. In conclusion, our findings clearly demonstrate that exposure of Aβ alone is sufficient to accelerate the senescence of human neuronal cells through the downregulation of SIRT1.

Keywords: Aβ, cell senescence, human neuronal cells, SIRT1, DNA damage

INTRODUCTION

Alzheimer's disease (AD) is an age-associated, progressive, and irreversible neurodegenerative disorder that exponentially increased with age (Baker and Petersen, 2018; Liu, 2022). Cell senescence, with the classical phenotypic hallmarks include senescence-associated β-galactosidase (SA-β-gal), cell cycle arrest, persistent DNA damage response (DDR), and senescence-associated secretory phenotype (SASP) including inflammatory cytokines, growth factor, matrix

metalloproteinases, and other proteinases (Coppé et al., 2010; Cuollo et al., 2020; Fafián-Labora and O'Loghlen, 2020), has been demonstrated to play an important role in onset and aggravation of AD (Martínez-Cué and Rueda, 2020). Recent studies have shown that plasminogen activator inhibitor-1 (PAI-1) also presents a key marker of cell senescence and contributes to various aging-associated morbidities (Gerenu et al., 2017; Vaughan et al., 2017; Kritsilis et al., 2018; Bryant et al., 2020; Tang et al., 2022). Mounting evidence has demonstrated that disease-associated microglia display several features of senescence and preventing microglia from senescence could lead to reduced amyloidosis and synaptic damage in age-related AD (Daria et al., 2017; Hu et al., 2021; Hu et al., 2022). Besides, it has been found that Aβ oligomers, one of the major players in AD, induced senescence in oligodendrocyte progenitor cells and in adult hippocampal neural stem/progenitor cells (He et al., 2013; Zhang et al., 2019). More importantly, the clearance of senescent cells was reported to decrease Aβ plaque size and improve cognition, further demonstrating senescent cells accelerate Aβ pathology (Zhang et al., 2019). However, neuronal senescence in AD models is relatively complicated, and there is a growing concern about cell senescence in brain post-mitotic cells. Many evidence demonstrated that terminally differentiated neurons show some phenotypes similar to senescence, such as cell cycle arrest, SA-β-gal activity, lipofuscin, DNA damage response, and activation of SASP both *in vitro* and *in vivo* (Wong et al., 2009; Geng et al., 2010; Jurk et al., 2012; Ota et al., 2012; Kang et al., 2015; Forero et al., 2016; Rocchi et al., 2021). Therefore, preventing neuronal cells from senescence might be beneficial in the prevention and treatment of age-related neurodegenerative disorders, such as AD.

Sirtuins family, as NAD^+-dependent deacetylases, plays the important roles in delaying cellular aging and extending the life cycle of organs through various complex cellular signaling regulation (Satoh et al., 2011; Zhao et al., 2020). Among the mammalian sirtuins, SIRT1 is widely recognized as a regulator of cellular and organismal processes, including gene regulation, genome stability maintenance, metabolism, autophagy, senescence, and tumorigenesis (Oberdoerffer et al., 2008; Zhang and Kraus, 2010; Xu J. et al., 2018; Xu et al., 2020). An increasing number of evidence suggests that elevated SIRT1 has beneficial effects on aging-related diseases. SIRT1 is involved in protecting endothelial cells from stress-induced premature senescence and replicative senescence (Ota et al., 2007; Zu et al., 2010; Wan et al., 2014). Also, knockdown of SIRT1 induced cell senescence and inhibited cell proliferation in young mesenchymal stem cells (hMSCs) while overexpression of SIRT1 resulted in delayed senescence in primary human lung fibroblasts and aged MSCs (Huang et al., 2008; Chen et al., 2014; Pi et al., 2021). However, whether SIRT1 can regulate human neuronal senescence and counteract Aβ-induced neuronal senescence is not well established. Aspirin, a widely used cardiovascular drug, was shown to reduce endothelial cell senescence and ameliorate doxorubicin-induced cell senescence in human and mouse fibroblasts (Bode-Böger et al., 2005; Feng et al., 2019), whereas the effect of aspirin on neuronal cell senescence is unknown in AD. In this study, we found that Aβ accelerated cell senescence in SK-N-SH cells, SH-SY5Y cells, and NSC-derived neuronal cells. Stimulation of neuronal cells with Aβ induced the reduction of SIRT1, and the exogeneous expression of SIRT1 could significantly alleviate Aβ-induced cell senescence, indicating Aβ-induced neuronal senescence through downregulation of SIRT1. To our surprise, we found aspirin could partially prevent human neuronal cell senescence by upregulating SIRT1.

MATERIALS AND METHODS

Cell Culture

SK-N-SH cells and SH-SY5Y cells were purchased from ATCC. SK-N-SH cell line was cultured in modified Eagle's medium (MEM), and SH-SY5Y cell line was cultured in MEM/F12 Medium, with 10% fetal bovine serum (FBS) and 100 U/ml penicillin and 0.1 mg/ml streptomycin in a humidified incubator with 5% CO2/95% air (v/v) at 37°C.

Human Neural Stem Cell Differentiation

Human induced pluripotent stem cell (iPSC)-derived NSCs (IxCell Biotechnology, Ltd.) were maintained as adherent culture in the medium, containing 50% Dulbecco's modified Eagle medium: nutrient mixture F-12 (DMEM/F12, Gibco), 50% neurobasal (Gibco), 1*N2 supplement (Gibco), 1*B27 supplement (Gibco), 1*MEM non-essential amino acids solution, 1*GlutaMAX (Gibco), 10 ng/μl bFGF, 10 ng/μl hlif, 3 μM CHIR99021 (Selleckchem), 5 μM SB431542 (Selleckchem), and 200 μM ascorbic acid (Sigma) and cultured in a humidified incubator with 5% CO2/95% air (v/v) at 37°C. For differentiation, the human NSCs were seeded in 24-well plates coated by poly-D-lysine and laminin, at the density of $5*10^4$ cells per well. On the second day, medium was changed to neuron differentiation medium, neurobasal with 1*B27, 1*CultureOne supplement (ThermoFisher Scientific), 1*GlutaMAX, and 200 μM ascorbic acid. The differential medium was refreshed every other day (Lu et al., 2019). At the day 12 of differentiation, cells were treated by Aβ for 48 h.

Plasmid Construction, Transfection, and siRNA

SIRT1 cDNA was generated from pCMV-SIRT1-t1-Flag (purchased from Sino Biological) *via* PCR amplification and then cloned into the FuGW vector by using Seamless Cloning Kit (Beyotime, D7010M) according to the manufacturer's instructions and confirmed by DNA sequencing. Cells were transfected with constructed SIRT1 plasmid using lipofectamine 3000 (ThermoFisher Scientific, L3000001). After transfection for 24 h, cells were stimulated by Aβ. The knockdown of SIRT1 was performed by the transfection with specific siRNA (Tsingke Biotechnology Co., Ltd.) using lipofectamine 3000.

The cloning primers were as follows:

Forward, TGGGCTGCAGGTCGACTCTAGAATGGCAGATGAAGCAGCTCTC;

Reverse, TTGATATCGAATTCTAGACTATGATTTGTTTGATGGATAGTTCATGTCT;

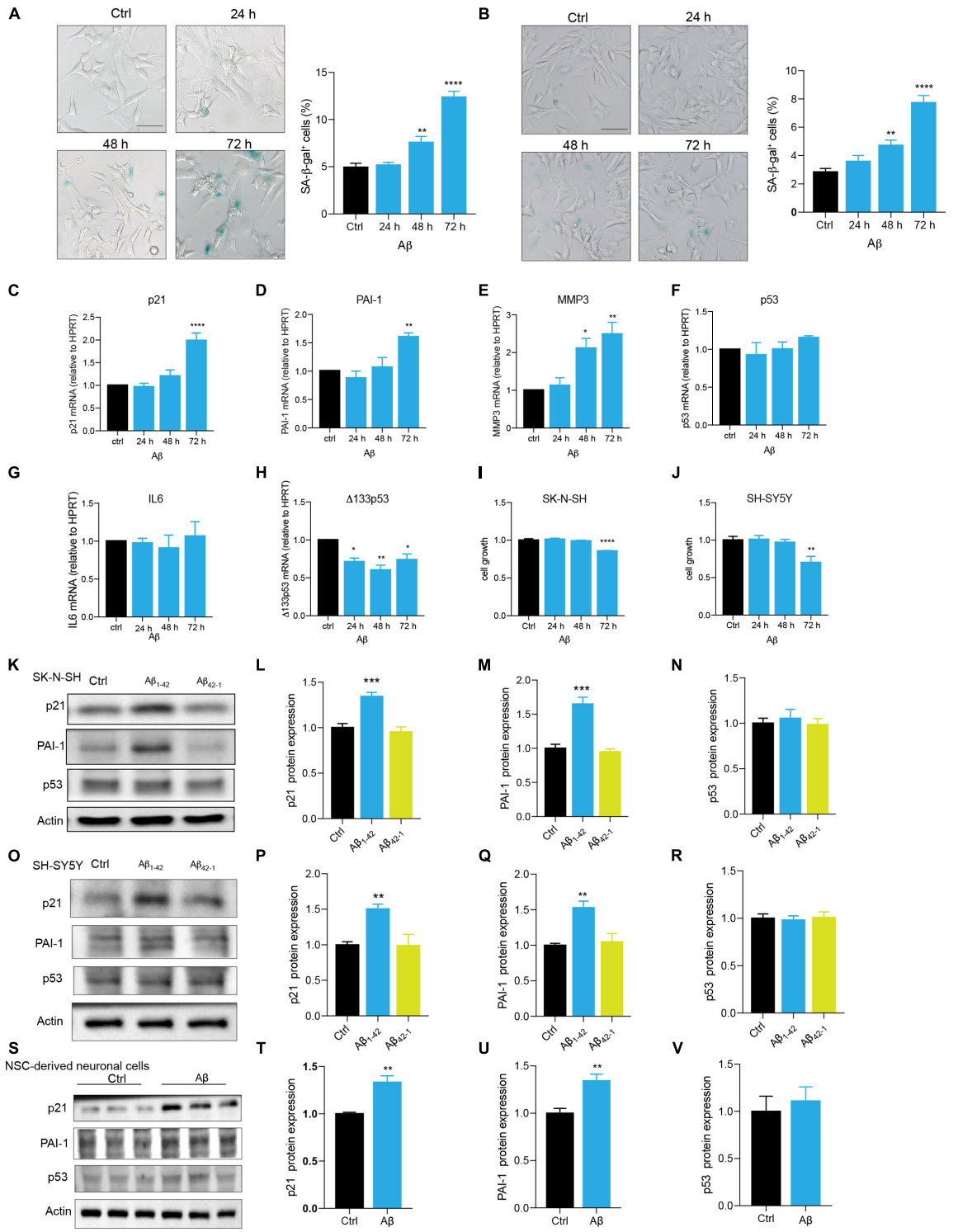

FIGURE 1 | Aβ accelerated cell senescence in human neuronal cells. **(A)** The representative images of SA-β-gal staining in SK-N-SH cells treated by Aβ (5 μM) at indicated time, and quantification of relative number of SA-β-gal-positive cells. The images were captured by Olympus IX73. Scale bars, 50 μm. **(B)** The representative images of SA-β-gal staining in SH-SY5Y cells challenged by Aβ (5 μM) at indicated time, and quantification of relative number of SA-β-gal-positive cells. The images were captured by Olympus IX73. Scale bars, 50 μm. **(C-H)** p21 **(C)**, PAI-1 **(D)**, MMP3 **(E)**, p53 **(F)**, IL6 **(G)**, Δ133p53 **(H)** mRNA levels were measured after treatment with Aβ (5 μM) at indicated time. **(I-J)** Cell growth was detected by luminescent cell viability assay in SK-N-SH cells **(I)** and SH-SY5Y cells **(J)** challenged by Aβ (5 μm) at indicated time. **(K-N)** Cells were incubated with $Aβ_{1-42}$ (5 μM) or $Aβ_{42-1}$ (5 μM) for 72 h in SK-N-SH cells, and cell lysates were prepared and analyzed using western blotting with p21, PAI-1, p53 antibody. Actin was used as a loading control.

(Continued)

FIGURE 1 | Quantification of relative p21 **(L)**, PAI-1 **(M)**, p53 **(N)** protein level in **(K)**. **(O-R)** Cells were incubated with $A\beta_{1-42}$ (5 μM) or $A\beta_{42-1}$ (5 μM) for 72 h in SH-SY5Y cells, and cell lysates were prepared and analyzed using western blotting with p21, PAI-1, and p53 antibody. Actin was used as a loading control. Quantification of relative p21 **(P)**, PAI-1 **(Q)**, p53 **(R)** protein level in **(O)**. **(S-V)** Cells were incubated with Aβ (5 μM) for 48 h in NSC-derived neuronal cells, and cell lysates were prepared and analyzed using western blotting with p21, PAI-1, and p53 antibody. Actin was used as a loading control. Quantification of relative p21 **(T)**, PAI-1 **(U)**, p53 **(V)** protein level in **(S)**. The data are presented as mean ± SEM, $n \geq 3$ independent experiments, $^{*}p < 0.05$, $^{**}p < 0.01$, $^{***}p < 0.001$, and $^{****}p < 0.0001$, analyzed by one-way ANOVA followed by Bonferroni test or unpaired Student's *t*-test (two-tailed).

The siRNA primers were as follows:
siSIRT1-1: Forward, CACCUGAGUUGGAUGAUAUTT;
siSIRT1-1: Reverse, AUAUCAUCCAACUCAGGUGTT;
siSIRT1-2: Forward, GUCUGUUUCAUGUGGAAUATT;
siSIRT1-2: Reverse, UAUUCCACAUGAAACAGACTT;

$A\beta_{42}$ Oligomer Preparation

$A\beta_{42}$ oligomers (Aβ) were prepared according to the previous publications (Li et al., 2020). In brief, 2 mg $A\beta_{42}$ peptides (CHINESE PEPTIDE, AMYD-003) dissolved in 2 ml cold hexafluoroisopropanol (HFIP) (Sigma) were dispensed into Protein LoBind tubes (Eppendorf, 030108094) and dried overnight at room temperature (RT). HFIP-treated $A\beta_{42}$ peptides were resuspended in dimethyl sulfoxide (DMSO) and diluted in phenol-red free DMEM/F12 medium to obtain a 100 μM stock solution. The diluted $A\beta_{42}$ peptides were vortexed for 15 s followed by incubation for 24 h at 4°C.

Cell Growth

SK-N-SH or SH-SY5Y cells were seeded in a 96-well plate at $1 * 10^4$ cells/well. The cells were treated with Aβ or aspirin at the indicated time. After the treatment for 72 h, cell viability was detected using luminescent cell viability assay (Vazyme, DD1101-02), following the manufacturer's guideline, and then were measured by BioTek SynergyNEO (BioTek, United States).

Long-Range PCR Lesion Assay

Genomic DNA was extracted from SK-N-SH or SH-SY5Y cells treated by Aβ for 72 h using TIANamp Genomic DNA kit (Tiangen, DP304-03), according to the manufacturer's instruction. The samples were quantified with Nanodrop (Gene Company Limited) and then diluted to 5 ng/μl. About 20 ng DNA as the template was used for quantitative PCR-based amplification nuclear DNA segment using TaKaRa LA Taq DNA Polymerase (TaKaRa LA). A small segment, 175-bp was amplified using 2*Taq PCR Master Mix (Tiangen) as an inner control.

The primers used are as follows:
12.2 kb Forward, CATGTCACCACTGGACTCTGCAC;
12.2 kb Reverse, CCTGGAGTAGGAACAAAAATTGCTG;
13.5 kb Forward, CGAGTAAGAGACCATTGTGGCAG;
13.5 kb Reverse, GCACTGGCTTTAGGAGTTGGACT;
175 bp Forward, GGGATAACATCCAGGGCATT;
175 bp Reverse, CCCTGACGTTTTAGGGCATA;

Senescence-Associated -β-Galactosidase (SA-β-Gal) Staining Assay

SA-β-gal staining of SK-N-SH or SH-SY5Y cells was performed as previously reported (Li et al., 2020). Cells were treated by Aβ or pre-incubated aspirin for 6 h with EX727 or without, followed by Aβ challenge for 72 h. Briefly, after treatment, cells were washed two times with phosphate buffer solution (PBS), and then stained using Senescence β-Galactosidase Staining Kit for 12 h according to the manufacturer's guideline (Beyotime, C0602). Images were captured with Olympus IX73 microscope. The numbers of SA-β-gal-positive cells were measured with Fiji.

Reverse Transfection and Quantitative Real-Time PCR

After treatment with Aβ at the indicated time, cells were harvested and total RNAs were isolated using an EZ-press RNA purification kit (EZBioscience, B0004D) according to the manufacturer's instructions. Reverse transfection was performed using PrimeScript RT Master Mix (Takara, RR036) under the following conditions: 37°C, 15 min and 85°C, 15 s. Then, gene transcripts were analyzed by quantitative real-time PCR conducted with 2x HotStart SYBR Green qPCR Master Mix (ExCell Bio, MB000-3013) on a Stratagene Mx3000P (Agilent Technologies). The reaction parameters were as follows: 95°C for 10 min; 95°C for 30 s, 40 cycles; 60°C for 30 s; and 72°C for 30 s. An additional cycle was performed for evaluation of primer's dissociation curve: 95°C for 1 min, 60°C for 30 s, and 95°C for 30 s. Each cDNA sample was amplified two times.

The primer sequences used were as follows:
p21-Forward, CGATGGAACTTCGACTTTGTCA;
p21-Reverse, GCACAAGGGTACAAGACAGTG;
PAI-1-Forward, ACCGCAACGTGGTTTTCTCA;
PAI-1-Reverse, TTGAATCCCATAGCTGCTTGAAT;
MMP3-Forward, CTGCTGTTGAGAAAGCTCTG;
MMP3-Reverse, AATTGGTCCCTGTTGTATCCT;
p53-Forward, CCCCTCCTGGCCCCTGTCATCTTC;
p53-Reverse, GCAGCGCCTCACAACCTCCGTCAT;
Δ133p53-Forward, TGACTTTCAACTCTGTCTCCTTCCT;
Δ133p53- Reverse, GGCCAGACCATCGCTATCTG;
IL6-Forward, GTGGCTGCAGGACATGACAA;
IL6-Reverse, TGAGGTGCCCATGCTACATTT;
HPRT-Forward, CCTGGCGTCGTGATTAGTGAT;
HPRT-Reverse, AGACGTTCAGTCCTGTCCATAA;

Immunofluorescence Staining

Immunostaining was performed as previously described with minor modification (Gao et al., 2019). Cells were treated by Aβ or pre-incubated aspirin for 6 h followed by Aβ challenge for 72 h. Briefly, cells for immunostaining were washed two times with PBS and fixed with 4% PFA for 15 min at RT. Then, cells were treated with permeabilization and blocking buffer (1% BSA and 0.3% Triton-X 100 in PBS) for 1 h at RT. Primary antibodies diluted in buffer (1% BSA and 0.3%

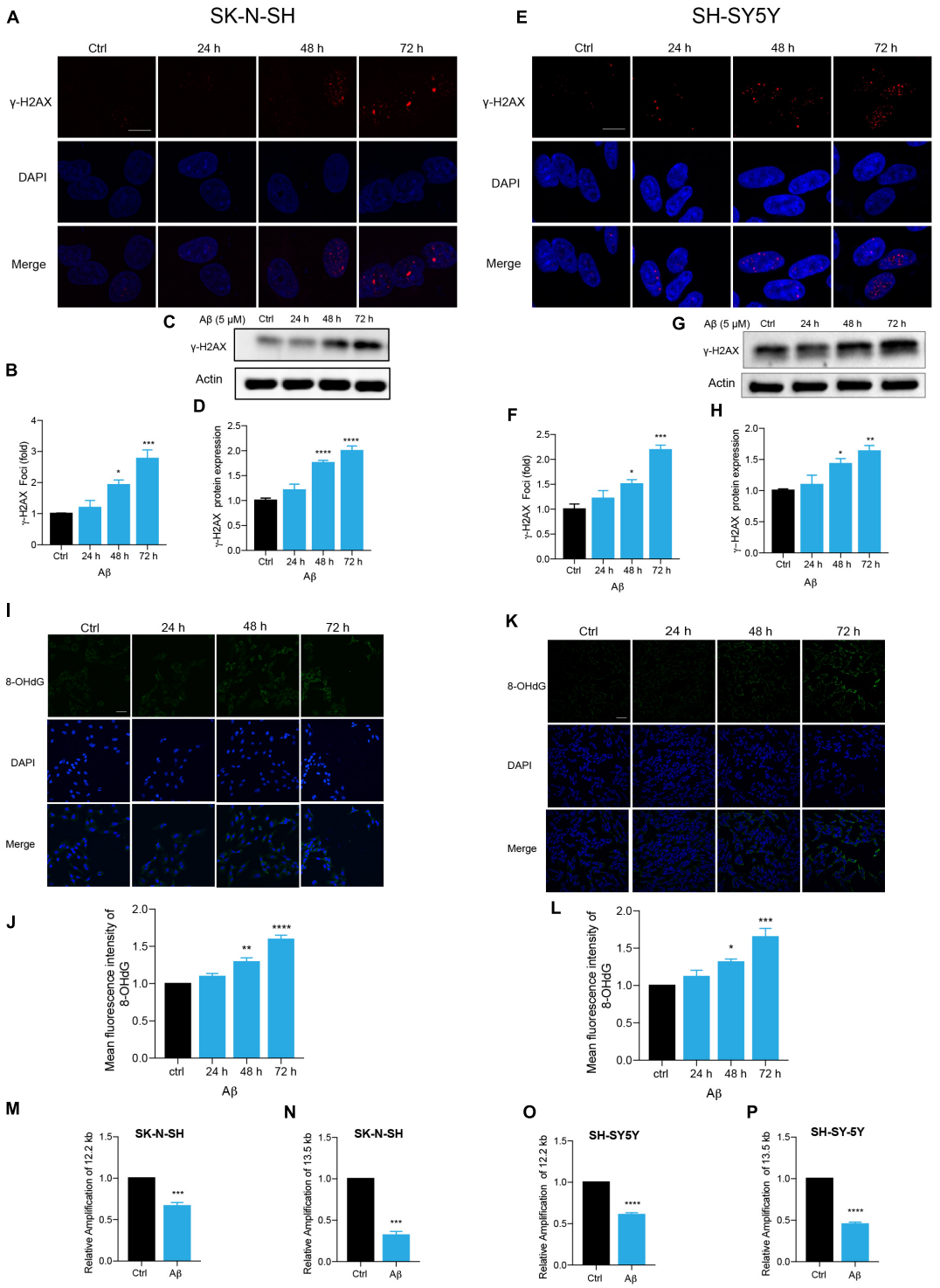

FIGURE 2 | Aβ induced senescence-associated DNA damage in human neuronal cells. **(A,B)** Representative images of DAPI and γ-H2AX fluorescent staining in Aβ (5 μM)-treated SK-N-SH cells at 24, 48, and 72 h. The quantificative analysis of γ-H2AX foci number in **(B)**. The pictures were captured by Leica TCS SP8 WLL. Scale bar, 10 μm. **(C,D)** Cells were incubated with Aβ for indicated time in SK-N-SH cells and western blot analysis of γ-H2AX protein in cell lysates **(C)**. Actin was used as a loading control. Quantification of γ-H2AX protein level in SK-N-SH cells **(D)**. **(E,F)** Representative images of DAPI and γ-H2AX fluorescent staining in Aβ-treated SH-SY5Y cells at 24, 48, and 72 h. The quantificative analysis of γ-H2AX foci number in SK-N-SH cells **(F)**. The pictures were captured by Leica TCS SP8 WLL. Scale bar, 10 μm. **(G,H)** Cells were incubated with Aβ for indicated time in SH-SY5Y cells, and western blot analysis of γ-H2AX protein in cell lysates **(G)**. Actin was used as a loading control. Quantification of γ-H2AX protein level **(H)**. **(I,J)** Representative images of 8-OHdG staining in SK-N-SH cells treated by Aβ (5 μM) at indicated time **(I)**. The quantification of 8-OHdG fluorescent intensity **(J)**. The pictures were obtained by Leica TCS SP8 WLL. Scale bar, 50 μm.

(Continued)

FIGURE 2 | (K,L) Representative images of 8-OHdG staining in SH-SY5Y cells treated by Aβ (5 μM) at indicated time **(K)**. The quantification of 8-OHdG fluorescent intensity **(L)**. The pictures were obtained by Leica TCS SP8 WLL. Scale bar, 50 μm. **(M,N)** Long-range PCR base-assessment of nDNA (12.2 kb) **(M)** and nDNA (13.5 kb) **(N)** damage in SK-N-SH cells incubated with Aβ (5 μM) for 72 h. 175 bp as inner control. **(O,P)** Long-range PCR base assessment of nDNA (12.2 kb) **(O)** and nDNA (13.5 kb) **(P)** damage in SH-SY5Y cells incubated with Aβ (5 μM) for 72 h. 175 bp as an inner control. The data are presented as mean ± SEM, $n \geq 3$ independent experiments, $^{*}p < 0.05$, $^{**}p < 0.01$, $^{***}p < 0.001$, and $^{****}p < 0.0001$, analyzed by one-way ANOVA followed by Bonferroni test or unpaired Student's *t*-test (two-tailed).

Triton-X 100 in PBS) were incubated overnight at 4°C. Cells were washed at least three times with PBS and incubated with fluorescent-dye conjugated secondary antibodies at RT for 1h, followed by incubation with DAPI (1:3000, Beyotime) for 15 min. Slides were mounted and images were captured with Leica TCS SP8 WLL microscope (Leica, German). Antibodies used for immunofluorescence analysis are as follows: anti-γ-H2AX (1:800, CST), anti-8-OHdG (1:1000, Rockland), anti-Tuj-1 (1:500, Abcam), and anti-Sox2 (1:200, R&D, system).

Western Blot

Western blot was performed following previous publications with minor modification. After cells were incubated with indicated treatment, total cell lysates were separated by 12% sodium dodecyl sulfate-polyacrylamide gel electrophoresis (SDS-PAGE) and transferred onto nitrocellulose membranes (400 mA constant current, 2 h, 4°C). Membranes were blocked with 5% non-fat milk in TBS containing 0.1% Tween-20 for 45 min at RT. Subsequently, membranes were treated with antibodies. Antibodies were used as follows: anti-p21 (1:1000, CST, 2947S), anti-PAI-1 (1:1000, CST, 11907), anti-p53 (1:1000, CST, 2527), anti-γ-H2AX (1:1000, CST, 9718), anti-SIRT1 (1:1000, CST, 8469), anti-SIRT5 (1:1000, Proteintech, 15122-1-AP), and actin (1:1000, Sigma, A2066).

Statistical Analysis

All data were analyzed using Prism 8.0. All quantified data were presented as mean ± SEM. Unpaired Student's *t*-test (two-tailed) was applied for the comparisons of two datasets and one-way or two-way analysis of variance (ANOVA) with Bonferroni's *post*-test was used where more than two datasets or groups were compared. Statistical significance was accepted at $p < 0.05$.

RESULTS

Aβ Accelerated Cell Senescence in Human Neuronal Cells

Neuronal cell senescence was examined by the detection of SA-β-gal activity, cell cycle arrest characterized by upregulation of p16, p21, and p53, PAI-1 expression, and SASP-related MMP3 and IL6. Compared with control, Aβ treatment significantly increased SA-β-gal-positive cells in dose- and time-dependent manners (**Supplementary Figures 1A,B** and **Figure 1A**) in SK-N-SH cells. This time dependence was consistently observed in another human neuronal cell line, SH-SY5Y cells (**Figure 1B**). Here, treatment with Aβ obviously upregulated the mRNA levels of cell senescence markers, p21 (**Figure 1C**), PAI-1 (**Figure 1D**), and MMP3 (**Figure 1E**), but not IL6 (**Figure 1G**). Although there was no change in p53 mRNA level (**Figure 1F**), Δ133p53, the isoform of p53, was markedly declined (**Figure 1H**). To further confirm, we detected the protein expression of the main cell senescence markers, p21, PAI-1, and p53 after the treatment with Aβ for 72 h. Consistent with mRNA results, Aβ significantly induced p21 and PAI-1 protein expression, but not p53 in SK-N-SH cells (**Figures 1K-N**) and SH-SY5Y cells (**Figures 1O-R**). By contrast, $A\beta_{42-1}$, as a negative control, had no obvious effect (**Figures 1K-R**). To examine this in a more relevant cell model, we differentiated NSC to neuronal cells (**Supplementary Figure 1C**), and as expected, Aβ increased the expression of cell senescence genes in SK-N-SH cells, SH-SY5Y cells, and NSC-derived neuronal cells (**Figures 1S-V**). The effect of Aβ treatment on cell growth was also detected and data showed that Aβ significantly decreased cell number at 72h in SK-N-SH cells (**Figure 1I**) and SH-SY5Y cells (**Figure 1J**). These findings revealed that Aβ is sufficient to accelerate human neuronal cell senescence.

Aβ Induced Senescence-Associated DNA Damage in Human Neuronal Cells

Persistent DDR is a characteristic feature of senescent cells (von Zglinicki et al., 2005; Chen et al., 2007; d'Adda di Fagagna, 2008; Kumari and Jat, 2021). DNA double-strand break (DSB) is the most dangerous type of DNA damage, and phosphorylation of H2AX, called γ-H2AX, in the position of Ser139 occurs in response to DSB formation (Mah et al., 2010, Podhorecka et al., 2010). Here, immunostaining of γ-H2AX presented increased DNA damage foci numbers by Aβ treatment in SK-N-SH cells (**Figures 2A,B**). Meanwhile, an increased protein expression of γ-H2AX was detected after Aβ treatment (**Figures 2C,D**). The location and expression of γ-H2AX were further verified in SH-SY5Y by immunostaining (**Figures 2E,F**) and western blot analysis (**Figures 2G,H**) and in NSC-derived neuronal cells by western blot (**Supplementary Figures 2A,B**). Oxidative DNA damage was evaluated by immunostaining of 8-hydroxy-2'deoxyguanosine (8-OHdG), a major oxidative DNA adduct involved in senescence and many disease processes (Nakae et al., 2000). The results revealed that Aβ markedly increased fluorescence intensity of 8-OHdG in SK-N-SH (**Figures 2I,J**) and SH-SY5Y cells (**Figures 2K,L**). Genomic DNA damage was then evaluated by long-range PCR lesion assay. A large nuclear segment is amplified with an efficiency that can be declined by the lesions of the DNA template. The results showed that Aβ significantly reduced the relative amplification of nuclear (12.2 and 13.5 kb) genomic DNA in SK-N-SH (**Figures 2M,N**) and SH-SY5Y cells (**Figures 2O,P**). The results were further confirmed by agarose gel electrophoresis (**Supplementary Figure 2C**). To sum up, these results suggested that Aβ accelerated DNA damage in human neuronal cells, which might contribute to cell senescence.

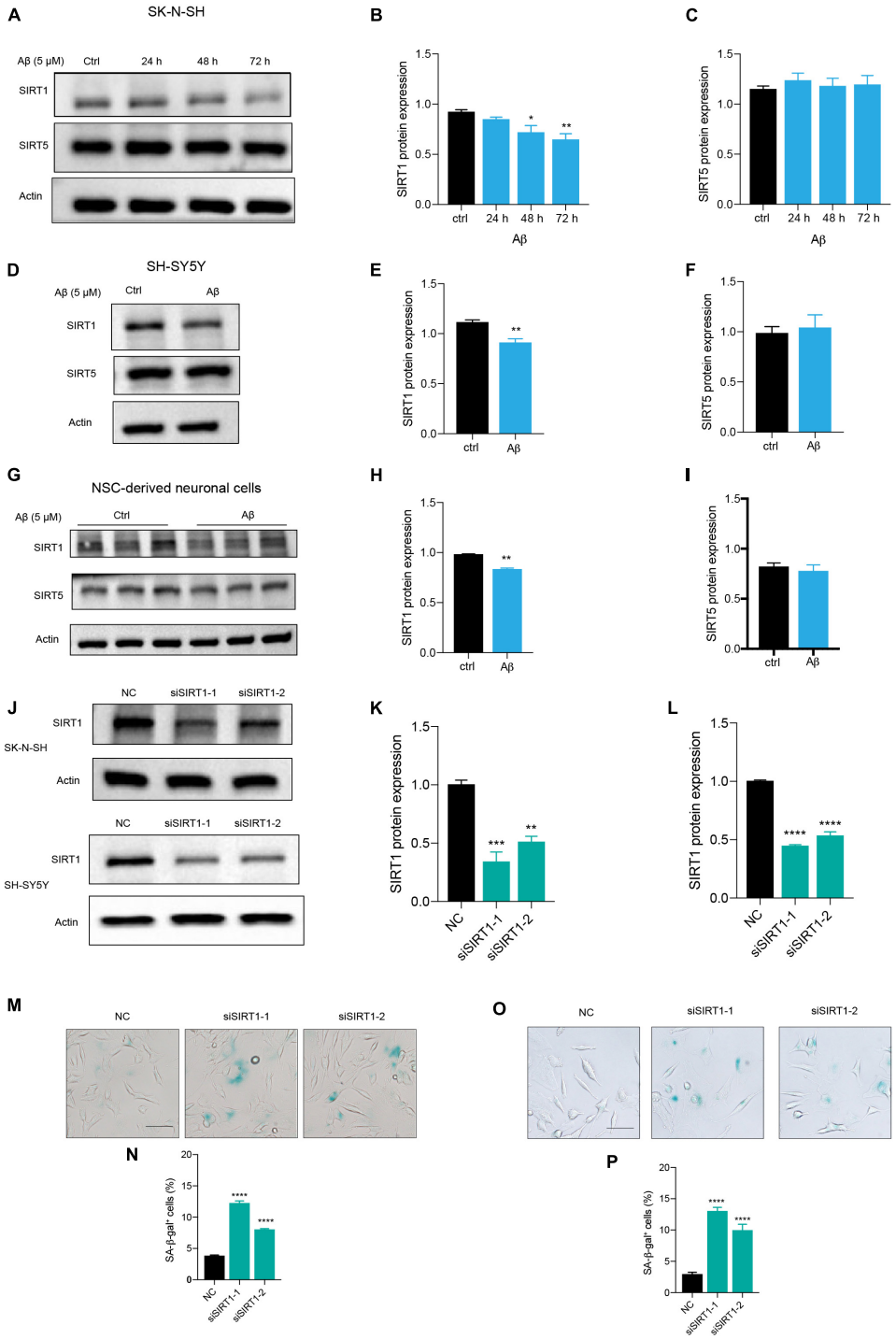

FIGURE 3 | Aβ induced neuronal cell senescence through suppressing SIRT1 expression. **(A)** Cells were incubated with Aβ for 24, 48, and 72 h in SK-N-SH cells, and cell lysates were prepared and analyzed using western blotting with SIRT1 and SIRT5 antibody. Actin was used as a loading control. **(B,C)** Quantification SIRT1 **(B)** and SIRT5 **(C)** protein level in **(A)**. **(D)** Cells were challenged with Aβ for 72 h in SH-SY5Y cells, western blot analysis of SIRT1 and SIRT5 protein. Actin was used as a loading control. **(E,F)** Quantification SIRT1 **(E)** and SIRT5 **(F)** protein level in **(D)**. **(G)** Cells were treated with Aβ for 48 h in NSC-derived neuronal cells and western blot analysis of SIRT1 and SIRT5. Actin was used as a loading control. **(H,I)** Quantification SIRT1 **(H)** and SIRT5 **(I)** protein level in **(G)**. **(J)** Cells were transfected with negative control (NC), siSIRT1-1, siSIRT1-2 in SK-N-SH and SH-SY5Y cells, and harvested after 72 h. Western blot analysis of SIRT1 protein level. Actin was used as a loading control. **(K,L)** Quantification of SIRT1 protein level in SK-N-SH cells **(K)** and in SH-SY5Y cells **(L)**. **(M,N)** The representative images of SA-β-gal staining in SK-N-SH cells transfected with siSIRT1 and stained after 72 h in **(M)**. The quantification analysis of SA-β-gal-positive cells in **(N)**. **(O,P)** The representative images of SA-β-gal staining in SH-SY5Y cells transfected with siSIRT1 and treated for 72 h in **(O)**. The quantification analysis of SA-β-gal-positive cells in **(P)**. The data are presented as mean ± SEM, $n \geq 3$ independent experiments, $^{*}p < 0.05$, $^{**}p < 0.01$, $^{***}p < 0.001$, and $^{****}p < 0.0001$, analyzed by one-way ANOVA followed by Bonferroni test or unpaired Student's *t*-test (two-tailed).

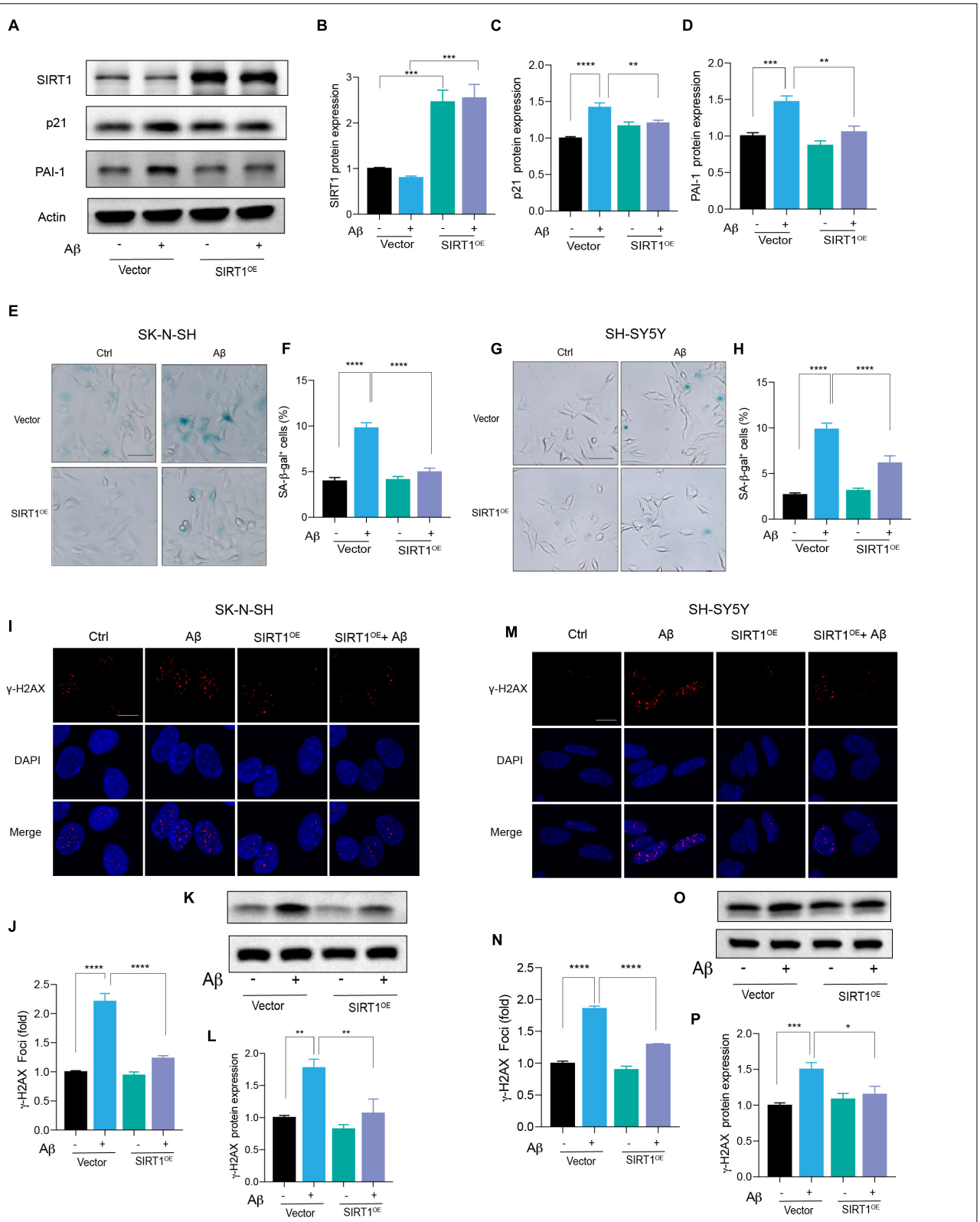

FIGURE 4 | Exogenous expression of SIRT1 rescued Aβ-induced cell senescence. **(A)** Cells were transfected with Vector and SIRT1 plasmid in SK-N-SH cells, and after 24 h transfection, cells were incubated with Aβ or without for another 72 h. Western blot analysis of SIRT1, p21, PAI-1 protein level. Actin was used a loading control. **(B-D)** Quantification of SIRT1 **(B)**, p21 **(C)**, and PAI-1 **(D)** protein level in (A). **(E,F)** The representative images of SA-β-gal staining in SK-N-SH cells treated with Aβ or without for 72 h, after transfected with Vector and SIRT1 plasmid for 24 h **(E)**. Quantification of relative number of SA-β-gal-positive cells in **(F)**. The

(Continued)

FIGURE 4 | pictures were obtained by Olympus IX73. Scale bar, 50 μm. **(G,H)** The representative images of SA-β-gal staining in SH-SY5Y cells incubated with Aβ or without for 72 h, after transfected with Vector and SIRT1 for 24 h **(G)**. Quantification of relative number of SA-β-gal-positive cells in **(H)**. The pictures were obtained by Olympus IX73. Scale bar, 50 μm. **(I-J)** Representative images of DAPI and γ-H2AX fluorescent staining in SK-N-SH cells transfected with SIRT1 plasmid for 24 h and then incubated with Aβ or without for another 72 h in **(I)**. The quantification of relative γ-H2AX foci number in SK-N-SH cells in **(J)**. **(K,L)** Western blot analysis of γ-H2AX protein in SK-N-SH cells transfected with SIRT1 plasmid for 24 h and then incubated with Aβ or without for another 72 h **(K)**. The quantification of γ-H2AX protein level in **(L)**. **(M,N)** Representative images of DAPI and γ-H2AX in SH-SY5Y cells transfected with SIRT1 plasmid for 24 h and followed with Aβ or without for another 72 h in **(M)**. The quantification of relative γ-H2AX foci number in **(N)**. **(O,P)** Western blot analysis of γ-H2AX protein in SH-SY5Y cells transfected with SIRT1 plasmid for 24 h and followed with Aβ or without for another 72 h **(O)**. The quantification of γ-H2AX protein level in **(P)**. The data are presented as mean ± SEM, n ≥ 3 independent experiments, $^{*}p < 0.05$, $^{**}p < 0.01$, $^{***}p < 0.001$, and $^{****}p < 0.0001$, analyzed by one-way ANOVA followed by Bonferroni test.

Aβ Induced Neuronal Cell Senescence Through Suppressing SIRT1 Expression

Among the sirtuins, we found that Aβ declined SIRT1, SIRT3, and SIRT6 protein levels in human neuronal cells, but the downregulation of SIRT1 is mostly remarkable (data not shown). The protein level of SIRT1 was significantly reduced after Aβ stimulation in a time-dependent manner, compared to the control in SK-N-SH cells (**Figures 3A,B**). By contrast, the SIRT5 expression was not changed (**Figures 3A,C**). The same results were obtained in SH-SY5Y cells (**Figures 3D,E,F**) and NSC-derived neuronal cells (**Figures 3G,H,I**). To further elucidate whether downregulation of SIRT1 plays a role in human neuronal cell senescence, we tested whether loss of SIRT1 expression increased senescence process of neuronal cells by the application of siRNA that specifically targets its transcript. Transfection of SK-N-SH cells with siSIRT1-1 or siSIRT1-2 successfully downregulated protein level of SIRT1 assessed by western blot (**Figures 3J,K**). This was consistently observed in SH-SY5Y cells (**Figures 3J,L**). The knockdown of SIRT1 resulted in a remarkable increase in the percentage of SA-β-gal-positive cells in SK-N-SH (**Figures 3M,N**) and SH-SY5Y cells (**Figures 3O,P**). These findings suggested that SIRT1 may be involved in human neuronal senescence and Aβ accelerated neuronal senescence by modulating SIRT1.

Exogenous Expression of SIRT1 Rescued Aβ-Induced Cell Senescence

Based on the above results, we suspected that the introduction of SIRT1 in human neuronal cells could alleviate Aβ-induced cell senescence. Therefore, the SIRT1 plasmid was constructed and transfected into neuronal cells. The successful overexpression of SIRT1 protein was confirmed by western blot (**Figures 4A,B**). The upregulation of SIRT1 significantly decreased p21 protein level under stimulation with Aβ (**Figures 4A,C**). Particularly, exogeneous SIRT1 almost rescued the Aβ-reduced PAI-1 protein levels to the untreated control (**Figures 4A,D**). Additionally, the number of SA-β-gal-positive cells in Aβ-treated neuronal cells was remarkably declined by SIRT1 overexpression. The results were verified in both SK-N-SH (**Figures 4E,F**) and SH-SY5Y (**Figures 4G,H**) cells. Finally, we assessed the effect of SIRT1 overexpression on Aβ-induced DNA damage response. The number of γ-H2AX foci was obviously decreased detected by immunofluorescence, and the protein level of γ-H2AX was also declined examined by western blot both in SK-N-SH (**Figures 4I-L**) and SH-SY5Y cells (**Figures 4M-P**). These results revealed that overexpression of SIRT1 can alleviate Aβ-induced cell senescence and senescence-associated DNA damage in human neuronal cells.

Aspirin Upregulated SIRT1 to Alleviate Aβ-Induced Senescence

Small-scale screening was used to find compounds that can slow cell senescence in human neuronal cells. To our surprise, aspirin, a widely used cardiovascular drug, inhibited Aβ-induced cell senescence. First, we found that aspirin which had no effect on cell viability at indicated dosage (**Supplementary Figure 2D**), dose-dependently declined the protein levels of p21 and PAI-1 in Aβ-treated neuronal cells (**Figures 5A,C,D**). Aspirin also increased SIRT1 protein expression in a dosage-dependent manner (**Figures 5A,B**). Next, we observed that the number of SA-β-gal-positive cells in Aβ-treated neuronal cells was remarkably declined by the pre-treatment with aspirin (**Figures 5E,F**). In addition, aspirin significantly decreased the proportion of γ-H2AX foci (**Figures 5G,H**) and the protein expression of γ-H2AX (**Figures 5I,J**). To verify whether the upregulation of SIRT1 is involved in the protective effect of aspirin on cell senescence and DNA damage, we introduced a SIRT1 inhibitor, EX527. Aspirin reduced Aβ-increased SA-β-gal-positive cells, and this effect was blocked when EX527 was applied with aspirin (**Figures 5K,L**). Finally, the result of aspirin on DNA damage was also confirmed in SH-SY5Ycells (**Figures 5M,N**). These finding suggested that aspirin could suppress Aβ-induced cell senescence and DNA damage in neuronal cells partially depending on the upregulation of SIRT1.

DISCUSSION

Cell senescence plays an important role in the development of many age-related diseases, such as AD. Increased senescent cells are found in the brains of AD mouse models and patients with AD with high expression of Aβ and tau protein (Kritsilis et al., 2018). Some *in vitro* studies have also shown that Aβ could induce astrocytes, microglia, and endothelial cell senescence (Bhat et al., 2012; Caldeira et al., 2017; Singh Angom et al., 2019). For the neuronal cells, there are several lines of evidence demonstrated that the exposure of oligomeric Aβ accumulated p16 protein level but not induced the SA-β-gal activity in cultured mouse neuron (Wei et al., 2016), and the other two studies showed that Aβ could promote some cell senescence-associated phenotypes without the detection of DNA damage in cultured M17 neuronal cell line (Wang et al., 2021; Gu et al., 2022). In this study, we further demonstrated that Aβ is

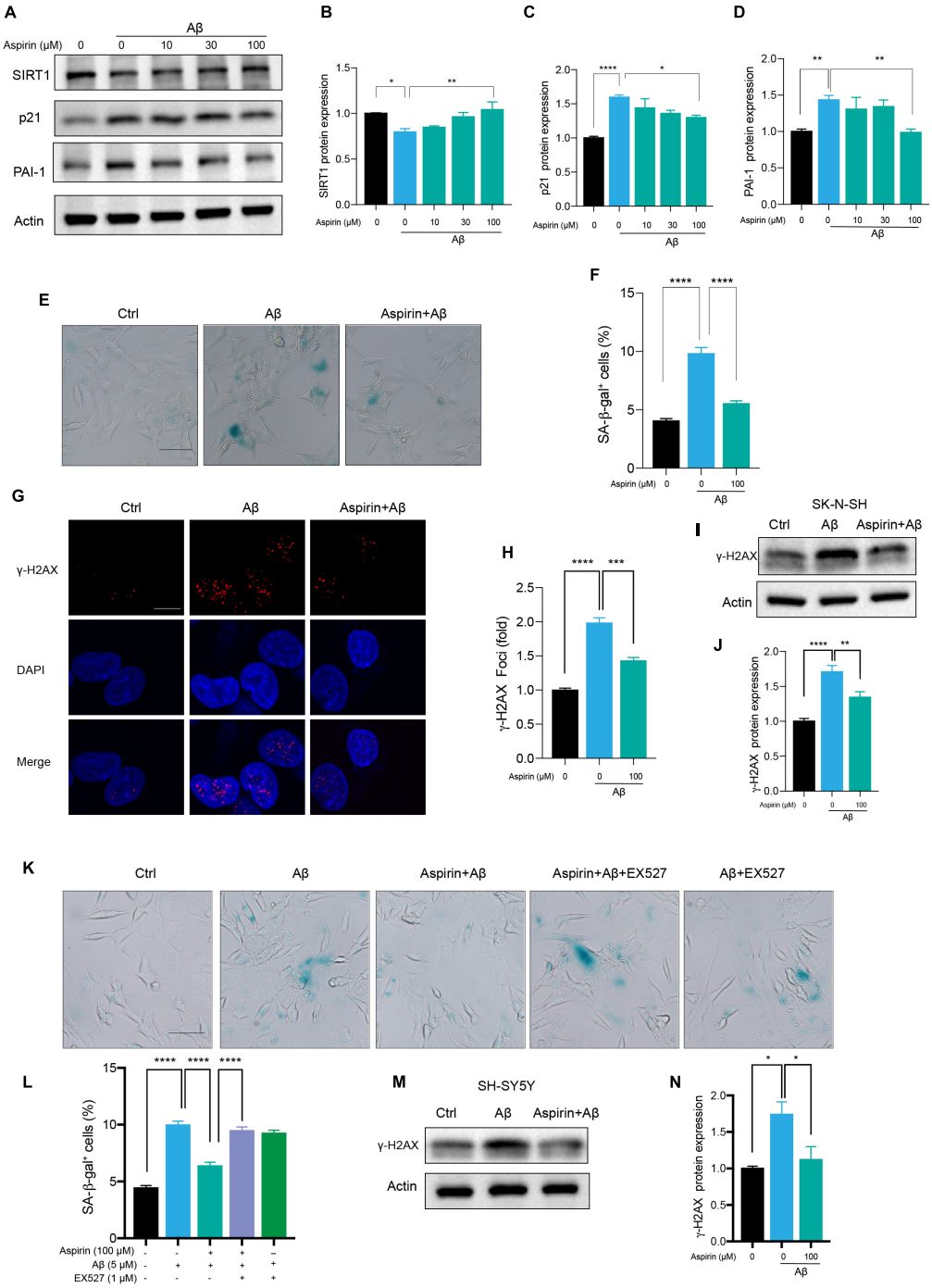

FIGURE 5 | Aspirin upregulated SIRT1 to alleviate Aβ-induced senescence. **(A)** Cells were incubated with aspirin at indicated dose for 6 h and then challenged with Aβ (5 μM) for another 72 h. Western blot analysis of SIRT1, p21, and PAI-1 protein level. Actin was used a loading control. **(B-D)** Quantification of SIRT1 **(B)**, p21 **(C)**, PAI-1 **(D)** protein level in **(A)**. **(E,F)** The representative images of SA-β-gal staining in SK-N-SH cells pre-incubated with aspirin (100 μM) for 6 h followed by Aβ (5 μM) challenge for 72 h **(E)**. The quantification of relative number of SA-β-gal-positive cells in **(F)**. The pictures were captured by Olympus IX73. Scale bars, 50 μm. **(G,H)** Representative images of γ-H2AX fluorescent staining in SK-N-SH cells pre-incubated with aspirin (100 μM) for 6 h followed by Aβ (5 μM) challenge for 72 h **(G)**. The quantification of relative γ-H2AX foci number in **(H)**. **(I,J)** Western blot analysis of γ-H2AX protein level in SK-N-SH cells pre-incubated with aspirin (100 μM) for 6 h followed by Aβ (5 μM) challenge for 72 h **(I)**. The quantification of γ-H2AX protein level in **(J)**. **(K,L)** The representative images of SA-β-gal staining in SK-N-SH cells pre-incubated with aspirin (100 μM) for 6 h with EX527 (1 μM) (SIRT1 inhibitor) or without, followed by Aβ (5 μM) challenge for 72 h **(K)**. The quantification of relative number of SA-β-gal-positive cells in **(L)**. The pictures were captured by Olympus IX73. Scale bars, 50 μm. **(M,N)** Western blot analysis of γ-H2AX protein level in SH-SY5Y cells pre-incubated with aspirin (100 μM) for 6 h followed by Aβ (5 μM) challenge for 72 h **(M)**. The quantification of γ-H2AX protein level in **(N)**. The data are presented as mean ± SEM, $n \geq 3$ independent experiments, $^{*}p < 0.05$, $^{**}p < 0.01$, $^{***}p < 0.001$, and $^{****}p < 0.0001$, analyzed by one-way ANOVA followed by Bonferroni test.

sufficient to accelerate cell senescence through upregulating p21 and PAI-1, increasing SA-β-gal-positive cells, and activating DNA damage response in multiple human neuronal cells including SK-N-SH cells, SH-SY5Y cells, and more relevant NSC-derived neuronal cells. Certainly, in addition to Aβ pathology, there are many other factors, including inflammation, tau pathology, APOE4 mutation, and mitochondrial dysfunction which may consequently trigger advanced cell senescence in the brain of patients with AD (Musi et al., 2018; Chapman et al., 2019; Guerrero et al., 2021).

The sirtuin family has beneficial effects on aging and AD. SIRT1 is widely reported to slow cell senescence in many different types of cells, including endothelial cells, fibroblast, and human mesenchymal stem cells (hMSCs) (Ota et al., 2007; Huang et al., 2008; Chen et al., 2014). Reduction of SIRT1 results in DNA damage response and cellular aging, whereas the research on human neuronal senescence and senescence-associated DNA damage has not been well documented in AD. Some chemicals have been shown to prevent Aβ-induced cell senescence through the modulation of SIRT1 (Wang et al., 2021; Gu et al., 2022) while whether SIRT1 can directly counteract Aβ effects on cellular senescence requires more investigations. Here, we found that Aβ treatment significantly declined SIRT1 protein expression in SK-N-SH cells in a time-dependent manner, and this result was consistently observed in SH-SY5Y cells and NSC-derived neuronal cells. Moreover, the reduction of SIRT1 by transfecting siRNA accelerated cell senescence, and the exogenous expression of SIRT1 reduced Aβ-induced senescence phenotypes and senescence-associated DNA damage response in both SK-N-SH and SH-SY5Y cells. These results revealed that modulating SIRT1 can regulate Aβ-induced senescence of human neuronal cells. Other than SIRT1, some other sirtuins play an essential factor in delaying cellular aging, such as SIRT3 (Diao et al., 2021) and SIRT6 (Nagai et al., 2015), and the underlying mechanism by which SIRT1 regulates Aβ-induced senescence requires further investigations.

Recent studies have reported that some clinically and preclinically used drugs, including metformin, rapamycin, resveratrol, and nicotinamide riboside (NR), have anti-aging effects. These chemicals can alleviate senescence phenotypes including the reduction of SA-β-gal, the decline of cell cycle genes, the suppression of DNA damage response, and the inhibition of inflammation through various signaling pathways. For example, metformin can reduce human cellular aging through upregulating GPx7 by Nrf2 signal pathway (Fang et al., 2018). Aspirin was observed to slower cognitive decline in patients with AD and to alleviate amyloid plaque pathology in an AD mouse model (Chandra et al., 2018; Weng et al., 2021). However, the effects on neuronal cell senescence are unknown in AD. Senolytics, a class of drugs that selectively clear senescent cells, are prevalently reported to reduce inflammation and SASP, improve tissue function, and prolong longevity (Xu M. et al., 2018; Zhang et al., 2019). These drugs can selectively induce apoptosis of senescent cells without influencing healthy cells. In our present study, we further demonstrated that aspirin reduced SA-β-gal-positive cells, p21 and PAI-1 expression, and DNA damage response partially through modulating SIRT1 in AD-associated human neuronal cells, suggesting that aspirin may be a potential drug for aging and age-related diseases. Of course, this needs to be further investigated using other methods such as gene editing.

In conclusion, this study revealed that Aβ accelerated cell senescence in multiple human neuronal cells, including SK-N-SH cells, SH-SY5Y cells, and human NSC-derived neuronal cells through downregulating SIRT1. Exogenous expression of SIRT1 rescued Aβ-induced cell senescence. In addition, aspirin reduced the levels of cell senescence markers at least partially through upregulating SIRT1, indicating that aspirin is possibly beneficial for aging-associated disorders.

DATA AVAILABILITY STATEMENT

The original contributions presented in the study are included in the article/**Supplementary Material**, further inquiries can be directed to the corresponding author/s.

ETHICS STATEMENT

This study was approved by the Institutional Ethics Committee of the Shanghai Institute of Biochemistry and Cell Biology, Chinese Academy of Sciences.

AUTHOR CONTRIBUTIONS

GP and SH supervised the project and revised the manuscript. YL designed and conducted most experiments, analyzed data, organized figures and drafted manuscript. JL provided critical technique supports and data analysis. YH revised the manuscript. All authors approved the submitted manuscript.

FUNDING

This study was supported by the National Key Research and Development Program of China (2018YFA0108003), the "Strategic Priority Research Program" of the Chinese Academy of Sciences (XDA16010309), and the National Science Foundation for Young Scientists of China (81901094).

ACKNOWLEDGMENTS

We thank Jing Lu for revising manuscript and providing technical assistance.

SUPPLEMENTARY MATERIAL

The Supplementary Material for this article can be found online at: https://www.frontiersin.org/articles/10.3389/fncel.2022.906270/full#supplementary-material

REFERENCES

Baker, D. J., and Petersen, R. C. (2018). Cellular senescence in brain aging and neurodegenerative diseases: evidence and perspectives. *J. Clin. Invest.* 128, 1208–1216. doi: 10.1172/JCI95145

Bhat, R., Crowe, E. P., Bitto, A., Moh, M., Katsetos, C. D., Garcia, F. U., et al. (2012). Astrocyte senescence as a component of Alzheimer's disease. *PLoS One* 7:e45069. doi: 10.1371/journal.pone.0045069

Bode-Böger, S. M., Martens-Lobenhoffer, J., Täger, M., Schröder, H., and Scalera, F. (2005). Aspirin reduces endothelial cell senescence. *Biochem. Biophys. Res. Commun.* 334, 1226–1232. doi: 10.1016/j.bbrc.2005.07.014

Bryant, A. G., Hu, M., Carlyle, B. C., Arnold, S. E., Frosch, M. P., Das, S., et al. (2020). Cerebrovascular Senescence Is Associated With Tau Pathology in Alzheimer's Disease. *Front. Neurol.* 11:575953. doi: 10.3389/fneur.2020.575953

Caldeira, C., Cunha, C., Vaz, A. R., Falcão, A. S., Barateiro, A., Seixas, E., et al. (2017). Key Aging-Associated Alterations in Primary Microglia Response to Beta-Amyloid Stimulation. *Front. Aging Neurosci.* 9:277. doi: 10.3389/fnagi.2017.00277

Chandra, S., Jana, M., and Pahan, K. (2018). Aspirin Induces Lysosomal Biogenesis and Attenuates Amyloid Plaque Pathology in a Mouse Model of Alzheimer's Disease via PPARα. *J. Neurosci.* 38, 6682–6699. doi: 10.1523/JNEUROSCI.0054-18.2018

Chapman, J., Fielder, E., and Passos, J. F. (2019). Mitochondrial dysfunction and cell senescence: deciphering a complex relationship. *FEBS Lett.* 593, 1566–1579. doi: 10.1002/1873-3468.13498

Chen, H., Liu, X., Zhu, W., Hu, X., Jiang, Z., Xu, Y., et al. (2014). SIRT1 ameliorates age-related senescence of mesenchymal stem cells via modulating telomere shelterin. *Front. Aging Neurosci.* 6:103. doi: 10.3389/fnagi.2014.00103

Chen, J. H., Hales, C. N., and Ozanne, S. E. (2007). DNA damage, cellular senescence and organismal ageing: causal or correlative? *Nucleic Acids Res.* 35, 7417–7428. doi: 10.1093/nar/gkm681

Coppé, J. P., Desprez, P. Y., Krtolica, A., and Campisi, J. (2010). The senescence-associated secretory phenotype: the dark side of tumor suppression. *Annu. Rev. Pathol.* 5, 99–118. doi: 10.1146/annurev-pathol-121808-102144

Cuollo, L., Antonangeli, F., Santoni, A., and Soriani, A. (2020). The Senescence-Associated Secretory Phenotype (SASP) in the Challenging Future of Cancer Therapy and Age-Related Diseases. *Biology* 9:485. doi: 10.3390/biology9120485

d'Adda di Fagagna, F. (2008). Living on a break: cellular senescence as a DNA-damage response. *Nat. Rev. Cancer* 8, 512–522. doi: 10.1038/nrc2440

Daria, A., Colombo, A., Llovera, G., Hampel, H., Willem, M., Liesz, A., et al. (2017). Young microglia restore amyloid plaque clearance of aged microglia. *EMBO J.* 36, 583–603. doi: 10.15252/embj.201694591

Diao, Z., Ji, Q., Wu, Z., Zhang, W., Cai, Y., Wang, Z., et al. (2021). SIRT3 consolidates heterochromatin and counteracts senescence. *Nucleic Acids Res.* 49, 4203–4219.

Fafián-Labora, J. A., and O'Loghlen, A. (2020). Classical and Nonclassical Intercellular Communication in Senescence and Ageing. *Trends Cell Biol.* 30, 628–639. doi: 10.1016/j.tcb.2020.05.003

Fang, J., Yang, J., Wu, X., Zhang, G., Li, T., Wang, X., et al. (2018). Metformin alleviates human cellular aging by upregulating the endoplasmic reticulum glutathione peroxidase 7. *Aging Cell* 17:e12765. doi: 10.1111/acel.12765

Feng, M., Kim, J., Field, K., Reid, C., Chatzistamou, I., and Shim, M. (2019). Aspirin ameliorates the long-term adverse effects of doxorubicin through suppression of cellular senescence. *FASEB Bioadv.* 1, 579–590. doi: 10.1096/fba.2019-00041

Forero, D. A., González-Giraldo, Y., ópez-Quintero, C. L., Castro-Vega, L. J., Barreto, G. E., and Perry, G. (2016). Meta-analysis of Telomere Length in Alzheimer's Disease. *J. Gerontol. Biol. Sci. Med. Sci.* 71, 1069–1073. doi: 10.1093/gerona/glw053

Gao, L., Zhang, Z., Lu, J., and Pei, G. (2019). Mitochondria Are Dynamically Transferring Between Human Neural Cells and Alexander Disease-Associated GFAP Mutations Impair the Astrocytic Transfer. *Front. Cell Neurosci.* 13:316. doi: 10.3389/fncel.2019.00316

Geng, Y. Q., Guan, J. T., Xu, X. H., and Fu, Y. C. (2010). Senescence-associated beta-galactosidase activity expression in aging hippocampal neurons. *Biochem. Biophys. Res. Commun.* 396, 866–869. doi: 10.1016/j.bbrc.2010.05.011

Gerenu, G., Martisova, E., Ferrero, H., Carracedo, M., Rantamäki, T., Ramirez, M. J., et al. (2017). Modulation of BDNF cleavage by plasminogen-activator inhibitor-1 contributes to Alzheimer's neuropathology and cognitive deficits. *Biochim. Biophys. Acta Mol. Basis Dis.* 1863, 991–1001. doi: 10.1016/j.bbadis.2017.01.023

Gu, X., Zhang, G., Qin, Z., Yin, M., Chen, W., Zhang, Y., et al. (2022). Safinamide protects against amyloid β (Aβ)-induced oxidative stress and cellular senescence in M17 neuronal cells. *Bioengineered* 13, 1921–1930. doi: 10.1080/21655979.2021.2022262

Guerrero, A., De Strooper, B., and Arancibia-Cárcamo, I. L. (2021). Cellular senescence at the crossroads of inflammation and Alzheimer's disease. *Trends Neurosci.* 44, 714–727. doi: 10.1016/j.tins.2021.06.007

He, N., Jin, W. L., Lok, K. H., Wang, Y., Yin, M., and Wang, Z. J. (2013). Amyloid-β(1-42) oligomer accelerates senescence in adult hippocampal neural stem/progenitor cells via formylpeptide receptor 2. *Cell Death Dis.* 4:e924. doi: 10.1038/cddis.2013.437

Hu, Y., Fryatt, G. L., Ghorbani, M., Obst, J., Menassa, D. A., and Martin-Estebane, M. (2021). Replicative senescence dictates the emergence of disease-associated microglia and contributes to Aβ pathology. *Cell Rep.* 35:109228. doi: 10.1016/j.celrep.2021.109228

Hu, Y., Huang, Y., Xing, S., Chen, C., Shen, D., and Chen, J. (2022). Aβ promotes CD38 expression in senescent microglia in Alzheimer's disease. *Biol. Res.* 55:10. doi: 10.1186/s40659-022-00379-1

Huang, J., Gan, Q., Han, L., Li, J., Zhang, H., Sun, Y., et al. (2008). SIRT1 overexpression antagonizes cellular senescence with activated ERK/S6k1 signaling in human diploid fibroblasts. *PLoS One* 3:e1710. doi: 10.1371/journal.pone.0001710.

Jurk, D., Wang, C., Miwa, S., Maddick, M., Korolchuk, V., Tsolou, A., et al. (2012). Postmitotic neurons develop a p21-dependent senescence-like phenotype driven by a DNA damage response. *Aging Cell* 11, 996–1004. doi: 10.1111/j.1474-9726.2012.00870.x

Kang, C., Xu, Q., Martin, T. D., Li, M. Z., Demaria, M., Aron, L., et al. (2015). The DNA damage response induces inflammation and senescence by inhibiting autophagy of GATA4. *Science* 349:aaa5612. doi: 10.1126/science.aaa5612

Kritsilis, M., Rizou, S. V., Koutsoudaki, P. N., Evangelou, K., Gorgoulis, V. G., and Papadopoulos, D. (2018). Ageing, Cellular Senescence and Neurodegenerative Disease. *Int. J. Mol. Sci.* 19:2937. doi: 10.3390/ijms19102937

Kumari, R., and Jat, P. (2021). Mechanisms of Cellular Senescence: cell Cycle Arrest and Senescence Associated Secretory Phenotype. *Front. Cell Dev. Biol.* 9:645593. doi: 10.3389/fcell.2021.645593

Li, Y., Lu, J., Cao, X., Zhao, H., Gao, L., Xia, P., et al. (2020). A Newly Synthesized Rhamnoside Derivative Alleviates Alzheimer's Amyloid-. *Oxid. Med. Cell Longev.* 2020:7698560. doi: 10.1155/2020/7698560

Liu, R. M. (2022). Aging, Cellular Senescence, and Alzheimer's Disease. *Int. J. Mol. Sci.* 23:1989.

Lu, J., Li, Y., Mollinari, C., Garaci, E., Merlo, D., and Pei, G. (2019). Amyloid-β Oligomers-induced Mitochondrial DNA Repair Impairment Contributes to Altered Human Neural Stem Cell Differentiation. *Curr. Alzheimer Res.* 16, 934–949. doi: 10.2174/1567205016666191023104036

Mah, L. J., El-Osta, A., and Karagiannis, T. C. (2010). gammaH2AX: a sensitive molecular marker of DNA damage and repair. *Leukemia* 24, 679–686. doi: 10.1038/leu.2010.6

Martínez-Cué, C., and Rueda, N. (2020). Cellular Senescence in Neurodegenerative Diseases. *Front. Cell Neurosci.* 14:16. doi: 10.3389/fncel.2020.00016

Musi, N., Valentine, J. M., Sickora, K. R., Baeuerle, E., Thompson, C. S., Shen, Q., et al. (2018). Tau protein aggregation is associated with cellular senescence in the brain. *Aging Cell* 17:e12840. doi: 10.1111/acel.12840

Nagai, K., Matsushita, T., Matsuzaki, T., Takayama, K., Matsumoto, T., Kuroda, R., et al. (2015). Depletion of SIRT6 causes cellular senescence, DNA damage, and telomere dysfunction in human chondrocytes. *Osteoarthritis Cartilage* 23, 1412–1420. doi: 10.1016/j.joca.2015.03.024

Nakae, D., Akai, H., Kishida, H., Kusuoka, O., Tsutsumi, M., and Konishi, Y. (2000). Age and organ dependent spontaneous generation of nuclear 8-hydroxydeoxyguanosine in male Fischer 344 rats. *Lab Invest.* 80, 249–261. doi: 10.1038/labinvest.3780028

Oberdoerffer, P., Michan, S., McVay, M., Mostoslavsky, R., Vann, J., and Park, S. K. (2008). SIRT1 redistribution on chromatin promotes genomic stability but alters gene expression during aging. *Cell* 135, 907–918. doi: 10.1016/j.cell.2008.10.025

Ota, H., Akishita, M., Akiyoshi, T., Kahyo, T., Setou, M., Ogawa, S., et al. (2012). Testosterone deficiency accelerates neuronal and vascular aging of SAMP8

mice: protective role of eNOS and SIRT1. *PLoS One* 7:e29598. doi: 10.1371/journal.pone.0029598

Ota, H., Akishita, M., Eto, M., Iijima, K., Kaneki, M., and Ouchi, Y. (2007). Sirt1 modulates premature senescence-like phenotype in human endothelial cells. *J. Mol. Cell Cardiol.* 43, 571–579. doi: 10.1016/j.yjmcc.2007.08.008

Pi, C., Ma, C., Wang, H., Sun, H., Yu, X., Gao, X., et al. (2021). MiR-34a suppression targets Nampt to ameliorate bone marrow mesenchymal stem cell senescence by regulating NAD. *Stem Cell Res. Ther.* 12:271. doi: 10.1186/s13287-021-02339-0

Podhorecka, M., Skladanowski, A., and Bozko, P. (2010). H2AX Phosphorylation: its Role in DNA Damage Response and Cancer Therapy. *J. Nucleic Acids* 2010:920161. doi: 10.4061/2010/920161

Rocchi, A., Carminati, E., De Fusco, A., Kowalska, J. A., Floss, T., and Benfenati, F. (2021). REST/NRSF deficiency impairs autophagy and leads to cellular senescence in neurons. *Aging Cell* 20:e13471. doi: 10.1111/acel.13471

Satoh, A., Stein, L., and Imai, S. (2011). The role of mammalian sirtuins in the regulation of metabolism, aging, and longevity. *Handb. Exp. Pharmacol.* 206, 125–162. doi: 10.1007/978-3-642-21631-2_7

Singh Angom, R., Wang, Y., Wang, E., Pal, K., Bhattacharya, S., Watzlawik, J. O., et al. (2019). VEGF receptor-1 modulates amyloid β 1-42 oligomer-induced senescence in brain endothelial cells. *FASEB J.* 33, 4626–4637.

Tang, M. Y., Gorin, F. A., and Lein, P. J. (2022). Review of evidence implicating the plasminogen activator system in blood-brain barrier dysfunction associated with Alzheimer's disease. *Ageing Neurodegener Dis* 2:2. doi: 10.20517/and.2022.05

Vaughan, D. E., Rai, R., Khan, S. S., Eren, M., and Ghosh, A. K. (2017). Plasminogen Activator Inhibitor-1 Is a Marker and a Mediator of Senescence. *Arterioscler. Thromb. Vasc. Biol.* 37, 1446–1452. doi: 10.1161/ATVBAHA.117.309451

von Zglinicki, T., Saretzki, G., Ladhoff, J., d'Adda di Fagagna, F., and Jackson, S. P. (2005). Human cell senescence as a DNA damage response. *Mech. Ageing Dev.* 126, 111–117.

Wan, Y. Z., Gao, P., Zhou, S., Zhang, Z. Q., Hao, D. L., Lian, L. S., et al. (2014). SIRT1-mediated epigenetic downregulation of plasminogen activator inhibitor-1 prevents vascular endothelial replicative senescence. *Aging Cell* 13, 890–899. doi: 10.1111/acel.12247

Wang, J., Zheng, B., Yang, S., and Zhou, D. (2021). Olmesartan Prevents Oligomerized Amyloid β (Aβ)-Induced Cellular Senescence in Neuronal Cells. *ACS Chem. Neurosci.* 12, 1162–1169.

Wei, Z., Chen, X. C., Song, Y., Pan, X. D., Dai, X. M., Zhang, J., et al. (2016). Amyloid β Protein Aggravates Neuronal Senescence and Cognitive Deficits in 5XFAD Mouse Model of Alzheimer's Disease. *Chin. Med. J.* 129, 1835–1844. doi: 10.4103/0366-6999.186646

Weng, J., Zhao, G., Weng, L., Guan, J., and Initiative, A. S. D. N. (2021). Aspirin using was associated with slower cognitive decline in patients with Alzheimer's disease. *PLoS One* 16:e0252969. doi: 10.1371/journal.pone.0252969

Wong, E. S., Le Guezennec, X., Demidov, O. N., Marshall, N. T., Wang, S. T., Krishnamurthy, J., et al. (2009). p38MAPK controls expression of multiple cell cycle inhibitors and islet proliferation with advancing age. *Dev. Cell* 17, 142–149. doi: 10.1016/j.devcel.2009.05.009

Xu, C., Wang, L., Fozouni, P., Evjen, G., Chandra, V., and Jiang, J. (2020). SIRT1 is downregulated by autophagy in senescence and ageing. *Nat. Cell Biol.* 22, 1170–1179. doi: 10.1038/s41556-020-00579-5

Xu, J., Jackson, C. W., Khoury, N., Escobar, I., and Perez-Pinzon, M. A. (2018). Brain SIRT1 Mediates Metabolic Homeostasis and Neuroprotection. *Front. Endocrinol.* 9:702. doi: 10.3389/fendo.2018.00702

Xu, M., Pirtskhalava, T., Farr, J. N., Weigand, B. M., Palmer, A. K., and Weivoda, M. M. (2018). Senolytics improve physical function and increase lifespan in old age. *Nat. Med.* 24, 1246–1256. doi: 10.1038/s41591-018-0092-9

Zhang, P., Kishimoto, Y., Grammatikakis, I., Gottimukkala, K., Cutler, R. G., Zhang, S., et al. (2019). Senolytic therapy alleviates Aβ-associated oligodendrocyte progenitor cell senescence and cognitive deficits in an Alzheimer's disease model. *Nat. Neurosci.* 22, 719–728.

Zhang, T., and Kraus, W. L. (2010). SIRT1-dependent regulation of chromatin and transcription: linking NAD(+) metabolism and signaling to the control of cellular functions. *Biochim. Biophys. Acta* 1804, 1666–1675. doi: 10.1016/j.bbapap.2009.10.022

Zhao, L., Cao, J., Hu, K., He, X., Yun, D., Tong, T., et al. (2020). Sirtuins and their Biological Relevance in Aging and Age-Related Diseases. *Aging Dis.* 11, 927–945. doi: 10.14336/AD.2019.0820

Zu, Y., Liu, L., Lee, M. Y., Xu, C., Liang, Y., Man, R. Y., et al. (2010). SIRT1 promotes proliferation and prevents senescence through targeting LKB1 in primary porcine aortic endothelial cells. *Circ. Res.* 106, 1384–1393. doi: 10.1161/CIRCRESAHA.109.215483

Conflict of Interest: The authors declare that the research was conducted in the absence of any commercial or financial relationships that could be construed as a potential conflict of interest.

Publisher's Note: All claims expressed in this article are solely those of the authors and do not necessarily represent those of their affiliated organizations, or those of the publisher, the editors and the reviewers. Any product that may be evaluated in this article, or claim that may be made by its manufacturer, is not guaranteed or endorsed by the publisher.

frontiers | Frontiers in Aging Neuroscience

SYSTEMATIC REVIEW
published: 22 July 2022
doi: 10.3389/fnagi.2022.860529

PSEN1 c.1292C<A Variant and Early-Onset Alzheimer's Disease: A Scoping Review

*Maribel Orozco-Barajas[1,2], Yulisa Oropeza-Ruvalcaba[2], Alejandro A. Canales-Aguirre[3] and Victor J. Sánchez-González[1,4]**

[1] Doctorado en Biociencias, Centro Universitario de los Altos, Universidad de Guadalajara, Guadalajara, Mexico, [2] Centro de Atención Psicológica, Tepatitlán de Morelos, Mexico, [3] Departamento de Biotecnología Médica y Farmacéutica, Centro de Investigación y Asistencia en Tecnología y Diseño del Estado de Jalisco A. C. (CIATEJ), Guadalajara, Mexico, [4] Departamento de Clínicas, Centro Universitario de los Altos, Universidad de Guadalajara, Guadalajara, Mexico

Alzheimer's disease (AD) is the most common cause of dementia, characterized by progressive loss of cognitive function, with β-amyloid plaques and neurofibrillary tangles being its major pathological findings. Although the disease mainly affects the elderly, c. 5–10% of the cases are due to *PSEN1*, *PSEN2*, and *APP* mutations, principally associated with an early onset of the disease. The A413E (rs63750083) *PSEN1* variant, identified in 2001, is associated with early-onset Alzheimer's disease (EOAD). Although there is scant knowledge about the disease's clinical manifestations and particular features, significant clinical heterogeneity was reported, with a high incidence of spastic paraparesis (SP), language impairments, and psychiatric and motor manifestations. This scoping review aims to synthesize findings related to the A431E variant of *PSEN1.* In the search, we followed the Preferred Reporting Items for Systematic Reviews and Meta-Analyses (PRISMA) statement and the guidelines proposed by Arksey and O'Malley. We searched and identified 247 studies including the A431E variant of *PSEN1* from 2001 to 2021 in five databases and one search engine. After the removal of duplicates, and apply inclusion criteria, 42 studies were finally included. We considered a narrative synthesis with a qualitative approach for the analysis of the data. Given the study sample conformation, we divided the results into those carried out only with participants carrying A431E (seven studies), subjects with *PSEN* variants (11 studies), and variants associated with EOAD in *PSEN1*, *PSEN2*, and *APP* (24 studies). The resulting synthesis indicates most studies involve Mexican and Mexican-American participants in preclinical stages. The articles analyzed included carrier characteristics in categories such as genetics, clinical, imaging techniques, neuropsychology, neuropathology, and biomarkers. Some studies also considered family members' beliefs and caregivers' experiences. Heterogeneity in both the studies found and carrier samples of EOAD-related gene variants does not allow for the generalization of the findings. Future research should focus on reporting data on the progression of carrier characteristics through time and reporting results independently or comparing them across variants.

Keywords: A431E, *c.1292C<A*, *PSEN1*, EOAD, founder effect, dementia, ADAD, scoping review

OPEN ACCESS

Edited by:
Jun Xu,
Capital Medical University, China

Reviewed by:
Mitsuru Shinohara,
National Center for Geriatrics and Gerontology (NCGG), Japan
Seong An,
Gachon University, South Korea

***Correspondence:**
Victor J. Sánchez-González
victor.sanchez@academicos.udg.mx

Specialty section:
This article was submitted to Alzheimer's Disease and Related Dementias, a section of the journal Frontiers in Aging Neuroscience

Received: *23 January 2022*
Accepted: *02 June 2022*
Published: *22 July 2022*

Citation:
Orozco-Barajas M, Oropeza-Ruvalcaba Y, Canales-Aguirre AA and Sánchez-González VJ (2022) PSEN1 c.1292C<A Variant and Early-Onset Alzheimer's Disease: A Scoping Review. Front. Aging Neurosci. 14:860529. doi: 10.3389/fnagi.2022.860529

INTRODUCTION

Alzheimer's disease causes c. 70% of dementia cases (World Health Organization, 2020), which is a neurodegenerative disease resulting in progressive cognitive deficits due to plaques and tangles accumulation leading to inflammation and oxidative stress responses (Amponsah et al., 2021).

Most cases are related to susceptibility genes and risk factors such as age, obesity, hypertension, diabetes, depression, and others (Livingston et al., 2020). Variants in the causality genes, including *PSEN1, PSEN2*, and *APP* (identified with high penetrance), are responsible for only 5–10% of the cases (Hoogmartens et al., 2021). With 326 reported, among them the A431E, *PSEN1* has the most pathogenic variants associated with EOAD (Alzforum, 2021).

With a 1292c> a, rs63750083 nomenclature, A431E is in the exon 12 of *PSEN1*, and in the transmembrane region nine, it changes an alanine by glutamic acid and alters its physical–chemical interaction (Landrum et al., 2018; Alzforum, 2021). A431E has the OMIM code 104311.0033 and is associated with EOAD type 3 (McKusick-Nathans Institute of Genetic Medicine JHU, 2019). A431E has complete penetrance (Bateman et al., 2012). According to the guidelines of the American College of Medical Genetics and Genomics and Association of Molecular Pathology (ACMG/AMP), it is classified as pathogenic due to studies indicating, in a moderate range, an effect on Aβ42/Aβ40 levels and a decreased ratio (PS3-M classification criteria), critical functional location (PM1-M) and low frequency or no control (PM2-M), and strong co-segregation (PP1-S) (Alzforum, 2022).

Rogaeva et al. (2001), made the first description of the variant, which was found in five unrelated cases with a family history of AD and onset before 65 years of age. Later, Yescas et al. (2006) identified 12 families and hypothesized a founder effect of A431E. At the same time, Murrell et al. (2006) added an extra 15 independent families with an A431E history.

A431E is one of the three variants in *PSEN1* with the highest number of affected individuals in Latin America (Dumois-Petersen et al., 2020; Llibre-Guerra et al., 2021). The estimated population varies from 381 (Llibre-Guerra et al., 2021) to 301 (Dumois-Petersen et al., 2020), while the number of people at risk ranges from 463 (Llibre-Guerra et al., 2021) to 560 (Dumois-Petersen et al., 2020). Therefore, an increase in A431E carriers is expected, as diagnostic studies and evaluations are still being held mostly by our group.

The distinctive phenotypic feature of A431E is the high frequency of SP (Santos-Mandujano et al., 2020; Llibre-Guerra et al., 2021). A431E is associated with generalized white matter abnormalities which precede SP (Soosman et al., 2016). In addition, Yescas et al. (2006) identified an exclusive motor presentation along with pyramidal signs, myoclonus, and seizures in cases where the onset of EOAD was before the average age of onset. Llibre-Guerra et al. (2021) reported such findings as uncommon in other *PSEN1* variants.

Cases such as the A431E offer the possibility of understanding the disease's genetic basis and pathology from the early stages (Fuller et al., 2019), which has triggered interest in genotypic and phenotypic characterization of its carriers. As studies involving individuals with a history of A431E continue to expand, it is necessary to have a reference framework regarding the findings of the phenotypic characteristics of this variant.

Previous literature reviews have focused on genetic aspects of EOAD caused by *PSEN1, PSEN2,* and *APP* variants (Tanzi, 2012; Ringman and Coppola, 2013; Ringman et al., 2014; Hoogmartens et al., 2021), and on the study of biomarkers in both cerebrospinal fluid (Ghidoni et al., 2011a,b; Rostgaard et al., 2015; Schindler et al., 2019) and plasma (Blennow et al., 2012). In addition, reviews focused on the clinical heterogeneity of *PSEN1* variants were also published (Larner and Doran, 2006, 2008; Larner, 2013). However, there are no articles specifically focused on reviewing the findings of A431E, which represents a gap in the literature.

In this article, we sought to review studies that include carriers of the A431E variant to describe and characterize findings (clinical, neuroanatomical, neuropathological, neuropsychological, and possible biomarkers) associated with EOAD through a narrative review synthesis with a qualitative approach. We choose an exploratory review to focus on providing scanning of existing knowledge evidence in response to a specific objective (Arksey and O'Malley, 2005).

This scoping review aims to identify and synthesize the characteristics of the A431E variant of *PSEN1* presented in the findings of EOAD-related studies.

METHODS

Study Design

An exploratory review was chosen to achieve the aim of this study. The search was conducted in accordance with the Preferred Reporting Items for Systematic Reviews and Meta-Analyses (PRISMA) (Page et al., 2021) statement and the guidelines proposed by Arksey and O'Malley (2005). The authors suggest that this type of study aims to quickly provide a general frame of reference for key aspects such as concepts, sources, and types of evidence. It was chosen to "evaluate the extent, range, and nature of the research activity" regarding the A431E variant associated with EOAD, which corresponds to the first of the aims of exploratory studies proposed by the authors (Arksey and O'Malley, 2005, p. 21).

Search Strategy

In order to identify the articles to be included, the search was conducted in medicine, biomedical, and multiple search field databases: MEDLINE, PubMed, Scopus, WOS (Web of Science), Ovid, BMC (BioMed Central) databases, and the search engine Google Scholar. Research articles were considered if they included the following keywords: A431E AND *PSEN1* OR *PS1* AND ALZHEIMER; although the following search codes were also used A431E AND *PSEN1* OR *PS1* AND ALZHEIMER NOT SPORADIC NOT LATE ONSET. Articles from all databases published from 2001 to September 2021 were considered. Subsequently, duplicates were removed.

Study Selection/Screening

An initial screening of the research papers' abstracts was independently conducted by two reviewers (MO-B and YO-R) considering the aim and the inclusion and exclusion criteria of the study.

Research papers included were those fulfilling the following inclusion criteria: (a) articles that report both the presence of the variant and disease; (b) scientific papers with an original contribution; (c) peer-reviewed publications; and (d) papers available in Spanish or English.

Articles were excluded when they met at least one of the following criteria: (a) a review paper; (b) abstracts of posters, conferences, or academic paper works where no access to the full text was available; (c) independent reviews or no peer-reviewed paper; and (d) experimental studies in cellular models. Full texts were also reviewed by the researchers to determine their eligibility by two reviewers (MO-B and YO-R). During this process, disagreements about the inclusion or exclusion of articles were discussed with third and fourth researchers (VJSG and AACA).

As a final criterion, we considered excluding experimental model studies. Articles were identified in which carriers and individuals with a history of the A431E were included along with participants with a history of other variants and even sporadic AD (SAD). Although in many of these papers the authors did not report the results separately or compared between groups, we highlight that in many of these studies the participant samples consisted mainly of people with a history of EOAD or A431E carriers. Therefore, we considered it appropriate to include the studies and, to facilitate the reading of results, separate them into those that included only people with a history of EOAD or A431E carriers, those including, in addition to the variant of interest, (a) other variants in *PSEN1*, (b) *PSEN1* and *PSEN2,* and (c) *PSEN* and *APP*.

Data Extraction and Analysis

General data extracted from the studies include the following: authors, year of publication, country, study group, type of sample, and stage/type of participant. In addition, information about techniques and instruments used, study aim, and key findings were also extracted.

Data for each article were extracted without distinguishing between (1) study aim, (2) discipline in which the study is framed, (3) significant findings in results, (4) size sample, (5) country of origin of author or group of authors, and (6) authors discipline.

Data extraction was carried out by two of the authors (MO-B and YO-R). The following types of findings were included in this review: beliefs, caregivers, clinical, genetics, neuroanatomical, neuropathology, neuropsychological, biochemical, electrophysiological, and cerebrospinal fluid (CSF) biomarkers.

Analysis and synthesis of the data were performed using a narrative review approach to capture the diversity of findings related to A431E. We consider this method to be the most appropriate given the heterogeneous characteristics of the results. Gaps in the literature were also identified.

RESULTS

Selection of Studies

The search has a date range from 2001 to September 2021. We identified a total of 484 articles in five electronic databases and one search engine. After duplicates were removed, a total of 247 articles were left. Following the inclusion criteria, 42 articles were finally considered to be included in this review. The process of identification, screening, eligibility, and inclusion as well as the articles identified in each phase are shown in **Figure 1**.

General Characteristics

Since 2001, there has been a gradual increase in the number of publications that consider the A431E *PSEN1* variant (see **Table 1**).

The number of participants in the studies is also variable, being the studies with the highest percentage of those evaluating c. 21–30 and 31–40 participants. Most of the studies are related to the Latino population, although studies conducted in Germany, Canada, and Sweden have also been performed.

Of the 42 studies, 14 were conducted in a preclinical phase, another 14 in both a preclinical and clinical phase, five were limited to the clinical phase, six of them were postmortem studies, two were in family members at risk for AD, and one included preclinical and clinical participants and individuals with SAD.

Variants in Studies

Seven of the studies were only on A431E, 11 studies with *PSEN* variants, and the remaining 24 articles are about EOAD [these studies also use the abbreviations FAD (familial Alzheimer's disease) and autosomal dominant Alzheimer's disease (ADAD)].

General details of the studies included in this review are presented in **Supplementary Table 1**, with a detailed study group sample and country, presented accordingly, based on the year of publication. All the studies were conducted in North America, with an exception of two articles in a collaboration with the United States, Canada, and Germany and another in a Swedish publication.

Category Combinations

The identified 42 studies are all cross-sectional and were classified into several categories according to what was analyzed. Among these, the main ones were beliefs, caregivers, clinical, genetics, studies using imaging techniques, neuropathology, and CSF biomarkers. Such categories are combined between them and with others including neuropsychological, biochemical, and electrophysiological. This classification is presented in **Table 2**.

Participant Type

Of the 42 studies, two were conducted on members of families with a history of EOAD (Withers et al., 2019, 2021). In the preclinical stage, two of the studies were conducted on *PSEN* variant carriers (Ringman et al., 2004, 2007a) and 12 on subjects with a history or carriers of EOAD-associated variants (Ringman et al., 2008a,b, 2011, 2012b,d,e; Golob et al., 2009; Medina et al., 2011, 2021; Braskie et al., 2013; Petok et al., 2018;

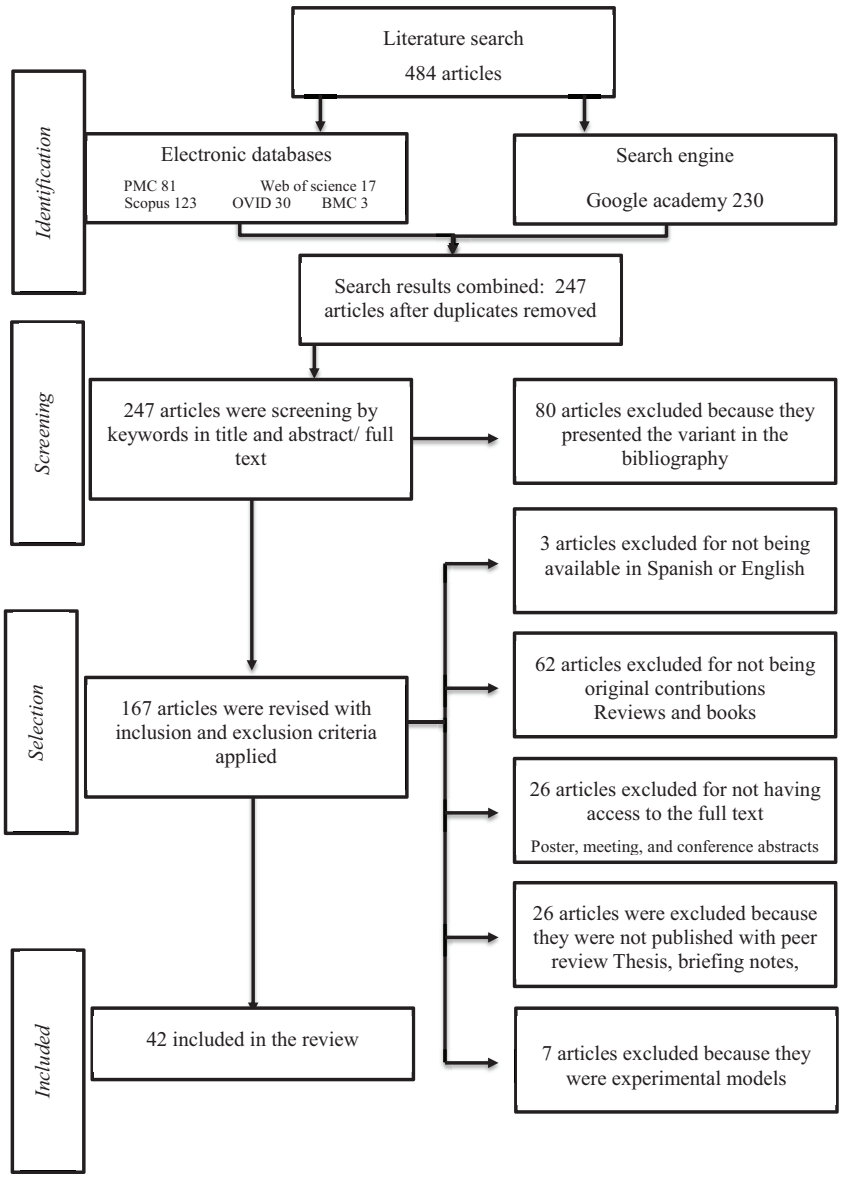

FIGURE 1 | Screening process.

Joe et al., 2019). In the clinical phase, three of the studies were conducted in A431E carriers (Parker et al., 2019; Alakkas et al., 2020; Dumois-Petersen et al., 2020), and two of the studies were conducted in *PSEN* variant carriers (Joshi et al., 2012; Soosman et al., 2016). Three studies were conducted on A431E carriers in both preclinical and clinical stages (Murrell et al., 2006; Yescas et al., 2006; Santos-Mandujano et al., 2020), "three in *PSEN* variant carriers (Rogaeva et al., 2001; Ringman et al., 2005; Leverenz et al., 2006), and eight in subjects with a history or carriers of EOAD-associated variants (Ringman et al., 2007b, 2010, 2012a,c; Apostolova et al., 2011; Braskie et al., 2012; Lee et al., 2013; Singer et al., 2021). One study included preclinical and clinical phase participants and individuals with SAD (Portelius et al., 2010). This is classified as part of the studies conducted in A431E carriers as the results were reported per participant. Of the studies conducted on brain tissue, four were performed in *PSEN* variant carriers (Maarouf et al., 2008; Roher et al., 2013; Beck et al., 2016; Gefen et al., 2020) and two in EOAD cases (Albrecht et al., 2009; Ringman et al., 2016).

Variants Presented in the Studies

A431E *PSEN1* Variant

Seven studies are focused on A431E (see **Table 3**). In 2006, a study hypothesized the founding effect of this variant in the Altos de Jalisco area (Yescas et al., 2006), a letter to the editor, further added 15 independent families to this finding (Murrell et al., 2006). Phenotypic variability reported in the studies, such as SP (Murrell et al., 2006; Yescas et al., 2006; Parker et al., 2019;

TABLE 1 | Summary of general study characteristics.

Study characteristic	Number of studies (*n* = 42)	Percentage
Publication year		
2001–2005	3	7%
2006–2010	12	29%
2011–2015	13	31%
2016–2021	14	33%
Number of participants in studies		
1–10	6	14%
11–20	5	12%
21–30	9	22%
31–40	9	22%
41–50	4	10%
51–60	3	7%
71–80	1	2%
100–200	3	7%
201–500	1	2%
Unknown	1	2%
Not applicable (experimental models)	7	–
Country of origin of the participants		
Latinos (in both Mexico and United States)	40	96%
Germans and Canadians	1	2%
Swedish	1	2%
Stage/participant type		
ADAD family members	2	5%
Preclinical	14	33%
Clinical	5	12%
Preclinical and clinical	14	33%
Preclinical, clinical, and sporadic	1	2%
Postmortem	6	14%
Variants in studies		
A431E	7	17%
PSEN	11	26%
FAD	24	57%

ADAD, autosomal dominant Alzheimer's disease.

TABLE 2 | Category combinations.

Category combinations		Number of studies (*n* = 42)	Percentage
Beliefs (psychological)		1	2%
Caregivers		1	2%
Clinical	Clinical	1	2%
	Genetics	4	10%
	Genetics, neuropsychological	1	2%
	Genetics, imaging technique	1	2%
Genetics	Genetics	3	7%
	Biomarkers	6	14%
	Linguistic	1	2%
	Imaging technique	5	12%
	Neuropathology	2	5%
	Neuropathology, biochemical	1	2%
	Neuropsychological	3	7%
	Neuropsychological, imaging technique	1	2%
	Electrophysiological	1	2%
Imaging technique	Electrophysiological	1	2%
	Imaging technique	2	5%
	Neuropsychological	2	5%
Neuropathology	Neuropathology	3	7%
	Biochemical	1	2%
CSF Biomarkers		1	2%
Total		42	100%

Dumois-Petersen et al., 2020), motor impairment, visuospatial deficits, olfactory dysfunctions, such as hyposmia and anosmia, as well as respiratory difficulties and visual impairment (Santos-Mandujano et al., 2020), language disorders (Dumois-Petersen et al., 2020), neuropsychiatric symptoms (Alakkas et al., 2020; Dumois-Petersen et al., 2020), atrophy disproportionate to age (Parker et al., 2019; Alakkas et al., 2020; Santos-Mandujano et al., 2020), chronic microhemorrhages within bilateral occipital, temporal, and right frontal lobes and pseudobulbar affect (Parker et al., 2019), and periventricular white matter hyperintensities (Santos-Mandujano et al., 2020), were reported. Two of these studies are case reports (Parker et al., 2019; Alakkas et al., 2020), one of them describing a case of a homozygous person (Parker et al., 2019). In two studies, the average age of dementia onset is mentioned as 42.5 ± 3.9 years (Dumois-Petersen et al., 2020) and 40 years (Yescas et al., 2006). One article identifies low levels of Aβ1–37, Aβ1–38, and Aβ1–39 in cerebrospinal fluid in carriers of this variant, compared to people with SAD (Portelius et al., 2010).

We found A431E in studies mixed with other genetic variants; in **Table 4**, we classified the articles analyzing *PSEN* variants. Eight studies focused on *PSEN1* variants (Rogaeva et al., 2001; Ringman et al., 2004, 2005, 2007a; Joshi et al., 2012; Beck et al., 2016; Soosman et al., 2016; Gefen et al., 2020) and, in three more, variants in *PSEN1* and *PSEN2* are analyzed (Leverenz et al., 2006; Maarouf et al., 2008; Roher et al., 2013).

PSEN1

One article in the Genetics category described novel missense variant substitutions (Rogaeva et al., 2001), among them, is the Ala431Glu. In four studies, the authors identified clinical and neuropsychological characteristics in the participants with variants in *PSEN1*. In the early stages, memory, visuospatial, and executive function deficits were found (Ringman et al., 2005). In a study using the Mini-Mental State Examination (MMSE), a decreased temporal orientation performance and divided attention were observed, whereas the three-word list subtest has no sensitivity in identifying changes in memory in the preclinical stage (Ringman et al., 2007a). In the case of women, depressive symptoms were identified (Ringman et al., 2004), and carriers of *PSEN1* mutations in the clinical stage more significantly presented headaches, myoclonus, gait abnormality, and pseudobulbar affect (Joshi et al., 2012). In these articles, the sample is composed primarily of people with the A431E variant.

TABLE 3 | A431E of *PSEN1* studies.

References	Sample	Category	Techniques and instruments used	Study aim	Key findings
Yescas et al., 2006	Carriers with early-onset AD (*n* = 12) and participants with a history of variant (*n* = 85) and healthy controls (*n* = 100).	Genetics	Analysis of microsatellite haplotypes, PCR and MMSE.	Describe a single missense mutation (Ala431Glu) in the *PSEN1* gene found in nine of the 12 apparently unrelated Mexican families with early onset AD.	• The Ala431Glu mutation in exon 12 of *PSEN1* was found in nine (75%) of these families, with autosomal dominant inheritance. • A founder effect was hypothesized. • Microsatellite haplotype analysis suggested a common ancestor in these nine kindreds.
Murrell et al., 2006	15 Families with a history of the A431E variant of *PSEN1*.	Genetics	PCR RFLP.	To expand the observation made by Yescas et al. (2006) by describing an additional 15 independent families with the Ala431Glu substitution in the *PSEN1* gene.	• Additional 15 independent families with the Ala431Glu substitution in the *PSEN1* gene. This mutation is not an uncommon cause of early-onset autosomal dominant AD in persons of Mexican origin.
Portelius et al., 2010	Subjects with sporadic AD (*n* = 18), carriers of the A431E variant in *PSEN1* (*n* = 7), people with depression (*n* = 6) and healthy controls (*n* = 17).	CSF Biomarkers	MMSE, CDR, lumbar puncture, immunoprecipitation analysis and mass spectrometry.	Test the hypothesis that AD is characterized by a specific CSF Ab isoform pattern that is distinct when comparing SAD and FAD due to different mechanisms underlying brain amyloid pathology in the two disease groups.	• Low CSF levels of Aβ1–42 and high levels of Aβ1–16 distinguished SAD patients and FAD mutation carriers from healthy controls and depressed patients. • SAD and FAD were characterized by similar changes in Aβ1–42 and Aβ1–16, but FAD mutation carriers exhibited very low levels of Aβ1–37, Aβ1–38, and Aβ1–39.
Parker et al., 2019	*A431E* (*n = 1*) *mutation carrier*.	Genetics, Clinical	Family history, MMSE, PCR, and MRI.	Report a 35-year-old male with childhood learning disability and early onset dementia who is homozygous for the A431E variant in the *PSEN1* gene.	• Homozygosity for the A431E variant in *PSEN1*. • Clinical evaluation demonstrated SP and pseudobulbar affect. • Brain MRI revealed cerebral atrophy disproportionate to age. • Chronic microhemorrhages within bilateral occipital, temporal, and right frontal lobes were seen.
Santos-Mandujano et al., 2020	Carriers of the A431E variant in *PSEN1* (*n* = 4), of which one was symptomatic and the rest asymptomatic.	Genetics, clinical, Imaging technique	PCR, MMSE, MOCA, CDR, UPSIT, and MRI.	Characterized three A431E mutation carriers, one symptomatic and two asymptomatic, from a Mexican family with a history of SP in all its affected members.	• Symptomatic subject showed an atypical non-amnestic mild cognitive impairment with visuospatial deficits, olfactory dysfunction, and significant parieto-occipital brain atrophy. • Several periventricular white matter hyperintensities whose progression pattern and localization correlated with their motor impairment.
Dumois-Petersen et al., 2020	Of the total number of participants (*n* = 54), *n* = 46 were carriers of the A431E variant.	Genetics, Clinical	PCR, Neuropsychiatric Inventory Questionnaire.	Present the initial evaluation of 46 individuals with AD-EOAD, all of whom from the Mexican state of Jalisco and carrying the A431E mutation in the *PSEN1* gene.	• The mean onset age was 42.5 ± 3.9 years. • Substantial clinical heterogeneity and high frequencies of SP, language disorders, and neuropsychiatric symptoms.
Alakkas et al., 2020	*n = 1 Woman with variant in PSEN1*.	Clinical	Electroencephalogram, Bush–Francis scale of Catatonia, clinical history, MRI, laboratory testing, genetic testing.	Report a case of a 35-year-old woman with significant deterioration in psychomotor functioning, depression, and catatonic features.	• This case is a cautionary reminder for clinicians that end stages of dementia can present similar to catatonia with mutism, lack of spontaneous movement, and refusal to eat. • The clues to the diagnosis were profound cortical atrophy and lack of improvement with optimal medical management.

Ab, amyloid β protein; AD, Alzheimer's disease; AD-EOAD, autosomal dominant early—onset Alzheimer's disease; CDR, Clinical Dementia Rating Scale; CSF, cerebrospinal fluid; FAD, familial Alzheimer's disease; MMSE, Mini-Mental State Examination; MOCA, Montreal Cognitive Assessment; MRI, magnetic resonance imaging; PCR, polymerase chain reaction; RFLP, restriction fragment length polymorphism analysis; SAD, sporadic Alzheimer's disease; SP, spastic paraparesis; and UPSIT, University of Pennsylvania Smell Identification Test.

TABLE 4 | *PSEN* studies.

References	Sample	Category	Techniques and instruments used	Study aim	Key findings
Studies whit variants in *PSEN1*					
Rogaeva et al., 2001	Total number of participants (n = 414), n = 372 had AD and n = 42 asymptomatic with a history. n = 48 of the participants had *PSEN1* variants, the most frequent being Glu206Ala (n = 25), Ala431Glu (n = 25) and Ile143Thr (n = 3), in addition, 21 new variants were identified.	Genetics	PCR	Report the experience of mutation screening in a series of consecutive patients with AD referred for diagnostic testing.	• Forty-eight independent patients screened had a *PS1* mutation including 21 novel mutations. • The majority of the mutations were missense substitutions.
Ringman et al., 2004	Of the total number of participants (n = 33), there were subjects from families with a history of the A431E variant (n = 22) between these carriers (n = 12) and non-carriers (n = 10). In addition to subjects with a history of L235V (n = 11) between these carriers (n = 5) and non-carriers (n = 6).	Genetics, clinical, neuropsychological	MMSE, Spanish Cognitive test, CDR, BDI, PCR RFLP.	To study depressive symptoms in preclinical *PS1* related Alzheimer's disease.	• Depressive symptoms can occur early in the course of *PS1* related Alzheimer's disease, at least in women. • Not demented mutation carriers tended to score lower than non-carriers on several neuropsychological tests.
Ringman et al., 2005	Participants without dementia with a history of variants in *PSEN1* (n = 51). carriers of A431E (n = 25), and L235V (n = 5) non-carriers (n = 21), of which 15 had a history of A431E and 6 of L235V.	Genetics, neuropsychological	MMSE, BDI, TMT (forms A and B), WMS-R, Rey Osterrieth Figure, 10-Word Learning List (immediate and delayed retrieval), Boston naming test, verbal fluency (semantics [fruits and animals] and phonological [F, A]), WAIS cube design and PCR.	To investigate these observations by the study of persons at risk for autosomal dominant forms of AD.	• Early problems with memory, visuospatial function, and particularly with executive function in *PS1* mutation carriers. • Depression, gender, and presence of an *APOE*ε4 allele did not demonstrate large influences on neuropsychological performance.
Ringman et al., 2007a	The participants were Mexicans (n = 50), who had a history of the A431E (n = 39) and L235V (n = 11) mutations, of which n = 29 were carriers and n = 21 were non-carriers.	Genetics, neuropsychological	Clinical interview, PCR RFLP, computerized version of MMSE.	Explore the sub-items on the MMSE that best differentiate *PSEN1* MCs and NCs and explore the relationship of age and education to these scores.	• Subjects in the earliest stage of *PSEN1*-related AD showed deficits on orientation to date and in divided attention when spelling backward. • The relative lack of deficits on delayed recall of three words probably represents the insensitivity of this measure in early AD. • This study supports the utility of ADAD as a model of the more common sporadic form of the disorder.

(Continued)

TABLE 4 | (Continued)

References	Sample	Category	Techniques and instruments used	Study aim	Key findings
Joshi et al., 2012	Subjects with familial AD associated with *PSEN1* (*n* = 32), of which *n* = 22 had the A431E variant, in addition the sample consisted of carriers of the following variants G206A (*n* = 2), L235V (*n* = 3), M146L (*n* = 1), S212Y (*n* = 1), R269H (*n* = 1), I238M (*n* = 1), and T245P (*n* = 1). Subjects with unfamiliar early-onset AD (*n* = 81). Results are not specified by mutation.	Clinical	MMSE and medical history review.	To identify clinical features that distinguish FAD from non-familial EAD.	• FAD patients with *PSEN1* mutations were more likely to have significant headaches, myoclonus, gait abnormality, and pseudobulbar affect. • Differences in pathophysiology between FAD and NF-EAD and findings in some contexts should lead to genetic counseling and appropriate recommendations for genetic testing for FAD.
Soosman et al., 2016	Carriers of variant A431E with paraparesis (*n* = 3) and carriers of variants A431E (*n* = 1), G206A (*n* = 2), I238M (*n* = 1), M146L (*n* = 1), R269H (*n* = 1), S212Y (*n* = 1) without paraparesis. All these variants are in *PSEN1*.	Electrophysiological, Imaging technique	MMSE, CDR, diffuser tensor, MRI, volumetric analysis, microbleed counting, amyloid PET using PiB and somatosensory and motor evoked potential studies and electrophysiological studies.	Compared diffusion and volumetric magnetic resonance measures between 3 persons with SP associated with the A431E mutation and 7 symptomatic persons with *PSEN1* mutations without SP matched for symptom duration.	• Decreases in FA and increases in mean diffusivity in widespread white matter areas including the corpus callosum, occipital, parietal, and frontal lobes in *PSEN1* mutation carriers with SP. • Volumetric measures were not different and amyloid imaging showed low signal in sensorimotor cortex and other areas in a single subject with SP. • Electrophysiological studies demonstrated both slowed motor and sensory conduction in the lower extremities.
Beck et al., 2016	Postmortem samples of frontal tissue (Brodmann's area 10) of cognitively intact controls (*n* = 9), sporadic-type AD (*n* = 8) and of the variants T115C, I143T, G209V, A260V, A431E (*n* = 8) of *PSEN1*.	Genetics, neuropathology	PCR and Western Blot.	To test whether mtUPR activation occurs in AD, we performed real-time quantitative PCR on postmortem frontal cortex samples from subjects classified as sporadic AD, familial AD linked to presenilin-1 mutations, or cognitively intact controls.	• Levels of all six mtUPR genes were significantly up-regulated by ∼70–90% in familial AD.
Gefen et al., 2020	Brain tissue of subjects with PPA (*n* = 16). Behavioral variant of frontotemporal dementia (*n* = 16). Alzheimer's type dementia (*n* = 16), of the latter two had variant H163R (*n* = 1) and A431E (*n* = 1) associated with *PSEN1*.	Neuropathology	Semiquantitative counting method to measure the degree of macroscopic atrophy, neuronal loss, and gliosis, superficial microvacuolation and pathological inclusions.	Determine whether leftward asymmetry is unique to PPA compared with the typical dementia of the Alzheimer's type and bvFTD.	• PPA has an exclusive pathologic signature, distinct from DAT and bv FTD, with PPA favoring the language-dominant hemisphere, typically left. This unique signature was consistent across all examinations of gross pathology, neuronal loss and gliosis, and microvacuolation, particularly in the temporal region.

(Continued)

TABLE 4 | (Continued)

References	Sample	Category	Techniques and instruments used	Study aim	Key findings
Studies whit variants in *PSEN1* and *PSEN2*					
Leverenz et al., 2006	Cases with *PSEN1* variants (*n* = 25), including: A260V (*n* = 7), G209V (*n* = 7), E120D (*n* = 3), A431E (*n* = 2), M233L (*n* = 2), H163R (*n* = 1), I143T (*n* = 1), L418F (*n* = 1) y M146L (*n* = 1). *PSEN2* variant N141I cases (*n* = 14).	Genetics, neuropathology	Lewy body neuropathology was examined using synuclein immunohistochemistry and sampling of multiple brainstem and cortical regions, and PCR.	To examine LBP in the brainstem, limbic cortex, and neocortex of a large number of familial AD cases with mutations in 2 *PSEN* genes.	• The amygdala was the most vulnerable site for LBP in *PSEN1* mutation cases. Genetic influences on the presence of LBP in familial AD as demonstrated by the differences between *PSEN1* and *PSEN2* mutation cases.
Maarouf et al., 2008	Brain tissue from carriers of *PSEN1* (*n* = 9) including: A79V (*n* = 1), A260V (*n* = 1), F105L (*n* = 1), Y115C (*n* = 1), A431E (*n* = 1), V261F (*n* = 1), V261I (*n* = 1), M146L (*n* = 1), P264L (*n* = 1); N141I of *PSEN2* (*n* = 1) carrier; subjects with sporadic AD (*n* = 4), and healthy controls (*n* = 2).	Genetics, neuropathology, biochemical	PCR, Western Blot, densitometry scanning and ELISA.	Compare neuropathological and biochemical findings among nine independent *PSEN1* and one *PSEN2* FAD cases, four SAD cases and two non-demented controls, determined Aβ40 and Aβ42 peptide levels, and the processing pattern and relative quantities of AβPP N-terminal and C-terminal peptides and soluble tau and investigated the differences among the *PSEN* mutations, as well as between the *PSEN* group and SAD or ND controls, with respect to Notch-1, N-cadherin and Erb-B4, molecules that are cleaved by the γ-secretase complex.	• Missense mutations in *PSEN* genes can alter a range of key γ-secretase activities to produce an array of subtly different biochemical, neuropathological, and clinical manifestations.
Roher et al., 2013	Brain tissue (white matter) of *PSEN1* variant carriers: A79V (*n* = 1), F105L (*n* = 1), Y115C (*n* = 1), M146L (*n* = 1), A260V (*n* = 1), V261F (*n* = 1), V261I (*n* = 1), P264L (*n* = 1), and A431E (*n* = 1); and substitution carriers in *PSEN2*: N141I (*n* = 1).	Neuropathology, biochemical	Western Blot and ELISA.	Examine the WM biochemistry by ELISA and Western blot analyses of key proteins in 10 FAD cases harboring mutations in the presenilin genes *PSEN1* and *PSEN2* as well as in 4 non-demented control individuals and 4 subjects with SAD.	• The *PSEN*-FAD mutations we examined did not produce uniform increases in the relative proportions of Aβ42 and exhibited substantial variability in total Aβ levels. Additional complexities in *PSEN*-FAD individuals. • Some direct substrates of γ-secretase, such as Notch, N-cadherin, Erb-B4 and *APP*, deviated substantially from the NDC group baseline for some, but not all, mutation types.

AD, Alzheimer's disease; ADAD, autosomal dominant Alzheimer's disease; BDI, Beck Depression Inventory; bvFTD, behavioral variant frontotemporal dementia; CDR, Clinical Dementia Rating Scale; DAT, dementia of the Alzheimer's type; EAD, Early-onset AD; FA, fractional anisotropy; FAD, familiar Alzheimer's disease; LBP, Lewy body pathology; MCs, mutation carriers; MMSE, Mini-Mental State Examination; mtUPR, mitochondrial unfolded protein response; NCs, non-carriers; ND, non-demented control; NDC, non-demented control; NF-EAD, non-familial EAD; PCR, polymerase chain reaction; PET, positron emission tomography; PiB, Pittsburgh Compound B; PPA, primary progressive aphasia; RFLP, restriction fragment length polymorphism analysis; SAD, sporadic Alzheimer's disease; SP, spastic paraparesis; TMT, Trail Making Test; WAIS, The Wechsler Adult Intelligence Scale; WM, white matter; and WMS-R, Wechsler Memory Scale–Revised.

One article reported findings related to electrophysiological and imaging techniques in carriers with and without SP, where SP carriers showed decreased fractional anisotropy, increased mean diffusivity in widespread white matter areas, and slow motor and sensory conduction in the inferior extremities (Soosman et al., 2016).

Two articles study brain tissue of carriers of *PSEN1* variants, and one presents a significant upregulation of six genes related to mitochondrial unfolded protein response (Beck et al., 2016) with primarily differences between primary progressive aphasia (PPA), AD, and a behavioral variant of frontotemporal dementia (Gefen et al., 2020).

PSEN1 and *PSEN2*

Three studies presented neuropathological features; differences among these genes were found in one article: in *PSEN1* mutation cases, the amygdala was more vulnerable to Lewy body pathology than in *PSEN2* (Leverenz et al., 2006). The other two analyze the biochemical and neuropathological implications (Maarouf et al., 2008; Roher et al., 2013), variation in levels of beta-amyloid, and differences in some substrates of gamma secretase (Roher et al., 2013) along with its dysfunction (Maarouf et al., 2008).

After presenting the studies exclusively to *PSEN,* we categorized those who reported in combination with *APP*. In **Table 5**, we present these articles in three categories: first, articles with *PSEN1* and *APP* (Ringman et al., 2007b, 2008a,b, 2010, 2011, 2012a,b,c,d,e; Golob et al., 2009; Apostolova et al., 2011; Braskie et al., 2012, 2013; Lee et al., 2013; Joe et al., 2019; Medina et al., 2021; Singer et al., 2021); second, articles with *PSEN1, PSEN2,* and *APP* variants (Albrecht et al., 2009; Medina et al., 2011; Ringman et al., 2016; Petok et al., 2018), and finally, those articles who reported families with a history of EOAD (Withers et al., 2019) and another with A431E *PSEN1* and an unknown mutation (Withers et al., 2021).

PSEN1 and *APP*

Six of the studies included genetic analysis in combination with biomarkers (Ringman et al., 2008b, 2012a,b,c,d,e): four CSF quantifications, two of which identified Aβ42 depletion (Ringman et al., 2008b, 2012e), one finds oligomers elevation (Ringman et al., 2012d), and one identified overlapped protein changes (Ringman et al., 2012a). Three articles measured plasma levels; one found elevated Aβ42 (Ringman et al., 2008b), other inflammatory markers (Ringman et al., 2012b), and other elevated MetO (Ringman et al., 2012c).

In imaging studies (Ringman et al., 2007b, 2010, 2011; Apostolova et al., 2011; Braskie et al., 2012, 2013; Lee et al., 2013; Joe et al., 2019; Singer et al., 2021), Ringman et al. (2007b) reported a decreased FA in white matter in the preclinical stage. Singer et al. (2021) found increased retinal perfusion also in presymptomatic carriers, and Joe et al. (2019) revealed that carriers had significantly lower levels of NAA and glutamine in the left pregenual anterior cingulate cortex, and lower levels of NAA and higher levels of myoinositol and choline in the precuneus, and a thinning of the posterior association and frontal cortices with hippocampal atrophy (Apostolova et al., 2011), lower thalamic, caudate, putamen volumes (Lee et al., 2013), and decreased BOLD activation in the anterior cingulate gyrus (Ringman et al., 2011). One article examined the ability of radiologists in the diagnosis of early AD stages in people in early stages of EOAD and found it to be suboptimal. Therefore, another marker is considered necessary for diagnosis (Ringman et al., 2010). Braskie et al. (2012) identified mutation carriers showing an increased fMRI activity in the fusiform and middle temporal gyri and a greater retrieval period signal, including in the frontal and temporal lobes (Braskie et al., 2013). These findings were related to the predementia phase.

Three of the studies with neuropsychological findings (Ringman et al., 2011; Braskie et al., 2012; Lee et al., 2013; Medina et al., 2021) reported no differences in cognitive tests between preclinical carriers of the mutations and non-carriers (Ringman et al., 2011; Braskie et al., 2012; Lee et al., 2013). However, in a memory retrieval task, a lower fMRI activity in the hippocampus was observed (Braskie et al., 2012) while for the executive function, the response gets slower as they approach the age onset of dementia (Medina et al., 2021). In carriers with mild cognitive impairment, lower memory, language, and visuospatial, executive functioning scores, were observed compared to preclinical carriers and controls (Lee et al., 2013).

In the clinical, a higher prevalence of headaches in MCs is held for different *PSEN1* and *APP* mutations (Ringman et al., 2008a) and electrophysiological features related to longer latencies of the N100, P200, N200, and P300 components, and smaller slow wave amplitudes (Golob et al., 2009).

PSEN1, *PSEN2,* and *APP*

Two of the studies analyzed brain tissue; Albrecht et al. (2009) identified that Casp-6 immunoreactivity was active in every participant, while Ringman et al. (2016) found Lewy body pathology in 27.1% of the ADAD cases and a higher Braak scores and cerebral amyloid angiopathy (CAA) prevalence. One study focused on linguistic aspects of the carriers (Medina et al., 2011), in which p-density was neither related to the status of participants with a history of EOAD nor with years to clinical onset of the disease, but it was associated with the presence of the *APOEe4* allele. The last article reported cognitive data in relation to neuroanatomical findings (Petok et al., 2018), in which more errors in generalization tasks were associated with smaller left hippocampal volume in carriers.

History of Early-Onset Alzheimer's Disease

Two studies were conducted on participants with a history of EOAD. One of the articles assessed cultural beliefs related to AD and genetic testing (Withers et al., 2019); in this study, some of the participants with a history of ADAD associated with genetic variants know their own risk of developing the disease. The authors found that providing information about the genetic bases of AD increased the interest of people with a history of ADAD for genetic testing. The other article assessed the experiences and needs of caregivers (Withers et al., 2021) and found the stress of informal caregivers comes from different sources beyond caregiving, such as knowing their own risk, caring for other family members including children, providing financially, their own health, and diagnosis access, and their main need is to access information in their own language.

DISCUSSION

The most common cause of hereditary EOAD is *PSEN1* mutations followed by *PSEN2* and *APP* mutations (Ramos et al., 2020). While the pathophysiology is similar, there are differences in the AD phenotype (Ringman et al., 2014). Among the variants in *PSEN1*, A431E is one of the primary three due to the number of carriers, which varies from 381 to 301 (Dumois-Petersen et al., 2020; Llibre-Guerra et al., 2021), and

TABLE 5 | *PSEN* and *APP* studies.

References	Sample	Category	Techniques and instruments used	Study aim	Key findings
Studies whit variants in *PSEN1* and *APP*					
Ringman et al., 2007b	Total number of participants (n = 23), n = 12 were carriers and n = 8 were non-carriers, among these n = 19 had a history of variants in *PSEN1* (including A431E) and n = 4 in *APP*. No quantities are specified.	Genetics, Imaging technique	CDR, MMSE, Diffuser Tensor, MRI, and PCR.	Compare global and localized fractional anisotropy measures in WM between FAD mutation carriers and non-carriers in the preclinical and presymptomatic stages of the disease.	• FA is decreased in the WM in preclinical and even presymptomatic FAD mutation carriers, particularly in the late-myelinating tracts connecting limbic structures. • Decreased FA in of the columns of the fornix is particularly robust in early FAD.
Ringman et al., 2008a	The participants (n = 27) were divided into carriers (n = 15) and non-carriers (n = 12), who came from 11 families, of which 9 had a history of variants in *PSEN1* (7 from A431E, one from L235V and another of G206A) and 2 of variants in *APP* (the results do not distinguish between carriers with different variants).	Genetics, clinical	Structured interview based on the ICHD-2; CDR; PCR RFLP.	Compare the prevalence of headaches between non-demented FAD MCs and NCs controls.	• The tendency for a higher prevalence of headaches in MCs held for different *PSEN1* and *APP* mutations but was not significant unless all families were combined. • Headache was more common in non-demented FAD MCs than NCs. Possible mechanisms for this include cerebral inflammation, aberrant processing of Notch3, or disrupted intracellular calcium regulation.
Ringman et al., 2008b	The participants (n = 21) were carriers of variants in *PSEN1* (n = 17) and in *APP* (n = 4). They came from families with variants in A431E (n = 4), L235V (n = 1), G206A (n = 1) of *PSEN1*, and families with V717I variants (n = 2) of *APP*.	Genetics, biomarkers	CDR, MMSE, ELISA, and PCR.	Measured levels of plasma (Aβ40, Aβ42, F2-isoprostanes) and CSF (F2-isoprostanes, t-tau, p-tau181, Aβ40, and Aβ42) biomarkers with putative relationships to AD status and progression in persons at risk for FAD to help clarify these relationships.	• Aβ42 is elevated in plasma in FAD MCs and suggests that this level may decrease with disease progression prior to the development of overt dementia. • The ratio of Aβ42 to Aβ40 was reduced in the CSF of non-demented MCs and that elevations of t-tau and p-tau181 are sensitive indicators of presymptomatic disease. • Elevated F2-isoprostane levels in the CSF of preclinical FAD MCs suggests that oxidative stress occurs downstream to metabolism of amyloid precursor protein.
Golob et al., 2009	Participants with a history of variants associated with *PSEN1* (n = 19), including a history of A431E (n = 14) and L235V (n = 5); and associated with *APP* V717I substitution (n = 5). Variant carriers in *PSEN1* and *APP* are not separated in the results.	Genetics, electrophysiological	Genetic testing, CDR, MMSE, CASI, PCR RFLP; target detection oddball task of listening to a sequence of tones at 2.5 s intervals; ERP.	To define changes in cortical function in persons inheriting FAD mutations before the onset of cognitive decline.	• FAD mutation carriers had significantly longer latencies of the N100, P200, N200, and P300 components, and smaller slow wave amplitudes. • Auditory sensory and cognitive cortical potentials in persons with FAD mutations are abnormal approximately 10 years before dementia will be manifest.
Ringman et al., 2010	Participants with dementia (n = 4), mild symptoms (n = 7), and asymptomatic (n = 28) from 13 families carrying variants in *APP* (n = 2) or *PSEN1* (n = 11). Among families with a history of *PSEN1* variants, one had L235V, one G206A, one S212Y, and eight had the A431E substitution. Number of carriers is not specified.	Imaging technique	CDR and MRI.	To assess the ability of radiologists to detect HA in persons destined to develop AD.	Radiologists' ability to detect HA in persons in whom the diagnosis of incipient AD is certain is suboptimal and quantitative MRI techniques or other biological markers of the disease are needed.

(Continued)

TABLE 5 | (Continued)

References	Sample	Category	Techniques and instruments used	Study aim	Key findings
Ringman et al., 2011	The participants (n = 23) came from families with a history of *PSEN1* variants, including: 1 with a history of L235V and 5 families with A431E. While the rest of the subjects belong to two families with a history of the V717I variant of *APP*. Of the total number of participants, n = 14 were carriers and n = 9 were non-carriers. The number of carrier and non-carrier participants per variant is not specified.	Genetics, neuropsychological, imaging technique	PCR RFLP, MRI, semantic verbal fluency test (animals), naming of objects, rey figure, WAIS cube design, word list retrieval and Stroop.	To study the effects of FAD mutation status and *APOE* genotype on fMRI activation during a novelty encoding task in a larger number of presymptomatic subjects at-risk for FAD mutations to differentiate the effects of these genes.	• FAD MCs (n = 14) showed decreased BOLD activation in the anterior cingulate gyrus relative to 9 NCs. • No increased activation was seen in MCs relative to NCs. • Increased fMRI activation associated with *APOE* genotype but not with FAD mutations.
Apostolova et al., 2011	Control subjects (n = 11). Carriers without dementia (n = 22) of variants A431E (n = 14), L235V and G206A (n = 3) associated with *PSEN1* and the V717I *APP* variant (n = 5). Carriers with dementia (n = 3), A431E (n = 1), L235V and G206A (n = 2).	Genetics, Imaging technique	MMSE, CDR, PCR RFLP, and MRI.	Define cortical and hippocampal atrophy in an independent cohort of persons at risk for FAD using different structural MRI analytical techniques.	• FAD is associated with thinning of the posterior association and frontal cortices and HA. • arger sample sizes may be necessary to reliably identify cortical atrophy in presymptomatic carriers.
Ringman et al., 2012a	Non-carriers (n = 5). Presymptomatic subjects (n = 10), including carriers of the A431E (n = 7) and L235V (n = 1) variants of *PSEN1* and the V717I variant (n = 2) of *APP*. Symptomatic carriers (n = 4), including carriers of the A431E (n = 2), L235V (n = 1) and S212Y (n = 1) variants of *PSEN1*.	Genetic, Biomarkers	CDR, PCR RFLP, and Lumbar puncture, mass spectrometry analysis, with ion trap analyzer.	To identify CSF protein changes in persons who will develop FAD due to *PSEN1* and *APP* mutations, using unbiased proteomics.	• Overlap in CSF protein changes between individuals with presymptomatic and symptomatic FAD. • Inflammation and synaptic loss early in FAD and suggest new presymptomatic biomarkers of potential usefulness in drug development.
Ringman et al., 2012b	Carriers (n = 21) and non-carriers (n = 12) from families with history of *PSEN1* variants (12 families, including 9 with A431E variant, 1 of L235V, 1 of G206A y 1 of S212Y) and *APP* (2 families with history of V717I variant).	Genetics, biomarkers	CDR, and PCR RFLP.	To study the effect of FAD mutations and *APOE* genotype on plasma signaling protein levels.	• Different patterns of inflammatory markers in young and middle-aged persons among *APOE* genotype groups. • The *APOE* ε4 carriers had the lowest levels of apolipoprotein E. • Young ε4 carriers have increased inflammatory markers that diminish with age.
Ringman et al., 2012c	Participants (n = 31) with a history of *PSEN1* mutations (n = 23) from 10 families, of which 14 had the mutation, n = 8 with A431E mutation, n = 1 with G206A, n = 1 with S212Y (does not mention the mutation of the rest of participants). Participants with a history of *APP* (n = 8) from 2 families with variant V7171 of which n = 5 were carriers. Of the total number of participants, n = 19 were carriers (n = 14) of *PSEN1* variants and n = 5 of *APP* variants, while n = 12 were non-carriers.	Genetics, biomarkers	CDR, western blot with a polyclonal anti-MetO antibody, isoprostane measurement, multiple protein analysis and PCR RFLP.	To ask if oxidation of methionine residues to methionine sulfoxide was increased in plasma proteins of persons carrying FADmutations.	Elevated MetO levels in persons carrying FAD mutations that correlate with other indices of oxidative stress.

(Continued)

TABLE 5 | (Continued)

References	Sample	Category	Techniques and instruments used	Study aim	Key findings
Ringman et al., 2012d	Participants (n = 7) were divided into asymptomatic carriers (n = 5) and non-carriers (n = 2). Participants had a history of L235V and A43E mutations in *PSEN1*, and V7171 in *APP* (specific mutations were not disclosed due to confidentiality).	Genetics, biomarkers	CDR, PCR RFLP, CSF with dot-blot using polyclonal antibodies A11 (anti-prefibrillar oligomer), OC and αAPF AB42 levels in CSF by ELISA; protein concentration was determined using the BCA Protein Assay Kit.	To identify oligomers during the presymptomatic stage of the disease in persons destined to develop FAD.	Evidence for an identifiable elevation of CSF oligomers during the presymptomatic phase of FAD.
Ringman et al., 2012e	Carriers (n = 13) and non-carriers (n = 5). Of the carriers, n = 11 had variants associated with *PSEN1* and n = 2 associated with *APP*. Among the variants associated with *PSEN1*, the participants had a history of A431E, L235V and S212Y, however, the number of carriers and non-carriers of this variant was not specified.	Genetics, biomarkers	MMSE and CDR. CSF analysis, innogenetics INNO-BIA AlzBio3 multiplex assays were used in standardized xMAP Luminex technology, and PCR RFLP.	Evaluate changes in CSF levels of 42-amino-acid β-amyloid (Aβ42), total tau protein (t-tau) and phosphorylated tau at residue 181 (p- tau181).	• There was a negative correlation between Aβ42 levels and age relative to the family-specific age of dementia diagnosis. • A decline in CSF Aβ42 levels occurring at least 20 years prior to clinical dementia in FAD.
Braskie et al., 2012	Subjects were asymptomatic or had mild cognitive impairment. Carriers (n = 18) and non-carriers (n = 8) had a history of the A431E and L235V variants of *PSEN1* and V717I of *APP*. Carrier variants are not specified.	Neuropsychological, imaging technique	CDR, MMSE, CASI, verbal fluency, Stroop, word list recall and fMRI.	Compared fMRI activity of non-demented autosomal dominant AD mutation carriers with fMRI activity in their non-carrier relatives as they performed a novelty encoding task in which they viewed novel and repeated images.	• Mutation carriers showed increased fMRI activity in the fusiform and middle temporal gyri. • During novelty encoding, increased fMRI activity in the temporal lobe may relate to incipient AD processes.
Braskie et al., 2013	Carriers (n = 9), of these n = 8 had the A431E variant of *PSEN1* while n = 1 had the V717I of *APP*, and non-carriers (n = 8).	Imaging technique	MMSE, CASI and fMRI performing a memory task.	Examine fMRI signal differences between carriers and non-carriers, and how signal related to fMRI task performance within mutation status group, controlling for relative age and education.	Poorer performing carriers showed greater retrieval period signal, including in the frontal and temporal lobes, suggesting underlying pathological processes.
Lee et al., 2013	Of the total number of participants (n = 35), n = 25 were carriers and n = 10 were non-carriers. Of the carriers, n = 21 had *PSEN1* A431E mutation and n = 4 *APP*-associated mutations. The results are not separated according to the mutation to respect the confidentiality of the participants.	Genetics, neuropsychological, imagine technique	CDR, MMSE, word list learning, MVP, Rey-Osterrieth figure, digit-symbol, Stroop, block design, category fluency, test object naming, WCST and MRI, PCR RFLP.	Examined brain volume differences between presymptomatic and symptomatic FAD mutation carriers and non-carrier relatives using tensor-based morphometry.	Cognitively intact FAD mutation carriers had lower thalamic, caudate and putamen volumes, and there is preliminary evidence for increasing caudate size during the predementia stage. These regions may be affected earliest during prodromal stages of FAD, while cortical atrophy may occur in later stages, when carriers show cognitive deficits.

(Continued)

TABLE 5 | (Continued)

References	Sample	Category	Techniques and instruments used	Study aim	Key findings
Joe et al., 2019	Of the total number of carriers (*n* = 16), *n* = 11 had the A431E variant and *n* = 2 L235V of *PSEN1*, while of *APP n* = 3 had the V717I variant. Non-carriers (*n* = 11) were subjects with a history of the A431E (*n* = 7), L235V (*n* = 2) variants of *PSEN1* and V717I (*n* = 2) of *APP*.	Genetics, imaging technique	MRI, MRS, CDR, and PCR.	Attempted to identify changes in levels of metabolites prior to the onset of clinical symptoms in carriers of ADAD mutations.	• MCs had significantly lower levels of NAA and Glx in the left pregenual anterior cingulate cortex, and lower levels of NAA and higher levels of mI and Cho in the precuneus. • Increased levels of mI were seen in these regions in association with increased proximity to expected age of dementia onset.
Medina et al., 2021	The sample of participants (*n* = 71) was divided into carriers (*n* = 40) and non-carriers (*n* = 31). Carriers had the following variants: A431E (*n* = 29) and L235V (*n* = 7) of *PSEN1*, and V717I (*n* = 4) of *APP*. While non-carriers had a history of the following variants A431E (*n* = 20), L235V (*n* = 7) and G206A (*n* = 1) of *PSEN1*, and V717I (*n* = 3) of *APP*.	Genetics, neuropsychological	Cognometer computer program including time reaction tasks, PCR RFLP.	Evaluate attention and working memory using a computerized battery in non-demented persons carrying ADAD mutations.	• MCs respond more slowly as they approach the age of dementia onset on tasks with greater demands on executive function. These effects were not explained by *APOEε4* status independently of ADAD mutation status. • Computerized reaction time tests can provide sensitive measures of the earliest cognitive changes in AD.
Singer et al., 2021	Of the total number of participants (*n* = 39), some had variants in *PSEN1*, including A431E (*n* = 11) and F388S (*n* = 1), while the rest of the carriers had variant V717I (*n* = 1) of *APP* and the rest of the participants (*n* = 21) were controls with a history of the previous variants.	Genetics, imaging technique	OCTA imaging protocol-quantitative capillary flow and morphometric, and PCR.	Characterize retinal capillary blood flow in subjects with ADAD-causing mutations.	Increased perfusion is a pathophysiologic feature of presymptomatic stages of ADAD.
Studies whit variants in *PSEN1*, *PSEN2,* and *APP*					
Albrecht et al., 2009	Brain tissue of cases with the variants *APP* K670N, M671L (*n* = 5), *APP* E693G (*n* = 1), *PSEN1* M146V (*n* = 2), *PSEN1* A431E (*n* = 2), *PSEN1* F105L (*n* = 2), *PSEN1* V261F (*n* = 2) *PSEN1* Y115C (*n* = 2) and *PSEN2* N141I (*n* = 1).	Neuropathology	Immunoreactivity with anti-active Casp-6 and Tau cleaved by Casp-6 y Semiquantitative Scoring of Immunostaining.	To determine if Casp-6 is activated in familial AD.	• Active Casp-6 immunoreactivity was found in all cases. • Caspase-6 immunoreactivity was observed in neuritic plaques or in some cases cotton-wool plaques, and in neuropil threads and neurofibrillary tangles.
Medina et al., 2011	Subjects without dementia (*n* = 35) with a history of variants associated with familial AD. Of these *n* = 30 had a history of *PSEN1* variants, *n* = 1 of *PSEN2* and *n* = 4 of *APP*.	Genetics, linguistic	CDR, PCR RFLP, CASI and writing biographical essays to determine propositional density (relationship between the number of unique ideas and the number of words in the text).	To explore the relationship between FAD mutation status, *APOE* genotype, and p-density.	• FAD mutation status was not significantly associated with p-density. • *APOE* ε4 carriers having lower p-density than non-carriers.

(Continued)

TABLE 5 | (Continued)

References	Sample	Category	Techniques and instruments used	Study aim	Key findings
Ringman et al., 2016	Neuropathologic (postmortem) data of cases with variants in *PSEN1* (*n* = 46), including A79V (*n* = 5), I143T (*n* = 2), M233L (*n* = 2), Y115C (*n* = 2), M146L (*n* = 2), L235V (*n* = 1), Y115H (*n* = 1), Y156insFl (*n* = 1), T245P (*n* = 2), E120D (*n* = 1), H163R (*n* = 4), V261F (*n* = 1), N135D (*n* = 1), S170F (*n* = 1), P267A (*n* = 1), N135S (*n* = 2), G206A (*n* = 6), A431E (*n* = 6), M139I (*n* = 1), G209V (*n* = 1), L435F (*n* = 1), M139V (*n* = 1) y L226R (*n* = 1). *APP* (*n* = 10), including E693G (*n* = 1), V717I (*n* = 3), V717F (*n* = 4) y V717L (*n* = 2). N141I in *PSEN2* (*n* = 4).	Neuropathology	CERAD and semi-quantification of diffuse and neuritic amyloid plaques on a scale of 0 to 3 (none, scarce, moderate, or frequent) in frontomedial, temporal, and inferior parietal regions.	Compare hallmark AD pathologic findings in 60 cases of ADAD and 120 cases of sporadic AD matched for sex, race, ethnicity, and disease duration.	• The finding of Lewy body pathology in a substantial minority of ADAD cases supports the assertion that development of Lewy bodies may be in part driven by abnormal b-amyloid protein precursor processing. • In persons with *PSEN1* mutations beyond codon 200 had higher average Braak scores and severity and prevalence of CAA.
Petok et al., 2018	Of the total number of participants (*n* = 45), *n* = 34 were carriers and *n* = 11 were non-carriers. Of these *n* = 13 had a history of variant V717I of *APP*, *n* = 12 of variant A431E, *n* = 5 of G206A, *n* = 4 L235V, *n* = 3 R269H, *n* = 1 A260V, *n* = 1 E184D, *n* = 1 E280A, *n* = 1 H163R, *n* = 1 S212Y, *n* = 1 C410Y, *n* = 1 G378E of *PSEN1*. While *n* = 1 had a history of *PSEN2* variant N14I.	Genetics, imaging technique	MMSE, CASI, PCR, generalization task on SuperCard and MRI.	Compared preclinical individuals carrying ADAD mutations to non-carrying kin to determine whether generalization (the ability to transfer previous learning to novel but familiar recombinations) is vulnerable early, before overt cognitive decline.	Preclinical ADAD mutation carriers made significantly more errors during generalization. This impairment correlated with left hippocampal volume, particularly in mutation carriers.
A431E and unknown mutation					
Withers et al., 2021	The participants (*n* = 27) came from families with a history of variants associated with early-onset AD. Five focus groups were held for discussion, of which four were conducted with people whose relatives are carriers of the A431E *PSEN1* variant, while the variant was not determined in the fifth focus group.	Caregivers	Demographic Survey, CBAD, ADKS and the Zarit Caregiver Burden Scale, focus groups.	To explore the experiences and needs of Latino caregivers of persons with EOAD.	• The stress of caregiving was compounded by other pressures and worries, such as taking care of young children, providing financially for family, caregivers' own co-morbidities, and contemplating their own risk of inheriting EOAD. • Resources for monolingual Spanish speakers were scarce. • Difficulty in obtaining a diagnosis from physicians who were uninformed about EOAD was also common.
ADAD families					
Withers et al., 2019	*n* = 86 relatives of Mexican patients and *n* = 37 Mexican Americans with ADAD (the CBAD scale was applied) and *n* = 18 surveyed in Mexico.	Beliefs (psychological)	CBAD and semi-structured interview.	Examine cultural beliefs about AD and genetic screening among at-risk populations of Mexican heritage.	The interviews demonstrated that very few at-risk respondents understood their own risk for harboring the mutation causing AD in their family. Once informed, most expressed a strong interest in genetic testing, largely motivated by the desire to be better prepared for the development of AD.

AD, Alzheimer's disease; ADAD, autosomal dominant Alzheimer's disease; ADKS, Alzheimer's Disease Knowledge Scale; CAA, cerebral amyloid angiopathy; CASI, Cognitive Abilities Screening Instrument; CBAD, Scale of Cultural beliefs about Alzheimer's Disease; CDR, Clinical Dementia Rating Scale; CERAD, Consortium to Establish a Registry for Alzheimer's Disease; Cho, choline; CSF, cerebrospinal fluid; EOAD, early-onset Alzheimer's disease; EAD, early-onset Alzheimer's disease; EOAD, autosomal dominant early–onset Alzheimer's disease; ERP, Event Related Potentials; FA, fractional anisotropy; FAD, familial Alzheimer's disease; fMRI, functional magnetic resonance imaging; Glx, glutamate/glutamine; HA, hippocampal atrophy; ICHD-2, International Classification of Headache Disorders; MCs, mutation carriers; MetO, methionine sulfoxide; mI, myo-inositol; MMSE, Mini-Mental State Examination; MRI, magnetic resonance imaging; MSR, magnetic resonance spectroscopy; MVP, memory verbal prose; NAA, N-acetyl-aspartate + N-acetyl-aspartyl-glutamate; NCs, non-carriers; OC, anti-fibrillar oligomer; OCTA, optical coherence tomography angiography; PCR, polymerase chain reaction; RFLP, restriction fragment length polymorphism analysis; WAIS, The Wechsler Adult Intelligence Scale; WCST, Wisconsin Card Sorting; WM, white matter; and αAPF, anti-annular protofibril.

more descendants have been reported to be at risk. Therefore, the incidence is currently open (Llibre-Guerra et al., 2021).

This scoping review aims to synthesize the findings related to the characteristics of the *PSEN1* A431E variant associated with EOAD. The results of this review integrated a few studies focused only on the variant of our interest; most studies included other *PSEN1, PSEN2,* and *APP* variants in addition to A431E.

In Mexico, a founder effect (Ala431Glu in *PSEN1*) was hypothesized in the Altos de Jalisco area by Yescas et al. (2006). This could explain why the carriers were mainly Mexican and Mexican Americans both in Mexico and in the United States.

The founder effect hypothesis and the identification of more families could be associated with the growing interest in the variant reflected in the considerable increase in studies between 2006 and 2010 and it has been rising since then.

Analyzing the pathophysiology of EOAD-associated variants, such as A431E, from the early stages of the disease, provides comprehensive knowledge especially to identify biomarkers and interventions with therapeutic potential (Pilotto et al., 2013; Russell et al., 2014). We consider this could be the reason why most of the identified studies have been performed at the preclinical stage.

Synthesizing the findings of the A431E variant is crucial, for it allows comparison of phenotypic features between this and other variants and with SAD cases as well, and provides a framework for clinicians working with individuals with such a history of AD. Therefore, we highlight the importance of constructing knowledge by means of independently reporting results or comparing variants in studies that involve people with a history of two or more variants.

A431E in *PSEN*

The average age of dementia onset is 40 years with a range of either 34–48 years (Yescas et al., 2006) or 42.5 ± 3.9 years of age (Dumois-Petersen et al., 2020). In both studies, the onset of symptoms was established based on reports from family members. Since families usually seek medical attention in advanced stages, we consider these reports may be biased. There were no longitudinal studies among the articles included in this review, only one study reported cross-sectional data over the course of 6 years of disease evolution (Dumois-Petersen et al., 2020). This lack of longitudinal studies may be due to the relatively recent identification of A431E, barriers that delay diagnosis such as the cost and time implications of assessments, and the attitudes of people with a history of the variant toward genetic analysis and research.

Evidence regarding phenotypic variability is not conclusive. Joshi et al. (2012) identified atypical features in carriers of variants associated with FAD, and these features were also reported by other authors: Pseudobulbar effect was identified also in the case of Parker et al. (2019); myoclonus was presented in one of the families identified by Yescas et al. (2006); gait abnormality was identified as a first symptom (Dumois-Petersen et al., 2020); and headaches were reported in the case of an A431E carrier (Alakkas et al., 2020), but the prevalence and intensity of the headaches could not be inquired; in addition, headaches were present in 67% of carriers in the study by Ringman et al. (2008a) and allowed for differentiating carriers and non-carriers of variants in both *PSEN1* and *APP* in a sample composed mainly of families with a history of A431E. Could these symptoms be part of a continuum or manifest at any moment is a topic of study and could be addressed in upcoming longitudinal studies. Spastic paraparesis is one of the main clinical features associated with A431E (Parker et al., 2019; Dumois-Petersen et al., 2020; Santos-Mandujano et al., 2020). In addition, pure motor presentations have been frequently identified in carriers of this variant (Llibre-Guerra et al., 2021). A431E has been associated with white matter abnormalities which correlate with motor impairments (Santos-Mandujano et al., 2020) which in some cases even preceded and exceeded cognitive symptoms.

Yescas et al., 2006, reported that one of the families in their study had a history of partial seizures 20 years prior to the clinical onset of AD, which they did not consider to be related to the A431E phenotype. However, seizures have been reported to occur in 15% of A431E carriers (Dumois-Petersen et al., 2020). The small population in the Yescas study may have been responsible for that finding and EEG evaluation in the early stages of the disease or a specific questioning for epileptic activity may be considered in EOAD cases, especially in those harboring the A431E variant.

Although evidence is still inconclusive, this type of manifestation could indicate A431E leads to an atypical presentation of EOAD whose early manifestations in the preclinical stage are not amnestic; therefore, this symptomatology should be explored as part of the clinical practice in this disease.

Given the heterogeneous characteristics of the studies involving carriers and non-carriers of different variants in the three principal genes associated with EOAD, we considered discussing the findings of A431E, *PSEN1*, *PSEN2*, and *APP* in a unified manner to contrast characteristic types among carriers of different variants.

Neuropsychological reports are inconsistent. Although memory deficits have been reported as the first cognitive symptom (Dumois-Petersen et al., 2020), verbal memory test scores did not allow differentiation between carriers and non-carriers at the preclinical stage (Ringman et al., 2004, 2011). In language, findings varied between those in which performance on language tests allowed differentiation (Lee et al., 2013) or not (Ringman et al., 2005; Medina et al., 2011) between carriers and non-carriers, and language disorders were observed as an initial symptom only in a minority (Dumois-Petersen et al., 2020). Visuospatial deficits are present since the early stages of the disease (Ringman et al., 2005; Lee et al., 2013; Santos-Mandujano et al., 2020). As for executive functioning, in mild cognitive impairment, both the carriers (Lee et al., 2013) and non-demented (Ringman et al., 2005) had lower and slower performance (Medina et al., 2021). These changes have been associated with Tau neurofibrillary tangles in the prefrontal areas (Weintraub et al., 2012) and may reflect dual protein participation in the early stages of the disease.

Neuropsychiatric manifestations complicate the diagnosis and even disguise some of the symptoms of the clinical onset of

EOAD, as in the case reported by Alakkas et al. (2020). Thus, we highlight the importance of exploring a family history of AD in the neuropsychiatric clinical practice and following up over time. Depressive symptoms are common during EOAD associated with A431E in 53% of the cases (Dumois-Petersen et al., 2020). In the case of female carriers, depressive symptoms usually appear in the first stages of the disease and could be associated with the neuropathology of AD (Ringman et al., 2004). Other neuropsychiatric symptoms were reported infrequently in the studies reviewed, including hallucinations in 11.8% of the A431E carriers (Dumois-Petersen et al., 2020), catatonia, mutism, lack of spontaneous movement, and refusal to eat (Alakkas et al., 2020).

The identified neuropathological and biomarker findings and distinctive clinical features, such as SP, support the classification of the A431E variant as pathogenic, as described by the ACMG/AMP guidelines (Alzforum, 2022).

A neuropathological characterization of a brain of an A431E carrier showed severe frontal atrophy, neuronal loss, and gliosis from moderate to severe, and a predominance of neurofibrillary tangles followed by cotton-wool plaques, with greater accumulation of the beta-amyloid 40. The type and concentration per area of amyloid deposits and neurofibrillary tangles have been reported to differ widely among carriers of *PSEN1* and *PSEN2* variants and SAD (Maarouf et al., 2008).

Lewy body pathology (LBP) was more common in the amygdala of carriers of variants in *PSEN1* (found in 96% of carriers) than in *PSEN2* (Leverenz et al., 2006). Ringman et al. (2016), when analyzing middle frontal, superior temporal, and inferior parietal regions, reported LBP in only 21.1% of the ADAD cases due to variants in *PSEN1*, *PSEN2,* and *APP*. In these regions, this pathology type was significantly higher in SAD.

In contrast, CAA scores were higher in ADAD due to variants in *PSEN1* beyond codon 200 (in 63.3% of the cases analyzed) than in SAD (39.2%) (Ringman et al., 2016). Cases with ADAD had a CAA mean score situated in the mild range with a trend toward the moderate (Ringman et al., 2016). Similarly, the case described by Maarouf et al. (2008) of A431E had a moderate CAA score.

Activation levels of mtUPR genes in the frontal cortex were significantly higher in *PSEN1* variant carriers (70–90%) compared with levels in those with SAD (40–60%) (Beck et al., 2016). This may result in increased vulnerability to pathological processes associated with this response in carriers of *PSEN1* variants.

Active Casp-6 immunoreactivity is present in cases of EOAD due to variants in *PSEN1*, *PSEN2,* and *APP*, and in SAD (Albrecht et al., 2009). The two A431E carriers in this study presented a neuritic plaque and neurofibrillary tangle in densities ranging from moderate to severe and mild to moderate neuropil threads in the superior/medial temporal gyrus, hippocampus, and entorhinal cortex (Albrecht et al., 2009).

Although the sample size of these studies was small and the minority were carriers of A431E, it is important to highlight that the neuropathological findings in postmortem studies allow in the first instance the differentiation between EOAD due to A431E variant or others in *PSEN1*, and variants in *PSEN2* or *APP*, SAD, and dementias caused by other conditions such as PPA and bvFTD (Gefen et al., 2020), and may ultimately be of help for the differential diagnosis (Braak and Braak, 1991; McKhann et al., 2011).

Case reports identified atrophy disproportionate to age (Parker et al., 2019; Alakkas et al., 2020; Santos-Mandujano et al., 2020) in structures such as thalamic, caudate, the putamen (Lee et al., 2013), hippocampus, and in posterior association and frontal cortices (Apostolova et al., 2011). As in the case of Alakkas et al. (2020), levels of cortical and subcortical atrophy are key in the differential diagnosis of the disease, but there are also other potential measures in the identification of EOAD, for example, decreased BOLD activation in the cingulate gyrus (Ringman et al., 2011), hyperactivity in the fusiform gyrus and medial temporal gyrus (Braskie et al., 2012), and lower levels of NAA and higher levels of myoinositol and choline in the precuneus (Joe et al., 2019).

Biomarkers are useful, especially CSF tau/ratio for differential diagnosis, therapeutic targets, and even to measure the progression of the disease (Pilotto et al., 2013; Russell et al., 2014). In CSF, toxic effects of Aβ42 oligomerization at synapses independent of amyloid plaque formation have been studied (Ringman et al., 2012d), and Ringman et al. (2012e) found elevated oligomers and low levels of Aβ42 in asymptomatic individuals with a history of variants in *PSEN1* (including A431E) and *APP*. Of the seven participants, five were carriers, with a significant elevation of ring protofibrils with a progressive reduction identified 20 years before to age of onset of dementia. In carriers, the Aβ42/Aβ40 ratio was lower (Ringman et al., 2008b) whereas SAD participants and A431E carriers had similar changes in Aβ42 and Aβ16, but symptomatic and asymptomatic carriers show a downward trending pattern of Aβ37, Aβ38, and Aβ39 isoform levels, suggesting that this variant determines the cleavage site of γ-secretase which is associated with disease manifestation (Portelius et al., 2010).

Plasma Aβ42 levels have been identified as elevated in carriers of variants associated with FAD and may decrease with disease progression prior to the development of dementia (Ringman et al., 2008b). An association was found between methionine sulfoxide levels with the amount of plasma F2-isoprostane and superoxide dismutase-1 (Ringman et al., 2012c); in addition, inflammatory markers and synaptic degeneration in presymptomatic carriers have been found, which has been indicated as a potential therapeutic target (Ringman et al., 2012b).

Providing information about the genetic basis of AD may increase the interest of people with a history of variants associated with EOAD to participate in clinical research and act focused on staying informed about the implications of this disease (Withers et al., 2019). However, it is important to consider that few studies have been conducted in this specific area. Other authors identified the factors leading to genetic testing in individuals with a history of variants associated with FAD were worry about the clinical onset of the disease and if they were carriers or not, and family and financial planning (Steinbart et al., 2001). The financial aspect was also an important stress source for caregivers of variant carriers associated with EOAD since some of them were also the main financial providers of their families (Withers et al., 2021).

An expansion of the findings regarding A431E is to be expected because a current area of research in our University is focused on studying the clinical, neuropsychological, social, and pathological hallmarks of these variants and has started collaborations with groups devoted to the ADAD. We expect that broader, longitudinal studies in both the preclinical and clinical stages will also help in a better understanding of the clinical course and the physiopathology of EOAD with the A431E variant.

Limitations

The limitations in the methodology consist of having only considered studies in humans or brain tissue. The exclusion of experimental studies could result in relevant information on pathophysiology, which was omitted from this review.

This article has described the extent, type, and research findings related to A431E in *PSEN1*. However, quality criteria were not applied to assess the methods of the included studies or the validity of their results.

Although among many of the studies identified, participants were carriers of other variants of *PSEN1* or associated with FAD, and most of the participants carried the A431E represents a limitation when characterizing these carriers. We recommend avoiding the generalization of the different findings.

In addition, the number of participants in each study and the design are variable.

Future systematic reviews should integrate more information about other variants mostly studied to contrast the information found.

CONCLUSION

This scoping review summarizes research associated with the A431E variant of *PSEN1* associated with EOAD.

In total, we reviewed 42 studies, all of them cross-sectional, seven focused on A431E, 11 analyzed that variant and others in the *PSEN1* and *PSEN2* genes, and 24 whose samples are composed of cases in the genes *PSEN* and *APP*.

The included studies indicate that A431E has been studied in several categories, such as genetics, clinical, imaging, neuropsychology, neuropathology, and biomarkers in carriers or participants with a history of the variant in the preclinical and clinical phases.

The key findings in these studies identify several changes that occur years before the age of onset of dementia. Further studies can be designed to monitor through time the early changes associated with the disease, allowing the establishment of programs to attend to the needs of these families.

The clinical heterogeneity found in the different studies is diagnosis challenging, which in clinical practice represents a burden for health professionals and public health measures, where families are affected by late diagnosis, delaying their intervention and support.

This study provides a helpful synthesis for researchers and clinicians who work with AD-related gene variants carriers, mostly with early-onset familial AD.

DATA AVAILABILITY STATEMENT

The original contributions presented in the study are included in the article/**Supplementary Material**, further inquiries can be directed to the corresponding author.

AUTHOR CONTRIBUTIONS

MO-B made the conception and study design. MO-B, YO-R, AC-A, and VS-G performed the database search. MO-B and YO-R performed data analysis. MO-B, YO-R, VS-G, and AC-A wrote the manuscript screening. All authors contributed with feedback and edited the manuscript.

FUNDING

Funding was given by the PROINPEP fund of the University of Guadalajara.

ACKNOWLEDGMENTS

We thank the support of the 727497 CONACYT grant.

SUPPLEMENTARY MATERIAL

The Supplementary Material for this article can be found online at: https://www.frontiersin.org/articles/10.3389/fnagi.2022.860529/full#supplementary-material

REFERENCES

Alakkas, A., Meyer, A., Debbold, E., Yagudayeva, R., and Bui, J. (2020). Early-Onset Alzheimer's Disease Masquerading as Catatonia. *Case. Rep. Neurol. Med.* 2020:1493481. doi: 10.1155/2020/149348

Albrecht, S., Bogdanovic, N., Ghetti, B., Winblad, B., and LeBlanc, A. C. (2009). Caspase-6 Activation in Familial Alzheimer Disease Brains Carrying Amyloid Precursor Protein or Presenilin I or Presenilin II Mutations. *J. Neuropathol. Exp. Neurol.* 68:12. doi: 10.1097/NEN.0b013e3181c1da10

Alzforum. (2021). *Mutations: PSEN-1*. Available online at https://www.alzforum.org/mutations/psen-1 (accessed Jun 28, 2021)

Alzforum. (2022). *Mutations; PSEN1 A431E*. Available online at https://www.alzforum.org/mutations/psen1-a431e (accessed on Apr 28, 2022)

Amponsah, A. E., Guo, R., Kong, D., Feng, B., He, J., Zhang, W., et al. (2021). Patient-derived iPSCs, a reliable *in vitro* model for the investigation of Alzheimer's disease. *Rev. Neurosci.* 32, 379–402. doi: 10.1515/revneuro-2020-0065

Apostolova, L. G., Hwang, K. S., Medina, L. D., Green, A. E., Braskie, M. N., Dutton, R. A., et al. (2011). Cortical and Hippocampal Atrophy in Patients with Autosomal Dominant Familial Alzheimer's Disease. *Dement. Geriatr. Cogn. Disord.* 32, 118–25. doi: 10.1159/000330471

Arksey, H., and O'Malley, L. (2005). Scoping studies: towards a methodological framework. *Int. J. Soc. Res. Methodol.* 8, 19–32. doi: 10.1080/1364557032000119616

Bateman, R. J., Xiong, C., Benzinger, T. L. S., Fagan, A. M., Goate, A., Fox, N. C., et al. (2012). Clinical and Biomarker Changes in Dominantly Inherited Alzheimer's Disease. *NEJM* 367, 795–804. doi: 10.1056/NEJMoa1202753

Beck, J. S., Mufson, E. J., and Counts, S. E. (2016). Evidence for Mitochondrial UPR Gene Activation in Familial and Sporadic Alzheimer's Disease. *Curr. Alzheimer. Res.* 13, :610–4. doi: 10.2174/1567205013666151221145445

Blennow, K., Zetterberg, H., and Fagan, A. M. (2012). Fluid Biomarkers in Alzheimer Disease. *Cold. Spring. Harb. Perspect. Med.* 2:a006221. doi: 10.1101/cshperspect.a006221

Braak, H., and Braak, E. (1991). Neuropathological stageing of Alzheimer-related changes. *Acta. Neuropathol.* 82, 239–59. doi: 10.1007/BF00308809

Braskie, M. N., Medina, L. D., Rodriguez-Agudelo, Y., Geschwind, D. H., Macias-Islas, M. A., Cummings, J. L., et al. (2012). Increased fMRI signal with age in familial Alzheimer's disease mutation carriers. *Neurobiol. Aging.* 33:424.e11–21. doi: 10.1016/j.neurobiolaging.2010.09.028

Braskie, M. N., Medina, L. D., Rodriguez-Agudelo, Y., Geschwind, D. H., Macias-Islas, M. A., Thompson, P. M., et al. (2013). Memory performance and fMRI signal in presymptomatic familial Alzheimer's disease: memory Performance and fMRI in Familial AD. *Hum. Brain. Mapp.* 34:3308–19. doi: 10.1002/hbm.22141

Dumois-Petersen, S., Gallegos-Arreola, M. P., Magaña-Torres, M. T., Perea-Díaz, F. J., Ringman, J. M., and Figuera, L. E. (2020). Autosomal dominant early onset Alzheimer's disease in the Mexican state of Jalisco: high frequency of the mutation PSEN1 c. 1292C> A and phenotypic profile of patients. *Am J Med. Genet. C. Semin. Med. Genet.* 184, 1023–1029. doi: 10.1002/ajmg.c.31865

Fuller, J. T., Cronin-Golomb, A., Gatchel, J. R., Norton, D. J., Guzmán-Vélez, E., Jacobs, H. I. L., et al. (2019). Biological and Cognitive Markers of Presenilin1 E280A Autosomal Dominant Alzheimer's Disease: a Comprehensive Review of the Colombian Kindred. *J. Prev. Alzheimers. Dis.* 6, 112–120. doi: 10.14283/jpad.2019.6

Gefen, T., Mao, Q., Kohler, M., Moeller, S., Kawles, A., Coventry, C., et al. (2020). Primary Progressive Aphasia has a Unique Signature Distinct from Dementia of the Alzheimer's Type and Behavioral Variant Frontotemporal Dementia Regardless of Pathology. *J. Neuropathol. Exp. Neurol.* 79, 1379–1381. doi: 10.1093/jnen/nlaa080

Ghidoni, R., Benussi, L., Paterlini, A., Albertini, V., Binetti, G., and Emanuele, E. (2011a). Cerebrospinal Fluid Biomarkers for Alzheimer's Disease: the Present and the Future. *J. Neurodegener. Dis.* 8, 413–20. doi: 10.1159/000327756

Ghidoni, R., Paterlini, A., Albertini, V., Stoppani, E., Binetti, G., Fuxe, K., et al. (2011b). A Window into the Heterogeneity of Human Cerebrospinal Fluid Aβ Peptides. *J. Biomed. Biotechnol* 2011:697036. doi: 10.1155/2011/697036

Golob, E. J., Ringman, J. M., Irimajiri, R., Bright, S., Schaffer, B., Medina, L. D., et al. (2009). Cortical event-related potentials in preclinical familial Alzheimer disease. *Neurology* 73, 1649–55. doi: 10.1212/WNL.0b013e3181c1de77

Hoogmartens, J., Cacace, R., and Van Broeckhoven, C. (2021). Insight into the genetic etiology of Alzheimer's disease: a comprehensive review of the role of rare variants. *Alzheimers. Dement.* 13:e12155. doi: 10.1002/dad2.12155

Joe, E., Medina, L. D., Ringman, J. M., and O'Neill, J. (2019). 1H MRS spectroscopy in preclinical autosomal dominant Alzheimer disease. *Brain Imaging and Behav.* 13, 925–932. doi: 10.1007/s11682-018-9913-1

Joshi, A., Ringman, J. M., Lee, A. S., Juarez, K. O., and Mendez, M. F. (2012). Comparison of clinical characteristics between familial and non-familial early onset Alzheimer's disease. *J. Neurol.* 259, 2182–8. doi: 10.1007/s00415-012-6481-y

Landrum, M. J., Lee, J. M., Benson, M., Brown, G. R., Chao, C., Chitipiralla, S., et al. (2018). ClinVar: improving access to variant interpretations and supporting evidence. *Nucleic. Acids. Res* 46, D1062–D1067. doi: 10.1093/nar/gkx1153

Larner, A. J. (2013). Presenilin-1 Mutations in Alzheimer's Disease: an Update on Genotype-Phenotype Relationships. *J. Alzheimers. Dis.* 37, 653–9. doi: 10.3233/JAD-130746

Larner, A. J., and Doran, M. (2006). Clinical phenotypic heterogeneity of Alzheimer's disease associated with mutations of the presenilin–1 gene. *J. Neurol.* 253, 139–58. doi: 10.1007/s00415-005-0019-5

Larner, A. J., and Doran, M. (2008). Genotype-Phenotype Relationships of Presenilin-1 Mutations in Alzheimer's Disease: an Update. *J. Alzheimers. Dis.* 17, 259–65. doi: 10.3233/JAD-2009-1042

Lee, G. J., Lu, P. H., Medina, L. D., Rodriguez-Agudelo, Y., Melchor, S., Coppola, G., et al. (2013). Regional brain volume differences in symptomatic and presymptomatic carriers of familial Alzheimer's disease mutations. *J. Neurol. Neurosurg. Psychiatry.* 84, 154–62. doi: 10.1136/jnnp-2011-302087

Leverenz, J. B., Fishel, M. A., Peskind, E. R., Montine, T. J., Nochlin, D., Steinbart, E., et al. (2006). Lewy Body Pathology in Familial Alzheimer Disease: evidence for Disease- and Mutation-Specific Pathologic Phenotype. *Arch. Neurol.* 63, 370–6. doi: 10.1001/archneur.63.3.370

Livingston, G., Huntley, J., Sommerlad, A., Ames, D., Ballard, C., Banerjee, S., et al. (2020). Dementia prevention, intervention, and care: 2020 report of the Lancet Commission. *Lancet* 396:10248. doi: 10.1016/S0140-6736(20)30367-6

Llibre-Guerra, J. J., Li, Y., Allegri, R. F., Mendez, P. C., Surace, E. I, Llibre-Rodriguez, J. J., et al. (2021). Dominantly inherited Alzheimer's disease in Latin America: genetic heterogeneity and clinical phenotypes. *Alzheimers. Dement.* 17, 653–664. doi: 10.1002/alz.12227

Maarouf, C. L., Daugs, I. D., Spina, S., Vidal, R., Kokjohn, T. A., Patton, R. L., et al. (2008). Histopathological and molecular heterogeneity among individuals with dementia associated with Presenilin mutations. *Mol. Neurodegener.* 3:20. doi: 10.1186/1750-1326-3-20

McKhann, G. M., Knopman, D. S., Chertkow, H., Hyman, B. T., Jack, C. R., Kawas, C. H., et al. (2011). The diagnosis of dementia due to Alzheimer's disease: recommendations from the National Institute on Aging-Alzheimer's Association workgroups on diagnostic guidelines for Alzheimer's disease. *Alzheimers. Dement.* 7, 263–9. doi: 10.1016/j.jalz.2011.03.005

McKusick-Nathans Institute of Genetic Medicine JHU. (2019). *Online Mendelian Inheritance in Man, OMIM®* . Available online at http://www.omim.org/entry/104311#0033 (accessed on Feb 02, 2021)

Medina, L. D., Rodriguez-Agudelo, Y., Geschwind, D. H., Gilbert, P. E., Liang, L. J., Cummings, J. L., et al. (2011). Propositional Density and Apolipoprotein E Genotype among Persons at Risk for Familial Alzheimer's Disease. *Dement. Geriatr. Cogn. Disord.* 32, 188–92. doi: 10.1159/000333023

Medina, L. D., Woo, E., Rodriguez-Agudelo, Y., Chaparro Maldonado, H., Yi, D., Coppola, G., et al. (2021). Reaction time and response inhibition in autosomal dominant Alzheimer's disease. *Brain Cogn.* 147:105656. doi: 10.1016/j.bandc.2020.105656

Murrell, J., Ghetti, B., Cochran, E., Macias-Islas, M. A., Medina, L., Varpetian, A., et al. (2006). The A431E mutation in PSEN1 causing Familial Alzheimer's Disease originating in Jalisco State. *Mexico: an additional fifteen families*. *Neurogenetics* 7, 277-9. doi: 10.1007/s10048-006-0053-1

Page, M. J., McKenzie, J. E., Bossuyt, P. M., Boutron, I., Hoffmann, T. C., Mulrow, C. D., et al. (2021). The PRISMA 2020 statement: an updated guideline for reporting systematic reviews. *BMJ.* 372:71. doi: 10.1136/bmj.n71

Parker, J., Mozaffar, T., Messmore, A., Deignan, J. L., Kimonis, V. E., and Ringman, J. M. (2019). Homozygosity for the A431E mutation in PSEN1 presenting with a relatively aggressive phenotype. *Neurosci. Lett.* 699, 195–198. doi: 10.1016/j.neulet.2019.01.047

Petok, J. R., Myers, C. E., Pa, J., Hobel, Z., Wharton, D. M., Medina, L. D., et al. (2018). Impairment of memory generalization in preclinical autosomal dominant Alzheimer's disease mutation carriers. *Neurobiol. Aging* 65, 149–157. doi: 10.1016/j.neurobiolaging.2018.01.022

Pilotto, A., Padovani, A., and Borroni, B. (2013). Clinical, Biological, and Imaging Features of Monogenic Alzheimer's Disease. *Biomed. Res. Int.* 2013:689591. doi: 10.1155/2013/689591

Portelius, E., Andreasson, U., Ringman, J. M., Buerger, K., Daborg, J., Buchhave, P., et al. (2010). Distinct cerebrospinal fluid amyloid β peptide signatures in sporadic and PSEN1 A431E-associated familial Alzheimer's disease. *Mol. Neurodegener.* 5:1. doi: 10.1186/1750-1326-5-2

Ramos, C., Aguillon, D., Cordano, C., and Lopera, F. (2020). Genetics of dementia: insights from Latin America. Dement. *Neuropsychol* 14, 223–236. doi: 10.1590/1980-57642020dn14-030004

Ringman, J. M., and Coppola, G. (2013). New Genes and New Insights from Old Genes: update on Alzheimer Disease. *Continuum.* 19, 358–71. doi: 10.1212/01.CON.0000429179.21977.a1

Ringman, J. M., Diaz-Olavarrieta, C., Rodriguez, Y., Chavez, M., Fairbanks, L., Paz, F., et al. (2005). Neuropsychological function in nondemented carriers of presenilin-1 mutations. *Neurology* 65, 552–8. doi: 10.1212/01.wnl.0000172919.50001.d6

Ringman, J. M., Diaz-Olavarrieta, C., Rodriguez, Y., Chavez, M., Paz, F., Murrell, J., et al. (2004). Female preclinical presenilin-1 mutation carriers unaware of their genetic status have higher levels of depression than their non-mutation carrying kin. *J. Neurol. Neurosurg. Psychiatry.* 75, 500–2. doi: 10.1136/jnnp.2002.005025

Ringman, J. M., Goate, A., Masters, C. L., Cairns, N. J., Danek, A., Graff-Radford, N., et al. (2014). Genetic Heterogeneity in Alzheimer Disease and Implications for Treatment Strategies. *Curr. Neurol. Neurosci. Rep.* 14:499. doi: 10.1007/s11910-014-0499-8

Ringman, J. M., Medina, L. D., Braskie, M., Rodriguez-Agudelo, Y., Geschwind, D. H., Macias-Islas, M. A., et al. (2011). Effects of Risk Genes on BOLD Activation in Presymptomatic Carriers of Familial Alzheimer's Disease Mutations during a Novelty Encoding Task. *Cereb. Cortex* 21, 877–83. doi: 10.1093/cercor/bhq158

Ringman, J. M., Monsell, S., Ng, D. W., Zhou, Y., Nguyen, A., Coppola, G., et al. (2016). Neuropathology of Autosomal Dominant Alzheimer Disease in the National Alzheimer Coordinating Center Database. *J. Neuropathol. Exp. Neurol.* 75, 284–90. doi: 10.1093/jnen/nlv028

Ringman, J. M., O'Neill, J., Geschwind, D., Medina, L., Apostolova, L. G., Rodriguez, Y., et al. (2007a). Diffusion tensor imaging in preclinical and presymptomatic carriers of familial Alzheimer's disease mutations. *Brain* 130, 1767–76. doi: 10.1093/brain/awm102

Ringman, J. M., Rodriguez, Y., Diaz-Olavarrieta, C., Chavez, M., Thompson, M., Fairbanks, L., et al. (2007b). Performance on MMSE sub-items and education level in presenilin-1 mutation carriers without dementia. *Int. Psychogeriatr.* 19, 323–32. doi: 10.1017/S1041610206003772

Ringman, J. M., Pope, W., and Salamon, N. (2010). Insensitivity of visual assessment of hippocampal atrophy in familial Alzheimer's disease. *J. Neurol.* 257, 839–42. doi: 10.1007/s00415-009-5436-4

Ringman, J. M., Elashoff, D., Geschwind, D. H., Welsh, B. T., Gylys, K. H., Lee, C., et al. (2012b). Plasma Signaling Proteins in Persons at Genetic Risk for Alzheimer Disease: influence of APOE Genotype. *Arch. Neurol.* 69, 757–64. doi: 10.1001/archneurol.2012.277

Ringman, J. M., Tomic, J. L., Coppola, G., Elashoff, D., Gylys, K. H., and Glabe, C. G. (2012d). Conformation-dependent oligomers in cerebrospinal fluid of presymptomatic familial Alzheimer's disease mutation carriers. *Dement. Geriatr. Cogn. Disord.* 2, 652–7. doi: 10.1159/000345771

Ringman, J. M., Coppola, G., Elashoff, D., Rodriguez-Agudelo, Y., Medina, L. D., Gylys, K., et al. (2012e). Cerebrospinal Fluid Biomarkers and Proximity to Diagnosis in Preclinical Familial Alzheimer's Disease. *Dement. Geriatr. Cogn. Disord.* 33, 1–5. doi: 10.1159/000335729

Ringman, J. M., Schulman, H., Becker, C., Jones, T., Bai, Y., Immermann, F., et al. (2012a). Proteomic Changes in Cerebrospinal Fluid of Presymptomatic and Affected Persons Carrying Familial Alzheimer Disease Mutations. *Arch. Neurol.* 69, 96–104. doi: 10.1001/archneurol.2011.642

Ringman, J. M., Fithian, A. T., Gylys, K., Cummings, J. L., Coppola, G., Elashoff, D., et al. (2012c). Plasma Methionine Sulfoxide in Persons with Familial Alzheimer's Disease Mutations. *Dement. Geriatr. Cogn. Disord.* 33, 219–25. doi: 10.1159/000338546

Ringman, J. M., Romano, J. D., Medina, L. D., Rodriguez-Agudelo, Y., Schaffer, B., Varpetian, A., et al. (2008a). Increased Prevalence of Significant Recurrent Headache in Preclinical Familial Alzheimer's Disease Mutation Carriers. *Dement. Geriatr. Cogn. Disord.* 25, 380–4. doi: 10.1159/000121986

Ringman, J. M., Younkin, S. G., Pratico, D., Seltzer, W., Cole, G. M., Geschwind, D. H., et al. (2008b). Biochemical markers in persons with preclinical familial Alzheimer disease. *Neurology.* 71, 85–92. doi: 10.1212/01.wnl.0000303973.71803.81

Rogaeva, E. A., Fafel, K. C., Song, Y. Q., Medeiros, H., Sato, C., Liang, Y., et al. (2001). Screening for PS1 Mutations in a Referral-Based Series of AD Cases: 21 Novel Mutations. *Neurology.* 57, 621–5. doi: 10.1212/WNL.57.4.621

Roher, A. E., Maarouf, C. L., Malek-Ahmadi, M., Wilson, J., Kokjohn, T. A., Daugs, I. D., et al. (2013). Subjects harboring presenilin familial Alzheimer's disease mutations exhibit diverse white matter biochemistry alterations. *Am. J. Neurodegener. Dis.* 2, 187–207.

Rostgaard, N., Waldemar, G., Nielsen, J. E., and Simonsen, A. H. (2015). Cerebrospinal Fluid Biomarkers in Familial Forms of Alzheimer's Disease and Frontotemporal Dementia. *Dement. Geriatr. Cogn. Dis. Extra.* 40, 54–62. doi: 10.1159/000381828

Russell, C. L., Koncarevic, S., and Ward, M. A. (2014). Post-Translational Modifications in Alzheimer's Disease and the Potential for New Biomarkers. *J. Alzheimers. Dis.* 41, 345–64. doi: 10.3233/JAD-132312

Santos-Mandujano, R. A., Ryan, N. S., Chávez-Gutiérrez, L., Sánchez-Torres, C., and Meraz-Ríos, M. A. (2020). Clinical Association of White Matter Hyperintensities Localization in a Mexican Family with Spastic Paraparesis Carrying the PSEN1 A431E Mutation. *J. Alzheimers. Dis.* 73, 1075–1083. doi: 10.3233/JAD-190978

Schindler, S. E., Bollinger, J. G., Ovod, V., Mawuenyega, K. G., Li, Y., Gordon, B. A., et al. (2019). High-precision plasma β-amyloid 42/40 predicts current and future brain amyloidosis. *J. Neurol.* 93, e1647–e1659. doi: 10.1212/WNL.0000000000008081

Singer, M. B., Ringman, J. M., Chu, Z., Zhou, X., Jiang, X., Shahidzadeh, A., et al. (2021). Abnormal retinal capillary blood flow in autosomal dominant Alzheimer's disease. *Alzheimer's Dement.* 13:e12162. doi: 10.1002/dad2.12162

Soosman, S. K., Joseph-Mathurin, N., Braskie, M. N., Bordelon, Y. M., Wharton, D., Casado, M., et al. (2016). Widespread white matter and conduction defects in PSEN1-related spastic paraparesis. *Neurobiol. Aging* 47, 201–209. doi: 10.1016/j.neurobiolaging.2016.07.030

Steinbart, E. J., Smith, C. O., Poorkaj, P., and Bird, T. D. (2001). Impact of DNA Testing for Early-Onset Familial Alzheimer Disease and Frontotemporal Dementia. *Arch. Neurol.* 58, 1828–31. doi: 10.1001/archneur.58.11.1828

Tanzi, R. E. (2012). The Genetics of Alzheimer Disease. *Cold. Spring. Harb. Perspect. Med.* 2, 10. doi: 10.1101/cshperspect.a006296

Weintraub, S., Wicklund, A. H., and Salmon, D. P. (2012). The neuropsychological profile of Alzheimer disease. *Cold. Spring. Harb. Perspect Med.* 2:a006171. doi: 10.1101/cshperspect.a006171

Withers, M., Cortez-Sanchez, K., Herrera, J., Ringman, J. M., and Segal-Gidan, F. (2021). "My backpack is so heavy": experiences of Latino caregivers of family with early-onset Alzheimer's. *J. Am. Geriatr. Soc.* 69, 1539–1547. doi: 10.1111/jgs.17091

Withers, M., Sayegh, P., Rodriguez-Agudelo, Y., Ernstrom, K., Raman, R., Montoya, L., et al. (2019). A mixed-methods study of cultural beliefs about dementia and genetic testing among Mexicans and Mexican-Americans at-risk for autosomal dominant Alzheimer's disease. *J. Genet. Couns.* 28, 921–932. doi: 10.1002/jgc4.1133

World Health Organization (2020). *Dementia*. Available online at: https://www.who.int/es/news-room/fact-sheets/detail/dementia (accessed June 28, 2021).

Yescas, P., Huertas-Vazquez, A., Villarreal-Molina, M. T., Rasmussen, A., Tusié-Luna, M. T., López, M., et al. (2006). Founder effect for the Ala431Glu mutation of the presenilin 1 gene causing early-onset Alzheimer's disease in Mexican families. *Neurogenetics.* 7, 195–200. doi: 10.1007/s10048-006-0043-3

Conflict of Interest: The authors declare that the research was conducted in the absence of any commercial or financial relationships that could be construed as a potential conflict of interest.

Publisher's Note: All claims expressed in this article are solely those of the authors and do not necessarily represent those of their affiliated organizations, or those of the publisher, the editors and the reviewers. Any product that may be evaluated in this article, or claim that may be made by its manufacturer, is not guaranteed or endorsed by the publisher.

Advantages of publishing in Frontiers

OPEN ACCESS
Articles are free to read for greatest visibility and readership

FAST PUBLICATION
Around 90 days from submission to decision

HIGH QUALITY PEER-REVIEW
Rigorous, collaborative, and constructive peer-review

TRANSPARENT PEER-REVIEW
Editors and reviewers acknowledged by name on published articles

Frontiers
Avenue du Tribunal-Fédéral 34
1005 Lausanne | Switzerland

Visit us: www.frontiersin.org
Contact us: frontiersin.org/about/contact

REPRODUCIBILITY OF RESEARCH
Support open data and methods to enhance research reproducibility

DIGITAL PUBLISHING
Articles designed for optimal readership across devices

FOLLOW US
@frontiersin

IMPACT METRICS
Advanced article metrics track visibility across digital media

EXTENSIVE PROMOTION
Marketing and promotion of impactful research

LOOP RESEARCH NETWORK
Our network increases your article's readership